

Abstract

Persistent Currents in Normal Metal Rings

William Ennis Shanks

2024

One striking phenomenon of mesoscopic physics is the ability of a resistive ring to sustain a constant electrical current while in thermal equilibrium and in the absence of an external excitation. The observability of persistent currents normal metal rings was first predicted in 1983 [1]. Subsequently, these persistent currents have been studied experimentally several times but with conflicting results due in part to the difficulty of the measurements.

In this work, I present measurements of persistent currents in normal metal rings performed with cantilever torsional magnetometry. With this technique, the typical persistent current (the component that varies randomly from ring to ring) was measured with high sensitivity. I report measured magnitudes ($\lesssim 1$ pA) over two orders of magnitude smaller than observed in previous studies. These measurements extend the range of temperature and magnetic field over which the typical current has been observed. The wide magnetic field range allowed us to study the effect of magnetic field penetrating the ring. It also enabled the recording of many independent measurements of the current magnitude in a single sample. These independent measurements are necessary to characterize the persistent current magnitude because it is a random quantity. From these measurements of the persistent current, I also characterize the parametric dependence of the typical current on sample orientation and number of rings.

In addition to presenting the experimental results, I thoroughly review the theory of the typical persistent current in the diffusive regime. I begin with the simplest model and build up to the case appropriate for the samples studied in our experiments. I also present in detail the experimental apparatus used to measure the persistent currents.

Persistent Currents in Normal Metal Rings

A Dissertation
Presented to the Faculty of the Graduate School
of
Yale University
in Candidacy for the Degree of
Doctor of Philosophy

by
William Ennis Shanks

Dissertation Director: Jack Harris

May 2011

Copyright © 2024 by William Ennis Shanks
All rights reserved.

Contents

Contents	iii
List of Figures	viii
List of Tables	xiv
Acknowledgments	xv
Glossary	xviii
1 Introduction	1
2 Review of theory relevant to mesoscopic persistent currents in the normal state	6
2.1 The ideal one-dimensional ring	6
2.1.1 Solution of Schrödinger's equation	7
2.1.2 The single-level and total current	14
2.2 Effects of finite temperature, finite cross-section, and the introduction of disorder on the persistent current of the ideal one-dimensional ring	18
2.2.1 Finite temperature	18
2.2.2 Finite ring cross-section	26
2.2.3 Introduction of disorder	39
2.3 Persistent currents in the diffusive regime	48
2.3.1 Typical persistent current magnitude in the diffusive regime	53
2.3.1.1 Zero temperature	54
2.3.1.2 Finite temperature	62
2.3.2 Refinements to the calculation of the typical current	65

2.3.2.1	Flux through the metal of the ring	65
2.3.2.2	Zeeman splitting	72
2.3.2.3	Spin-orbit scattering	78
2.3.3	Contributions to the average current in the diffusive regime	85
2.3.3.1	Single particle contribution	86
2.3.3.2	Electron-electron contribution	91
3	Review of previous work on persistent currents in normal metal rings	99
3.1	Overview of the theoretical literature	100
3.2	Previous measurements of persistent currents	105
3.2.1	Measurements of the typical current	106
3.2.2	Measurements of the average current	110
4	Cantilever torsional magnetometry	113
4.1	Introduction to cantilever torsional magnetometry	113
4.2	Cantilever as a simple harmonic oscillator	115
4.3	Cantilever frequency shift due to persistent currents in the small amplitude limit	118
4.4	The effect of finite cantilever oscillation amplitude on the frequency shift due to the persistent current	124
5	Experimental set-up and measurement	134
5.1	Cantilever sample fabrication	134
5.1.1	Preliminary thermometry cantilevers	134
5.1.2	Persistent current cantilever-with-ring sample fabrication	136
5.2	Experimental apparatus	138
5.2.1	Dewar and refrigerator	138
5.2.2	Cantilever detection set-up	139
5.2.2.1	Laser source	140
5.2.2.2	Fiber optic components	141
5.2.2.3	Cantilever detection fiber termination and mounting	143
5.2.2.4	Sample holder	145
5.2.2.5	Electronics	148
5.2.3	Transport measurement set-up	149

5.3	Calibrations and measurement procedures	153
5.3.1	Cantilever detection calibrations and measurement procedures	153
5.3.1.1	Model of the cantilever-fiber interferometer	153
5.3.1.2	Optimal interferometer fringe position and laser wavelength tuning	158
5.3.1.3	Determination of resonant phase for the cantilever drive signal . . .	160
5.3.1.4	Calibration of the cantilever drive and interferometer signal	161
5.3.1.5	Cantilever measurement procedure	163
5.3.2	Transport calibrations and measurement procedures	166
5.3.2.1	Mathematical relations for the resistance bridge	166
5.3.2.2	Calibration of the applied voltage V_{XY}	167
5.3.2.3	Determination of lead resistances R_l and R'_l	168
5.3.2.4	Magnetoresistance measurement procedure	169
6	Sensitivity of cantilever torsional magnetometry to persistent currents	172
6.1	Sources of uncertainty in cantilever torsional magnetometry measurements	172
6.1.1	Fluctuating forces acting on the cantilever	172
6.1.2	Interferometer readout noise	175
6.1.3	Measurement electronics noise	178
6.2	Derivation of the error in the frequency measurement of a cantilever driven in a phase-locked loop	179
6.2.1	Fluctuations $\sigma_{f,\text{cant}}$ in the frequency of motion of the driven cantilever	179
6.2.2	Frequency fluctuations $\sigma_{f,\text{int}}$ added to the cantilever signal by detector noise	186
6.3	Optimal cantilever dimensions for measuring persistent currents	189
6.4	Experimental characterization of the sensitivity of the cantilever detection apparatus	197
6.4.1	Cantilever and sample thermometry measurements	197
6.4.1.1	Measurements of the cantilever's noise temperature	198
6.4.1.2	Measurements of the electron temperature of a metallic sample at the end of a cantilever	202
6.4.1.3	Effect of a localized heat source on the cantilever temperature . . .	204
6.5	Characterization of uncertainty in measurement of persistent current samples	208

7	Data from and analysis of persistent current measurements	217
7.1	Signal processing of the measured cantilever frequency shift	217
7.1.1	Description of signal processing	217
7.1.2	Step-by-step walk-through of signal processing	221
7.2	Persistent current measurement diagnostics	230
7.3	Persistent current measurements	238
7.3.1	Qualitative discussion	238
7.3.2	Quantitative discussion	246
7.3.2.1	Power spectral density of the persistent current	246
7.3.2.2	Determination of the temperature dependence from the measured persistent current	253
7.3.2.3	Analysis of the temperature dependence of the persistent current . .	260
7.3.2.4	Analysis of persistent current autocorrelation and estimation of sta- tistical uncertainty of persistent current magnitude	262
7.3.3	Complete persistent current traces	269
8	Outlook	285
A	Mathematical relations	290
A.1	Poisson summation formula	290
A.1.1	General formula	290
A.1.2	Application to $\nu(\varepsilon, \phi)$ for the one-dimensional ring	291
A.2	Fourier transform of $\text{sech}^2(t)$	292
A.3	Integral of $\text{sech}^2(\sigma + \frac{\varepsilon}{2})\text{sech}^2(\sigma - \frac{\varepsilon}{2})$ in current-current correlation function calculation	294
A.4	Summation form of the normalized temperature dependence of the current-current correlation function	297
A.5	Trigonometric identities	299
A.6	Jacobi-Anger expansion	299
A.7	Select integral identities	301
A.7.1	$\frac{\sin^2(x/2)}{1+(x/\alpha)^2}$	301
A.7.2	$\frac{1}{x^2} \frac{\sin^2(x/2)}{1+(x/\alpha)^2}$	301

B	Green functions in mesoscopics	303
B.1	General properties	303
B.2	The diffuson and cooperon	313
B.2.1	Density of states correlation function	318
B.2.2	Magnetic field effects	323
B.2.3	Spin effects	324
C	Classical perturbation theory using action-angle variables	329
C.1	Classical mechanics formalism	329
C.1.1	Hamiltonian mechanics	329
C.1.2	Canonical transformations	330
C.1.3	Hamilton-Jacobi formalism	331
C.1.4	Action-angle variables	332
C.1.5	Action-angle variables of the simple harmonic oscillator	333
C.2	Perturbation theory with action-angle variables	334
D	Persistent current cantilever-with-ring sample fabrication	338
D.1	Cantilever-with-ring fabrication recipe	339
D.2	Supplementary figures related to sample fabrication	352
E	Transport characterization of persistent current samples	360
E.1	Transport measurements of the diffusion constant	361
E.1.1	Resistance measurement	361
E.1.2	Superconducting critical field measurement	361
E.2	Determination of electron phase coherence length and spin-orbit scattering length from low field magnetoresistance measurements	363
E.2.1	Theoretical predictions for the magnetoresistance of thin wires	363
E.2.2	Measurement and analysis of low field magnetoresistance measurements	365
F	Measurements of persistent currents in the superconducting state	369
G	Cumulants of the persistent current in arrays of rings	377
	Bibliography	385

List of Figures

2.1	A perfect one-dimensional ring	8
2.2	Eigenenergies of a perfect one-dimensional ring	9
2.3	Energy levels of a perfect one-dimensional ring	10
2.4	Current versus flux for a perfect one-dimensional ring	17
2.5	The thermal averaging function $y(\epsilon)$	21
2.6	Spread of energy level occupancy at finite temperature in an ideal ring	24
2.7	Temperature dependence of the harmonics of the persistent current in a one-dimensional ring	25
2.8	Persistent current in a one-dimensional ring versus flux for a series of temperatures	25
2.9	Energy levels of a perfect three-dimensional ring	32
2.10	Temperature dependence of a perfect three-dimensional ring	38
2.11	Energy spectrum of a disordered one-dimensional ring	42
2.12	Energy spectrum of a disordered multichannel ring	44
2.13	Drawing of energy level spectrum in the diffusive regime	50
2.14	Drawing of distribution of occupancy of the energy level spectrum in the diffusive regime	51
2.15	Alternate drawing of energy level spectrum in the diffusive regime	52
2.16	Current-current harmonic correlation function $H_1^{(0)}$ versus energy difference	61
2.17	Temperature weighting function f_2 plotted against energy difference $\delta\epsilon$	64
2.18	Temperature dependence of the persistent current in the diffusive regime	64
2.19	Current-current harmonic correlation function $H_1^{(0)}$ versus energy difference for different values of the toroidal field B_M^\pm	69
2.20	Current-current correlation function versus toroidal field	70

2.21	Zero-temperature current-current correlation function versus energy difference at finite Zeeman splitting	74
2.22	Typical magnitude of the persistent current harmonics versus Zeeman energy at finite temperature	76
2.23	Typical magnitude of the p^{th} harmonic of the current versus temperature for finite Zeeman splitting	77
2.24	Current-current correlation function versus toroidal field at finite Zeeman splitting .	77
2.25	Zero-temperature current-current correlation function versus energy difference at finite spin-orbit scattering and Zeeman splitting	82
2.26	Typical persistent current magnitude versus spin-orbit scattering strength	83
2.27	Typical persistent current magnitude versus temperature at finite spin-orbit scattering strength	83
2.28	Current-current correlation function versus toroidal field in the presence of spin orbit scattering	84
2.29	Typical persistent current magnitude versus Zeeman splitting with finite spin-orbit scattering	84
2.30	Typical persistent current magnitude versus temperature at finite Zeeman splitting and spin-orbit scattering	85
4.1	Cantilever mode shapes	115
4.2	Labeled diagram of an unflexed cantilever	118
4.3	Flexed cantilever schematic	121
4.4	Potential energy landscapes of cantilever and ring	127
4.5	Persistent current signal suppression factor due to finite cantilever amplitude	133
5.1	Bare cantilever used for Brownian motion measurements.	135
5.2	Cantilever with aluminum grain glued on tip	135
5.3	Persistent current sample fabrication schematic	137
5.4	Scanning electron micrograph images of cantilevers with integrated aluminum rings .	137
5.5	Schematic of Dewar and helium-3 refrigerator	139
5.6	Cantilever measurement schematic	142
5.7	Optical fiber holder drawing	144

5.8	Persistent current sample holder stage photograph	147
5.9	Transport measurement sample holder	151
5.10	Circuit diagram of the four-point AC resistance bridge	152
5.11	Cantilever-fiber interferometer diagram	156
5.12	Fiber-cantilever interferometer fringe pattern	157
5.13	Effect of the optical lever term on the cantilever interferometer signal	159
5.14	Normalized magnitude and frequency response of a simple harmonic oscillator	160
5.15	Cantilever first harmonic signal as measured by the lock-in as a function of piezo driving voltage	163
5.16	Example of a decade resistance scan	168
6.1	Power spectral density of cantilever motion	200
6.2	Mean square cantilever displacement versus refrigerator temperature	201
6.3	Resonant frequency versus magnetic field for the Al grain-mounted cantilever	203
6.4	Superconducting critical field versus refrigerator temperature	204
6.5	Measured cantilever temperature versus incident laser power	205
6.6	Comparison of observed cantilever heating to a phonon thermal conductivity model	207
6.7	Power spectral density of cantilever displacement for sample CL14	208
6.8	Quadratures of cantilever motion at a series of amplitudes of motion	210
6.9	Standard deviation $\sigma(x_{\max})$ of cantilever amplitude versus mean cantilever amplitude $\langle x_{\max} \rangle$	213
6.10	Measured frequency uncertainty as a function of cantilever amplitude	216
7.1	Frequency versus time for a typical data set	222
7.2	Frequency shift versus magnetic field for a typical data set	223
7.3	Frequency shift versus magnetic field frequency β for a typical data set	224
7.4	Fourier coefficients dI_p^A for a typical data set	225
7.5	Derivative of persistent current I^A versus magnetic field for a typical data set	226
7.6	Frequency shift and inferred persistent current derivative I^A over a large range of magnetic field	227
7.7	Persistent current I^A versus magnetic field without background subtraction for a typical data set	228

7.8	Fourier transform of the persistent current for a typical data set	229
7.9	Persistent current versus magnetic field with smooth background removed for a typical data set	229
7.10	Frequency shift and inferred persistent current versus magnetic field for a series of cantilever amplitudes	231
7.11	Frequency shift versus cantilever amplitude	233
7.12	Persistent current measurements taken while exciting the first and second flexural modes of the cantilever	235
7.13	Persistent current versus magnetic field for a series of readout laser powers	236
7.14	Persistent current versus magnetic field observed with the magnet in different modes of operation	237
7.15	Persistent current versus magnetic field measured for both magnet polarities	237
7.16	Comparison of persistent current measured for samples with three different ring sizes	240
7.17	Comparison of persistent current observed in sample CL15 for two different angles θ_0	242
7.18	Comparison of persistent current observed in sample CL17 for two different angles θ_0	243
7.19	Comparison of the persistent current signal from a single ring with the signal from an array of rings	245
7.20	Persistent current power spectral density for sample CL17 at 45°	250
7.21	Persistent current power spectral density for sample CL15 at 45°	251
7.22	Persistent current power spectral density for sample CL17 at 6°	251
7.23	Persistent current power spectral density for sample CL15 at 6°	252
7.24	Persistent current power spectral density for sample CL14 at 45°	252
7.25	Persistent current power spectral density for sample CL11 at 6°	253
7.26	Fit to the background of the persistent current power spectral density for sample CL17 at 45°	254
7.27	Persistent current versus magnetic field for a series of temperatures	256
7.28	Fourier transform of the persistent current signal for a series of temperatures	257
7.29	Typical magnitude of the persistent current versus temperature	258
7.30	Persistent current autocorrelation for sample CL17 at $\theta_0 = 45^\circ$	264
7.31	Persistent current autocorrelation for sample CL15 at $\theta_0 = 45^\circ$	265
7.32	Persistent current autocorrelation for sample CL17 at $\theta_0 = 6^\circ$	266

7.33	Persistent current autocorrelation for sample CL15 at $\theta_0 = 6^\circ$	266
7.34	Persistent current autocorrelation for sample CL14	267
7.35	Persistent current autocorrelation for sample CL11	267
7.36	Full current versus magnetic field trace for CL17 at 45° , part 1	270
7.37	Full current versus magnetic field trace for CL17 at 45° , part 2	271
7.38	Full current versus magnetic field trace for CL17 at 45° , part 3	272
7.39	Full current versus magnetic field trace for CL15 at 45° , part 1	273
7.40	Full current versus magnetic field trace for CL15 at 45° , part 2	274
7.41	Full current versus magnetic field trace for CL15 at 45° , part 3	275
7.42	Full current versus magnetic field trace for CL15 at 45° , part 4	276
7.43	Full current versus magnetic field trace for CL17 at 6°	277
7.44	Full current versus magnetic field trace for CL15 at 6°	277
7.45	Full current versus magnetic field trace for CL14 at 45°	278
7.46	Full current versus magnetic field trace for CL11 at 6°	279
7.47	Full frequency shift versus magnetic field trace for CL14 at 45°	281
7.48	Spectral density of the measured frequency shift for CL14 at 45°	282
7.49	Full frequency shift versus magnetic field trace for CL11 at 6°	283
7.50	Spectral density of the measured frequency shift for CL11 at 6°	284
A.1	Exponential fit to $g_D(0, y)$	298
B.1	Contributions to the Green function in the presence of disorder	315
B.2	Contributions to the diffuson	316
B.3	Contribution to the cooperon	317
B.4	Long-range contributions of the diffuson and cooperon to the density of states correlation function	320
B.5	Short-range contributions of the diffuson and cooperon to the density of states correlation function	322
D.1	Wafer map displaying typical SOI wafer uniformity	353
D.2	Images of cantilever sample mask designs	354
D.3	Image of transport sample mask design	355
D.4	Scanning electron micrograph of transport sample	355

D.5	Optical microscope images of underetched silicon surrounding two sample chips . . .	356
D.6	Optical microscope images of residual oxide film on two cantilever sample chips . . .	356
D.7	Images of aluminum wires displaying characteristic linewidths of measured samples.	357
D.8	Atomic force microscope analysis of persistent current sample thickness	358
D.9	Dark field optical microscope images of cantilevers	358
D.10	Scanning electron micrographs of sample chip: side views	358
D.11	Overhead scanning electron micrographs of cantilever with array of rings	359
D.12	Angled scanning electron micrographs of array of rings on end of cantilever	359
E.1	Magnetic field sweep through the superconducting transition of sample WL115 . . .	362
E.2	Superconducting critical field of transport sample versus temperature	363
E.3	Magnetoresistance of sample WL115 at several temperatures	366
E.4	Fitted electron phase coherence length for sample WL115 versus temperature	367
F.1	Frequency shift due to superconductivity in sample CL10	374
F.2	Fit to frequency shift of sample CL10 at low magnetic field	375
F.3	Frequency shift observed for sample CL10 in the superconducting state at several temperatures	376
G.1	Magnitude and phase of the persistent current signal	379
G.2	Quadratures of the persistent current signal	380
G.3	Autocorrelation of the persistent current quadratures	381
G.4	Cross-correlation of the persistent current quadratures	381
G.5	Cumulants of the persistent current for samples CL15 and CL17	384

List of Tables

7.1	Cantilever parameters of persistent current samples	239
7.2	Ring specifications of persistent current samples	239
7.3	Extracted parameters for persistent current samples	261
E.1	Dimensions and properties of sample WL115	360
F.1	Cantilever parameters of superconducting ring sample	373
F.2	Superconducting ring specifications	373

Acknowledgments

I wish to begin this text by acknowledging my advisor Jack Harris to whom I am very grateful. I feel fortunate to have been involved in the beginnings of the persistent currents experiment in the Harris Lab. When I decided to attend Yale for my graduate work, I knew that I wanted to do something involving electronic systems behaving quantum mechanically, but I did not even know Jack, in his first year as a professor at the time, was at Yale. Fortuitously, I happened across the Harris Lab website in time to work for Jack over the summer and found both the lab and the persistent current project to be perfect fits. Over the past six years, Jack has displayed all the traits of a great advisor: patience, striking physical intuition, strong managerial skills, and general wisdom.

Continuing the discussion of my good fortune as a graduate student, I must also acknowledge Ania Bleszynski Jayich with whom I built the persistent current experiment. While I had worked in a couple experimental labs over the previous few years, it was my time with Ania during which I learned to be an experimentalist. Her strong work ethic, openness to new ideas, and positive attitude in the face of challenges have had great influences on me (I hope!).

Jack's good judgment of character was exemplified by the lab's early roster. It is hard to imagine a lab environment with better camaraderie than the early Harris Lab composed of myself, Ben Zwickl, Andrew Jayich, Jeff Thompson, and Ania. Amongst us all there was a shared vision of how a lab should operate, which allowed work to progress smoothly. I will remember Ben for his positive attitude towards all things including Notre Dame during the Charlie Weis era and Mathematica's ability to perform any task, Andrew for his infectious enthusiasm for "taking data" (and doing pretty much everything else really), and Jeff for his massive intellect and healthy skepticism of authority.

I worked directly with several other Harris Lab members on the persistent current experiment. Sofia Magkiriadou wrote the basic LabVIEW shell on which the vi's that recorded all of the persis-

tent current data were based. She also had a great sense of humor and was a pleasure to work with. Bruno Peaudecerf helped build several electronic components and brought a meticulous attention to detail to calculations of the cantilever frequency shift due to the persistent current. Dustin Ngo, my successor as graduate student on the persistent current experiment, contributed most directly to the work discussed here through his characterization of the fiber-and-lens version of the cantilever detection set up. Dustin has a wide-ranging intellectual curiosity, and I expect him to shed further light on the persistent current phenomena in the coming years.

Lastly, I worked closely over my last five months in the lab with Manuel Castellanos Beltran. Manuel's greatest contribution to this text is that he read it in its entirety and has probably corrected more errors in it than I have myself. Most of my work with Manuel was devoted to the fabrication and measurement of single ring persistent current samples, the discussion of which goes beyond the scope of this text. I will remember Manuel for the alacrity with which he attacked all problems and for his humility, perhaps best exemplified by his tendency to say he understands nothing while actually understanding almost everything.

Though he did not work on persistent currents, Jack Sankey's ability to identify the puzzling aspects of any problem led him to contribute to our understanding of the persistent current measurement. Jack also impressed upon me a healthy respect for Python and the open source revolution. This text would not have been written in LyX without him. I would also like to acknowledge the indirect contributions of other Harris Lab members Brian Yang, Nathan Flowers-Jacobs, Jason Merrill, and Matthew Harrison.

Many people outside of the Harris Lab contributed to the work discussed here. First, there are my direct collaborators and co-authors, Eran Ginossar, Leonid Glazman, Felix von Oppen, and Rob Ilic. The first three were responsible for understanding the effects of a strong magnetic field on the persistent current. Rob's vast knowledge of fabrication of silicon micromechanical devices was invaluable when developing the persistent current sample recipe. Dan Prober provided insight, equipment, and old theses relevant to the transport measurements used to characterize the electron phase coherence length. In addition to sharing his keen insight into mesoscopic physics, Michel Devoret allowed us to use his clean aluminum evaporator for depositing persistent current samples. Luigi Frunzio also provided help with the evaporator as well as with some early stages of the persistent current sample fabrication. Several members of the labs of Michel Devoret and Rob Schoelkopf provided assistance with sample preparation and characterization, in particular Markus

Brink, Nico Bergeal, and Julie Wyatt. Finally, while mentioning people who worked in the Becton Engineering and Applied Science Center, I'd also like to acknowledge Eric Akkermans, from whose course and textbook I base much of my understanding of mesoscopies. I have also useful exchanges with John Mamin, Martino Poggio, and Hendrik Bluhm.

Within Sloane Physics Laboratory, I have been surrounded by many bright, helpful people over the past six years. Dave DeMille, Sean Barrett, Dan McKinsey, and members of their labs have provided equipment and occasional advice. I am grateful to Sid Cahn for reminding me not to hurt myself in the machine shop and for several loans of liquid helium. Many people in the administrative offices upstairs, including John Fox, SJ Compton, Lilian Snipes, and Julie Murphy, made it easy to focus on research rather than paperwork. Outside of Yale, the hospitality of Evan and Colleen at the Inn at City Lights in Ithaca made the long trips to the Cornell NanoScale Facility for sample fabrication much more bearable.

This text was written primarily on the wide screen television of Tera Gahlsdorf. I am thankful for her daily company and support throughout the writing process.

I thank my parents, Bill and Jean, and my sister Amanda for their unflagging support over many years. My family has always encouraged my pursuit of physics despite not understanding it, and I likely would have taken a different path long ago without their faith in me. Over the long period between when I finished a complete draft of this work and when I finally completed the ultimate version for print, my father would ask regularly to be sent the finished copy when it was ready despite knowing that he would likely not understand much of it. To me, this work will always be a symbol of the love of my family, without which it could not have been created.

Finally, I thank you, the reader, for being brave enough to open this document. I have struggled to make it as perfect as I could, working on it well after the submission date and stopping only when I discovered that my edits had reached a steady state in which they introduced as many errors as they corrected.

This work was performed in part at the Cornell NanoScale Facility, a member of the National Nanotechnology Infrastructure Network, which is supported by the National Science Foundation (Grant ECS-0335765).

Glossary

Many symbols are employed in this work. The most used ones are given below along with the quantities they represent. Some symbols are used multiple times to represent different quantities when that symbol is the most fitting choice for each quantity and the chance of ambiguity is low. These different quantities are given in the order in which they appear and are separated by semicolons. References to the equation or section where the quantity is first introduced are given in parentheses.

$\langle \dots \rangle$	Average taken over disorder (Sections 2.3, 2.3.2.1)
$\overline{\dots}$	Average over a quantity other than disorder (Section 2.2.2)
α	Derivative of the normalized cantilever mode shape U with respect to the normalized displacement η (Eq. 4.12)
β	Magnetic field frequency (Section 7.1.1)
β_1	Magnetic field frequency of the first harmonic of the persistent current (Section 7.1.1)
γ	Geometric factor relating the toroidal magnetic field to the uniform one applied in experiment (Section 7.3.2.4)
Δ_1	Mean energy level spacing of a single transverse channel of a ring (Section 2.2.1)
$\Delta_{1,M}$	Mean energy level spacing of a single transverse channel averaged over all channels in a ring (Section 2.2.2)
Δ_M	Mean energy level spacing of a ring with a finite cross-section (Eq. 2.38)
Δf	Cantilever frequency shift (Section 4.3)

ε	Energy of electrons within a ring
ε_{\perp}	Transverse eigenvalues of the persistent current diffusion constant (Eq. 2.78)
ε_F	Fermi energy (Section 2.2.1)
η	Ratio of the statistical uncertainty in a quantity found from a number of measurements M_{eff} to the expected value of that quantity
θ	Angle between magnetic field and cantilever beam axis (Section 4.3)
κ_i	The i^{th} cumulant of a statistical distribution (Eq. G.6)
λ	Optical wavelength (Section 5.3.1.1)
λ_0	First order scale factor for the magnitude of the persistent current due to electron-electron interactions (Eq. 2.91); mean optical wavelength (Fig. 5.12)
λ_{eff}	Renormalized scale factor for the magnitude of the persistent current due to electron-electron interactions (Eq. 2.94)
μ	Magnetic moment (Section 4.3)
ν	Density of states (Section 2.2.1)
ν_0	Density of states in the absence of disorder (Section 2.2.3)
τ	Torque (Eq. 4.17)
ϕ	Magnetic flux through a ring (Section 2.1.1)
ϕ_0	Magnetic flux quantum h/e
Ω	Grand canonical free energy (Eq. 2.44)
ω	Angular frequency (usually $2\pi f$) (Section 4.2)
A	Area enclosed by a ring (typically the mean area in the case of a ring with finite linewidth) (Section 4.3)
B	Magnetic field
B_c	Superconducting critical field (Eq. 6.44)

$B_{c,p}$	Persistent current correlation field for the p^{th} harmonic (Eq. 2.79)
B_M	Toroidal magnetic field (Section 2.3.2.1)
b_L	Lorentzian function (Section 2.2.3)
$C_1^{(0)}$	Zero temperature persistent current autocorrelation in energy (Eq. 2.51)
c_p^0	Normalized p^{th} harmonic of the zero temperature persistent current autocorrelation in energy (Eq. 2.81)
c_p^T	Normalized square of the p^{th} harmonic of the temperature dependent persistent current magnitude (Eq. 2.82)
D	Diffusion constant (Eq. B.23)
dI_p	Estimated p^{th} harmonic of the derivative of the persistent current with respect to field including a correction for finite cantilever amplitude of motion (Eq. 7.3)
E	Energy of the ring-cantilever system
E_c	Correlation scale of the energy levels of a ring in the diffusive regime (Eq. 2.57)
E_n	Longitudinal eigenvalues of the persistent current diffusion equation (Eq. 2.52)
E_{SO}	Spin-orbit energy scale (Section 2.3.2.3)
E_Z	Zeeman energy (Section 2.3.2.2)
e	Absolute value of the electron charge
F_p	Helper function defined in the calculation of the persistent current autocorrelation function (Eq. 2.62)
f	Fermi-Dirac distribution function; cantilever frequency (Eq. 2.7)
G	Gain (Eq. 6.15); Green function (Appendix B)
g_1	Normalized temperature dependence of an ideal, one-dimensional ring (Eq. 2.23)
g_D	Normalized temperature dependence of the typical current of a diffusive ring (Eq. 2.72)
g_M	Normalized temperature dependence of an ideal ring of finite cross-section (Eq. 2.36)

$H_1^{(0)}$	Helper function defined in the calculation of the persistent current autocorrelation function (Eq. 2.66)
h	Planck's constant
I	Persistent current (Eq. 2.7)
I'	Magnetic field derivative of the persistent current scaled by $1/2\pi\beta_1$ so that the first harmonic amplitude should have the same magnitude as the persistent current (Eq. 7.6)
I_0	Characteristic magnitude ev_F/L of the persistent current in an ideal, one-dimensional ring (Eq. 2.12)
I^{can}	Contribution to the average persistent current present in the canonical ensemble but not the grand canonical ensemble (Section 2.3.3.1)
I^{ee}	Contribution to the average persistent current due to electron-electron interactions (Section 2.3.3.2)
i	Single energy level persistent current (Section 2.1.2)
K_p	Normalized and scaled autocorrelation in magnetic field of the p^{th} harmonic of the persistent current (Eq. 7.14)
k	Cantilever spring constant (Eq. 4.6)
k_B	Boltzmann's constant
$k_{F,M}$	Effective Fermi wave vector of one channel as a function of channel indices in a three dimensional ring (Eq. 2.32)
L	Ring circumference (Fig. 2.1); wire length (Appendix E)
L_ϕ	Phase coherence length of the electron (Section E.2)
l	Cantilever length (Fig. 4.2)
l_e	Elastic mean free path of the electron (Eq. B.16)
L_{so}	Spin-orbit scattering length (Eq. 2.83)

M	Number of transverse channels in a three-dimensional ring (Eq. 2.31)
M_{eff}	Effective number of transverse channels in the diffusive regime (Eq. 2.69); effective number of independent measurements contained in a trace of persistent current versus magnetic field (Eq. 7.15)
m	Mass
N	Number of rings in an array (Eq. 6.36)
P	Optical power (Eq. 5.2)
p	Harmonic index of frequency shift or persistent current (Eq. 2.13)
p_{zero}	Lowest value of the harmonic index p for which the finite drive correction results in no cantilever frequency shift (Eq. 7.4)
Q	Mechanical quality factor of a cantilever (Eq. 4.3)
R	Optical reflection coefficient (Eq. 5.2); electrical resistance
S	Power spectral density (Section 6.1.1)
S_{pc}	Ratio of persistent current signal to measurement noise (Eq. 6.35)
T	Temperature; optical transmission coefficient (Eq. 5.2)
T_b	Temperature of the refrigerator in thermometry measurements (Section 6.4.1)
T_c	Superconducting transition temperature (Eq. 6.44)
T_e	Electron temperature in thermometry measurements (Eq. 6.44)
T_n	Brownian motion noise temperature of the cantilever (Eq. 6.4.1.1)
T_p	Characteristic temperature of the p^{th} harmonic of the persistent current (Eqs. 2.24 and 2.73)
t	Time; thickness (cantilever, ring, or wire where appropriate) depending context
t_r	Ring thickness (denoted by t when there is no ambiguity)
typ	Superscript used to denote the square root of the square of a quantity averaged over disorder (e.g. $I^{\text{typ}} = \sqrt{\langle I^2 \rangle}$) (Eq. 2.64)

U_m	Normalized cantilever flexural mode shape for mode m (Eq. 4.1)
V	Disorder potential in a metal ring; voltage
w	Width (cantilever, ring, or wire where appropriate)
w_r	Ring linewidth (denoted by w when there is no ambiguity)
w_w	Wire linewidth (denoted by w when there is no ambiguity)
x	Displacement of the cantilever tip from its equilibrium position (Eq. 4.10)
x_0	Distance from optical fiber to cantilever equilibrium position (Fig. 5.11)
x_1	Displacement of the cantilever at the point addressed by the fiber (Section 5.3.1.1)
$x_{f,\max}$	Amplitude of displacement of the cantilever at the point addressed by the fiber (Eq. 5.3.1.1)
x_{\max}	Amplitude of displacement at the tip of an oscillating cantilever (Eq. 4.23)
z	Expression composed various energy scales and introduced for convenience in Chapter 2 (Eq. 2.61); distance to a point on the cantilever from the base (Fig. 4.3)
z_f	Distance from the base to the point on the cantilever where the laser is incident (Section 5.3.1.1)

Chapter 1

Introduction

The main goals of my graduate research were to develop a high quality cantilever torsional magnetometer and most importantly to apply this magnetometer to the measurement of persistent currents in normal metal rings. In this text, I describe the success that I and my lab mates had in achieving these goals. I document in detail each step of this process including the theoretical description of persistent currents, the nanofabrication of persistent current samples, the physical implementation of the magnetometer, and the analysis of our torsional magnetometry measurements. The results which I report here both add to an existing body of research on persistent currents in normal metal rings and open up the possibility of new measurements using torsional magnetometry.

In this text, I use “persistent current” to mean an electrical current flowing around a ring which is constant in time and which is not driven by a power source external to the ring. As such, it is a thermal equilibrium property of the ring system. While persistent currents are usually associated with superconductors and atomic and molecular quantum systems, quantum mechanics allows, surprisingly, for such a current to exist in a resistive material as well. For the persistent current in a ring of resistive material to be measurable, the ring must be cold ($\lesssim 1$ K) and small ($\lesssim 1$ μ m).

The specific focus of my experimental work is what I refer to in this text as the “typical” persistent current I^{typ} in normal metal rings. In practice, the atomic lattice of a metal contains many microscopic defects upon which electrons scatter. The typical persistent current depends sensitively on the microscopic details of the metal’s disorder and varies seemingly randomly in magnitude and sign across an ensemble of rings fabricated with the same dimensions. As a random quantity, the

typical persistent current must be characterized by its typical root-mean-square magnitude $I^{\text{typ}} = \sqrt{\langle I^2 \rangle}$ averaged across an ensemble of rings with the same dimensions but different microscopic arrangements of defects (here $\langle \dots \rangle$ denotes averaging over all possible realizations of disorder with the same density of scatterers). The typical persistent current may be contrasted with a related quantity, the average persistent current $I^{\text{avg}} = \langle I \rangle$, which is the same for each ring in an ensemble.¹

At the beginning of this project, two measurements of the typical persistent current in normal metal rings had been performed, one in 1991 and the other in 2001 [2, 3]. Despite the fact that in both cases gold rings of similar size were studied using SQUID magnetometers, the reported magnitudes of the persistent current for the two experiments were inconsistent with each other. The first experiment observed persistent currents two orders of magnitude larger than what was expected by theory and an order of magnitude larger than what was observed in the second experiment. The second measurement had reasonable agreement with theory.² Adding to the intrigue surrounding persistent currents, measurements of the average persistent current performed between 1990 and 2002 observed currents that differed from theory in both magnitude and sign [3–7]. For completeness, I note that the typical persistent current was also studied in semiconductor rings and found to agree roughly with theory [8, 9]. Additionally, the typical current was measured again in gold rings at about the same time as the measurements discussed here and was found to agree well with theory [10].³

The measurements which I report greatly expand the range of parameters over which the typical persistent current has been measured. We studied aluminum in which normal state persistent

¹This distinction between the typical and average components of the persistent current is somewhat artificial because for any single ring or array of rings there is only one persistent current signal (i.e. the typical and average values of the persistent current are not measured separately). However, the distinction is useful for discussing the measurements of this text and their implications for the study of persistent currents. As discussed in Chapter 2, our measurements can not distinguish between the typical and average values of the persistent current because, at the strong magnetic fields employed in our measurements, the signal from an array of rings with moderate variation in ring radius would appear random. In Chapter 2, different physical mechanisms (electron-electron interactions, simple quantum interference in a diffusive system, flux-dependence of the density of states in an isolated system, etc.) are identified as being responsible for the leading contributions to the average and typical values of the persistent current in a metal ring. Each of these mechanisms is of theoretical and experimental interest. At strong magnetic fields, all contributions to the average current are expected to be strongly suppressed. I use the typical/average distinction in order to signal to other researchers in the field of persistent currents that our measurements (according to my interpretation of them) mainly provide insight into one persistent current mechanism, namely that of non-interacting electrons in the diffusive regime, without addressing the others. I use “typical persistent current” as a shorthand for “the typical magnitude of the fluctuations of the persistent current of non-interacting electrons in the diffusive regime” because I know of no other contribution to the fluctuations of the persistent current that is not negligible compared to this contribution.

²Because the sample in the second experiment was observed to have a diffusion constant D larger than that of the first experiment, the magnitude of the current expected using the analysis of Chapter 2 was an order of magnitude larger than in the first experiment.

³In this brief introduction, I leave out the experiment of Ref. 11 which studied persistent currents in a different parameter regime (the ballistic regime with few electrons per ring). It is notable that this measurement also used a torsional magnetometry technique, though not one employing a high quality factor micromechanical device.

currents had not previously been investigated. Across all samples (Tables 7.1 and 7.2), the range of observed current magnitudes span three orders of magnitude from ~ 0.7 pA to ~ 700 pA whereas previous measurements had observed currents spanning less than two orders of magnitude and had never observed currents smaller than ~ 200 pA. The dimensions of the samples discussed here varied sufficiently to possess characteristic temperatures T_p (see Table 7.3) differing by a factor of ~ 8 . No previous experiment had studied the temperature dependence of co-deposited samples with significantly different characteristic temperatures. Our measurements increase the maximum temperature at which the typical current has been observed in normal metal rings from 500 mK to 2.5 K. We observe hundreds of oscillations of the persistent current, which is roughly sinusoidal in applied magnetic field, whereas previous measurements had measured only a few oscillations, and we raise the maximum field at which the typical persistent current has been observed from ~ 10 mT to 8.4 T.

These many additions to the existing body of work on persistent currents are made possible in large part by the torsional magnetometry measurement technique. All of the previous measurements of the typical persistent current had been performed using SQUID magnetometers. The torsional magnetometry measurement increases in sensitivity with applied magnetic field and is thus complementary to the SQUID measurement which requires a weak applied magnetic field. The large magnetic field range afforded by torsional magnetometry enabled the study of the magnetic field correlation of the persistent current oscillation. This correlation had never been studied previously.

The torsional magnetometry measurement technique permits the study of persistent currents in a quiet electromagnetic environment. All previous measurements of both the typical and average persistent current had employed either a SQUID magnetometer or a superconducting resonator. In the SQUID magnetometry measurements, the high frequency Josephson current present in the measurement SQUID coupled inductively to the ring sample.⁴ The superconducting resonators used to measure persistent currents were also coupled inductively to the rings and possessed resonant frequencies greater than 100 MHz. In attempting to explain the experimental results obtained using these techniques, several theoretical studies of non-equilibrium effects due to the presence of high frequency electromagnetic radiation found that these effects could mimic the equilibrium persistent current [13–34]. Thus the torsional magnetometry technique demonstrated here, which does not necessitate the presence of high frequency electromagnetic radiation, is advantageous

⁴In principle, the high frequency components of the magnetic flux produced by the SQUID could have been shielded from the sample [12].

because it allows the equilibrium persistent current to be studied without the need to account for the possibility of non-equilibrium effects.

Beyond non-equilibrium effects, persistent currents in the normal state have been studied theoretically in many regimes (see chapter 3). Experimental progress has lagged behind. Besides the work described in this text, only three experiments have been reported in the last eight years [10, 11, 35]. The demonstration of cantilever torsional magnetometry as a powerful alternative to SQUID and resonator based measurements is perhaps as important a contribution to the field of persistent currents as our experimental results themselves. Some possible follow up work to the measurements described here is proposed in chapter 8.

My main goal with this thesis is to provide a thorough account of my experiment as well as a detailed theoretical description of persistent currents. A secondary goal of mine is to present these topics beginning at the level of a first year physics graduate student. Often in my graduate tenure, I have been puzzled by an aspect of a published journal article and dug up the thesis of the lead author only to be disappointed by the lack of a clarification in its text. I hope that anyone searching for additional explanation on any point in one of my published works is aided by this text. If a section seems tedious, it is likely that I struggled with its subject and want to dispel confusion from anyone else dealing with it. I have tried to push the topics somewhat tangential to persistent currents and their measurement into the appendices.

In chapter 2, I present a thorough theoretical description of the basic persistent current phenomena. I begin with the simplest possible model and build up to the regime relevant to the measurement which I discuss in chapter 7. Chapter 2 draws heavily on the presentation given in Ref. [36] and follows closely the results of Refs. 37–42 among others. I believe some small aspects of chapter 2, namely the discussion of the perfect three dimensional ring, the detailed consideration of the effects of Zeeman splitting and spin-orbit scattering, and the extension of the toroidal field model to the average persistent current, to be novel. The theoretical machinery needed for chapter 2 is reviewed in Appendix B. In chapter 3, I review the persistent current literature thoroughly, providing more detail to many of the points touched upon in this introduction.

In chapter 4, I discuss the physics of cantilever torsional magnetometry. This torsional magnetometry technique was developed by myself, Ania Jayich, Jack Sankey, and Jack Harris to take advantage of the unique magnetic properties of the persistent current effect. In torsional magnetometry, one studies a magnetic moment $\boldsymbol{\mu}$ through the torque $\boldsymbol{\tau} = \boldsymbol{\mu} \times \boldsymbol{B}$ that it experiences in

a magnetic field \mathbf{B} . For our cantilever torsional magnetometry technique, one infers the magnetic properties of a sample by monitoring the spring constant of the cantilever on which it is mounted. Because the persistent current depends strongly on the orientation of the applied field, the frequency shift of the cantilever varies quadratically in \mathbf{B} (rather than the typical linear dependence). This quadratic dependence on magnetic field is what leads to the high sensitivity to persistent currents which I discuss in chapter 6. The torsional magnetometry of persistent currents discussed in chapter 4 makes use of some classical physics which is reviewed in Appendix C.

In chapter 5 I present the experimental apparatus and the procedures used to apply it to the persistent current measurement. I was the first member of the Harris lab to work on the persistent current project and began working in nearly an empty lab. Most of equipment used in this experiment was acquired or designed by myself and Ania Jayich under the direction of Jack Harris. The sample fabrication process is also discussed in this chapter (with a more detailed recipe given in Appendix D). The difficult process of trial and error involved in developing a sample fabrication recipe was done mostly by Ania Jayich along with Rob Ilic. Ania and I designed the samples reported on in chapter 7 together. We each did roughly half of the cleanroom work for these samples. We took all of the measurements together. Most of the LabVIEW routines used in the measurements were programmed by me.

In chapter 7, I outline the signal analysis procedure developed by myself along with Ania Jayich and Jack Harris. I also present analysis of all of our measurements of the persistent current. All of the analysis presented in this chapter was performed by myself.⁵ Transport measurements and analysis of a co-deposited wire are presented in Appendix E. These measurements allowed us to check some properties of the samples independent of the persistent current measurement. In chapter 8, I discuss future measurements which could build upon the results discussed in chapter 7.

⁵Ania also performed the analysis independently so we could check each other for errors.

Chapter 2

Review of theory relevant to mesoscopic persistent currents in the normal state

In this chapter we will review the basic theoretical results describing persistent currents in small normal metal rings. We will begin with the simplest possible model for the ring system and then refine it to be applicable to three-dimensional rings of a normal metal in large magnetic fields. We will acknowledge the original publications of the results we summarize where appropriate but will reserve most discussion of the persistent current literature for Chapter 3. In all cases, we assume that the ring dimensions are less than the electron phase coherence length L_ϕ so that decoherence effects may be ignored.

2.1 The ideal one-dimensional ring

The normal state persistent current studied in this dissertation is an equilibrium property of the system. It is a quantum effect related to the Aharonov-Bohm phase (discussed in Section 2.1.1) picked up by a charged particle moving in a magnetic field. Although it is possible for collective effects to contribute to an equilibrium current, we will primarily be concerned with the current due to non-interacting electrons (sometimes referred to as the “single-particle” current). This current arises from the fact that for any disorder configuration of the ring each energy eigenstate possesses

a non-zero expectation value for its angular momentum. Since the electron is a charged particle, this angular momentum has a current associated with it. These eigenstates with finite angular momentum are analogous to the eigenstates of an electron orbiting a nucleus which also possess finite angular momenta for electrons outside of the s -orbital. In principle, the calculation of the current in a ring of many electrons boils down to calculating the current associated with each energy eigenstate and then summing up each of these currents with an appropriate weighting factor reflecting the thermal population of that state.

2.1.1 Solution of Schrödinger's equation

We begin with the simplest possible model for the ring: a clean, one-dimensional ring into which we put a single electron of mass m and charge $-e$. The task of describing this system is the textbook particle-in-a-box problem from introductory quantum mechanics, here with periodic boundary conditions. We parametrize the ring by the coordinate u and call its circumference L , as shown in Fig. 2.1. The time-independent Schrödinger equation for the Hamiltonian $\hat{H} = \hat{P}^2/2m$ is

$$-\frac{\hbar^2}{2m} \frac{d^2\psi_n}{du^2} = \varepsilon_n \psi_n \quad (2.1)$$

with the wavefunction ψ subject to the boundary condition

$$\psi(u + L) = \psi(u). \quad (2.2)$$

The eigenfunctions and eigenenergies indexed by integer n are

$$\psi_n(u) = \frac{1}{\sqrt{L}} \exp\left(2\pi i n \frac{u}{L}\right) \quad (2.3)$$

and

$$\varepsilon_n = \frac{\hbar^2}{2mL^2} n^2.$$

We consider the effects of applying a constant, uniform magnetic field \mathbf{B} to the system. We choose coordinates so that the ring lies in the xy -plane and is centered on the origin. We assume that the magnetic field $\mathbf{B} = B\hat{z}$ is parallel to the z -axis.

In the presence of a magnetic field, the canonical momentum \mathbf{P}_{can} for a particle of charge $-e$ and mass m becomes $\mathbf{P}_{\text{can}} = \mathbf{P}_{\text{mech}} - e\mathbf{A}$ where $\mathbf{P}_{\text{mech}} = m\mathbf{v}$ is the particle's mechanical momentum

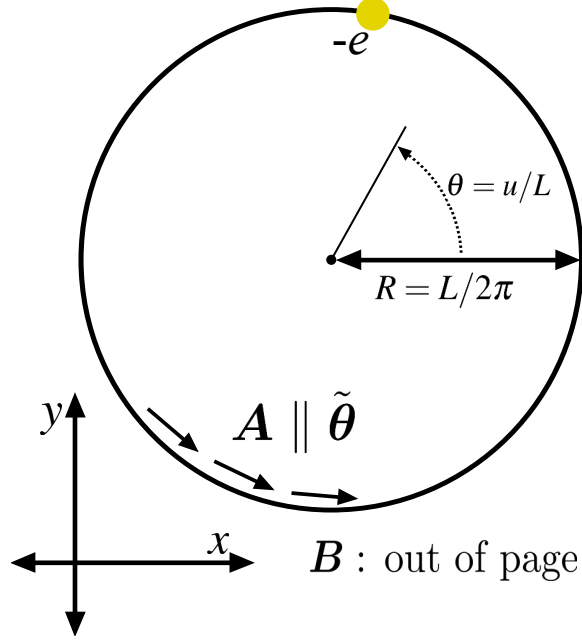


Figure 2.1: A perfect one-dimensional ring. The figure shows the orientation relative to an applied magnetic field of a perfect, one-dimensional ring of radius $L/2\pi$ to which a particle with charge $-e$ is confined. The applied magnetic field \mathbf{B} is parallel to the \tilde{z} direction and points out of the page. The vector potential \mathbf{A} chosen in the text is everywhere tangent to the ring and parallel to the cylindrical unit vector $\tilde{\theta}$.

at velocity \mathbf{v} and \mathbf{A} is the vector potential of the magnetic field satisfying $\mathbf{B} = \nabla \times \mathbf{A}$. Only the mechanical momentum contributes to the particle's energy. Thus the Hamiltonian becomes $\hat{H} = (\hat{\mathbf{P}} + e\mathbf{A}(\hat{\mathbf{X}}))^2/2m$, where $\hat{\mathbf{X}}$ is the position operator.¹

For $\mathbf{B} = B\tilde{z}$, we can write $\mathbf{A} = (-B/2)(y\tilde{x} - x\tilde{y})$. Defining cylindrical coordinates (r, θ) and corresponding unit vectors $(\tilde{r}, \tilde{\theta})$ satisfying

$$x = r \cos \theta$$

$$y = r \sin \theta$$

$$r = \sqrt{x^2 + y^2}$$

$$\theta = \tan^{-1}(y/x)$$

$$\tilde{r} = \cos \theta \tilde{x} + \sin \theta \tilde{y}$$

¹We will sometimes suppress the dependence of \mathbf{A} on the operator $\hat{\mathbf{X}}$ by expressing the vector potential as an operator $\hat{\mathbf{A}}$.

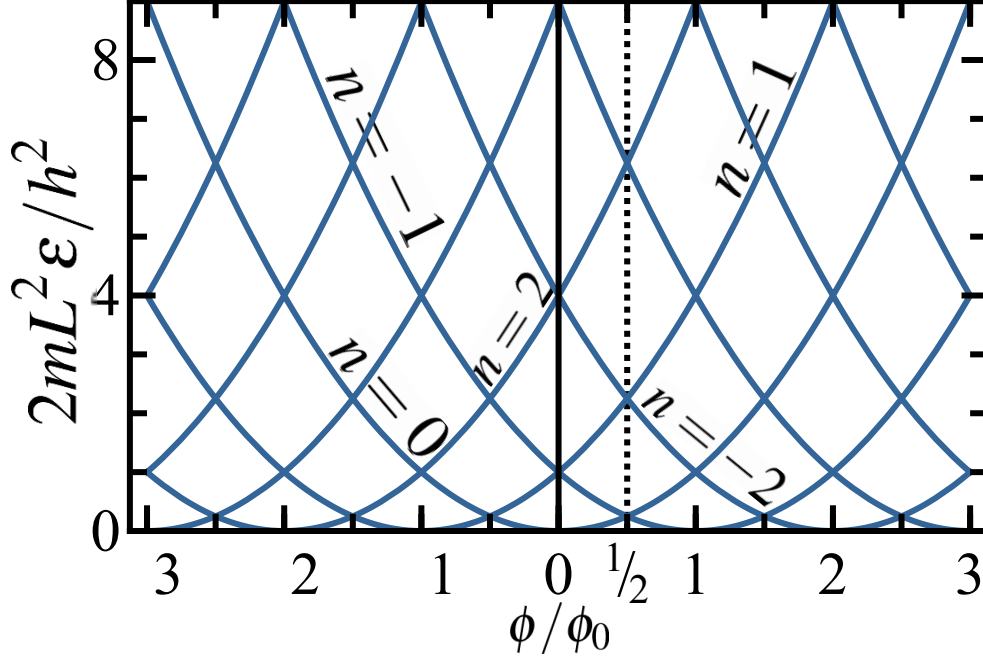


Figure 2.2: Eigenenergies of a perfect one-dimensional ring. The figure shows the first few eigenenergies ε_n of Eq. 2.4 plotted versus the normalized flux ϕ/ϕ_0 . The flux periodicity of the energy spectrum discussed in the text can clearly be seen. The dashed line marks the point $\phi = \phi_0/2$. In the range $0 < \phi < \phi_0/2$, the energy levels are, in increasing order, $n = 0, -1, +1, -2, +2$, etc.

$$\tilde{\boldsymbol{\theta}} = -\sin \theta \tilde{\boldsymbol{x}} + \cos \theta \tilde{\boldsymbol{y}},$$

we can write $\boldsymbol{A} = Br\tilde{\boldsymbol{\theta}}/2$. Confined to $r = L/2\pi$ along the ring, we can also write $\boldsymbol{A} = \frac{\phi}{L}\tilde{\boldsymbol{\theta}}$ where $\phi = \pi(L/2\pi)^2 B$ is the flux enclosed by the ring. The coordinate $u = L\theta/2\pi$ follows the ring in a circle about the origin, and thus the derivative $\frac{d}{du}$, which is everywhere tangent to the ring, is always parallel to $\tilde{\boldsymbol{\theta}}$. Thus, in the presence of \boldsymbol{B} , the one-dimensional time-independent Schrödinger equation parametrized by u becomes

$$\frac{1}{2m} \left(-i\hbar \frac{d\psi_n}{du} + e \frac{\phi}{L} \right)^2 = \varepsilon_n \psi_n.$$

The eigenfunctions ψ_n are again given by Eq. 2.3 with the eigenenergies now

$$\begin{aligned} \varepsilon_n &= \frac{1}{2m} \left(\frac{2\pi\hbar}{L} n + e \frac{\phi}{L} \right)^2 \\ &= \frac{\hbar^2}{2mL^2} \left(n + \frac{\phi}{\phi_0} \right)^2 \end{aligned} \quad (2.4)$$

where we have introduced the flux quantum $\phi_0 = h/e$.

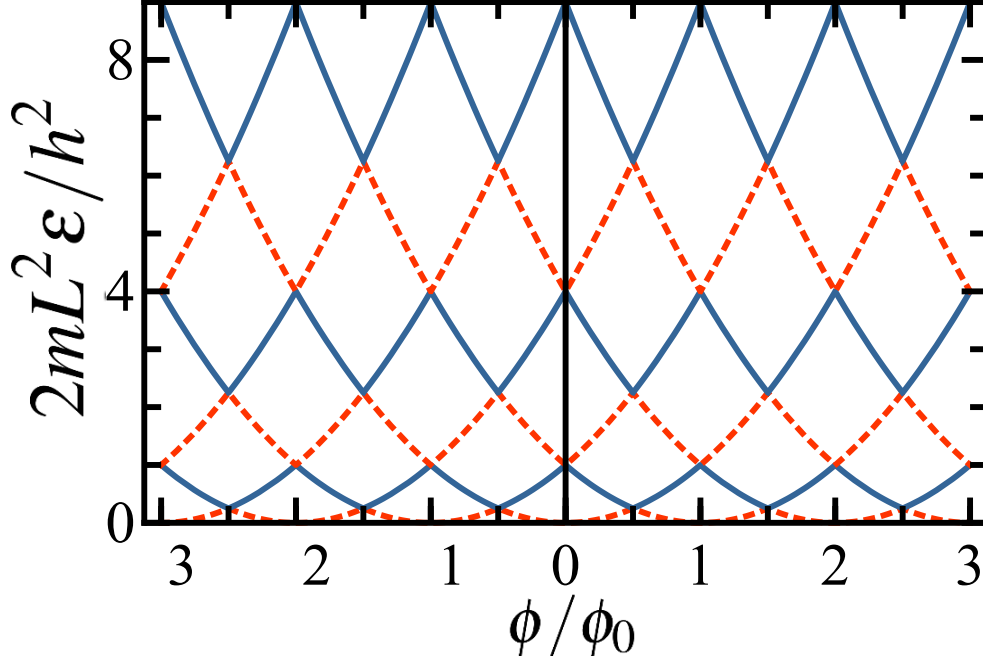


Figure 2.3: Energy levels of a perfect one-dimensional ring. The figure shows the energy spectrum of Fig. 2.2 with each single energy level drawn either with a solid or a dashed curve. Each energy level has a kink at the points $\phi = m\phi_0/2$ for integer m where two of the eigenenergy parabolae intersect. These kinks are smoothed out with the introduction of disorder to the ring.

The energies ε_n are plotted versus flux ϕ in Fig. 2.2. Although the eigenenergy ε_n of the n^{th} eigenstate is a parabola, the even spacing of the different ε_n in ϕ produces a spectrum that is periodic overall. We will discuss this flux periodicity shortly. First, we note that in later sections it will often be preferable to discuss the energy spectrum as a set of “levels” rather than a set of eigenenergies corresponding to particular eigenstates. By energy levels, we mean ε curves which are periodic in flux. In Fig. 2.3, the energy spectrum of Fig. 2.2 is replotted with the energy levels, rather than the eigenenergies, indicated by the alternating use of solid and dashed lines for each level. Since the energy spectrum is symmetric under both $\phi \rightarrow -\phi$ and $\phi \rightarrow \phi + \phi_0$, the spectrum is totally specified by its set of values in the range $0 < \phi < \phi_0/2$. We could thus label the energy levels by the index n of the corresponding eigenenergy over this range, in which case the energy levels are in increasing order: $n = 0, -1, +1, -2, +2$, etc.

Rather than solving the Schrödinger equation with \mathbf{A} included explicitly, it is possible to use a gauge transformation to remove it from the Hamiltonian, restoring the original $\mathbf{B} = 0$ Hamiltonian.

In quantum mechanics, a gauge transformation involves replacing \mathbf{A} and ψ by

$$\mathbf{A}' = \mathbf{A} + \nabla\Lambda$$

and

$$\psi' = \psi \exp\left(-i\frac{e\Lambda}{\hbar}\right)$$

where Λ is some smooth function of position. Since $\nabla \times \nabla\Lambda = 0$ for all Λ , this modification to \mathbf{A} does not change \mathbf{B} . The product rule then gives

$$\begin{aligned} (\hat{\mathbf{P}} + e\hat{\mathbf{A}}')\psi' &= (-i\hbar\nabla)\psi' + (e\hat{\mathbf{A}} + e\nabla\Lambda)\psi' \\ &= \left(-i\hbar\exp\left(-i\frac{e\Lambda}{\hbar}\right)\nabla\psi - e(\nabla\Lambda)\psi'\right) + (e\hat{\mathbf{A}} + e\nabla\Lambda)\psi' \\ &= \exp\left(-i\frac{e\Lambda}{\hbar}\right)(-i\hbar\nabla + e\hat{\mathbf{A}})\psi \\ &= \exp\left(-i\frac{e\Lambda}{\hbar}\right)(\hat{\mathbf{P}} + e\hat{\mathbf{A}})\psi. \end{aligned}$$

Often in quantum mechanics an overall phase factor such as the factor $\exp(-ie\Lambda/\hbar)$ introduced in the gauge transformation has no impact on the calculation of any physical observable and so the vector potential can be freely shifted by $\nabla\Lambda$ without consequence. However, Ehrenberg and Siday [43], and later Aharonov and Bohm [44], showed that, when two trajectories enclosing a magnetic flux ϕ interfere, the phase factor due the vector potential plays an important role, shifting the overall phase of the interference by $2\pi\phi/\phi_0$. A similar effect holds for eigenfunctions of the ideal ring which we have been considering.

In the case of the ring, we can choose

$$\begin{aligned} \Lambda &= -\frac{1}{2}RBu \\ &= -\frac{1}{2}R^2B\theta \\ &= -\phi\frac{\theta}{2\pi}. \end{aligned}$$

In cylindrical coordinates, $\nabla\Lambda = \tilde{\mathbf{r}}\frac{\partial\Lambda}{\partial r} + \tilde{\boldsymbol{\theta}}\frac{1}{r}\frac{\partial\Lambda}{\partial\theta} + \tilde{\mathbf{z}}\frac{\partial\Lambda}{\partial z}$, so along the ring $\nabla\Lambda = -\frac{\phi}{L}\tilde{\boldsymbol{\theta}}$ and $\mathbf{A}' = 0$. With this gauge transformation, we thus return to the Hamiltonian given in Eq. 2.1. The new

wavefunctions are

$$\psi'(u) = \exp\left(2\pi i \frac{\phi}{\phi_0} \frac{u}{L}\right) \psi(u).$$

Using the original boundary condition of Eq. 2.2, the new boundary condition on ψ' is

$$\psi'(u + L) = \exp\left(2\pi i \frac{\phi}{\phi_0}\right) \psi'(u). \quad (2.5)$$

This boundary condition, which determines which combinations of the eigenfunctions given in Eq. 2.3 are permitted, now depends periodically on ϕ with period ϕ_0 . Since this is a general property of the solutions of the Hamiltonian, it follows that *all* properties of the system are periodic in ϕ with period ϕ_0 . This property carries over in the generalization to a disordered, three-dimensional ring and is one of the key signatures of the persistent current.

The phrase “carries over” is to be taken loosely here. When the ring has a finite linewidth, the flux threading the ring is not a well-defined quantity. In this case, we can define ϕ to be the flux through the mean radius of the ring. The persistent current is no longer strictly periodic in ϕ , but its Fourier transform with respect to ϕ

$$I(p) = \int_{-\infty}^{\infty} d\phi I(\phi) e^{-2\pi i p \phi / \phi_0}$$

is peaked near $p = 1$, with its peak width determined by the ring’s finite cross-section.

Often the persistent current is discussed using an idealized “Aharonov-Bohm flux” ϕ threading the ring but not penetrating the linewidth of the ring itself, similar to the arrangement presented by Refs. [43] and [44]. It is possible to attain all of the results given here for the one-dimensional, perfect ring using this idealized flux. If the flux ϕ is taken to be produced by a field B threading a disk of radius a , then the vector potential can be written as

$$\mathbf{A} = \begin{cases} Br\tilde{\theta}/2, & r < a \\ \phi\tilde{\theta}/2\pi r, & r > a \end{cases} \quad (2.6)$$

which will give the same values for \mathbf{A} along the ring as we found above.

More generally, we can consider any arrangement of field $\mathbf{B}(\mathbf{r})$ for which $B = 0$ everywhere inside the ring. Choosing the Lorenz gauge for which $\nabla \cdot \mathbf{A} = 0$ (a condition which the \mathbf{A} defined

in Eq. 2.6 satisfies), the line integral

$$\Lambda(\mathbf{r}) = - \int_{\mathbf{r}_0}^{\mathbf{r}} d\mathbf{r}' \cdot \mathbf{A}(\mathbf{r}')$$

is independent of the path of integration within the ring, as long as the path does not encircle the ring. The choice of \mathbf{r}_0 is arbitrary and shifts Λ by a constant with no physical significance. If the path does encircle the ring, the line integral can be decomposed into

$$\Lambda(\mathbf{r}) = - \int_{\mathbf{r}_0}^{\mathbf{r}} d\mathbf{r}' \cdot \mathbf{A}(\mathbf{r}') - n \oint d\mathbf{r}' \cdot \mathbf{A}(\mathbf{r}')$$

where the first integral does not encircle the ring, the second integral represents a closed loop encircling the ring, and n is the number of times that the original path encircled the ring. Since $\nabla \times \mathbf{A} = \mathbf{B} = 0$ over the path of integration, Stokes' theorem can be applied to state

$$\begin{aligned} \oint d\mathbf{r}' \cdot \mathbf{A}(\mathbf{r}') &= \iint d\mathbf{S} \cdot (\nabla \times \mathbf{A}) \\ &= \iint d\mathbf{S} \cdot \mathbf{B} \\ &= \phi \end{aligned}$$

where the surface integral is taken over the enclosed path and thus is equal to the total flux ϕ threading the ring. If we take this Λ to be the function in the gauge transformation introduced above, the transformed potential is $\mathbf{A}' = \mathbf{A} + \nabla\Lambda(\mathbf{r}) = 0$ and the magnetic field is eliminated from the Hamiltonian. Under the gauge transformation, the boundary condition of Eq. 2.2 becomes

$$\begin{aligned} \psi(u+L) &= \exp(2\pi i (\Lambda(\mathbf{r}+L) - \Lambda(\mathbf{r})) / \phi_0) \psi(u) \\ &= \exp\left(2\pi i \left(\oint d\mathbf{r}' \cdot \mathbf{A}(\mathbf{r}')\right) / \phi_0\right) \psi(u) \\ &= \exp(2\pi i \phi / \phi_0) \psi(u) \end{aligned}$$

where $\Lambda(\mathbf{r}+L)$ represents a line integral following a path from \mathbf{r}_0 to point \mathbf{r} plus the integral representing one closed curve encircling the ring. Thus, this more general treatment results in the same flux periodic boundary condition as was given above in Eq. 2.5. With this last, general form of the gauge transformation, we have derived this flux periodicity without specifying the

dimensionality of the ring nor the potential energy term $V(\mathbf{r})$ of the Hamiltonian. Thus, for this idealized Aharonov-Bohm flux threading the ring but not penetrating the metal, the property of flux periodicity carries over exactly from the perfect ring to the three-dimensional, disordered ring. Due to the micrometer size scale necessary for the persistent current to be observable, such an idealized flux would be nearly impossible to impose in practice and is useful only as a conceptual device (and as a first approximation for a ring with a reasonable aspect ratio).

2.1.2 The single-level and total current

We now find the current associated with each eigenstate. A particle moving at velocity v around a ring of circumference L makes one round trip in time $\Delta t = L/v$. If the particle has charge $-e$, then the average current, the charge passing any given point of the ring per unit time averaged over one period, is $i = -e/\Delta t = -ev/L$. As we stated above, the velocity of such a charged particle in a magnetic field can be written as $v = P_{\text{mech}}/m = (P_{\text{can}} + eA)/m$. Then for the system we have been considering, the velocity v_n associated with the n^{th} eigenstate as given in Eq. 2.3 satisfies

$$\begin{aligned} v_n \psi_n(u) &= \frac{(P_{\text{can}} + eA)}{m} \psi_n(u) \\ &= \frac{1}{m} \left(-i\hbar \frac{d}{du} + e \frac{\phi}{L} \right) \left(\frac{1}{\sqrt{L}} \exp\left(2\pi i n \frac{u}{L}\right) \right) \\ &= \frac{\hbar}{mL} \left(n + \frac{\phi}{\phi_0} \right) \left(\frac{1}{\sqrt{L}} \exp\left(2\pi i n \frac{u}{L}\right) \right), \end{aligned}$$

giving a current

$$\begin{aligned} i_n &= -\frac{e}{L} v_n \\ &= -\frac{e\hbar}{mL^2} \left(n + \frac{\phi}{\phi_0} \right). \end{aligned}$$

We note that in terms of the energy ε_n given in Eq. 2.4 the current i_n may be written as

$$i_n = -\frac{\partial \varepsilon_n}{\partial \phi}.$$

Having described the single-particle states of the ideal ring, we now consider the case of a ring filled with many electrons, as would be the case in a real metal ring. We assume that the electrons are non-interacting. This assumption is often appropriate due to charge screening which suppresses

long-range interactions within the metal [45], but it is one which we will revisit later. To find the total current I at temperature T , we sum over the contributions of each individual level with the weighting factor $f(\varepsilon, \mu, T)$ given by the Fermi-Dirac distribution function²

$$\begin{aligned}
I &= \sum_n i_n f(\varepsilon_n, \mu, T) \\
&= \sum_n \left(-\frac{\partial \varepsilon_n}{\partial \phi} \right) \left(1 + \exp \left(-\frac{(\mu - \varepsilon_n)}{k_B T} \right) \right)^{-1} \\
&= -\frac{\partial \Omega}{\partial \phi}
\end{aligned} \tag{2.7}$$

where

$$\Omega = -k_B T \sum_n \left(\ln \left(1 + \exp \left(\frac{(\mu - \varepsilon_n)}{k_B T} \right) \right) \right)$$

is the grand potential of thermodynamics and n also indexes both spin states. We assume that the temperature is well below the Fermi temperature so that the chemical potential $\mu \approx \varepsilon_F$ where ε_F is the Fermi energy. In the limit of low temperature $T \rightarrow 0$, the Fermi-Dirac distribution function $f(\varepsilon_n, \varepsilon_F, T)$ becomes $\theta(\varepsilon_F - \varepsilon_n)$ where $\theta(x)$ is the Heaviside function equal to 1 for $x > 0$ and 0 otherwise. Thus the sum in the first two lines of Eq. 2.7 becomes a sum over the single-level currents of all energy levels below the Fermi level.

Within the flux range $0 < \phi < \phi_0/2$, the energy levels in ascending order are 0, -1, +1, -2, +2, etc. as shown in Fig. 2.2. For $-\phi_0/2 < \phi < 0$, the ordering of the levels $+n$ and $-n$ is reversed for each n . If we consider filling up all of the levels to $n = \pm N$ as is appropriate for this flux range and $T = 0$, we will get a contribution $(-eh/mL^2)\phi/\phi_0$ to the current due to the $n = 0$ level and a total contribution $2(-eh/mL^2)\phi/\phi_0$ due to each pair $\pm n$. Denoting the total current due to all levels $|n| \leq N$ by I_N and accounting for the twofold degeneracy of each level due to spin,³ we find

$$I_N = -\frac{eh}{mL^2} (4N + 2) \frac{\phi}{\phi_0}.$$

²This analysis is appropriate for the grand canonical ensemble in which the ring can exchange electrons with a reservoir. Technically, such a model is not accurate for the isolated ring system which we study. However, it can be shown that for a gas of Fermions in the grand canonical ensemble the typical fluctuations $\sqrt{\langle \Delta N^2 \rangle}$ in particle number N scale as \sqrt{T} and so are negligible at sufficiently low temperature. Many of the early and most cited publications on persistent currents, such as Refs. [37, 38, 41, 42, 46, 47], use this model to calculate the current. We note that some authors have taken issue with the use of the grand canonical ensemble [48], while others have argued that the calculation in the grand canonical ensemble can be related to the one in the canonical ensemble by making the chemical potential flux dependent so that as the energy levels change with ϕ the number of occupied levels remains constant [40, 49, 50]. We will touch on the difference between the canonical and grand canonical ensemble again when discussing the average current in the diffusive regime.

³Note that, including spin degeneracy, I_N is the current in a ring filled with $4N + 2$ electrons, and, in the notation used below, I_{N+n} is the current for a ring with $4N + 2 + n$ electrons.

Since we summed each pair $\pm n$, this result does not depend on the ordering and is valid for $-\phi_0/2 < \phi < \phi_0/2$.

Over this range, the contributions of the next three electrons⁴ to the total current are $\frac{e\hbar}{mL^2}(\sigma N - \phi/\phi_0)$, $\frac{e\hbar}{mL^2}(\sigma N - \phi/\phi_0)$, and $\frac{e\hbar}{mL^2}(-\sigma N - \phi/\phi_0)$ respectively with $\sigma = \text{sgn}(\phi)$ the sign of ϕ . The velocity of the N^{th} level at $\phi = 0$ is hN/mL . Taking $N \gg 1$ and denoting the magnitude of the velocity of the highest filled as $v_F \approx hN/mL$, we can write

$$I_{N+0} \approx -4 \frac{ev_F}{L} \frac{\tilde{\phi}}{\phi_0} \quad (2.8)$$

$$I_{N+1} \approx \sigma \frac{ev_F}{L} - 4 \frac{ev_F}{L} \frac{\tilde{\phi}}{\phi_0} \quad (2.9)$$

$$I_{N+2} \approx 2\sigma \frac{ev_F}{L} - 4 \frac{ev_F}{L} \frac{\tilde{\phi}}{\phi_0} \quad (2.10)$$

$$I_{N+3} \approx \sigma \frac{ev_F}{L} - 4 \frac{ev_F}{L} \frac{\tilde{\phi}}{\phi_0} \quad (2.11)$$

where we have used the reduced flux $\tilde{\phi} = \phi - M\phi_0$ where M is the integer required to satisfy $-\phi_0/2 < \tilde{\phi} < \phi_0/2$.⁵

The current for various numbers of electrons in the ring as given in Eqs. 2.8 through 2.11 is plotted against flux threading the ring in Fig. 2.4. In all cases, the typical current magnitude is of order

$$I_0 = \frac{ev_F}{L}. \quad (2.12)$$

Since this value has the same magnitude as that of the electron in the highest occupied level, each additional electron has a strong effect on the flux dependence of the current. These conclusions can also be drawn from Fig. 2.2. Since the single-level currents are equal to the slopes of the energy levels $-\partial\varepsilon/\partial\phi$ and the slopes of successive energy levels are anti-correlated, the current of each electron added to the ring tends to cancel out the contribution of the previous electron resulting in a total current with a magnitude of the order of the current contribution from the highest energy level and with a flux dependence that is sensitive to the number of electrons in the ring.

Taking the analysis one more step, we can calculate the harmonics of the current. We note that the current is in all cases periodic in ϕ and antisymmetric about $\phi = 0$ and can thus be expanded

⁴Here we are switching back temporarily to the canonical ensemble. In the grand canonical ensemble, each level is either doubly filled or empty, so the expressions below for singly occupied levels (I_{N+1} and I_{N+3}) are never applicable.

⁵More precisely, $M = \lfloor (\phi + \phi_0/2)/\phi_0 \rfloor$ where $\lfloor z \rfloor$ denotes the nearest integer less than z .

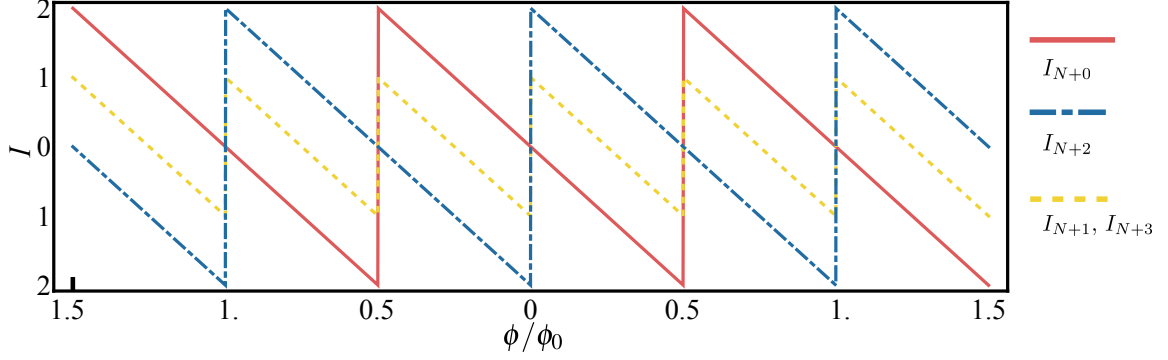


Figure 2.4: Current versus flux for a perfect one-dimensional ring. The currents for different numbers of electrons as given in Eqs. 2.8 through 2.11 are plotted versus ϕ/ϕ_0 . The current axis is scaled in units of I_0 . For each filling of the ring, the current has a diamagnetic slope and is of the same order of magnitude. However, the discontinuous jumps in the current occur at different values of ϕ/ϕ_0 for different fillings. The jump at $\phi = 0$ for I_{N+2} results in its odd Fourier components taking positive values despite the fact that the slope is always negative (except at the points of discontinuity). As is discussed below, in the presence of finite temperature or disorder, higher harmonics are suppressed, meaning that I_{N+2} is dominated by its first harmonic and thus has a paramagnetic slope at $\phi = 0$.

as

$$I = \sum_p I_p \sin 2\pi p \frac{\phi}{\phi_0}. \quad (2.13)$$

Using $I_p = \frac{4}{\phi_0} \int_0^{\phi_0/2} d\phi I(\phi) \sin(2\pi p \phi/\phi_0)$, $\int_0^{1/2} dx x \sin(2\pi p x) = -(-1)^p/4\pi p$, and $\int_0^{1/2} dx \sin(2\pi p x) = (1 - (-1)^p)/2\pi p$, we find the harmonics of the current for the different fillings of the energy levels to be

$$I_{p,N+0} = \frac{4}{\pi p} (-1)^p I_0 \quad (2.14)$$

$$I_{p,N+1} = \frac{2}{\pi p} (1 + (-1)^p) I_0$$

$$I_{p,N+2} = \frac{4}{\pi p} I_0 \quad (2.15)$$

$$I_{p,N+3} = I_{p,N+1}.$$

Notably, for p odd $I_{p,N+0} = -I_{p,N+2}$ and $I_{p,N+1} = I_{p,N+3} = 0$, whereas for p even the harmonic is the same for each number of electrons. For an ensemble of rings with a spread in the number of electrons per ring greater than four, the ensemble average of the harmonics I_p with odd p will be zero, while for even harmonics it will be $4I_0/\pi p$.

Much of what we have seen for the perfect one-dimensional ring has a counterpart in the case

of the disordered, three-dimensional ring. In that case, the perfectly anti-correlated single energy levels are replaced by bands of energy levels correlated on an energy scale E_c . Anti-correlation of successive bands (as well as lack of correlation beyond a certain energy scale) causes the current contributions of most bands to cancel out. This cancellation results in a typical total current of the order of the current of the top-most filled band of levels instead of the top-most filled energy level as we found for the perfect, one-dimensional ring. Likewise, the sensitivity to electron number of the odd harmonics of the current for the perfect ring can be likened to the sensitivity of the disordered ring to its microscopic disorder configuration.⁶ Averaging over the various possible disorder configurations also results in the odd harmonics of the current vanishing. Survival of the finite disorder average for the even harmonics is discussed in 2.3.3.

2.2 Effects of finite temperature, finite cross-section, and the introduction of disorder on the persistent current of the ideal one-dimensional ring

2.2.1 Finite temperature

First we consider finite disorder which can be addressed using Eq. 2.7. We begin by writing the grand canonical potential as

$$\Omega = -k_B T \int_{-\infty}^{\infty} d\varepsilon \nu(\varepsilon, \phi) \left(\ln \left(1 + \exp \left(-\frac{(\varepsilon - \varepsilon_F)}{k_B T} \right) \right) \right) \quad (2.16)$$

where $\nu(\varepsilon, \phi) = \sum_n 2\delta(\varepsilon_n(\phi) - \varepsilon)$ is the flux-dependent density of states. The factor of 2 has been added to ν to account for spin degeneracy. We perform two integrations by parts on the integral in Eq. 2.16. Because $\nu(\varepsilon, \phi)$ and its integrals are zero for $\varepsilon < 0$ and the ln term and its derivatives are zero at $\varepsilon = \infty$, the boundary terms can be discarded. Using the Poisson summation formula

⁶The odd harmonics in a perfect three-dimensional ring are also sensitive to the exact values of the cross-sectional dimensions. See Section 2.2.2.

(see Eq. A.3), the first term in the integral in Eq. 2.16 becomes

$$\begin{aligned}
\int_0^\varepsilon d\varepsilon' \int_0^{\varepsilon'} d\varepsilon'' \nu(\varepsilon'', \phi) &= 2 \int_0^\varepsilon d\varepsilon' \int_0^{\varepsilon'} d\varepsilon'' \sum_p \sqrt{\frac{2mL^2}{h^2\varepsilon''}} \cos\left(2\pi p \sqrt{\frac{2mL^2\varepsilon''}{h^2}}\right) e^{2\pi i p \phi / \phi_0} \\
&= 4 \int_0^\varepsilon d\varepsilon' \int_0^{\varepsilon'} d\varepsilon'' \sum_{p>0} \sqrt{\frac{2mL^2}{h^2\varepsilon''}} \cos\left(2\pi p \sqrt{\frac{2mL^2\varepsilon''}{h^2}}\right) \cos\left(2\pi p \frac{\phi}{\phi_0}\right) \\
&\quad + \int_0^\varepsilon d\varepsilon' \int_0^{\varepsilon'} d\varepsilon'' \sqrt{\frac{2mL^2}{h^2\varepsilon''}} \\
&= 4 \sum_{p>0} \cos\left(2\pi p \frac{\phi}{\phi_0}\right) \int_0^\varepsilon d\varepsilon' \frac{1}{\pi p} \sin\left(2\pi p \sqrt{\frac{2mL^2\varepsilon'}{h^2}}\right) \\
&\quad + \frac{8}{3} \sqrt{\frac{2mL^2}{h^2}} \varepsilon^{3/2}. \tag{2.17}
\end{aligned}$$

Changing variables to $k = \sqrt{2m\varepsilon}/\hbar$,

$$\begin{aligned}
\int_0^\varepsilon d\varepsilon' \int_0^{\varepsilon'} d\varepsilon'' \nu(\varepsilon'', \phi) - \frac{8}{3} \sqrt{\frac{2mL^2}{h^2}} \varepsilon^{3/2} &= 4 \sum_{p>0} \cos\left(2\pi p \frac{\phi}{\phi_0}\right) \int_0^\varepsilon d\varepsilon' \frac{1}{\pi p} \sin\left(2\pi p \sqrt{\frac{2mL^2\varepsilon'}{h^2}}\right) \\
&= 4 \sum_{p>0} \cos\left(2\pi p \frac{\phi}{\phi_0}\right) \int_0^k dk' \frac{\hbar^2 k'}{m} \frac{1}{\pi p} \sin(pk'L) \\
&= 4 \sum_{p>0} \cos\left(2\pi p \frac{\phi}{\phi_0}\right) \frac{\hbar^2}{m\pi p} \int_0^k dk' k' \sin(pk'L).
\end{aligned}$$

Integrating by parts and setting the constant of integration to zero gives

$$\begin{aligned}
\int_0^\varepsilon d\varepsilon' \int_0^{\varepsilon'} d\varepsilon'' \nu(\varepsilon'', \phi) - \frac{8}{3} \sqrt{\frac{2mL^2}{h^2}} \varepsilon^{3/2} &= 4 \sum_{p>0} \cos\left(2\pi p \frac{\phi}{\phi_0}\right) \frac{\hbar^2}{m\pi p} \left(\frac{\sin(pkL)}{p^2 L^2} - k \frac{\cos(pkL)}{pL} \right) \\
&= \sum_{p>0} \frac{4\hbar^2 k}{m\pi p^2 L} \cos\left(2\pi p \frac{\phi}{\phi_0}\right) \left(\frac{\sin(pkL)}{pkL} - \cos(pkL) \right).
\end{aligned}$$

Meanwhile, the second term in the integral in Eq. 2.16 becomes

$$\begin{aligned}
\partial_\varepsilon^2 \left(\ln \left(1 + \exp \left(-\frac{(\varepsilon - \varepsilon_F)}{k_B T} \right) \right) \right) &= \partial_\varepsilon \left(\frac{-1/k_B T}{1 + \exp((\varepsilon - \varepsilon_F)/k_B T)} \right) \\
&= \left(\frac{1}{k_B T} \right)^2 \left(\frac{\exp((\varepsilon - \varepsilon_F)/k_B T)}{(1 + \exp((\varepsilon - \varepsilon_F)/k_B T))^2} \right) \\
&= \left(\frac{\operatorname{sech}((\varepsilon - \varepsilon_F)/2k_B T)}{2k_B T} \right)^2.
\end{aligned}$$

Using these results the persistent current is

$$\begin{aligned}
I &= -\frac{\partial\Omega}{\partial\phi} \\
&= -\sum_{p>0} \sin\left(2\pi p\frac{\phi}{\phi_0}\right) \int_{-\infty}^{\infty} d\varepsilon \frac{8\hbar^2 k}{mpL\phi_0} \left(\frac{\sin(pkL)}{pkL} - \cos(pkL)\right) \frac{\text{sech}^2((\varepsilon - \varepsilon_F)/2k_B T)}{4k_B T}.
\end{aligned}$$

The last factor

$$-f'(\varepsilon, \varepsilon_F, T) = \frac{\text{sech}^2((\varepsilon - \varepsilon_F)/2k_B T)}{4k_B T} \quad (2.18)$$

is the negative derivative of the Fermi-Dirac distribution and is peaked around the Fermi energy ε_F with characteristic width $k_B T$. The function $-f'(\varepsilon, \varepsilon_F, T)$ is plotted in Fig. 2.5. Typically, the temperatures considered satisfy $k_B T \ll \varepsilon_F$, so the factors of k in the integral over ε will be of order $k_F = \sqrt{2m\varepsilon_F}/\hbar$. Since $k_F L \gg 1$, we can approximate the current as

$$I \approx \sum_{p>0} \sin\left(2\pi p\frac{\phi}{\phi_0}\right) \int_{-\infty}^{\infty} d\varepsilon \frac{8\hbar^2 k}{mpL\phi_0} \cos(pkL) (-f'(\varepsilon, \varepsilon_F, T)). \quad (2.19)$$

The integral $-\int_{-\infty}^{\infty} d\varepsilon f'(\varepsilon, \varepsilon_F, T) = 1$ for all T , while the integrand is $1/k_B T$ at $\varepsilon = \varepsilon_F$. Thus, as temperature decreases, this factor maintains a constant integral while becoming more and more sharply peaked at ε_F and can be represented by $\delta(\varepsilon - \varepsilon_F)$ in the limit $T \rightarrow 0$. In this limit of $T \rightarrow 0$, the current becomes

$$\begin{aligned}
I &= \sum_{p>0} \frac{8\hbar^2 k_F}{mpL\phi_0} \cos(pk_F L) \sin\left(2\pi p\frac{\phi}{\phi_0}\right) \\
&= \sum_{p>0} \left(\frac{e v_F}{L}\right) \frac{4}{\pi p} \cos(pk_F L) \sin\left(2\pi p\frac{\phi}{\phi_0}\right).
\end{aligned} \quad (2.20)$$

If we take $k_F = 2\pi(N + (n + 1)/2)/L$ for $n = 0, 1$, we find

$$I = \sum_{p>0} I_0 \frac{4}{\pi p} (-1)^{p(n+1)} \sin\left(2\pi p\frac{\phi}{\phi_0}\right),$$

which has harmonic coefficients $I_p = I_0 \frac{4}{\pi p} (-1)^{p(n+1)}$. As expected, these coefficients match the $I_{p, N+2n}$ given in Eqs. 2.14 and 2.15 for the case of a fixed number of electrons at zero temperature.

We now evaluate the thermal averaging integral of Eq. 2.19. To evaluate this integral, we

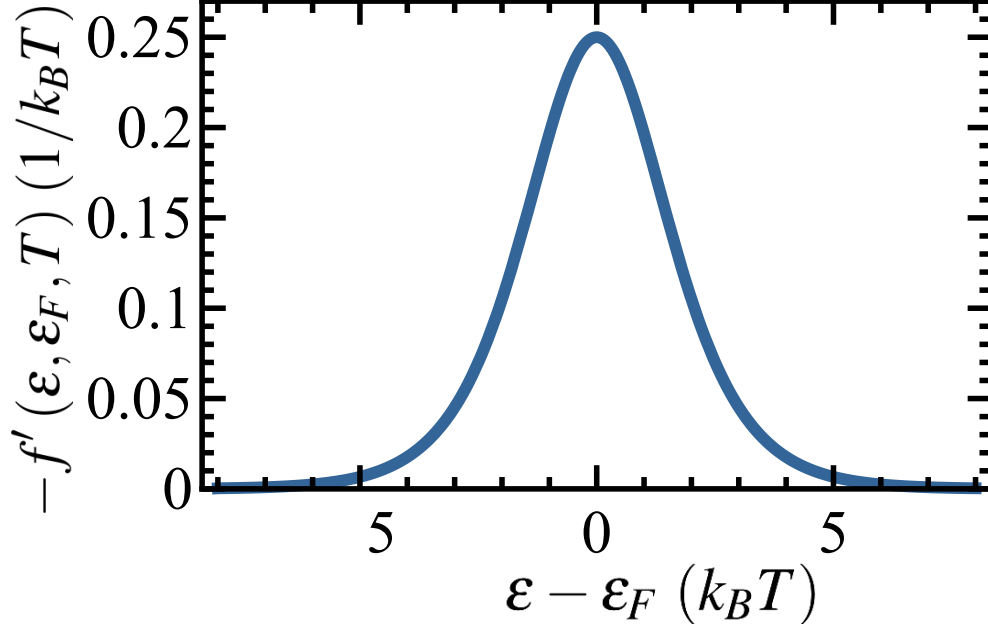


Figure 2.5: The thermal averaging function $-f'(\varepsilon, \varepsilon_F, T)$. The function $-f'(\varepsilon, \varepsilon_F, T)$ represents the weighting of different energy components in the calculation of the thermally averaged persistent current at finite temperature T . The vertical axis is plotted in units of $1/k_B T$ while the horizontal axis is centered on ε_F and in units of $k_B T$. The functional form of $-f'(\varepsilon, \varepsilon_F, T)$ is given in Eq. 2.18.

rewrite the relation $k = \sqrt{2m\varepsilon}/\hbar$ as

$$\begin{aligned}
 k &= \frac{\sqrt{2m\varepsilon_F}}{\hbar} \sqrt{1 + \left(\frac{\varepsilon}{\varepsilon_F} - 1\right)} \\
 &\approx k_F \left(1 + \frac{1}{2} \left(\frac{\varepsilon}{\varepsilon_F} - 1\right) - \frac{1}{8} \left(\frac{\varepsilon}{\varepsilon_F} - 1\right)^2 + \mathcal{O}\left(\left(\frac{\varepsilon}{\varepsilon_F} - 1\right)^3\right) \right). \quad (2.21)
 \end{aligned}$$

Assuming $k_B T \ll \varepsilon_F$, as noted above, the $f'(\varepsilon, \varepsilon_F, T)$ factor in the integral will be sharply peaked around $\varepsilon = \varepsilon_F$ with width of order $k_B T$. Thus, the integrand is appreciable only when $|\frac{\varepsilon}{\varepsilon_F} - 1| \ll 1$. We can thus replace the prefactor k in the integral by k_F . Using Eq. 2.4, we can write $k_F \approx 2\pi N/L$ where $N \gg 1$ is the highest occupied level. Then using Eq. 2.21, we have that the change of the argument of the $\cos(pkL)$ factor in Eq. 2.19 as ε varies from ε_F to $\varepsilon_F + k_B T$ (i.e., over the range over which the thermal averaging function in Fig. 2.5 is appreciable) is

$$pkL - pk_F L \sim \pi N \left(\frac{k_B T}{\varepsilon_F}\right) - \frac{\pi N}{4} \left(\frac{k_B T}{\varepsilon_F}\right)^2.$$

As this factor is in the argument of a cosine, variations small compared to π may be neglected. For

$v_F = 10^6$ m/s, $T = 1$ K, $L = 1 \mu\text{m}$, and $m = 9.1 \times 10^{-31}$, we have $N \sim 10^3$ and $(k_B T / \varepsilon_F) \sim 10^{-5}$.

Thus, we can to good approximation drop all powers of $\varepsilon / \varepsilon_F$ beyond the first. With this linearization of k , Eq. 2.19 gives a current of

$$\begin{aligned}
I &= \sum_{p>0} \sin\left(2\pi p \frac{\phi}{\phi_0}\right) \int_{-\infty}^{\infty} d\varepsilon \frac{8\hbar^2 k_F}{mpL\phi_0} \cos\left(pk_F L + \frac{pk_F L}{2\varepsilon_F} (\varepsilon - \varepsilon_F)\right) (-f'(\varepsilon, \varepsilon_F, T)) \\
&= \sum_{p>0} \sin\left(2\pi p \frac{\phi}{\phi_0}\right) \int_{-\infty}^{\infty} d\varepsilon \frac{4ev_F}{\pi pL} \cos\left(pk_F L + \frac{pk_F L}{2\varepsilon_F} \varepsilon\right) \frac{\text{sech}^2(\varepsilon/2k_B T)}{4k_B T} \\
&= \sum_{p>0} \frac{4}{\pi p} I_0 \sin\left(2\pi p \frac{\phi}{\phi_0}\right) \int_{-\infty}^{\infty} d\varepsilon \cos(pk_F L) \cos\left(\frac{pk_F L}{2\varepsilon_F} \varepsilon\right) \frac{\text{sech}^2(\varepsilon/2k_B T)}{4k_B T} \\
&= \sum_{p>0} \frac{4}{\pi p} I_0 \cos(pk_F L) \sin\left(2\pi p \frac{\phi}{\phi_0}\right) \int_{-\infty}^{\infty} d\varepsilon \exp\left(-i \frac{pk_F L}{2\varepsilon_F} \varepsilon\right) \frac{\text{sech}^2(\varepsilon/2k_B T)}{4k_B T} \\
&= \sum_{p>0} \frac{4}{\pi p} I_0 \cos(pk_F L) \sin\left(2\pi p \frac{\phi}{\phi_0}\right) \int_{-\infty}^{\infty} dx \frac{1}{2} \exp\left(-i \frac{4mpLk_B T}{\hbar^2 k_F} x\right) \text{sech}^2(x)
\end{aligned}$$

In several steps above, we have made use of the symmetry of $\text{sech}(x)$. The last integral is just the Fourier transform of $\text{sech}^2(x)$ which is given in Eq. A.4. Using this relation, the current can be written as

$$I = \sum_{p>0} \left(\frac{4}{\pi p} I_0 \cos(pk_F L)\right) \left(\frac{T/T_p}{\sinh(T/T_p)}\right) \sin\left(2\pi p \frac{\phi}{\phi_0}\right) \quad (2.22)$$

where $T_p = \frac{1}{\pi p k_B} \frac{\hbar^2 k_F}{2m} \frac{k_F}{L}$. We denote the normalized temperature dependence of the harmonics of the single-channel ring as

$$g_1(T/T_p) = \frac{T/T_p}{\sinh(T/T_p)}. \quad (2.23)$$

If we denote the highest index n in Eq. 2.4 for the energy levels ε_n by N , then there are $2N$ levels between the lowest at $\varepsilon \approx 0$ and $\varepsilon_F \approx \hbar^2 N^2 / 2mL^2$. The mean level spacing Δ_1 can be written as

$$\begin{aligned}
\Delta_1 &= \varepsilon_F / 2N \\
&= \frac{\pi^2 \hbar^2 N}{mL^2} \\
&= \frac{\pi \hbar^2 k_F}{2mL}.
\end{aligned}$$

The characteristic temperature of the p^{th} harmonic of the current can be written in terms of Δ_1 as

$$T_p = \frac{1}{k_B} \frac{\hbar^2 k_F}{2\pi m p L} = \frac{1}{k_B} \frac{\Delta_1}{\pi^2 p}. \quad (2.24)$$

For $T > T_p$, the p^{th} harmonic of the current decays exponentially in T .

As we noted when introducing Eq. 2.7, the calculation of the current at finite temperature is performed by taking a weighted sum of the single level currents i_n with each energy level ε_n weighted by the Fermi-Dirac distribution function $f(\varepsilon_n, \varepsilon_F, T)$. In Fig. 2.6, we plot the Fermi-Dirac distribution alongside the energy levels previously shown in Fig. 2.2 for three different temperatures. As the temperature becomes an appreciable fraction of the mean level spacing Δ_1 , adjacent energy levels begin to have comparable thermal occupancy. We found in the previous section that the current contributions of adjacent levels tend to cancel producing at net current at $T = 0$ of the same order as the current in the highest occupied level. Thus, it is quite sensible to expect the current to decay quickly once the spread in energy $k_B T$ of the occupied levels becomes comparable to the spacing between levels and levels with nearly opposite currents are given roughly equal weights.

Fig. 2.7 displays this decay by plotting the magnitude of the p^{th} harmonic

$$I_p(T) = \left(\frac{4}{\pi p} I_0 \cos(pk_F L) \right) \left(\frac{T/T_p}{\sinh(T/T_p)} \right) \quad (2.25)$$

as a function of temperature. Fig. 2.8 shows the decay in a different way by plotting the current I given in Eq. 2.22 as a function of normalized flux ϕ/ϕ_0 for the same values of temperature as used in Fig. 2.6. At finite temperature, the discontinuities in $I(\phi)$ are rounded out. For temperatures $T \gtrsim 0.3\Delta_1/k_B$, the higher harmonics of the current are suppressed resulting in a sinusoidal form for I .

Similar results will hold for the case of the three-dimensional ring in the diffusive regime. In that case, the current begins to decay once the spread in energy of the occupied levels becomes comparable to the correlation energy E_c discussed in the previous section. Likewise, the p^{th} harmonic of the current decays on a characteristic scale T_p which scales as p^{-1} , meaning that for most achievable temperatures the current is sinusoidal to a good approximation.

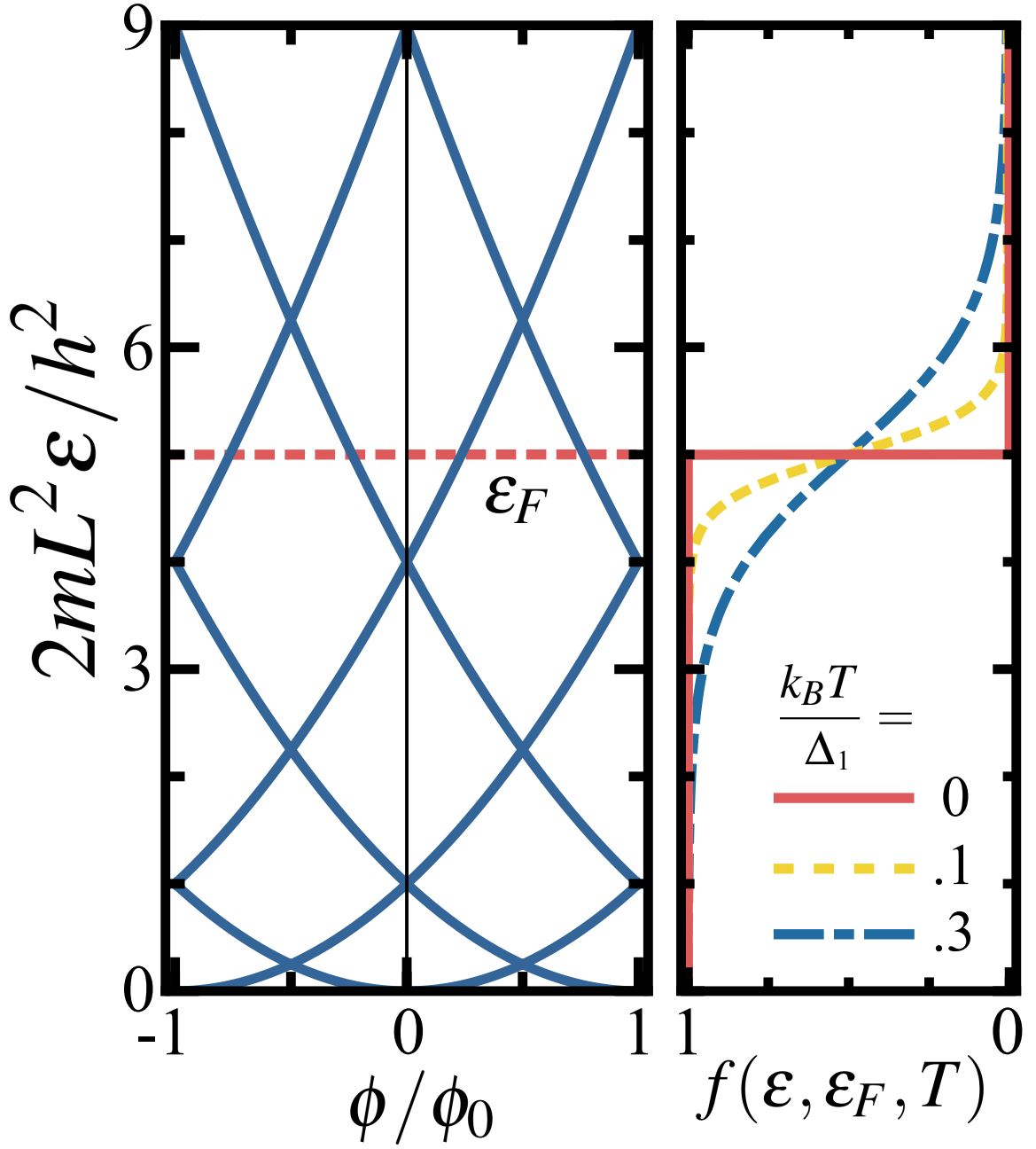


Figure 2.6: Spread of energy level occupancy at finite temperature in an ideal ring. The left plot shows the same energy levels as Fig. 2.2 while the right plot shows the Fermi-Dirac distribution function $f(\varepsilon, \varepsilon_F, T)$ on the horizontal axis for the same vertical axis as the left plot. This vertical energy axis is scaled by $2mL^2/h^2$ so that at $\phi = 0$ the n^{th} energy level should be at n^2 . In the plot on the right, the Fermi-Dirac distribution is plotted for temperatures representing 0 , $0.1\Delta_1/k_B$, and $0.3\Delta_1/k_B$ where Δ_1 is the mean level spacing. For the plot, $2mL^2\varepsilon_F/h^2 = 5$ and $2mL^2\Delta_1/h^2 \approx 2.2$. These small values were chosen for the figure for the sake of clarity, but the expressions derived in the text are only appropriate when these values are $\gg 1$.

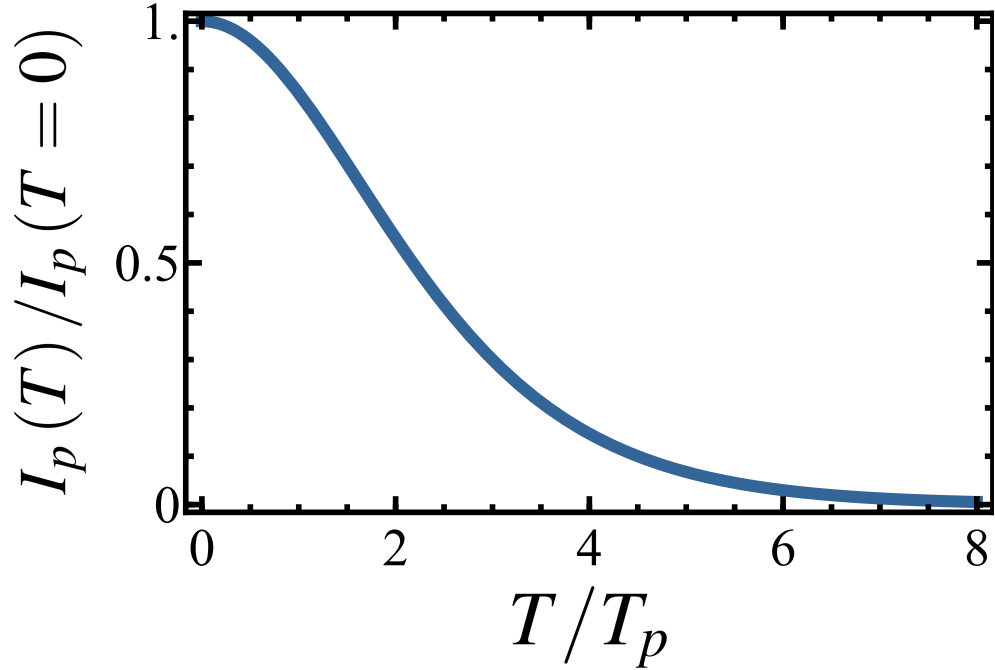


Figure 2.7: Temperature dependence of the harmonics of the persistent current in a one-dimensional ring. The figure plots the magnitude of the p^{th} harmonic I_p (see Eq. 2.25) scaled by its value at $T = 0$ as a function temperature T scaled by the characteristic temperature $T_p = \Delta_1/p\pi^2 k_B$ of the p^{th} harmonic (see Eq. 2.24). At low temperatures, the current is not affected by temperature, but, once $k_B T$ reaches a value of $\sim \Delta_1/p\pi^2$, I_p begins to decay quickly with T/T_p .

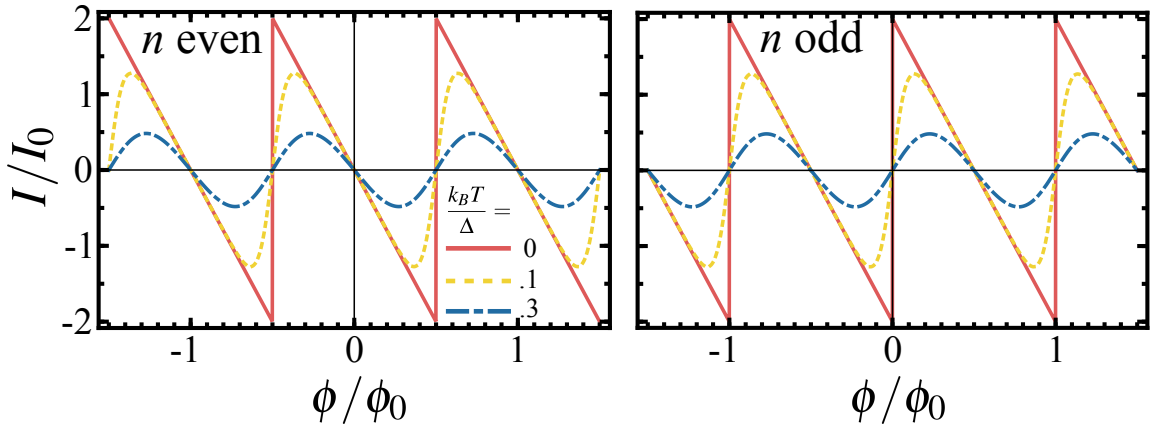


Figure 2.8: Persistent current in a one-dimensional ring versus flux for a series of temperatures. The figure shows I of Eq. 2.22, scaled by $I_0 = ev_F/L$, with $k_F L = 2\pi(N + (n + 1)/2)$ for N and n integers. The top panel corresponds to n even and matches I_{N+0} derived in Eq. 2.8, while the bottom panel corresponds to n odd and thus I_{N+2} of Eq. 2.10. As temperature is increased, the current transitions from a sawtooth to a sinusoid. The three temperatures plotted ($T = 0, 0.1\Delta_1$, and $0.3\Delta_1$ as indicated in the legend) are the same as those of Fig. 2.6.

2.2.2 Finite ring cross-section

We now consider a three-dimensional ring with a finite cross-section. Giving the ring a finite cross-section introduces additional energy bands to the spectrum plotted in Fig. 2.2. For this discussion, we ignore the effects of magnetic flux penetrating the finite cross-section of the ring by considering the applied flux ϕ to be an idealized Aharonov-Bohm flux threading the ring like that introduced at the end of Section 2.1.1. We will describe one way of accounting for the magnetic flux penetrating the metal in 2.3.2.1.

We denote the ring thickness by t and its linewidth by w , with the mean radius still $L/2\pi$. For simplicity, we use the vector potential given in Eq. 2.6. For the function

$$\Lambda(\mathbf{r}) = \int_{\mathbf{r}_0}^{\mathbf{r}} d\mathbf{r}' \cdot \mathbf{A}(\mathbf{r}')$$

we choose $\mathbf{r}_0 = (L/2\pi - w/2)\tilde{\mathbf{x}}$. For the point $\mathbf{r} = x\tilde{\mathbf{x}} + y\tilde{\mathbf{y}} + z\tilde{\mathbf{z}}$ in the argument of Λ , we can first integrate along the path given by $\mathbf{r}_0 + tz\tilde{\mathbf{z}}$ as t goes from 0 to 1 and then along the path from $\mathbf{r}_0 + z\tilde{\mathbf{z}} + t(\sqrt{x^2 + y^2} - (L/2\pi - w/2))\tilde{\mathbf{x}}$ as t goes from 0 to 1. Since \mathbf{A} is parallel to $\tilde{\boldsymbol{\theta}}$ and $d\mathbf{r}'$ is parallel to $\tilde{\mathbf{z}}$ along the first path and $\tilde{\mathbf{r}}$ along the second, both of these integrals are zero. Finally, we integrate along the path $\sqrt{x^2 + y^2}(\cos(\theta')\tilde{\mathbf{x}} + \sin(\theta')\tilde{\mathbf{y}}) + z\tilde{\mathbf{z}}$ for θ' from 0 to $\theta = \tan^{-1}(y/x)$. This final path integration gives

$$\begin{aligned} \Lambda(\mathbf{r}) &= \int_0^\theta \left(\sqrt{x^2 + y^2} \tilde{\boldsymbol{\theta}} d\theta' \right) \cdot \left(\frac{\phi}{2\pi\sqrt{x^2 + y^2}} \tilde{\boldsymbol{\theta}} \right) \\ &= \int_0^\theta d\theta' \left(\frac{\phi}{2\pi} \right) \\ &= \frac{\theta}{2\pi} \phi. \end{aligned}$$

The relation between the gauge transformed wave function ψ' and the untransformed ψ is $\psi' = \exp(i\theta\phi/\phi_0)\psi$.

Solving the time-independent Schrödinger equation

$$-\frac{\hbar^2}{2m} \left(\nabla + i\frac{e}{\hbar} \mathbf{A} \right)^2 \psi = \varepsilon \psi \quad (2.26)$$

boils down to solving

$$\nabla^2 \psi' = -\frac{2m\varepsilon}{\hbar^2} \psi'$$

with ψ' subject to the constraint that it goes smoothly to zero at the edges of the ring and that ψ' is a periodic function of θ up to a factor of $\exp(i\theta\phi/\phi_0)$. This equation can be solved by standard separation of variables. Taking $\psi' = P(r) \exp(i\theta\phi/\phi_0)Q(\theta)Z(z)$, the equation in cylindrical coordinates becomes

$$\frac{1}{P(r)} \frac{1}{r} \frac{\partial}{\partial r} \left(r \frac{\partial P}{\partial r} \right) + \frac{e^{-i\theta\phi/\phi_0}}{Q(\theta)} \frac{1}{r^2} \frac{\partial^2}{\partial \theta^2} \left(e^{i\theta\phi/\phi_0} Q(\theta) \right) + \frac{1}{Z(z)} \frac{\partial^2 Z}{\partial z^2} = -\frac{2m\varepsilon}{\hbar^2}.$$

Since all of the z dependence is contained in one term, that term must be independent of z and $\ddot{Z} = -k_z^2 Z$ for some constant k_z . The function Z must then be some linear combination of the functions $\exp(ik_z z)$ and $\exp(-ik_z z)$. Taking the z coordinate of the ring to range from 0 to t , the boundary conditions $Z(0) = Z(t) = 0$ require $Z = \sin(k_z z)$ with $k_z = \pi n_z/t$ for a positive integer n_z ($-n_z$ gives the same function as n_z).

Writing $\varepsilon(n_z) = \hbar^2 k_z^2/2m$, the Schrödinger equation can be rewritten as

$$\frac{1}{P(r)} r \frac{\partial}{\partial r} \left(r \frac{\partial P}{\partial r} \right) + \frac{e^{-i\theta\phi/\phi_0}}{Q(\theta)} \frac{\partial^2}{\partial \theta^2} \left(e^{i\theta\phi/\phi_0} Q(\theta) \right) = -r^2 \frac{2m(\varepsilon - \varepsilon(n_z))}{\hbar^2}$$

where now the θ dependence has been isolated to one term, so that

$$\frac{\partial^2}{\partial \theta^2} \left(e^{i\theta\phi/\phi_0} Q(\theta) \right) = -a(\phi) e^{i\theta\phi/\phi_0} Q(\theta)$$

must hold for some a . The boundary conditions on $Q(\theta)$ require that it be periodic in θ with period 2π . Thus $Q(\theta)$ must be some linear combination of terms of the form $\exp(in\theta)$.⁷ Each of these terms already satisfies the boundary on its own with $a_n(\phi) = (n + \phi/\phi)^2$ for $Q = \exp(in\theta)$.

Schrödinger's equation can now be rewritten as

$$r^2 \frac{\partial^2 P}{\partial r^2} + r \frac{\partial P}{\partial r} + \left(\frac{2m(\varepsilon - \varepsilon(n_z))}{\hbar^2} r^2 - (n + \phi/\phi)^2 \right) P = 0 \quad (2.27)$$

which bears solutions for P that are linear combinations of $J_{n+\phi/\phi_0}(k_r(n_r, n, \phi)r)$ and $Y_{n+\phi/\phi_0}(k_r(n_r, n, \phi)r)$ (Bessel functions of the first and second kind respectively) for some constant

$$k_r(n_r, n, \phi) = \sqrt{\frac{2m\varepsilon_r}{\hbar^2}}$$

⁷We could denote n by n_θ to follow the convention used with the other indices. We use n in order to emphasize the connection with the index n from the previous sections.

where $\varepsilon_r = \varepsilon - \varepsilon(n_z)$. The radial boundary conditions can be stated as

$$J_{n+\phi/\phi_0}(k_r(n_r, n, \phi)(L/2\pi - w/2)) + C_{n_r} Y_{n+\phi/\phi_0}(k_r(n_r, n, \phi)(L/2\pi - w/2)) = 0$$

and

$$J_{n+\phi/\phi_0}(k_r(n_r, n, \phi)(L/2\pi + w/2)) + C_{n_r} Y_{n+\phi/\phi_0}(k_r(n_r, n, \phi)(L/2\pi + w/2)) = 0$$

for some constant C_{n_r} . These boundary conditions admit a series of possible k_r 's which we index by n_r (justifying the notation introduced above). The k_r satisfy the equation

$$J_{n+\phi/\phi_0}\left(x\left(1 - \frac{\delta}{2}\right)\right) Y_{n+\phi/\phi_0}\left(x\left(1 + \frac{\delta}{2}\right)\right) - J_{n+\phi/\phi_0}\left(x\left(1 + \frac{\delta}{2}\right)\right) Y_{n+\phi/\phi_0}\left(x\left(1 - \frac{\delta}{2}\right)\right) = 0 \quad (2.28)$$

where $x = k_r L/2\pi$ and $\delta = 2\pi w/L$.

In the limit of $2\pi w/L \ll 1$, the values of x satisfying Eq. 2.28 must be large since the arguments of the different Bessel functions must be significantly different for the two terms to cancel. For example, for $2\pi w/L = .3$ and $n = \phi/\phi_0 = 0$, the lowest value of x satisfying Eq. 2.28 is ~ 10 . In the limit of $x \gg \alpha^2$, the Bessel functions take the asymptotic forms⁸

$$J_\alpha(x) \sim \sqrt{\frac{\pi}{2x}} \left(\cos\left(x - \frac{\pi\alpha}{2} - \frac{\pi}{4}\right) - \frac{4\alpha^2 - 1}{8x} \sin\left(x - \frac{\pi\alpha}{2} - \frac{\pi}{4}\right) \right)$$

and

$$Y_\alpha(x) \sim \sqrt{\frac{\pi}{2x}} \left(\sin\left(x - \frac{\pi\alpha}{2} - \frac{\pi}{4}\right) + \frac{4\alpha^2 - 1}{8x} \cos\left(x - \frac{\pi\alpha}{2} - \frac{\pi}{4}\right) \right).$$

Taking

$$\begin{aligned} \alpha &= n + \phi/\phi_0, \\ \beta &= \pi\alpha/2 + \pi/4, \\ x_\pm &= x \left(1 \pm \frac{\delta}{2}\right), \end{aligned}$$

⁸The actual form for the coefficients (ignoring the $\sqrt{\pi/2x}$ term) is $\sum_n \frac{1}{n!} \left(\frac{-1}{8x}\right)^n \prod_{p,\text{odd}}^n (4\alpha^2 - p^2)$ where the sum over n runs over the odd integers for the first term (the cosine term for J_α) and the even integers for the second term (the sine term for J_α) and the index p runs over the first n odd integers (the product is defined to be 1 for $n = 0$). In the text, we give the asymptotic forms keeping up to $n = 1$. In order to drop the $n = 2$ term, it must hold that $(4\alpha^2 - 1)(4\alpha^2 - 9)/(2(8x)^2) \ll 1$. For $\alpha \gtrsim 4$, the condition can be written as $\alpha^4 \ll 8x^2$. For more discussion of the asymptotic form of the Bessel functions, see e.g. Ref. 51.

and $\delta \ll 1$ so that $x \gg \alpha^2$, Eq. 2.28 can be written as

$$\begin{aligned}
0 &= \left(\cos(x_- - \beta) - \frac{4\alpha^2 - 1}{8x_-} \sin(x_- - \beta) \right) \left(\sin(x_+ - \beta) + \frac{4\alpha^2 - 1}{8x_+} \cos(x_+ - \beta) \right) \\
&\quad - \left(\cos(x_+ - \beta) - \frac{4\alpha^2 - 1}{8x_+} \sin(x_+ - \beta) \right) \left(\sin(x_- - \beta) + \frac{4\alpha^2 - 1}{8x_-} \cos(x_- - \beta) \right) \\
&\approx \cos(x_- - \beta) \sin(x_+ - \beta) - \cos(x_+ - \beta) \sin(x_- - \beta) \\
&\quad + \frac{4\alpha^2 - 1}{8} \left(\frac{1}{x_+} - \frac{1}{x_-} \right) (\cos(x_+ - \beta) \cos(x_- - \beta) + \sin(x_- - \beta) \sin(x_+ - \beta))
\end{aligned}$$

Using the Eqs. A.9 and A.10, the condition on x becomes

$$\begin{aligned}
0 &= \sin(x_+ - x_-) + \frac{4\alpha^2 - 1}{8} \left(\frac{x_- - x_+}{x_+ x_-} \right) \cos(x_+ - x_-) \\
&= \sin(x\delta) - \frac{4\alpha^2 - 1}{8} \left(\frac{x\delta}{x^2 (1 - \delta^2/4)} \right) \cos(x\delta) \\
&\approx \sin(x\delta) - \frac{4\alpha^2 - 1}{8} \left(\frac{\delta}{x} \right) \cos(x\delta).
\end{aligned}$$

From the conditions on x and δ , we know that the coefficient of the second term is very small so that the sum of the two terms goes to zero near where the first does at $x = n_r \pi / \delta$ for n_r a non-zero integer. Performing a Taylor expansion on x about $n_r \pi / \delta$, we have to first order in $(x - \pi n_r / \delta)$

$$\begin{aligned}
\sin(x\delta) - \frac{4\alpha^2 - 1}{8} \left(\frac{\delta}{x} \right) \cos(x\delta) &\approx \\
&(-1)^{n_r} \delta \left(x - \frac{n_r \pi}{\delta} \right) - \frac{4\alpha^2 - 1}{8} (-1)^{n_r} \delta \left(\frac{\delta}{n_r \pi} - \left(\frac{\delta}{n_r \pi} \right)^2 \left(x - \frac{n_r \pi}{\delta} \right) \right)
\end{aligned}$$

This expression is equal to zero for

$$\begin{aligned}
x &= \frac{n_r \pi}{\delta} + \frac{4\alpha^2 - 1}{8} \frac{\delta}{n_r \pi} \left(1 + \frac{4\alpha^2 - 1}{8} \left(\frac{\delta}{n_r \pi} \right)^2 \right)^{-1} \\
&\approx \frac{n_r \pi}{\delta} + \frac{4\alpha^2 - 1}{8} \frac{\delta}{n_r \pi}
\end{aligned}$$

where we have dropped terms of the order of δ^3 . Restoring the expressions for x , α and δ , we find the values of k_r are

$$k_r(n_r, n, \phi) = \frac{\pi n_r}{w} - \frac{\pi}{2n_r} \frac{w}{L^2} + \frac{2\pi}{n_r} \frac{w}{L^2} \left(n + \frac{\phi}{\phi_0} \right)^2.$$

Note that Eq. 2.27 is unchanged for $r \rightarrow -r$ and thus for $k_r \rightarrow -k_r$ and $n_r \rightarrow -n_r$. We can restrict the index n_r to be a positive integer without discarding any unique solutions.

Having obtained the form of the eigenfunctions of the Schrödinger equation, we can now write down the eigenvalues. For

$$\begin{aligned} \psi'(n_r, n, \phi, n_z) &= (J_{n+\phi/\phi_0}(k_r(n_r, n, \phi)r) + C(n_r, n, \phi)Y_{n+\phi/\phi_0}(k_r(n_r, n, \phi)r)) \\ &\times \exp\left(i\left(n + \frac{\phi}{\phi_0}\right)\theta\right) \sin\left(\frac{\pi n_z z}{t}\right) \end{aligned} \quad (2.29)$$

with

$$C(n_r, n, \phi) = -\frac{J_{n+\phi/\phi_0}(k_r(n_r, n, \phi)\left(\frac{L}{2\pi} - \frac{w}{2}\right))}{Y_{n+\phi/\phi_0}(k_r(n_r, n, \phi)\left(\frac{L}{2\pi} - \frac{w}{2}\right))},$$

we have

$$\begin{aligned} -\frac{\hbar^2}{2m}\nabla^2\psi' &= -\frac{\hbar^2}{2m}\left(\frac{1}{r}\frac{\partial}{\partial r}\left(r\frac{\partial\psi'}{\partial r}\right) + \frac{1}{r^2}\frac{\partial^2}{\partial\theta^2}(\psi') + \frac{\partial^2\psi'}{\partial z^2}\right) \\ &= \frac{\hbar^2}{2m}(k_r^2(n_r, n, \phi) + k_z^2). \end{aligned}$$

In the limit, $\frac{2\pi w}{L} \ll 1$ discussed in the preceding paragraph, we can write the eigenenergy indexed by (n_r, n, n_z) and parametrized by ϕ as

$$\begin{aligned} \varepsilon(n_r, n, \phi, n_z) &= \frac{\hbar^2}{2m}\left(\left(\frac{\pi n_r}{w} - \frac{\pi}{2n_r}\frac{w}{L^2} + \frac{2\pi}{n_r}\frac{w}{L^2}\left(n + \frac{\phi}{\phi_0}\right)^2\right)^2 + \left(\frac{\pi n_z}{t}\right)^2\right) \\ &\approx \frac{\hbar^2}{2m}\left(\frac{4\pi^2}{L^2}\left(n + \frac{\phi}{\phi_0}\right)^2 + \left(\frac{\pi n_r}{w}\right)^2 - \frac{\pi^2}{L^2} + \left(\frac{\pi n_z}{t}\right)^2\right) \\ &= \frac{\hbar^2}{2mL^2}\left(n + \frac{\phi}{\phi_0}\right)^2 + \frac{\hbar^2 n_r^2}{8mw^2} + \frac{\hbar^2 n_z^2}{8mt^2} - \frac{\hbar^2}{8mL^2}. \end{aligned} \quad (2.30)$$

The first term in Eq. 2.30 matches Eq. 2.4 for the energies of the one-dimensional ring plotted in Fig. 2.2. The other terms offset the energy levels of the one-dimensional ring by an amount that depends on the indices n_r and n_z associated with the transverse dimensions. We refer to the different sets of eigenstates indexed by (n_r, n_z) as “transverse modes,” “subbands,” or “transverse channels.” We also see from Eq. 2.30 that the “one-dimensional limit” is reached when w and t are sufficiently small so that

$$\frac{\hbar^2 n_r^2}{8mw^2}, \frac{\hbar^2 n_z^2}{8mt^2} > \varepsilon_F$$

for $n_r, n_z \geq 2$. In this case, only the lowest transverse mode $n_r = n_z = 1$ is occupied.

When the one-dimensional limit does not hold, several transverse modes will be occupied and the energy spectrum of Fig. 2.2 will be overlaid with additional sets of energy bands offset in ε by amounts determined by n_r, n_z, w , and t as described in Eq. 2.30. In Fig. 2.9, we plot the energy levels of Eq. 2.30 versus flux ϕ for $t^2/L^2 = 1/12$ and $w^2/L^2 \leq 1/144$. As can be seen in the figure, the energy spectrum begins to become complicated as more channels become occupied.

Writing $x = \pi n_r/w$, $y = \pi n_z/w$, and $\varepsilon_F = \hbar^2 k_F^2/2m$, we can rewrite the condition

$$\frac{\hbar^2 n_r^2}{8mw^2} + \frac{\hbar^2 n_z^2}{8mt^2} \leq \varepsilon_F$$

for a channel (n_r, n_z) to be occupied as

$$x^2 + \left(\frac{w}{t}\right)^2 y^2 \leq k_F^2.$$

The total number of occupied levels, M , can be found by summing up all of the occupied levels

$$M = \sum_{n_r, n_z} 1$$

such that

$$\left(\frac{n_r}{w}\right)^2 + \left(\frac{n_z}{t}\right)^2 \leq \frac{8m\varepsilon_F}{\hbar^2}.$$

When $\varepsilon_F \gg \frac{\hbar^2}{8mw^2}, \frac{\hbar^2}{8mt^2}$ (for which $M \gg 1$), the sum over n_r and n_z can be approximated by an integral

$$M \approx \frac{1}{4} \left(\frac{w}{\pi}\right)^2 \iint_{x^2 + \left(\frac{w}{t}\right)^2 y^2 \leq k_F^2} dx dy$$

where the factor of $1/4$ accounts for the fact that $n_r, n_z > 0$. This integral is just the area of an ellipse with major and minor diameters of k_F and $\frac{t}{w}k_F$. Thus,

$$\begin{aligned} M &= \frac{1}{4} \left(\frac{w}{\pi}\right)^2 \left(\pi \frac{t}{w} k_F^2\right) \\ &= \frac{1}{4\pi} w t k_F^2. \end{aligned} \tag{2.31}$$

We now consider the total persistent current in a ring of finite cross-section. As we have seen, each channel (n_r, n_z) possesses the same energy spectrum as the one-dimensional ring considered

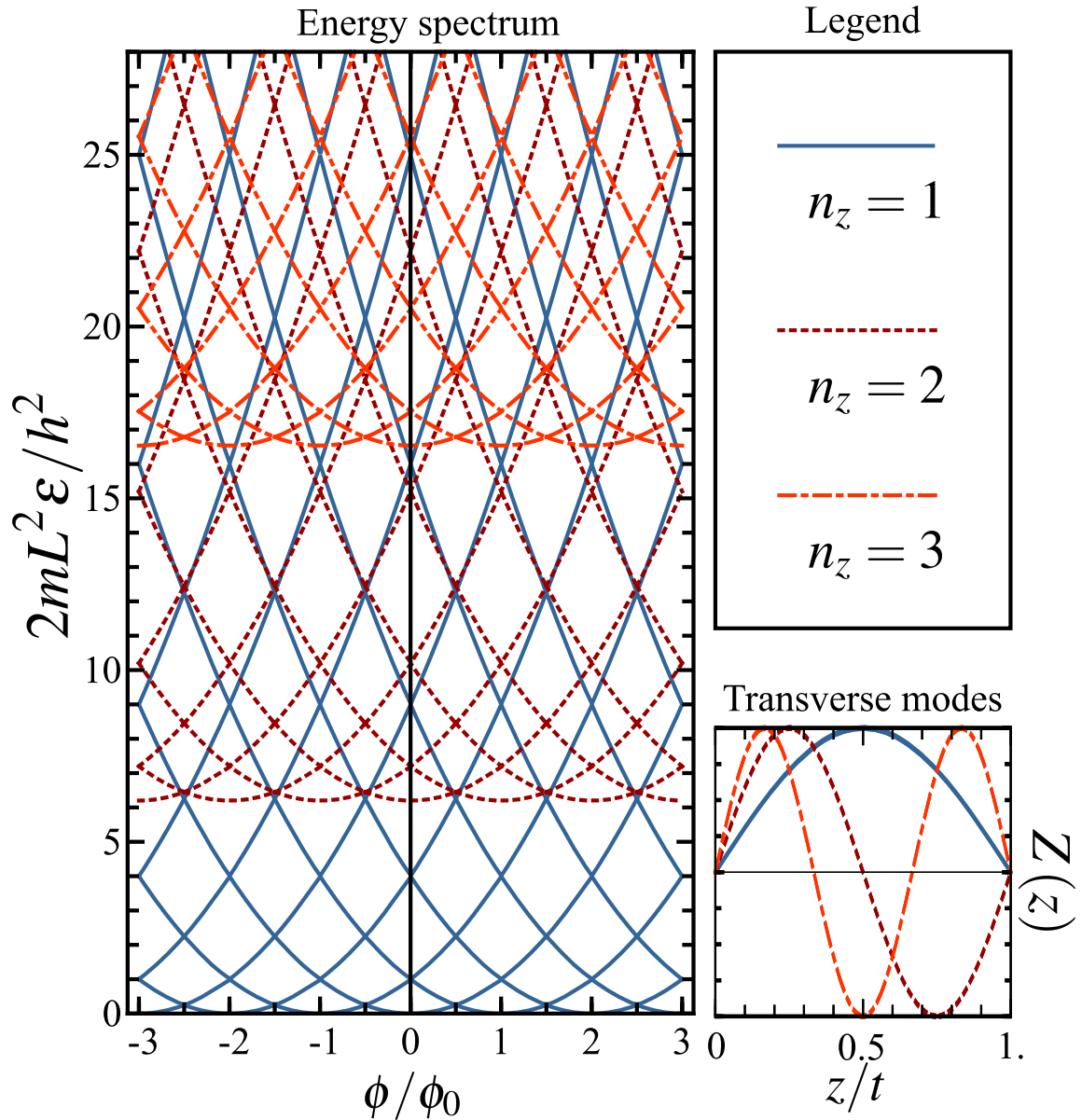


Figure 2.9: Energy levels of a perfect three-dimensional ring. The panel on the left plots the energy levels of the three lowest transverse channels versus flux ϕ for $t/L = 0.38$ and $w/L \leq 0.16$ (so that only $n_r = 1$ is shown). The three channels plotted correspond to $n_z = 1, 2, 3$ and $n_r = 1$. The energy axis has been shifted so that the lowest energy level within the ring is at $\varepsilon = 0$. All levels within one channel are plotted in the same style as indicated by the legend on the right. Below the legend, the transverse mode shape $Z(z) = \sin(n_z\pi z/t)$ along the z direction is shown. When w and t are of comparable dimensions and ε_F is high enough to allow many modes to be occupied, the energy spectrum becomes very dense.

in previous sections with only the energy offset

$$\varepsilon_M(n_r, n_z) = \frac{\hbar^2 n_r^2}{8mw^2} + \frac{\hbar^2 n_z^2}{8mt^2} - \frac{\hbar^2}{8mL^2}$$

varying from channel to channel. Thus the total current of any single channel is given by Eq. 2.22 with k_F replaced by

$$k_{F,M}(n_r, n_z) = \sqrt{\frac{2m}{\hbar^2} (\varepsilon_F - \varepsilon_M(n_r, n_z))}. \quad (2.32)$$

The expression for the current becomes

$$\begin{aligned} I_M &= \sum_{n_r, n_z} \sum_{p>0} I_{p,M}(n_r, n_z) \sin\left(2\pi p \frac{\phi}{\phi_0}\right) \\ &= \sum_{n_r, n_z} \sum_{p>0} \left(\frac{4}{\pi p} \left(\frac{e\hbar}{mL} k_{F,M}\right) \cos(pk_{F,M}L)\right) \left(\frac{T/T_p(k_{F,M})}{\sinh(T/T_p(k_{F,M}))}\right) \sin\left(2\pi p \frac{\phi}{\phi_0}\right) \end{aligned} \quad (2.33)$$

with

$$T_p(k_{F,M}) = \frac{1}{\pi p k_B} \frac{\hbar^2 k_{F,M}}{2m} \frac{1}{L}$$

For the case of many occupied channels ($M \gg 1$) and large aspect ratio ($L \gg w, t$), the quantity $k_{F,M}L$ can depend strongly on the dimensions of the ring and the channel indices (n_r, n_z). To see this, we note that for channels (n_r, n_z) with $\varepsilon_M \ll \varepsilon_F$

$$\begin{aligned} k_{F,M}(n_r + 1, n_z) &= \sqrt{\frac{2m}{\hbar^2} \left(\varepsilon_F - \varepsilon_M(n_r, n_z) - \frac{\hbar^2(2n_r + 1)}{8mw^2}\right)} \\ &\approx \sqrt{\frac{2m}{\hbar^2} \varepsilon_F} \left(1 - \frac{1}{2} \frac{\pi^2 \hbar^2 (2n_r + 1)}{2mw^2 \varepsilon_F}\right) \\ &\approx k_{F,M}(n_r, n_z) - \frac{\pi^2 (2n_r + 1)}{2w^2 k_F}. \end{aligned}$$

Thus, the variation in $k_{F,M}L$ satisfies

$$\begin{aligned} \Delta(k_{F,M}L) &= k_{F,M}(n_r + 1, n_z)L - k_{F,M}(n_r, n_z)L \\ &= -\frac{\pi^2}{2} (2n_r + 1) \left(\frac{L}{w}\right) \left(\frac{1}{k_F w}\right). \end{aligned}$$

For a ring with roughly symmetric cross-section, the condition $M \gg 1$ implies $k_F w, k_F t \gg 2\sqrt{\pi}$, so the expression above is the product of a large quantity L/w and a small quantity $(k_F w)^{-1}$. (A similar expression is of course possible for the other channel index by replacing n_r with n_z)

and w with t). To estimate $\Delta(k_{F,M}L)$, we use the typical values for a metal of $v_F = 10^6$ m/s and $m = 10^{-30}$ kg and for standard lithographically realizable dimensions $w = 60 \times 10^{-9}$ m and $L = 2 \times 10^{-6}$ m. Then we have $k_F = mv_F/h = 9 \times 10^9$ m⁻¹, $M \sim 2 \times 10^5$, the number of electrons per channel $N_M \sim 5 \times 10^4$ and

$$\Delta(k_{F,M}L) = -0.3(2n_{r,z} + 1).$$

Thus the argument of the $\cos(pk_{F,M}L)$ factor in Eq. 2.33 for the current of the multichannel ring can vary by $\gg \pi$ from channel to channel with the exact magnitude of the variation depending on w/L , t/L , k_F , and the channel indices n_r and n_z . This large variation leads to a lack of correlation in the sign of the current in channels with similar values of $k_{F,M}$. Similarly, when varying w , t , or k_F over a small range about its typical value, we expect $\cos(pk_{F,M}L)$ to vary between -1 and 1. We would thus expect the average current of each channel to be zero upon averaging over such a small range of w , t , or k_F . Since the sign of the current in nearby channels is uncorrelated, the total current should also average to zero.

Since the current I_M varies strongly with the ring dimensions and the Fermi level, we consider its typical value $\overline{I_M^2}$, where the average $\overline{\dots}$ is over some range of parameters sufficient to produce a range of uncorrelated values for $\cos(pk_{F,M}L)$ between the different channels. In this case, each $I_{p,M}(n_r, n_z)$ in Eq. 2.33 is uncorrelated and we have

$$\begin{aligned} \overline{I_M^2} &= \overline{\left(\sum_{n_r, n_z} \sum_{p>0} I_{p,M}(n_r, n_z) \sin\left(2\pi p \frac{\phi}{\phi_0}\right) \right)^2} \\ &= \sum_{n_r, n_z} \sum_{p>0} \overline{I_{p,M}^2}(n_r, n_z) \sin^2\left(2\pi p \frac{\phi}{\phi_0}\right) \\ &= \sum_{p>0} \left(\frac{4}{\pi p} \frac{e\hbar}{mL}\right)^2 \left(\sum_{n_r, n_z} k_{F,M}^2 \overline{\cos^2(pk_{F,M}L)} \left(\frac{T/T_p(k_{F,M})}{\sinh(T/T_p(k_{F,M}))}\right)^2 \right) \sin^2\left(2\pi p \frac{\phi}{\phi_0}\right) \\ &= \sum_{p>0} \frac{1}{2} \left(\frac{4}{\pi p} \frac{e\hbar}{mL}\right)^2 \left(\sum_{n_r, n_z} k_{F,M}^2 \left(\frac{T/T_p(k_{F,M})}{\sinh(T/T_p(k_{F,M}))}\right)^2 \right) \sin^2\left(2\pi p \frac{\phi}{\phi_0}\right) \\ &= \sum_{p>0} \overline{I_{p,M}^2} \sin^2\left(2\pi p \frac{\phi}{\phi_0}\right) \end{aligned}$$

where we have averaged the \cos^2 term to 1/2 and otherwise left the expressions for $k_{F,M}$ unchanged, assuming that the average over the small range of $k_{F,M}$ of these slowly varying expressions is roughly

equal to their value evaluated at the mean $k_{F,M}$.⁹ The quantity $T_p(k_{F,M})$ is

$$\begin{aligned} T_p(k_{F,M}) &= \frac{1}{\pi p k_B} \frac{\hbar^2}{2m} \frac{k_{F,M}(n_r, n_z)}{L} \\ &= \frac{k_{F,M}}{k_F} T_p, \end{aligned}$$

where T_p is the characteristic temperature of the single channel ring with the same Fermi energy ε_F as the three-dimensional ring under consideration. In the limit $M \gg 1$, the sum over channels can be replaced by an integral. We first evaluate this integral at $T = 0$ to find

$$\begin{aligned} \sum_{n_r, n_z} k_{F,M}^2 &= \frac{1}{4} \int_{k_r^2 + k_z^2 \leq k_F^2} dk_r dk_z \left(\frac{wt}{\pi^2} \right) (k_F^2 - k_r^2 - k_z^2) \\ &= \frac{wt}{4\pi^2} \int_0^{k_F} dk \int_0^{2\pi} d\theta k (k_F^2 - k^2) \\ &= \frac{wt}{2\pi} k_F^4 \int_0^1 dx x (1 - x^2) \\ &= \frac{wt}{2\pi} \frac{k_F^4}{4}. \end{aligned}$$

We can thus write the typical magnitude of the p^{th} harmonic of the current for the multichannel ring at $T = 0$ as

$$\begin{aligned} I_{p,M}^{\text{typ}} &= \sqrt{I_{p,M}^2} \tag{2.34} \\ &= \left(\frac{1}{4} \left(\frac{4}{\pi p} \right)^2 \left(\frac{e\hbar}{mL} k_F \right)^2 \left(\frac{wt k_F^2}{4\pi} \right) \right)^{1/2} \\ &= \frac{\sqrt{M}}{2} \left(\frac{4}{\pi p} I_0 \right), \end{aligned}$$

which is $\sqrt{M}/2$ times the magnitude of the single channel value given in Eqs. 2.14 and 2.15. The typical current of the perfect ring grows as the number of transverse channels is increased.

⁹Replacing $\cos^2(pk_{F,M}L)$ by $1/2$ is correct for the grand canonical ensemble where $k_{F,M}$ can vary freely. For the canonical ensemble, the $\cos(pk_{F,M}L)$ must be ± 1 so $\cos^2(pk_{F,M}L)$ should be replaced by 1 in the average and in this case I_M^2 is a factor of 2 larger. Our temperature dependence is appropriate only for the grand canonical ensemble.

In the case of finite temperature, the sum over channels becomes

$$\begin{aligned}
\sum_{n_r, n_z} k_{F,M}^2 \left(\frac{T/T_p(k_{F,M})}{\sinh(T/T_p(k_{F,M}))} \right)^2 &= \frac{wt}{4\pi^2} \int_0^{k_F} dk \int_0^{2\pi} d\theta k k_{F,M}^2 \left(\frac{T}{k_{F,M} T_p / k_F} \right)^2 \frac{1}{\sinh^2 \left(\frac{T}{k_{F,M} T_p / k_F} \right)} \\
&= \frac{wt}{4\pi^2} \int_0^{k_F} dk \int_0^{2\pi} d\theta k \frac{k_F^2 (T/T_p)^2}{\sinh^2 \left(\frac{T}{T_p} \left(1 - \frac{k^2}{k_F^2} \right)^{-1/2} \right)} \\
&= \left(\frac{wt k_F^4}{2\pi \cdot 4} \right) \left(4 \left(\frac{T}{T_p} \right)^2 \int_0^1 dx \frac{x}{\sinh^2 \left(\frac{T}{T_p} (1-x^2)^{-1/2} \right)} \right).
\end{aligned}$$

For the single channel ring, we wrote T_p in terms of the mean level spacing Δ_1 in Eq. 2.24. For the multichannel ring, we can calculate $\Delta_{1,M}$, the mean level spacing within a single channel by averaging Δ_1 over all occupied channels. This averaging gives

$$\begin{aligned}
\Delta_{1,M} &= \frac{\pi \hbar^2}{2mL} \left(\frac{1}{M} \sum_{n_r, n_z} k_{F,M}(n_r, n_z) \right) \\
&= \frac{\pi \hbar^2}{2mL} \left(\frac{1}{M} \left(\frac{wt}{\pi^2} \right) \left(\frac{2\pi}{4} \right) \int_0^{k_F} dk k \sqrt{k_F^2 - k^2} \right) \\
&= \frac{\pi \hbar^2}{2mL} \left(\frac{1}{M} \left(\frac{wt}{4\pi} \right) 2k_F^3 \int_0^1 dx x \sqrt{1-x^2} \right) \\
&= \frac{\pi \hbar^2}{2mL} \left(2k_F \int_0^{\pi/2} d\theta \cos^2 \theta \sin \theta \right) \\
&= \frac{2}{3} \Delta_1.
\end{aligned}$$

We could also define a characteristic temperature $T_{p,M}$ in analogy to Eq. 2.24 by

$$\begin{aligned}
T_{p,M} &= \frac{1}{k_B} \frac{\Delta_{1,M}}{\pi^2 p} \\
&= \left(\frac{2}{3} \right) \frac{1}{k_B} \frac{\Delta_1}{\pi^2 p} \\
&= \left(\frac{2}{3} \right) T_p.
\end{aligned} \tag{2.35}$$

However, since this temperature scale differs from that of the single channel ring by a simple numerical factor, we continue to use T_p for simplicity. Defining

$$g_M^2 \left(\frac{T}{T_p} \right) = 4 \left(\frac{T}{T_p} \right)^2 \int_0^1 dx \frac{x}{\sinh^2 \left(\frac{T}{T_p} (1-x^2)^{-1/2} \right)}, \tag{2.36}$$

the typical magnitude of the p^{th} harmonic of the current for the multichannel ring is

$$I_{p,M}^{\text{typ}} = \frac{\sqrt{M}}{2} \left(\frac{4}{\pi p} I_0 \right) g_M \left(\frac{T}{T_p} \right). \quad (2.37)$$

The function $g_M(y)$ does not have a closed analytic form.¹⁰ In Fig. 2.10, we plot $g_M(T/T_p)$ as well as $g_1(1.2T/T_p)$. The function $g_1(T/T_p)$ was defined in Eq. 2.23 to give the normalized temperature dependence of the single channel ring. The factor of 1.2 was chosen so that the two curves agree over the range $T/T_p \lesssim 1$ shown. This agreement indicates that the temperature dependence of the multichannel ring is determined by the single-channel level spacing $\Delta_{1,M}$ rather than the average level spacing Δ_M across all levels

$$\begin{aligned} \Delta_M &= \frac{\Delta_{1,M}}{M} \\ &= \frac{4\pi}{3} \frac{1}{wtk_F^2} \frac{\hbar v_F}{L}, \end{aligned} \quad (2.38)$$

which depends on the transverse dimensions of the ring.

The correspondence between the temperature dependence of the single-channel and multichannel rings is due to the fact that the levels within a given channel are all anti-correlated as described in Section 2.2.1 while we have taken different channels to be uncorrelated. From the assumption of no correlation between different channels, it follows that the current from levels in different channels does not add up to a net average current and so does not cancel out with the thermal broadening of the energy range over which levels are partially occupied.

The decay with temperature of the multichannel ring is stronger than the single channel ring by a factor of ~ 1.2 . To explain this stronger decay, we note that, in the limit of many electrons, the mean level spacing $\Delta_{1,M}(n_r, n_z)$ of the lowest indexed channel ($n_r = 1, n_z = 1$) is approximately the same as the mean level spacing Δ_1 of a single-channel ring with the same Fermi energy. For higher indexed channels, the mean level spacing $\Delta_{1,M}(n_r, n_z)$ is smaller and so is the characteristic temperature of decay for that channel. Since the current in the higher channels decays more quickly than the single channel current, the current summed over all channels does as well.

The results of this section for the multichannel ring provide a striking contrast to those found for a ring in the diffusive limit. Here we found that the typical magnitude of the current scales with the square-root of the number of transverse channels. In the diffusive regime, the current magnitude

¹⁰At least, my efforts to find one were unsuccessful.

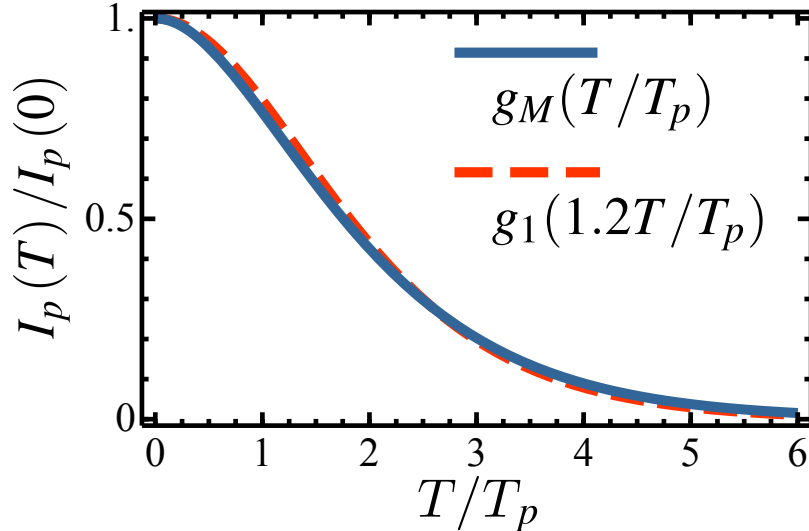


Figure 2.10: Temperature dependence of a perfect three-dimensional ring. The solid curve gives the normalized temperature dependence g_M of the typical p^{th} harmonic of the current for the three-dimensional ring as given by Eq. 2.36 in the text. The dashed curve gives the normalized magnitude g_1 of the p^{th} harmonic of the current for the single channel ring defined in Eq. 2.23. The temperature axis is scaled by the characteristic temperature T_p , which was defined in Eq. 2.24. The argument of the single channel ring function g_1 was scaled by an additional factor of 1.2 so that the two curves would overlap.

is independent of the number of transverse channels. As we will see in the next section, disorder distorts the shape of the individual energy levels. This distortion leads to correlation between levels from different channels but near each other in energy and destroys the anti-correlation of the levels within a single channel because the energy scale E_c of the correlation is less than Δ_1 .¹¹ Thus, the different channels no longer make large, uncorrelated contributions to the current. In the presence of disorder the total current magnitude is actually a fraction of the disorder-free single channel current. As discussed in Section 2.2.1, the temperature dependence in the diffusive regime is set by the correlation scale E_c . Since $E_c < \Delta_1$, the decay of the current with temperature is also stronger in the diffusive regime. Similar results to the ones discussed in this section were obtained in 1970 by Kulik for a two-dimensional ring ($w \ll t, L$) [52]. For a more detailed account of the finite cross-section ring, see Ref. [37].

¹¹The relationship between E_c and Δ_1 is not obvious at this point in our discussion. In Eq. 2.57, we will define $E_c = \hbar D/L^2$. The correlation energy E_c can be rewritten in terms of Δ_1 as $E_c = (2/\pi)(l_e/L)\Delta_1$ where the elastic mean free path l_e is a measure of the strength of the disorder (we note though that this definition of E_c was chosen for its notational simplicity. In Fig. 2.16, it can be seen that the energy levels are actually correlated on a scale of $\sim 10E_c$). In the diffusive regime, $l_e \ll L$, and thus $E_c \ll \Delta_1$.

2.2.3 Introduction of disorder

Before discussing the diffusive regime in the next section, we make a few general remarks about the introduction of disorder to the perfect ring which has been considered in this section.

First we examine the effect of disorder on two levels in the energy spectrum (Figs. 2.2, 2.6, and 2.9). We label states by $|\psi_1\rangle$ and $|\psi_2\rangle$ and their flux-dependent energies by $\varepsilon_1(\phi)$ and $\varepsilon_2(\phi)$. In the $[|\psi_1\rangle, |\psi_2\rangle]$ basis, we can write the unperturbed Hamiltonian as

$$\hat{H}_0(\phi) = \begin{bmatrix} \varepsilon_1(\phi) & 0 \\ 0 & \varepsilon_2(\phi) \end{bmatrix}.$$

We consider the effect of introducing a spatially-dependent disorder potential

$$\hat{V} = \begin{bmatrix} V_{11} & V_{12} \\ V_{12}^* & V_{22} \end{bmatrix}$$

to the Hamiltonian $\hat{H} = \hat{H}_0 + \hat{V}$, where

$$\begin{aligned} V_{ij} &= \langle \psi_i | \hat{V} | \psi_j \rangle \\ &= \int_{R-w/2}^{R+w/2} dr \int_0^t dz \int_0^{2\pi} d\theta r \psi_i^*(n_{ri}, n_i, \phi, n_{zi}) V(r, \theta, z) \psi_j'(n_{rj}, n_j, \phi, n_{zj}) \end{aligned} \quad (2.39)$$

where $\psi_j'(n_{rj}, n_j, \phi, n_{zj})$ is the eigenfunction (with (r, θ, z) dependence suppressed) given in Eq. 2.29.

The diagonal values V_{11} and V_{22} merely shift ε_1 and ε_2 and can be absorbed into these terms by taking $\varepsilon_i + V_{ii} \rightarrow \varepsilon_i$. Dropping the explicit use of V_{ii} , the Hamiltonian in the presence of disorder is

$$\hat{H}(\phi) = \begin{bmatrix} \varepsilon_1(\phi) & V_{12} \\ V_{12}^* & \varepsilon_2(\phi) \end{bmatrix}.$$

In the presence of \hat{V} , the Hamiltonian is no longer diagonalized, indicating that $\{|\psi_1\rangle, |\psi_2\rangle\}$ are no longer the energy eigenstates. Instead \hat{V} produces mixed eigenstates which are linear combinations of the form $A|\psi_1\rangle + B|\psi_2\rangle$. From Eq. 2.39 and the orthogonality of the different factors of the eigenstates as expressed in Eq. 2.29, some general conclusions can be reached about the effect of \hat{V} on the energy levels. In order for \hat{V} to mix two levels from different orbitals $n_1 \neq n_2$, it

must have a non-zero Fourier component $\tilde{V}(n_1 - n_2, r, z) \neq 0$ when expanded in a Fourier series $V(r, \theta, z) = \sum_n \tilde{V}(n, r, z)e^{in\theta}$. Additionally, to mix levels from different channels $V(r, \theta, z)$ can not be uniform in r and z , $V(r, \theta, z) \neq V(\theta)$, since the transverse eigenfunctions are themselves orthogonal in (r, z) .

The new eigenenergies are found by solving

$$\begin{aligned} 0 &= \det \left[\hat{H} - \lambda \hat{I} \right] \\ &= (\varepsilon_1 - \lambda)(\varepsilon_2 - \lambda) - |V_{12}|^2 \\ &= \lambda^2 - (\varepsilon_1 + \varepsilon_2)\lambda + \varepsilon_1\varepsilon_2 - |V_{12}|^2. \end{aligned}$$

Setting $V^2 = |V_{12}|^2$, the quadratic formula gives the new eigenenergies λ_{\pm} as

$$\begin{aligned} \lambda_{\pm} &= \frac{1}{2}(\varepsilon_1 + \varepsilon_2) \pm \frac{1}{2}\sqrt{(\varepsilon_1 + \varepsilon_2)^2 - 4\varepsilon_1\varepsilon_2 + 4V^2} \\ &= \frac{1}{2}(\varepsilon_1 + \varepsilon_2) \pm \frac{1}{2}\sqrt{(\varepsilon_1 - \varepsilon_2)^2 + 4V^2}. \end{aligned} \quad (2.40)$$

When $|\varepsilon_1 - \varepsilon_2| \gg 2V$, the new eigenenergies match the original ones, with $\lambda_+ \approx \max(\varepsilon_1, \varepsilon_2)$ and $\lambda_- \approx \min(\varepsilon_1, \varepsilon_2)$. When $\varepsilon_1 \approx \varepsilon_2 = \varepsilon_D$, the new eigenenergies are split from the degenerate value ε_D by $2V$, $\lambda_{\pm} \approx \varepsilon_D \pm V$. When the ε_i are functions of some parameter ϕ so that $|\varepsilon_1 - \varepsilon_2|$ changes as well, the splitting of (λ_+, λ_-) at a point in ϕ where $|\varepsilon_1 - \varepsilon_2| \rightarrow 0$ is referred to as an ‘‘avoided crossing.’’ Taking $\varepsilon_2 > \varepsilon_1$, we can write

$$\lambda_+ = \varepsilon_2 + \frac{1}{2} \left(\sqrt{(\varepsilon_2 - \varepsilon_1)^2 + 4V^2} - (\varepsilon_2 - \varepsilon_1) \right) \quad (2.41)$$

$$\lambda_- = \varepsilon_1 - \frac{1}{2} \left(\sqrt{(\varepsilon_2 - \varepsilon_1)^2 + 4V^2} - (\varepsilon_2 - \varepsilon_1) \right) \quad (2.42)$$

from which it is easily seen that the deviations from $(\varepsilon_1, \varepsilon_2)$ are always $\leq V$. Since V only changes the levels close to each other, this two-level analysis can be extended to many levels as long as V is small enough that only two adjacent levels are ever within V of each other at a time (otherwise a treatment handling the three or more relevant levels would be necessary).

As a special case, we note that for $\varepsilon_{1,2} = (\pm n + \phi)^2$ (which is the case of the one-dimensional

ring with $\hbar^2/2mL^2$ and ϕ_0 set to 1) the eigenenergies are

$$\begin{aligned}\lambda_{\pm} &= \frac{1}{2} \left((n + \phi)^2 + (n - \phi)^2 \right) \pm \frac{1}{2} \sqrt{\left((n + \phi)^2 - (n - \phi)^2 \right)^2 + 4V^2} \\ &= (\phi^2 + n^2) \pm \sqrt{2n^2\phi^2 + V^2}.\end{aligned}$$

Near the crossing at $\phi = 0$, the eigenenergies become to lowest order in ϕ

$$\begin{aligned}\lambda_{\pm} &\approx (\phi^2 + n^2) \pm \left(V + \frac{n^2\phi^2}{V} \right) \\ &= n^2 \pm V + \left(1 \pm \frac{n^2}{V} \right) \phi^2.\end{aligned}$$

All energy level crossings¹² for the one-dimensional ring are of this form and thus all crossings in the spectrum are replaced by these quadratic avoided crossings, as indicated in Fig. 2.11. In that figure, it can be seen that the kinks in the energy levels are smoothed out while the ϕ_0 periodicity of the spectrum is maintained, as expected from the discussion in Section 2.1.1. It can also be seen that this smoothing reduces the range of energy ε and energy slope $\partial\varepsilon/\partial\phi$ experienced by each level. Since the current in a given level is proportional to this slope, the disorder reduces the single level currents and the total current as a result.

In Fig. 2.12, the energy spectrum of the multichannel ring shown in Fig. 2.9 is replotted for the case of a disordered ring. The energy levels were calculated by applying Eq. 2.40 to each pair of intersecting unperturbed levels.¹³ The same disorder potential V ($V_{ij} = 0.2\hbar^2/2mL^2$ for each pair of levels $i \neq j$ and $V_{ii} = 0$ for each level i) as used in Fig. 2.11 was employed for this figure so the low-lying levels ($\varepsilon < 5\hbar^2/2mL^2$) of Fig. 2.12 reproduce Fig. 2.11. At higher energies the density of levels increases. Each individual level represents the result several avoided crossings and takes on quite a complicated, but still periodic, flux dependence. As was the case for the single channel ring of Fig. 2.11, the disorder smooths out the energy levels and so reproduces the associated single level currents.

¹²Pairs of levels degenerate at $\phi = m\phi_0/2$ with $m \neq 0$ can be put in this form by shifting ϕ by $-m\phi_0/2$.

¹³More precisely, for two levels ε_1 and ε_2 which cross at ϕ_c and for which $\varepsilon_1 < \varepsilon_2$ when $\phi < \phi_c$, the quantity

$$\frac{1}{2} \left(\sqrt{(\varepsilon_2 - \varepsilon_1)^2 + 4V^2} - (\varepsilon_2 - \varepsilon_1) \right) \quad (2.43)$$

was subtracted from level ε_1 and added to ε_2 in order to create two new perturbed levels (see Eqs. 2.41 and 2.42). For levels undergoing multiple crossings, this procedure was repeated for each crossing with a term such as the one in Eq. 2.43 above being added or subtracted at each crossing. In calculating the new levels, the terms given by Eq. 2.43 were calculated using the unperturbed levels. Thus the figure does not include the second order effects that occur when two distant unperturbed levels are shifted by other levels close enough to each other that they should be subject to a repulsion away from each other as well.

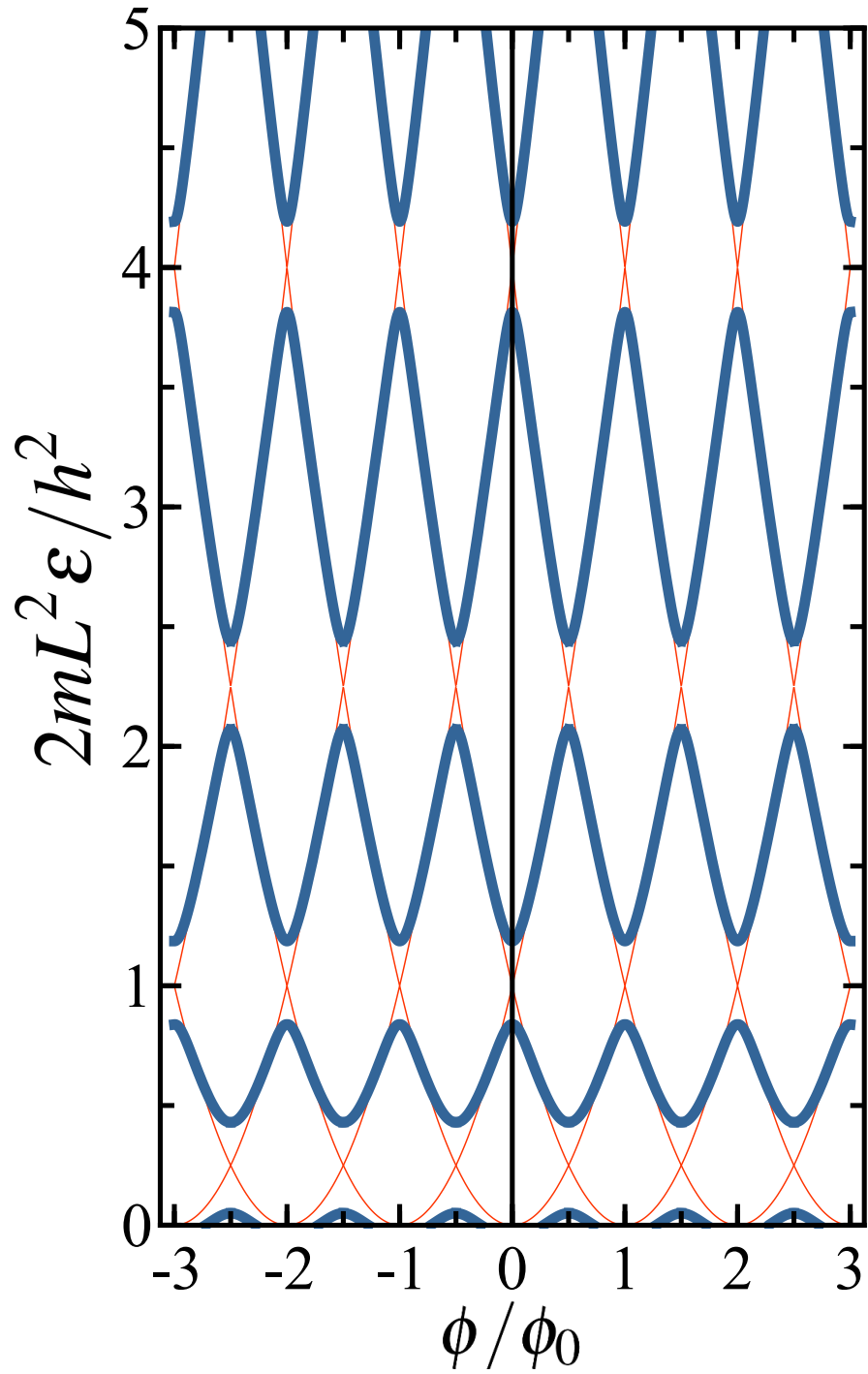


Figure 2.11: Energy spectrum of a disordered one-dimensional ring. The thick lines show the energy levels calculated using Eq. 2.40 with $V_{ij} = 0.2\hbar^2/2mL^2$ for each pair of levels $i \neq j$ and $V_{ii} = 0$ for each level i . The thinner lines reproduce the unperturbed ($V = 0$) spectrum of the one-dimensional ring shown in Figs. 2.2 and 2.3.

As the ratio V/Δ_M of the disorder strength V to the level spacing Δ_M is increased to ~ 1 , the two-level picture no longer remains valid. The disorder induced level repulsion becomes strong enough to push one of the two repulsed levels into a third nearby level. Since the avoided crossing derivation is quite general, it is also valid for the level pushed into the third level and they repel each other as well. When this multi-level repulsion occurs for many levels, neighboring levels become correlated on an energy scale set by the disorder. Also, the long-range anti-correlation of the levels of each unperturbed channel noted previously is destroyed. The effect of this energy level correlation on the total persistent current is addressed in the next section.

It is possible to obtain a quantitative expression for the effect of weak disorder within the framework introduced in this section for the ideal ring. To show this, we use the result from Eq. B.17 for a Gaussian disorder potential characterized by an elastic scattering time τ_e . In the weak disorder limit $k(\varepsilon)l_e \gg 1$ (where $l_e = v_F\tau_e$ is the elastic mean free path), the disorder averaged density of states $\nu(\varepsilon)$ is related to the density of states¹⁴ $\nu_0(\varepsilon)$ in the absence of disorder by

$$\nu(\varepsilon) = \int_0^\infty d\varepsilon' \nu_0(\varepsilon') b_L\left(\varepsilon - \varepsilon', \frac{\hbar}{2\tau_e}\right)$$

where $b_L(\varepsilon, \delta)$ is the Lorentzian function

$$b_L(\varepsilon, \delta) = \frac{1}{\pi} \frac{\delta}{\varepsilon^2 + \delta^2}.$$

In Section 2.2.1, we argued that the grand canonical potential Ω expressed in Eq. 2.16 could be rewritten using two integrations by parts (for which the boundary terms could be dropped) as

$$\Omega = \int_0^\infty d\varepsilon \left(\int_0^\varepsilon d\varepsilon' \int_0^{\varepsilon'} d\varepsilon'' \nu(\varepsilon'', \phi) \right) f'(\varepsilon, \varepsilon_F, T). \quad (2.44)$$

Because we have defined the energy levels to begin at $\varepsilon = 0$, we can freely extend the lower limit of integration of ν and ν_0 from 0 to $-\infty$ when it is convenient. We can rewrite the integral of the

¹⁴In this section, we will use “0” in subscripts to denote quantities calculated previously for a ring without disorder.

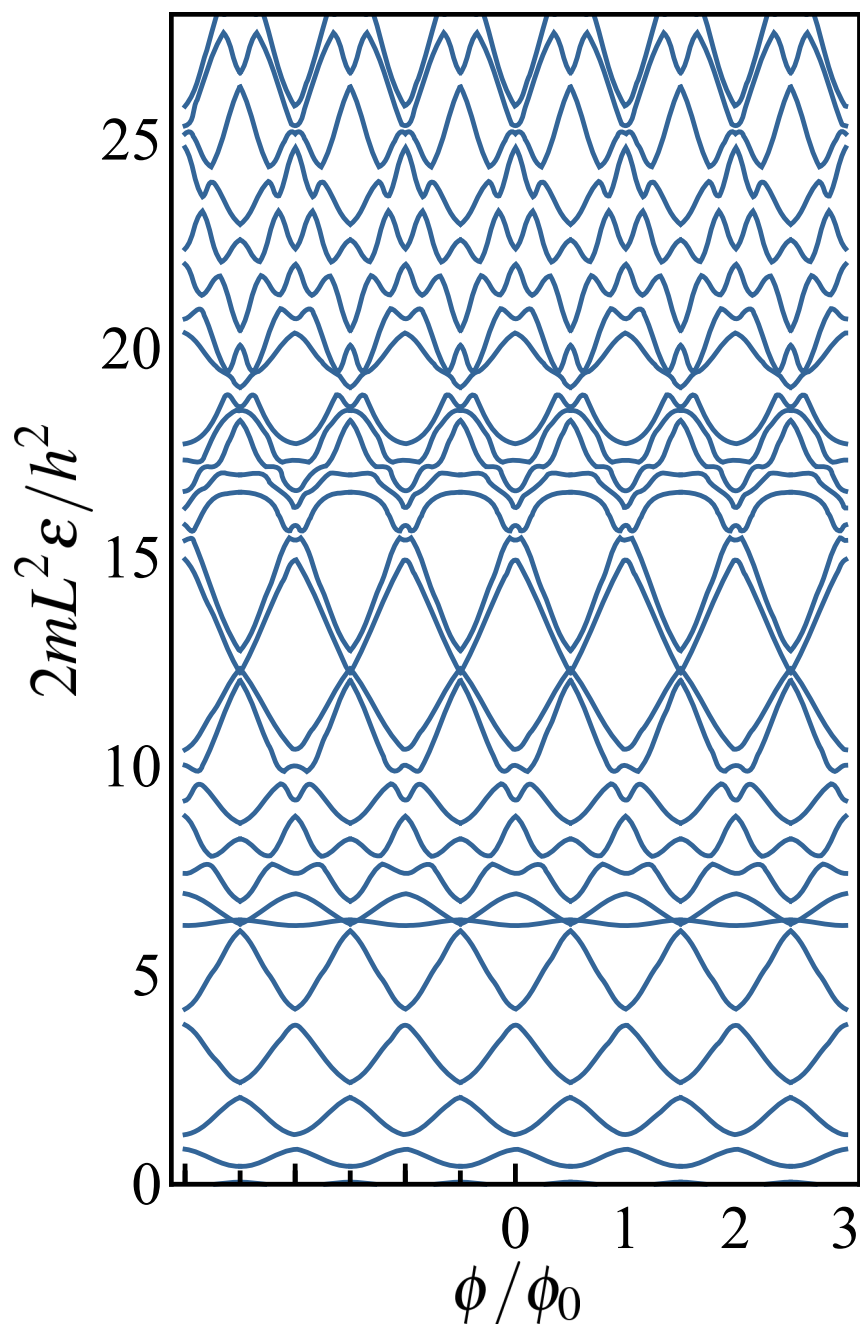


Figure 2.12: Energy spectrum of a disordered multichannel ring. The figure shows the spectrum for a ring with the same dimensions ($t/L = 0.38$ and $w/L \leq 0.16$) as those used to make Fig. 2.9 but with an off-diagonal perturbation applied to break the level degeneracies. Towards the top of the plot, the energy level density is higher and the two-level limit is not strictly valid. Because of this fact, some levels are pushed quite close to each other and appear to intersect. These intersections can be viewed as very close avoided crossings for which the finite thickness of the curves depicting adjacent energy levels overlap.

disorder averaged density of states as

$$\begin{aligned}
\int_0^\varepsilon d\varepsilon_1 \nu(\varepsilon_1) &= \int_{-\infty}^\varepsilon d\varepsilon_1 \int_{-\infty}^\infty d\varepsilon_2 \nu_0(\varepsilon_2) b_L\left(\varepsilon_1 - \varepsilon_2, \frac{\hbar}{2\tau_e}\right) \\
&= - \int_{-\infty}^\infty d\varepsilon_2 \left(\int_{-\infty}^{\varepsilon_2} d\varepsilon_3 \nu_0(\varepsilon_3) \right) \int_{-\infty}^\varepsilon d\varepsilon_1 (-1) b_L'\left(\varepsilon_1 - \varepsilon_2, \frac{\hbar}{2\tau_e}\right) \\
&\quad + \left(\int_{-\infty}^{\varepsilon_2} d\varepsilon_3 \nu_0(\varepsilon_3) \right) \left(\int_{-\infty}^\varepsilon d\varepsilon_1 b_L\left(\varepsilon_1 - \varepsilon_2, \frac{\hbar}{2\tau_e}\right) \right) \Big|_{\varepsilon_2=-\infty}^{\infty}
\end{aligned}$$

where we have used integration by parts with respect to ε_2 . Since $b_L(\varepsilon) \rightarrow 0$ as $\varepsilon \rightarrow \pm\infty$, the boundary term can be dropped. We then have

$$\int_0^\varepsilon d\varepsilon_1 \nu(\varepsilon_1) = \int_{-\infty}^\infty d\varepsilon_2 \left(\int_{-\infty}^{\varepsilon_2} d\varepsilon_3 \nu_0(\varepsilon_3) \right) b_L\left(\varepsilon - \varepsilon_2, \frac{\hbar}{2\tau_e}\right). \quad (2.45)$$

This integration by parts did not make use of any properties of ν_0 and can be repeated replacing $\nu_0(\varepsilon)$ with $\int_{-\infty}^\varepsilon d\varepsilon_1 \nu_0(\varepsilon_1)$ so that

$$\left(\int_{-\infty}^\varepsilon d\varepsilon_1 \int_{-\infty}^{\varepsilon_1} d\varepsilon_2 \nu(\varepsilon_2, \phi) \right) = \int_{-\infty}^\infty d\varepsilon_1 \left(\int_{-\infty}^{\varepsilon_1} d\varepsilon_2 \int_{-\infty}^{\varepsilon_2} d\varepsilon_3 \nu_0(\varepsilon_3, \phi) \right) b_L\left(\varepsilon - \varepsilon_1, \frac{\hbar}{2\tau_e}\right). \quad (2.46)$$

At $T = 0$, $f'(\varepsilon, \varepsilon_F, T) = \delta(\varepsilon - \varepsilon_F)$ and the persistent current is

$$\begin{aligned}
I &= -\frac{\partial \Omega}{\partial \phi} \\
&= -\frac{\partial}{\partial \phi} \left(\int_{-\infty}^{\varepsilon_F} d\varepsilon' \int_{-\infty}^{\varepsilon'} d\varepsilon'' \nu(\varepsilon'', \phi) \right). \quad (2.47)
\end{aligned}$$

By Eq. 2.46, the disorder average is accomplished by convolving the clean ring result at energy ε with the Lorentzian $b_L(\varepsilon_F - \varepsilon, \hbar/2\tau_e)$. Using the result of Eq. 2.20 for $T = 0$, we can write the disorder averaged current as

$$\begin{aligned}
I &= \int_{-\infty}^\infty d\varepsilon I_{1D,0}(\varepsilon) b_L\left(\varepsilon_F - \varepsilon, \frac{\hbar}{2\tau_e}\right) \\
&= \sum_{p>0} \sin\left(2\pi p \frac{\phi}{\phi_0}\right) \frac{8\hbar^2}{mpL\phi_0} \int_{-\infty}^\infty d\varepsilon k(\varepsilon) \cos(pk(\varepsilon)L) b_L\left(\varepsilon_F - \varepsilon, \frac{\hbar}{2\tau_e}\right).
\end{aligned}$$

The function $b_L(\varepsilon_F - \varepsilon, \hbar/2\tau_e)$ is sharply peaked near the Fermi energy ε_F so we can once again

use the expansion given in Eq. 2.21 for $k(\varepsilon)$ about ε_F ,

$$k(\varepsilon) \approx k_F \left(1 + \frac{1}{2} \left(\frac{\varepsilon}{\varepsilon_F} - 1 \right) - \frac{1}{8} \left(\frac{\varepsilon}{\varepsilon_F} - 1 \right)^2 + \mathcal{O} \left(\left(\frac{\varepsilon}{\varepsilon_F} - 1 \right)^3 \right) \right).$$

The function $b_L(\varepsilon_F - \varepsilon, \hbar/2\tau_e)$ is appreciable for $|\varepsilon - \varepsilon_F| \lesssim \hbar/2\tau_e$. Note that

$$\begin{aligned} \frac{\hbar}{2\tau_e} &= \frac{\hbar v_F}{2l_e} \\ &= \frac{\hbar}{2l_e} \left(\frac{\hbar k_F}{m} \right) \\ &= \frac{\varepsilon_F}{k_F l_e}, \end{aligned}$$

so that over this same range with $\alpha \leq 1$

$$k \left(\varepsilon_F + \alpha \frac{\hbar}{2\tau_e} \right) \approx k_F \left(1 + \frac{1}{2k_F l_e} \alpha - \frac{1}{8(k_F l_e)^2} \alpha^2 \right).$$

Since we are assuming weak disorder $k_F l_e \gg 1$, it is sufficient to replace the first factor of k in the expression for I by k_F . We make the additional assumption that $L \gtrsim l_e$ so that $k_F l_e \gg L/l_e$. Only up to the first order term in $\varepsilon - \varepsilon_F$ must be kept in the argument of the cosine factor of the expression for I . Thus, we have

$$\begin{aligned} &\int_{-\infty}^{\infty} d\varepsilon k(\varepsilon) \cos(pk(\varepsilon)L) b_L \left(\varepsilon_F - \varepsilon, \frac{\hbar}{2\tau_e} \right) \\ &\approx k_F \int_{-\infty}^{\infty} d\varepsilon \cos \left(pk_F L + p \frac{k_F L}{2\varepsilon_F} (\varepsilon - \varepsilon_F) \right) b_L \left(\varepsilon_F - \varepsilon, \frac{\hbar}{2\tau_e} \right) \\ &\approx k_F \int_{-\infty}^{\infty} d\varepsilon \left(\cos(pk_F L) \cos \left(\frac{pk_F L}{2\varepsilon_F} \varepsilon \right) - \sin(pk_F L) \sin \left(\frac{pk_F L}{2\varepsilon_F} \varepsilon \right) \right) b_L \left(\varepsilon, \frac{\hbar}{2\tau_e} \right) \\ &= k_F \cos(pk_F L) \int_{-\infty}^{\infty} d\varepsilon \exp \left(i \frac{pk_F L}{2\varepsilon_F} \varepsilon \right) b_L \left(\varepsilon, \frac{\hbar}{2\tau_e} \right) \end{aligned}$$

where we made use of the narrowness and symmetry of $b_L(\varepsilon)$. The last line is the Fourier transform of the Lorentzian which has the well-known form

$$\begin{aligned} \int_{-\infty}^{\infty} d\varepsilon k(\varepsilon) \cos(pk(\varepsilon)L) b_L \left(\varepsilon_F - \varepsilon, \frac{\hbar}{2\tau_e} \right) &= k_F \cos(pk_F L) \exp \left(-\frac{|p| \hbar k_F L}{4\varepsilon_F \tau_e} \right) \\ &= k_F \cos(pk_F L) \exp \left(-\frac{|p| L}{2l_e} \right). \end{aligned} \quad (2.48)$$

We can write the single-channel, disorder averaged persistent current as

$$\begin{aligned}
I &= \sum_{p>0} \frac{8\hbar^2 k_F}{mpL\phi_0} \cos(pk_F L) \exp\left(-p\frac{L}{2l_e}\right) \sin\left(2\pi p\frac{\phi}{\phi_0}\right) \\
&= \sum_{p>0} I_{p,0} \exp\left(-p\frac{L}{2l_e}\right) \sin\left(2\pi p\frac{\phi}{\phi_0}\right)
\end{aligned} \tag{2.49}$$

where the coefficients $I_{p,0}$ are the harmonic amplitudes of the current in the absence of disorder. Note that the suppression factors have no dependence on k_F so that the result in Eq. 2.49 remains valid at finite temperature just by using the temperature dependent form for the $I_{p,0}(T)$ given in Eq. 2.49.

Similarly, the typical harmonic magnitudes $I_{p,M,0}^{\text{typ}}$ given in Eq. 2.37 for the multichannel ring can be multiplied by the factor $\exp(-pL/2l_e)$ to give the disorder averaged result (since each single channel in the ring is suppressed by this same factor). Recall that, in the absence of disorder and for rings with dimensions similar to those studied in this text, the p^{th} harmonic $I_{p,M}$ of the multichannel ring was found to fluctuate strongly in sign and magnitude under small changes of the Fermi wave vector k_F , thickness t , or width w . Because of this strong dependence on dimensions, the current from nominally identical rings could differ greatly in magnitude and sign due to lithographic imperfections. To describe the current in the multi-channel ring quantitatively, we introduced in Eq. 2.34 the typical magnitude $I_{p,M,0}^{\text{typ}}$ of the p^{th} harmonic of the current. This typical magnitude was found by averaging $I_{p,M,0}^2$ over small variations in k_F , w , or t and then taking the square root. To account for disorder, one replaces $I_{p,M,0}$ with $I_{p,M,0} \exp(-pL/2l_e)$. The calculation of the typical current magnitude under variations of k_F , w , or t proceeds as before with this additional factor of $\exp(-pL/2l_e)$. To be precise, this quantity $I_{p,M,0}^{\text{typ}} \exp(-pL/2l_e)$ is the result of finding the disorder averaged current of a multichannel ring and then finding its standard deviation over a small range of k_F , t , or w .

By taking the disorder average of the current first, we obtain the exponential dependence on L/l_e . If it were possible to fabricate many rings with precisely the same dimensions but different realizations of the microscopic disorder, we would expect the average current in all of these rings to be $I_{p,M,0} \exp(-pL/2l_e)$ where the sign and magnitude of the $I_{p,M,0}$ can be found exactly from Eq. 2.33. In practice, this calculation requires unrealistic precision in the specification of the ring dimensions (namely k_F , w , and t). For this reason, we calculate the typical current by averaging over dimensions. It turns out that this quantity $I_{p,M}^{\text{typ}}$ is not especially useful for us. In 2.3, we

consider the fluctuations of the persistent current with disorder by averaging the square of the current over disorder (rather than averaging the current over disorder and then taking the square average over k_F, w, t). The typical current magnitude found in this way does not depend sensitively on the ring dimensions, nor does it decay exponentially in L/l_e . Consequently, it is much larger than $I_{p,M}^{\text{typ}}$ for the rings studied experimentally in this text for which $L/l_e \gg 1$. The subtlety of this distinction in the method of disorder averaging perhaps explains why the possibility of measuring persistent currents experimentally was overlooked for as long as it was.

The reason for the strong suppression of the current in L/l_e is best described in terms of Green's functions (see Appendix B). From Eq. B.4, it is seen that the density of states, which is intimately related to the persistent current (see Eq. 2.47), can be written as a spatial average of Green's function amplitudes for closed paths within the ring. The disorder average effectively throws away the contributions of all closed paths in which the electron wavefunction is scattered from one wavevector \mathbf{k} to another \mathbf{k}' , which happens when the electron travels an average distance l_e (albeit with $|\mathbf{k}| = |\mathbf{k}'|$ unchanged because the scattering is elastic). It was pointed out by Landauer, Büttiker, and Imry that, because the electron maintains phase coherence over these discarded trajectories, many of them produce sizable contributions to the persistent current [1]. We discuss the contribution of these diffusive trajectories to the persistent current in the next section.

2.3 Persistent currents in the diffusive regime

With all of the framework for describing persistent currents established in the previous sections, we consider the diffusive regime relevant for metal rings. As discussed in Section 2.2.3, in the presence of disorder, the energy levels of the clean ring are distorted and nearby levels repelled from each other. A ring with a cross-section on the order of tens of nanometers can have on the order of $M = 10^5$ transverse channels resulting in relatively dense channels.

As all of these dense channels repel each other strongly in the diffusive regime, the flux-dependence of the energy levels is smoothed out leading to a reduction in the current $i_n = -\partial\varepsilon_n/\partial\phi$ of each single level ε_n . However, this strong repulsion of dense levels also results in a correlation in the features of neighboring levels, as illustrated in Fig. 2.13. Although the spectrum as a whole still consists of energy levels with currents $\langle i_n \rangle = 0$ which have no net disorder average, this correlation means that a large number $M_{\text{eff}} \gg 1$ of levels add coherently to the total current $I = \sum_n i_n$. While the current of most levels will cancel out, the net current will have a typical magnitude $I^{\text{typ}} = \sqrt{\langle I^2 \rangle}$

of $M_{\text{eff}}\sqrt{\langle i^2 \rangle}$ rather than simply $\sqrt{\langle i^2 \rangle}$. It turns out the number of correlated levels $M_{\text{eff}} = \frac{l_c}{L}M$.

The correlation of energy levels means that levels within $\sim M_{\text{eff}}\Delta$ about the Fermi energy ε_F all give the same contribution to the current and thus the thermal occupancy, shown in Fig. 2.14, must be broadened to this energy scale $k_B T \sim M_{\text{eff}}\Delta$ rather than the smaller scale of the single level spacing Δ before the current begins to decay. Because the correlation in the energy spectrum results from level repulsion, changing the density of levels (e.g. by varying the ring cross-section and so the number of transverse channels M) does not affect the typical current magnitude. A greater density of levels means a greater number of correlated levels contribute to I^{typ} . However, a greater density of levels also means that each level n is further flattened and so possesses less current i_n . These two effects cancel each other out. An indication of this phenomena is given in Fig. 2.15 which shows an energy spectrum twice as dense as that shown in Fig. 2.13 but with a typical level slope of half the magnitude of Fig. 2.13. We will now discuss all of these effects more quantitatively.

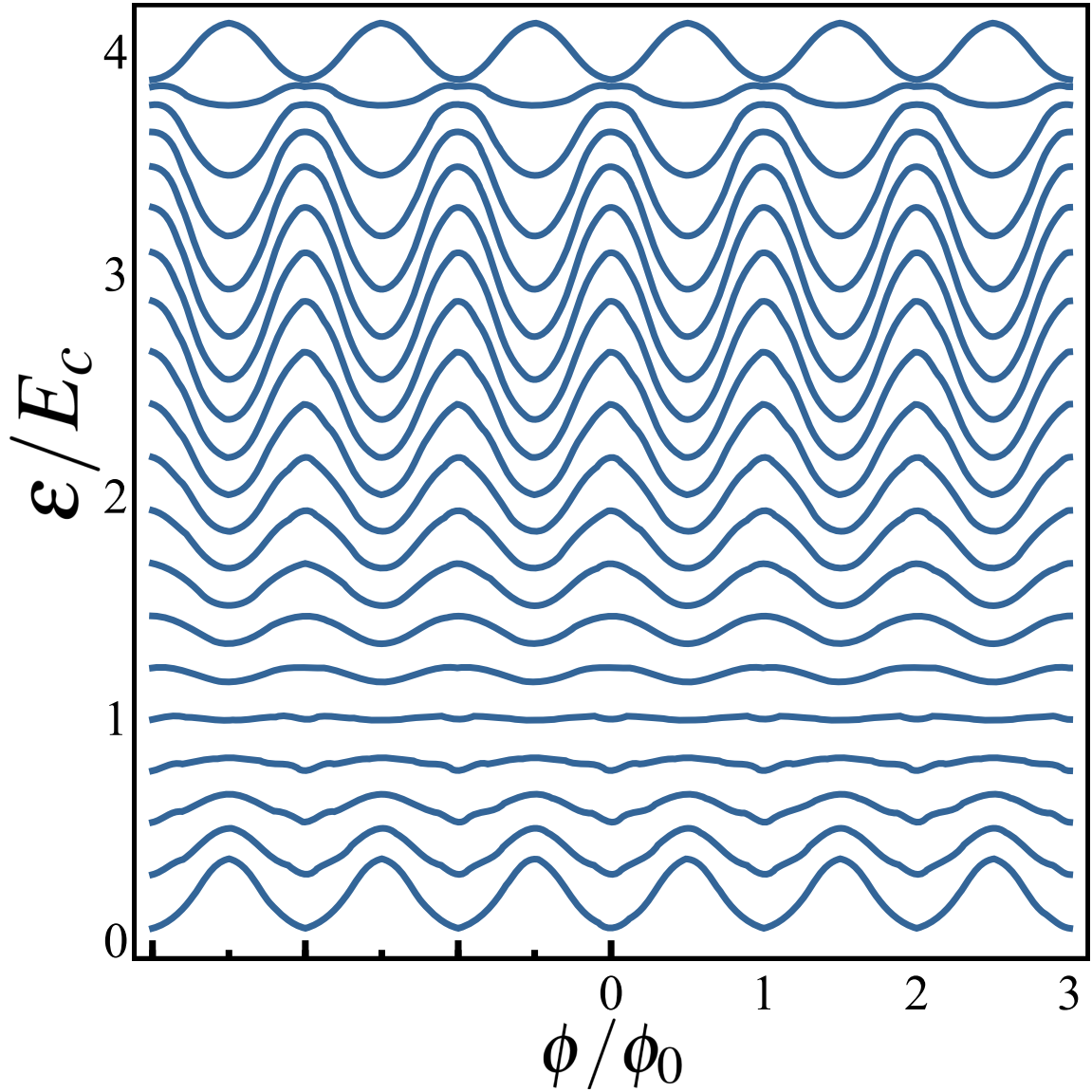


Figure 2.13: Drawing of energy level spectrum in the diffusive regime. The figure represents a cartoon of the energy level spectrum for one disorder realization of a ring in the diffusive regime. The spectrum was designed to have a correlation scale of $M_{\text{eff}} = 4$ energy levels. The energy axis is scaled by the correlation energy while the flux axis is scaled by the flux quantum.

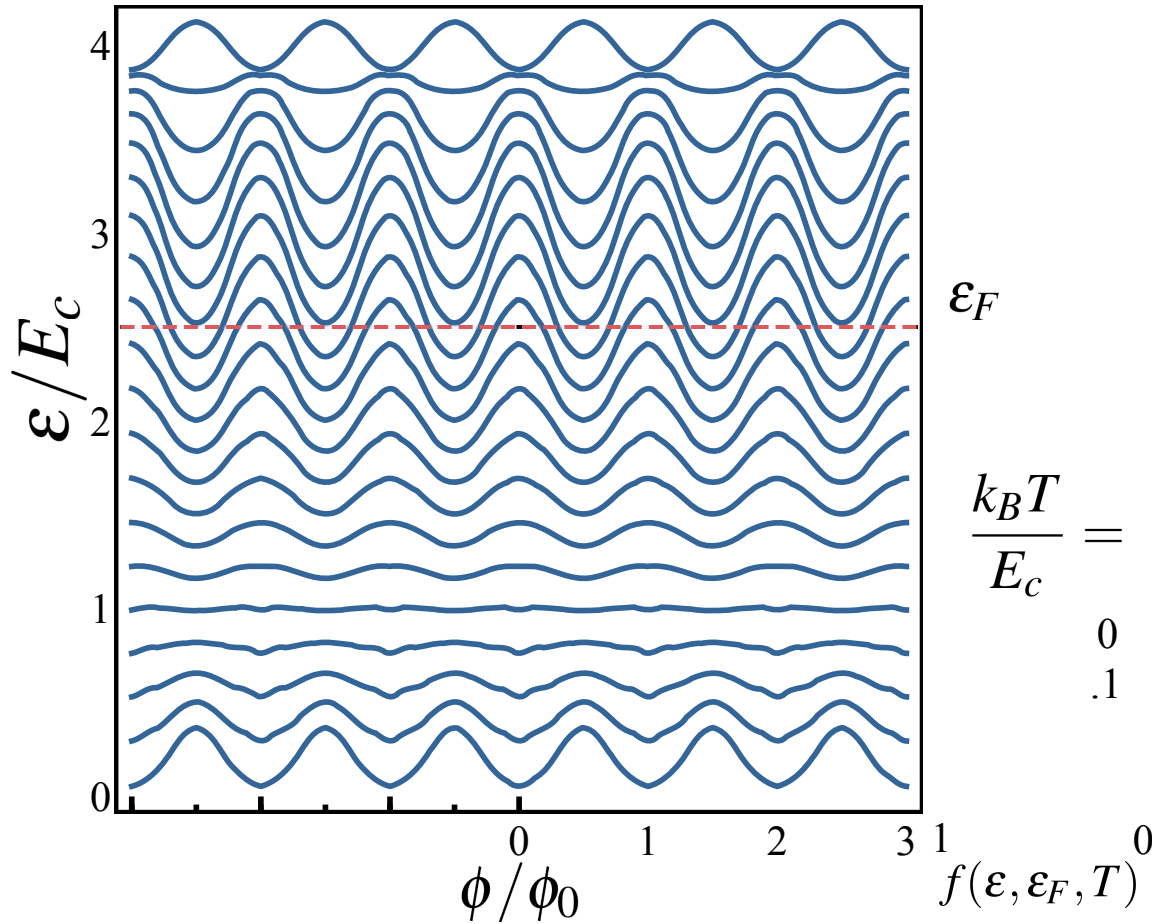


Figure 2.14: Drawing of distribution of occupancy of the energy level spectrum in the diffusive regime. The same spectrum as shown in Fig. 2.13 is replotted alongside a plot of the Fermi-Dirac distribution $f(\varepsilon, \varepsilon_F, T)$ for three different temperatures ($0 \times E_c/k_B$, $0.1 \times E_c/k_B$, $0.3 \times E_c/k_B$). By the highest temperature shown the level occupancy begins spread out over levels with different shapes from those right at the Fermi level ε_F .

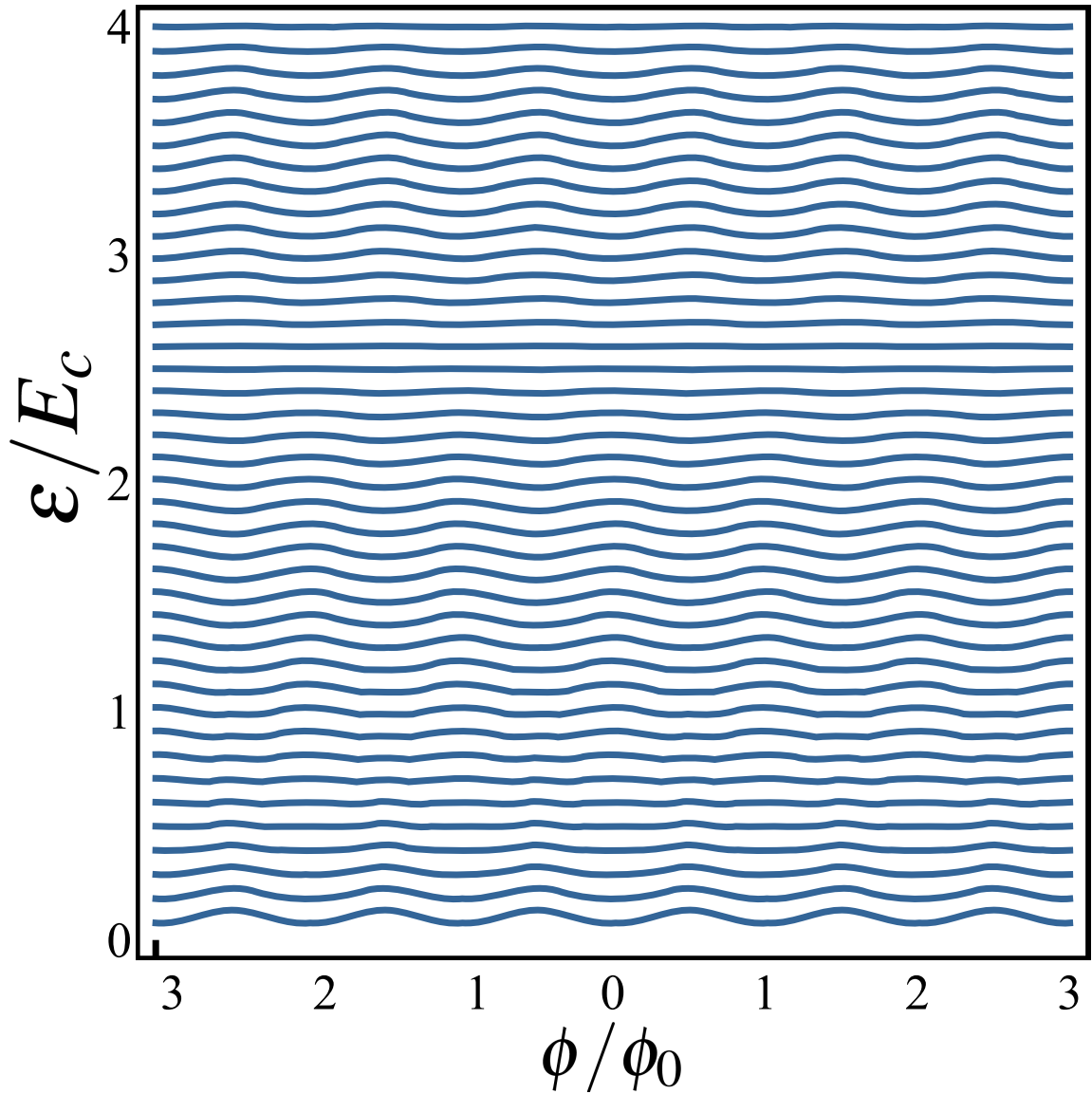


Figure 2.15: Alternate drawing of energy level spectrum in the diffusive regime. A spectrum is shown for which eight neighboring energy levels are correlated. In contrast to Fig. 2.13, this spectrum (for the same correlation energy scale E_c) is denser and has less steeply sloped energy curves. As discussed in the text, this spectrum and that of Fig. 2.13 have the same typical current because the larger number of coherent levels $M_{\text{eff}} = 8$ is compensated for by the smaller single level current $i = \partial\varepsilon/\partial\phi$. The typical current of each spectrum could be calculated, for example, by finding $I_N = \sum_{n=1}^N i_n$ for a range of highest occupied levels N and then averaging I_N^2 over N .

2.3.1 Typical persistent current magnitude in the diffusive regime

To calculate the persistent current in the diffusive regime,¹⁵ we return to the general formula

$$I = -\frac{\partial \Omega}{\partial \phi},$$

which we rewrite using Eq. 2.44 and integration by parts on ε' as

$$\begin{aligned} I &= -\frac{\partial}{\partial \phi} \int_0^\infty d\varepsilon \left(\int_0^\varepsilon d\varepsilon' \int_0^{\varepsilon'} d\varepsilon'' \nu(\varepsilon'', \phi) \right) f'(\varepsilon, \varepsilon_F, T) \\ &= -\frac{\partial}{\partial \phi} \int_0^\infty d\varepsilon \left(\int_0^\varepsilon d\varepsilon' (\varepsilon - \varepsilon') \nu(\varepsilon', \phi) \right) f'(\varepsilon, \varepsilon_F, T). \end{aligned}$$

In Section 2.2.3, we found that the current averaged over disorder decays as $\exp(-L/2l_e)$. This same conclusion can also be reached by noting that Eq. B.4 relates $\nu(\varepsilon)$ to a Green function and that according to Eq. B.16 this Green function decays on a characteristic length scale $2l_e$ when averaged over disorder. Since the average value of the current decays strongly, we focus here on the typical magnitude $\sqrt{\langle I^2 \rangle}$ of the fluctuations of the current and revisit the average current in Section 2.3.3.

We begin by considering a ring threaded by an ideal Aharonov-Bohm flux ϕ (see Section 2.1.1). We calculate the current-current correlation function

$$\begin{aligned} \langle I(\phi) I(\phi') \rangle &= \frac{\partial^2}{\partial \phi \partial \phi'} \langle \Omega(\phi) \Omega(\phi') \rangle \\ &= \int_0^\infty d\varepsilon_1 \int_0^\infty d\varepsilon'_1 (f'(\varepsilon_1) f'(\varepsilon'_1)) C_1^{(0)}(\varepsilon_1, \phi; \varepsilon'_1, \phi') \end{aligned} \quad (2.50)$$

where $f'(\varepsilon_1)$ is short for $f'(\varepsilon_1, \varepsilon_F, T)$ and

$$C_1^{(0)}(\varepsilon_1, \phi; \varepsilon'_1, \phi') = \frac{\partial^2}{\partial \phi \partial \phi'} \int_0^{\varepsilon_1} d\varepsilon_2 \int_0^{\varepsilon'_1} d\varepsilon'_2 (\varepsilon_1 - \varepsilon_2) (\varepsilon'_1 - \varepsilon'_2) \langle \nu(\varepsilon_2, \phi) \nu(\varepsilon'_2, \phi') \rangle. \quad (2.51)$$

As we have noted before the derivative of the Fermi-Dirac distribution obeys $f'(\varepsilon, \varepsilon_F, T) \rightarrow \delta(\varepsilon - \varepsilon_F)$ as $T \rightarrow 0$. Thus the current-current correlation function at zero temperature is

$$\langle I(\phi) I(\phi') \rangle = C_1^{(0)}(\varepsilon_F, \phi; \varepsilon_F, \phi').$$

¹⁵In addition to Refs. 41 and 42, I acknowledge private communication with Eran Ginossar and Felix von Oppen in the composition of this derivation.

The function $C_1^{(0)}(\varepsilon, \phi, \varepsilon', \phi')$ can be thought of as the current-current correlation function at zero temperature for a ring at two different Fermi energies ε and ε' and Aharonov-Bohm fluxes ϕ and ϕ' :

$$\langle I(\varepsilon, \phi) I(\varepsilon', \phi') \rangle = C_1^{(0)}(\varepsilon, \phi; \varepsilon', \phi').$$

Because this quantity is rather abstract, we will use the more general-looking syntax $C_1^{(0)}$ rather than the correlation function syntax $\langle I(\phi)I(\phi') \rangle$. We first evaluate the current-current correlation function at zero temperature and then consider the more general case.

2.3.1.1 Zero temperature

Because of the flux derivatives in Eq. 2.51, we need only consider the flux-dependent portion of the disorder averaged density of states correlation function. This flux dependent part of the correlation function is specified by Eq. B.30,

$$\langle \nu(\varepsilon, B) \nu(\varepsilon - \hbar\omega, B') \rangle_{d,c} = 2 \left(\frac{1}{2\pi\hbar} \right)^2 \sum_{\mp} \sum_n \text{Re} \left(\left(\frac{1}{i\omega + DE_n(B_{\mp})} \right)^2 \right),$$

and Eq. B.31,

$$\left(\nabla' + i \frac{e}{\hbar} \mathbf{A}_{\mp} \right)^2 P_{d,c}(\mathbf{r}, \mathbf{r}', \omega) = E_n^{d,c}(B_{\mp}) P_{d,c}(\mathbf{r}, \mathbf{r}', \omega). \quad (2.52)$$

Since $\langle \nu(\varepsilon_2, \phi) \nu(\varepsilon'_2, \phi') \rangle$ depends only on $|\varepsilon_2 - \varepsilon'_2|$, we can rewrite this correlation function as

$$\begin{aligned} C_1^{(0)}(\varepsilon_1, \phi; \varepsilon'_1, \phi') &= \frac{\partial^2}{\partial\phi\partial\phi'} \int_{-\infty}^{\varepsilon_1} d\varepsilon_2 \int_{-\infty}^{\varepsilon'_1} d\varepsilon'_2 (\varepsilon_1 - \varepsilon_2) (\varepsilon'_1 - \varepsilon'_2) \langle \nu(\varepsilon_2, \phi) \nu(\varepsilon'_2, \phi') \rangle \\ &= \frac{\partial^2}{\partial\phi\partial\phi'} \int_{-\infty}^0 d\varepsilon_2 \int_{-\infty}^0 d\varepsilon'_2 \varepsilon_2 \varepsilon'_2 \langle \nu(\varepsilon_2 + \varepsilon_1, \phi) \nu(\varepsilon'_2 + \varepsilon'_1, \phi') \rangle \\ &= \frac{\hbar}{8} \frac{\partial^2}{\partial\phi\partial\phi'} \int_{-\infty}^0 d\varepsilon \int_{\varepsilon/\hbar}^{-\varepsilon/\hbar} d\omega (\varepsilon^2 - \hbar^2\omega^2) \left\langle \nu \left(\frac{\varepsilon + \hbar\omega}{2} + \varepsilon_1, \phi \right) \nu \left(\frac{\varepsilon - \hbar\omega}{2} + \varepsilon'_1, \phi' \right) \right\rangle \end{aligned} \quad (2.53)$$

where we have used the change of variables $\varepsilon = \varepsilon_2 + \varepsilon'_2$ and $\hbar\omega = \varepsilon_2 - \varepsilon'_2$ and again extended the integrals to $-\infty$.

Before evaluating the integrals, we must evaluate the disorder averaged density of states correlation function. For a ring subject to an ideal Aharonov-Bohm flux ϕ , Eq. B.31 for the eigenvalues $E_n(\phi_{\pm})$ of the diffuson and cooperon is identical to the Schrödinger equation, Eq. 2.26, considered

in Section 2.2.2 with $\hbar^2/2m \rightarrow 1$ and the boundary conditions changed to Eq. B.32,

$$\tilde{\mathbf{n}} \cdot \left(\nabla' + i \frac{e}{\hbar} \mathbf{A}_{\mp} \right) P_{d,c}(\mathbf{r}, \mathbf{r}', \omega) = 0. \quad (2.54)$$

The eigenvalues are thus given by Eq. 2.30 except that the new boundary conditions change the indices allowed for the transverse degrees of freedom. Using the same gauge considered in that section, we have that $\tilde{\mathbf{n}} \cdot \mathbf{A} = 0$ on all surfaces, and thus the boundary condition becomes

$$\tilde{\mathbf{n}} \cdot \nabla' P_{d,c}(\mathbf{r}, \mathbf{r}', \omega) = 0$$

which admits (amongst others) solutions of the form $P_{d,c}(r, \theta, z) = P_{d,c}(\theta)$, which are independent of r and z . These functions correspond to $n_r = n_z = 0$, which were not allowed for Eq. 2.30.¹⁶ The eigenvalues for the diffuson and cooperon are then¹⁷

$$E_n(\phi_{\pm}) = \frac{(2\pi)^2}{L^2} \left(n + \frac{\phi}{\phi_0} \right)^2 + \frac{\pi^2 n_r^2}{2w^2} + \frac{\pi^2 n_z^2}{2t^2}.$$

We will write these eigenvalues as

$$E_n(\phi_{\pm}) = \frac{(2\pi)^2}{L^2} \left(n + \frac{\phi_{\pm}}{\phi_0} \right)^2 + \frac{1}{L^2} \varepsilon_{\perp}^{\pm} \quad (2.55)$$

where $\varepsilon_{\perp}^{\pm}$ stands in for all transverse eigenvalues scaled by $1/L^2$. We can then write the density of states correlation function as

$$\begin{aligned} & \left\langle \nu \left(\frac{\varepsilon + \hbar\omega}{2} + \varepsilon_1, \phi \right) \nu \left(\frac{\varepsilon - \hbar\omega}{2} + \varepsilon'_1, \phi' \right) \right\rangle \\ &= \frac{1}{2\pi^2 \hbar^2} \sum_{\pm} \sum_{\varepsilon_{\perp}^{\pm}} \sum_n \operatorname{Re} \left(\left(i\omega + i(\varepsilon_1 - \varepsilon'_1) + \frac{(2\pi)^2 D}{L^2} \left(n + \frac{\phi_{\pm}}{\phi_0} \right)^2 + \frac{D\varepsilon_{\perp}}{L^2} \right)^{-2} \right) \\ &= \frac{1}{2\pi^2} \sum_{\pm} \sum_{\varepsilon_{\perp}^{\pm}} \sum_n \operatorname{Re} \left(\left(i\hbar\omega + i(\varepsilon_1 - \varepsilon'_1) + E_c \varepsilon_{\perp} + (2\pi)^2 E_c \left(n + \frac{\phi_{\pm}}{\phi_0} \right)^2 \right)^{-2} \right) \end{aligned} \quad (2.56)$$

¹⁶The new boundary condition also changes the form of the eigenfunctions. For example, instead of $Z(z) = \sin(\pi n_z z/t)$ we would have $Z(z) = \cos(\pi n_z z/t)$. However, the eigenvalue is the same in both cases. Since we are concerned only with the eigenvalues and not the eigenfunctions here, we do not write out the new form for the eigenfunctions.

¹⁷A few more steps are necessary to show that the extra constant offset in Eq. 2.30 drops out when the radial eigenvalues are recalculated for the new boundary conditions.

where we have introduced the energy scale

$$E_c = \frac{\hbar D}{L^2} \quad (2.57)$$

known in the literature as the Thouless or correlation energy.¹⁸ Using the Poisson summation formula given in Eq. A.2, we can replace the sum over n by a sum over p . Writing

$$\alpha = i\hbar\omega + i(\varepsilon_1 - \varepsilon'_1) + E_c\varepsilon_\perp,$$

we have

$$\begin{aligned} \sum_n \frac{1}{\left(\alpha + (2\pi)^2 E_c \left(n + \frac{\phi_\pm}{\phi_0}\right)^2\right)^2} &= -\frac{\partial}{\partial\alpha} \sum_n \frac{1}{\alpha + 4\pi^2 E_c \left(n + \frac{\phi_\pm}{\phi_0}\right)^2} \\ &= -\frac{1}{2\sqrt{E_c}} \frac{\partial}{\partial\alpha} \sum_{p=-\infty}^{\infty} e^{2\pi i p \phi_\pm / \phi_0} \frac{1}{\sqrt{\alpha}} \int_{-\infty}^{\infty} d\phi \frac{1}{\pi} \frac{\frac{\phi_0 \sqrt{\alpha}}{2\pi \sqrt{E_c}} e^{-2\pi i p \phi / \phi_0}}{\frac{\phi_0^2 \alpha}{4\pi^2 E_c} + \phi^2} \end{aligned} \quad (2.58)$$

where the last integral is now the Fourier transform of a Lorentzian. Performing the Fourier transform gives

$$\begin{aligned} \sum_n \frac{1}{\left(\alpha + (2\pi)^2 E_c \left(n + \frac{\phi_\pm}{\phi_0}\right)^2\right)^2} &= -\frac{1}{2\sqrt{E_c}} \frac{\partial}{\partial\alpha} \sum_{p=-\infty}^{\infty} e^{2\pi i p \phi_\pm / \phi_0} \frac{1}{\sqrt{\alpha}} \exp\left(-|p| \sqrt{\frac{\alpha}{E_c}}\right) \\ &= \frac{1}{\sqrt{E_c}} \frac{i}{\hbar} \frac{\partial}{\partial\omega} \sum_{p=1}^{\infty} \cos\left(2\pi p \frac{\phi_\pm}{\phi_0}\right) \frac{1}{\sqrt{\alpha}} \exp\left(-p \sqrt{\frac{\alpha}{E_c}}\right) \end{aligned} \quad (2.59)$$

where in the last line we have prematurely dropped the $p = 0$ term. This term will drop out under the derivatives with respect to ϕ and ϕ' which will be performed when evaluating $C_1^{(0)}(\varepsilon_1, \phi; \varepsilon'_1, \phi')$.

Putting the results of Eqs. 2.56 and 2.59 into Eq. 2.53 for the current current correlation

¹⁸This energy scale is defined with various factors of 2 and π by different authors.

function gives

$$\begin{aligned}
C_1^{(0)}(\varepsilon_1, \phi; \varepsilon'_1, \phi') &= \frac{\hbar}{8} \frac{\partial^2}{\partial \phi \partial \phi'} \int_{-\infty}^0 d\varepsilon \int_{\varepsilon/\hbar}^{-\varepsilon/\hbar} d\omega (\varepsilon^2 - \hbar^2 \omega^2) \dots \\
&\dots \times \frac{1}{2\pi^2} \sum_{\pm} \sum_{\varepsilon_{\pm}} \operatorname{Re} \left(\frac{1}{\sqrt{E_c}} \frac{i}{\hbar} \frac{\partial}{\partial \omega} \sum_{p=1}^{\infty} \cos \left(2\pi p \frac{\phi_{\pm}}{\phi_0} \right) \frac{1}{\sqrt{\alpha}} \exp \left(-p \sqrt{\frac{\alpha}{E_c}} \right) \right) \\
&= \frac{1}{4} \sum_{p=1}^{\infty} \sum_{\pm} \sum_{\varepsilon_{\pm}} \left(\pm \frac{p^2}{\phi_0^2} \cos \left(2\pi p \frac{\phi_{\pm}}{\phi_0} \right) \right) \int_{-\infty}^0 d\varepsilon \int_{\varepsilon/\hbar}^{-\varepsilon/\hbar} d\omega (\varepsilon^2 - \hbar^2 \omega^2) \dots \\
&\dots \times \operatorname{Im} \left(\frac{1}{\sqrt{E_c}} \frac{\partial}{\partial \omega} \frac{1}{\sqrt{\alpha}} \exp \left(-p \sqrt{\frac{\alpha}{E_c}} \right) \right) \\
&= \frac{\hbar^2}{2} \operatorname{Im} \sum_{p=1}^{\infty} \sum_{\pm} \sum_{\varepsilon_{\pm}} \left(\pm \frac{p^2}{\phi_0^2} \cos \left(2\pi p \frac{\phi_{\pm}}{\phi_0} \right) \right) \int_{-\infty}^0 d\varepsilon \int_{\varepsilon/\hbar}^{-\varepsilon/\hbar} d\omega \frac{\omega}{\sqrt{\alpha E_c}} \exp \left(-p \sqrt{\frac{\alpha}{E_c}} \right) \\
&= -\frac{\hbar^2}{2\sqrt{E_c}} \operatorname{Im} \sum_{p=1}^{\infty} \sum_{\pm} \sum_{\varepsilon_{\pm}} \left(\pm \frac{p^2}{\phi_0^2} \cos \left(2\pi p \frac{\phi_{\pm}}{\phi_0} \right) \right) \int_{-\infty}^0 d\varepsilon \int_{-\varepsilon/\hbar}^{\varepsilon/\hbar} d\omega \frac{\omega}{\sqrt{\alpha}} \exp \left(-p \sqrt{\frac{\alpha}{E_c}} \right)
\end{aligned}$$

where in the next to last line we have used integration by parts on ω . To perform the final two integrals, we first use the change of variables $x = \sqrt{\alpha}$ and the abbreviations $\sigma = i(\varepsilon_1 - \varepsilon'_1) + E_c \varepsilon_{\perp}$ and $\kappa = p/\sqrt{E_c}$ to find

$$\begin{aligned}
\int_{-\varepsilon/\hbar}^{\varepsilon/\hbar} d\omega \frac{\omega}{\sqrt{\alpha}} \exp \left(-p \sqrt{\frac{\alpha}{E_c}} \right) &= -\frac{2}{\hbar^2} \int_{\sqrt{-i\varepsilon+\sigma}}^{\sqrt{i\varepsilon+\sigma}} dx (x^2 - \sigma) \exp(-\kappa x) \\
&= -\frac{2}{\hbar^2} \int_{\sqrt{-i\varepsilon+\sigma}}^{\sqrt{i\varepsilon+\sigma}} dx \left(\frac{\partial^2}{\partial \kappa^2} - \sigma \right) \exp(-\kappa x) \\
&= \frac{2}{\hbar^2} \left(\frac{\partial^2}{\partial \kappa^2} - \sigma \right) \sum_{\pm} \pm \frac{1}{\kappa} \exp \left(-\kappa \sqrt{\sigma \pm i\varepsilon} \right).
\end{aligned}$$

The final integral over ε involves only the last factor of this expression. Using another change of variables $y = \sqrt{\sigma \pm i\varepsilon}$, we have

$$\begin{aligned}
\int_{-\infty}^0 d\varepsilon \exp \left(-\kappa \sqrt{\sigma \pm i\varepsilon} \right) &= \int_{\sqrt{\sigma \mp i(\varepsilon_1 + \varepsilon'_1)}}^{\sqrt{\sigma}} dy (\mp 2iy) \exp(-\kappa y) \\
&= \pm 2i \frac{\partial}{\partial \kappa} \int_{\sqrt{\sigma \mp i\infty}}^{\sqrt{\sigma}} dy \exp(-\kappa y) \\
&\approx \mp 2i \frac{\partial}{\partial \kappa} \left(\frac{1}{\kappa} \exp(-\kappa \sqrt{\sigma}) \right)
\end{aligned}$$

where in the last line we dropped the term $\exp(-\kappa \sqrt{\sigma \mp i\infty}) \rightarrow 0$. Because the derivatives of

the Fermi-Dirac distribution function in Eq. 2.50 are peaked around $\varepsilon_F \gg E_c$, this term will be proportional to approximately $\exp(-\sqrt{2\varepsilon_F/\pi E_c}) \approx 0$. Together the two integrals are

$$\begin{aligned}
\int_{-\infty}^0 d\varepsilon \int_{-\varepsilon/\hbar}^{\varepsilon/\hbar} d\omega \frac{\omega}{\sqrt{\alpha}} \exp\left(-\frac{p}{\pi} \sqrt{\frac{\alpha}{E_c}}\right) &= \frac{2}{\hbar^2} \left(\frac{\partial^2}{\partial \kappa^2} - \sigma \right) \sum_{\pm} \pm \frac{1}{\kappa} \left(\mp 2i \frac{\partial}{\partial \kappa} \left(\frac{1}{\kappa} \exp(-\kappa\sqrt{\sigma}) \right) \right) \\
&= -\frac{8i}{\hbar^2} \left(\frac{\partial^2}{\partial \kappa^2} - \sigma \right) \left(\frac{1}{\kappa} \frac{\partial}{\partial \kappa} \left(\frac{1}{\kappa} \exp(-\kappa\sqrt{\sigma}) \right) \right) \\
&= -\frac{8i}{\hbar^2} \left(\frac{\partial^2}{\partial \kappa^2} - \sigma \right) \left(\left(-\frac{1}{\kappa^3} - \frac{\sqrt{\sigma}}{\kappa^2} \right) \exp(-\kappa\sqrt{\sigma}) \right) \\
&= -\frac{8i}{\hbar^2} \left(\left(\frac{\sigma}{\kappa^3} + \frac{\sigma\sqrt{\sigma}}{\kappa^2} \right) \exp(-\kappa\sqrt{\sigma}) \right) \\
&\quad - \frac{8i}{\hbar^2} \frac{\partial}{\partial \kappa} \left(\left(\frac{3}{\kappa^4} + \frac{\sqrt{\sigma}}{\kappa^3} + \frac{2\sqrt{\sigma}}{\kappa^3} + \frac{\sigma}{\kappa^2} \right) \exp(-\kappa\sqrt{\sigma}) \right) \\
&= -\frac{8i}{\hbar^2} \exp(-\kappa\sqrt{\sigma}) \left(\frac{\sigma}{\kappa^3} + \frac{\sigma\sqrt{\sigma}}{\kappa^2} - \frac{12}{\kappa^5} - \frac{9\sqrt{\sigma}}{\kappa^4} - \frac{2\sigma}{\kappa^3} \right. \\
&\quad \left. \dots - \frac{3\sqrt{\sigma}}{\kappa^4} - \frac{3\sigma}{\kappa^3} - \frac{\sigma\sqrt{\sigma}}{\kappa^2} \right) \\
&= -\frac{8i}{\hbar^2} \left(-\frac{4\sigma}{\kappa^3} - \frac{12\sqrt{\sigma}}{\kappa^4} - \frac{12}{\kappa^5} \right) \exp(-\kappa\sqrt{\sigma}).
\end{aligned}$$

With this result for the integrals, we can write down a final expression for the zero temperature current autocorrelation function:

$$\begin{aligned}
C_1^{(0)}(\varepsilon_1, \phi; \varepsilon'_1, \phi') &= \frac{\hbar^2}{2\sqrt{E_c}} \text{Im} \sum_{p=1}^{\infty} \sum_{\pm} \left(\pm \frac{p^2}{\phi_0^2} \cos\left(2\pi p \frac{\phi_{\pm}}{\phi_0}\right) \right) \frac{8i}{\hbar^2} \left(-\frac{4\sigma}{\kappa^3} - \frac{12\sqrt{\sigma}}{\kappa^4} - \frac{12}{\kappa^5} \right) \exp(-\kappa\sqrt{\sigma}) \\
&= -16 \frac{E_c^2}{\phi_0^2} \text{Re} \sum_{p=1}^{\infty} \sum_{\pm} \left(\pm \cos\left(2\pi p \frac{\phi_{\pm}}{\phi_0}\right) \right) \left(\frac{3}{p^3} + \frac{3\sqrt{z}}{p^2} + \frac{z}{p} \right) \exp(-p\sqrt{z}) \quad (2.60)
\end{aligned}$$

where we have introduced the notation

$$z = \varepsilon_{\perp} + \frac{i(\varepsilon_1 - \varepsilon'_1)}{E_c}. \quad (2.61)$$

For convenience, we define the function

$$F_p(z) = \text{Re} \left[\left(\frac{3}{p^3} + \frac{3\sqrt{z}}{p^2} + \frac{z}{p} \right) \exp(-p\sqrt{z}) \right] \quad (2.62)$$

which allows us to write the zero temperature correlation function as

$$C_1^{(0)}(\varepsilon_1, \phi; \varepsilon'_1, \phi') = -16 \frac{E_c^2}{\phi_0^2} \sum_{\varepsilon_{\perp}^{\pm}} \sum_{p=1}^{\infty} \pm F_p(z) \cos\left(2\pi p \frac{\phi \pm \phi'}{\phi_0}\right) \quad (2.63)$$

We note that, with the definition of ε_{\perp} in Eq. 2.55, the exponential in $F_p(z)$ takes the form $\exp(-p\sqrt{\frac{L^2\pi^2 n_r^2}{2w^2} + \frac{L^2\pi^2 n_z^2}{2t^2} + i\delta})$ where δ is a purely real number. For a high aspect ratio ring $L \gg w, t$, this exponential is negligible for $n_r, n_z > 0$. Thus we can discard these higher order transverse terms and use ε_{\perp} to signify the first term in the sum with $n_r = n_z = 0$. With the system we have considered so far, this first transverse energy term ε_{\perp} is equal to zero. Despite this fact, we do not drop the transverse energy ε_{\perp} term from our derivations. In Section 2.3.2, we will consider an effect, magnetic flux penetrating the metal of the ring, which leads to a non-zero value for ε_{\perp} . With this effect, ε_{\perp} takes different values for the diffuson and cooperon, so we also retain the \pm notation to distinguish these two terms where necessary. When only $\varepsilon_{\perp} = 0$ is significant, we can write

$$\begin{aligned} \langle I(\varepsilon_1, \phi) I(\varepsilon'_1, \phi') \rangle &= C_1^{(0)}(\varepsilon_1, \phi; \varepsilon'_1, \phi') \\ &= 32 \frac{E_c^2}{\phi_0^2} \sum_{\varepsilon_{\perp}^{\pm}} \sum_{p=1}^{\infty} F_p(z) \left(\sin\left(2\pi p \frac{\phi}{\phi_0}\right) \sin\left(2\pi p \frac{\phi'}{\phi_0}\right) \right). \end{aligned}$$

As noted at the beginning of this section, setting $\varepsilon_1 = \varepsilon'_1 = \varepsilon_F$ gives the zero temperature current-current correlation function

$$\begin{aligned} \langle I(\phi) I(\phi') \rangle_{T=0} &= C_1^{(0)}(\varepsilon_F, \phi; \varepsilon_F, \phi') \\ &= 96 \frac{E_c^2}{\phi_0^2} \sum_{p=1}^{\infty} \frac{1}{p^3} \sin\left(2\pi p \frac{\phi}{\phi_0}\right) \sin\left(2\pi p \frac{\phi'}{\phi_0}\right) \end{aligned}$$

or in terms of the ring parameters

$$\langle I(\phi) I(\phi') \rangle_{T=0} = \left(1.11 \frac{eD}{L^2}\right)^2 \sum_{p=1}^{\infty} \frac{2}{p^3} \sin\left(2\pi p \frac{\phi}{\phi_0}\right) \sin\left(2\pi p \frac{\phi'}{\phi_0}\right)$$

where the numerical factor is $2\sqrt{3}/\pi = 1.11$. We also define the typical magnitude I_p^{typ} of the p^{th}

harmonic (per spin) by

$$\begin{aligned} I_p^{\text{typ}} &= \frac{4\sqrt{3} E_c}{p^{1.5} \phi_0} \\ &= \frac{1.11 eD}{p^{1.5} L^2} \end{aligned} \quad (2.64)$$

so that

$$\langle I(\phi) I(\phi') \rangle_{T=0} = \sum_{p=1}^{\infty} 2 (I_p^{\text{typ}})^2 \sin\left(2\pi p \frac{\phi}{\phi_0}\right) \sin\left(2\pi p \frac{\phi'}{\phi_0}\right). \quad (2.65)$$

So far we have neglected the spin of the electron. Assuming the two spin states are degenerate, we simply multiply $\nu(\varepsilon)$ by a factor of 2 which results in a factor of 4 for $C_1^{(0)}$. We will neglect this factor of 2 for spin degeneracy until considering spin effects more closely in Sections 2.3.2.2 and 2.3.2.2.

For convenience in plotting normalized curves, we define the normalized correlation function $H_1^{(0)}(x)$ as

$$H_1^{(0)}(x) = \text{Re} \left[\left(1 + \sqrt{x} + \frac{x}{3}\right) \exp(-\sqrt{x}) \right] \quad (2.66)$$

so that the current-current correlation function $C_1^{(0)}(\varepsilon_1, \phi; \varepsilon'_1, \phi')$ can be expanded as

$$\begin{aligned} \langle I(\varepsilon_1, \phi) I(\varepsilon'_1, \phi') \rangle &= C_1^{(0)}(\varepsilon_1, \phi; \varepsilon'_1, \phi') \\ &= 3 \times 32 \frac{E_c^2}{\phi_0^2} \sum_p \frac{H_1^{(0)}(p^2 z)}{p^3} \sin\left(2\pi p \frac{\phi}{\phi_0}\right) \sin\left(2\pi p \frac{\phi'}{\phi_0}\right) \end{aligned} \quad (2.67)$$

$$= \sum_{p=1}^{\infty} 2 (I_p^{\text{typ}})^2 H_1^{(0)}(p^2 z) \sin\left(2\pi p \frac{\phi}{\phi_0}\right) \sin\left(2\pi p \frac{\phi'}{\phi_0}\right). \quad (2.68)$$

The function $H_1^{(0)}(p\sqrt{z})$ gives the normalized autocorrelation function of the harmonics of the current at the energy difference $\varepsilon_1 - \varepsilon'_1$. That is,

$$H_1^{(0)}\left(p\sqrt{\varepsilon_{\perp} + i\frac{\delta\varepsilon}{E_c}}\right) = \frac{\langle I_p(\varepsilon_1) I_p(\varepsilon_1 + \delta\varepsilon) \rangle}{\langle (I_p(\varepsilon_1))^2 \rangle}.$$

In Fig. 2.16, we plot $H_1^{(0)}(\sqrt{ip^2 \delta\varepsilon/E_c})$ versus $p^2 \delta\varepsilon/E_c$. The figure shows that the amplitude of the p^{th} harmonic of the total current is correlated over an energy range $\sim \pm 14E_c/p^2$. Interestingly, it can also be seen that the harmonics of the current possess some anti-correlation, reminiscent of the perfect anti-correlation of the single level currents of the ideal one-dimensional ring. For

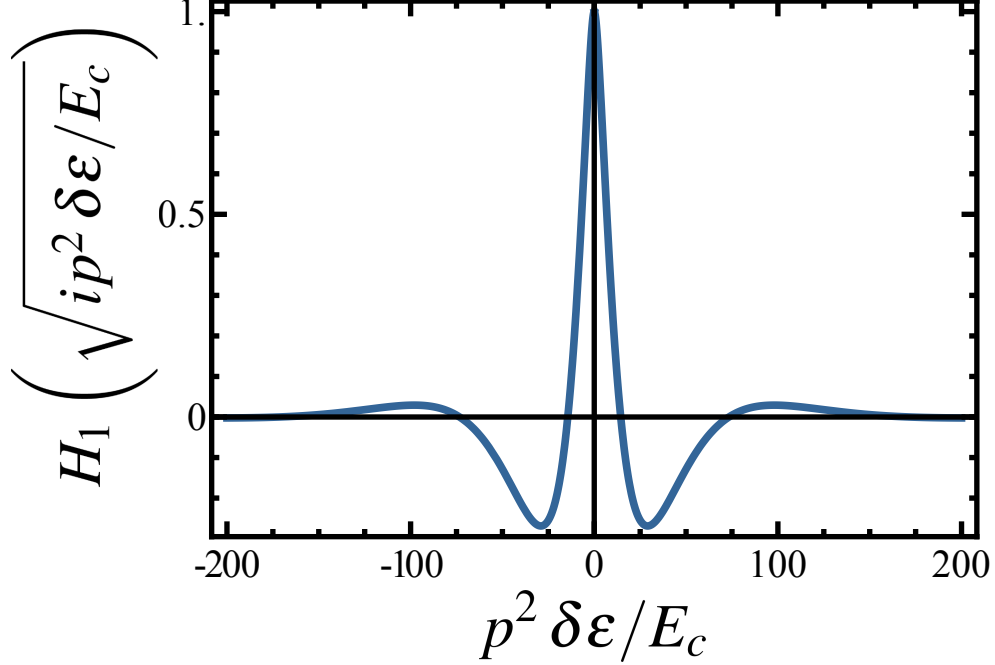


Figure 2.16: Current-current harmonic correlation function $H_1^{(0)}$ versus energy difference. The p^{th} harmonic of the total current is seen to be correlated over an energy range $\delta\varepsilon \sim 14E_c/p^2$. The correlation function shows a sizable amount of anti-correlation before decaying significantly.

more discussion of $H_1^{(0)}$ see Ref. 41,¹⁹ where it is argued that an increase $\delta\varepsilon$ in the Fermi energy equal to the single level spacing Δ_M is equivalent to an increase in the number of electrons in the ring by 1. Among the results of this argument is the conclusion that, for a large number M_{eff} of correlated levels and low harmonic index p , the typical single level current harmonic magnitude $i_p^{\text{typ}} = \sqrt{\langle i_p^2 \rangle} = p^{-1/2} \sqrt{2} \Delta_M / \phi_0$ scales with the single level spacing Δ_M . This result is reasonable given the conclusions drawn above that the single level current is proportional to the slope of that level with respect to flux and that adjacent levels are repelled from each other. That the total current is larger than this figure reinforces the interpretation given at the beginning of this section that a certain number of levels are correlated. By comparing the single level current and the total current

$$\frac{I_p^{\text{typ}}}{i_p^{\text{typ}}} = \frac{8\sqrt{3} E_c}{\sqrt{2} p \Delta_M},$$

¹⁹While mentioning this paper, I would also like to point out its discussion of the sensitivity of the persistent current to the location of impurities. It is argued that in the diffusive regime the autocorrelation function of the current as a function of the location of a single scattering center (with the rest of the disorder potential held fixed) decays exponentially on the length scale k_F^{-1} . In other words, the current is completely randomized when one scattering center within the ring is moved by a distance of one Fermi wavelength.

we can estimate that the number M_{eff} of correlated levels correlated for the p^{th} harmonic is

$$M_{\text{eff}} \sim 10E_c/p\Delta_M. \quad (2.69)$$

With $D = v_F l_e/3$, we can see that the typical current magnitude is approximately the single channel perfect ring current I_0 (Eq. 2.12) reduced by the factor l_e/L . From the sinusoidal factors, it can be seen that, although each harmonic has a random sign, its phase with respect to flux is well defined. The p^{th} harmonic of the current always is zero for $\phi = N\phi_0/2p$ with N an integer.

2.3.1.2 Finite temperature

We now evaluate the integrals of Eq. 2.50 in order to find the temperature dependence of the current-current correlation function. From Eq. 2.60, we can see that $C_1^{(0)}(\varepsilon_1, \phi; \varepsilon'_1, \phi')$ depends only on the difference $\varepsilon_1 - \varepsilon'_1$. This dependence motivates using the change of variables of Eq. 2.53 on the integrals of Eq. 2.50. Since $f'(\varepsilon, \varepsilon_F, T)$ is well localized around $\varepsilon_F \gg E_c$ and $C_1^{(0)}(\varepsilon_1, \phi; \varepsilon'_1, \phi')$ decays for $|\varepsilon_1 - \varepsilon'_1| \gg E_c$, we extend the lower bound of the ε_1 and ε'_1 integrals to $-\infty$. Using Eq. 2.18 for the form of $f'(\varepsilon, \varepsilon_F, T)$, we can then write

$$\begin{aligned} \langle I(\phi) I(\phi') \rangle &= \int_0^\infty d\varepsilon_1 \int_0^\infty d\varepsilon'_1 (f'(\varepsilon_1) f'(\varepsilon'_1)) C_1^{(0)}(\varepsilon_1, \phi; \varepsilon'_1, \phi') \\ &\approx \int_{-\infty}^\infty d\varepsilon_1 d\varepsilon'_1 \left(\frac{1}{4k_B T} \right)^2 \text{sech}^2 \left(\frac{\varepsilon_1 - \varepsilon_F}{2k_B T} \right) \text{sech}^2 \left(\frac{\varepsilon'_1 - \varepsilon_F}{2k_B T} \right) C_1^{(0)}(\varepsilon_1, \phi; \varepsilon'_1, \phi') \\ &\approx \left(\frac{1}{4k_B T} \right)^2 \int_{-\infty}^\infty d\varepsilon_1 d\varepsilon'_1 \text{sech}^2 \left(\frac{\varepsilon_1}{2k_B T} \right) \text{sech}^2 \left(\frac{\varepsilon'_1}{2k_B T} \right) C_1^{(0)}(\varepsilon_1, \phi; \varepsilon'_1, \phi') \\ &= \frac{1}{4} \int_{-\infty}^\infty d\varepsilon C_1^{(0)}(\varepsilon_1, \phi; \varepsilon'_1, \phi') \int_{-\infty}^\infty d\sigma \text{sech}^2 \left(\sigma + \frac{\varepsilon}{2} \right) \text{sech}^2 \left(\sigma - \frac{\varepsilon}{2} \right) \end{aligned}$$

where we have used $\varepsilon = (\varepsilon_1 - \varepsilon'_1)/2k_B T$ and $\sigma = (\varepsilon_1 + \varepsilon'_1)/4k_B T$. Using the expression for the integral over σ given in Eq. A.5, we find

$$\langle I(\phi) I(\phi') \rangle = \int_{-\infty}^\infty d\varepsilon f_2(\varepsilon) C_1^{(0)}(\varepsilon_1, \phi; \varepsilon'_1, \phi').$$

with the thermal weighting function (see Fig. 2.17)

$$f_2(\varepsilon) = \frac{\varepsilon \cosh \varepsilon - \sinh \varepsilon}{\sinh^3 \varepsilon}. \quad (2.70)$$

Using Eq. 2.60, we can write the current-current correlation function in terms of its harmonics as

$$\langle I(\phi) I(\phi') \rangle = \sum_{p=1}^{\infty} (I_p^{\text{typ}})^2 \sum_{\pm} \left(\mp \cos \left(2\pi p \frac{\phi_{\pm}}{\phi_0} \right) \right) g_D \left(p^2 \varepsilon_{\perp}, 20.8 \frac{T}{T_p} \right) \quad (2.71)$$

where the normalized temperature dependence (see Fig. 2.18) is

$$g_D(x, y) = \int_{-\infty}^{\infty} d\varepsilon f_2(\varepsilon) H_1^{(0)}(x + iy\varepsilon) \quad (2.72)$$

and the characteristic temperature of decay is

$$\begin{aligned} T_p &= \frac{10.4 E_c}{k_B p^2} \\ &= \frac{10.4 \hbar D}{k_B p^2 L^2}. \end{aligned} \quad (2.73)$$

We can also define a temperature dependent form for the typical magnitude I_p^{typ} of the persistent current harmonics (keeping only $\varepsilon_{\perp} = 0$)

$$\begin{aligned} I_p^{\text{typ}}(T) &= I_p^{\text{typ}}(T=0) \sqrt{g_D \left(0, 20.8 \frac{T}{T_p} \right)} \\ &= \frac{1.11 e D}{p^{1.5} L^2} \sqrt{g_D \left(0, 20.8 \frac{T}{T_p} \right)}. \end{aligned} \quad (2.74)$$

As discussed in Section A.4, the function $g_D(x, y)$ can also be expressed as the sum

$$g_D(x, y) = \frac{\pi^2 y^2}{12} \sum_{N=1}^{\infty} N \text{Re} \left(\exp \left(-\sqrt{x + \pi N y} \right) \right).$$

When $x = 0$, this sum takes the simpler form

$$g_D(0, y) = \frac{\pi^2 y^2}{12} \sum_{N=1}^{\infty} N \exp \left(-\sqrt{\pi N y} \right).$$

Over the experimentally relevant range of $y < 50$, the temperature dependence is roughly exponential (see Section A.4) with

$$g_D(0, y) \approx \exp(-0.096y), \quad (2.75)$$

meaning that the typical magnitude I_p^{typ} decays exponentially on the temperature scale $\sim T_p$.

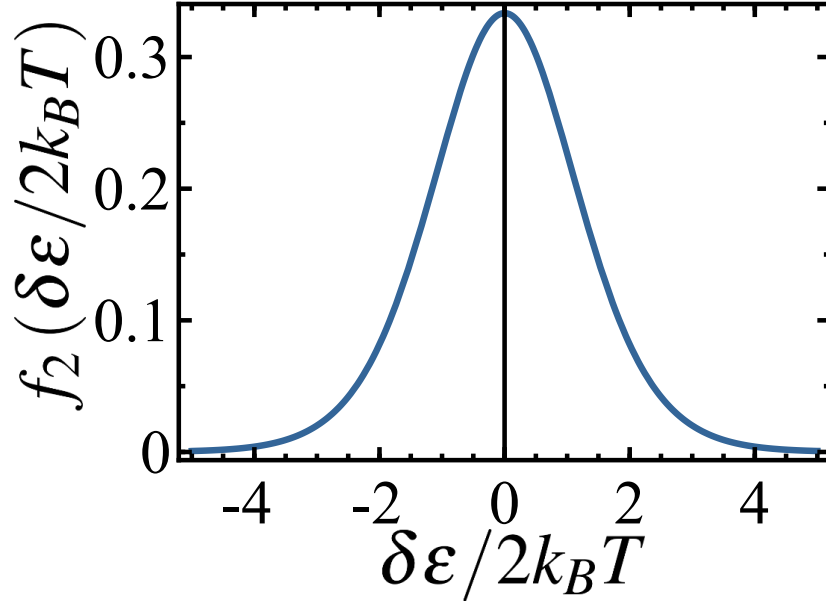


Figure 2.17: Temperature weighting function f_2 plotted against energy difference $\delta\varepsilon$. The figure shows the function f_2 of Eq. 2.70 which provides the weighting given to the current-current correlation function $H_1^{(0)}(ip^2 \delta\varepsilon/E_c)$ (Fig. 2.16) in the integral of Eq. 2.72 for the suppression of I_p^{typ} due to finite temperature (with $\varepsilon_\perp = 0$). As temperature increases, $f_2(\delta\varepsilon/2k_B T)$ becomes broader in $\delta\varepsilon$ and less weight is given to the central peak of $H_1^{(0)}(ip^2 \delta\varepsilon/E_c)$.

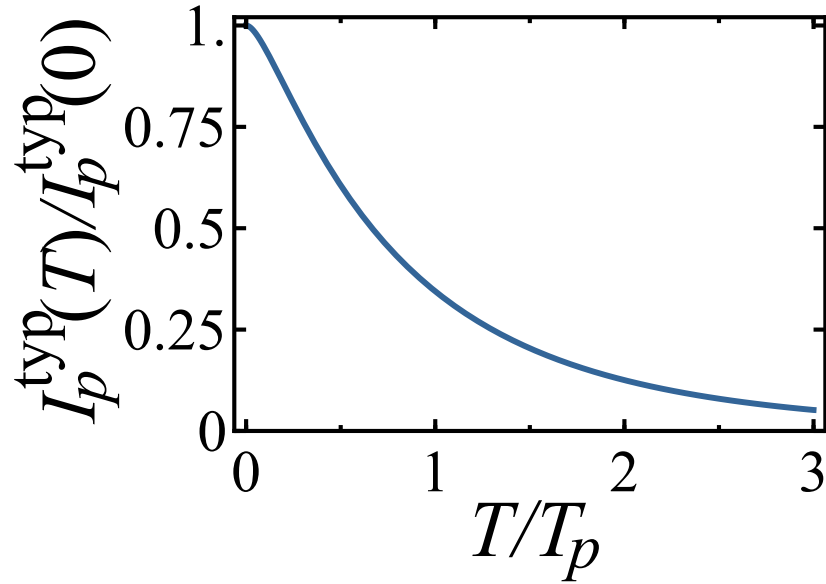


Figure 2.18: Temperature dependence of the persistent current in the diffusive regime. The typical magnitude $I_p^{\text{typ}}(T)$ of the p^{th} harmonic of the current, given in Eq. 2.74, is shown as a function of temperature. The vertical axis is normalized by the magnitude $I_p^{\text{typ}}(0)$ of the current at zero temperature, while the horizontal axis is normalized by the characteristic temperature T_p defined in Eq. 2.73.

2.3.2 Refinements to the calculation of the typical current

In the previous section, we investigated the persistent current in a ring threaded by an idealized Aharonov-Bohm flux. In practice, our measurements were performed at high magnetic field where the flux through the metal can not be ignored. The flux through the metal affects the persistent current in two ways. First, it modifies the vector potential \mathbf{A}_\pm of Eq. 2.52 and so changes the eigenvalues $E_n^{d,c}(B_\pm)$. The major result of this modification is the suppression of the cooperon contribution to $\langle I(\phi)I(\phi') \rangle$. Additionally, the Zeeman effect lifts the spin degeneracy of the electrons. Spin degeneracy is also lifted by spin orbit scattering, which is non-negligible in the samples we measured (see Appendix E). All of these effects were considered recently in Ref. 42.

2.3.2.1 Flux through the metal of the ring

In Eq. 2.65, we wrote the current-current correlation function as a sum over harmonics. This form was a rearrangement of a previous form (see e.g. Eq. 2.63) involving the sum and difference of fluxes. These two forms are

$$\begin{aligned} \langle I(\phi) I(\phi') \rangle &= \sum_{p=1}^{\infty} \langle I_p^2 \rangle \left(\cos \left(2\pi \frac{\phi - \phi'}{\phi_0} \right) - \cos \left(2\pi \frac{\phi + \phi'}{\phi_0} \right) \right) \\ &= \sum_{p=1}^{\infty} 2 \langle I_p^2 \rangle \sin \left(2\pi \frac{\phi}{\phi_0} \right) \sin \left(2\pi \frac{\phi'}{\phi_0} \right). \end{aligned} \quad (2.76)$$

Looking back over the derivation of Section 2.3.1.1, the term involving $\phi_+ = \phi + \phi'$ can be linked to the cooperon, while the term involving $\phi_- = \phi - \phi'$ is due to the diffuson. For $\phi = \phi'$, we have

$$\langle I^2(\phi) \rangle = \sum_p \langle I_p^2 \rangle \left(1 - \cos \left(2\pi \frac{2\phi}{\phi_0} \right) \right),$$

from which it can be seen that the diffuson term provides a constant contribution to typical magnitude of each harmonic while the cooperon contribution oscillates with period $\phi_0/2$. The role of the cooperon is to provide a definite phase reference for the oscillations of $I(\phi)$ with respect to ϕ . Because of the cooperon, the average variance of the current $\langle I^2(N\phi_0/2) \rangle$ is zero at flux values $\phi = N\phi_0/2$ for all integer N . Consider the quantity

$$\overline{\langle I^2 \rangle} = \frac{1}{\phi_0} \int_0^{\phi_0} d\phi \langle I^2(\phi) \rangle,$$

where the bar $\overline{\dots}$ denotes that the variance of the current is averaged over one period ϕ_0 . The contribution of the p^{th} harmonic to $\overline{\langle I^2 \rangle}$ can be broken up into the contribution from the diffuson

$$\begin{aligned}\overline{\langle I_p^2 \rangle}_d &= \frac{1}{\phi_0} \int_0^{\phi_0} d\phi \langle I_p^2 \rangle \\ &= \langle I_p^2 \rangle\end{aligned}$$

and the cooperon

$$\begin{aligned}\overline{\langle I_p^2 \rangle}_c &= \frac{1}{\phi_0} \int_0^{\phi_0} d\phi \langle I_p^2 \rangle \cos\left(2\pi \frac{2\phi}{\phi_0}\right) \\ &= 0.\end{aligned}$$

With this breakdown of the contributions to $\overline{\langle I^2 \rangle}$, it can be seen that all of the magnitude of the variance of the current $\overline{\langle I^2 \rangle}$ is due to the diffuson, while the role of the cooperon is solely to modify the flux dependence of the variance of the current.

We note that the suppression of the cooperon is consistent with the randomization of the phases of the persistent current harmonics. We can write the persistent current in the form

$$\begin{aligned}I(\phi) &= \sum_p \sqrt{2} I_p \sin\left(2\pi p \frac{\phi}{\phi_0} + \alpha_p\right) \\ &= \sum_p \sqrt{2} I_p \left(\cos(\alpha_p) \sin\left(2\pi p \frac{\phi}{\phi_0}\right) + \sin(\alpha_p) \cos\left(2\pi p \frac{\phi}{\phi_0}\right) \right),\end{aligned}$$

where with the cooperon unsuppressed all phases α_p must be zero and the factor of $\sqrt{2}$ is included so that I_p is the same quantity as in Eq. 2.76. The amplitude I_p and phase α_p are assumed to vary independently with disorder configuration and to be independent from harmonic to harmonic:

$$\begin{aligned}\langle I_p I_{p'} \rangle &= \langle I_p^2 \rangle \delta_{pp'} \\ \langle \sin(\alpha_p) \sin(\alpha_{p'}) \rangle &= \frac{\delta_{pp'}}{2} \\ \langle \cos(\alpha_p) \cos(\alpha_{p'}) \rangle &= \frac{\delta_{pp'}}{2} \\ \langle \sin(\alpha_p) \cos(\alpha_{p'}) \rangle &= 0 \\ \langle I_p f(\alpha_{p'}) \rangle &= \langle I_p \rangle \langle f(\alpha_{p'}) \rangle\end{aligned}$$

where f is any function. With these assumptions, we can write

$$\begin{aligned}\langle I(\phi) I(\phi') \rangle &= \sum_p 2 \langle I_p^2 \rangle \left(\frac{1}{2} \sin \left(2\pi p \frac{\phi}{\phi_0} \right) \sin \left(2\pi p \frac{\phi'}{\phi_0} \right) + \frac{1}{2} \cos \left(2\pi p \frac{\phi}{\phi_0} \right) \cos \left(2\pi p \frac{\phi'}{\phi_0} \right) \right) \\ &= \sum_p \langle I_p^2 \rangle \cos \left(2\pi p \frac{\phi - \phi'}{\phi_0} \right).\end{aligned}$$

This final expression matches Eq. 2.76 with the $\phi_+ = \phi + \phi'$ term associated with the cooperon dropped. We now consider the effects of magnetic flux penetrating the metal of the ring, which leads to such a suppression of the cooperon.

In the experimental arrangement discussed in this text, the metal ring is subjected to a uniform field applied at an angle relative to the plane of the ring. Ideally, we would like to decompose the field $\mathbf{B} = \mathbf{B}_\phi + \mathbf{B}_M$ into the fields \mathbf{B}_ϕ threading flux through the ring and \mathbf{B}_M penetrating the metal, so that we can use the results of the previous section with \mathbf{B}_ϕ leading to the dependence on ϕ in the results of that section and \mathbf{B}_M providing perturbative corrections to that result. Such an approach is complicated, however, by the boundary conditions given in Eq. 2.54 for the diffuson and cooperon. In principle, \mathbf{B}_M , and thus the corresponding vector potential \mathbf{A}_M , varies in a non-uniform manner throughout the ring. Because of the boundary condition's dependence on the vector potential \mathbf{A} , the diffuson and cooperon eigenfunctions depend on the perturbing field \mathbf{B}_M , complicating the simple perturbation theory approach.

In Ref. 42, the complications associated with an arbitrary \mathbf{B}_M are circumvented by choosing a particular form of \mathbf{B}_M , the toroidal field, for which $\mathbf{A}_M \cdot \tilde{\mathbf{n}} = 0$ and thus for which the boundary condition of Eq. 2.54 is independent of \mathbf{B}_M . The toroidal field is specified by $\mathbf{B}_M = B_M \tilde{\boldsymbol{\theta}}$ within the ring. While such a form for \mathbf{B}_M is geometrically quite distinct from the experimental arrangement, it does allow an analytical solution for the current-current correlation function for the case of a magnetic field inside the ring. As is argued in Ref. 42, this analytical solution differs from the solution for the field $\mathbf{B}_{M,\text{exp}}$ appropriate for the experimental set-up only by a geometrical scaling $\alpha_M \sim 1$ of the field strength as $\mathbf{B}_{M,\text{exp}} = \gamma \mathbf{B}_M$.

In order to solve for the current-current correlation function analytically in the presence of the toroidal field, a couple other approximations must be made. First, the ring is taken to have a circular cross-section rather than a rectangular one. We keep the cross-sectional area of the ring constant by taking the radius of the circular cross-section to be $r_T = \sqrt{wt/\pi}$. Second, the high aspect ratio limit is taken where the curvature of the ring can be ignored. In this limit, the ring

can be viewed as a cylinder centered along the z -axis. The quantity $L\theta/2\pi$ then becomes z , with the condition $\theta + 2\pi = \theta$ becoming $z + L = z$ and $\mathbf{A}_\phi = \phi\tilde{\boldsymbol{\theta}}/2\pi r \rightarrow \phi\tilde{\mathbf{z}}/L$. Eq. 2.52 then becomes, for $\mathbf{A}_M = 0$,

$$\begin{aligned} \left(\nabla' + i\frac{e}{\hbar}\mathbf{A}_\mp\right)^2 P_{d,c}(\mathbf{r}, \mathbf{r}', \omega) &= E_n^{d,c}(B_\mp) P_{d,c}(\mathbf{r}, \mathbf{r}', \omega) \\ \left(\frac{\partial^2}{\partial x'^2} + \frac{\partial^2}{\partial y'^2} + \left(\frac{\partial}{\partial z'} + \frac{2\pi i}{L}\frac{\phi_\mp}{\phi_0}\right)^2\right) P_{d,c}(\mathbf{r}, \mathbf{r}', \omega) &= E_n^{d,c}(B_\mp) P_{d,c}(\mathbf{r}, \mathbf{r}', \omega), \end{aligned}$$

which once again separates to allow eigenfunctions of the form $P_{d,c}(\mathbf{r}, \mathbf{r}', \omega) = X(x, y) \exp(2\pi i n z/L)$ and has eigenvalues of the form of Eq. 2.55. With this coordinate system, the toroidal field is $\mathbf{B}_M = B_M \hat{\mathbf{z}}$, for which the vector potential can be written as

$$\mathbf{A}_M = -\frac{B_M}{2}y\tilde{\mathbf{x}} + \frac{B_M}{2}x\tilde{\mathbf{y}}.$$

This form for \mathbf{A}_M is always parallel to the surface of the ring (it is always orthogonal to the vector $x\tilde{\mathbf{x}} + y\tilde{\mathbf{y}}$ normal to the ring surface).

For the lowest transverse mode at $B_M = 0$, the eigenvalue is $\varepsilon_\perp = 0$ and the eigenfunction $X_0(x, y) = (\pi r_T^2)^{-1/2}$ is a constant. Treating the toroidal field as a perturbation with

$$wtB_M \ll \phi_0, \quad (2.77)$$

we find the leading correction to the lowest transverse eigenvalue to the cooperon (+) and diffuson (-) to be

$$\begin{aligned} \varepsilon_\perp^\pm &= L^2 \left\langle X_0 \left| \left(\nabla + 2\pi i \frac{\mathbf{A}_M^\pm}{\phi_0} \right)^2 \right| X_0 \right\rangle \\ &= L^2 \iint dx dy X_0^2(x, y) \left(\frac{\pi^2 (B_M^\pm)^2 y^2}{\phi_0^2} + \frac{\pi^2 (B_M^\pm)^2 x^2}{\phi_0^2} \right) \\ &= \frac{L^2}{wt} \int_0^{\sqrt{wt/\pi}} dr \int_0^{2\pi} d\theta r^3 \frac{\pi^2 (B_M^\pm)^2}{\phi_0^2} \\ &= \frac{\pi (B_M^\pm)^2 wt L^2}{2 \phi_0^2} \end{aligned} \quad (2.78)$$

where the factor of L^2 comes from the scaling used when ε_\perp was introduced in Eq. 2.55.

In the previous section, we retained the ε_\perp in most expressions despite concluding that for a

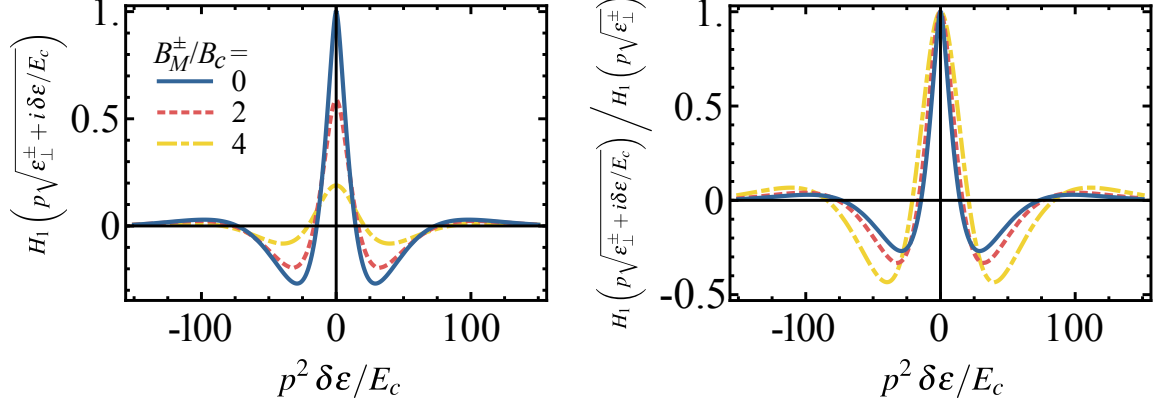


Figure 2.19: Current-current harmonic correlation function $H_1^{(0)}$ versus energy difference for different values of the toroidal field B_M^{\pm} . The left plot shows $H_1^{(0)}(p\sqrt{\varepsilon_{\perp}^{\pm} + i\delta\varepsilon/E_c})$ versus the normalized energy difference $p^2\delta\varepsilon/E_c$ for different values of the toroidal field $B_M^{\pm}/B_{c,p}$. The main effect of finite B_M^{\pm} is an overall reduction of the current-current correlation function, with otherwise minor effects on $H_1^{(0)}$'s dependence on $\delta\varepsilon$, as seen in the right plot where the same curves are scaled so that they are all unity at $\delta\varepsilon = 0$.

high aspect ratio ring we could take $\varepsilon_{\perp} = 0$. We did this so that the relations derived there would be valid for the case of the toroidal field with ε_{\perp} as given in Eq. 2.78. Adapting Eq. 2.63 (and ignoring the factor of 4 for spin degeneracy), we find that the current-current correlation function in the presence of a toroidal field is

$$C_1^{(0)}(\varepsilon_1, \phi, B_M; \varepsilon'_1, \phi', B'_M) = 16 \frac{E_c^2}{\phi_0^2} \sum_{p=1}^{\infty} \sum_{\pm} F_p(z_{\pm}) \left(\mp \cos\left(2\pi p \frac{\phi \pm \phi'}{\phi_0}\right) \right)$$

where

$$z_{\pm} = \varepsilon_{\perp}^{\pm} + \frac{i(\varepsilon_1 - \varepsilon'_1)}{E_c}.$$

In Fig. 2.19, we plot the correlation function $H_1^{(0)}$ defined in Eq. 2.66 and shown previously in Fig. 2.16 now for different, finite values of B_M . This function gives the normalized correlation in energy of the p^{th} harmonic of the current at zero temperature,

$$H_1^{(0)}\left(p\sqrt{\varepsilon_{\perp}^{\pm} + i\frac{\delta\varepsilon}{E_c}}\right) = \frac{\langle I_p(\varepsilon_1, B_M) I_p(\varepsilon_1 + \delta\varepsilon, B'_M) \rangle}{\langle (I_p(\varepsilon_1, B_M^{\pm} = 0))^2 \rangle}.$$

At finite temperature, the current-current correlation function, following Eq. 2.71, is

$$\langle I(\phi, B_M) I(\phi', B'_M) \rangle = \sum_p (I_p^{\text{typ}})^2 \sum_{\pm} \left(\mp \cos\left(2\pi p \frac{\phi \pm \phi'}{\phi_0}\right) \right) g_D\left(p^2\varepsilon_{\perp}^{\pm}, 20.8 \frac{T}{T_p}\right).$$

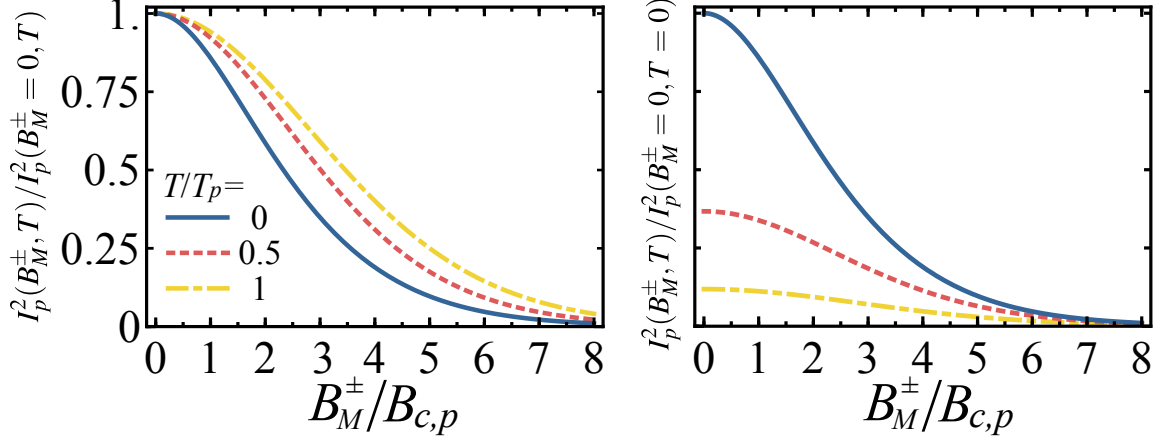


Figure 2.20: Current-current correlation function versus toroidal field. The correlation function $I_p^2(B_M^\pm, T)$ of the p^{th} harmonic of the current is plotted against the scaled toroidal field $B_M^\pm/B_{c,p}$ for three different scaled temperatures $T = 0, 0.5T_p$, and T_p . The correlation function is scaled by its value $I_p^2(B_M^\pm = 0, T)$ at zero field and finite temperature. In the inset, the same curves are shown scaled by the zero-temperature, zero-field value $I_p^2(B_M^\pm = 0, T = 0)$ of the correlation function. The correlation function is seen to decay on a field scale $B_M^\pm \sim 3B_{c,p}$, indicating that the cooperon is suppressed at large field. The diffuson is not suppressed with absolute field but does have a finite correlation in field difference $B_M^- = B_M - B_M'$. Temperature has only a small effect on the field dependence of $I_p^2(B_M^\pm, T)$ in the temperature range between 0 and T_p .

We can also write this function as

$$\langle I(\phi, B_M) I(\phi', B_M') \rangle = \sum_p \sum_{\pm} I_p^2(B_M^\pm, T) \left(\mp \cos\left(2\pi p \frac{\phi_{\pm}}{\phi_0}\right) \right)$$

with

$$I_p^2(B_M^\pm, T) = (I_p^{\text{typ}})^2 g_D \left(p^2 \varepsilon_{\pm}^{\pm}, 20.8 \frac{T}{T_p} \right)$$

the temperature dependent correlation function of the p^{th} harmonic with respect to the toroidal field B_M . In Fig. 2.20, the persistent current harmonic correlation function $I_p^2(B_M^\pm, T)$ is plotted for several temperatures T against B_M^\pm scaled by the field scale

$$B_{c,p} = \frac{1}{p} \sqrt{\frac{2}{\pi}} \frac{\phi_0}{L\sqrt{wt}}. \quad (2.79)$$

The field scale $B_{c,p}$ is of the order of the field required to thread flux ϕ_0/p through the shadow cast by the ring onto the plane perpendicular to the applied magnetic field.²⁰

The persistent current correlation $I_p^2(B_M^\pm, T)$ decays over the toroidal field scale $B_M^\pm \sim 3B_{c,p}$.

²⁰For typical ring dimensions, this projected area changes by no more than a factor of three as the ring is rotated so this flux is of the appropriate magnitude for all ring orientations.

For the cooperon, this result means that the cooperon contribution to the persistent current correlation function decays for $B_M \sim 1.5B_c$. For the diffuson, this decay means that the amplitude of the harmonics of the current become uncorrelated on the scale $B_M - B'_M \sim 3B_{c,p}$. For the experimentally relevant case of a large uniform magnetic field applied at an angle θ with respect to the plane of the ring, the quantities the threaded flux ϕ through the ring and the toroidal field B_M penetrating the metal are proportional and related to each other through the aspect ratio of the ring and the geometrical factor γ mentioned above. As the applied magnetic field B is swept, the current undergoes oscillations of frequency $\beta_0 = \phi_0/(\pi R^2 \sin \theta)$ as the component of B perpendicular to the ring plane changes by enough to thread ϕ_0 through it. At the same time, the field B_M through the metal of the ring is changing. Once B_M changes by around

$$B_c \equiv B_{c,p=1},$$

the oscillations of the current in B are no longer correlated. Effectively, the amplitude and phase of the oscillations of the persistent are randomized on this field scale. Since the autocorrelation function and the power spectral density are related by a Fourier transform, we can rephrase this result, by stating that the flux through the finite linewidth of the ring introduces a broadening of the persistent current's magnetic field frequency β of $\sim 1/3B_c$.

While it is extremely useful for the correlation field $3B_c$ to be larger than the period $1/\beta$ of the persistent current oscillation so that the current signal has a well-defined magnetic field frequency which can be distinguished from background noise, we note in passing that the finite correlation of the persistent current also brings benefits from an experimental point of view. By appeal to the ergodic hypothesis, it can be argued that the finite correlation of the persistent current oscillation leads to measurements separated by a field $> 3B_c$ being statistically independent [53, 54]. By measuring over a field range covering many B_c , a statistical distribution of the persistent current can be built up from measurements of only a single sample.²¹

²¹Additionally, the fact that different regions of magnetic field correspond to independent samples means that every physical sample should be capable of producing a signal of roughly the same magnitude. For SQUID and superconducting resonator techniques, the measurement is confined to a field region less than $3B_c$. For some samples, the current will be small as it is being drawn from a probability distribution centered around 0. For a measurement over a wide field range, it is possible that the current will be small (compared to I^{typ}) in some field regions. However, it is also statistically unlikely that the current will be small over the entirety of a region much greater than $3B_c$. In fact, because the phase of the persistent current becomes randomized, the persistent current becomes a random phasor. If the underlying distribution of the current is the normal distribution with standard deviation I^{typ} , then the amplitude of each quadrature of the persistent current phasor should be drawn from a normal distribution as well. The amplitude of the persistent current phasor then follows the Rayleigh distribution, which is peaked at I^{typ} . That is, the most probable amplitude of the current is I^{typ} . The fact that each sample should produce a measurable signal is useful when trying to “debug” a measurement.

2.3.2.2 Zeeman splitting

An applied magnetic field also affects the persistent current through its interaction with the electron spins. A spin σ in a magnetic field \mathbf{B} receives an energy shift E_Z proportional to $\sigma \cdot \mathbf{B}$. The degeneracy of up and down spins is broken by this splitting. As the Zeeman energy E_Z is turned up, the entire sets of spin up and spin down energy levels are shifted relative to each other. From Fig. 2.16, it was seen that the energy levels in the diffusive ring are correlated only over an energy range $\sim 14E_c$. In the absence of Zeeman splitting, the amplitude $I_{p\uparrow}$ of the p^{th} harmonic of the current associated with the spin up states is identical to the amplitude $I_{p\downarrow}$ of the spin down states so that the typical total amplitude of this harmonic is

$$\begin{aligned}\sqrt{\langle I_{p,\text{tot}}^2 \rangle} &= \sqrt{\langle (I_{p\uparrow} + I_{p\downarrow})^2 \rangle} \\ &= \sqrt{\langle (2I_{p\uparrow})^2 \rangle} \\ &= 2\sqrt{\langle I_{p\uparrow}^2 \rangle},\end{aligned}$$

twice the typical current of the single spin set of levels. In the presence of strong Zeeman splitting $E_Z \gg 14E_c$, the current associated with the spin up and spin down states is no longer correlated, $\langle I_{p\uparrow} I_{p\downarrow} \rangle = 0$. The typical harmonic amplitude is then reduced by a factor of $\sqrt{2}$:

$$\begin{aligned}\sqrt{\langle I_{p,\text{tot}}^2 \rangle} &= \sqrt{\langle (I_{p\uparrow} + I_{p\downarrow})^2 \rangle} \\ &= \sqrt{\langle I_{p\uparrow}^2 \rangle + \langle I_{p\downarrow}^2 \rangle + 2\langle I_{p\uparrow} I_{p\downarrow} \rangle} \\ &= \sqrt{2}\sqrt{\langle I_{p\uparrow}^2 \rangle},\end{aligned}$$

where we make use of the fact that the typical current of each set of spin states is unaffected by Zeeman splitting.

In order to find the current in between these two extremes, we re-perform the preceding calculation using the modified form of the density of states correlation function $\langle \nu(\varepsilon_1, B) \nu(\varepsilon'_1, B') \rangle$ given in Eq. B.35 which accounts for the Zeeman splitting.²² The result for the current-current correlation

²²For simplicity, it is assumed that magnetic field used to calculate the Zeeman energy is the same for both B and B' . Such an approximation is exact for any quantity calculated for which $B = B'$. Additionally, it is accurate for finite $B_M^- = B_M - B'_M \ll B_M$, which is the regime of interest when calculating the field correlation of the diffuson at large toroidal field.

function (Eq. 2.63) is

$$C_1^{(0)}(\varepsilon_1, \phi, B_M; \varepsilon'_1, \phi', B'_M; E_Z) = 16 \frac{E_c^2}{\phi_0^2} \sum_{p=1}^{\infty} \sum_{\pm} \left(\mp \cos \left(2\pi p \frac{\phi_{\pm}}{\phi_0} \right) \right) \left(2F_p(z) + F_p \left(z - 2i \frac{E_Z}{E_c} \right) + F_p \left(z + 2i \frac{E_Z}{E_c} \right) \right) \quad (2.80)$$

with F_p given by Eq. 2.62 and $z = \varepsilon_{\perp}^{\pm} + i(\varepsilon_1 - \varepsilon'_1)/E_c$, or, following Eqs. 2.64 and 2.68,

$$\begin{aligned} C_1^{(0)}(\varepsilon_1, \phi, B_M; \varepsilon'_1, \phi', B'_M; E_Z) &= \sum_{p=1}^{\infty} (I_p^{\text{typ}})^2 \sum_{\pm} \left(\mp \cos \left(2\pi p \frac{\phi_{\pm}}{\phi_0} \right) \right) c_p^0(\varepsilon_1 - \varepsilon'_1, B_M^{\pm}, E_Z, E_{SO} = 0) \\ &= \sum_{p=1}^{\infty} (I_p^{\text{typ}})^2 \sum_{\pm} \left(\mp \cos \left(2\pi p \frac{\phi_{\pm}}{\phi_0} \right) \right) \times \dots \\ &\quad \times \left(2H_1^{(0)}(p^2 z) + H_1^{(0)} \left(p^2 z - 2ip^2 \frac{E_Z}{E_c} \right) + H_1^{(0)} \left(p^2 z + 2ip^2 \frac{E_Z}{E_c} \right) \right), \end{aligned} \quad (2.81)$$

where we have introduced the notation $c_p^0(\varepsilon, B_M^{\pm}, E_Z, E_{SO})$ as an abbreviation for the normalized p^{th} harmonic and \pm component of $C_1^{(0)}$. We include a dependence on E_{SO} in anticipation of the results of the next section. At finite temperature, Eq. 2.71 is modified to

$$\begin{aligned} \langle I(\phi) I(\phi') \rangle &= \sum_{p=1}^{\infty} (I_p^{\text{typ}})^2 \sum_{\pm} \left(\mp \cos \left(2\pi p \frac{\phi_{\pm}}{\phi_0} \right) \right) c_p^T(T, B_M^{\pm}, E_Z, E_{SO} = 0) \\ &= \sum_{p=1}^{\infty} (I_p^{\text{typ}})^2 \sum_{\pm} \left(\mp \cos \left(2\pi p \frac{\phi_{\pm}}{\phi_0} \right) \right) \times \dots \\ &\quad \times \left(2g_D \left(p^2 \varepsilon_{\perp}^{\pm}, 20.8 \frac{T}{T_p} \right) + \dots \right. \\ &\quad \left. + g_D \left(p^2 \left(\varepsilon_{\perp}^{\pm} - 2i \frac{E_Z}{E_c} \right), 20.8 \frac{T}{T_p} \right) + \dots \right. \\ &\quad \left. + g_D \left(p^2 \left(\varepsilon_{\perp}^{\pm} + 2i \frac{E_Z}{E_c} \right), 20.8 \frac{T}{T_p} \right) \right) \end{aligned} \quad (2.82)$$

where we have again introduced a normalized notation c_p^T for the p^{th} harmonic and \pm component of the sum (note that c_p^0 is a zero temperature correlation in energy, whereas c_p^T is a finite-temperature correlation in field B_M^{\pm}).

From Eqs. 2.80 and 2.82, it can be seen that in the presence of Zeeman splitting the zero-

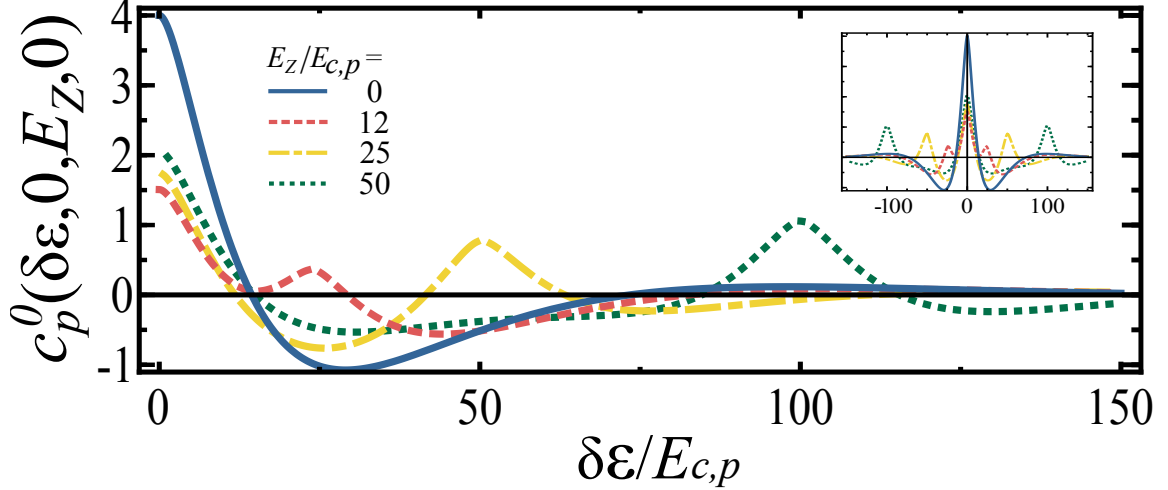


Figure 2.21: Zero-temperature current-current correlation function versus energy difference at finite Zeeman splitting. The curves show the normalized current-current correlation function $c_p^0(\delta\varepsilon, B_M^\pm, E_Z, E_{SO})$ versus the normalized energy difference $\delta\varepsilon/E_c$ for values of the Zeeman energy $E_Z/E_c = 0, 12, 25, 50$ (and $B_M^\pm = E_{SO} = 0$). For $E_Z = 0$, the correlation function is four times that of the spin-less case. At large E_Z , it is reduced to half its value near $\delta\varepsilon = 0$ and has additional copies of the spin-less correlation function centered at $\pm 2E_Z$. At intermediate E_Z , these shifted correlation functions overlap leading to a complicated form for the total correlation function. Interestingly, the two intermediate curves have lower values for c_p^0 at $\delta\varepsilon = 0$ than either the weak or strong E_Z regimes. The inset shows the same curves plotted over a different range of $\delta\varepsilon$. It is seen that c_p^0 remains symmetric in $\delta\varepsilon$ at finite E_Z .

temperature current-current correlation function $C_1^{(0)}(\varepsilon_1, \phi; \varepsilon'_1, \phi')$ is modified from being from four times its value for spin-less particles to being twice its value for spin-less particles plus two terms shifted in energy difference $\delta\varepsilon = \varepsilon_1 - \varepsilon'_1$ by $\pm 2E_Z$. These latter two terms represent the shifting in energy of the up and down spin states due to the Zeeman effect. The levels that are correlated are shifted to finite energy difference.

These shifts are shown in Fig. 2.21 where the normalized current-current correlation function $c_p^0(\delta\varepsilon, B_M^\pm, E_Z, E_{SO})$ is plotted versus $\delta\varepsilon/E_{c,p}$ for several values of $E_z/E_{c,p}$ (and $B_M^\pm = E_{SO} = 0$) with $E_{c,p} = E_c/p^2$. Interestingly, due to the anti-correlation in $C_1^{(0)}(\varepsilon_1, \phi; \varepsilon'_1, \phi')$ near $\varepsilon_1 - \varepsilon'_1 \sim \pm 25E_c$, the value of c_p^0 for $\delta\varepsilon = 0$ and $E_Z \sim \pm 12E_{c,p}$ drops below 2, its value at $\delta\varepsilon = 0$ in the limit of large E_Z where the levels of the two spin states are uncorrelated, because the Zeeman splitting causes these anti-correlated levels to overlap. We note that, for typical values of the diffusion constant $D = 0.02 \text{ m}^2/\text{s}$ and the ring circumference $L = 2 \mu\text{m}$, the Zeeman energy $E_Z = 2\mu_B B$ at 1 T corresponds to $E_Z \approx 35E_c$.

The oscillation of the current-current correlation function's magnitude near $\delta\varepsilon = 0$ with E_Z corresponds to an oscillation in the typical magnitude of the current as a function of E_Z . From

Eq. 2.82 it can be seen that the quantity $c_p^T(T, B_M^\pm, E_Z, E_{SO})$ gives the square magnitude of the p^{th} harmonic of the current at finite T , B_M^\pm , E_Z , and E_{SO} , normalized by the single-spin value at $T = B_M^\pm = E_Z = E_{SO} = 0$. That is,

$$c_p^T(T, B_M^\pm, E_Z, E_{SO}) = \frac{\langle I^2(T, B_M^\pm, E_Z, E_{SO}) \rangle_{\text{both spins}}}{\langle I^2(T = 0, B_M^\pm) \rangle_{\text{single spin}}}.$$

In Fig. 2.22, the normalized typical magnitude

$$\frac{I_{p,2s}^{\text{typ}}(T, E_Z)}{I_{p,1s}^{\text{typ}}(T)} = \sqrt{\frac{c_p^T(T, 0, E_Z, 0)}{g_D\left(0, 20.8\frac{T}{T_p}\right)}}$$

of the p^{th} harmonic of the current is plotted versus E_Z for several values of temperature. The label $2s$ denotes a quantity that accounts for the two spin states, while $1s$ ignores spin. The label $1s$ could be applied to results of all preceding calculations in the diffusive regime as up to now we have ignored spin. Whenever a Zeeman or spin-orbit dependence is written, the two spin label $2s$ is implied since Zeeman splitting and spin orbit scattering are spin-dependent effects. The magnitude of the current is seen to decay in an oscillatory fashion from twice the single-spin value $I_{p,1s}^{\text{typ}}$ for the spin-degenerate case of $E_Z = 0$ to $\sqrt{2}I_{p,1s}^{\text{typ}}$ in the uncorrelated spin regime of $E_Z \gg E_c$. The transition between these two regimes occurs more slowly at higher temperature.

The explanation for this interplay between the temperature and Zeeman energy on the typical current magnitude can be deduced by consulting Figs. 2.17 (showing the thermal weighting function $f_2(\delta\varepsilon/2k_B T)$) and 2.21 (showing $c_p^0(\delta\varepsilon, 0, E_Z, 0)$). The typical current is found by integrating the product of these two functions and taking the square root. As E_Z is increased, the correlation close to $\delta\varepsilon = 0$ is decreased at the expense of greater correlation at larger $\delta\varepsilon$ as the Zeeman split terms are shifted. As temperature is increased, the range of $\delta\varepsilon$ given an appreciable weight by f_2 increases and the Zeeman shifted features in the correlation at larger values of $\delta\varepsilon$ contribute more to the integral. Physically speaking, as E_Z is increased, the correlated orbitals of opposite spin are shifted apart and the correlation becomes less significant. At finite temperature, the occupancy of the levels is spread out, allowing the electrons to occupy the displaced correlated levels. The large Zeeman splitting regime requires both $E_Z \gg E_c$ and $E_Z \gg k_B T$. The temperature dependence of the transition for weak to strong Zeeman splitting also results in added features in the plot of the typical current versus temperature, (Fig. 2.23). Other than an overall suppression, the

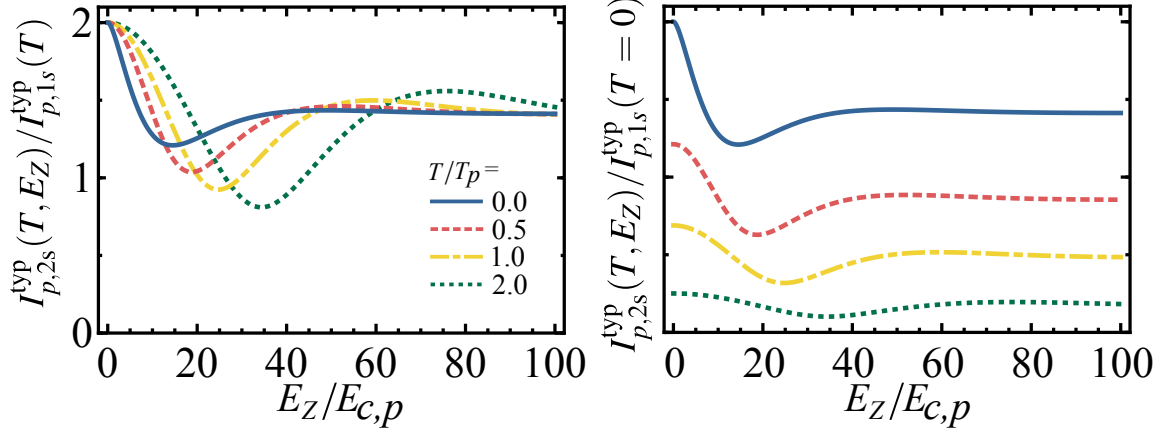


Figure 2.22: Typical magnitude of the persistent current harmonics versus Zeeman energy at finite temperature. In the left plot, the curves represent the typical magnitude of the current at finite T and E_Z normalized by the single spin magnitude of the current at finite T , so that all curves agree at $E_Z = 0$. The curves represent the normalized current magnitude for $T/T_p = 0, 0.5, 1,$ and 2 . As E_Z is increased, the typical magnitude of the current decays from $2I_{p,1s}^{typ}(T)$ to $\sqrt{2}I_{p,1s}^{typ}(T)$ in an oscillatory fashion which indicates the anti-correlation of the current in different regions of energy $\delta\varepsilon$. This transition is seen to occur more slowly at higher temperatures. The right plot shows, on the same scale and for the same series of temperatures, the quantity $\sqrt{c_p^T(T, 0, E_Z, 0)}$ which represents $I_{p,2s}^{typ}(T, E_Z) / I_{p,1s}^{typ}(T = 0)$.

current-current correlation as a function of toroidal field B_M^\pm is only slightly affected by E_Z (Fig. 2.24).

In order to get a more quantitative estimate of the cross-over from weak Zeeman splitting to strong Zeeman splitting at finite temperature, we fit the normalized square magnitude of the current $(I_{p,2s}^{typ}(T, E_Z) / I_{p,1s}^{typ}(T))^2$ to

$$h(E_Z) = 2 + 2 \cos\left(2\pi \frac{E_Z}{E_{Z,\text{period}}(T)}\right) \exp\left(-\frac{E_Z}{E_{Z,\text{decay}}(T)}\right)$$

at a series of temperatures. This fit function was chosen as a rough approximation to the shape of the current magnitude's dependence on E_Z and provides a functional but inexact match. The extracted values for $E_{Z,\text{decay}}(T)$ are roughly hyperbolic in T with $E_{Z,\text{decay}}(T) \approx 11E_c$ for $T \lesssim 0.3T_p$ and $E_{Z,\text{decay}}(T) \approx 30E_c(T/T_p)$ for $.3T_p \lesssim T \lesssim 3T_p$. With these results, we can state that the weak Zeeman splitting regime is $E_Z \ll E_{Z,\text{CO}}$ while the strong Zeeman splitting regime is $E_Z \gg E_{Z,\text{CO}}$, where the cross-over energy is

$$E_{Z,\text{CO}} = \max(11E_c, 30E_c(T/T_p)).$$

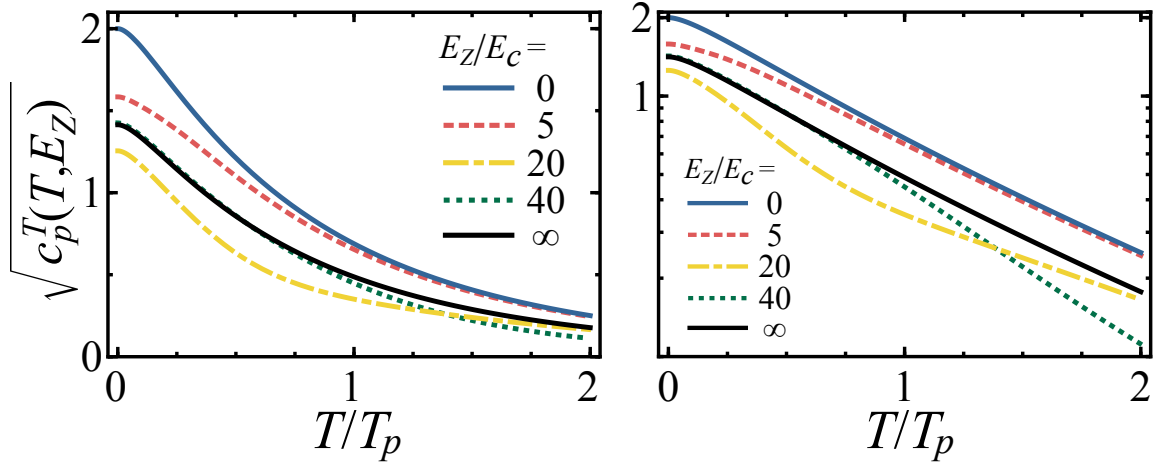


Figure 2.23: Typical magnitude of the p^{th} harmonic of the current versus temperature for finite Zeeman splitting. The two plots show the normalized typical magnitude of the p^{th} harmonic of the current $\sqrt{c_p^T(T, 0, E_Z, 0)}$ versus the normalized temperature T/T_p for the Zeeman splittings $E_Z/E_c = 0, 5, 20, 40,$ and ∞ on both linear (left plot) and log (right plot) scales. The curve for $E_Z = 0$ is exactly a factor of $\sqrt{2}$ larger than that for $E_Z = \infty$ for all values of T . For the measurements discussed in this work, E_Z was always greater than $84E_c$.

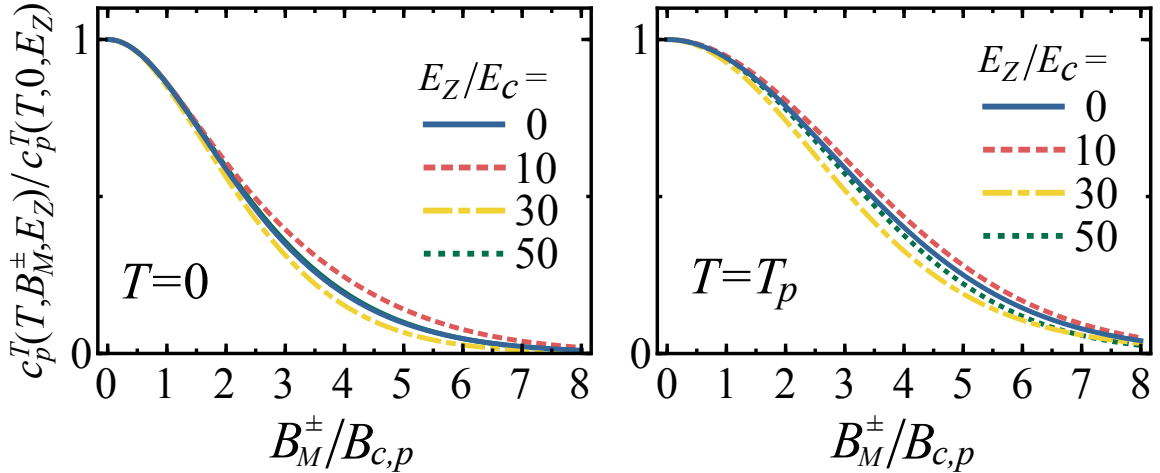


Figure 2.24: Current-current correlation function versus toroidal field at finite Zeeman splitting. The curves show the current-current correlation function $c_p^T(T, B_M^\pm, E_Z, E_{SO})$ at fixed values of E_Z and T (and $E_{SO} = 0$) versus the normalized toroidal field $B_M^\pm/B_{c,p}$. The curves display the autocorrelation of the p^{th} harmonic of the current as a function of the toroidal field. Each curve has been normalized by its value at B_M^\pm , which removes the overall suppression of the current due to finite E_Z and finite T . Qualitatively, the curves are all very similar, indicating that the main role of E_Z and T is to reduce the typical magnitude of the current-current correlation without affecting its dependence on B_M^\pm .

For sample CL17 with the smallest rings, the ratio $E_Z/E_c \approx 84$ in the low range of the applied magnetic field which was ~ 3 T. This range was measured at low temperature for which $E_{Z,CO} = 11E_c$. At the highest temperatures $T \sim 5T_p$, the cross-over to the strong Zeeman splitting limit is $E_{Z,CO} \sim 150E_c$. Measurements at this temperature occurred at fields greater than 5 T for which E_Z was close to this cross-over value. The majority of the data was taken at larger magnetic fields and lower values of T/T_p (and, for the larger ring samples, smaller values of E_c) for which E_Z does exceed $E_{Z,CO}$ and the strong Zeeman splitting limit applies. The main impact of the Zeeman energy introduced by the large magnetic field used in the measurement is thus to reduce the typical current magnitude by an overall factor of $1/\sqrt{2}$.

2.3.2.3 Spin-orbit scattering

In addition to coupling to an external field through the Zeeman effect, the spin degrees of freedom of electrons in a ring can also couple directly to the disordered medium of the ring. This interaction can be either in the form of a direct coupling of the electron spin to magnetic impurities or an indirect coupling to the disorder potential through the spin-orbit interaction. Both interactions can be important. However, for measurements discussed in this text, high purity aluminum was used to fabricate the rings in order to minimize the effects of magnetic impurities. Additionally, it has previously been observed in copper samples that for magnetic fields $B \gtrsim 5k_B T/\mu_B$ magnetic impurities become polarized and spin-flip interactions are suppressed [55]. Most of our measurements, those with $T \lesssim 1$ K, were performed in this regime. Moreover, no magnetic impurity has been observed to retain a localized moment when dissolved into aluminum [56]. For these reasons, we neglect interactions with magnetic impurities.

The coupling of the spin degrees of freedom of an electron to the disorder potential of its metallic host is relativistic in origin. The disorder potential is essentially a spatially inhomogeneous electric field through which the electron moves. In the rest frame of the moving electron, the purely electric field is transformed into a mixture of electric and magnetic fields. Thus the spin of the electron experiences an effective magnetic field that varies with the velocity of the electron and the strength of the disorder potential. A more detailed description of the spin-orbit interaction is provided in Section B.2.3.

The spin-orbit interaction mixes the spin up and spin down states. The result of this mixing is that the spectrum of doubly degenerate states is replaced by a non-degenerate spectrum which

is twice as dense. As was argued in the introduction to this section, in the diffusive regime the magnitude of the persistent current should be independent of the density of states because a denser spectrum leads to a greater number of levels contributing to the current at the expense of a smaller single-level current. Therefore, if we expect that with spin-orbit scattering the typical persistent current magnitude is $2I^{\text{typ}}$, twice the typical current of a spin-less system, we expect that in the presence of a strong spin-orbit coupling the typical persistent current magnitude will be reduced to I^{typ} , the same magnitude as the spin-less case.

We now calculate the current in the presence of finite spin-orbit interaction, confirming the two limiting cases just described. We restrict our focus to the diffuson contribution to the persistent current. Our measurements were performed at large magnetic fields where the cooperon contribution to the typical current should be strongly suppressed according to the analysis of Section 2.3.2.1. The cooperon contribution is straightforward to calculate but takes a slightly different form than the diffuson. Because the cooperon involves reversed paths, it couples to different pairs of spins than the diffuson. Namely, it mixes the $\uparrow\downarrow$ and $\downarrow\uparrow$ pairs split by the Zeeman effect (see Section B.2.3) and consequently results in a more complicated expression for the typical current in the presence of both finite Zeeman and spin-orbit interactions.

As was the case for the Zeeman interaction in the preceding section, to calculate the typical persistent current in the presence of finite spin-orbit interaction we must recalculate the density of states correlation function $\langle \nu(\varepsilon)\nu(\varepsilon') \rangle$. This calculation is discussed in Section B.2.3 and the result is given in Eq. B.36. Repeating the calculation of the current-current correlation function of the preceding sections with this form for the density of states correlation function, we find for the zero-temperature current-current correlation function

$$\begin{aligned}
C_1^{(0)}(\varepsilon_1, \phi, B_M; \varepsilon'_1, \phi', B'_M; E_Z, E_{SO}) = \\
16 \frac{E_c^2}{\phi_0^2} \sum_{p=1}^{\infty} \cos\left(2\pi p \frac{\phi - \phi'}{\phi_0}\right) \left(F_p(z) + F_p\left(z + \frac{4}{3} \frac{E_{SO}}{E_c}\right) + F_p\left(z - 2i \frac{E_Z}{E_c} + \frac{4}{3} \frac{E_{SO}}{E_c}\right) + \dots \right. \\
\left. + F_p\left(z + 2i \frac{E_Z}{E_c} + \frac{4}{3} \frac{E_{SO}}{E_c}\right) \right)
\end{aligned}$$

with F_p given by Eq. 2.62, $z = \varepsilon_{\perp}^{-} + i(\varepsilon_1 - \varepsilon'_1)/E_c$, ε_{\perp}^{-} given by Eq. 2.78, and the energy scale

$$E_{SO} = \frac{\hbar}{\tau_{SO}} = \frac{\hbar D}{L_{SO}^2}. \quad (2.83)$$

The spin-orbit scattering time τ_{SO} was introduced in Section B.2.3. Here we introduce the spin-orbit scattering length $L_{SO} = \sqrt{\tau_{SO}}$ as well. Following Eqs. 2.64, 2.68, and 2.81, we can also write this correlation function in terms of the normalized zero-temperature correlation function of the p^{th} harmonic, c_p^0 :

$$\begin{aligned} C_1^{(0)}(\varepsilon_1, \phi, B_M; \varepsilon'_1, \phi', B'_M; E_Z, E_{SO}) &= \sum_{p=1}^{\infty} (I_p^{\text{typ}})^2 \cos\left(2\pi p \frac{\phi - \phi'}{\phi_0}\right) c_p^0(\varepsilon_1 - \varepsilon'_1, B_M^{\pm}, E_Z, E_{SO}) \\ &= \sum_{p=1}^{\infty} (I_p^{\text{typ}})^2 \cos\left(2\pi p \frac{\phi - \phi'}{\phi_0}\right) \left(H_1^{(0)}(p^2 z) + H_1^{(0)}\left(p^2 z + \frac{4 E_{SO}}{3 E_{c,p}}\right) + \dots \right. \\ &\quad \left. + H_1^{(0)}\left(p^2 z + \frac{4 E_{SO}}{3 E_{c,p}} - 2i \frac{E_Z}{E_{c,p}}\right) + \dots \right. \\ &\quad \left. + H_1^{(0)}\left(p^2 z + \frac{4 E_{SO}}{3 E_{c,p}} + 2i \frac{E_Z}{E_{c,p}}\right) \right), \quad (2.84) \end{aligned}$$

where we use the notation

$$E_{c,p} = \frac{E_c}{p^2}.$$

At finite temperature, Eqs. 2.71 and 2.82 are modified to

$$\begin{aligned} \langle I(\phi) I(\phi') \rangle &= \sum_{p=1}^{\infty} (I_p^{\text{typ}})^2 \cos\left(2\pi p \frac{\phi - \phi'}{\phi_0}\right) c_p^T(T, B_M^-, E_Z, E_{SO}) \\ &= \sum_{p=1}^{\infty} (I_p^{\text{typ}})^2 \cos\left(2\pi p \frac{\phi - \phi'}{\phi_0}\right) \times \dots \\ &\quad \times \left(g_D\left(p^2 \varepsilon_{\perp}^{-}, 20.8 \frac{T}{T_p}\right) + \dots \right. \\ &\quad \left. + g_D\left(p^2 \left(\varepsilon_{\perp}^{-} + \frac{4 E_{SO}}{3 E_c}\right), 20.8 \frac{T}{T_p}\right) + \dots \right. \\ &\quad \left. + g_D\left(p^2 \left(\varepsilon_{\perp}^{-} + \frac{4 E_{SO}}{3 E_c} - 2i \frac{E_Z}{E_c}\right), 20.8 \frac{T}{T_p}\right) + \dots \right. \\ &\quad \left. + g_D\left(p^2 \left(\varepsilon_{\perp}^{-} + \frac{4 E_{SO}}{3 E_c} + 2i \frac{E_Z}{E_c}\right), 20.8 \frac{T}{T_p}\right) \right), \quad (2.85) \end{aligned}$$

where $c_p^T(T, B_M^-, E_Z, E_{SO})$ gives the normalized magnitude of the autocorrelation of the p^{th} harmonic of the current at finite T , B_M^- , E_Z , and E_{SO} . The typical magnitude of the p^{th} harmonic of the current can be written as

$$I_p^{\text{typ}}(T, E_Z, E_{SO}) = I_p^{\text{typ}} \sqrt{c_p^T(T, 0, E_Z, E_{SO})}. \quad (2.86)$$

As this is the final form of the persistent current in the diffusive limit presented in this text, we restate the following relevant expressions for ease of reference:

$$I_p^{\text{typ}} = \frac{1.11 eD}{p^{1.5} L^2} = \frac{4\sqrt{3} E_c}{p^{1.5} \phi_0},$$

$$T_p = \frac{10.4 \hbar D}{k_B p^2 L^2} = \frac{10.4 E_c}{p^2 k_B},$$

$$E_c = \frac{\hbar D}{L^2},$$

$$\varepsilon_{\perp}^- = \frac{\pi (B_M^-)^2 \omega t L^2}{2 \phi_0^2},$$

$$B_{c,p} = \frac{1}{p} \sqrt{\frac{2}{\pi}} \frac{\phi_0}{L \sqrt{\omega t}},$$

and

$$\begin{aligned} g_D(x, y) &= \int_{-\infty}^{\infty} d\varepsilon f_2(\varepsilon) H_1^{(0)}(x + iy\varepsilon) \\ &= \int_{-\infty}^{\infty} d\varepsilon \left(\frac{\varepsilon \cosh \varepsilon - \sinh \varepsilon}{\sinh^3 \varepsilon} \right) \text{Re} \left[\left(1 + \sqrt{x + iy\varepsilon} + \frac{x + iy\varepsilon}{3} \right) \exp(-\sqrt{x + iy\varepsilon}) \right] \end{aligned}$$

with $g_D(0, y) \approx \exp(-0.096y)$.

Referring to each of the four terms summed together at fixed p as “modes,” we see that the spin-orbit interaction affects three of the modes, including the two affected by Zeeman splitting, in exactly the same fashion as the toroidal field does the spin-less mode. These three modes are thus suppressed with L/L_{SO} in a similar fashion to how the current-current correlation was seen to be suppressed at finite toroidal fields. This suppression, including the weakening of features associated with Zeeman splitting, can be seen in Fig. 2.25 showing the normalized zero-temperature current-current correlation function $c_p^0(\delta\varepsilon, 0, E_Z, E_{SO})$ versus $\delta\varepsilon$ and in Fig. 2.26 showing the typical magnitude of the p^{th} current harmonic normalized by its value in the absence of spin-

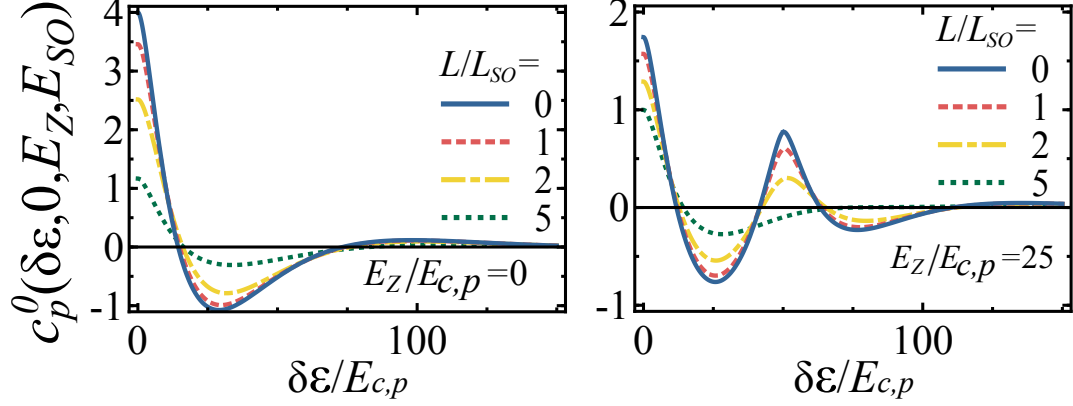


Figure 2.25: Zero-temperature current-current correlation function versus energy difference at finite spin-orbit scattering and Zeeman splitting. The top graph shows $c_p^T(T, 0, E_Z, E_{SO})$ with $E_Z = 0$ and $L/L_{SO} = 0, 1, 2,$ and 5 . The bottom graph shows the correlation function for the same series of values for L/L_{SO} but with $E_Z = 25E_c$. The figure can be meaningfully contrasted with Figs. 2.19 and 2.21, which show the same correlation function in different parameter regimes. As L/L_{SO} is increased with $E_Z = 0$, the current-current correlation function is reduced to one fourth of its value in the absence of spin-orbit scattering but otherwise largely unchanged (left graph). For finite E_Z , features at larger energy difference are reduced as the modes coupling to the Zeeman interaction are suppressed (right graph).

orbit scattering $\sqrt{c_p^T(T, 0, 0, E_{SO})/c_p^T(T, 0, 0, 0)}$ versus L/L_{SO} . With $E_Z = 0$, the current-current correlation function is mostly unchanged as a function of $\delta\varepsilon$ at finite E_{SO} other than an overall suppression, leading to a weak temperature dependence when $c_p^T(T, 0, 0, E_{SO})$ is normalized by its value $c_p^T(T, 0, 0, 0)$ in the absence of spin-orbit scattering. This weak temperature dependence is also visible in Fig. 2.27 which shows the normalized magnitude $\sqrt{c_p^T(T, 0, 0, E_{SO})}$ of the p^{th} harmonic of the current versus temperature. Similarly, the main effect of spin-orbit scattering on the correlation $c_p^T(T, B_M^-, 0, E_{SO})$ of the current at finite B_M^- is largely just to scale down the magnitude of the correlation without affecting the toroidal field dependence (Fig. 2.28).

From all of these observations, we can summarize the effect of the spin-orbit interaction on the persistent current as reducing the overall magnitude of the current by correlating the spin and spatial degrees of freedom and thus removing the spin degeneracy. In the strong spin-orbit scattering limit, the current magnitude is reduced by a factor of two and thus is the same as in the spin-less case. As indicated in Fig. 2.25, the other major consequence of spin-orbit scattering is to diminish the importance of the Zeeman splitting. The reduction of the features associated with Zeeman splitting is shown in Figs. 2.29 and 2.30. In 2.29, the oscillatory feature of $I_p(E_Z)$ versus E_Z is seen to be flattened out by increasing L/L_{SO} . Similarly, in Fig. 2.30, the corresponding oscillatory feature in $I_p(T)$ at finite E_Z is suppressed with increasing L/L_{SO} .

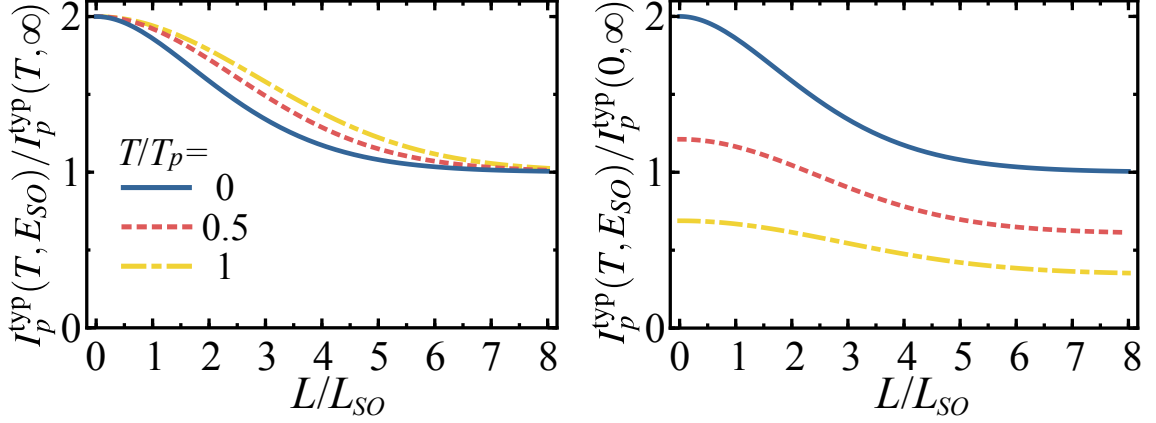


Figure 2.26: Typical persistent current magnitude versus spin-orbit scattering strength. The function $\sqrt{c_p^T(T, 0, 0, E_{SO})/c_p^T(T, 0, 0, \infty)}$, representing the magnitude $I_p^{\text{typ}}(T, E_{SO})/I_p^{\text{typ}}(T, \infty)$ of the p^{th} harmonic of the persistent current at finite T and E_{SO} normalized by its magnitude in the strong spin-orbit scattering (“spin-less”) limit, is plotted on the left against L/L_{SO} . The normalized temperatures plotted are $T/T_p = 0, 0.5$, and 1 . It is seen that the current magnitude decays to the spin-less value for $L/L_{SO} \sim 4$, with the cross-over point increasing weakly with temperature. The right plot shows the typical current magnitude $I_p^{\text{typ}}(T, E_{SO})/I_p^{\text{typ}}(0, \infty)$ (or $\sqrt{c_p^T(T, 0, 0, E_{SO})/c_p^T(0, 0, 0, \infty)}$) normalized by the zero temperature magnitude of the current so that the decay with temperature can be seen.

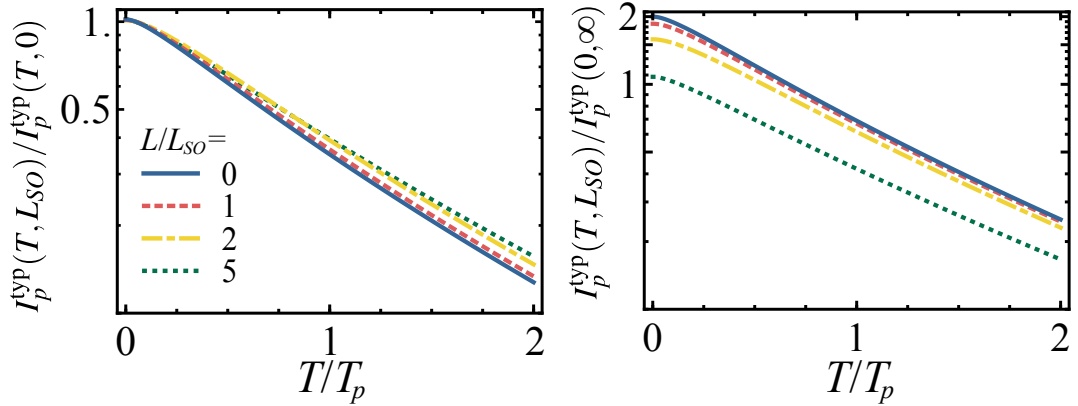


Figure 2.27: Typical persistent current magnitude versus temperature at finite spin-orbit scattering strength. The left plot shows $\sqrt{c_p^T(T, 0, 0, E_{SO})/c_p^T(T, 0, 0, 0)}$, which represents the typical magnitude $I_p^{\text{typ}}(T, L_{SO})/I_p^{\text{typ}}(T, 0)$ of the current at finite L_{SO} normalized by its magnitude in the absence of spin-orbit scattering, versus normalized temperature T/T_p . The curves correspond to $L/L_{SO} = 0, 1, 2$, and 5 . The normalized magnitudes change very little with $L/L_{SO} \lesssim 5$. In the right plot which shows $\sqrt{c_p^T(T, 0, 0, E_{SO})}$ (effectively $I_p^{\text{typ}}(T, L_{SO})/I_p^{\text{typ}}(0, \infty)$), the suppression of the current magnitude by a factor of 2 with increasing L/L_{SO} can be observed.

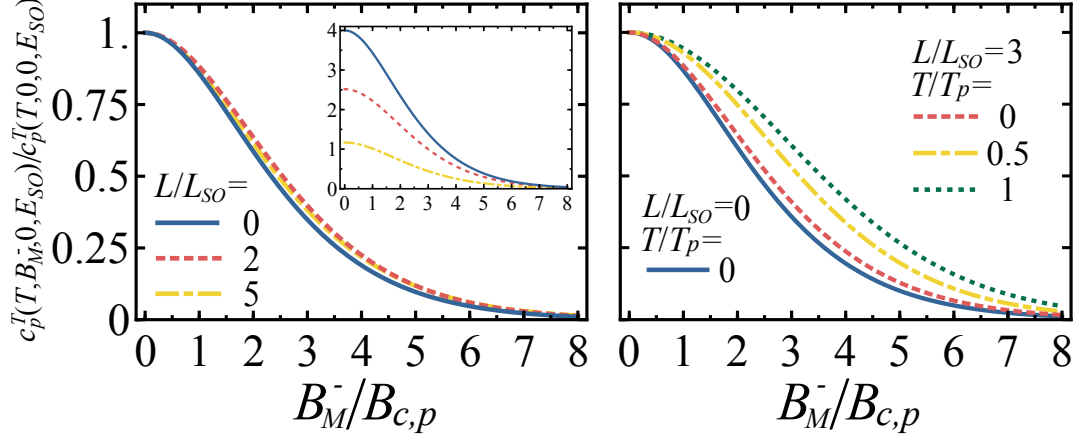


Figure 2.28: Current-current correlation function versus toroidal field in the presence of spin orbit scattering. Both the left and right plots show $c_p^T(T, B_M^-, 0, E_{SO})/c_p^T(T, 0, 0, E_{SO})$ versus the normalized toroidal field difference $B_M^-/B_{c,p}$. The curves represent $\langle I_p(B_M + B_M^-)I_p(B_M) \rangle$ normalized by its $B_M^- = 0$ value for different values of L/L_{SO} and T . The left plot shows the $T = 0$ case for $L/L_{SO} = 0, 2$, and 5 . The inset shows $c_p^T(0, B_M^-, 0, E_{SO})$ which corresponds to $\langle I_p(B_M + B_M^-)I_p(B_M) \rangle$ at $T = 0$ and finite E_{SO} normalized by its value at $E_{SO} = \infty$. Spin-orbit scattering has very little effect on the correlation in B_M^- other than to suppress the overall magnitude by a factor of 4. In the right figure, the $T = 0, L/L_{SO} = 0$ case is replotted along with three curves representing $L/L_{SO} = 3$ and $T/T_p = 0, 0.5$, and 1 . This plot can be compared to Fig. 2.20 where a similar 33% increase in the scale of correlation field is observed with increasing T/T_p from 0 to 1 in the absence of spin-orbit scattering. Other than the overall suppression of the current magnitude, spin-orbit scattering has negligible effect on the correlation of the current with toroidal field.

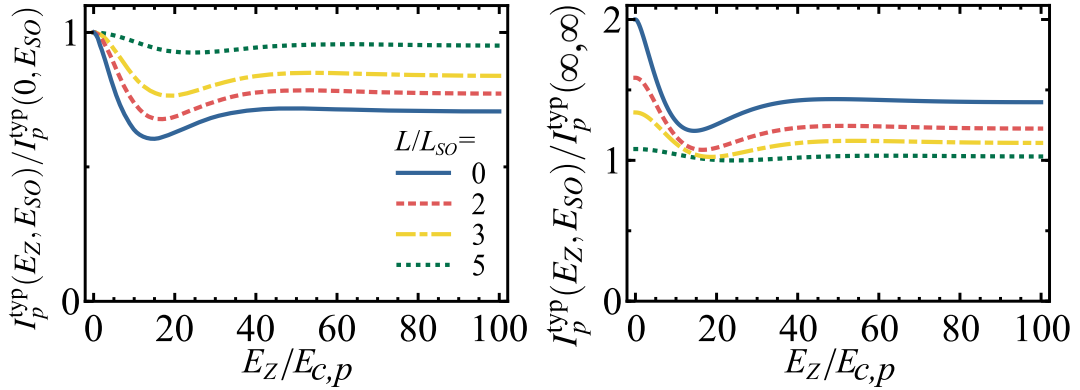


Figure 2.29: Typical persistent current magnitude versus Zeeman splitting with finite spin-orbit scattering. The left plot shows the typical current magnitude $I_p^{\text{typ}}(E_Z, E_{SO})/I_p^{\text{typ}}(0, E_{SO})$ (or $\sqrt{c_p^0(0, 0, E_Z, E_{SO})/c_p^0(0, 0, 0, E_{SO})}$) at zero temperature versus the normalized Zeeman splitting $E_Z/E_{c,p}$. The current magnitude has been normalized by its value at $E_Z = 0$ so that all curves begin 1. As the spin-orbit scattering strength is increased, the oscillatory feature in the current magnitude is flattened out. The right plot shows the current magnitude $I_p^{\text{typ}}(E_Z, E_{SO})/I_p^{\text{typ}}(\infty, \infty)$ normalized by the spin-less typical current. In the limit of strong Zeeman splitting and no spin-orbit scattering, the persistent current magnitude is reduced from $2I_p^{\text{typ}}$ to $\sqrt{2}I_p^{\text{typ}}$, where I_p^{typ} is the spin-less typical current magnitude. In the limit of strong spin-orbit scattering the current magnitude is reduced to I_p^{typ} , independent of the strength E_Z of the Zeeman splitting.

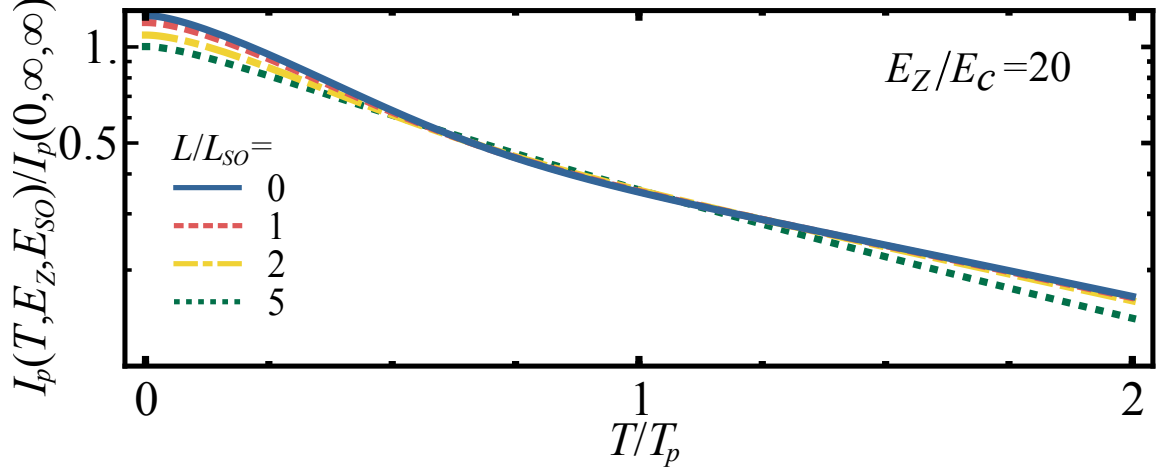


Figure 2.30: Typical persistent current magnitude versus temperature at finite Zeeman splitting and spin-orbit scattering. The normalized typical magnitude of the p^{th} harmonic $I_p(T, E_Z, E_{SO})/I_p(0, \infty, \infty)$ (or $\sqrt{c_p^T(T, 0, E_Z, E_{SO})/c_p^T(T, 0, \infty, \infty)}$) at finite Zeeman splitting and spin-orbit scattering is plotted versus the normalized temperature T/T_p . The current magnitude, which has been normalized by its value in the large Zeeman splitting, strong spin-orbit scattering limit (the spin-less case), is shown for $E_Z/E_c = 20$ and $L/L_{SO} = 0, 1, 2,$ and 5 . The value of E_Z was chosen because, on a log scale, it produced the largest deviations from a straight line in Fig. 2.23 (which showed the current magnitude's temperature dependence in the absence of spin-orbit scattering for several values of E_Z/E_c). With increasing spin orbit strength, it is seen that the persistent current magnitude decreases slightly and loses much of its non-linearity on the log scale.

2.3.3 Contributions to the average current in the diffusive regime

We now briefly describe two contributions to the average persistent current and explain why these contributions are negligible for the measurements discussed in the text. Addressing the average current contributions is important because the measurements discussed in Chapter 7 were performed on arrays of $\sim 10^3$ rings. The total typical current in an array of N rings due to a random current contribution with typical value $I^{\text{typ}} = \sqrt{\langle I^2 \rangle}$ is $\sqrt{N}I^{\text{typ}}$ per ring, while the total current in the array due to an average current contribution $I^{\text{avg}} = \langle I \rangle$ per ring is NI^{avg} . Thus the average current contribution to the total current signal could be a factor of \sqrt{N} times smaller than the contribution from the random component and still contribute equally to the total current in an array.

The first contribution I^{can} arises when one constrains the number of particles in the ring to be a fixed number, which was not done for most of the preceding calculations. It can be understood as a single-level effect. The second contribution I^{ee} results from incorporating electron-electron interactions into the calculation and thus is a collective effect. As discussed in Section B, the diffuson and cooperon depend on magnetic fields B and B' through $B^- = B - B'$ and $B^+ = B + B'$

respectively. When considering an average quantity, there is only one magnetic field $B = B'$. The average persistent current is defined in terms of a magnetic field derivative and thus has no diffuson contribution (since $B^- = 0$ for average quantities). The gist of the argument for why these two contributions may be neglected in our analysis is that they are derived from the cooperon contribution to the current, which, as seen in Section 2.3.2.1, is suppressed in the presence of a strong magnetic field penetrating the diffusive medium of the ring, as is the case in our measurements.

2.3.3.1 Single particle contribution

We first discuss the contribution to the average current referred to alternately as the “single-particle,” “mesoscopic,” “canonical,” or “non-interacting electron” contribution. This contribution was first calculated independently by three different groups [40, 49, 57]. Our discussion is based off of Ref. [36] (which, in turn, was based on the three previously cited references). We will refer to this current as I^{can} .

The starting point for the calculation is the observation that the samples measured in experiments, consisting of metal rings on insulating substrates, are more appropriately described by the canonical ensemble in which the number N of electrons is fixed rather than the grand canonical ensemble in which the Fermi level ε_F is fixed and the particle number is allowed to fluctuate. One method of correcting for this inaccuracy is to make the Fermi level $\varepsilon_F(\phi)$ depend on flux ϕ by enforcing the condition

$$N = \int_0^{\varepsilon_F} d\varepsilon \nu(\varepsilon, \phi)$$

for fixed N and all ϕ . Eq. 2.7 defining the persistent current then becomes

$$I = -\frac{\partial \Omega(\varepsilon_F(\phi), \phi)}{\partial \phi}$$

which now has an extra dependence upon ϕ through $\varepsilon_F(\phi)$. Because of the arguments given in Section 2.1.1, the quantity $\varepsilon(\phi)$ is periodic in flux with period ϕ_0 .

Assuming that the variations of $\varepsilon_F(\phi)$ with ϕ are small compared to its average

$$\varepsilon_F = \frac{1}{\phi_0} \int_0^{\phi_0} d\phi \varepsilon_F(\phi),$$

we can expand the expression for I to first order about ε_F as

$$I = -\frac{\partial}{\partial\phi} \left(\Omega(\varepsilon_F, \phi) + \frac{\partial\Omega(\varepsilon_F, \phi)}{\partial\varepsilon_F} (\varepsilon_F(\phi) - \varepsilon_F) \right).$$

The first term calculated at constant ε_F is simply the quantity calculated in previous sections in the grand canonical ensemble at constant ε_F . It was found to decay exponentially in L/l_e and thus was negligible in the diffusive regime. The second term can be rewritten using a couple of thermodynamic relations. First, we recall that at low temperature the Fermi level is equal to the chemical potential $\mu \approx \varepsilon_F$ to lowest order in temperature. The derivative of the grand potential with respect to μ is

$$\frac{\partial\Omega}{\partial\mu} = -N.$$

Additionally, a change in the chemical potential at fixed particle number $\delta\mu|_N$ can be related to a change in average particle number at fixed chemical potential $\delta N|_\mu$ by

$$\delta\mu|_N = \left(\frac{\partial\mu}{\partial N} \right)_N \delta N|_\mu = \Delta_M \delta N|_\mu$$

where Δ_M is the energy level spacing at the Fermi level, roughly equal to the quantity given in Eq. 2.38. Using these two relations (and dropping the term already found to be negligible in the diffusive regime), we have

$$\begin{aligned} I &= \Delta_M \frac{\partial N(\phi)}{\partial\phi} (N(\phi) - N) \\ &= \frac{\Delta_M}{2} \frac{\partial}{\partial\phi} (N(\phi) - N)^2, \end{aligned}$$

where the expressions are for fixed Fermi level with N corresponding to ε_F and $N(\phi)$ to $\varepsilon_F(\phi)$. We can write these quantities in terms of the density of states as

$$N = \int_0^{\varepsilon_F} d\varepsilon \nu(\varepsilon)$$

and

$$N(\phi) = \int_0^{\varepsilon_F(\phi)} d\varepsilon \nu(\varepsilon) = \int_0^{\varepsilon_F} d\varepsilon \nu(\varepsilon, \phi).$$

The disorder averaged current is

$$I^{\text{can}} = \langle I \rangle = \frac{\Delta_M}{2} \left(\frac{\partial}{\partial \phi} \langle N^2(\phi) \rangle - 2N \frac{\partial}{\partial \phi} \langle N(\phi) \rangle \right).$$

In the absence of disorder, the number of levels below energy ε

$$N_0(\varepsilon, \phi) = \int_0^\varepsilon d\varepsilon' \nu_0(\varepsilon', \phi)$$

was calculated in Eq. 2.17 as

$$N_0(\varepsilon, \phi) = 4 \sum_{p>0} \cos\left(2\pi p \frac{\phi}{\phi_0}\right) \frac{1}{\pi p} \sin\left(2\pi p \sqrt{\frac{2mL^2\varepsilon}{\hbar^2}}\right),$$

where we have dropped the flux independent term. In Eq. 2.45, it was found that the disorder averaged number of levels $N(\varepsilon, \phi) = \langle N_0(\varepsilon, \phi) \rangle$ was the convolution of N_0 with a Lorentzian:

$$N(\varepsilon, \phi) = \int^\varepsilon d\varepsilon_1 \nu(\varepsilon_1, \phi) = \int_0^\infty d\varepsilon_2 N_0(\varepsilon_2, \phi) b_L\left(\varepsilon - \varepsilon_2, \frac{\hbar}{2\tau_e}\right)$$

with flux-dependent part of the n

$$b_L(\varepsilon, \delta) = \frac{1}{\pi} \frac{\delta}{\varepsilon^2 + \delta^2}.$$

Taking $\varepsilon = \varepsilon_F$ and expanding ε_2 about ε_F , we have

$$\begin{aligned} N(\phi) &= \sum_p \frac{4}{\pi p} \cos\left(2\pi p \frac{\phi}{\phi_0}\right) \int_0^\infty d\varepsilon \sin\left(2\pi p \sqrt{\frac{2mL^2\varepsilon_F}{\hbar^2}} \left(1 + \frac{\varepsilon - \varepsilon_F}{2\varepsilon_F}\right)\right) b_L\left(\varepsilon_F - \varepsilon, \frac{\hbar}{2\tau_e}\right) \\ &\approx \sum_p \frac{4}{\pi p} \cos\left(2\pi p \frac{\phi}{\phi_0}\right) \int_{-\infty}^\infty d\varepsilon \sin\left(pk(\varepsilon_F)L \left(1 + \frac{\varepsilon}{2\varepsilon_F}\right)\right) b_L\left(\varepsilon, \frac{\hbar}{2\tau_e}\right) \\ &= \sum_p \frac{4}{\pi p} \cos\left(2\pi p \frac{\phi}{\phi_0}\right) \left(\sin(pk(\varepsilon_F)L) \int_{-\infty}^\infty d\varepsilon \cos\left(pk(\varepsilon_F)L \frac{\varepsilon}{2\varepsilon_F}\right) b_L\left(\varepsilon, \frac{\hbar}{2\tau_e}\right) + \dots \right. \\ &\quad \left. + \cos(pk(\varepsilon_F)L) \int_{-\infty}^\infty d\varepsilon \sin\left(pk(\varepsilon_F)L \frac{\varepsilon}{2\varepsilon_F}\right) b_L\left(\varepsilon, \frac{\hbar}{2\tau_e}\right) \right) \end{aligned}$$

where we have that $\varepsilon_F \gg \hbar/2\tau_e$. The last term is zero by symmetry. The other term is the Fourier

transform of the Lorentzian which was previously encountered in Eq. 2.48:

$$\begin{aligned}
N(\phi) &= \sum_p \frac{4}{\pi p} \cos\left(2\pi p \frac{\phi}{\phi_0}\right) \sin(pk(\varepsilon_F)L) \int_{-\infty}^{\infty} d\varepsilon \cos\left(\pi p k(\varepsilon_F)L \frac{\varepsilon}{2\varepsilon_F}\right) b_L\left(\varepsilon, \frac{\hbar}{2\tau_e}\right) \\
&= \sum_p \frac{4}{\pi p} \cos\left(2\pi p \frac{\phi}{\phi_0}\right) \sin(pk(\varepsilon_F)L) \exp\left(-\frac{\hbar}{2\tau_e} \frac{\pi p k(\varepsilon_F)L}{2\varepsilon_F}\right) \\
&= \sum_p \frac{4}{\pi p} \cos\left(2\pi p \frac{\phi}{\phi_0}\right) \sin(pk(\varepsilon_F)L) \exp\left(-\frac{pL}{2l_e}\right).
\end{aligned}$$

In the diffusive regime, this leads to a negligible contribution to the current.

Dropping the $\langle N(\phi) \rangle$ term, we have

$$I^{\text{can}} = \frac{\Delta_M}{2} \frac{\partial}{\partial \phi} \langle N^2(\phi) \rangle.$$

The second moment of $N(\phi)$ can be written as

$$\langle N^2(\phi) \rangle = \int_0^{\varepsilon_F} d\varepsilon \int_0^{\varepsilon_F} d\varepsilon' \langle \nu(\varepsilon, \phi) \nu(\varepsilon', \phi) \rangle,$$

which has the cooperon as given in Eq. B.30 as its leading flux dependent contribution (the diffuson is flux independent since $B' = B$ in Eq. B.30 in this case). Adapting Eqs. 2.56 and 2.59, we can write

$$\begin{aligned}
\langle \nu(\varepsilon, \phi) \nu(\varepsilon', \phi) \rangle_c &= \frac{1}{2\pi^2} \sum_n \text{Re} \left(\left(i\hbar\omega + E_c \varepsilon_{\perp} + (2\pi)^2 E_c \left(n + \frac{2\phi}{\phi_0} \right)^2 \right)^{-2} \right) \\
&= \frac{1}{2\pi^2} \frac{1}{\sqrt{E_c}} \frac{1}{\hbar} \text{Im} \frac{\partial}{\partial \omega} \sum_{p=1}^{\infty} \cos\left(4\pi p \frac{\phi}{\phi_0}\right) \frac{1}{\sqrt{i\hbar\omega + E_c \varepsilon_{\perp}}} \exp\left(-p \sqrt{\frac{i\hbar\omega + E_c \varepsilon_{\perp}}{E_c}}\right)
\end{aligned}$$

with $\hbar\omega = \varepsilon - \varepsilon'$. Using the change of variables $\varepsilon_1 = \varepsilon + \varepsilon'$ and $\hbar\omega = \varepsilon - \varepsilon'$,

$$\begin{aligned}
\langle N^2(\phi) \rangle_c &= \int_0^{\varepsilon_F} d\varepsilon \int_0^{\varepsilon_F} d\varepsilon' \langle \nu(\varepsilon, \phi) \nu(\varepsilon', \phi) \rangle_c \\
&= \frac{1}{4\pi^2} \frac{1}{\sqrt{E_c}} \sum_{p=1}^{\infty} \cos\left(4\pi p \frac{\phi}{\phi_0}\right) \text{Im} \int_0^{2\varepsilon_F} d\varepsilon_1 \int_{-\varepsilon_1/\hbar}^{\varepsilon_1/\hbar} d\omega \frac{\partial}{\partial \omega} \frac{\exp\left(-p \sqrt{i\hbar\omega/E_c + \varepsilon_{\perp}}\right)}{\sqrt{i\hbar\omega + E_c \varepsilon_{\perp}}} \\
&= \frac{1}{4\pi^2} \frac{1}{\sqrt{E_c}} \sum_{p=1}^{\infty} \cos\left(4\pi p \frac{\phi}{\phi_0}\right) \text{Im} \int_0^{2\varepsilon_F} d\varepsilon_1 \frac{\exp\left(-p \sqrt{i\hbar\omega/E_c + \varepsilon_{\perp}}\right)}{\sqrt{i\hbar\omega + E_c \varepsilon_{\perp}}} \Bigg|_{-\varepsilon_1/\hbar}^{\varepsilon_1/\hbar}
\end{aligned}$$

$$= \frac{1}{2\pi^2} \frac{1}{\sqrt{E_c}} \sum_{p=1}^{\infty} \cos\left(4\pi p \frac{\phi}{\phi_0}\right) \text{Im} \int_0^{2\varepsilon_F} d\varepsilon_1 \frac{\exp\left(-p\sqrt{i\varepsilon_1/E_c + \varepsilon_\perp}\right)}{\sqrt{i\varepsilon_1 + E_c\varepsilon_\perp}}$$

where in the last line we used the fact that $\text{Im}(a - a^*) = \text{Im}(2i\text{Im}(a)) = 2\text{Im}(a)$. Performing the final integral, we have

$$\begin{aligned} \langle N^2(\phi) \rangle_c &= \frac{1}{2\pi^2} \frac{1}{\sqrt{E_c}} \sum_{p=1}^{\infty} \cos\left(4\pi p \frac{\phi}{\phi_0}\right) \text{Im} \left(\frac{2i\sqrt{E_c}}{p} \exp\left(-p\sqrt{\frac{i\varepsilon_1 + E_c\varepsilon_\perp}{E_c}}\right) \Big|_0^{2\varepsilon_F} \right) \\ &\approx -\frac{1}{\pi^2} \sum_{p=1}^{\infty} \frac{1}{p} \cos\left(4\pi p \frac{\phi}{\phi_0}\right) \text{Re}(\exp(-p\sqrt{\varepsilon_\perp})) \end{aligned}$$

where we used the fact that $\varepsilon_F \gg E_c$ to drop the oscillatory term. The average current is then

$$\begin{aligned} I^{\text{can}} &= \frac{\Delta_M}{2} \frac{\partial}{\partial \phi} \langle N^2(\phi) \rangle \\ &= \frac{2}{\pi} \frac{\Delta_M}{\phi_0} \sum_{p=1}^{\infty} \sin\left(4\pi p \frac{\phi}{\phi_0}\right) \text{Re}[\exp(-p\sqrt{\varepsilon_\perp})]. \end{aligned} \quad (2.87)$$

From this expression, we see that the average current is of the order of the single level current Δ_M/ϕ_0 . Additionally, the current is periodic with period $\phi_0/2$ and is paramagnetic ($\partial\langle I \rangle/\partial\phi > 0$) at $\phi = 0$. This result could perhaps have been anticipated from Eqs. 2.8 through 2.11 which predicted a paramagnetic current for the even harmonics of the current in the ideal ring with a fixed number of electrons. We have retained the transverse eigenvalues of the cooperon with the term ε_\perp . Within the toroidal field model,

$$p^2\varepsilon_\perp = \left(\frac{2B_M}{B_{c,p}}\right)^2 \quad (2.88)$$

where B_M is the toroidal field strength and $B_{c,p}$ was given in terms of the ring parameters in Eq. 2.79. Thus, this average current decays exponentially on the characteristic field scale $B_{c,p}/2$. For this reason, we may neglect this term as it is strongly suppressed at large field.

Since this contribution is negligible, we do not calculate its temperature dependence or the effects of Zeeman splitting or spin-orbit scattering. In passing, we note that the temperature dependence goes, very roughly, as $T^2 \exp(-\sqrt{k_B T/E_c})$ at low temperature and over the range of experimental interest decays more strongly with temperature than the interaction contribution (characteristic temperature $\sim 3E_c/k_B$) and the typical current contribution (characteristic tem-

perature $\sim 10E_c/k_B$ as seen in Eq. 2.73) [49, 58]. To account for spin, the expression in Eq. 2.87 should be multiplied by 4 for the case of spin degeneracy. For Zeeman splitting, the factor of $\text{Re}[\exp(-p\sqrt{\varepsilon_\perp})]$ should be replaced by

$$\text{Re} \left[2 \exp(-p\sqrt{\varepsilon_\perp}) + \exp\left(-p\sqrt{\varepsilon_\perp + 2i\frac{E_Z}{E_c}}\right) + \exp\left(-p\sqrt{\varepsilon_\perp - 2i\frac{E_Z}{E_c}}\right) \right],$$

and for spin orbit scattering the factor should be replaced by

$$\exp(-p\sqrt{\varepsilon_\perp}) + 3 \exp\left(-p\sqrt{\varepsilon_\perp + \frac{4E_{SO}}{3E_c}}\right)$$

following the procedure of Refs. B.2.3, 2.3.2.2 and 2.3.2.3. As mentioned in Section B.2.3, the expression accounting for both Zeeman splitting and spin-orbit, using the eigenvalues given in the comment 9 on page 327 requires replacing $\text{Re}[\exp(-p\sqrt{\varepsilon_\perp})]$ by

$$\begin{aligned} & \text{Re} \left[2 \exp\left(-p\sqrt{\varepsilon_\perp + \frac{4E_{SO}}{3E_c}}\right) + \exp\left(-p\sqrt{\varepsilon_\perp + \frac{2E_{SO}}{3E_c} + \sqrt{\left(\frac{2E_{SO}}{3E_c}\right)^2 - 4\left(\frac{E_Z}{E_c}\right)^2}}\right) \right. \\ & \left. + \exp\left(-p\sqrt{\varepsilon_\perp + \frac{2E_{SO}}{3E_c} - \sqrt{\left(\frac{2E_{SO}}{3E_c}\right)^2 - 4\left(\frac{E_Z}{E_c}\right)^2}}\right) \right], \end{aligned}$$

from which it can be seen that this contribution is suppressed for large Zeeman splitting and strong spin-orbit scattering even in the absence of a toroidal field.

In principle, we should also consider the contribution of this canonical current to the typical current. Such a contribution would involve two fluxes ϕ and ϕ' and could thus contain a diffuson which would survive at high field. However, we neglect this term as we expect it to remain of order Δ_M/ϕ_0 which is smaller than the contribution calculated in the previous sections by a factor of $M_{\text{eff}} \sim 10^3$. The small size of this correction justifies the use of the grand canonical ensemble in the previous sections.

2.3.3.2 Electron-electron contribution

We now briefly discuss the contribution to the average current due to electron-electron interactions, a contribution which was first investigated in the normal state in Refs. 39, 59. Our discussion is once again based on Ref. 36. We refer to this contribution to the average current as I^{ee} .

The interaction between electrons is handled by introducing a two-body potential $U(\mathbf{r} - \mathbf{r}')$ describing the energy associated with two electrons located at \mathbf{r} and \mathbf{r}' . It is typically taken to be short-ranged due to the tendency of the electron gas in a metal to screen any net charge. For simplicity, we work at zero temperature where the free energy is simply the sum of the energies of the N occupied states. Denoting by $\psi_i(\mathbf{r})$ the i^{th} energy eigenfunction and by

$$n(\mathbf{r}) = \sum_{m=1}^N |\psi_m(\mathbf{r})|^2$$

the spatial density of electrons, the classical electro-static energy due to the interaction for the i^{th} eigenstate is

$$\begin{aligned} \delta\varepsilon_i^{ee,H} &= \int d\mathbf{r} \int d\mathbf{r}' U(\mathbf{r} - \mathbf{r}') (n(\mathbf{r}) - \bar{n}) |\psi_i(\mathbf{r}')|^2 \\ &= \sum_{m=1}^N \int d\mathbf{r} \int d\mathbf{r}' U(\mathbf{r} - \mathbf{r}') (|\psi_m(\mathbf{r})|^2 - \bar{n}) |\psi_i(\mathbf{r}')|^2 \end{aligned}$$

where \bar{n} is the electron density averaged over all of the occupied states and over disorder. The average density \bar{n} is assumed to give a uniformly neutral charge distribution when combined with the positive ions making up the metal. This term does not take the anti-symmetry of the wave function into account. Following the standard second-quantization procedure of many-body physics, accounting for the anti-symmetry of the wave function is accomplished by adding the exchange term

$$\delta\varepsilon_i^{ee,F} = - \sum_{m \neq i}^N \int d\mathbf{r} \int d\mathbf{r}' U(\mathbf{r} - \mathbf{r}') \psi_i^*(\mathbf{r}) \psi_m(\mathbf{r}') \psi_m^*(\mathbf{r}) \psi_i(\mathbf{r}')$$

to $\delta\varepsilon_i^{ee,H}$ where the sum over m and i is taken only over states of opposite spin.

To find the contribution of these interaction terms to the average persistent current at zero temperature, we calculate the disorder averaged contribution F^{ee} of the interaction to the free energy (the same as the energy at zero temperature) and take the derivative with respect to flux:

$$I^{ee} = - \frac{\partial \langle F^{ee} \rangle}{\partial \phi}.$$

Referring to the N^{th} level as the Fermi level with $\varepsilon_N = \varepsilon_F$ and making use of the non-local density

of states $\nu(\mathbf{r}, \mathbf{r}', \varepsilon)$ defined in Eq. B.7, we can write

$$\begin{aligned}
F^{ee} &= \sum_{i=1}^N \left(\delta\varepsilon_i^{ee,H} + \delta\varepsilon_i^{ee,F} \right) \\
&= \frac{1}{2} \int_0^{\varepsilon_F} d\varepsilon \int_0^{\varepsilon_F} d\varepsilon' \int d\mathbf{r} \int d\mathbf{r}' U(\mathbf{r} - \mathbf{r}') \nu(\mathbf{r}, \mathbf{r}, \varepsilon) \nu(\mathbf{r}', \mathbf{r}', \varepsilon') \\
&\quad - \int_0^{\varepsilon_F} d\varepsilon \int_0^{\varepsilon_F} d\varepsilon' \int d\mathbf{r} \int d\mathbf{r}' U(\mathbf{r} - \mathbf{r}') \nu(\mathbf{r}, \mathbf{r}', \varepsilon) \nu(\mathbf{r}', \mathbf{r}, \varepsilon')
\end{aligned} \tag{2.89}$$

where we have dropped the term like $\bar{n}\nu(\mathbf{r}, \mathbf{r}, \varepsilon)$ because we have seen previously (e.g. the preceding section) that this term produces a contribution to the current which decays as $\exp(-pL/2l_e)$. For simplicity, we assume that the range of the interaction is very short so that $U(\mathbf{r} - \mathbf{r}') \approx U\delta(\mathbf{r} - \mathbf{r}')$. In this case, we have

$$F^{ee} = -\frac{U}{2} \int_0^{\varepsilon_F} d\varepsilon \int_0^{\varepsilon_F} d\varepsilon' \int d\mathbf{r} \nu(\mathbf{r}, \mathbf{r}, \varepsilon) \nu(\mathbf{r}, \mathbf{r}, \varepsilon'). \tag{2.90}$$

The cooperon and diffuson contributions to the disorder averaged product $\langle \nu(\mathbf{r}, \mathbf{r}, \varepsilon) \nu(\mathbf{r}', \mathbf{r}', \varepsilon') \rangle$ were given as the integrand of Eq. B.25 (long-range contribution) and the expression of Eq. B.28 (short-range contribution). Since only the cooperon depends on ϕ (because we are considering $\langle \nu(\phi) \nu(\phi) \rangle$), we only need to consider the cooperon term. For the long-range contribution, setting $\mathbf{r}' = \mathbf{r}$ and then performing the spatial integral leads to a contribution to Eq. 2.90 proportional to

$$\sum_{n,n'} \int d\mathbf{r} \frac{\phi_n^*(\mathbf{r}) \phi_n(\mathbf{r}) \phi_{n'}^*(\mathbf{r}) \phi_{n'}(\mathbf{r})}{(i\omega + DE_n^c)(i\omega + DE_{n'}^c)}$$

where we have used the eigenfunction expansion for $P_c(\mathbf{r}, \mathbf{r}', \omega)$ introduced in Eq. B.26 and $\omega = (\varepsilon - \varepsilon')/\hbar$. Since the terms in this sum have no reason to add coherently (there is no reason for pairs of eigenfunctions to have appreciable magnitudes over the same spatial region), we take this integral to be negligible. Again using the eigenfunction expansion of Eq. B.26, we can write the short-range contribution to Eq. 2.90 as

$$\begin{aligned}
\int d\mathbf{r} \langle \nu(\mathbf{r}, \mathbf{r}, \varepsilon) \nu(\mathbf{r}, \mathbf{r}, \varepsilon') \rangle_c &= \text{Re} \left(\frac{\nu_0 L^d}{\pi} \right) \int d\mathbf{r} \sum_n \frac{|\phi_n(\mathbf{r})|^2}{i\omega + DE_n^c} \\
&= \text{Re} \left(\frac{\nu_0 L^d}{\pi} \right) \sum_n \frac{1}{i\omega + DE_n^c},
\end{aligned}$$

leading to

$$\langle F^{ee} \rangle = -\frac{U}{2} \int_0^{\varepsilon_F} d\varepsilon \int_0^{\varepsilon_F} d\varepsilon' \operatorname{Re} \left(\frac{\nu_0 L^d}{\pi} \right) \sum_n \frac{1}{i\omega + DE_n^c}.$$

Using the Poisson summation given in Eqs. 2.58 and 2.59 and setting $\lambda_0 = U\nu_0 L^d/2$, we write

$$\langle F^{ee} \rangle = -\frac{\lambda_0}{\pi} \int_0^{\varepsilon_F} d\varepsilon \int_0^{\varepsilon_F} d\varepsilon' \operatorname{Re} \frac{1}{\sqrt{E_c}} \sum_{p=1}^{\infty} \cos \left(4\pi p \frac{\phi}{\phi_0} \right) \frac{1}{\sqrt{i\hbar\omega + E_c \varepsilon_{\perp}}} \exp \left(-p \sqrt{\frac{i\hbar\omega + E_c \varepsilon_{\perp}}{E_c}} \right). \quad (2.91)$$

We use the standard change of variables $\varepsilon_1 = \varepsilon + \varepsilon'$ and $\hbar\omega = \varepsilon - \varepsilon'$ to write

$$\begin{aligned} \langle F^{ee} \rangle &= -\frac{\lambda_0}{\pi} \sum_{p=1}^{\infty} \cos \left(4\pi p \frac{\phi}{\phi_0} \right) \operatorname{Re} \int_0^{2\varepsilon_F} d\varepsilon_1 \int_{-\varepsilon_1/\hbar}^{\varepsilon_1/\hbar} d\omega \frac{\hbar}{2\sqrt{E_c}} \frac{1}{\sqrt{i\hbar\omega + E_c \varepsilon_{\perp}}} \exp \left(-p \sqrt{\frac{i\hbar\omega + E_c \varepsilon_{\perp}}{E_c}} \right) \\ &= -\frac{\lambda_0}{\pi} \sum_{p=1}^{\infty} \cos \left(4\pi p \frac{\phi}{\phi_0} \right) \operatorname{Re} \int_0^{2\varepsilon_F} d\varepsilon_1 \frac{\hbar}{\sqrt{E_c}} \left(\frac{\sqrt{E_c} i}{p\hbar} \right) \exp \left(-p \sqrt{\frac{i\hbar\omega + E_c \varepsilon_{\perp}}{E_c}} \right) \Big|_{-\varepsilon_1/\hbar}^{\varepsilon_1/\hbar} \\ &= -\frac{\lambda_0}{\pi} \sum_{p=1}^{\infty} \cos \left(4\pi p \frac{\phi}{\phi_0} \right) \operatorname{Im} \int_0^{2\varepsilon_F} d\varepsilon_1 \left(\frac{2}{p} \right) \exp \left(-p \sqrt{i \frac{\varepsilon_1}{E_c} + \varepsilon_{\perp}} \right). \end{aligned}$$

Using a couple changes of variables ($x = \varepsilon_1/E_c$, $y = ix + \varepsilon_{\perp}$, and $z = p\sqrt{y}$), we can evaluate the integral to find

$$\begin{aligned} \langle F^{ee} \rangle &= -\frac{\lambda_0}{\pi} E_c \sum_{p=1}^{\infty} \cos \left(4\pi p \frac{\phi}{\phi_0} \right) \operatorname{Im} \int_0^{2\varepsilon_F/E_c} dx \left(\frac{2}{p} \right) \exp \left(-p \sqrt{ix + \varepsilon_{\perp}} \right) \\ &= -\frac{\lambda_0}{\pi} E_c \sum_{p=1}^{\infty} \cos \left(4\pi p \frac{\phi}{\phi_0} \right) \operatorname{Im} \int_{\varepsilon_{\perp}}^{2i\varepsilon_F/E_c + \varepsilon_{\perp}} dy (-i) \left(\frac{2}{p} \right) \exp \left(-p \sqrt{y} \right) \\ &= \frac{\lambda_0}{\pi} E_c \sum_{p=1}^{\infty} \cos \left(4\pi p \frac{\phi}{\phi_0} \right) \operatorname{Re} \int_{p\sqrt{\varepsilon_{\perp}}}^{p\sqrt{2i\varepsilon_F/E_c + \varepsilon_{\perp}}} dz \left(\frac{4}{p^3} \right) z e^{-z}. \end{aligned}$$

The final integral can be evaluated using integration by parts:

$$\begin{aligned} \int_{p\sqrt{\varepsilon_{\perp}}}^{p\sqrt{2i\varepsilon_F/E_c + \varepsilon_{\perp}}} dz z e^{-z} &= - \int_{p\sqrt{\varepsilon_{\perp}}}^{p\sqrt{2i\varepsilon_F/E_c + \varepsilon_{\perp}}} dz (-e^{-z}) + z (-e^{-z}) \Big|_{p\sqrt{\varepsilon_{\perp}}}^{p\sqrt{2i\varepsilon_F/E_c + \varepsilon_{\perp}}} \\ &= -(1+z) e^{-z} \Big|_{p\sqrt{\varepsilon_{\perp}}}^{p\sqrt{2i\varepsilon_F/E_c + \varepsilon_{\perp}}} \\ &\approx (1 + p\sqrt{\varepsilon_{\perp}}) \exp(-p\sqrt{\varepsilon_{\perp}}). \end{aligned}$$

where the upper boundary term is dropped since it decays exponentially with $\varepsilon_F/E_c \gg 1$. Ulti-

mately, the persistent current due to the interaction is

$$\begin{aligned}
I^{ee} &= -\frac{\partial \langle F^{ee} \rangle}{\partial \phi} \\
&= 16\lambda_0 \frac{E_c}{\phi_0} \sum_p \sin\left(4\pi p \frac{\phi}{\phi_0}\right) \frac{1}{p^2} (1 + p\sqrt{\varepsilon_\perp}) \exp(-p\sqrt{\varepsilon_\perp}).
\end{aligned} \tag{2.92}$$

Within the toroidal field model, we can write

$$I^{ee} = 16\lambda_0 \frac{E_c}{\phi_0} \sum_p \sin\left(4\pi p \frac{\phi}{\phi_0}\right) \frac{1}{p^2} \left(1 + \frac{2B_M}{B_{c,p}}\right) \exp\left(-\frac{2B_M}{B_{c,p}}\right) \tag{2.93}$$

with $B_{c,p}$ given in terms of the ring parameters by Eq. 2.79.

Before interpreting the expression in Eq. 2.93 for I^{ee} , we must state a few important caveats regarding the way in which we handled the interaction $U(\mathbf{r} - \mathbf{r}')$. First, the assumption $U(\mathbf{r} - \mathbf{r}') \approx U\delta(\mathbf{r} - \mathbf{r}')$ of a local form for the interaction while fairly accurate is not necessary. It is possible to evaluate the spatial integrals of Eq. 2.89 using an analytical function for $U(\mathbf{r} - \mathbf{r}')$ (typically an exponentially screened r^{-1} potential) and for $\langle \nu(\mathbf{r}, \mathbf{r}, \varepsilon)\nu(\mathbf{r}', \mathbf{r}', \varepsilon') \rangle$ and $\langle \nu(\mathbf{r}, \mathbf{r}', \varepsilon)\nu(\mathbf{r}', \mathbf{r}, \varepsilon') \rangle$. Doing so simply rescales the value of λ_0 in our derivation. Additionally, our derivation consisted of finding the average contribution of the interaction to the total energy using the eigenstates of the system in the absence of the interaction, essentially a perturbative calculation of the first order contribution of the interaction to the total energy of the system. Taking higher orders leads to higher order corrections in U . Carrying out the calculation to n^{th} order leads to a term proportional to U^n so that, very roughly, the full calculation of the interaction contribution to the current leads to a sum of terms similar to the geometric series $U + U^2 + U^3 + \dots = U/(1 - U)$ and essentially rescales λ_0 to λ_{eff} , giving

$$I^{ee} = 16\lambda_{\text{eff}} \frac{E_c}{\phi_0} \sum_p \sin\left(4\pi p \frac{\phi}{\phi_0}\right) \frac{1}{p^2} \left(1 + \frac{2B_M}{B_{c,p}}\right) \exp\left(-\frac{2B_M}{B_{c,p}}\right). \tag{2.94}$$

We gloss over these details because, as discussed in Chapter 3, the exact nature of the interaction and the correct value for λ_{eff} is one of the outstanding questions in persistent current research.²³

Theoretical and experimental values for λ_{eff} have fallen in the range of $\sim 0.02 - 0.5$ [3, 5-7, 39, 58-61], putting this current on roughly the same order of magnitude as the typical current

²³Note that the comparison to a geometric series is provided just to give a sense of the kind of effect that performing the full calculation has on the prefactor in the expression for I^{ee} . The actual calculation is not as simple as summing a geometric series.

$I^{\text{typ}} \sim 6E_c/\phi_0$ found in Section 2.3.1. Additionally, we note that this current oscillates with a fundamental period of $\phi_0/2$ and the sign of its slope $\partial I^{ee}/\partial\phi$ at zero flux $\phi = 0$ is determined by the sign of the interaction $\lambda_{\text{eff}} \propto U$. For a repulsive interaction such as the Coulomb interaction, $U > 0$ and the current is paramagnetic at low field, while for an attractive interaction, such as the phonon-mediated interaction leading to superconductivity, the current is diamagnetic at low field.

As noted at the outset of this section, for an array of N rings such as those measured in the experiments described in this text, an average current I^{ee} per ring of comparable size to the typical current fluctuations I^{typ} per ring should dominate the total current in the array with $\sum I^{ee}/\sum I^{\text{typ}} \sim \sqrt{N}$ where the sums are over all the rings in the array. However, as can be seen in Eq. 2.94, the contribution I^{ee} to the current becomes strongly suppressed on the field scale $\gamma B_{c,p}/2$, which is typically ~ 10 mT.²⁴ The measurements discussed in this text were performed at fields > 3 T where this interaction contribution to the average current should be negligible. The expression given in Eq. 2.94 is valid for low fields (Eq. 2.77). In Ref. 42, the high-field limit $wtB \gg \phi_0/2$ was considered. It was found that the prefactor of the p^{th} harmonic in Eq. 2.94 becomes

$$0.14 \frac{1}{p^{2.5}} \sqrt{\frac{wt}{L}} \left(\frac{B_M}{\phi_0}\right)^{1/4} \left(1 + 2.75p \sqrt{\frac{L^2 B_M}{\phi_0}}\right) \exp\left(-2.75p \sqrt{\frac{L^2 B_M}{\phi_0}}\right),$$

which gives currents of $\sim 10^{-61} \lambda_{\text{eff}} E_c/\phi_0$ for typical ring parameters and $B_M = 3$ T (assuming the geometric factor $\gamma = 1$). Despite the strong suppression with magnetic field, the magnitude of the current given in Eq. 2.94 is actually large enough that it could be measured using the torsional magnetometry technique discussed in Chapters 4 and 6. Such a measurement would need to be performed at a field scale of $\sim \gamma B_{c,p}$ where Eq. 2.94 is valid and would require a large cantilever with $\sim 10^6$ rings.

To measure the average current in a large ensemble of rings, it is important that the phases of the persistent current oscillations of each individual ring remain synchronized. The frequency β of persistent current oscillation in magnetic field B applied at angle θ relative to the plane of the rings is given by

$$\beta = \frac{\pi R^2 \sin \theta}{\phi_0/2}$$

for the average current oscillation with period $\phi_0/2$. We call the mean area of each ring in the ensemble A_0 and the mean magnetic field frequency $\beta_0 = 2A_0 \sin \theta/\phi_0$. In any fabricated ensemble

²⁴This figure was calculated using Eq. 2.79, sample dimensions similar to those given in Table 7.2, and a geometrical factor of γ . It should be possible to fabricate smaller rings for which $B_{c,p}/2 \gtrsim 50$ mT.

of rings, there will be ring-to-ring variations in the dimensions and thus the area. We characterize these variations by a normal distribution of ring areas with mean A_0 and standard deviation αA_0 . This distribution in ring area results in distribution of magnetic field frequencies with mean β_0 and standard deviation $\alpha\beta_0$. For an ensemble of N rings with $N \gg 1$, the total current signal I^{tot} is well approximated by N times the ensemble-averaged current:

$$I^{\text{tot}}(B) = N \sum_{p=1}^{\infty} I_p^{ee}(B) \int_{-\infty}^{\infty} d\beta \sin(2\pi p\beta B) \left(\frac{1}{\sqrt{2\pi\alpha^2\beta_0^2}} \exp\left(-\frac{(\beta - \beta_0)^2}{2\alpha^2\beta_0^2}\right) \right).$$

The integral giving the ensemble-averaged oscillation is just the imaginary part of the well-known Fourier transform of the Gaussian function. Evaluating the Fourier transform gives

$$I^{\text{tot}} = N \sum_{p=1}^{\infty} I_p^{ee}(B) \sin(2\pi p\beta_0 B) \exp(-2\pi^2 p^2 \alpha^2 \beta_0^2 B^2). \quad (2.95)$$

The ensemble average introduces a new field scale of suppression

$$B_{\text{var},p} = \frac{1}{\sqrt{2\pi p \alpha \beta_0}}.$$

The functions $\exp(-b^2)$ and $(1+2b)\exp(-2b)$ are, very roughly, equal for $b \lesssim 1$. Thus, which effect is more important to calculating the average current in an ensemble of rings, the suppression of the cooperon governed by Eq. 2.94 or the dephasing of the oscillation due to variations in persistent current frequency governed by Eq. 2.95, depends on the relative magnitudes of the field scales $\gamma B_{c,p}$ and $B_{\text{var},p}$, with the shorter field scale being the more significant. Writing out the ratio of the two field scales in terms of the ring parameters, one finds

$$\frac{B_{\text{var},p}}{\gamma B_{c,p}} = \frac{\sqrt{\pi}}{\alpha \gamma \sin \theta} \frac{\sqrt{wt}}{L}.$$

Typically, $w \sim t \sim L/20$, $\gamma \sim 1$, and $\sin \theta \sim 1/\sqrt{2}$ so that $B_{\text{var},p}/B_{c,p} \approx 1/8\alpha$. Typically, $\alpha < 1/8$ for current electron-beam tolerances,²⁵ so that the suppression of the cooperon dominates over these ring-to-ring variations. We note, however, that this dephasing of the average current due to geometric variations would suppress its total magnitude on a field scale of ~ 1 T for $\alpha = 0.01$ and ring dimensions of the order of those studied in this text. Thus, even in the absence of

²⁵Note that α is the fractional variation of the mean ring area. Calculating the area of each ring averages over the small variations in radius within a single ring.

cooperon suppression any average contribution to the current should be strongly dephased for the measurements discussed in Chapter 7, which were performed at fields greater than 3 T.

Since this interaction contribution to the persistent current is strongly suppressed for the measurements discussed in this text, we do not consider the effects of temperature or spin in any detail. Over the temperature range of experimental interest, it can be shown that I^{ee} decays roughly exponentially with a characteristic temperature of $\sim 3E_c/k_B$, which is slightly smaller than that of the typical current contribution ($\sim 10E_c/k_B$ as seen in Eq. 2.73) [49, 58]. Spin effects are less straightforward than in the previous derivations due to the exchange term in the Hartree-Fock model for the interaction. It can be argued that spin-orbit scattering does not affect I^{ee} because the spin-dependence of the interaction (through the exchange term) results in only the spin-orbit independent term of expressions like Eq. B.36 contributing [36]. Because of this spin dependence, the dependence of I^{ee} on Zeeman splitting takes on a slightly complicated form.

Finally, we address the effect of electron-electron interactions on the typical fluctuations of the persistent current. While some have argued the typical current in the presence of interactions could be as large as $I^{ee,typ} \sim ev_F/L$ [62, 63], it has generally been accepted that interactions do not change the form of the typical current derived in Section 2.3.1 [64–67].

Chapter 3

Review of previous work on persistent currents in normal metal rings

In this chapter, we discuss previous theoretical and experimental work on persistent currents in normal metal rings. By my accounting, there have been over 450 papers published which investigate persistent currents theoretically, while there have been nine published measurements of persistent currents.¹ This large discrepancy is due in part to the difficulty of measuring persistent currents and to the surprising nature of some of the early experimental findings. Additionally, theorists have found that the topology of the persistent current system grants access to several different kinds of physical phenomena, many of which remain unstudied experimentally.

We will first review the major theoretical results in chronological order and then discuss the experiments. In order to put the theoretical work into the proper context, we first give a brief summary of the experiments. The earliest measurement of the typical persistent current in a single normal metal ring reported current magnitudes over one order of magnitude larger than that expected from Eq. 2.71 [2]. This large magnitude was not reproduced in later experiments [3, 10, 68]. The earliest measurement of the average current in an ensemble of normal metal (copper) rings reported a current magnitude somewhat smaller than expected from Eq. 2.93 using the λ_{eff}

¹I have cataloged many of these publications at <http://www.citeulike.org/user/willshanks/tags/persistent-current>.

corresponding to a repulsive screened Coulomb interaction. Additionally, the low-field sign of the current was found to be diamagnetic, corresponding to an attractive electron-electron interaction. This result was unexpected as none of the materials studied was thought to possess electrons with an attractive interaction. These findings were confirmed by experiments on different materials [5–7]. A large portion of the theoretical literature has been devoted to the explanation of the large currents found in the first measurement of individual rings as well as the low-field sign of the average current.

3.1 Overview of the theoretical literature

Various different papers have been cited as the earliest precursor to the phenomenon of persistent currents in a ring of a diffusive system. A reasonable choice is Bohr’s early work in 1913 on the quantization of electron orbits in atoms and molecules [69]. All of the calculations of the persistent current in the preceding chapter depend critically on the quantization of electron orbits, as the Bohr-van Leeuwen theorem states that classically the magnetization of any system of charged particles in thermal equilibrium is zero [56, 70].

The next step towards the prediction of persistent currents in solid state systems was taken by Ehrenfest, who in 1925 conjectured that the anomalous diamagnetism of bismuth could be explained by electron orbits enclosing several atoms in the crystal lattice [71, 72]. This conjecture was developed by Landau in 1930 into his theory of diamagnetism [73, 74]. Landau’s theory was further developed in the 1930’s by, among others, Peierls [75] and Blackman [76] to explain the de Haas-van Alphen effect (which is described briefly from an experimental perspective in 4.1). Landau diamagnetism and the de Haas-van Alphen effect are both magnetization effects arising from the orbital motion of conduction electrons in a solid. In a sense, they can be thought of as the analogues to the persistent current (ring topology) for a singly-connected topology.

The earliest studies of the magnetization due the orbital motion of electrons in a ring structure were performed by Pauling in 1936 [77] and London in 1937 [78]. Both of these authors were concerned with the anisotropic magnetization of aromatic compounds such as benzene. The large diamagnetic susceptibility perpendicular to the hexagonal lattice of such compounds was attributed to the “ring currents” of electrons free to move in an orbit encircling one hexagonal unit of the lattice. Shortly afterward in 1938, Hund published the first quantum mechanical investigation of the magnetization of a metal system with a ring topology [79]. In 1952, Dingle elaborated upon

Hund's work [70]. Both works considered two and three dimensional cylinders and treated the effect of the magnetic field perturbatively to first order.

The flux quantum periodicity of electron interference effects was first noted by Ehrenberg and Siday in 1949 [43] and again ten years later by Aharonov and Bohm [44]. The flux quantum periodicity of all equilibrium properties of a system with a ring topology was shown by Byers and Yang in 1961 [80]. Following this work, several authors (including Refs. 81–84) made generalizations to the normal state while studying persistent currents and flux quantization in superconducting rings. A particularly noteworthy work along these lines was the 1970 paper of Kulik in which he obtained the one-dimensional persistent current expression given in Eq. 2.22 and argued for the exponential suppression with disorder given in Eq. 2.49.

The most important work in the history of persistent current research was the 1983 paper of Landauer, Büttiker, and Imry [1]. In the Landauer formalism for microscopic electron conduction developed by one of the authors, transport through a narrow conductor with dimensions smaller than the electron phase coherence length L_ϕ is decomposed into the transport through many transverse channels each characterized by a transmission coefficient t . These transverse channels, similar to those discussed in 2.2.2, act as one dimensional conductors in parallel with each other. Electrons entering the conductor from a reservoir at chemical potential μ_1 on the left side of the conductor are transmitted to the reservoir at chemical potential $\mu_2 < \mu_1$ on the right side with probability $|t|^2$ and are otherwise scattered elastically back into the first reservoir. In either case, the kinetic energy of the electron is conserved. In this picture, the Joule heating usually associated with the transport of electrons through a disordered conductor in the normal state occurs not in the conductor itself but in the reservoirs as the electrons transported from left to right equilibrate from a distribution associated with μ_1 to one associated with μ_2 through inelastic processes in the right reservoir (as the electrons travel over distances much larger than L_ϕ within the reservoir itself). Likewise, the energy loss associated with transport through a normal conductor occurs in the left reservoir as the higher energy states associated with the electrons transported from left to right must be re-populated. This picture of transport in which energy loss occurs in the leads led the authors to consider what would happen if the reservoirs were eliminated by closing the conductor upon itself in a ring geometry. The authors conjectured that it was possible that a realistic disordered ring with dimensions larger than the elastic scattering length l_e but smaller than the inelastic length L_ϕ could sustain a significant persistent current. This conjecture was further developed by the authors in

subsequent works [85–87]. In 1983, the importance of the distinction between elastic and inelastic scattering was just becoming appreciated with the experiments of Sharvin and Sharvin in 1981² [89] and Washburn, Webb, *et al.* in 1984 and 1985 [90, 91]. A review of the advances leading to the understanding of the difference between elastic and inelastic processes in disordered conductors, an understanding which was critical to the serious consideration of persistent currents in the normal state, was written by Washburn and Webb [92].

Following the work of Landauer, Büttiker, and Imry, Riedel and colleagues performed several analytical calculations using Green function methods and numerical simulations using the tight-binding model to study the effect of disorder and finite temperature on the typical magnitude of the persistent current in the ballistic and diffusive regimes [37, 38, 46, 47, 93, 94]. Results similar to those of 2.3.1 for the typical current magnitude and temperature dependence in the diffusive regime were first presented in Ref. 46 in 1989. This calculation was refined by Riedel and von Oppen in 1993 by including additional Green function diagrams [41]. In 2010, the applicability of this calculation was expanded to the regime of strong magnetic fields and strong spin-orbit scattering by Ginossar *et al.* for analysis of the measurements discussed in this text [42].

Montambaux, Bouchiat *et al.* performed additional early numerical studies in 1990 which predicted that the ensemble average of the persistent current for non-interacting electrons in the diffusive regime had an appreciable contribution with a half flux quantum $\phi_0/2$ periodicity [60, 95]. This result was corroborated analytically by several different groups which each derived the result given in 2.3.3.1 [40, 49, 57, 96]. However, this result for non-interacting electrons has largely been insignificant as it is predicted to be much smaller than the contribution to the average persistent current due to electron-electron interactions (see 2.3.3.2) first calculated by Ambegaokar and Eckern in 1990 [39, 59]. The previously cited work of Ginossar *et al.* extended the calculation of both of these contributions to large magnetic fields, where both contributions are strongly suppressed [42].

The magnitude of the persistent current is a random quantity which in the diffusive regime depends on the microscopic details of the disorder configuration. The average and typical values of the persistent current characterize the first two moments of the statistical distribution from which the current is drawn. In 1992, Eckern and Schmid argued that in the presence of electron-electron interactions the typical persistent current would be $I^{\text{typ}} \sim e v_F / L$ (with L the circumference of the ring), a factor of L/l_e larger than the value in the non-interacting case [62]. They also calculated

²A similar experiment had previously been performed in 1974 [88], but it had been interpreted in terms of superconducting fluctuations rather than single electron coherence.

the higher-order cumulants of the current and found that cumulants of order $2n + 1$ and $2n + 2$ with $n > 1$ were suppressed by a factor of N^{-n} where N is the number of electrons in the ring. In the same year, Smith and Ambegaokar challenged Eckern and Schmid's calculation of the typical current in the presence of interactions (arguing that the leading contribution to the typical current was that of the non-interacting electron case) but confirmed the form of the suppression of the higher order cumulants [64]. Smith and Ambegaokar also questioned the conclusion that the persistent current followed a Gaussian distribution, citing the possibility of a long tail to the distribution. Subsequently, Eckern and Schmid published a new calculation in which they addressed the criticism of Smith and Ambegaokar and confirmed their earlier result for the typical current in the presence of electron-electron interactions [63]. Later in 1995, Eckern and Schwab described the determination of the typical current in the presence of electron-electron interactions as an open question due to the ambiguities involved in the previously published calculations [65]. In 1994, Cattaneo *et al.* found that the persistent current follows a Gaussian distribution in the idealized one dimensional limit [97]. In 1997, Bussemaker and Kirkpatrick used the nonlinear sigma model to confirm the results of Smith and Ambegaokar for the cumulants of the persistent current in the presence of interactions [66]. In 2010, Houzet used the nonlinear sigma model to derive the full distribution function for persistent currents in the diffusive regime, finding a Gaussian distribution both with and without electron-electron interactions [67]. This result is valid for values of the current $|I| \ll \sqrt{g}I^{\text{typ}}$ where $g = 2\pi E_c/\Delta_M$ is the dimensionless conductance. Also in 2010, Danon and Brouwer calculated the leading correction in g to the third order correlation function $\langle I(\phi)I(\phi')I(\phi'') \rangle$, finding a correction of order $(I^{\text{typ}})^3/g$ [98]. For reference, we note that $g \sim 2.5 \times 10^4$ for sample CL17 of Table 7.2, resulting in $\langle I(\phi)I(\phi')I(\phi'') \rangle^{1/3}/I^{\text{typ}} \sim 0.03$. In related work, several authors have investigated the statistics of the individual energy levels [99–103], and Feldmann *et al.* calculated the distribution of the flux dependent density of states in the limit $l_e \ll L$ [104].

The preceding discussion touches upon all of the results directly relevant to analyzing the measurements discussed in this text. Before concluding this section, however, we give a brief overview of some of the other aspects of persistent currents which have been investigated theoretically. Excluding the measurements discussed in Chapter 7, only the magnitude, low-field susceptibility, temperature dependence, and flux periodicity of the current have been measured. The theoretical predictions described below can be viewed as additional motivation for our measurements. Although our measurements do not test the predictions directly, they demonstrate a new method of

persistent current detection and raise the possibility of observing many of these to date untested hypotheses.

As mentioned above, much theoretical effort has been put into attempting to explain the large current magnitude reported in early measurements. One strategy has been to calculate the non-equilibrium currents associated with rings the presence of an externally applied, time-varying electromagnetic field [13–34]. A ring studied experimentally could potentially be subject to such electromagnetic radiation through the back-action of the measurement apparatus. Following the work of Ambegaokar and Eckern mentioned above [39, 59, 62–64], many authors have investigated the possibility of additional contributions to the persistent current due to electron-electron interactions [105–125]. Others have considered the role of magnetic impurities, mostly finding that they suppress the current [126–130]. However, Schwab and Eckern have identified a large contribution to the average current due to magnetic impurities [131]. More recently, Bary-Soroker and colleagues have predicted that a dilute amount of magnetic impurities could totally quench superconductivity in a metal while only weakly suppressing the effect of the attractive BCS interaction on the persistent current (as calculated by Ambegaokar and Eckern [132, 133]). Various other mechanisms, including effects related to the nature of the disorder potential, have also been considered as possible explanations of the large observed magnitude of the persistent current [134–144].

Several authors have considered the behavior of persistent currents in systems beyond the simplest case of a ring in a uniform magnetic field. Some studies have been done on the persistent current in rings connected to leads [86, 135, 142, 145, 146] and in networks of many connected rings [147, 148]. Others have considered normal-superconducting hybrid rings [149, 150]. Additionally, it has been predicted that the interaction of a non-uniform magnetic field with the spin of the electrons in a ring can lead to a Berry phase and associated persistent current distinct from the one considered in this text [151–153].

The work discussed so far has had potential applications to persistent currents in the diffusive regime appropriate for metal rings. Persistent currents have also been studied extensively in the ballistic regime and the localized regime (mainly in the framework of the Hubbard model in, e.g., Refs. [117, 154–158]). The ballistic regime is of particular interest for this text because it is realizable in semi-conductor heterostructures for which a current magnitude similar to that observed in normal metal rings is possible. It should be possible to integrate semiconductor rings onto cantilevers and to employ the measurement technique discussed in Chapter 4 to study their persistent currents.

Many of the works cited above are also applicable to the ballistic (or localized) case. Several interesting phenomena unique to the ballistic case have also been studied. Many authors have considered rings with integrated quantum dots, either within the ring or side-coupled to it. Such systems have been identified as test-systems for studying Kondo physics [159–174], adiabatic quantum pumping [175–177], a noise-induced quantum phase transition [178], and quantum zero-point fluctuations [179–181]. Ballistic rings have also been proposed as potential qubits for quantum computation [182–193] and more broadly as model systems for the study of non-classical light, quantum gambling, and the quantum Smoluchowski regime [23, 31, 189, 191, 194–198]. Quite recently, Bary-Soroker *et al.* have studied the transition of the persistent current from the ballistic to the diffusive regime [199].

While the work discussed above is most directly applicable to the measurements discussed in this text, persistent currents have also been studied in other regimes. The study of persistent currents in superconductors is too broad of an area of research to discuss here, but we note that persistent currents have been measured experimentally in rings of similar size to those measured in this text, both in rings made entirely of superconducting material [200] and in rings consisting of superconducting material interrupted by Josephson junctions [201]. In superconductors in their normal state, persistent currents due to thermal and quantum fluctuations have been studied theoretically [202–204], with the persistent currents due to thermal fluctuations having also been measured experimentally [35]. Persistent currents have been studied theoretically [205–207] and observed experimentally with torsional magnetometry [11] in few-electron quantum rings. Other regimes for which persistent currents have been studied theoretically but as yet unprobed experimentally include the Luttinger liquid [208–210], the quantum Hall state [211–213], carbon nanotubes [214–217], graphene [34, 218, 219], and topological insulators [220].

For reference, we conclude this summary of previous work by noting that persistent currents in the normal state have been the subject of several reviews and introductory articles [36, 50, 65, 103, 183, 207, 221–229].

3.2 Previous measurements of persistent currents

We now review the measurements of persistent currents reported prior to those discussed in this text. The experiments may be divided into two types, measurements of the typical current and measurements of the average current. We discuss these two types separately rather than reviewing

all of them in chronological order. Some of the measurements, the first two in particular [2, 4], were published prior to the most plausible theoretical prediction describing them. Rather than summarizing the interpretations of these experiments given by the authors, we will discuss their results in the context of the theoretical framework reviewed in Chapter 2. We know of no proposed theory that accurately describes all of the reported measurements. Besides the measurements discussed below, persistent currents have been observed in superconducting rings above the superconducting transition temperature [35] and in self-assembled InAs quantum rings [11].

3.2.1 Measurements of the typical current

The measurement of the typical persistent current with h/e flux periodicity was reported by Chandrasekhar *et al.* in 1991 [2]. Measurements were performed on single gold rings with circumferences L of 7.5, 8.0, and 12.6 μm at a base temperature of 4.5 mK. The current in the two smaller rings was observed to decrease with temperature, consistent with an exponential decay with a characteristic temperature of $T_0 = 22$ mK. Using Eq. 2.73 for the characteristic temperature $T_{p=1}$ of a diffusive ring, we find values of 0.0156 and 0.0178 m^2/s for the diffusion constant $D = L^2 k_B T_0 / 10.4 \hbar$ in these samples. Using $v_F = 1.4 \times 10^6$ m/s for gold [56], these values of D correspond to elastic mean free paths $l_e = 3D/v_F$ of 34 and 38 nm respectively, slightly smaller than the value of 70 nm measured by Chandrasekhar *et al.* in codeposited wires. From Eqs. 2.74 and 2.75, the expected current magnitude $I = \sqrt{2}(1.11eD/L^2) \exp(-T/T_0)$ for both samples at 4.5 mK is 57 pA. Using the mean value of D from the two small samples and the associated $T_0 = 10.4 \hbar D / k_B L^2 = 8.3$ mK, the expected current magnitude for the for the 12.6 μm sample at 4.5 mK is 11 pA. All of these values stand in striking contrast to the reported values of 6 and 30 nA for the two smaller rings and 3 nA for the larger one. Due to the variability of the observed background in this experiment and the substantial filtering of the data presented, it is difficult to assign a signal to noise ratio to the measured persistent current magnitude. However, I would estimate it to be no larger than 4.

Following the experiment of Chandrasekhar *et al.*, Mailly *et al.* measured persistent currents in a single ring etched into the two dimensional electron gas of a GaAs/GaAlAs heterostructure [8, 230]. The ring was etched with leads so that the ring's conductance and magnetization could be measured simultaneously. The mean circumference of the ring was $L \sim 8.5 \mu\text{m}$, while the elastic mean free path measured via transport was $l_e \sim 11 \mu\text{m}$, placing this sample in the ballistic regime $L < l_e$ described in 2.1 and 2.2. For this two dimensional ring, the number $M = 2w/\lambda_F$ of

transverse channels was ~ 8 for the reported width $w = 160$ nm and Fermi wavelength $\lambda_F = 42$ nm. Repeating the analysis of 2.2.2 for two dimensions, one can show that the typical amplitude of the p^{th} harmonic of the current (the two dimensional analogue of Eq. 2.37) is

$$I_{p,2D,\text{ballistic}}^{\text{typ}} = 2 \times \sqrt{\frac{2M}{3}} \frac{4}{\pi p} I_0 g_{M,2D} \left(\frac{T}{T_p} \right) \exp \left(-\frac{pL}{2l_e} \right) \quad (3.1)$$

with

$$g_{M,2D}(x) = \sqrt{\frac{3}{2} x^2 \int_0^1 dy \operatorname{csch}^2 \left(\frac{x}{\sqrt{1-y^2}} \right)}$$

and T_p the single-channel characteristic temperature of Eq. 2.24. Additionally, in the expression for $I_{p,2D,\text{ballistic}}^{\text{typ}}$ we have included the correction for finite elastic scattering length l_e first introduced in Eq. 2.48 and a factor of 2 for spin. Using the reported value $v_F = 2.6 \times 10^5$ m/s (and corresponding $T_{p=1} = 37$ mK), one finds an expected value of $I_{p,2D,\text{ballistic}}^{\text{typ}} = 18$ nA for the fundamental h/e periodic component of the current,³ which is a bit larger than the measured value 4 ± 2 nA. During the measurement, the disorder configuration of the ring changed due to slow relaxation processes in the semiconductor. This effect allowed measurements of the current to be made for a few different realizations of disorder but could also have introduced some averaging over disorder within a single measurement. The change of the disorder configuration was monitored by measuring the h/e transport signal at the same time as the measurement of the persistent current.⁴ The authors attributed some of the discrepancy in the current magnitude to the small number of independent samples of the current magnitude. The temperature dependence of the current was not studied. Due to the large low frequency feature in the measured persistent current spectrum of Mailly *et al.*, it is difficult to define a signal to noise ratio from the results presented in Refs. 8, 230, but it appears to be no greater than 2.

In 2001, Jariwala *et al.* published a study of the magnetization of $N = 30$ gold rings similar in dimensions ($L = 8 \mu\text{m}$) to those studied individually by the same group in 1991 [3]. Oscillatory currents with flux periodicities of both h/e and $h/2e$ were observed. Focusing first on the h/e signal, the observed characteristic temperature $T_{h/e}$ was 166 mK, which corresponds to a diffusion constant $D = L^2 k_B T_{h/e} / 10.4 \hbar$ of $0.134 \text{ m}^2/\text{s}$ following Eq. 2.73. This diffusion constant corresponds to a

³In the analysis of Refs. 8, 230, the expected current is listed as half this value with no mention of including spin degeneracy.

⁴Several theoretical works have investigated the effects of a transport current on the behavior of the persistent current, including Refs. 231–233. It goes beyond the scope of this text to analyze the effects of the transport current in the experiment of Mailly *et al.*

current $I_{h/e} = \sqrt{2}(1.11eD/L^2) \exp(-T/T_0)$ of 510 pA at 5.5 mK, in reasonable agreement with the measured value of 350 pA per ring. This value of the current per ring was obtained by scaling the total magnetization by $1/\sqrt{N}$ because the current is expected to vary randomly in sign from ring to ring. On a separate wire with the same cross-section (thickness $t = 60$ nm) as the rings, the sheet resistance R_{\square} was measured to be $0.15 \Omega/\square$, which by Eq. E.1 corresponds to a diffusion constant of $D = 0.131 \text{ m}^2/\text{s}$,⁵ in agreement with the value inferred from the h/e persistent current signal. Due to the substantial filtering of the data presented, it is difficult to assign a signal to noise ratio to the measured h/e persistent current magnitude.

Analysis of the $h/2e$ signal from the array of gold rings is more problematic. From the value of D found for the h/e signal, the expected characteristic temperature of the second harmonic of the typical current $T_{p=2} = T_{h/e}/4$ is 42 mK while the characteristic temperature $T_{ee} = 3\hbar D/k_B L^2$ of the interaction contribution to the average current discussed in 2.3.3.2 is 48 mK. In contrast, the decay of the $h/2e$ signal observed by Jariwala *et al.* displayed a characteristic temperature of $T_{h/2e} = 89$ mK. The expected magnitude $I_{p=2} = (1.11eD/2^{1.5}L^2) \exp(-T/T_{p=2})$ of the second harmonic of the typical current at 5.5 mK was 115 pA, giving a typical contribution to the total $h/2e$ current signal for the entire array of $\sqrt{30} \times 115 \text{ pA} = 0.63 \text{ nA}$. Assuming a repulsive Coulomb interaction, the expected magnitude $I^{ee} = 8\lambda_{\text{eff}}eD/\pi L^2 \exp(-T/T_{ee})$ of the interaction contribution to the average $h/2e$ signal at 5.5 mK was 41 pA, giving an average contribution to the total $h/2e$ current signal for the entire array of $30 \times 41 \text{ pA} = 1.22 \text{ nA}$.⁶ The expected values of $I_{p=2}$ and I^{ee} are consistent with the measured 1.98 nA for the total $h/2e$ current signal of the array at 5.5 mK. However, the sign of the total $h/2e$ current was found to be diamagnetic at low field, while a paramagnetic sign is expected for the Coulomb interaction. Although the typical contribution to the $h/2e$ current has a random sign, a diamagnetic fluctuation of $I_{p=2}$ of five times its typical value is required to mask the expected paramagnetic value of I^{ee} and match the data.⁷ The $h/2e$

⁵This number differs from the value quoted in Ref. [3]. The measured resistivity $\rho = tR_{\square}$ was $9 \times 10^{-9} \Omega \text{ m}$. The density of states per unit volume was $\eta = (2\Delta V)^{-1} = 3.3 \times 10^{46} \text{ J}^{-1}\text{m}^{-3}$ for the reported ring volume $V = wtL = 5.76 \times 10^{-20} \text{ m}^{-3}$ and mean level spacing $\Delta = k_B \times 19 \mu\text{K}$. The value of D given above was found using these numbers and Eq. E.1.

⁶Here following Refs. 59 and 36, we use the formula $\lambda_{\text{eff}} = \ln(\epsilon_F e^{\lambda_0^{-1}}/E_c)$ with $\lambda_0 = x^2 \ln(1 + 4/x^2)/8$ and $x = 0.81\sqrt{(r_s/a_0)(m^*/m)}$. The quantity r_s/a_0 is the radius of a sphere with volume equal to the volume of the ring divided by the number of conduction electrons and normalized by the Bohr radius (see Table 1.1 of Ref. 56), ϵ_F is the Fermi energy (see Table 2.1 of Ref. 56), and m^*/m is the ratio of the effective mass to the bare electron mass (see Table 2.3 of Ref. 56). This expression is valid assuming a screened Coulomb repulsion between the electrons. With the values from the tables in Ref. 56 and the E_c inferred from the h/e data of the array of gold rings, one finds $\lambda_{\text{eff}} = 0.053$.

⁷If one infers a value of D from the observed $T_{h/2e}$ and either the expression for $T_{p=2}$ or T_{ee} , one finds larger expected values for the typical current $I_{p=2} \sim 266 \text{ pA}$ (D from $T_{p=2}$) and interaction current $I_{ee} \sim 80 \text{ pA}$ (D from T_{ee}), giving $\sqrt{30} \times I_{p=2} = 1.5 \text{ nA}$ and $30 \times I_{ee} = 2.4 \text{ nA}$. With these numbers it is slightly more plausible that the observed sign could be due to insufficient averaging of the typical fluctuations of the $h/2e$ current signal. However,

signal was observed to decay consistently with the form given in Eq. 2.94 with $B_{c,p=1} = 0.51$ mT, roughly a factor of 10 smaller than the value of $B_{c,p=1}$ expected from Eq. 2.79. This discrepancy could possibly be due to the geometrical correction factor between the toroidal field model and the orientation of the magnetic field (perpendicular to the plane of the rings) in the experiment. As with the h/e signal, due to the substantial filtering of the data presented, it is difficult to assign a signal to noise ratio to the measured $h/2e$ persistent current magnitude.

Also in 2001, Rabaud *et al.* reported measurements on an array of 16 connected GaAs/GaAlAs rings similar to the single GaAs/GaAlAs ring studied in 1993 by some of the same authors [9]. The ring array sample was fabricated in such a way that all of the rings could be isolated from each other by applying a gate voltage. For these rings, the perimeter $L = 12 \mu\text{m}$ was slightly larger than the measured elastic mean free path $l_e = 8 \mu\text{m}$, putting this sample closer to the diffusive regime than the previously measured single semiconductor ring. Using the expression in Eq. 3.1 for the current expected for the ballistic regime gives a much larger typical current (~ 25 nA) than the measured 0.35 nA per ring at 20 mK. The expression for the diffusive ring $I = 2 \times \sqrt{2}(1.11eD/L^2) \exp(-T/T_0)$ gives an expected current of 4.3 nA for $D = v_F l_e / 2 = 1.26 \text{ m}^2/\text{s}$ and $T_0 = 10.4\hbar D/L^2 = 695$ mK. The authors cited the finite phase coherence length $L_\phi = 20 \mu\text{m}$ and the geometry of the square-shaped rings as possible explanations of the smaller magnitude of the current. It is noteworthy that, because of instabilities in the semiconductor leading to changes in the disorder configuration, hundreds of independent measurements of the current were able to be taken. As with the single semiconductor ring, the instability of the disorder configuration could also have slightly reduced the magnitude of the measured current. Although it is not directly relevant to the measurements of this text, we note that the measured magnitude of the current in the connected rings, 0.40 nA per ring, was slightly larger than for the disconnected rings while expected to be a factor of 0.58 smaller. The signal to noise ratio was ~ 5 .

The four measurements described above constituted the entire body of published experimental research on the typical persistent current when the work detailed in this text was undertaken. Shortly before the measurements of Chapter 7 were published in 2009, Bluhm *et al.* published a third study of the typical current in gold rings [10, 234]. For rings with $L = 4.2 \mu\text{m}$, the persistent current was observed to decay exponentially on a scale of 380 mK, in good agreement with the characteristic temperature $T_{p=1} = 10.4\hbar D/k_B L^2 = 402$ mK expected for the value of the diffusion

there is no theoretical justification for assuming a different value for D for the $h/2e$ current contributions compared to that observed for the h/e contribution.

constant $D = 0.09 \text{ m}^2/\text{s}$ found in transport measurements on codeposited wires. The typical current magnitude $I_{h/e} = 0.9 \text{ nA}$ observed in measurements of 15 such rings at 150 mK was also in good agreement with the magnitude expected $I_{p=1} = \sqrt{2}1.11eD/L^2 \exp(-T/T_{p=1}) = 0.88 \text{ nA}$ for this diffusion constant. Similar current magnitudes were observed in measurements on four rings with $L = 3.6 \mu\text{m}$. Due to the need to remove the ensemble-averaged background signal, no inference of the average current could be made. It is noteworthy that the base temperature of this measurement was an order of magnitude larger than that of the earlier measurements due to heating of the samples from the 10 GHz Josephson current in the SQUID detector pickup loop. The signal to noise ratio of this measurement at base temperature was ~ 6 .

Summarizing the measurements of the typical persistent current prior to the work of this text, we find that the two measurements in semiconductor rings reported current magnitudes close to, but slightly smaller than, that expected by theory while two of the three measurements on gold rings reported h/e currents in agreement with theory. All of these measurements employed various forms of SQUID magnetometers. No generally accepted explanation for the contradiction between the earliest measurement on gold rings and the two subsequent measurements has been proposed. Additionally, we note that at least in the experiment of Bluhm *et al.* the high frequency electromagnetic signal of the SQUID detector was observed to have an effect on the sample. The absolute signal to noise ratio in all of these experiments was quite small, ranging from $\sim 4 - 6$.

3.2.2 Measurements of the average current

The first measurement of persistent currents in normal metal rings was reported by Levy *et al.* in 1990 on an array of 10^7 copper rings of circumference $L = 2.2 \mu\text{m}$ [4, 61]. The magnetization signal, which oscillated with an $h/2e$ flux periodicity, was observed to decay exponentially with temperature on a characteristic scale $T_{h/2e} = 80 \text{ mK}$. Using the form for the characteristic temperature $T_{ee} = 3\hbar D/L^2$ of the interaction contribution to the average current discussed in 2.3.3.2, one finds that the observed $T_{h/2e}$ corresponds to a diffusion constant of $D = 0.017 \text{ m}^2/\text{s}$, in good agreement with the value found from transport measurements on codeposited wires.⁸ This value of D leads to an expected average current due to the repulsive Coulomb interaction $I^{ee} = (8\lambda_{\text{eff}}eD/\pi L^2) \exp(-k_B T/T_{ee})$ of 71 pA at 7 mK,⁹ a bit smaller than the observed 400 pA.

⁸Note that the value of l_e was revised in Ref. 61 from the value first reported in Ref. 4. The revised value of 30 nm corresponds to a diffusion constant of $D = v_F l_e/3 = 0.016 \text{ m}^2/\text{s}$, using $v_F = 1.57 \times 10^6 \text{ m/s}$ from Ref. 56.

⁹This estimate assumes $\lambda_{\text{eff}} = 0.054$ following the procedure described in note 6 on page 108.

However, the low-field sign of the current was found to be diamagnetic, while, as noted above and in 2.3.3.2, a paramagnetic current is expected for a repulsive electron-electron interaction. The signal to noise ratio of this measurement was ~ 7 .

All of the measurements discussed so far were performed using SQUID magnetometers operated at frequencies of order 10 Hz (though high frequency electromagnetic signals were still present due to the Josephson oscillations of the SQUIDs). The remaining two studies were performed by inductively coupling arrays of rings to a high Q superconducting resonator. The resonant frequencies of the resonators were all over 200 MHz. As noted in 3.1 and by the authors themselves, it is possible that the presence of high frequency electromagnetic radiation could produce non-equilibrium effects in the rings which behave similarly to the equilibrium persistent current, complicating the analysis.

Two similar measurements of the persistent currents in arrays of 10^5 GaAs/GaAlAs rings were reported first by Reulet *et al.* in 1995 [5] and later by Deblock *et al.* in 2002 [6]. The same group later noted (see note 16 in Ref. [7]) that electric and magnetic responses of the rings were not well separated in the earlier measurement of Reulet *et al.*, so we focus on the results of Deblock *et al.* Qualitatively the results of the two measurements were similar, with the second set of measurements reporting an $h/2e$ periodic current ~ 5 times smaller. For the measurements of Deblock, the rings were in the intermediate regime between ballistic and diffusive motion of the electrons with $L = 5.2 \mu\text{m}$ and $l_e = 3 \mu\text{m}$. For the ideal ring, we found in Eqs. 2.14 and 2.15 a current magnitude $I_{p=2}$ which was independent of electron number and could be written as $I_{p=2} = (4/\pi)\Delta_1/\phi_0$ where Δ_1 is the mean level spacing of the single channel ring (including a factor of 2 for spin). The mean level spacing averaged over all the transverse channels (in two dimensions) is $\Delta_{1,M} = \pi\Delta_1/4$. Taking all transverse channels into account, one would then expect an average current in the ballistic ring at zero temperature of $I_{p=2} = M(\Delta_1/\phi_0) \exp(-L/l_e)$. However, using the values of Ref. [6] ($v_F = 2.2 \times 10^5$ m/s and $w = 200$ nm) gives an expected current of ~ 10 nA, much greater than the observed 0.25 nA per ring at 20 mK. The expected average current $I^{\text{can}} = 8\Delta_M/\pi\phi_0$ in the diffusive, non-interacting electron regime described by Eq. 2.87 predicts a current of 0.7 nA at zero temperature (following Ref. 58, this contribution is not expected to be strongly attenuated for $k_B T/E_c \sim 0.25$ as is the case for this measurement; this contribution is more significant for the semiconductor rings than the metal ones because of the larger mean level spacing). The expected average current contribution $I^{ee} = (8\lambda_{\text{eff}}eD/\pi L^2) \exp(-k_B T/T_{ee})$

due to the repulsive Coulomb interaction is 0.36 nA.¹⁰ So both the diffusive non-interacting and the interacting electron contributions to the average current are on the same order as the observed current. However, once again the low field sign of the current was observed to be diamagnetic, while both of these contributions correspond to paramagnetic behavior.

The final measurement of the average persistent current was reported by Deblock *et al.* in 2002 for an array of 10^5 silver rings with circumference $L = 4 \mu\text{m}$. The $h/2e$ current signal was observed to decay on a temperature scale of 39 mK, corresponding to a diffusion constant of $D = k_B T_{ee} L^2 / 3\hbar = 0.027 \text{ m}^2/\text{s}$ in rough agreement with the value ($0.018 \text{ m}^2/\text{s}$) measured in codeposited wires. At $T = 40 \text{ mK}$, the expected current $I^{ee} = 8\lambda_{\text{eff}} e D / \pi L^2 \exp(-T/T_{ee}) = 13 \text{ pA}$ for the inferred diffusion constant is smaller than the observed current $I_{h/2e} = 330 \text{ pA}$.¹¹ Additionally, the low field sign of the current was observed to be diamagnetic, in contradiction to the expectation of a repulsive Coulomb interaction between the electrons.

Including the $h/2e$ signal measured by Jariwala *et al.* in the array of gold rings, the low field sign of the average persistent current has been observed to be diamagnetic in Cu, Au, GaAs, and Ag rings, in contradiction to the sign predicted both for non-interacting electrons and for electrons with a repulsive interaction. As described in 3.1, non-equilibrium effects and an attractive electron-electron interaction have been proposed as possible explanations of these observations. An attractive electron-electron interaction would be surprising as none of these materials has been observed to superconduct. Additionally, the measured current in each of the samples was somewhat larger in magnitude than that expected for the current due to the Coulomb interaction. These results highlight the need for further study. While the measurements described in this text do not detect the average persistent current, they demonstrate a measurement technique that could be applied to the study of the average persistent current. Finally, we note that the difficulty in interpreting the experimental results for the average persistent currents results an advantage on the measurements described in Chapter 7 over previous work. Because we operate in a regime of magnetic field where all contributions to the average persistent current are strongly suppressed, we can analyze our measurements, and our observed $h/2e$ signal in particular, assuming that the current is entirely due to the non-interacting diffusive contribution and ignoring the poorly understood average contributions.

¹⁰The scale factor λ_{eff} is once again calculated following the procedure of note 6 on page 108. In the expression for λ_0 given there, we use $x = \lambda_F / 2\pi\lambda_s$, where λ_s is the Thomas Fermi screening length specified to be 16 nm in Ref. [6]. The calculated value for λ_{eff} is then 0.077.

¹¹This estimate assumes $\lambda_{\text{eff}} = 0.053$ following the procedure described in note 6 on page 108.

Chapter 4

Cantilever torsional magnetometry

4.1 Introduction to cantilever torsional magnetometry

Cantilever torsional magnetometry has a long history and has been applied to the study of many different physical problems. The origins of torsional magnetometry can be traced back to the development of the compass which took place in China no later than the eleventh century . These early compasses took the form of a floating magnet in a bowl of water or a magnetic needle suspended by a long, thin thread, a form not unlike modern torsional magnetometers. In the thirteenth century, Petrus Peregrinus wrote the earliest text to describe the use of a freely pivoting magnet with a graduated circle to study the properties of magnetic materials [235]. While the compass is capable of measuring magnetic field direction, it was not until the first of half of the nineteenth century that Gauss and Weber devised a magnetometer capable of measuring magnetic field strength on an absolute scale [236]. Again, the instrument was a torsional magnetometer composed of a permanent magnet suspended by a long, thin thread. Gauss and Weber's method required measuring the frequency of oscillation of the suspended magnet when it was angularly displaced from its equilibrium position. This technique, used previously by von Humboldt to measure relative magnetic field strength, is quite similar to that described in this chapter and used in the measurements discussed in this text [237].

Following the work of Gauss and Weber, one of the most notable scientific achievements involving torsional magnetometry was the precise measurement of the de Haas-van Alphen effect, the most important element in the experimental confirmation of the concept of the Fermi surface [238].

While the original measurements were performed with a Faraday balance [239–241], much more precise data over a wider field range was obtained by Shoenberg using a torsional magnetometer developed by Krishnan [242]. In this case, torsional magnetometry takes advantage of a sample’s anisotropic magnetization by using a uniform magnetic field. The magnetic field gradient of the Faraday balance becomes problematic when the resulting variation in magnetic field across the sample is of the same order of magnitude as the magnetic field scale of the experimental features of interest [243]. It is of historical interest to note that the first measurements of the de Haas-van Alphen effect in a material other than bismuth were performed at Yale in Rooms 16 and 17 of Sloane Physics Laboratory [244],¹ the same location as the measurements discussed in this text, using a Faraday balance [245, 246] and using a torsional magnetometer [247, 248]. These measurements were important for demonstrating that the de Haas-van Alphen effect was not a peculiarity of bismuth and led to numerous experiments by other groups outside of Yale [238]. Although a variety of alternate magnetometers such as the superconducting quantum interference device (SQUID), Hall effect probe, and cesium vapor magnetometer have been developed, torsional magnetometry using a sample suspended by a wire has continued to be used up to the present day [249–251], including notably for the measurement of persistent currents in self-assembled semiconductor quantum rings [11].

Cantilever magnetometry was first developed in the late 1980s, arising out of advances over the previous two decades in micromachining. These advances allowed for the fabrication of single crystal oscillators with high quality factors [252, 253] and led to the subsequent development of the atomic force microscope [254]. The earliest applications of cantilever magnetometry were magnetic force microscopy [255, 256] and studies of flux lattice melting in high temperature superconductors by cantilever torsional magnetometry [257]. Much of the pioneering work on cantilever magnetometry was performed by Dan Rugar and collaborators at IBM for magnetic resonance force microscopy [258], who have reported detection of the magnetic moment of single electrons [259] and small ensembles of atomic nuclei [260]. Dovetailing nicely with our discussion of the de Haas-van Alphen effect and its historical connection to the measurements discussed in this text, another major highlight for cantilever torsional magnetometry was the work done by my advisor Jack Harris to study magnetization effects, including the de Haas-van Alphen effect, in two dimensional electron

¹To be completely accurate and discreet, I note that I have only been able to confirm that the helium liquefier of C. T. Lane was located in Room 17 of Sloane Physics Laboratory, but it seems highly likely that these cryogenic experiments would be performed in the same location as the source of the cryogen.

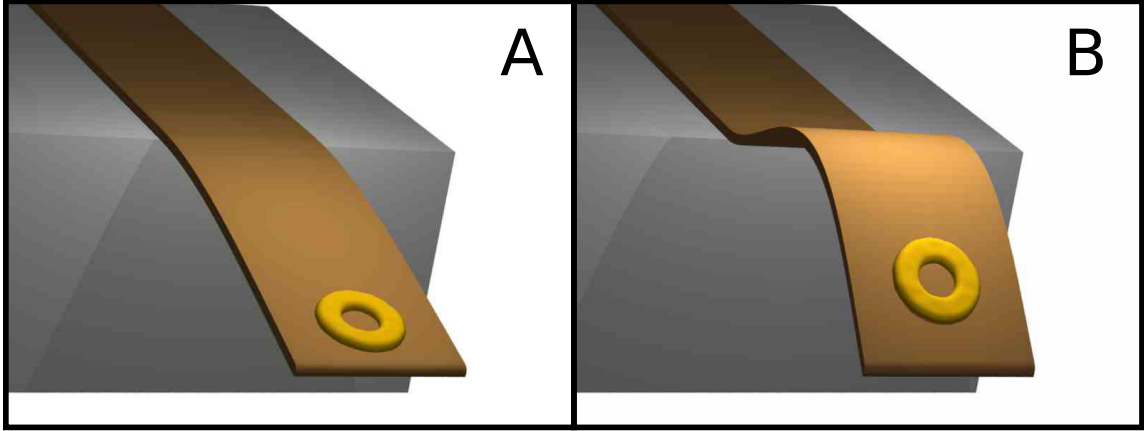


Figure 4.1: Cantilever mode shapes. Panel A shows a cantilever with a normal metal ring deformed from its equilibrium position according to its fundamental flexural mode of vibration, while panel B shows the same cantilever deformed according to the second flexural mode of vibration.

gases [261, 262].

4.2 Cantilever as a simple harmonic oscillator

A cantilever's motion can be decomposed into sets of indexed normal modes, including flexural and torsional modes, each associated with a particular deformation of the beam. The shapes of the first two flexural modes of a cantilever are shown in Fig. 4.1. Focusing on the flexural modes, the beam's deformation consists in a displacement at each point of the beam in the direction perpendicular to the plane defined by the unflexed beam. The beam's deformation varies as a function of position but follows a fixed functional form which is scaled by an overall factor. The motion of each mode can be treated as an independent, one-dimensional simple harmonic oscillator, with this overall scaling (which can be written as the maximum displacement at the cantilever tip) serving as the single degree of freedom [263]. In this section, we will introduce many terms and symbols which will be used throughout the text to discuss the cantilever motion explicitly.

To describe the motion of the cantilever quantitatively, we consider a cantilever of length l with its long dimension parallel to the z -axis and with its wide face parallel to the yz -plane (see Fig. 4.2). When the cantilever undergoes motion in its m^{th} flexural mode, a point located a distance z from the cantilever base moves a distance $x_z = xU_m(z/l)$ in the \tilde{x} direction where x is the amount of displacement at the cantilever tip and U_m , the normalized mode shape for the m^{th} flexural mode, scales the \tilde{x} displacement appropriately for position z . All of the flexural mode shapes are

independent of y . The normalized mode shape is given by

$$U_m(\eta) = \frac{a_m(\cos(\beta_m\eta) - \cosh(\beta_m\eta)) + \sin(\beta_m\eta) - \sinh(\beta_m\eta)}{a_m(\cos(\beta_m) - \cosh(\beta_m)) + \sin(\beta_m) - \sinh(\beta_m)} \quad (4.1)$$

where β_m and a_m are constants associated with mode m [263]. The constant β_m is given by the solution of

$$\cos\beta_m \cosh\beta_m + 1 = 0, \quad (4.2)$$

and

$$a_m = -\frac{\sin\beta_m + \sinh\beta_m}{\cos\beta_m + \cosh\beta_m}.$$

When the cantilever is elastically deformed, it experiences a restoring force $F_{\text{restoring}}$ which can be modeled as a force acting on the cantilever tip and obeying by Hooke's law $F_{\text{restoring}} = -kx$ for spring constant k . Additionally, when the cantilever moves, it experiences a viscous damping force proportional to its velocity

$$F_{\text{damping}} = -m_{\text{eff}}\omega_0\dot{x}/Q, \quad (4.3)$$

where ω_0 is the angular resonant frequency of the cantilever and Q is the cantilever mechanical quality factor. The equation of motion for x can be written as

$$\ddot{x} + \frac{\omega_0}{Q}\dot{x} + \omega_0^2x = \frac{F(t)}{m_{\text{eff}}}, \quad (4.4)$$

where $F(t)$ is the effective external force acting on the cantilever tip at time t and m_{eff} is the cantilever effective mass.² In Eq. 4.4, the spring constant has been eliminated using the expression for the angular resonant frequency

$$\omega_0 = \sqrt{k/m_{\text{eff}}}. \quad (4.5)$$

The cantilever spring constant k can be defined as the product

$$k = \frac{Q}{m_{\text{eff}}} \frac{F(\omega_0)}{x(\omega_0)} \quad (4.6)$$

where $F(\omega_0)$ is the amplitude of an effective force applied at the resonant frequency at the cantilever tip³ and $x(\omega_0)$ is the amplitude of the cantilever response at that frequency. The spring constant

² t is such a natural symbol for both time and thickness that it will be used for both in this document. Which quantity is denoted by t should be clear by context

³Unlike a true mass-and-spring simple harmonic oscillator, it is not possible to define the spring constants of the

of the m^{th} flexural mode can be written in terms of the cantilever's mechanical parameters as

$$k_m = \frac{\beta_m^4}{48} E_Y \frac{wt^3}{l^3} \quad (4.7)$$

where E_Y is Young's modulus for the cantilever material and w , t , and l are the cantilever width, thickness, and length respectively (see Fig. 4.2). The effective mass of the cantilever m_{eff} satisfies

$$m_{\text{eff}} = \frac{\rho}{4} wtl \quad (4.8)$$

where ρ is the cantilever density. Using the relation $x(\omega) = \int_{-\infty}^{\infty} dt e^{-i\omega t} x(t)$ for the Fourier transform,⁴ the equation of motion (4.4) can be rewritten as $x(\omega) = G(\omega)F(\omega)$ where $G(\omega)$ is the cantilever transfer function given by

$$G(\omega) = \frac{1/m_{\text{eff}}}{\omega_0^2 - \omega^2 - i\omega_0\omega/Q}. \quad (4.9)$$

From these relations we see that the cantilever motion is fully characterized by the cantilever's dimensions and material properties and the quality factor Q . The mechanical quality factor Q describes the rate of energy transfer from the cantilever's mechanical motion to its environment. While the geometrical dimensions can be specified during fabrication and the material properties are fixed and can be easily looked up, a complete understanding of the mechanisms determining the mechanical quality factor in micro-electromechanical systems is lacking [264]. The mechanical quality factor can be extracted from measurements of the cantilever's motion. For example, the mechanical quality factor satisfies the relation $Q = \omega_0/\Delta\omega$, where $\Delta\omega$ is the full width at half maximum of $|G(\omega)|^2$. The transfer function $G(\omega)$ can be measured by monitoring the cantilever amplitude as the frequency of a fixed amplitude excitation is varied. Alternatively, in the absence of an applied force and the limit of $Q \gg 1$, the cantilever position as a function of time is

$$x(t) = x_i e^{-\omega_0 t/2Q} \cos(\omega_0 t), \quad (4.10)$$

flexural modes of the cantilever as the ratio of an applied static force to the corresponding static displacement. The static deflection of the beam is described by a different set of equations. Although we do not always write the mode index m , the cantilever spring constant and resonant frequency vary with m .

⁴We will favor the ordinary frequency definition of the Fourier transform and its inverse, namely $x(f) = \int_{-\infty}^{\infty} dt e^{-2\pi i f t} x(t)$ and $x(t) = \int_{-\infty}^{\infty} df e^{2\pi i f t} x(f)$, though as above we will sometimes use the angular frequency form when convenient. These two forms for the Fourier transform are totally equivalent under the substitution $\omega = 2\pi f$, though their inverse transforms are not.

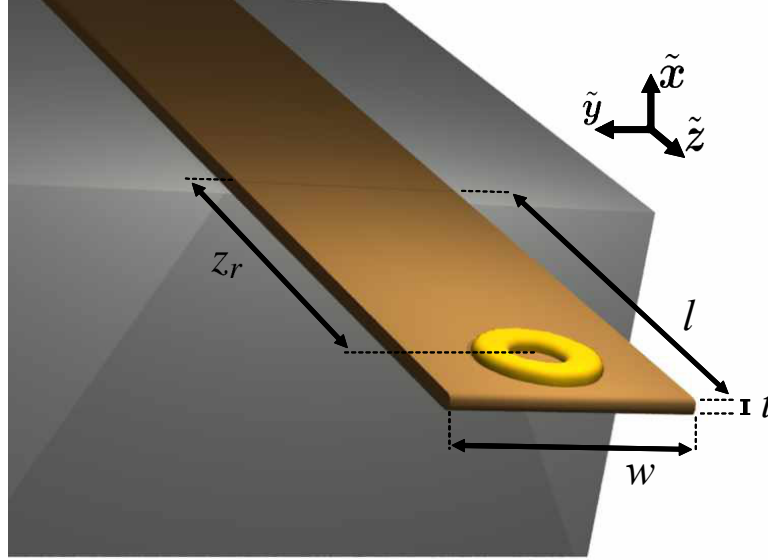


Figure 4.2: Labeled diagram of an unflexed cantilever. The cantilever has a length l , a width w , and a thickness t . The cantilever's beam axis is parallel to the z -axis with the wide surface of the cantilever parallel to the yz -plane. The center of the normal metal ring sitting on the cantilever is located a distance z_r from the base of the cantilever. The ring is also parallel to the yz -plane. A circulating current in the ring would produce a magnetic moment pointed in the \tilde{x} direction.

where x_i is the position of the cantilever at $t = 0$.⁵ In this case, the cantilever oscillates with an amplitude that decays exponentially. By monitoring this decay and determining its characteristic time scale $\tau = 2Q/\omega_0$, the mechanical quality factor Q can be extracted.

4.3 Cantilever frequency shift due to persistent currents in the small amplitude limit

For the measurements of cantilever motion discussed in this text, the primary effect of placing a normal metal ring onto the end of the cantilever is to produce a shift in the cantilever's resonant frequency proportional to the persistent current in the ring.⁶ In this section, we derive the change in the resonant frequency of the cantilever due to the interaction of an integrated normal metal ring

⁵Here, we have assumed that the cantilever has no kinetic energy at $t = 0$. This assumption can be removed at the cost of including an additional phase factor ϕ in the argument of the cosine in Eq. (4.10) satisfying $\tan(\phi) = -v_0/\omega_0 x_0$ where v_0 is the value of \dot{x} at $t = 0$. For completeness, we note here that the $Q \gg 1$ limit mentioned above was used to drop a factor of $\sqrt{1 - 1/4Q^2}$ in the argument of the cosine in Eq. (4.10).

⁶One could also imagine using a time varying flux through the ring to excite the cantilever resonantly and extracting the magnitude of the persistent current from the amplitude of the cantilever's motion. Similarly, one could vary the flux through the ring at twice the cantilever's resonant frequency and use the influence of the ring on the cantilever to amplify the cantilever motion parametrically.

with an applied magnetic field. We will ignore corrections due to the finite extent of the cantilever's motion, which will be discussed in 4.4.

To begin the derivation of the frequency shift, it is more convenient to discuss the cantilever spring constant than the resonant frequency. The cantilever spring constant represents a force gradient experienced by the cantilever tip, $k = -\partial F/\partial x$, or equivalently the curvature of the cantilever's potential energy E_{elastic} , $k = \partial^2 E_{\text{elastic}}/\partial x^2$, at equilibrium. The ring has its own potential energy E_{ring} which depends on its position and orientation in an applied magnetic field. When the ring is integrated onto the cantilever as in Fig. 4.2, the position of the ring becomes coupled to the position of the cantilever. We can then write the total potential energy curvature (or spring constant) as $k_{\text{tot}} = k + \Delta k$ with $\Delta k = \partial^2 E_{\text{ring}}/\partial x^2$. Using the relation (Eq. 4.5) between frequency and spring constant from the preceding section, we can write the frequency of the cantilever-ring system as

$$\begin{aligned}\omega_0 + \Delta\omega &= \sqrt{(k + \Delta k)/m_{\text{eff}}} \\ &\approx \omega_0 \left(1 + \frac{\Delta k}{2k}\right)\end{aligned}$$

so that $\Delta f/f_0 \approx \Delta k/2k$ where f_0 and Δf are the resonant frequency of the bare cantilever and the shift in the resonant frequency due to the ring. The resonant frequency shift of the cantilever due to the ring can be written as

$$\Delta f = \frac{f_0}{2k} \frac{\partial^2 E_{\text{ring}}}{\partial x^2}. \quad (4.11)$$

To describe the dependence of the ring's energy E_{ring} on the motion of the cantilever, it is convenient to introduce a coordinate representing the position of the ring. We use the angular deflection of the ring θ . We will see shortly that the angular deflection of the ring couples to the magnitude of the magnetic field, while the linear position of the ring couples to the magnetic field gradient. In the measurements described in this text, a uniform magnetic field was applied, so the angular deflection θ is the more natural variable to use. In Fig. 4.3, we show a schematic, two-dimensional diagram of the cantilever depicted in Figs. 4.1 and 4.2. We place the center of the ring a distance z_r from the base of the cantilever. The linear displacement of the ring from its equilibrium position x_r is given by $x_r = xU_m(z_r)$. We can also relate the linear displacement of

the ring to its angular deflection by

$$\begin{aligned}\theta &= \alpha_m(z_r) \frac{x}{l} \\ &= \frac{\alpha_m(z_r)}{U_m(z_r)} \frac{x_r}{l}\end{aligned}$$

where

$$\alpha_m(z_r) = \partial_\eta U_m \Big|_{\eta = \frac{z_r}{l}} \quad (4.12)$$

is the normalized, dimensionless derivative of the cantilever mode shape. We will usually abbreviate $U_m(z_r)$ by U and $\alpha_m(z_r)$ by α when it is clear that we are discussing a particular mode and particular z_r coordinate on the cantilever. With this definition, Eq. 4.11 for the resonant frequency shift becomes

$$\Delta f = \frac{f_0}{2k} \left(\frac{\alpha_m(z_r)}{l} \right)^2 \frac{\partial^2 E_{\text{ring}}}{\partial \theta^2}. \quad (4.13)$$

We will consider the motion of the cantilever-ring system in the presence an arbitrary magnetic field $\mathbf{B} = B_x \tilde{\mathbf{x}} + B_y \tilde{\mathbf{y}} + B_z \tilde{\mathbf{z}}$ which could be spatially inhomogeneous. The ring has a mean radius r and so mean area $A = \pi r^2$ (we ignore finite linewidth effects in the present discussion). We also define the vectorial form of the ring area $\mathbf{A} = A(\cos \theta \tilde{\mathbf{x}} - \sin \theta \tilde{\mathbf{z}})$ which is orthogonal to the plane containing the ring. The magnetic moment of the ring can be written as $\boldsymbol{\mu} = I \mathbf{A}$ where I is the current in the ring [265]. We assume that the persistent current is a function of the flux threading the ring with period ϕ_0 so that it can be expanded as

$$I = \sum_p I_p \sin(2\pi p \phi_{\text{tot}} / \phi_0 + \psi_p) \quad (4.14)$$

with the I_p and ψ_p constant but otherwise arbitrary and $\phi_{\text{tot}} = \mathbf{A} \cdot \mathbf{B}$ the total flux threading the mean radius of the ring.⁷

The energy of a magnetic moment in an applied magnetic field can be written as

$$E = - \int^{\mathbf{B}} d\mathbf{B}' \cdot \boldsymbol{\mu}(\mathbf{B}') \quad (4.15)$$

⁷For an ideal Aharonov-Bohm flux, the current should possess nonzero Fourier coefficients only for integral values of p . However, the finite magnetic field correlation of the persistent current discussed in 2.3.2.1 results in a broadening of the magnetic flux frequency peaks of the persistent current oscillation. The persistent current Fourier coefficients for p close to each integral value then take on nonzero values as well.

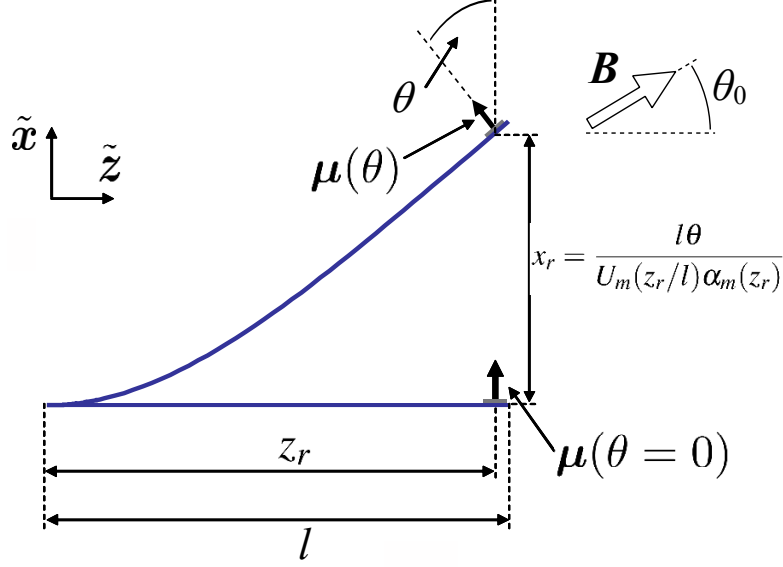


Figure 4.3: Flexed cantilever schematic. Profiles of a cantilever beam (purple lines) unflexed and flexed in its fundamental mode shape are shown. The coordinate axes and cantilever length l are the same as those used in Figs. 4.1 and 4.2. A ring carrying a persistent current which produces a magnetic moment $\boldsymbol{\mu}(\theta)$ is located a distance z_r from the cantilever base and is represented by a thick, solid arrow pointing in the direction of $\boldsymbol{\mu}(\theta)$. When the cantilever flexes, the ring is displaced a distance x_r along the \hat{x} direction. The ring is also tilted an angle $\theta = \alpha_m(z_r)x/l$. The factor $\alpha_m(z_r)$ corrects for the bending of the beam. This factor would be unity and independent of z if the beam were totally rigid and merely pivoted about its base. When the ring is tilted, the direction of $\boldsymbol{\mu}$ is rotated by the same angle θ . In the presence of a magnetic field \mathbf{B} , the magnitude of $\boldsymbol{\mu}$ also varies with θ due the change in magnetic flux through the ring as described in the Chapter 2. The component of \mathbf{B} in the xz -plane, represented by a hollow arrow, is oriented at an angle θ_0 relative to the \hat{z} axis.

where the lower bound of the integral produces an irrelevant shift in the energy. Performing this integral for the case of the ring as described above, we obtain

$$\begin{aligned}
 E_{\text{ring}} &= \sum_p E_{p,\text{ring}} \\
 &= \sum_p \frac{I_p \phi_0}{2\pi p} \cos \left(2\pi p \frac{A(B_x \cos \theta - B_z \sin \theta)}{\phi_0} + \psi_p \right). \tag{4.16}
 \end{aligned}$$

Taking the angular derivative of E_{ring} , we find the torque on the ring due to the magnetic field

$$\begin{aligned}
 \tau_{\text{ring}} &= - \frac{\partial E_{\text{ring}}}{\partial \theta} \\
 &= \sum_p I_p A \sin \left(2\pi p \frac{A(B_x \cos \theta - B_z \sin \theta)}{\phi_0} + \psi_p \right) \\
 &\quad \times \left(\frac{\partial B_x}{\partial \theta} \cos \theta - B_x \sin \theta - \frac{\partial B_z}{\partial \theta} \sin \theta - B_z \cos \theta \right). \tag{4.17}
 \end{aligned}$$

Setting $\theta = 0$, Eq. (4.17) reduces to

$$\tau_{\text{ring}} = \sum_p I_p A \sin \left(2\pi p \frac{\phi_{\text{tot}}}{\phi_0} + \psi_p \right) \left(U \frac{l}{\alpha} \frac{\partial B_x}{\partial x_r} - B_z \cos \theta \right),$$

and follows the expected form for the torque and force on a fixed magnetic moment

$$\boldsymbol{\tau} = \boldsymbol{\mu} \times \mathbf{B} + \frac{U_m(z)}{\alpha_m(z)} \mathbf{l} \times ((\boldsymbol{\mu} \cdot \nabla) \mathbf{B})$$

where the first term is the usual expression for the torque and the second term is the usual expression for the force but converted into a torque by the operation $[(U_m(z)/\alpha_m(z))\mathbf{l} \times]$ where \mathbf{l} has a magnitude l and points along the cantilever beam axis (in the $\tilde{\mathbf{y}}$ direction in Fig. 4.2) [266].

Performing a second derivative on Eq. (4.17) and setting $\theta = 0$, we obtain the cantilever resonant frequency shift in the limit of zero drive

$$\begin{aligned} \Delta f &= \frac{f_0}{2k} \left(\frac{\alpha}{l} \right)^2 \frac{\partial^2 E_{\text{ring}}}{\partial \theta^2} \\ &= -\frac{f_0}{2k} \left(\frac{\alpha}{l} \right)^2 \sum_p I_p A \left[\left(\frac{2\pi p}{\phi_0} A \right) \left(\frac{\partial B_x}{\partial \theta} - B_z \right)^2 \cos \left(\frac{2\pi p}{\phi_0} A B_x + \psi_p \right) + \dots \right. \\ &\quad \left. + \left(-B_x + \frac{\partial^2 B_x}{\partial \theta^2} - 2 \frac{\partial B_z}{\partial \theta} \right) \sin \left(\frac{2\pi p}{\phi_0} A B_x + \psi_p \right) \right]. \end{aligned} \quad (4.18)$$

We can rewrite this expression as

$$\Delta f = -\frac{f_0}{2k} \left[\left(A \frac{\partial \mu}{\partial \phi} \right) \left(U \frac{\partial B_x}{\partial x} - \frac{\alpha}{l} B_z \right)^2 + \mu \left(-\left(\frac{\alpha}{l} \right)^2 B_x - 2 \frac{\alpha}{l} U \frac{\partial B_z}{\partial x} + U^2 \frac{\partial^2 B_x}{\partial x^2} \right) \right]. \quad (4.19)$$

The various terms in Eq. (4.19) have different physical origins. As discussed above, the frequency shift is proportional to the sum of the torque and force gradients, $\partial_\theta \tau_y$ and $\partial_x F_x$ respectively, experienced by the ring.

The terms proportional to μ in Eq. (4.19) represent the torque and force gradients felt by a rigid magnetic moment of fixed magnitude whose orientation and position are coupled to those of the cantilever. The B_x term is usually the dominant term in cantilever torsional magnetometry and represents the restoring torque which tends to align $\boldsymbol{\mu}$ parallel to a uniform \mathbf{B} . Similarly, the $\partial_x B_z$ term represents the fact that, although a uniform \mathbf{B} along $\tilde{\mathbf{z}}$ produces a uniform torque with no torque gradient for our chosen cantilever and corresponding magnetic moment orientation, giving the B_z a gradient along $\tilde{\mathbf{x}}$ allows the torque due to the $\tilde{\mathbf{z}}$ component of \mathbf{B} to produce a torque

gradient along $\tilde{\mathbf{x}}$. This term is usually dominant in magnetic force microscopy. Finally, the $\partial_x^2 B_x$ term corresponds to the force gradient arising from the force experienced by a magnetic moment in a magnetic field gradient when that field gradient itself is non-uniform.

Unlike the terms in Eq. (4.19) proportional to μ , the terms proportional to $\partial_\phi \mu$ represent the force gradient felt by the ring that arise from the fact that the ring's magnetic moment itself varies with cantilever position.⁸ The magnetic moment of the ring is modulated by the magnetic flux threading it, and this flux changes when the cantilever moves. When the cantilever moves, the flux through the ring can change in two ways. First, it can change because the ring moves in the $\tilde{\mathbf{x}}$ direction and the magnitude of the magnetic field itself changes due to a gradient, $\partial_x B_x$. Second, the flux can change because the ring tilts slightly so that \mathbf{A} picks up a $\tilde{\mathbf{z}}$ component and the component of \mathbf{B} along $\tilde{\mathbf{z}}$, B_z now contributes to the flux. It is interesting to note that for typical parameters used for measuring the persistent current, $U = 1$, $\alpha_1 = 1.377$, $l = 150 \mu\text{m}$, and $B = 9$ T, the product $\alpha B/l = 8.3 \times 10^4$ T/m is a bit less than two orders of magnitude smaller than the largest magnetic field gradients, $\partial_x B_x = 4 \times 10^6$ T/m reported in the literature [260].

Although the numbers seem promising for measuring persistent currents in a magnetic field gradient,⁹ we will now drop the magnetic field gradient terms in order to focus more closely on the experiments described in this text which were all performed in a uniform magnetic field. We note that the $\tilde{\mathbf{y}}$ component of \mathbf{B} does not appear in Eqs. (4.18) and (4.19). Without loss of generality,

⁸It will be shown presently that this term is the dominant contribution to the persistent current signal in our detection scheme. Without this term, measuring persistent currents would have been much more difficult. I would like to add a few remarks regarding it to the historical record. We overlooked this contribution for quite a long time in our analysis of the persistent current signal. For the first couple of years of work on the persistent current project, we experimented unsuccessfully with various measurement schemes including conventional frequency modulation magnetometry with \mathbf{B} parallel to \mathbf{A} , static deflection magnetometry with \mathbf{B} orthogonal to \mathbf{A} , and a variant of resonant force magnetometry in which a time-varying flux through the ring is applied on resonance with the cantilever as described in [267]. Ania Jayich and I independently discovered this flux-through-the-ring dependent contribution to the cantilever frequency shift, without much physical intuition on our parts, while following an exhortation from Jack Harris to revisit the frequency shift derivation with a more careful approach (which evolved into the analysis covered in this section). Jack Sankey also played a role in leading us to perform the derivation more carefully. The impetus for revisiting the frequency shift derivation was the unexpectedly strong signal that we measured with the rings in the superconducting state (see Appendix F). In an earlier version of the experiment, the cantilevers were oriented at $\theta_0 = 0^\circ$ while we attempted to thread flux through the rings with a second, smaller superconducting coil which we had wound ourselves. Expecting only the term proportional to μ (which is 0 at $\theta_0 = 0^\circ$), we were initially quite surprised by the large frequency shift signal which we observed at low magnetic field. Once we understood its origin and implications, we removed the second coil, introduced a known, non-zero amount of tilt θ_0 , and performed the measurements described in this text.

⁹Based on the numerical values for $\alpha B/l$ and $\partial_x B_x$ presented in the previous paragraph and the equivalence of these two terms in the expression for the frequency shift given in Eq. 4.19, any results derived for the magnitude of the persistent current signal and its signal to noise ratio in the presence of a uniform field can be translated over to the case of a field gradient. While the uniform field measurement is more straightforward and was thus chosen for the measurements discussed in this text, there are some effects, namely those discussed in 2 which involve the cooperon, which are strongly suppressed at high field. Measuring these effects with a uniform field would be highly difficult due to low fields required. A magnetic field gradient measurement could be a better choice in these cases since it can achieve the same ratio of frequency shift to current as the strong uniform field measurement but can be conducted at low field.

we will set $B_y = 0$ (which also matches the experimental arrangement discussed in this text). We can then write $\mathbf{B} = B \sin \theta_0 \tilde{\mathbf{x}} + B \cos \theta_0 \tilde{\mathbf{z}}$ with θ_0 the angle between \mathbf{B} and the unflexed cantilever beam (see Fig. (4.3)). With these simplifications, Eq. (4.18) reduces to

$$\Delta f = -\frac{f_0}{2k} \left(\frac{\alpha}{l}\right)^2 \sum_p I_p A \left[\left(\frac{2\pi p}{\phi_0} A\right) B^2 \cos^2 \theta_0 \cos \left(\frac{2\pi p}{\phi_0} AB \sin \theta_0 + \psi_p\right) - B \sin \theta_0 \sin \left(\frac{2\pi p}{\phi_0} AB \sin \theta_0 + \psi_p\right) \right] \quad (4.20)$$

The first term will dominate the second when the condition $B \gg [(\tan \theta_0 / \cos \theta_0) (\phi_0 / 2\pi A)]$ is met. The first factor $(\tan \theta_0 / \cos \theta_0)$ is no larger than 10 as long as $\theta_0 < 70^\circ$. For a typical ring size for measuring the normal state persistent current, the second factor $(\phi_0 / 2\pi A)$ is on the order of a millitesla. All of the measurements of the normal state persistent current reported in this text were performed under the conditions $\theta_0 \leq 45^\circ$ and $B > 1$ T. Retaining only the dominant term, we arrive at the simplified expression for the frequency shift due to the persistent current valid for all measurements reported in this text (in the limit of zero drive)

$$\begin{aligned} \Delta f &= -\frac{f_0}{2k} \left(\frac{\alpha}{l} AB \cos \theta_0\right)^2 \sum_p I_p \left(\frac{2\pi p}{\phi_0}\right) \cos \left(\frac{2\pi p}{\phi_0} AB \sin \theta_0 + \psi_p\right) \\ &= -\frac{f_0}{2k} \left(\frac{\alpha}{l} AB \cos \theta_0\right)^2 \frac{\partial I}{\partial \phi}. \end{aligned} \quad (4.21)$$

4.4 The effect of finite cantilever oscillation amplitude on the frequency shift due to the persistent current

The cantilever frequency measurement is made by monitoring the cantilever position as a function of time while the cantilever is driven at some fixed amplitude and by then extracting the dominant frequency of the resulting time trace. The main sources of noise in the measurement of the cantilever position, the cantilever's Brownian motion and the technical noise of the measurement system, are independent of the cantilever's amplitude. The sensitivity to persistent current thus increases with cantilever amplitude since the measurement signal increases while the magnitude of the noise remains constant.¹⁰

There is a limit to the effectiveness of increasing the cantilever amplitude in the measurement

¹⁰We ignore here the effects of cantilever non-linearity which lead to an amplitude dependence of the cantilever frequency and can complicate an analysis of the uncertainties involved in extracting the cantilever frequency from a time trace of the cantilever position.

of the frequency shift due to the persistent current. This limit results from the fact that the flux through the ring changes when the cantilever is displaced. For sufficiently large displacements the flux through the ring varies by more than ϕ_0 in one period of cantilever oscillation and the current in the ring, which follows the form given by Eq. 4.14, tends to be washed out when averaged over the cantilever motion. We will now discuss this effect more quantitatively.

When the cantilever flexes and the ring undergoes a small angular deflection θ from its equilibrium position, the amount of flux threading the ring changes by $\phi = |\mathbf{A}(\theta = 0) \times \mathbf{B}|\theta$.¹¹ Due to the proportionality between ϕ and θ , we can parametrize the motion of the cantilever and ring either in terms of the angle θ or in terms of this change in flux ϕ . As the ring-cantilever system evolves in time, the cantilever position moves through the potential energy landscape (see Fig. 4.4) given by the sum of the parabola corresponding to cantilever's energy E_{elastic} of elastic deformation plus the energy E_{ring} of the ring in the presence of a magnetic field given in Eq. 4.16. For simplicity, we will consider only the p^{th} term from the sum in Eq. 4.16 defining the energy of the ring. All of our analysis will be linear so that the effects of the full ring potential can be found by summing over p .

In Fig. 4.4, the potential energy landscape of both the cantilever and the ring are plotted versus ϕ . The potential energy of the ring can be written as the sum of terms proportional to $\cos(2\pi p\phi/\phi_0)$ and $\sin(2\pi p\phi/\phi_0)$ as

$$\begin{aligned} E_{p,\text{ring}} &= \frac{I_p\phi_0}{2\pi p} \cos\left(2\pi p\frac{\phi_{\text{tot}} - \phi}{\phi_0} + \psi_p\right) \\ &= \frac{I_p\phi_0}{2\pi p} \left(\cos\left(2\pi p\frac{\phi_{\text{tot}}}{\phi_0} + \psi_p\right) \cos\left(2\pi p\frac{\phi}{\phi_0}\right) + \dots \right. \\ &\quad \left. + \sin\left(2\pi p\frac{\phi_{\text{tot}}}{\phi_0} + \psi_p\right) \sin\left(2\pi p\frac{\phi}{\phi_0}\right) \right). \end{aligned} \quad (4.22)$$

where ϕ_{tot} is the total flux threading the mean radius of the ring. These two terms are plotted individually in Fig. 4.4. For cantilever motion traversing a sufficiently small range of ϕ , the cosine term (dashed blue line) merely adjusts the curvature of the parabolic shape of E_{elastic} while the sine term shifts the minimum of E_{elastic} without changing the curvature. Since the frequency of a system with a parabolic potential is given by the potential's curvature, these observations are sufficient to determine the shift of the cantilever's resonant frequency due to the ring as described

¹¹We follow the convention that x , θ , and ϕ represent deviations in the different parameters due to the displacement of the cantilever from its equilibrium position while x_0 , θ_0 , and ϕ_{tot} denote the values of those parameters at the equilibrium position (the symbol ϕ_0 is traditionally reserved for the flux quantum). The symbols x_{max} , θ_{max} , and ϕ_{max} represent the amplitudes of x , θ , and ϕ when the cantilever moves periodically.

in 4.3. However, once $\phi \sim \phi_0/2$, the parabolic and linear approximations are no longer good enough and a more detailed analysis of the cantilever's motion is needed.

To perform this more detailed analysis, we use perturbation theory in the Hamilton-Jacobi formalism with action-angle variables. The basic principles behind this technique are outlined in Appendix C. For a more detailed account, see Ref. [268]. Our perturbative approach gives the shift in the frequency of the cantilever's periodic free evolution due to interaction of the persistent current ring with the magnetic field. The calculation ignores cantilever damping (the term proportional to \dot{x} in Eq. 4.4) and external, time dependent forces acting on the cantilever ($F(t)$ in Eq. 4.4). In the case of the unperturbed simple harmonic oscillator driven on resonance, the force of friction is exactly canceled by the resonant external driving force so that the energy of the oscillator is constant in time. In practice, we will measure the resonant frequency of the cantilever by measuring its position while exciting it with such an external driving force. We assume that even in the presence of the perturbation the only appreciable effect of damping is to offset the energy added to the oscillator by the external driving force. This assumption will be justified by agreement between the expressions derived below and our measurements. However, a quantitative analysis of the effect of the perturbation on the cantilever's motion accounting for damping and an external driving force would be worthwhile.

The full Hamiltonian of the cantilever-ring system in the presence of a magnetic field is given by

$$H = H_0 + H_1$$

with

$$H_0 = E_{\text{ring}} = \frac{1}{2m_{\text{eff}}} \frac{\alpha^2 p_\theta^2}{l^2} + \frac{1}{2} m_{\text{eff}} \omega_0^2 \frac{l^2 \theta^2}{\alpha^2}$$

the Hamiltonian of the bare cantilever expressed in terms of θ and its canonically conjugate angular momentum p_θ and

$$H_1 = E_{p,\text{ring}} = \frac{I_p \phi_0}{2\pi p} \cos \left(2\pi p \frac{AB \sin(\theta_0 - \theta)}{\phi_0} + \psi_p \right)$$

the p^{th} harmonic of the perturbing Hamiltonian due to the ring as written in Eq. (4.22) with $\phi_{\text{tot}} + \phi = AB \sin(\theta_0 - \theta)$. At this point, we have not yet taken the small angle approximation for θ which results in $\phi_a \propto \theta$ as discussed qualitatively above. We will make this approximation explicitly below.

In order to find the shift in the resonant frequency of the system due to H_1 , we rewrite $H_1(\theta, p_\theta)$

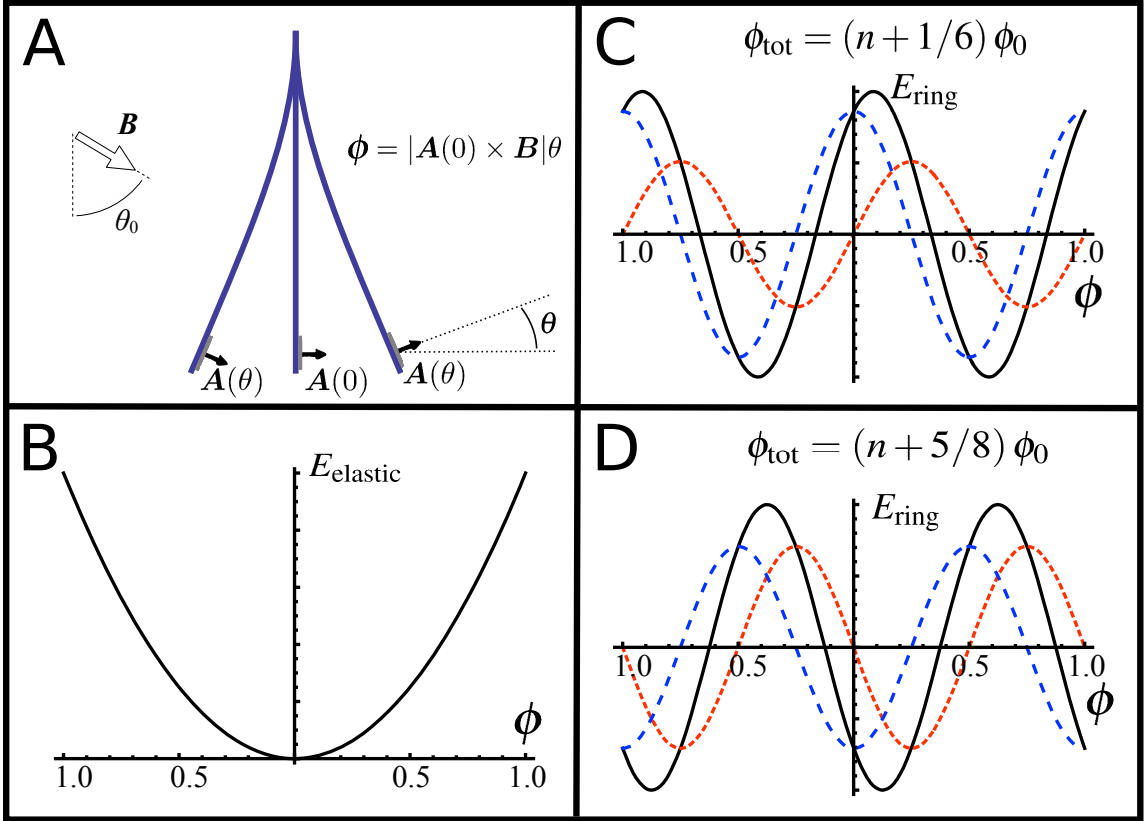


Figure 4.4: Potential energy landscapes of cantilever and ring. Panel A shows a profile of the cantilever beam in both flexed and unflexed positions. A side view of the ring is shown near the end of the cantilever along with an arrow indicating the direction of \mathbf{A} , the ring area vector which always points normal to the plane containing the ring. When the cantilever is flexed, the direction of \mathbf{A} changes by θ . Also indicated in this panel is the direction of the vector \mathbf{B} and the angle θ_0 that it makes relative to the unflexed cantilever beam. When the cantilever flexes and \mathbf{A} changes direction by θ , the flux through the ring changes by $\phi = |\mathbf{A}(0) \times \mathbf{B}|\theta$ from its value when the cantilever is unflexed. For fixed \mathbf{B} , the flux ϕ is proportional the displacement of the cantilever. In panel B, the potential energy of the bare cantilever E_{elastic} is plotted versus the displacement of the cantilever, expressed as ϕ . This energy landscape displays the familiar parabolic form for a simple harmonic oscillator. In panels C and D, the potential energy of the ring E_{ring} (solid black curves) is shown for two different values of the total flux ϕ_{tot} through the ring when the cantilever is unflexed. For simplicity, only the $p = 1$ term of Eq. 4.16 is shown, and ψ_p is take to be 0. The values of ϕ_{tot} in panels C and D are $(n + 1/6)\phi_0$ and $(n + 5/8)\phi_0$ respectively where n is an integer. The scale of the horizontal axes in panels B, C and D is in units of the flux quantum ϕ_0 . The scale of the vertical axes is arbitrary. For the measurements reported in this text, the vertical scale of panel B is typically seven or more orders of magnitude larger than that of panels C and D. Panels C and D also show the components of E_{ring} proportional to $\sin 2\pi\phi/\phi_0$ (red dotted line) and $\cos 2\pi\phi/\phi_0$ (blue dashed line) described in Eq. 4.22. The total value of E_{ring} (solid black curves) is equal to the sum of these two components.

in terms of the action-angle variables (η, J) as $K_1(\eta, J)$ where J is the action variable of the unperturbed system. In Appendix C, we wrote the transformed perturbation Hamiltonian as $K_1(\eta, j)$ where j is the action variable of the perturbed system. However, K_1 is already first order in the perturbation parameter ε and the two action variables J and j differ only by a term proportional to ε . Thus using J rather than j leads to a correction to the frequency shift that is second order in ε and can be discarded. Using Eq. C.7, we find

$$K_1(\eta, J) = \frac{I_p \phi_0}{2\pi p} \cos \left(2\pi p \frac{AB}{\phi_0} \sin \left(\theta_0 - \frac{\alpha}{l} \sqrt{\frac{J}{2\pi^2 m f_0}} \sin 2\pi\eta \right) + \psi_p \right) \quad (4.23)$$

where we take $J = kx_{\max}^2/2f_0$ with x_{\max} the amplitude of motion of the tip of the cantilever. The first order correction to the resonant frequency of the cantilever due to the persistent current is given by Eq. C.12 as

$$\Delta f = \frac{\partial}{\partial J} \int_0^1 d\eta K_1(\eta, J). \quad (4.24)$$

To simplify the analysis, we make the abbreviations

$$\begin{aligned} M &= 2\pi p \frac{AB}{\phi_0} \sin \theta_0, & F(J) &= \frac{\alpha}{l} \sqrt{\frac{J}{2\pi^2 m f_0}}, \\ N &= 2\pi p \frac{AB}{\phi_0} \cos \theta_0, & \varepsilon_p &= \frac{I_p \phi_0}{2\pi p}. \end{aligned}$$

Using the identities in Eqs. A.9 and A.10, we expand Eq. 4.23 to

$$\begin{aligned} K_1(\eta, J) = \varepsilon_p \left[& \cos \psi_p \cos (M \cos (F(J) \sin 2\pi\eta)) \cos (N \sin (F(J) \sin 2\pi\eta)) \right. \\ & + \sin \psi_p \cos (M \cos (F(J) \sin 2\pi\eta)) \sin (N \sin (F(J) \sin 2\pi\eta)) \\ & + \cos \psi_p \sin (M \cos (F(J) \sin 2\pi\eta)) \sin (N \sin (F(J) \sin 2\pi\eta)) \\ & \left. - \sin \psi_p \sin (M \cos (F(J) \sin 2\pi\eta)) \cos (N \sin (F(J) \sin 2\pi\eta)) \right]. \end{aligned}$$

The quantity $F(J)$ represents the amplitude of angular deflection of the cantilever. Generally, this is a small quantity no larger than a few degrees. We use the small angle approximations $\cos \theta \approx 1 - \theta^2/2$ and $\sin \theta \approx \theta$ to remove one level from the nested series of sines and cosines operating on η in the expression for K_1 . We keep to second order in θ because in Section 4.3 we evaluated δf in the small amplitude limit by taking two derivatives of $E_{p,\text{ring}}$ with respect to θ before taking $\theta \rightarrow 0$.

With these approximations and the trigonometric identity of Eq. A.12, the Hamiltonian takes on the unwieldy form

$$\begin{aligned}
K_1(\eta, J) &= \varepsilon_p \left[\cos \psi_p \cos \left(M - M \frac{F^2}{4} + M \frac{F^2}{4} \cos(4\pi\eta) \right) \cos(NF \sin 2\pi\eta) \right. \\
&\quad + \sin \psi_p \cos \left(M - M \frac{F^2}{4} + M \frac{F^2}{4} \cos(4\pi\eta) \right) \sin(NF \sin 2\pi\eta) \\
&\quad + \cos \psi_p \sin \left(M - M \frac{F^2}{4} + M \frac{F^2}{4} \cos(4\pi\eta) \right) \sin(NF \sin 2\pi\eta) \\
&\quad \left. - \sin \psi_p \sin \left(M - M \frac{F^2}{4} + M \frac{F^2}{4} \cos(4\pi\eta) \right) \cos(NF \sin 2\pi\eta) \right] \\
&= \varepsilon_p \left[\cos \psi_p \cos \left(M - M \frac{F^2}{4} \right) \cos \left(M \frac{F^2}{4} \cos(4\pi\eta) \right) \cos(NF \sin 2\pi\eta) \right. \\
&\quad - \cos \psi_p \sin \left(M - M \frac{F^2}{4} \right) \sin \left(M \frac{F^2}{4} \cos(4\pi\eta) \right) \cos(NF \sin 2\pi\eta) \\
&\quad + \sin \psi_p \cos \left(M - M \frac{F^2}{4} \right) \cos \left(M \frac{F^2}{4} \cos(4\pi\eta) \right) \sin(NF \sin 2\pi\eta) \\
&\quad - \sin \psi_p \sin \left(M - M \frac{F^2}{4} \right) \sin \left(M \frac{F^2}{4} \cos(4\pi\eta) \right) \sin(NF \sin 2\pi\eta) \\
&\quad + \cos \psi_p \sin \left(M - M \frac{F^2}{4} \right) \cos \left(M \frac{F^2}{4} \cos(4\pi\eta) \right) \sin(NF \sin 2\pi\eta) \\
&\quad + \cos \psi_p \cos \left(M - M \frac{F^2}{4} \right) \sin \left(M \frac{F^2}{4} \cos(4\pi\eta) \right) \sin(NF \sin 2\pi\eta) \\
&\quad - \sin \psi_p \sin \left(M - M \frac{F^2}{4} \right) \cos \left(M \frac{F^2}{4} \cos(4\pi\eta) \right) \cos(NF \sin 2\pi\eta) \\
&\quad \left. - \sin \psi_p \cos \left(M - M \frac{F^2}{4} \right) \sin \left(M \frac{F^2}{4} \cos(4\pi\eta) \right) \cos(NF \sin 2\pi\eta) \right]. \tag{4.25}
\end{aligned}$$

In order to simplify Eq. 4.25, we use the Jacobi-Anger identity given in Eqs. (A.17), (A.18), (A.19), and (A.20) to expand out the nested trigonometric functions of η . Then the integral over η in (4.23) can be evaluated. We have four different integrals to evaluate, which give

$$\begin{aligned}
&\int_0^1 d\eta \cos \left(M \frac{F^2}{4} \cos(4\pi\eta) \right) \cos(NF \sin 2\pi\eta) \\
&= \int_0^1 d\eta \left(\sum_{n=-\infty}^{\infty} (-1)^n J_{2n} \left(M \frac{F^2}{4} \right) \cos(8\pi n\eta) \right) \left(\sum_{m=-\infty}^{\infty} J_{2m}(NF) \cos(4\pi m\eta) \right) \\
&= \sum_{n=-\infty}^{\infty} (-1)^n J_{2n} \left(M \frac{F^2}{4} \right) J_{4n}(NF),
\end{aligned}$$

$$\begin{aligned}
&\int_0^1 d\eta \sin \left(M \frac{F^2}{4} \cos(4\pi\eta) \right) \cos(NF \sin 2\pi\eta) \\
&= \int_0^1 d\eta \left(\sum_{n=-\infty}^{\infty} (-1)^{n+1} J_{2n-1} \left(M \frac{F^2}{4} \right) \cos(4\pi(2n-1)\eta) \right) \\
&= \sum_{n=-\infty}^{\infty} (-1)^{n+1} J_{2n-1} \left(M \frac{F^2}{4} \right) J_{4n-2}(NF),
\end{aligned}$$

$$\begin{aligned}
& \int_0^1 d\eta \cos\left(M\frac{F^2}{4}\cos(4\pi\eta)\right) \sin(NF\sin 2\pi\eta) \\
&= \int_0^1 d\eta \left(\sum_{n=-\infty}^{\infty} (-1)^n J_{2n}\left(M\frac{F^2}{4}\right) \cos(8\pi n\eta) \right) \\
&\quad \times \left(\sum_{n=-\infty}^{\infty} J_n(NF) \sin(2\pi n\eta) \right) \\
&= 0,
\end{aligned}$$

and

$$\begin{aligned}
& \int_0^1 d\eta \sin\left(M\frac{F^2}{4}\cos(4\pi\eta)\right) \sin(NF\sin 2\pi\eta) \\
&= \int_0^1 d\eta \left(\sum_{n=-\infty}^{\infty} (-1)^{n+1} J_{2n-1}\left(M\frac{F^2}{4}\right) \cos(4\pi(2n-1)\eta) \right) \\
&\quad \times \left(\sum_{n=-\infty}^{\infty} J_n(NF) \sin(2\pi n\eta) \right) \\
&= 0,
\end{aligned}$$

where we have made use of the relations given in Eqs. (A.13), (A.14), and (A.15). Using these results and the trigonometric identities of Eqs. (A.9) and (A.10), we find for the integral of the entire Hamiltonian in Eq. (4.25)

$$\begin{aligned}
\int_0^1 d\eta K_1(\eta, J) = & \varepsilon_p \left(\cos\left(M - M\frac{F^2}{4} + \psi_p\right) \left(\sum_{n=-\infty}^{\infty} (-1)^n J_{2n}\left(M\frac{F^2}{4}\right) J_{4n}(NF) \right) \right. \\
& \left. + \sin\left(M - M\frac{F^2}{4} + \psi_p\right) \left(\sum_{n=-\infty}^{\infty} (-1)^n J_{2n-1}\left(M\frac{F^2}{4}\right) J_{4n-2}(NF) \right) \right).
\end{aligned}$$

The frequency shift of Eq. 4.24 becomes

$$\begin{aligned}
\frac{\Delta f}{\varepsilon_p} = & \frac{MF^2}{4J} \sin Q \left(\sum_{n=-\infty}^{\infty} (-1)^n J_{2n}\left(\frac{MF^2}{4}\right) J_{4n}(NF) \right) \\
& + \frac{NF}{4J} \cos Q \left(\sum_{n=-\infty}^{\infty} (-1)^n J_{2n}\left(\frac{MF^2}{4}\right) (J_{4n-1}(NF) - J_{4n+1}(NF)) \right) \\
& + \frac{MF^2}{8J} \cos Q \left(\sum_{n=-\infty}^{\infty} (-1)^n \left(J_{2n-1}\left(\frac{MF^2}{4}\right) - J_{2n+1}\left(\frac{MF^2}{4}\right) \right) J_{4n}(NF) \right) \\
& + \dots
\end{aligned}$$

$$\begin{aligned}
& -\frac{MF^2}{4J} \cos Q \left(\sum_{n=-\infty}^{\infty} (-1)^n J_{2n-1} \left(\frac{MF^2}{4} \right) J_{4n-2}(NF) \right) \\
& + \frac{NF}{4J} \sin Q \left(\sum_{n=-\infty}^{\infty} (-1)^n J_{2n-1} \left(\frac{MF^2}{4} \right) (J_{4n-3}(NF) - J_{4n-1}(NF)) \right) \\
& + \frac{MF^2}{8J} \sin Q \left(\sum_{n=-\infty}^{\infty} (-1)^n \left(J_{2n-2} \left(\frac{MF^2}{4} \right) - J_{2n} \left(\frac{MF^2}{4} \right) \right) J_{4n-2}(NF) \right).
\end{aligned}$$

where we have used the identities $\partial_J F = F/2J$ and $J'_n = (J_{n-1} - J_{n+1})/2$ and the abbreviation $Q = M - MF^2/4 + \psi_p$.

To simplify the expression for the shift in the resonant frequency of the cantilever, we need to make further approximations. We note that $F = \alpha x_{\max}/l$ and $M = 2\pi p \phi_{\text{tot}}/\phi_0$. In the case of the experiment, $F \lesssim 1.377 \times (200 \text{ nm})/(150 \mu\text{m}) \approx 2 \times 10^{-3}$ and $M \lesssim 3 \times 10^4$ for $p = 1$, $B = 9 \text{ T}$ and $r = 780 \text{ nm}$. Thus, the relations $MF^2/4 \ll 1$ and $F^2/4 \ll 1$ both hold. In the limit $x \ll 1$, the Bessel functions obey $J_n(x) \propto x^n$. Retaining only the lowest order terms (with $J_0(MF^2/4) \sim 1$) and taking $F^2/4 \sim 0$, we have

$$\Delta f \approx \varepsilon_p \left(-\frac{NF}{2J} \cos(M + \psi_p) J_1(NF) + \frac{MF^2}{4J} \sin(M + \psi_p) J_0(NF) \right).$$

Specifically, we have kept the $n = 0$ term of the first two lines of the previous expression for Δf and allowed the $n = 0$ and $n = 1$ terms of the last line to cancel. All other terms in all of the sums were dropped because they contain a factor $J_n(MF^2/4)$ with $|n| > 0$. Restoring the full expressions for ε_p , M , N , and F and the sum over p and writing $J = kx_{\max}^2/2f_0$, we find

$$\begin{aligned}
\Delta f &= \frac{f_0}{2k} \sum_p I_p \left(-\frac{2\pi p}{\phi_0} \left(AB \cos \theta_0 \frac{\alpha}{l} \right)^2 \cos \left(2\pi p \frac{AB}{\phi_0} \sin \theta_0 + \psi_p \right) \text{jinc} \left(2\pi p \frac{AB}{\phi_0} \cos \theta_0 \frac{\alpha}{l} x_{\max} \right) \right. \\
&\quad \left. + AB \sin \theta_0 \left(\frac{\alpha}{l} \right)^2 \sin \left(2\pi p \frac{AB}{\phi_0} \sin \theta_0 + \psi_p \right) J_0 \left(2\pi p \frac{AB}{\phi_0} \cos \theta_0 \frac{\alpha}{l} x_{\max} \right) \right) \\
&= \frac{f_0}{2k} \sum_p I_p \left(-\frac{2\pi p}{\phi_0} \left(AB \cos \theta_0 \frac{\alpha}{l} \right)^2 \cos \left(2\pi p \frac{\phi_{\text{tot}}}{\phi_0} + \psi_p \right) \text{jinc} \left(2\pi p \frac{\phi_{\text{max}}}{\phi_0} \right) \right. \\
&\quad \left. + AB \sin \theta_0 \left(\frac{\alpha}{l} \right)^2 \sin \left(2\pi p \frac{\phi_{\text{tot}}}{\phi_0} + \psi_p \right) J_0 \left(2\pi p \frac{\phi_{\text{max}}}{\phi_0} \right) \right).
\end{aligned}$$

where we define $\text{jinc}(x) = 2J_1(x)/x$ and use $\phi_{\text{max}} = AB \cos \theta_0 \alpha x_{\max}/l$ to represent amplitude of the change ϕ in flux. In the limit $x_{\max} \rightarrow 0$, this expression matches Eq. (4.20) as expected.¹² As

¹²One might wonder why we did not drop the second order terms earlier in the derivation. Doing so greatly simplifies the derivation. However, it also misses the second term in the expression above and thus does not match Eq. (4.20) in the limit of zero cantilever amplitude. Since either of the two terms in Eq. (4.20) can be dominant depending on the parameters chosen, I find it more reassuring to follow the derivation in a way that produces both of them.

before, for the conditions of the experiment the first term dominates and we can take

$$\begin{aligned}\Delta f &= -\frac{f_0}{2k} \sum_p \frac{2\pi p}{\phi_0} I_p \left(AB \cos \theta_0 \frac{\alpha}{l} \right)^2 \cos \left(2\pi p \frac{AB}{\phi_0} \sin \theta_0 + \psi_p \right) \text{jinc} \left(2\pi p \frac{AB}{\phi_0} \cos \theta_0 \frac{\alpha}{l} x_{\max} \right) \\ &= -\frac{f_0}{2k} \sum_p \frac{2\pi p}{\phi_0} I_p \left(AB \cos \theta_0 \frac{\alpha}{l} \right)^2 \cos \left(2\pi p \frac{\phi_{\text{tot}}}{\phi_0} + \psi_p \right) \text{jinc} \left(2\pi p \frac{\phi_{\max}}{\phi_0} \right)\end{aligned}\quad (4.26)$$

as the shift in the resonant frequency of the cantilever due to the persistent current for the case of finite cantilever amplitude.

In Fig. (4.5), the suppression factor $\text{jinc}(2\pi p \phi_{\max}/\phi_0)$ is plotted versus ϕ_{\max}/ϕ_0 for $p = 1$. The main consequence of the form of the suppression factor is that during measurements of the persistent current the amplitude x_{\max} of the cantilever tip must be kept small enough that $\phi_{\max} = AB \cos \theta_0 \alpha x_{\max}/l \lesssim \phi_0/3p$ for the highest p of interest. The suppression factor also has an impact on the analysis of the measured frequency signal. At first, it might appear that Eq. (4.26) states that the frequency shift of the cantilever is proportional to the convolution of $\partial I/\partial \phi_{\text{tot}}$ with the inverse Fourier transform of the jinc suppression factor. However, note that this factor depends on both the transform variable p and the original variable ϕ_{tot} .¹³ This dependency on p and ϕ_{tot} complicates the analysis. Dealing with this factor will be covered in more detail when data analysis is discussed in 7.1.

Finally, we address one concern that might be raised regarding this analysis. In deriving Eq. 4.26, we have treated I_p and ψ_p as constants while in 2.3.2.1 it was shown that the persistent current oscillation has a finite range of correlation in magnetic field due to the effect of magnetic field penetrating the metal of the ring. One might wonder whether I_p and ψ_p change as the ring tilts in the static magnetic field and the flux ϕ_{tot} changes. We believe that such changes in I_p and ψ_p should be small because, although the tilting of the ring with the cantilever's motion results in changes of ϕ_{tot} on the order of ϕ_0 , the change in the flux ϕ_M actually penetrating the metal of the ring should be small as long as the aspect ratio of the ring cross-section is not extreme.

¹³It is $\phi_{a,\max}$ that appears in the jinc factor, but experimentally $\phi_{a,\max}$ and ϕ_{tot} are not independent since they are both proportional to the applied magnetic field B .

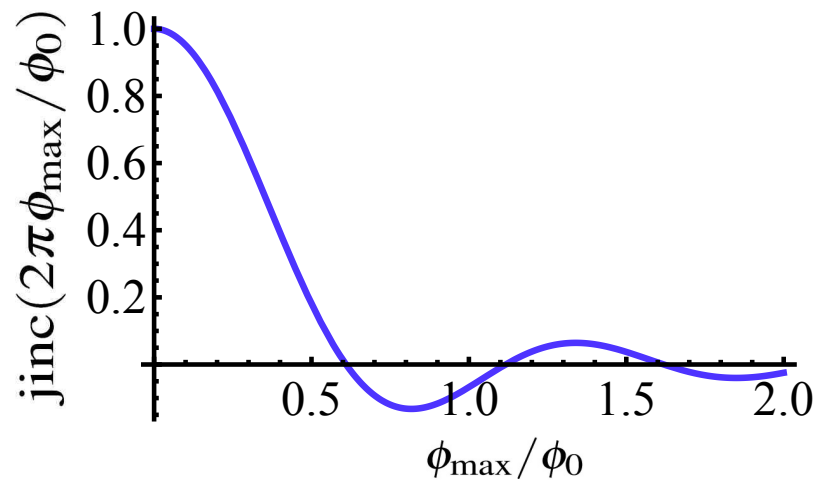


Figure 4.5: Persistent current signal suppression factor due to finite cantilever amplitude. As the amplitude $\phi_{\max} = AB \cos \theta_0 \alpha x_{\max} / l$ of the change in flux threading the ring during cantilever oscillation increases, the resonant frequency shift due to the persistent current is suppressed. The characteristic scale of this suppression is $\phi_{\max} = \phi_0 / 2p$ (in the figure $p = 1$). The suppression has an oscillatory component, but the subsequent peaks are successively smaller and never surpass 14% of the value of the peak at $\phi_{a,\max} = 0$.

Chapter 5

Experimental set-up and measurement

5.1 Cantilever sample fabrication

5.1.1 Preliminary thermometry cantilevers

For the preliminary experiment discussed in 6.4.1, commercially available atomic force microscope (AFM) cantilevers were used. In particular, we used the ArrowTM TL8 chip from NanoWorld (NanoWorld, Neuchâtel, Switzerland). These are tipless cantilevers with nominal dimensions of $500\ \mu\text{m}$ by $100\ \mu\text{m}$ by $1\ \mu\text{m}$ and typical spring constant and resonant frequency of $0.03\ \text{N/m}$ and $6\ \text{kHz}$, respectively. A single chip contains eight cantilevers with a center to center pitch of $250\ \mu\text{m}$ between cantilevers. A picture of a typical chip is shown in the inset of Fig. 5.1.

Various samples were glued to the ends of the arrow cantilevers using thermally conductive Stycast[®] 2850 FT epoxy cured with Catalyst 23LV (Henkel Emerson & Cuming, Billerica, MA, USA). In principle, up to eight different samples could be measured in one cool down of the cryostat using an ArrowTM TL8 chip. In practice, we only measured two cantilevers in any detail: the bare cantilever shown in Fig. 5.1 used for the Brownian motion thermometry measurements and the aluminum grain-mounted cantilever shown in Fig. 5.2 used for the superconducting transition thermometry measurements. The aluminum grain was taken from a 99.99% pure aluminum shot sample (ESPI, Ashland, OR, USA).

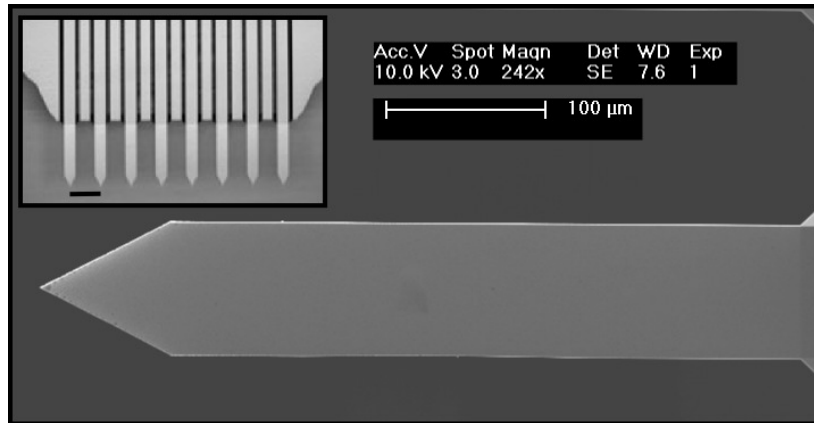


Figure 5.1: Bare cantilever used for Brownian motion measurements. The main figure shows the bare cantilever used in Brownian motion thermometry measurements described in 6.4.1. The inset shows a typical ArrowTM TL8 chip with no samples attached to the cantilever tips. The scale bar in the inset is 250 μm long.

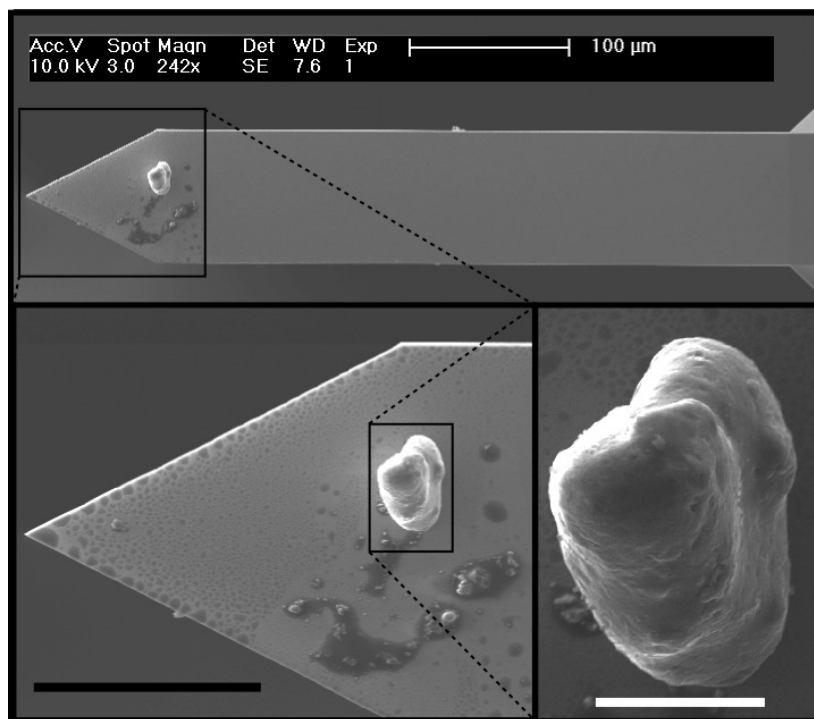


Figure 5.2: Cantilever with aluminum grain glued on tip. The top panel shows the cantilever used for the aluminum superconducting transition thermometry measurements described in 6.4.1. The lower two panels show successive magnified images of the aluminum grain. The discolorations near the grain are puddles of epoxy and smaller pieces of aluminum. The scale bar in the lower left panel is 50 μm long, and the one in the lower right is 10 μm long.

5.1.2 Persistent current cantilever-with-ring sample fabrication

The persistent current samples discussed in this text were created at the Cornell NanoScale Facility (CNF) located on the campus of Cornell University in Ithaca, NY, USA. The majority of the preliminary work determining dosages, exposure times, etc. was performed by Ania Jayich with guidance from Rob Ilic of the CNF. Ania and I fabricated most of the samples reported on in this text together.

An outline of the major steps in the persistent current sample fabrication procedure is depicted in Fig. 5.3. We begin with a clean silicon-on-insulator (SOI) wafer. The microelectronics industry has developed etching procedures highly selective to silicon and silicon dioxide. The insulator/oxide layer of the SOI wafer serves as an etch stop for both frontside and backside processing during the cantilever fabrication. The cantilevers are defined on the frontside by using standard photolithography and a reactive ion etch (RIE) to remove the surrounding frontside silicon. Then the rings and wires are defined with electron beam lithography and created with standard electron beam evaporation and lift-off. After this, the backside silicon is removed by deep reactive ion etch (DRIE) of windowed regions defined by another step of photolithography. Finally the cantilevers are released with a wet etch of the silicon dioxide membrane and dried in a critical point dryer. Images of fully fabricated persistent current samples are shown in Fig. 5.4. A more detailed account of the fabrication procedure is given in Appendix D.

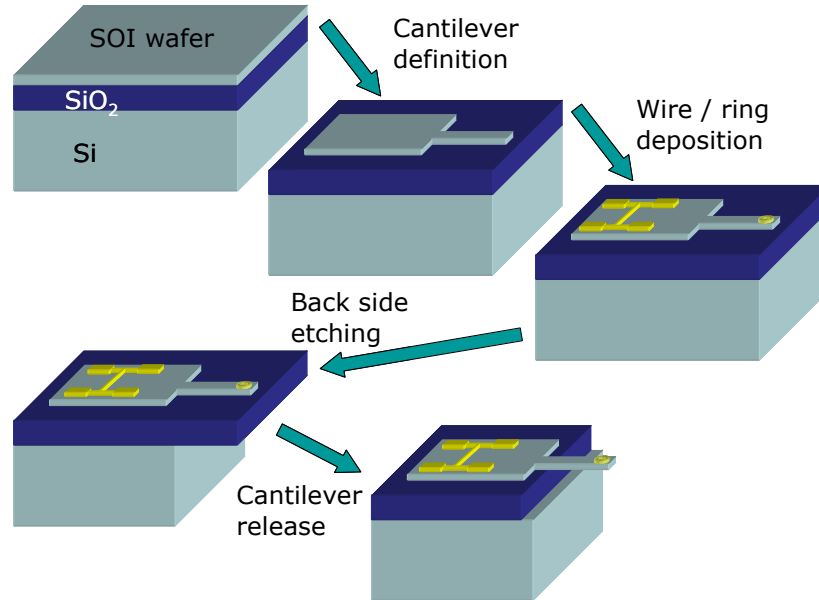


Figure 5.3: Persistent current sample fabrication schematic. **Cantilever definition:** photolithography and reactive ion etch. **Wire / ring deposition:** electron beam lithography and electron beam evaporation of aluminum. **Backside etching:** photolithography and deep reactive ion etching. **Cantilever release:** wet etch with buffered oxide etchant and critical point dry.

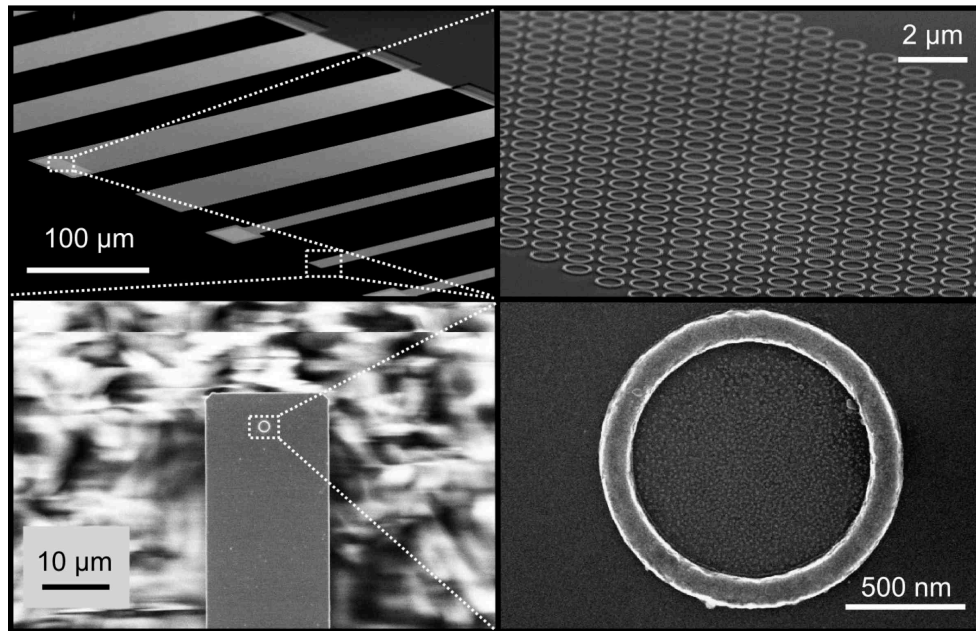


Figure 5.4: Scanning electron micrograph images of cantilevers with integrated aluminum rings. The upper left panel shows an angled view of several cantilevers on one cantilever chip. The samples on the ends of the cantilevers alternate between arrays and single rings. The other panels show magnified images of an array of rings and a cantilever with a single ring as indicated by the dotted lines in the figure. Some of the distortion in the array image is due to cantilever vibration which is difficult to eliminate when imaging released cantilevers. The samples shown in the lower two panels were part of different chips but have similar dimensions to the regions indicated in adjacent panels.

5.2 Experimental apparatus

5.2.1 Dewar and refrigerator

All experiments discussed in this text were performed in a helium-3 refrigerator (He-3-SSV, Janis Research Company, Inc., Wilmington, MA, USA) inserted into a 70 L helium Dewar (Precision Cryogenic Systems, Inc., Indianapolis, IN, USA) equipped with a 9 T magnet (American Magnetics Inc., Oak Ridge, TN, USA).¹ The magnet had a 3" bore which fit snugly around the outside of the refrigerator's inner vacuum chamber. The Dewar was mounted on a felt-covered aluminum frame (1" by 2" cross-section aluminum beams, 80/20 Inc., Columbia City, IN, USA) with four feet. Each foot was supported by a stack of 2.5" by 2.5" by .25" pieces of ultra-soft polyurethane (McMaster-Carr, Elmhurst, IL, USA) and ribbed elastomer (Vib-X-Pads, Vibrasciences, Branford, CT, USA) separated by similarly sized pieces of aluminum. These stacks were the only form of vibration isolation added to the cryostat.² A schematic of the refrigerator and Dewar is shown in Fig. 5.5.

The refrigerator was outfitted with thermometers on its charcoal sorption pump, 1 K pot, and helium-3 pot and with resistive heaters on the charcoal sorption pump and helium-3 pot. An additional thermometer (RX-202A, Lake Shore Cryotronics, Inc., Westerville, OH, USA) was glued into each sample mounting piece with the sample with Stycast[®] 2850 FT in order to achieve good thermal contact. This thermometer was wired with the refrigerator's 0.005" manganin wire. The thermometers were measured and the heaters controlled by a piece of electronics from Lake Shore (Model 340 Temperature Controller, Lake Shore Cryotronics, Inc., Westerville, OH, USA). The usual mode of operation³ of the refrigerator after condensing the helium-3 was to leave the 1 K pot's needle valve and exhaust valve open (so that it was well anchored to 4 K) and to heat the charcoal sorption pump slightly (~ 20 K) to control the sample stage temperature. A constant sample temperature was maintained by a PID feedback loop controlling the charcoal sorption pump heater while monitoring the sample stage thermometer. The feedback loop was implemented by the Lake Shore controller. The lowest temperatures were reached by allowing the 1 K pot to fill completely, then closing the needle valve, and pumping on the 1 K pot's exhaust line (using a SC

¹The magnet was controlled with the Model 420 Power Supply Programmer (American Magnetics Inc., Oak Ridge, TN, USA) and the 4Q050100PS Four Quadrant Power Supply (American Magnetics Inc., Oak Ridge, TN, USA).

²It is possible that the structure of the cryostat naturally provides some vibration isolation itself. The magnet also provided some vibration reduction through eddy current damping.

³For fine temperature control close to the refrigerator base temperature and for temperatures above 4.2 K, the helium-3 pot heater was used.

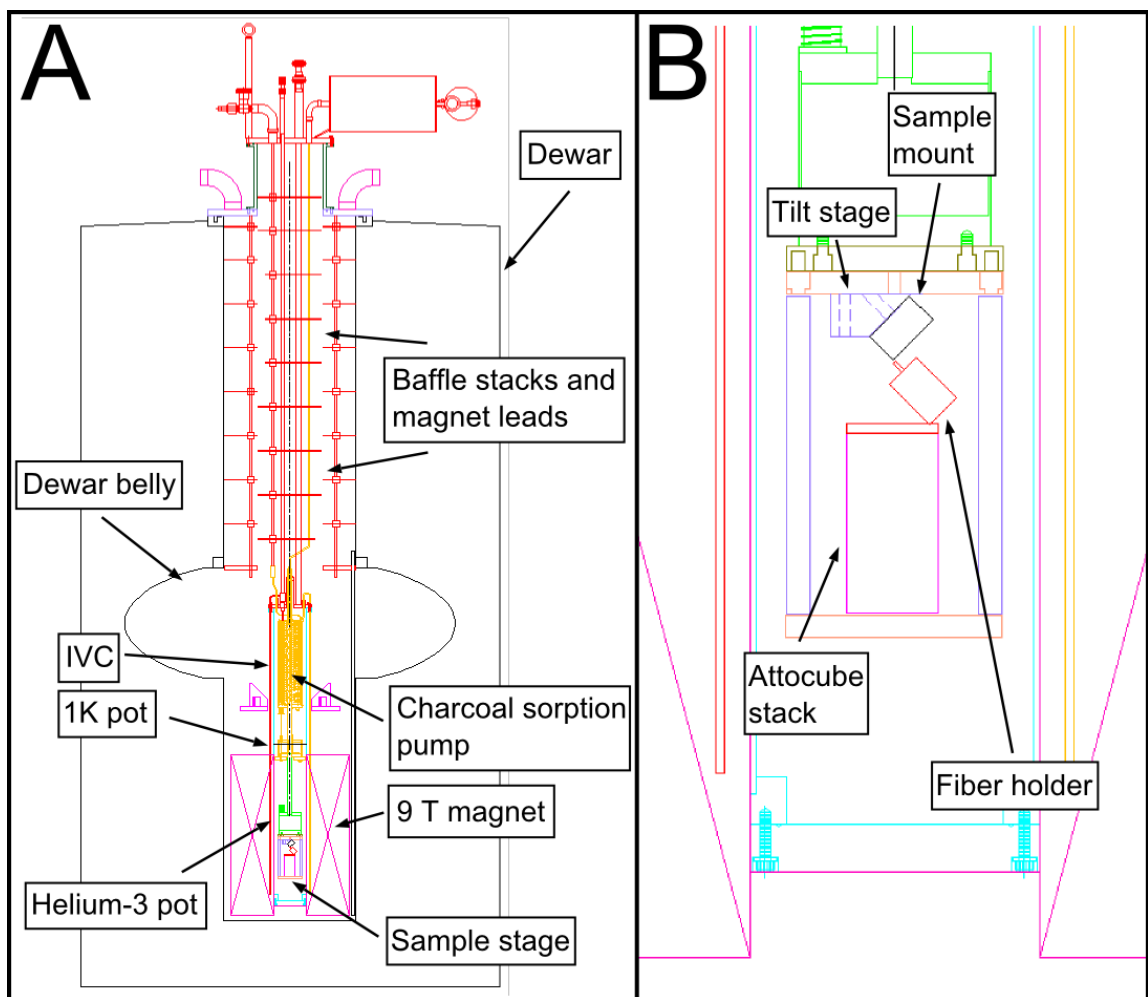


Figure 5.5: Schematic of Dewar and helium-3 refrigerator. Panel A shows the entire Dewar and refrigerator layout with the main elements labeled. The IVC is the inner vacuum chamber. Panel B shows a close-up of the sample stage hanging from the bottom of the refrigerator. The configuration for cantilevers mounted at 45° is shown.

15 D scroll pump from Oerlikon Leybold Vacuum GmbH, Cologne, Germany). A base temperature of 287 mK was achieved by this method with the cantilever detection apparatus mounted to the refrigerator.

5.2.2 Cantilever detection set-up

The basic cantilever detection set-up is shown in Fig. 5.6. The cantilever motion is detected optically using a fiber-based interferometer in a manner similar to that described in Refs. [269], [270], and [271]. The cantilever signal is converted to a voltage signal using a photodiode-amplifier package and measured with a lock-in amplifier. The cantilever is mounted on a piezoelectric actuator which

is driven in a phase-locked loop by the local oscillator of the lock-in which uses the cantilever signal as its clock. Various feedback circuits were used to control the laser power and wavelength and the cantilever amplitude of motion. We will now discuss each component of the set-up in more detail.

5.2.2.1 Laser source

The laser source used in all persistent current measurements was a 1550 nm fiber-coupled diode laser from JDS Uniphase (CQF935/66 26 50 mW 1550 nm CW DFB Laser with PM fiber for WDM applications, JDS Uniphase, Milpitas, CA, USA).⁴ The laser was powered by a low noise current source from ILX (LDX-3620 Ultra low noise current source, ILX Lightwave, Bozeman, MT, USA). The driving current of the laser was approximately 100 mA for all measurements. During measurement, the LDX-3620 current source powering the laser was operated in its constant power mode. In constant power mode, the LDX-3620 current source stabilized its output drive to the laser by feeding back on the output of the reference photodiode (described below). The voltage output of the reference photodiode package was connected through a 1 k Ω resistor to the LDX-3620 photodiode reference port, which required a current input. The laser wavelength was tuned via its temperature using a thermoelectric cooler mount (LM14S2 Universal 14-Pin Butterfly Laser Diode Mount, Thorlabs, Newton, NJ, USA) and controller (TED200C Thermoelectric Temperature Controller, Thorlabs, Newton, NJ, USA). The thermoelectric cooler mount was equipped with a bias-T adapter which allowed for RF modulation of the laser driving current.

We employed a constant RF modulation of the laser current in order to reduce optical feedback noise and optical interference noise [272–274]. The ~ 1 MHz RF modulation signal was generated by a voltage-controlled oscillator (ZX95-850W+, Mini-Circuits, Brooklyn, NY, USA) which passed through a voltage-variable attenuator (ZX73-2500+, Mini-Circuits, Brooklyn, NY, USA) and an amplifier (ZFL-1000VH2, Mini-Circuits, Brooklyn, NY, USA). After the laser was first turned on, the RF components were turned on⁵ and the voltage-controlled oscillator and voltage-variable attenuator were tuned while watching the interferometer signal (to be described below) on an oscilloscope (DPO 2014, Tektronix, Beaverton, OR, USA) until the signal became quiet. The transition from noisy to quiet interferometer signal was very sharp and typically reflected the reduction of interference between unwanted reflectors in the fiber interferometer path through the

⁴The thermometry experiments discussed in 6.4.1 and preliminary attempts at measuring persistent currents were made using a laser source from Thorlabs (S3FC 1550 nm DFB Benchtop Laser Source, Thorlabs, Newton, NJ, USA). This laser source was less tunable than the JDS Uniphase laser. We did not implement feedback schemes for this laser’s wavelength or power.

⁵It is important to turn the laser on before the RF components to avoid reverse biasing the laser diode.

shortening of the laser coherence length. The shortened coherence length used during measurements of the cantilever motion was approximately 1 cm.

5.2.2.2 Fiber optic components

The optical beam path used to monitor the cantilever position is shown in Fig. 5.6. The fiber-coupled output of the laser was connected in series first to an optical isolator (4015SAFC, Thorlabs, Newton, NJ, USA) and then to a variable attenuator (VOA50-FC, Thorlabs, Newton, NJ, USA). The attenuator could be adjusted by hand to change the laser power between measurements. The driving current of the laser was not varied to change the laser power. The attenuator output was connected to the input port of a 99:1 directional coupler (10202A-99-FC, Thorlabs, Newton, NJ, USA). The through port of the directional coupler was connected to a fiber-coupled photodiode package (2011-FC 200-kHz Front-End Photoreceiver, New Focus, Santa Clara, CA, USA) which we refer to as the reference photodiode. The coupled port of the directional coupler was connected to a long fiber which was fed into the inner vacuum chamber (IVC) of the cryostat and mounted with its end addressing the cantilever to be detected. The details of this fiber are discussed more below. The isolated port of the directional coupler (which is also the through port from the perspective of the optical signal returning from the cantilever) was connected to another photodiode package identical to the reference photodiode's and is known as the signal photodiode in this text.

The optical path from the directional coupler down to the cantilever was composed of one single fiber (custom-ordered 8 m 9/125 bare fiber pigtailed with 5 m of furcation tubing, Fiber Instrument Sales, Inc., Oriskany, NY, USA).⁶ Early on, we attempted to use various commercial fiber vacuum feedthroughs. However, all feedthroughs we used had sizable losses which seemed to vary when the fiber was disconnected and reconnected. We chose to do away with the fiber feedthrough element to simplify determination of the incident laser power on the cantilever. The vacuum feedthrough was achieved by epoxying the fiber into a 2" long copper tube with outer diameter chosen to match the inner diameter of a Swagelok[®] Ultra-Torr fitting (Swagelok, Solon, OH, USA). From outside to inside, the optical fiber layers were a 3 mm yellow PVC jacket, a woven layer of yellow aramid yarn, a 1.7 mm Teflon tube, a 250 μm acrylate buffer coating, and the 9/125 μm fiber core/cladding. In order to make the feedthrough the outer PVC, aramid yarn, and teflon tube layers were terminated inside the copper tube.⁷ The PVC jacket of the fiber was then glued into place using 5-Minute[®]

⁶The optical fibers were made by Corning (SMF-28, Corning Inc., Corning, NY, USA).

⁷Alternatively, the Teflon tube was terminated just after the the copper tube, but a section of the teflon which

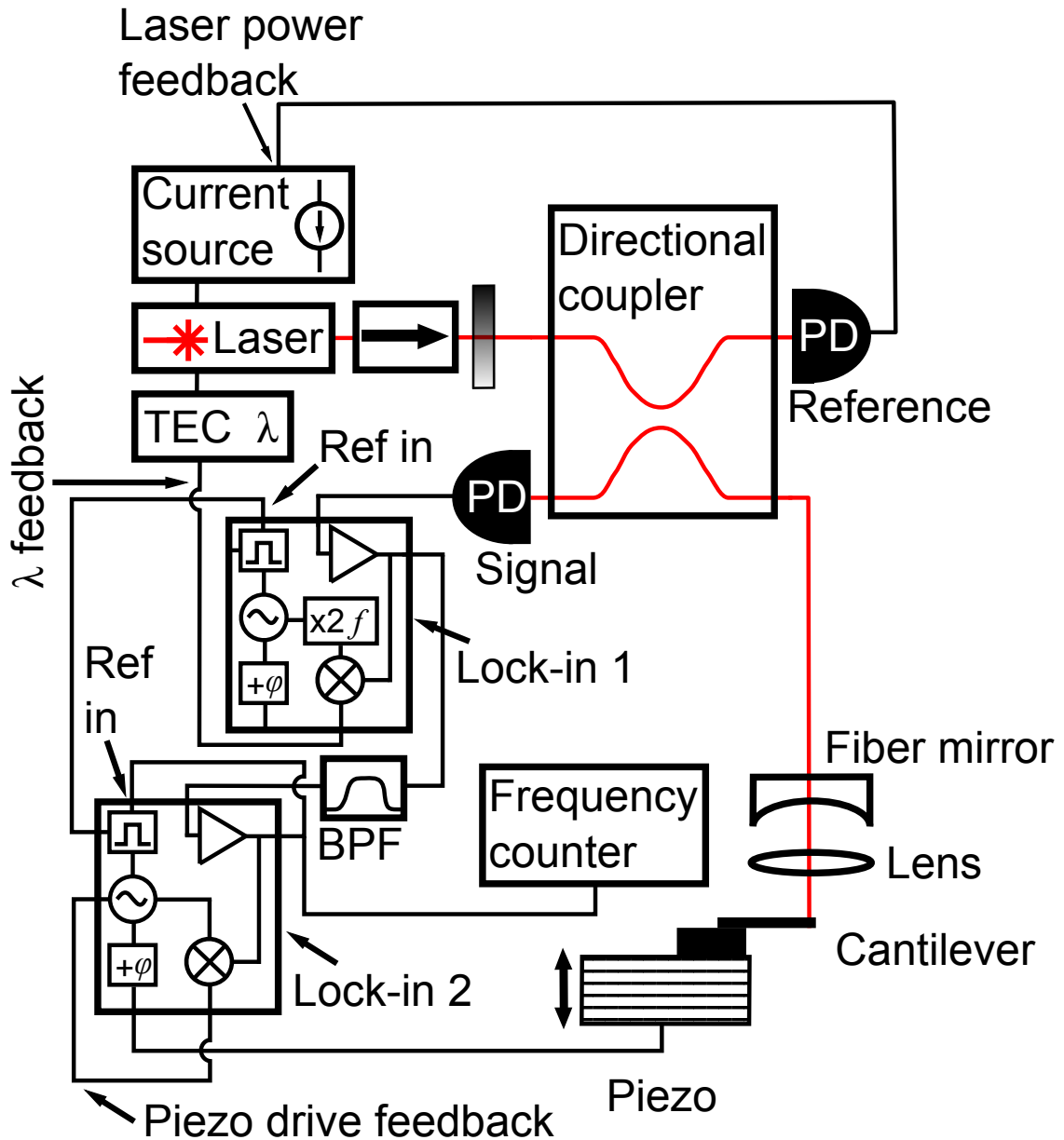


Figure 5.6: Cantilever measurement schematic. The figure displays the arrangement of optical and electronic components during a typical measurement of the cantilever's motion, such as during a persistent current measurement. The laser first passes through an optical isolator and variable attenuator before entering the 99:1 directional coupler. Two of the directional coupler ports are connected to photodiodes (PD) while the other passes through a feedthrough into the fridge and down to the cantilever. The reference photodiode reading is used to stabilize the input laser power. The signal photodiode reading is fed through two lock-in amplifiers and a band pass filter (BPF). The second lock-in drives the piezo actuator holding the cantilever in a phase-locked loop with the signal photodiode as its reference. The outputs of the lock-in mixers (circles with crosses) are to be understood schematically as containing both magnitude and phase information which is processed externally by a computer to implement the feedback loops on the cantilever amplitude through the piezo drive and laser wavelength through the thermoelectric temperature controller (TEC). More details of the cantilever measurement are given in the text.

Epoxy (ITW Devcon, Danvers, MA, USA) to form a plug on the atmosphere side of the copper tube. The tube was then turned atmosphere side down and filled with Stycast[®] 1266 A/B epoxy (Henkel Emerson & Cuming, Billerica, MA, USA). 1266 was chosen for its low viscosity, which allowed it to fill the small openings between different fiber jacket layers.

5.2.2.3 Cantilever detection fiber termination and mounting

The preparation of the termination of the fiber directed at the cantilever changed over the course of the experiment. In the earliest measurements (such as the thermometry measurements discussed in 6.4.1), the fiber was epoxied into a thin copper tube and then cleaved. The copper tube was epoxied to a piece of brass which was screwed down to the Attocube positioners described below. The fiber tip was then positioned $\sim 100 \mu\text{m}$ away from the cantilever for measurement.

For the majority of the measurements discussed in this text, the fiber was modified to include an integrated Bragg grating reflector (fabricated by Avensys, Montreal, QC, Canada) with reflectivity $\sim 20\%$ located $\sim 8 \text{ mm}$ from the cleaved end of the fiber. Again, the fiber tip was positioned $\sim 100 \mu\text{m}$ from the cantilever. However, the effective cavity length with the Bragg reflector was $\sim 8 \text{ mm}$ rather than $\sim 100 \mu\text{m}$.⁸ This longer cavity length is useful for the wavelength tuning described below. With the Bragg reflector fiber, the fiber holder design was also changed. The fiber end was fed into a 14 mm long, $129 \mu\text{m}$ inner diameter / 1 mm outer diameter borosilicate ferrule (Vitrocom, Mountain Lakes, NJ, USA). One end of the ferrule had a tapered opening to allow the fiber to be fed in. The buffer coating layer was carefully stripped from the end of the fiber so that when the fiber was inserted into the ferrule the tip of the fiber extended the desired distance ($\sim 1 \text{ mm}$) from the ferrule while the end of the buffer coating layer fit inside of the tapered ferrule lead-in.⁹ The fiber was then glued into the ferrule using Stycast[®] 2850 FT at the buffer coating end (and not on the cleaved tip side). This ferrule was then slid into a brass holder piece similar to the one shown in Fig. 5.7 with the cleaved fiber tip extending a bit past the end of the fiber holder. In the center of the brass piece was a tube with a diameter 0.001" wider than the ferrule (this tight tolerance¹⁰ was more important for the lens set-up described below). Two set screws

would be inside of the copper tube was cut away so that epoxy could seep into the tube. This arrangement provided extra strain relief for the buffer coated fiber emerging from the epoxy.

⁸One can think of the section of fiber between the Bragg reflector and the fiber tip as playing the role of the "Lens" in Fig. 5.6 because it keeps the light from diverging over most of the length between the Bragg reflector and the cantilever. In the early cleaved fiber set-up, there was no analogue to the lens.

⁹It is very important that the buffer coating mate with the ferrule lead-in. The bare fiber cladding (with the buffer coating removed) is extremely brittle and will easily break at the epoxy joint if it is not sufficiently strain-relieved.

¹⁰Great care must taken in cleaning and deburring the fiber holder due to this tight tolerance, especially with the lens set-up described below. It is nearly impossible to clean the inside of the fiber holder without damaging the lens

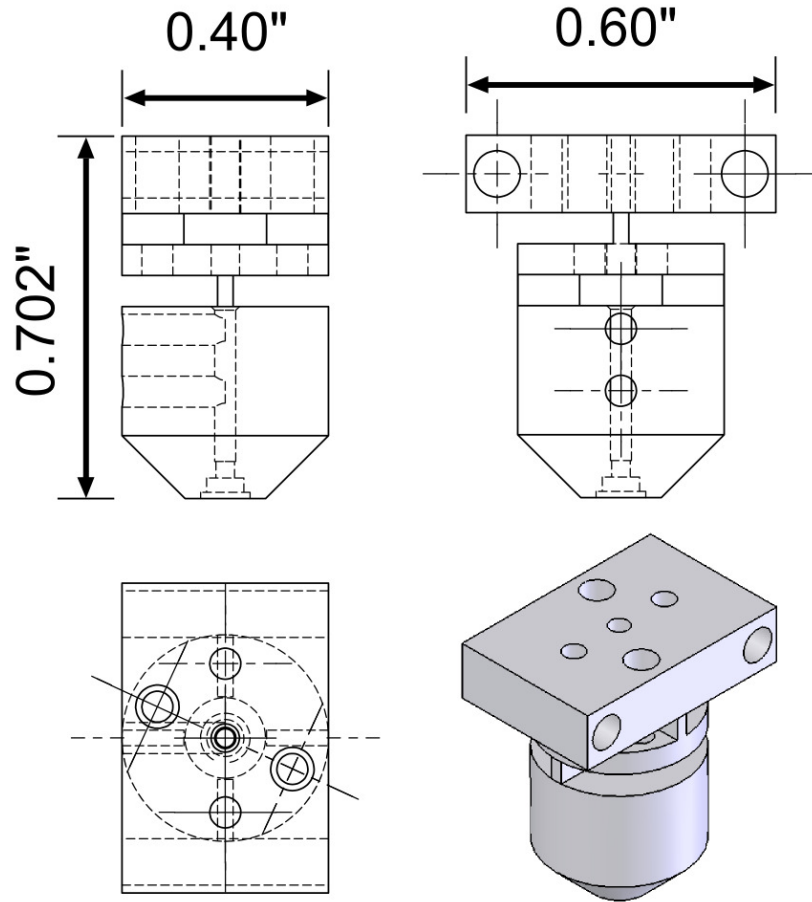


Figure 5.7: Optical fiber holder drawing. The figure shows technical drawings of the fiber holder from three different angles and a three dimensional rendition viewed from an angle askew to the principle axes of symmetry. The drawings represent the lens-mounted version of the fiber holder discussed in the text. The pocket for the lens is located on the bottom of the part in the top two drawings. The fiber holder for the Bragg reflector fiber looked similar but did not have this pocket.

oriented perpendicularly to the axis of the ferrule were used to hold the ferrule in place.

In the latest design of fiber holder with which I worked, an anti-reflection coated aspheric lens (352140-C $f=1.45$ mm, $NA=0.55$, Unmounted Geltech Aspheric Lens, Thorlabs, Newton, NJ, USA) was incorporated into the fiber holder. The drawing shown in Fig. 5.7 depicts the fiber holder with a lens mount at one end. Other than the cut-out for the lens mount, the only functional difference between the lens-mounted fiber holder and the fiber holder for the Bragg reflector fiber was the addition of a slight constriction of the cylinder inside the fiber holder which prevented the ferrule from bumping into the lens. This constriction was approximately one focal length away from the

once the lens has been mounted.

lens. The lens was glued into the fiber holder with Stycast[®] 2850 FT.¹¹ A bare cleaved fiber (no Bragg reflector) was used in the lens set-up.¹² With the lens set-up, the fiber holder was positioned with the lens approximately two focal lengths (~ 3 mm) away from the cantilever for measurement. The lens set-up thus has a similar cavity length to the Bragg reflector set-up but did not require that an object be brought into close proximity with the cantilever. Interactions (e.g. electrostatic) between the cantilever and a nearby surface can reduce the mechanical quality factor and also modify the cantilever resonant frequency.

5.2.2.4 Sample holder

The sample holder stage used in the cantilever thermometry measurements and preliminary persistent current measurements consisted of a top plate and cylindrical bottom piece both machined out of brass. The sample holder stage used in the persistent current measurements consisted of a copper top plate, three brass¹³ rods, and a brass bottom plate screwed together in a fashion similar to that shown in Fig. 5.5 (see note in figure caption).

The fiber holder in each of its incarnations was screwed down to a stack of Attocube linear positioners (2 ANPx101/LT/HV and 1 ANPz101/LT/HV, Attocube systems AG, Munich, Germany).¹⁴ The Attocubes had ~ 6 mm of travel in each direction, allowing access to an entire sample chip, and a minimum step size of ~ 40 nm. For most of the persistent current measurements, the Attocubes were stacked with their central axis parallel to gravity, as indicated in panel B of Fig. 5.5. When the lens was incorporated into the fiber holder, an angled Attocube mount was also added to the sample stage so that the central axis of the Attocubes was parallel to the cantilevers as shown in Fig. 5.8. The Attocube wiring consisted of 0.005" copper wires from the top of the fridge down

¹¹To prevent accidental smudging of the lens with epoxy, we applied the epoxy with a bit of Kapton which we taped to thin wire which in turn was taped to a three-dimensional translation stage with micrometer screws (Ultra-align 561D, Newport Corporation, Irvine, CA, USA). The Kapton tip was used to prevent scratching of the lens coating and surface (which occurred with the wire tip). The wire tip was used to make the object touching the lens extremely pliable and unlikely to knock the lens out of its seat. The translation stage was used to steady the epoxy applicator. Different translation stages were used in different lens mounting attempts, and there were no stringent specification requirements on stage performance. The epoxy was applied while viewing the lens with a microscope.

¹²A higher reflectivity surface would boost the cantilever signal. We experimented with gold coated fibers (Evaporated Coatings, Inc., Willow Grove, PA, USA) but were not able to mount a coated fiber successfully because the fibers had been stripped too far prior to being coated and were very fragile as noted above. It is possible to obtain coated fibers with less stripped coating. Our fibers were stripped so far because we wanted to attempt to ground the coating to eliminate possible electrostatic effects between the fiber tip and the cantilever. These effects should not be a concern with the lens set-up.

¹³For some measurements, parts of the sample holder were machined from copper nickel rather than brass in order to increase material resistivity and reduce eddy current damping when ramping the magnetic field. No significant change was observed using the copper nickel components instead their brass counterparts.

¹⁴Early measurements were performed using an earlier generation of Attocube positioners (2 ANPx100/LT and 1 ANPz100/LT). At one point during the persistent current measurements, one of the ANPx101 models stopped working and one of the ANPx100 versions was used while it was repaired.

to the 4K plate at the top of the inner vacuum chamber, then heat-sunk superconducting twisted pairs down to a connector bracket on the sample stage, and finally short 32 AWG copper jumpers connected to the Attocubes. The Attocubes were operated with a controller created by Attocube (ANC150/3, Attocube systems AG, Munich, Germany).

Sample chips were held to a block of copper by means of a clip cut out of a beryllium-copper gasket (9-78D-A Finger stock gaskets, Leader Tech, Tampa, FL, USA), and epoxied to the copper block with Stycast[®] 2850 FT. The sample stage thermometer was glued into a hole drilled into the copper block. Thick (16 AWG) copper wires were silver soldered to the copper block and to a copper bobbin which was screwed down to top plate of the sample stage holder in order to ensure good thermal contact between the sample and the refrigerator. The copper block was the top layer of a stack that also included a 0.032" G-10 (Grade G-10/FR4 Garolite, McMaster-Carr, Elmhurst, IL, USA) spacer, a 0.5" diameter piezoelectric actuator (EDO, West Salt Lake City, UT, USA), and a 0.1" G-10 spacer. Each layer of this stack was glued together with Stycast[®] 2850 FT. The stack was screwed down to a sample tilt stage piece which provided the desired angle between cantilever and magnetic field. 32 AWG Copper wires were soldered to either side of the piezoelectric actuator and to the center pins of two SMA coaxial connectors. These connectors were connected to the refrigerator's UT-85-BSS semi-rigid coaxial lines via jumpers of flexible UT-085B-SS micro-coax (Janis, Wilmington, MA, USA) and 80 MHz low pass filters (VLFX-80, Mini-Circuits, Brooklyn, NY, USA). At the top of the refrigerator, these coaxial lines were connected to 1.9 MHz low pass filters (SLP-1.9+, Mini-Circuits, Brooklyn, NY, USA).

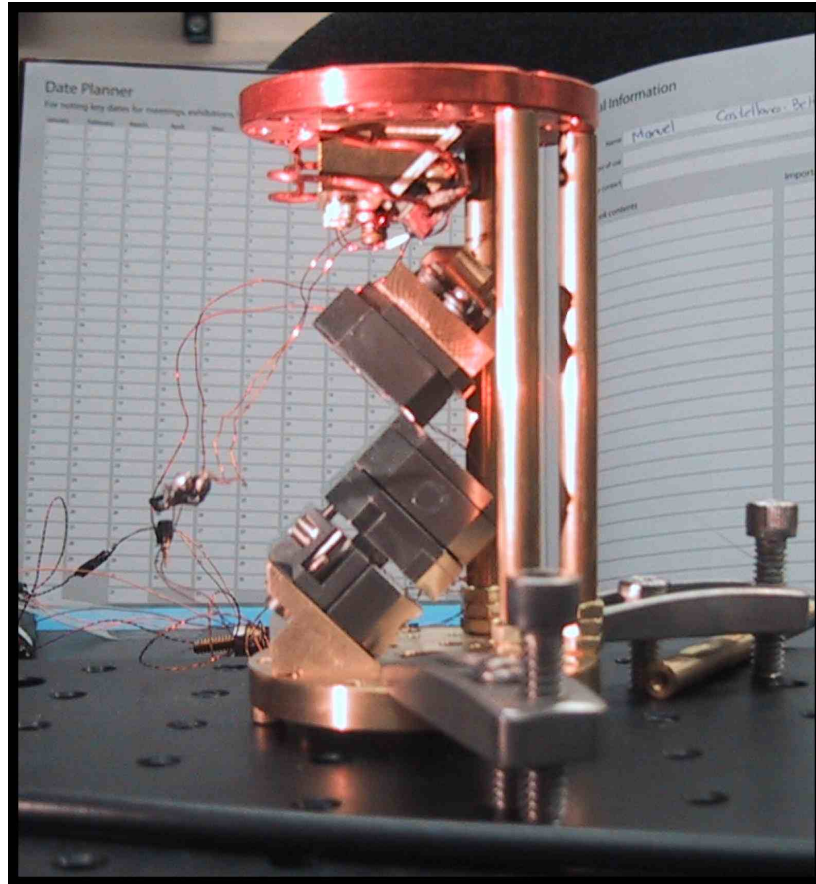


Figure 5.8: Persistent current sample holder stage photograph. The image shows the lens-mounted fiber holder seated on top of a set of three Attocube linear positioners. The Attocubes are mounted on a 45° tilt stage. The unusual stacking of the Attocubes is necessary for them to fit within the inner vacuum chamber while tilted at this angle. The 45° sample tilt stage is mounted to the copper top plate above the fiber holder. Insulating spacers, a piezoelectric actuator, and a copper block for mounting the cantilever (with thick heat sink leads) are mounted on the sample tilt stage. During measurement three posts were arranged symmetrically about the sample stage but were moved for the picture. The figure gives a representative depiction of the sample stage used during measurement with only a connector bracket used for interfacing the fridge wiring with the sample stage thermometer, piezo, and Attocubes missing.

5.2.2.5 Electronics

For measurements of the cantilever frequency, the arrangement of electronics was adopted from [270] as indicated in Fig. 5.6. The output of the signal photodiode (with 2011 internal filters set to 300 Hz and 30 kHz for most measurements) was fed into the input port of lock-in 1 (7265 DSP Lock-in Amplifier, AMETEK Advanced Measurement Technology, Oak Ridge, TN, USA). The signal monitor output of lock-in 1, the result of applying the lock-in's amplifier to the input signal, was then passed through low and high pass filters (SIM 965 Analog Filter, SIM900 Mainframe, Stanford Research Systems, Sunnyvale, CA, USA) set to $\sim \pm 10\%$ of the cantilever frequency and then into the input of lock-in 2 (identical to lock-in 1). The signal monitor of lock-in 2 was then connected to its own reference input. Lock-in 2's reference output, a square wave version of its reference input, was connected to lock-in 1's reference input. Both lock-ins were operated in external reference mode. The cantilever was driven in a phase-locked loop by connecting the oscillator output of lock-in 2 to the piezoelectric actuator on which the cantilever was mounted. The oscillator output phase was chosen to maximize the amplitude of motion of the cantilever. By setting lock-in 1 to measure the second harmonic of the input and lock-in 2 to measure the first harmonic, the magnitude and phase of the first two harmonics of the interferometer signal could be measured simultaneously.

The frequency of the cantilever was recorded in one of two ways. First, the reference output of lock-in 2 was fed into a frequency counter (Agilent 53132A 225 MHz Universal Counter with 012 US oven option, Agilent, Loveland, CO, USA). Second, the signal monitor output of lock-in 2 was fed into a data acquisition (DAQ) board (NI PCI-6251, National Instruments Corporation, Austin, TX, USA), which used the oven-stabilized clock of the frequency counter as its timebase. The digitized interferometer signal was then analyzed to determine its frequency. An early implementation of the analysis software fit the digitized signal to a sine wave and produced comparable results to the frequency counter. A less computationally intensive and more informative implementation took the Hilbert transform of the digitized signal in order to obtain a trace of phase versus time, which could be differentiated to give the real time frequency of the cantilever interferometer signal.

The analysis of the cantilever interferometer signal described above was performed using LabVIEW software (National Instruments Corporation, Austin, TX, USA), which was also used to record all the readings of all other electronic components of the experiment. Most other recordings of instrument readings were made via GPIB connections. The other quantities typically measured

in this way were the temperature readings of the various thermometers, the magnitude and phase of the input of both lock-in amplifiers, the magnetic field strength, the reference photodiode voltage (as measured by an Agilent 34410A 6¹/₂ Digit Multimeter, Agilent, Loveland, CO, USA), and the thermistor reading of the laser’s thermoelectric temperature controller (measured by an analog to digital input of one of the lock-in amplifiers). Additionally, LabVIEW routines controlled via GPIB the magnetic field strength, the lock-in amplifier’s oscillator output amplitude and phase, and the laser’s thermoelectric temperature controller setting.

5.2.3 Transport measurement set-up

Magnetoresistance measurements were performed on wires codeposited with the aluminum persistent current rings onto the sample chips whose fabrication was described in 5.1.2. The original magnetoresistance measurements of quasi-one dimensional aluminum wires at low temperature were performed in the lab of Daniel Prober at Yale University. In particular, the dissertations of Santhanam [275], Rooks [276], Wind [277], and Chandrasekhar [278] (as well as personal communication from Dan himself) were useful references.

All magnetoresistance measurements were performed using a four-point AC resistance bridge modeled after the one described in the dissertations of Rooks [276] and Chandrasekhar [278]. A diagram of the bridge circuit is shown in Fig. 5.10. The bridge was excited and measured by the 7265 Signal Recovery lock-in amplifier discussed in 5.2.2.5. In order to avoid ground loops between voltage excitation and the voltage measurement, a battery powered isolation amplifier (AD202JY Isolation Amplifier, Analog Devices, Inc., Norwood, MA, USA) was inserted between the lock-in’s voltage output and the bridge circuit. The bridge resistors were chosen to be well matched to a high tolerance and to have good thermal stability (Vishay Intertechnology, Inc., Malvern, PA, USA).¹⁵ Each bridge resistor had a bridge resistance $R_b = 47\text{k}\Omega$.¹⁶ The bridge resistors were soldered to a small scrap piece of circuit board which was screwed down to a large block of copper (approximately $1/2'' \times 1'' \times 2''$) and enclosed in an aluminum box to ensure thermal stability and to shield from stray electromagnetic radiation. The refrigerator’s coaxial lines were used for all transport measurements with 80 MHz filters just before the sample on the sample stage and

¹⁵I believe we used VSMP series resistors with a 0.01% tolerance and a 0.1 ppm/°C temperature coefficient, but I can not find the exact part number in my notes.

¹⁶This choice of bridge resistance was the result of following the thesis of Chandrasekhar a bit too closely. His samples had significantly smaller resistance than ours so that his sample resistance was negligible compared to the bridge resistance. Our sample resistance of around $R_s \sim 300\Omega$ was a bit less than 1% of R_b , but a bit higher bridge resistance of around $1\text{M}\Omega$ would have been more strongly into the limit of $R_s \ll R_b$.

1.9 MHz just outside the refrigerator (in an arrangement identical to that used for the connections to the piezoelectric actuator described in 5.2.2.5). The sample resistance R_s was balanced by a decade resistor (GenRad 1433-X Decade Resistor, General Radio Co., Concord, MA).

A photograph of the sample chip holder is shown in Fig. 5.9. The sample chip was mounted onto a patterned circuit board. The circuit board was a copper-coated dielectric onto which a circuit pattern of our design was printed and then etched away to create six leads and a ground plane.¹⁷ The sample itself was mounted with a cryogenic grease (Apiezon[®] N Cryogenic High Vacuum Grease, Manchester, UK) onto the ground plane, which was connected directly to the refrigerator via a 16 AWG gauge copper wire for heat sinking. The sample chip was then wire bonded to the leads on the circuit board.¹⁸ Each chip had several wire samples fabricated onto it and in principal four-point measurements of two wire samples could be performed in one cool down using the six coaxial leads of the refrigerator. Let A and B label the two bond pads on the same side of one wire sample and C and D label the two bond pads on the same side of a second wire sample. By connecting one coaxial lead to both A and C and another coaxial lead to B and D, these leads could serve a dual role in measuring the two wire samples. In practice, due to frequent lead blow outs on the sample chips, we only measured one chip (and that chip only had three leads available for that measurement as described below).

The circuit board leads were soldered to 32 AWG gauge copper wires which were all soldered into one single-in-line (SIP) connector for interfacing with the refrigerator wiring (all of the components connecting the sample to the refrigerator's coaxial lines are shown in Fig. 5.9 other than the micro-coax jumpers mentioned in 5.2.2.5). Additionally, another set of SIP connectors was soldered to directly to the circuit board leads. Another set of electrically connected SIP connectors could be plugged into the circuit board SIP connectors in order to ground the sample chip. This grounding plug was plugged in during the wire bonding step. It was only removed after the other set of leads had been connected to the fridge and then grounded (with the heat sink connector also connected to the refrigerator and the refrigerator itself tied to ground) in order avoid blowing out samples by electrostatic discharge. The leads emerging from the refrigerator were connected to a junction box. Inside the box, each lead was connected to a switch which controlled whether the lead was grounded or electrically connected to a connector on the other side of the box. When the sample

¹⁷We are indebted to the Devoret Lab, and Nicolas Bergeal in particular, for supplying us with the necessary materials and assistance to fabricate this board.

¹⁸We are indebted to the Devoret and Schoelkopf labs for the use of their wire bonder and for assistance in wire bonding.

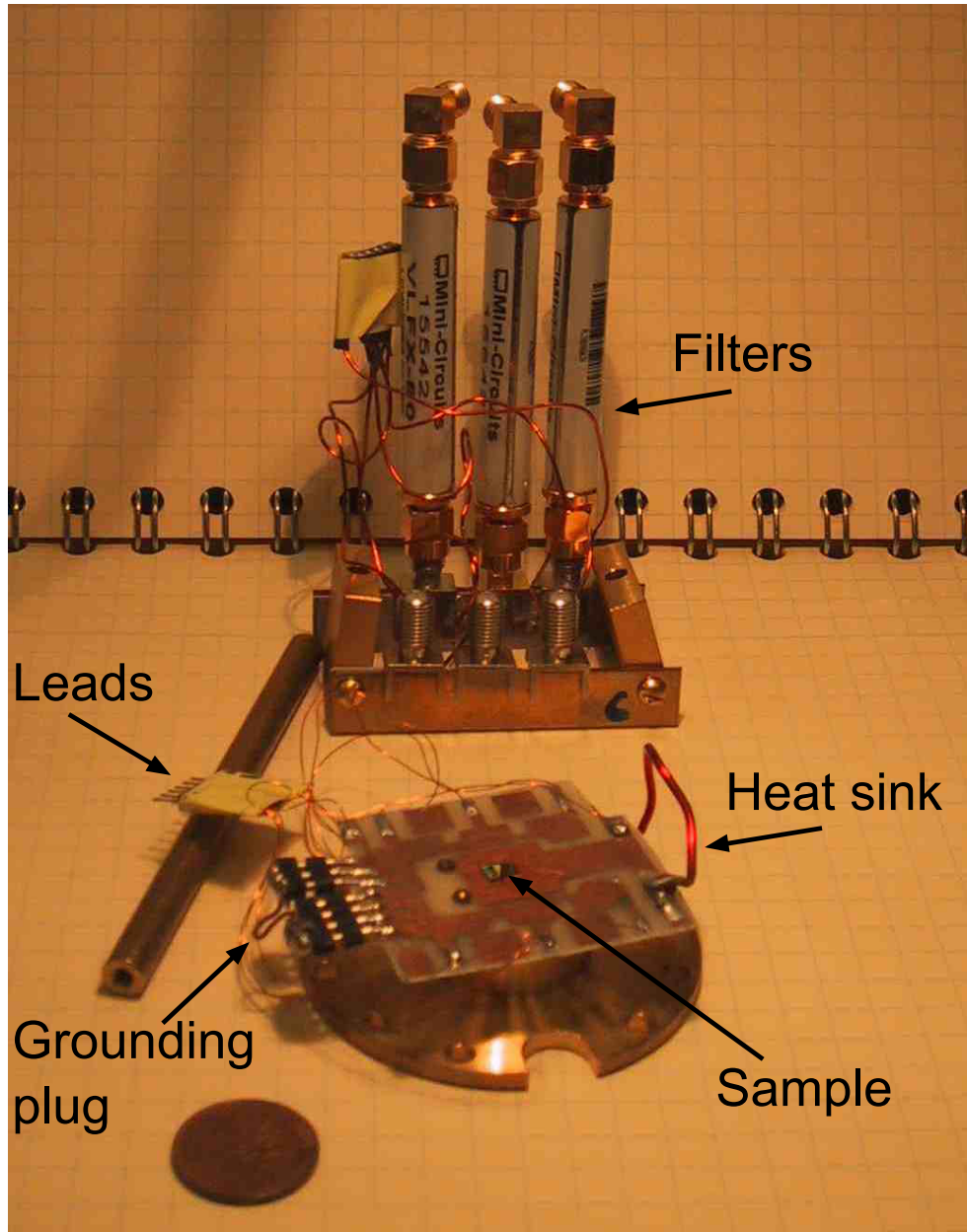


Figure 5.9: Transport measurement sample holder. The sample chip is indicated on top of the ground plane, which is electrically and thermally linked to the refrigerator by the 16 AWG gauge copper wire shown (the other end of the wire is soldered to a copper washer which is screwed down onto the refrigerator at a point below the 3-helium cold plate). Each pad on the sample chip is connected by a wire bond to one of the copper regions on the circuit board. Each of these copper regions is connected to two sets of SIP connectors (Series X518, Aries Electronics, Inc., Bristol, PA, USA), one on the circuit board (grounding plug) and one separated from the circuit board by 32 AWG gauge copper wire (leads). The circuit board is shown screwed down to a stub of brass machined so that it can be bolted to the top plate of the sample holder (not in figure). In the background of the figure, the low pass filters, which hang below the sample by brass rods like the one in the picture, can be seen, as well as the plug for the sample leads.

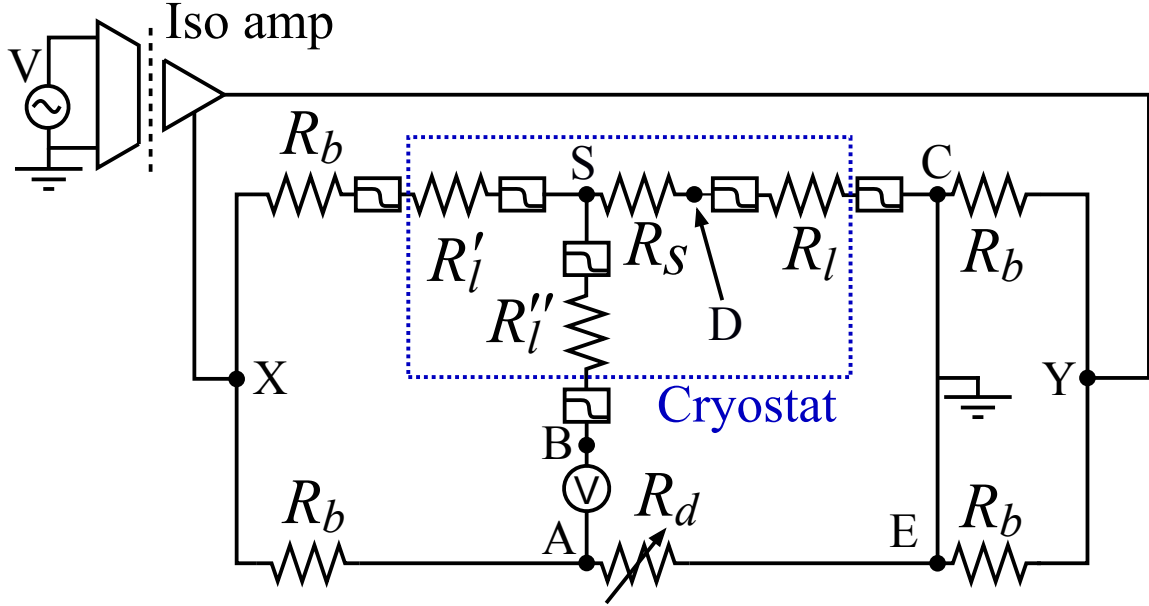


Figure 5.10: Circuit diagram of the four-point AC resistance bridge. The figure depicts a “three point” resistance bridge driven by a lock-in amplifier (V) through an isolation amplifier (Iso amp). The resistances for the bridge resistors (R_b), sample (R_s), decade (R_d), and sample leads (R_l and primed equivalents) are indicated. Additionally, all low-pass filters are indicated. The filters within the cryostat had a 3 dB point of 80 MHz, while that of those outside it was 1.9 MHz. Note that the resistances R_l really encompass the entire lead resistance on each side of these filters. The lock-in performed a differential measurement between the decade (A) and the sample (B). More discussion of the connections in the diagram is provided in the main text.

chip was first plugged into the refrigerator, all of these switches were set to ground. Whenever an external wire was connected to or disconnected from the sample, these switches were always set to ground first. Despite all of these precautions, many sample chips were blown out, and we ultimately settled on making a three lead measurement of a single sample.

We now step briefly through the circuit depicted in Fig. 5.10. An excitation voltage (V) is supplied by the lock-in amplifier to the isolation amplifier (Iso amp). In order to ensure accurate excitation voltages, a voltage divider (not shown) was often included between the lock-in and isolation amplifiers so that the lock-in output could be operated at a higher setting. The frequency of the excitation was typically around 200 Hz. The isolation amplifier output is split off into the two arms of the bridge (X) passing through two balanced bridge resistors R_b . The sample side of the bridge then goes through two low pass filters and the refrigerator and sample chip leads R'_l (indicated schematically between the filters, but in actuality distributed around both of them) before connecting to the sample (S). Another lead attached to the other wire bond pad on this same side of the sample (S, see Figs. D.3 and D.4) goes into the lock-in amplifier’s B input, while

the lock-in's A input is connected to the other side of the bridge. The other side of the sample (D) is then connected (again through filters and leads) to a bridge resistor (C). On the other side of the bridge, the bridge resistor is connected to the decade (A), which in turn connects to a fourth bridge resistor (E). These two bridge resistors on opposite sides of the decade and sample from X are then tied together at Y where they are also connected to the other side of the isolation amplifier. Additionally, the other sides of these two bridge resistors (C and E) were both tied to the lock-in's ground.

The circuit described in this way is really a “three-point” bridge. For a true four-point measurement, the sample-side connection to ground should really be at point D connected to the sample through a second sample bond pad lead (before the lead resistance R_l). In the experiment, this fourth lead was unintentionally blown out, so that only this three-point measurement arrangement was possible.

5.3 Calibrations and measurement procedures

5.3.1 Cantilever detection calibrations and measurement procedures

5.3.1.1 Model of the cantilever-fiber interferometer

We model the cantilever-fiber system as a Fabry-Perot interferometer in the limit of low finesse. A diagram of the interferometer is shown in Fig. 5.11. We call the distance from the point of reflection in the fiber (either the Bragg reflector or the cleaved fiber end) to the cantilever surface at equilibrium x_0 , and we call the cantilever displacement from equilibrium x_1 . We describe the incident laser light with a complex electric field amplitude $E_{\text{inc}} \exp(2\pi i x / \lambda)$ at point x where E_{inc} is the magnitude of the electric field amplitude of the incident light and λ is its wavelength.

At each interface, the light is partially reflected and partially transmitted. Additionally, there can be loss associated with the light propagation. With the materials involved, absorptive loss should be negligible. However, a large degree of loss is still possible due to misalignment of the optical components and due to the mismatch of the beam profile and the fiber core shape. We call the electric field amplitude reflection and transmission coefficients for the fiber r_f and t_f respectively and the cantilever reflection coefficient r_c (see e.g. Ref. [279] for a description of how to treat a series of dielectric surfaces as one optical unit characterized by its reflection and transmission coefficients). We denote by $p_{ft,n}$, $p_{fr,n}$, and $p_{cr,n}$ the additional reduction factors associated with the laser light

being transmitted into the fiber, reflected off of the fiber, and reflected off of the cantilever on the n^{th} trip. The index is necessary since these factors can be different after different numbers of round trips around the cavity (due to diffraction of the laser beam, for example).

As shown in Fig. 5.11, the ratio of the total light amplitude traveling back down the fiber away from the cantilever to the incident light amplitude, $E_{\text{cant}}/E_{\text{inc}}$, is found by summing the infinite series of successively higher numbers of reflections as

$$\begin{aligned} \frac{E_{\text{cant}}}{E_{\text{inc}}} = & r_f - t_f r_c p_{cr,1} t_f p_{ft,1} \exp\left(\frac{4\pi i(x_0 + x_1)}{\lambda}\right) \\ & - t_f r_c p_{cr,1} r_f p_{fr,1} r_c p_{cr,2} t_f p_{ft,2} \exp\left(\frac{8\pi i(x_0 + x_1)}{\lambda}\right) \\ & + \dots \end{aligned} \quad (5.1)$$

where the factors have been written sequentially. Ignoring common factors, the ratio of the third term to the second in Eq. 5.1 is $r_c r_f p_{cr,2} p_{ft,2} (p_{fr,1}/p_{ft,1})$.

The amplitude reflection coefficient r_f is typically around .2 for a bare fiber and .45 for the Bragg reflectors in our fibers, while the maximum possible value for the cantilever reflection coefficient r_c is .85.¹⁹ A typical value for $p_{cr,1} p_{ft,1}$ in either of our interferometer arrangements is .19, and the value of $p_{cr,2} p_{ft,2}$ should be smaller since misalignment and similar effects should be more pronounced for higher orders of reflections. The ratio $(p_{fr,1}/p_{ft,1})$ should be less than one since misalignment/mismatch effects should be more pronounced in reflection than transmission. Thus, we find that the ratio of magnitudes between the third and second terms in Eq. 5.1 has an upper bound of 0.07 and should in fact be less than this figure. We make the low finesse approximation by dropping all terms beyond the first two in Eq. 5.1 (all of which should be at least a factor of ~ 0.07 smaller), keeping only the first reflection off of the cantilever.

So far we have ignored the motion of the cantilever. When the cantilever moves, it tilts in addition to changing its linear position and thus changes the factor $p_{cr,1} p_{ft,1}$ which parametrizes the coupling of light from the cantilever back into the fiber. For small cantilever displacements, we can account for this ‘‘optical lever’’ effect by replacing $r_c p_{cr,1} p_{ft,1}$ by $r_c(1 - \epsilon x_1)$, where we have combined the loss factors into r_c for simplicity of notation. The factor ϵx_1 is typically small for the cantilever displacements used in the experiment. With these modifications, we obtain the simplified

¹⁹This value is obtained by using $n \approx 3.5$ for the refractive index of silicon [280] and treating the cantilever as an Fabry-Perot etalon of optimal thickness [281].

form for the amplitude E_{cant} of electric field returning from the cantilever,

$$\frac{E_{\text{cant}}}{E_{\text{inc}}} = r_f - t_f^2 r_c (1 - \epsilon x_1) \exp\left(\frac{4\pi i (x_0 + x_1)}{\lambda}\right).$$

We measure light intensity P_{cant} which is proportional to the square modulus of E_{cant} , satisfying

$$\frac{P_{\text{cant}}}{P_{\text{inc}}} = R_f + T_f^2 R_c (1 - 2\epsilon x_1) - 2T_f \sqrt{R_c R_f} (1 - \epsilon x_1) \cos\left(\frac{4\pi}{\lambda}(x_0 + x_1)\right) \quad (5.2)$$

to leading order in ϵ . In the previous equation we have introduced the power reflectivities given by the square of the amplitude coefficients, $R_f = r_f^2$, $T_f = t_f^2$, and $R_c = r_c^2$. When $x_0 \gg \lambda$ and x_1 is held constant, the cantilever interferometer signal P_{cant} should trace out a sinusoidal curve over small changes in λ . Our observations of a highly sinusoidal P_{cant} (not shown) as a function of wavelength justifies the use of the low finesse approximation.

Generally, in the experiment the cantilever signal is measured by a lock-in amplifier, which monitors a single frequency component. Therefore, a Fourier decomposition of the time dependence of P_{inc} is appropriate. The time dependence enters the expression for P_{inc} through the motion of the cantilever which we write as $x_1 = x_{f,\text{max}} \cos \omega t$ where $x_{f,\text{max}}$ is the amplitude of motion of the cantilever at the position z_f addressed by the optical fiber and ω is the angular frequency of the cantilever's oscillation. We obtain a harmonic decomposition by writing

$$\cos\left(\frac{4\pi}{\lambda}(x_0 + x_1)\right) = \cos\left(\frac{4\pi}{\lambda}x_0\right) \cos\left(\frac{4\pi}{\lambda}x_{f,\text{max}} \cos \omega t\right) - \sin\left(\frac{4\pi}{\lambda}x_0\right) \sin\left(\frac{4\pi}{\lambda}x_{f,\text{max}} \cos \omega t\right)$$

and applying the Jacobi-Anger identity given in Eqs. A.19 and A.20. The first three terms are

$$\begin{aligned} \left(\frac{P_{\text{cant}}}{P_{\text{inc}}}\right)_0 &= R_f + T_f^2 R_c - T_f \sqrt{R_f R_c} \cos\left(\frac{4\pi}{\lambda}x_0\right) J_0\left(\frac{4\pi}{\lambda}x_{f,\text{max}}\right) \\ &\quad + T_f \sqrt{R_f R_c} \sin\left(\frac{4\pi}{\lambda}x_0\right) \epsilon x_{f,\text{max}} J_1\left(\frac{4\pi}{\lambda}x_{f,\text{max}}\right) \end{aligned} \quad (5.3)$$

$$\begin{aligned} \left(\frac{P_{\text{cant}}}{P_{\text{inc}}}\right)_1 &= 4T_f \sqrt{R_f R_c} \sin\left(\frac{4\pi}{\lambda}x_0\right) J_1\left(\frac{4\pi}{\lambda}x_{f,\text{max}}\right) + 2T_f^2 R_c \epsilon x_{f,\text{max}} \\ &\quad + 2T_f \sqrt{R_f R_c} \cos\left(\frac{4\pi}{\lambda}x_0\right) \epsilon x_{f,\text{max}} \left(J_0\left(\frac{4\pi}{\lambda}x_{f,\text{max}}\right) - J_2\left(\frac{4\pi}{\lambda}x_{f,\text{max}}\right)\right) \end{aligned} \quad (5.4)$$

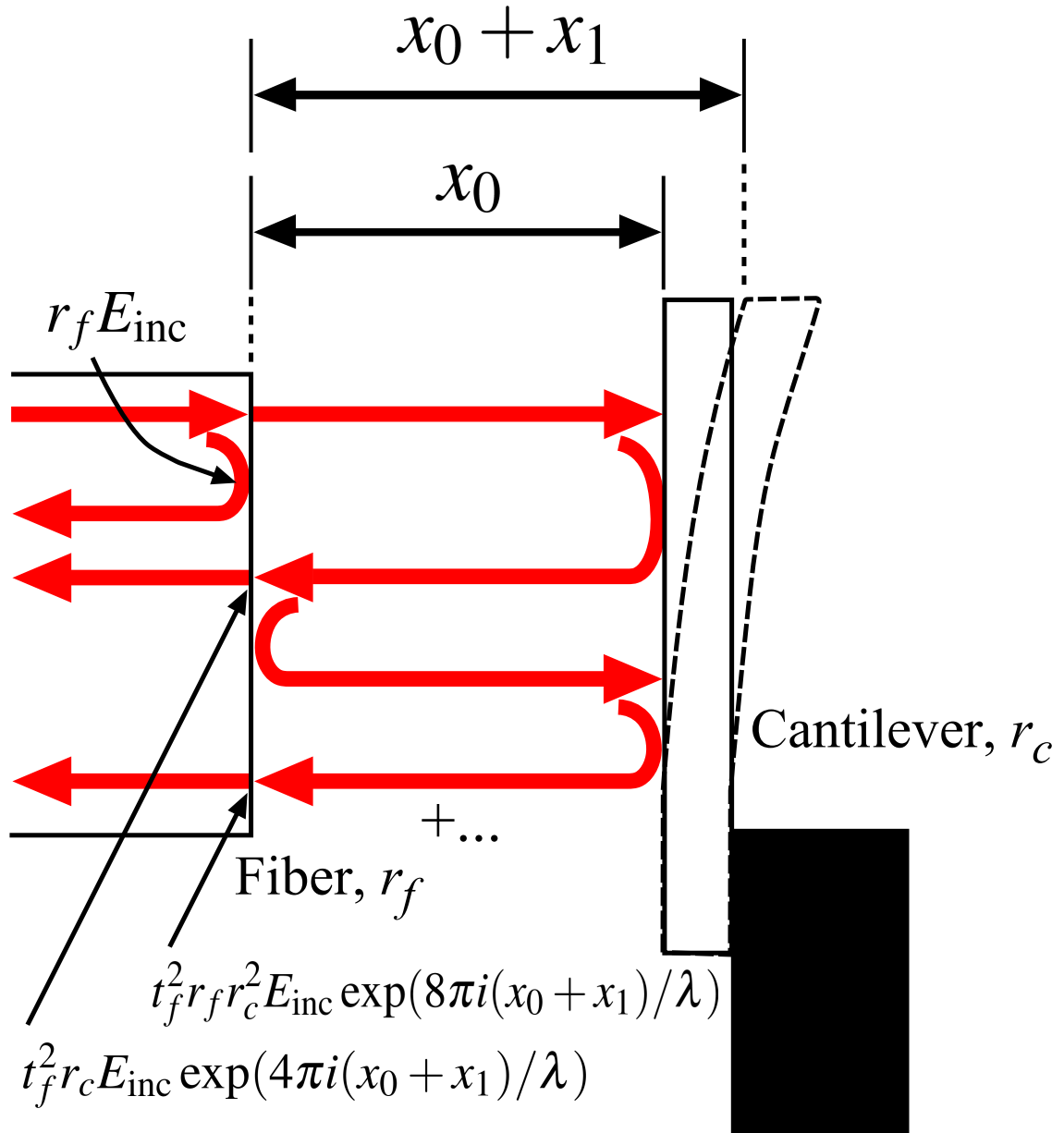


Figure 5.11: Cantilever-fiber interferometer diagram. The laser light with electric field amplitude E_{inc} enters the interferometer from the left and is partially reflected off the end of the fiber (or Bragg reflector) which has a reflection coefficient r_f . The rest of the laser light proceeds to the cantilever from which it is either reflected back to the fiber or transmitted through the cantilever and lost. The light reentering the fiber has amplitude $t_f^2 r_c E_{\text{inc}}$ and also picks up a phase factor given by 2π times the round trip cavity distance, $2(x_0 + x_1)$, divided by laser wavelength λ . Here x_0 is the cavity length with the cantilever at its equilibrium position and x_1 is the displacement of the cantilever from equilibrium. The second roundtrip of the light inside the cavity is also shown. On each trip, some amount of the light is transmitted through the cantilever (not shown). The loss factors discussed in the text are omitted from the figure for simplicity.

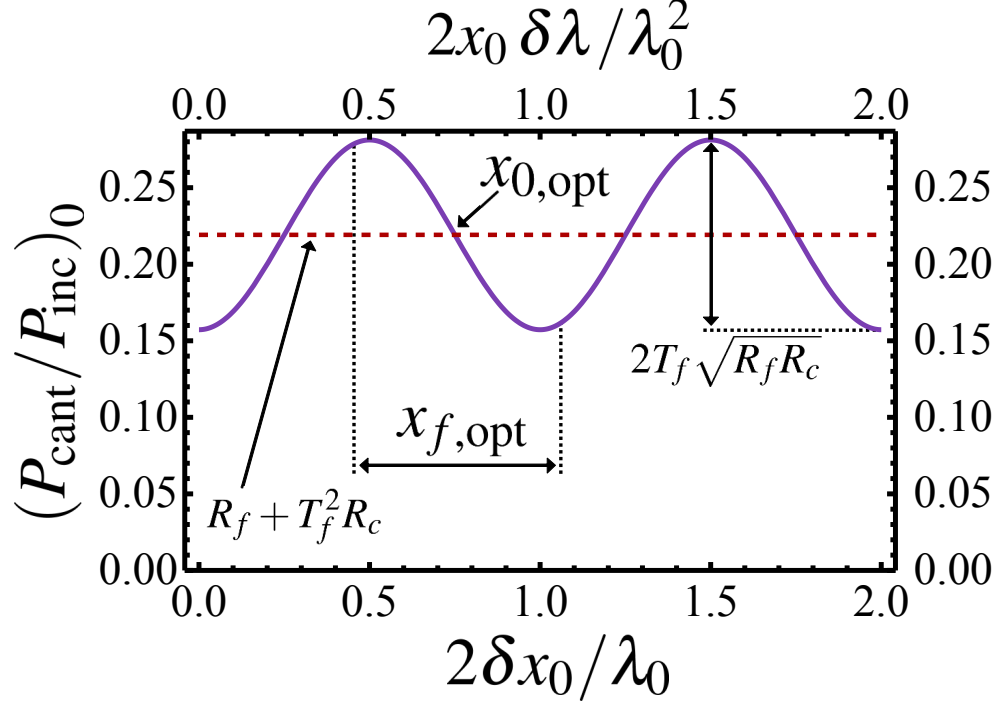


Figure 5.12: Fiber-cantilever interferometer fringe pattern. The figure plots Eq. 5.3 with $R_f = .2$, $T_f = .8$, $R_c = .03$, and $x_0 = 5300\lambda$. The horizontal axis is parametrized in two equivalent ways. On the bottom axis, the fringe pattern is measured in terms of a small detuning $\delta x_0 = x_0 - 5300\lambda$ away from a value of $x_0 = 5300\lambda$ that is an integral multiple of the fixed wavelength λ . On the top axis, the wavelength λ itself is detuned through the parameter $\delta\lambda = \lambda - x_0/5300$ for fixed cavity length x_0 . In the limit of $x_0/\lambda \gg 1$, these two parametrizations are equivalent when δx_0 and $\delta\lambda$ are scaled as indicated in the labels of these axes. Additionally, the figure indicates $x_{0,\text{opt}}$, the optimal fringe position where the first harmonic of the cantilever interferometer signal is maximal (assuming $\epsilon \sim 0$) as discussed in Section 5.3.1.2. The range $x_{f,\text{opt}} = 1.84\lambda/4\pi$ indicated in the figure depicts the peak-to-peak amplitude $2x_{f,\text{max}}$ of the cantilever oscillation, centered at the optimal fringe position $x_{0,\text{opt}}$, that maximizes the first harmonic signal of the interferometer (again for $\epsilon \sim 0$).

$$\begin{aligned} \left(\frac{P_{\text{cant}}}{P_{\text{inc}}}\right)_2 &= 4T_f \sqrt{R_f R_c} \cos\left(\frac{4\pi}{\lambda} x_0\right) J_2\left(\frac{4\pi}{\lambda} x_{f,\text{max}}\right) \\ &\quad - 2T_f \sqrt{R_f R_c} \sin\left(\frac{4\pi}{\lambda} x_0\right) \epsilon x_{f,\text{max}} \left(J_1\left(\frac{4\pi}{\lambda} x_{f,\text{max}}\right) - J_3\left(\frac{4\pi}{\lambda} x_{f,\text{max}}\right) \right) \end{aligned} \quad (5.5)$$

where we have expanded

$$\left(\frac{P_{\text{cant}}}{P_{\text{inc}}}\right) = \sum_n \left(\frac{P_{\text{cant}}}{P_{\text{inc}}}\right)_n \cos n\omega t. \quad (5.6)$$

For $x_0 = \lambda(n + 1/4)/2$ with n an integer, the first harmonic $(P_{\text{cant}})_1$ of the interferometer signal is proportional to $J_1(4\pi x_{f,\text{max}}/\lambda) + A x_{f,\text{max}}$ for A as given by Eq. 5.3 and is proportional to $x_{f,\text{max}}$ for $x_{f,\text{max}} \ll 0.14\lambda$. We refer to such a value of x_0 as an “optimal fringe position” of the interferometer.

5.3.1.2 Optimal interferometer fringe position and laser wavelength tuning

The constant value $(P_{\text{cant}}/P_{\text{inc}})_0$ of the cantilever interferometer signal when plotted as a function of wavelength λ or cavity length x_0 is known as the interferometer “fringe.” In Fig. 5.12, the interferometer fringe pattern is plotted for the case of $x_{f,\text{max}} = 0$ and typical interferometer parameters for the Bragg reflector set-up. In the limit $\epsilon \rightarrow 0$, the condition $x_0 = \lambda(n + 1/4)/2$ maximizes the first harmonic of the cantilever interferometer signal $(P_{\text{cant}}/P_{\text{inc}})_1$ and causes the second harmonic $(P_{\text{cant}}/P_{\text{inc}})_2$ to be zero. With both the Bragg reflector and the lens, the length of the interferometer was ~ 8 mm, so $x_0 \sim 5300\lambda$. In this case, the required change $\delta\lambda$ in wavelength necessary to change x_0/λ by $1/2$ (and so to move from optimal fringe position n to optimal fringe position $n \pm 1$) is given by

$$\begin{aligned} \frac{1}{2} &= \frac{x_0}{\lambda} - \frac{x_0}{\lambda + \delta\lambda} = \frac{x_0}{\lambda^2} \delta\lambda \\ \implies \delta\lambda &\approx .15 \text{ nm.} \end{aligned}$$

With the thermoelectric cooler, the wavelength of the JDS Uniphase laser was tunable between 1549 nm and 1554 nm. Thus the wavelength could be tuned to the optimal fringe position for any cantilever displacement x_0 .

With $\epsilon = 0$, the peak response of the first harmonic $(P_{\text{cant}}/P_{\text{inc}})_1$ of the cantilever interferometer signal occurs at the first peak of $J_1(4\pi x_{f,\text{max}}/\lambda)$ where $x_{f,\text{max}} \approx 1.84\lambda/4\pi \approx 227$ nm. Typical values of $x_{f,\text{max}}$ during persistent current measurements ranged from 10 nm to 227 nm, so that the arguments of each of the Bessel functions in Eqs. 5.3, 5.4, and 5.5 were below the locations of all of the Bessel functions’ non-trivial zeros (i.e. those for non-zero argument). For $\epsilon = 0$, the location on the interferometer “fringe” can be adjusted by tuning the laser wavelength to maximize the first harmonic of the interferometer signal either by tuning to the midpoint of the constant interferometer response value $(P_{\text{cant}}/P_{\text{inc}})_0$, tuning to the maximum of the first harmonic $(P_{\text{cant}}/P_{\text{inc}})_1$ directly, or tuning to the zero of the second harmonic $(P_{\text{cant}}/P_{\text{inc}})_2$. In practice, tuning to the zero of the second harmonic is the most practical because it can be measured more precisely (via a lock-in measurement) than the constant interferometer reading and provides feature more sensitive to laser wavelength than the first harmonic reading which varies only to second order about its maximum value.

The optical lever effect can modify the locations of the peaks and zeros of the various harmonics

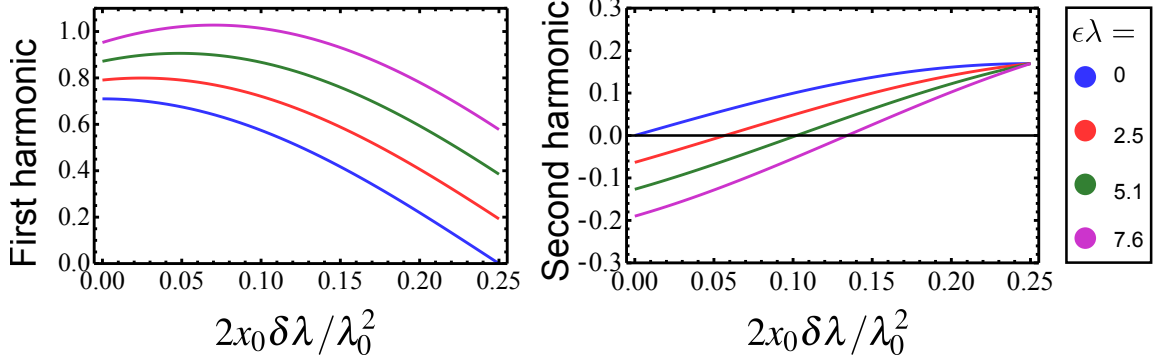


Figure 5.13: Effect of the optical lever term on the cantilever interferometer signal. The figure shows the first harmonic $(P_{\text{cant}}/P_{\text{inc}})_1$ and the second harmonic $(P_{\text{cant}}/P_{\text{inc}})_2$ of the cantilever interferometer signal as a function of wavelength $\delta\lambda = \lambda - \lambda_0$ for different values of the optical lever coefficient ϵ . The cavity length is set to $x_0 = (5300 + 1/4)\lambda_0/2$ and the amplitude $x_{f,\text{max}}$ of motion of the cantilever is set to $x_{f,\text{max}} = 1.84\lambda/8\pi$, half of the value giving the maximum response of the first harmonic in the absence of the optical lever effect. The two harmonics have been normalized by the maximum value of the first harmonic in the absence of the optical lever effect. For $\epsilon = 0$ and $\delta\lambda = 0$, the first harmonic is maximized while the second harmonic is zero. As ϵ increases, the location of both these conditions moves to the right. However, even for $\epsilon\lambda = 7.6$, the first harmonic is still within 10% of its maximum at the zero of the second harmonic

of the cantilever interferometer signal. Typical values for the optical lever coefficient ϵ ($\epsilon\lambda$) were $4.1 \times 10^{-5} \text{ nm}^{-1}$ (0.064) and $4.9 \times 10^{-3} \text{ nm}^{-1}$ (7.6) for the Bragg reflector and lens set-ups respectively. The larger optical lever effect for the lens set-up is due to the much longer lever arm. The fiber to cantilever distance was only $\sim 100 \mu\text{m}$ for the Bragg reflector set-up whereas it was closer to 8 mm for the lens set-up. However, the optical lever effect tends to shift the maximum of the first harmonic and the zero of the second harmonic of the cantilever interferometer signal in the same way as seen in Fig. 5.13 where we plot $(P_{\text{cant}}/P_{\text{inc}})_1$ and $(P_{\text{cant}}/P_{\text{inc}})_2$ as functions of λ for various values of ϵ and for values of other parameters similar to those of the experimental conditions. The location of the zero of the second harmonic of the interferometer signal is nearly insensitive to cantilever amplitude $x_{f,\text{max}}$ for the experimentally relevant range of drives. Thus, the zero of the second harmonic provides a stable reference point for the wavelength that is close to the maximum response of the first harmonic. We note that for the Bragg reflector case the zero of the second harmonic is less than 1% away from its value in the absence of the optical lever effect. For large ϵ , it may be necessary to characterize the difference between operating the system with λ chosen to maximize the first harmonic and with λ chosen to minimize the second harmonic. In order to use the second harmonic to stabilize the fringe position at a value that provides a large first harmonic response, the second harmonic would need to be tuned to a non-zero value.

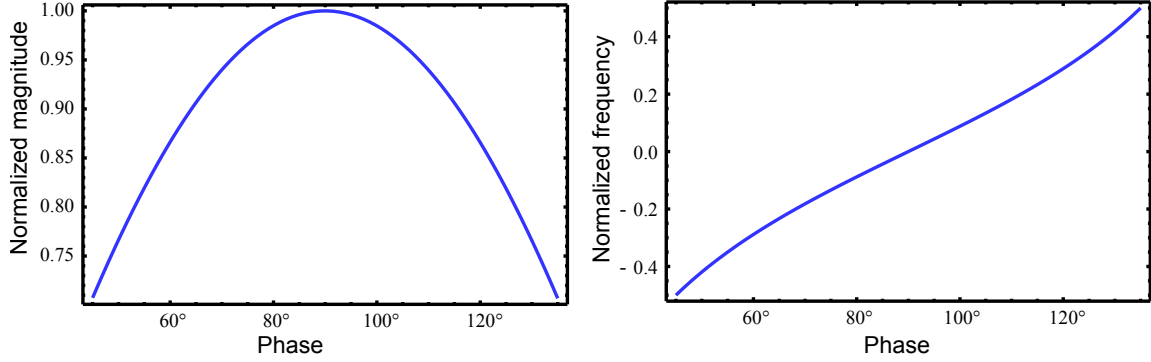


Figure 5.14: Normalized magnitude and frequency response of a simple harmonic oscillator. The magnitude and frequency of a damped, driven simple harmonic oscillator are plotted as a function of the phase difference between the oscillator’s motion and the driving signal. The magnitude has been normalized so that it is unity on resonance. The normalized frequency $Q \frac{\omega - \omega_0}{\omega_0}$ represents the difference between the oscillator’s frequency ω and the resonant frequency ω_0 multiplied by the oscillator’s quality factor Q and divided by the resonant frequency. The phase ϕ is found by writing the transfer function given in Eq. 4.9 as $G(\omega) = |G(\omega)| \exp(i\phi)$ and solving for ϕ .

5.3.1.3 Determination of resonant phase for the cantilever drive signal

For the cantilever frequency measurements, the cantilever was driven in a phase-locked loop using the arrangement described in 5.2.2. In this set-up, a lock-in amplifier drives the cantilever while in external mode using the cantilever interferometer signal as its reference. In this mode, the lock-in maintains a fixed phase between its reference and the cantilever drive signal, effectively adjusting its output frequency to do so. On resonance, a simple harmonic oscillator’s motion is 90° out of phase with its drive as shown in Fig. 5.14. However, due to extra phase shifts from the leads, filters, and amplifiers in the phase-locked loop, the reference phase of the lock-in required to drive the cantilever on resonance often differs from 90° .

In order to find the resonant phase, the magnitude of the first harmonic of the cantilever interferometer signal was measured while the lock-in’s reference phase was scanned. The cantilever was driven sufficiently weakly that the first harmonic of the interferometer signal was nearly proportional to the cantilever displacement as mentioned at the end of 5.3.1.1. In this case, the magnitude of the first harmonic of the cantilever interferometer signal traces out a curve similar to the one shown in Fig. 5.14. The measured magnitude can be fit to the expected oscillator response function to determine the resonant phase. In practice, it is sufficient to determine the resonant phase by eye from a measured phase scan. Because the frequency of the simple harmonic oscillator as a function of phase is linear over tens of degrees (Fig. 5.14), the phase-locked loop is relatively insensitive to the choice of the reference phase.

5.3.1.4 Calibration of the cantilever drive and interferometer signal

The amount of displacement per voltage V_{piezo} applied to the piezoelectric actuator can be difficult to calibrate. Even when this calibration is known, it is not straightforward to model the coupling of this motion to the motion of a cantilever sitting on top of the piezo. In principal, the interferometer signal could be converted into a displacement from knowledge of the incident laser power and wavelength and the relevant reflection and transmission coefficients. However, the optical lever term complicates the conversion of this signal into cantilever amplitude. The difficulties associated with calibrating both the interferometer signal and the piezo voltage in units of cantilever amplitude can be overcome by performing a cantilever amplitude scan.

An amplitude scan is taken, for an experimental arrangement like the one shown in Fig. 5.6, by measuring the value of the first harmonic of the cantilever interferometer signal at a series of drive voltages to the piezo. The drive frequency must be the cantilever's resonant frequency. If the cantilever frequency drifts significantly over time or has an amplitude dependence, the amplitude scan must be performed with the lock-in maintaining a phase-locked loop (which requires the resonant phase to be shifted by 180° when the interferometer signal changes sign, a complication that can be avoided by using the lock-in's internal reference when the cantilever frequency is constant as a function of time and amplitude). Before the scan begins, the laser wavelength must be tuned to the optimal fringe position as described in 5.3.1.2 (or adjusting the constant value of the interferometer signal to its midpoint).

With the conditions described in the previous paragraph, the lock-in first harmonic magnitude V_1 can be fit to a function of the form

$$V_1 = \frac{V_{1,\max}}{0.582} \left| J_1 \left(1.841 \frac{V_{\text{piezo}}}{V_{\text{peak}}} \right) + \epsilon_V V_{\text{piezo}} \right| \quad (5.7)$$

where, in the absence of the optical lever effect (i.e. for $\epsilon = 0$), $V_{1,\max}$ is the maximum value of V_1 and V_{peak} the value of V_{piezo} corresponding to that maximum (0.582 and 1.841 are approximations for the magnitude and location of the first peak of J_1). Here we assume that the piezo motion and consequently the cantilever motion are proportional to V_{piezo} . By comparison with Eq. 5.4, we can write the calibration of the piezo drive as

$$\frac{x_{f,\max}}{V_{\text{piezo}}} = \frac{1.841\lambda}{4\pi V_{\text{peak}}}$$

and the calibration of the lock-in magnitude at small cantilever amplitudes as

$$\left. \frac{dV_1}{dx_{f,\max}} \right|_{x_{f,\max}=0} = \frac{2\pi V_0}{.582\lambda} \left(1 + \frac{2\epsilon_V V_{\text{peak}}}{1.841} \right).$$

The ratio $x_{f,\max}/V_{\text{piezo}}$ allows the calculation of the cantilever amplitude $x_{f,\max}$ from the voltage drive to the piezo. The cantilever amplitude can also be calculated from the measured value of V_1 using

$$V_1 = \frac{V_{1,\max}}{0.582} \left| J_1 \left(\frac{4\pi x_{f,\max}}{\lambda} \right) + \frac{4\pi\epsilon_V V_{\text{peak}} x_{f,\max}}{1.841\lambda} \right|$$

without reference to the piezo driving voltage. This method is useful when the ratio $x_{f,\max}/V_{\text{piezo}}$ is not reliably constant (such as when the cantilever quality factor is drifting in time). The quantity $dV_1/dx_{f,\max}|_{x_{f,\max}=0}$ allows for the lock-in voltage V_1 to be converted into displacement $x_{f,\max}$ when the cantilever amplitude is very small ($x_{f,\max} \ll \lambda/2\pi$ so that $V_1 \propto x_{f,\max}$), as is the case during measurements of the Brownian motion of an undriven cantilever (see Chapter 6). Assuming the distance z_f of the laser spot from the cantilever base is known, all of the calibrations can be expressed in terms of the motion of the cantilever tip x_{\max} by using $x_{\max} = x_{f,\max}/U_m(z_f/l)$ with U_m as given by Eq. 4.1. We can write the conversion factor $\Gamma_{V \text{ to } x}$ from the lock-in reading V_1 to x_{\max} (valid for $x_{f,\max} \ll \lambda/2\pi$) as

$$\Gamma_{V \text{ to } x} = \left(U_m(z_f/l) \left. \frac{dV_1}{dx_f} \right|_{x_{f,\max}=0} \right)^{-1} \quad (5.8)$$

and the conversion factor g_{piezo} from piezo voltage V_{piezo} to x_{\max} as

$$g_{\text{piezo}} \equiv \frac{x_{\max}}{V_{\text{piezo}}} = \frac{1.841\lambda}{4\pi V_{\text{peak}}} \frac{1}{U_m(z_f/l)}. \quad (5.9)$$

The optical lever coefficient ϵ is given by

$$\epsilon = \frac{8\pi V_{\text{peak}} \epsilon_V}{1.841\lambda T_f \sqrt{R_c/R_f}}.$$

A typical amplitude scan and fit are shown in Fig. 5.15.

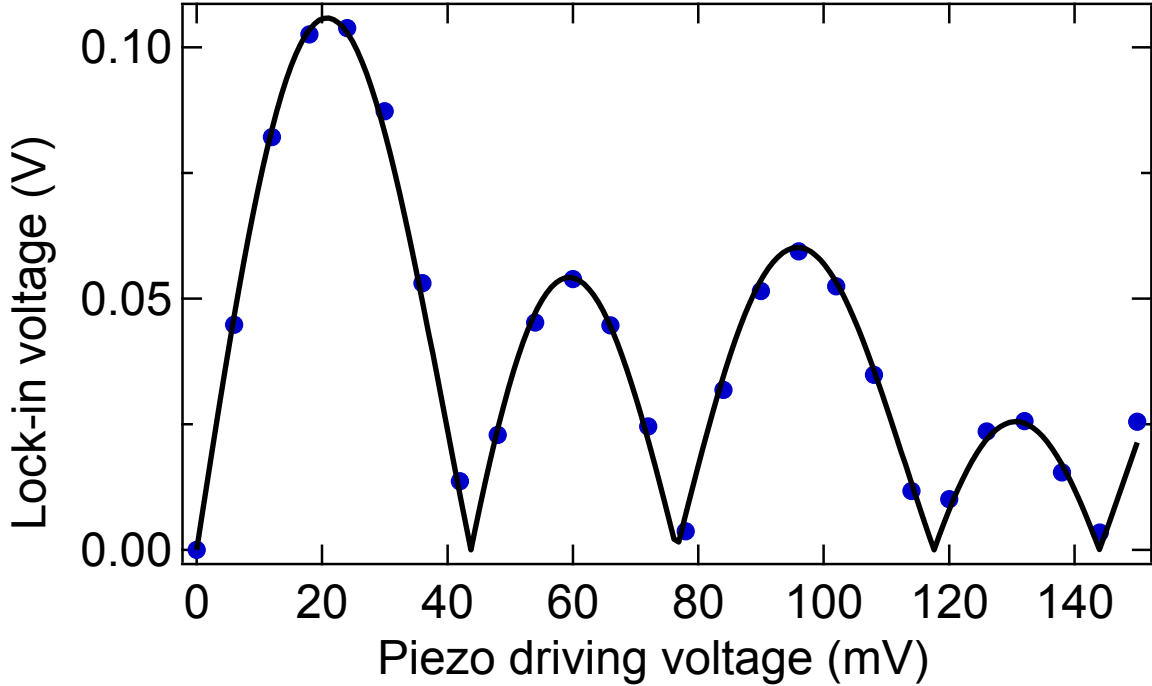


Figure 5.15: Cantilever first harmonic signal as measured by the lock-in as a function of piezo driving voltage. The figure shows the first harmonic V_1 of the cantilever interferometer signal as measured by the lock-in as a function of piezo driving voltage V_{piezo} as well as a fit to Eq. 5.7. The extracted fit coefficients are $V_{1,\text{max}} = 0.10$ V, $V_{\text{peak}} = 20.6$ mV, and $\epsilon_V = 1.17 \times 10^{-6} \text{ V}^{-1}$. This amplitude scan was taken with the cantilever shown in Fig. 5.1 and was used to calibrate the Brownian motion measurements discussed in 6.4.1.

5.3.1.5 Cantilever measurement procedure

We now give a brief step by step summary of the operations necessary to go from new cantilever samples to persistent current (or aluminum grain thermometry) measurements.

1. Preliminary steps at room temperature.
 - (a) Arrange all optical and electronic components as in Fig. 5.2.2.
 - (b) Mount new sample chip.
 - (c) Position fiber holder so that the laser is shining on a cantilever at room temperature with a fiber to cantilever distance at least $500 \mu\text{m}$ to allow for drift during the cool down (for the lens set up, the lens should be positioned so that the laser spot is focused on a cantilever).
 - (d) Cool down refrigerator.
2. Reposition the fiber holder.

- (a) Scan the fiber holder laterally to move the laser spot onto a cantilever if it drifted off during the cool down.
- (b) Calibrate the step size in nanometers of the Attocube that moves the fiber closer to and further away from the sample chip. This can be done by monitoring the position on the interferometer fringe over the course of many steps. The constant interferometer power or the magnitude of the first harmonic response to shaking of the Attocube itself can be monitored and fit to $P \sin(4\pi N dz/\lambda + \phi)$ where N is the number of Attocube steps and dz is displacement per step (and P and ϕ are the other fit parameters besides dz).
- (c) Adjust the fiber to cantilever distance. With a cleaved fiber tip, this adjustment is made by carefully moving the fiber towards the cantilever until it just touches (indicated by the abrupt absence of cantilever motion in the interferometer signal) and then retracting the fiber tip by the desired amount. With the lens, the lens to cantilever distance is adjusted to locate the point of maximum reflected power and maximum depth of modulation of the reflected power when the wavelength is tuned.
- (d) Determine laser spot position on the sample chip, and move to the desired cantilever. Identification of chip position is usually determined by scanning the laser spot laterally until the chip window is located. The chip window is distinguished by being much wider than the cantilevers and shaking less (as observed by the interferometer signal). Then the laser spot is scanned back to the desired cantilever. The individual cantilevers are easily distinguished from empty space by their modulation of the interferometer signal.
- (e) Calibrate the step size of the Attocubes which move parallel to the sample chip. This calibration is performed by noting the number of steps required to move between two points separated by a known distance. Typically, the number of steps required to move between two adjacent cantilevers can be used for the direction perpendicular to the cantilever beams, and the number of steps required to move from the cantilever tip to the base (by moving to the tip, moving just off to the side of the cantilever, and then moving back towards the base until it appears again in the interferometer signal) is used for the direction parallel to the cantilever beams.
- (f) Position the laser spot at a known distance z_f from the base of the cantilever.

3. Calibrate and characterize cantilever motion.

- (a) Determine the resonant phase for the piezo driving voltage by performing a phase scan as described in 5.3.1.3.
 - (b) Tune the laser wavelength to the optimal fringe position as described in 5.3.1.2 and perform an amplitude scan as described in 5.3.1.4 to find the relationship between piezo drive voltage and cantilever tip motion and between lock-in magnitude and cantilever tip motion.
 - (c) Characterize the cantilever signal noise.
 - i. Determine the cantilever quality factor Q from cantilever ringdown measurements. The cantilever ringdown measurement procedure consists of exciting the cantilever, setting the piezo driving voltage to zero, and measuring the first harmonic of the cantilever interferometer signal as a function of time. The portion of the signal corresponding to $x_{f,\max} \ll \lambda/2\pi$ (where the interferometer signal is proportional to the cantilever motion) can then be fit to Eq. 4.10 for Q .
 - ii. Measure the power spectral density of the undriven cantilever's motion. If this motion is larger than the thermal limit (Brownian motion), external vibrations or heating may be contributing appreciably to the motion of the cantilever.
 - iii. Measure the power spectral density of the driven cantilever's frequency (by using the Hilbert transform method of frequency measurement) at various cantilever excitation amplitudes. This measurement allows one to detect contributions to the uncertainty in the frequency measurement beyond the unavoidable thermal contribution and to determine the optimal conditions for the frequency measurement.
4. Measure the cantilever frequency as a function of magnetic field
- (a) Drive the cantilever in a phase-locked loop at the desired amplitude (often chosen to give a certain amplitude of flux ϕ_a through the ring as discussed in 4.4; alternatively chosen to minimize uncertainty in the frequency measurement for the case of cantilevers which show increasing frequency noise with amplitude).
 - (b) Make a series of measurements at constant magnetic field of the cantilever frequency and any other parameters to be recorded.
 - (c) Ramp the magnetic field by the desired magnetic field step.

- i. While the magnetic field is ramped, a PID feedback loop is run in LabVIEW to minimize the second harmonic of the cantilever interferometer signal by tuning the laser wavelength via the thermoelectric temperature controller. This feedback loop corrects for any shift in the interferometer length x_0 due to tilting of the sample stage with magnetic field.
 - ii. At the end of the magnetic field ramp, after the laser wavelength has been tuned to the optimal fringe position, another PID feedback loop can be run by LabVIEW to set the first harmonic of the cantilever interferometer signal to the desired set point by adjusting the piezo driving voltage. This feedback loop corrects for any change in the calibration of the piezo driving voltage in units of cantilever amplitude which can occur if, for example, the cantilever quality factor or phase-locked loop resonant phase changes with time or magnetic field. Because the piezo drive should not change much in time or with magnetic field and because each adjustment to the piezo driving voltage must be given a cantilever ringdown time to take full effect, this feedback loop was not usually run at each magnetic field point and was instead run when the first harmonic of the cantilever interferometer signal moved outside of a specified tolerance window.
- (d) Steps 4b and 4c are repeated over the desired field range. In order to counteract low frequency noise due to drift in the cantilever frequency as a function of time, the number of measurements of the cantilever frequency made at any one magnetic field value is usually kept to a small number so that whole field range can be swept over several times. These sweeps can then be averaged together.

5.3.2 Transport calibrations and measurement procedures

5.3.2.1 Mathematical relations for the resistance bridge

In the magnetoresistance measurements, the lock-in is used to measure the difference V_{AB} between the voltage dropped across the sample (plus a lead) V_{ss} and that dropped across the decade resistor V_{ds} . In Fig. 5.10, V_{ss} (“sample side”) and V_{ds} (“decade side”) are, respectively, the voltages from points B and A to ground. We can write these voltages by using Ohm’s law. If we call the voltage across the entire bridge V_{XY} (dropped between points X and Y in Fig. 5.10), the sample side current I_{ss} and decade side current I_{ds} satisfy $I_{ss} = V_{XY}/(2R_b + R_l + R'_l + R_s)$ and $I_{ds} = V_{XY}/(2R_b + R_d)$,

respectively. The voltage measured by the lock-in is then

$$\begin{aligned} V_{AB} &= I_{ss}(R_s + R_l) - I_{ds}R_d \\ &= V_{XY} \left(\frac{R_s + R_l}{2R_b + R_l + R'_l + R_s} - \frac{R_d}{2R_b + R_d} \right). \end{aligned} \quad (5.10)$$

In the experiment, the voltage V_{AB} is measured while the sample resistance R_s is varied by sweeping the magnetic field. If we write the sample resistance as $R_s = R_{s0} + \delta R_s$ where R_{s0} is the sample resistance at zero magnetic field, we can invert the change in voltage $\delta V_{AB} = V_{AB}(R_{s0} + \delta R_s) - V(R_{s0})$ to find the change in resistance δR_s as

$$\delta R_s = \left(\frac{\delta V_{AB}}{V_{XY}} \right) \frac{(2R_b + R_l + R'_l)^2}{2R_b + R_l - (\delta V_{AB}/V_{XY})(2R_b + R_l + R'_l)}. \quad (5.11)$$

Typical values for the difference resistances in bridge were $R_b = 4.7 \times 10^4 \Omega$, $R_l, R'_l = 30 \Omega$, and $R_s = 300 \Omega$. In the limit of $R_b \gg R_l, R'_l, R_s$, Eq. 5.11 becomes

$$\delta R_s \approx 2R_b \frac{\delta V_{AB}}{V_{XY}}. \quad (5.12)$$

5.3.2.2 Calibration of the applied voltage V_{XY}

The output of the isolation amplifier used in the bridge circuit did not have unity gain. In fact, the gain factor of its output to its input was observed to drift slowly over time, possibly due to the fact it was powered by batteries in order to minimize its output noise. To calibrate the output of the isolation amplifier, “decade scans” were taken each day.

A decade scan consisted of measuring the sample-decade voltage difference V_{AB} at a series of values of the decade resistance R_d . Typically, R_d was stepped up from the value used for the magnetoresistance measurements over a range of about 30Ω . The measured values of V_{AB} were then fit to Eq. 5.10 in the form

$$V_{AB} = V_{XY} \left(w_{\text{offset}} - \frac{R_d}{2R_b + R_d} \right)$$

for V_{XY} and w_{offset} using the known value of R_b . This fitted value for V_{XY} was then used with Eq. 5.11 (or Eq. 5.12) to find δR_s for the magnetic field sweeps. The data from one decade scan along with the corresponding fit are shown in Fig. 5.16.

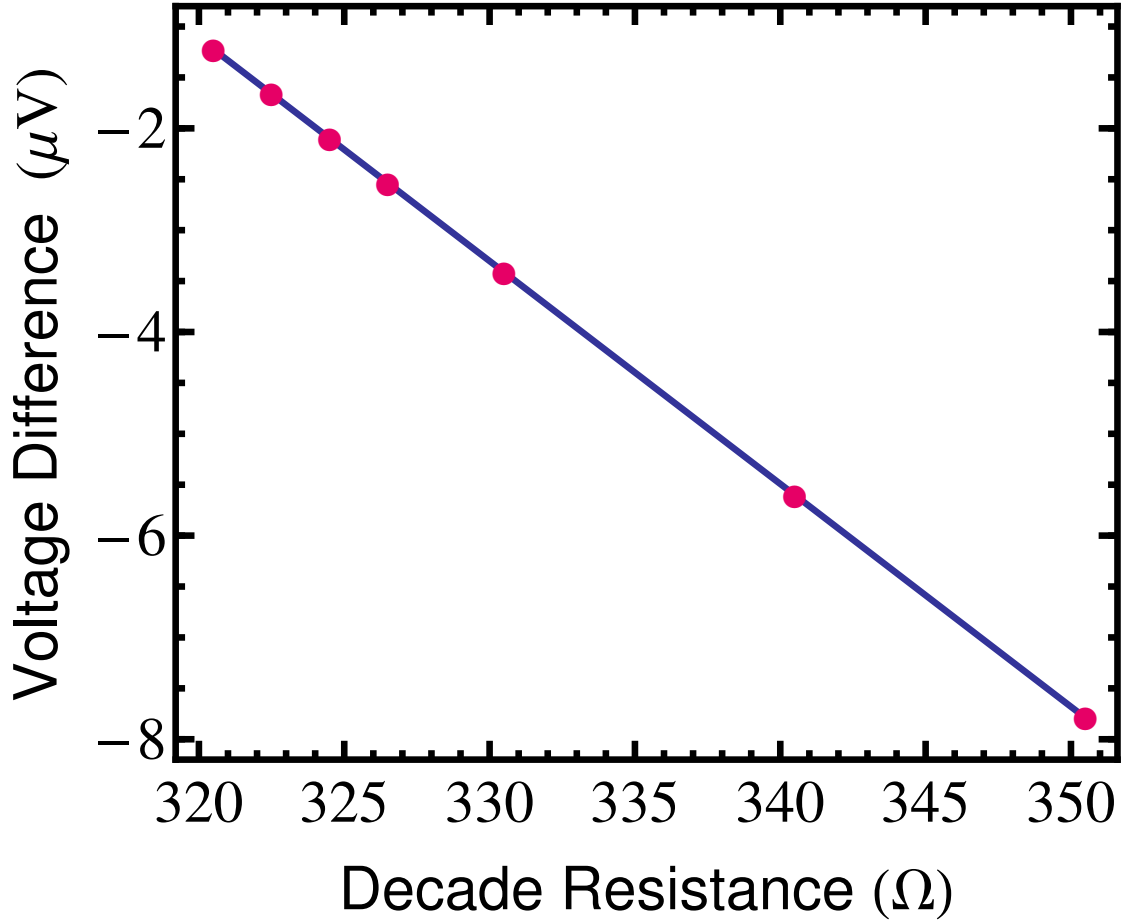


Figure 5.16: Example of a decade resistance scan. The voltage difference V_{AB} is plotted against the decade resistance R_d along with a fit. For this particular scan, the bridge voltage V_{XY} was -20.7 mV and the factor w_{offset} was -3.34×10^{-3} .

5.3.2.3 Determination of lead resistances R_l and R'_l

Since a three-point rather than a four-point measurement was used, it was helpful to determine the resistances of the leads attached to either side of the sample labeled R_l and R'_l in Fig. 5.10 (though to a good approximation they could be ignored when finding δR_s since $R_b \gg R_l, R'_l$). The lead resistance R_l was found by noting the resistance of the decade necessary to null out V_{AB} while the sample was in the superconducting state. The resistance R'_l could then be determined by measuring the resistance through R'_l , R_s , and R_l while the sample was superconducting and subtracting the known value for R_l . The resistance of the sample can also be inferred by measuring its superconducting transition and using the inferred values for R_l and R'_l and solving Eq. 5.10 for

R_s . The value of both lead resistances was about $34 \pm 5 \Omega$ (where the imprecision is due to the uncertainty in determining the end of the superconducting transition in Fig. E.1).

5.3.2.4 Magnetoresistance measurement procedure

We now give a brief outline of the steps for mounting and measuring a transport sample.

1. Mount a sample chip (for details regarding the elements discussed in all of these steps see 5.2.3)
 - (a) The guiding principle behind the following steps is that an unknown voltage should never be connected to the sample. The sample and any connectors should always be grounded before making a new connection in order to avoid a blow out.
 - (b) Wire bond the sample. During part of the wire bonding process, the sample may be ungrounded in order to measure its resistance and verify that the wire bonding was successful. The end result though should be that the sample is bonded to the circuit board with the grounding plug in place.
 - (c) Mount the sample chip holder onto the refrigerator.
 - (d) Connect the sample chip holder leads to the refrigerator leads and connect the heat sink/ground plane to the refrigerator.
 - (e) Connect the leads coming out of the refrigerator to the junction box and set all of the junction box switches to ground.
 - (f) Remove grounding plug from sample chip holder.
 - (g) Cool down the refrigerator.
 - (h) Connect external electronics. Always ground the leads to the sample (with the junction box switches) before changing external electronics connections or settings.
2. Measure Magnetoresistance
 - (a) Perform a decade scan to calibrate the applied bridge voltage V_{XY} (see 5.3.2.2).
 - (b) Set the decade resistance to null out V_{AB} .
 - i. When a four-point measurement is used, this decade setting gives the sample resistance R_s . If only a three-point measurement is possible, determine the lead resistances as described in 5.3.2.3.

ii. Due to stray capacitance in the leads, it is not possible to completely null out V_{AB} because tuning the decade resistance only adjusts the real part of the bridge impedance. The following approaches can be employed to minimize the effect of the stray capacitance on the measurement:

A. Theoretically, it is possible to null out the difference in capacitance between the two sides of the bridge using a variable capacitor. We never attempted to do this in our measurements.

B. Alternatively, the reference phase of the lock-in can be adjusted so that the lock-in's X quadrature voltage is entirely due to resistance offsets in the two sides of the bridge and the Y quadrature contains a constant voltage due to the constant capacitive offset. The voltage in this quadrature should function as the voltage V_{AB} . We did not use this approach in our measurements.

C. In practice, we addressed this issue by tuning the decade resistance $\sim 20 \Omega$ away from its balanced value. Because the capacitive offset is small, it contributed negligibly to the magnitude of V_{AB} at this bridge imbalance, so changes in voltage with magnetic field could be treated as being proportional to changes in the sample resistance. For this 20Ω bridge imbalance, V_{AB} was, for example, $2.6 \mu V$ at 2.2 K and changes in V_{AB} of $\sim 5 \text{ nV}$ could be resolved with the lock-in. If higher resolution were needed, it would be necessary to null out the capacitive offset so that the gain of the lock-in could be increased (nulling out the offset voltage being the whole point of the bridge circuit in the first place).

(c) Measure magnetoresistance

- i. Measure the voltage difference across the bridge several times at one field point.
- ii. Ramp to the next field point (at a ramp rate of $\sim .1 \text{ mT/s}$).
- iii. Repeat over desired field range (this ramp used the same LabVIEW routine as that used in the persistent current measurement procedure discussed in 5.3.1.5).

(d) Repeat the magnetoresistance measurements at several different excitation voltages to verify that the signal does not depend on excitation. This check is to make sure that the electrons are not being heated. A good guide for the choice of excitation is that $eI_{ss}R_s \lesssim k_B T$ where $I_{ss}R_s$ is the voltage drop across the sample. When measuring at

many temperatures, it is a safe assumption that a sufficiently low excitation voltage for temperature T_1 will also be sufficiently low for $T_2 > T_1$. Thus, it is advisable to perform temperature measurements in order of increasing temperature so that this check need not be made at each new temperature value. However, due to the need for a high signal to noise ratio, it will be necessary to as temperature increases.

Chapter 6

Sensitivity of cantilever torsional magnetometry to persistent currents

6.1 Sources of uncertainty in cantilever torsional magnetometry measurements

There are many potential sources of uncertainty in the estimation of the frequency of a cantilever excited in the phase-locked loop circuit depicted in Fig. 5.6. Almost every component in the figure can in principal be assigned a contribution to the measurement noise. These noise sources can be broken up into four general classes: fluctuations of the cantilever's position due to unavoidable applied forces, noise in the readout of the interferometer signal, and the input voltage noise associated with each piece of electronics, and the output noise of the driving voltage sent to the piezoelectric actuator.

6.1.1 Fluctuating forces acting on the cantilever

When the cantilever is sufficiently well isolated from external vibrations, the two fluctuating forces intrinsic to the cantilever detection arrangement are those of the thermal noise associated with the cantilever's finite temperature and the radiation pressure shot noise due to the backaction of the readout laser on the cantilever [266, 270]. We treat both noise sources as white and thus

characterized by their respective force power spectral densities, $S_{F,\text{th}}$ and $S_{F,\text{RP}}$.¹

The magnitude of the thermal force noise can be computed from the equipartition theorem [282], which states that at thermal equilibrium

$$k \langle x^2 \rangle = k_B T, \quad (6.1)$$

where k and x are the spring constant and displacement of the cantilever tip, $\langle \dots \rangle$ denotes thermodynamic ensemble averaging, and T is the cantilever temperature. The mean square displacement is given by Parseval's theorem $\langle x^2 \rangle = (1/2\pi) \int_0^\infty d\omega S_{x,\text{th}}(\omega)$ where $S_{x,\text{th}}(\omega)$ is the power spectral density of the cantilever's displacement when the cantilever is driven by the thermal force noise. Using the transfer function given in Eq. 4.9, we can relate displacement to force as $S_{x,\text{th}}(\omega) = |G(\omega)|^2 S_{F,\text{th}}$ and then evaluate the expression for the mean square displacement:

$$\begin{aligned} \langle x^2 \rangle &= \frac{S_{F,\text{th}}}{2\pi m_{\text{eff}}^2} \int_0^\infty d\omega \frac{1}{(\omega^2 - \omega_0^2)^2 + \omega^2 \omega_0^2 / Q^2} \\ &= \frac{S_{F,\text{th}}}{2\pi m_{\text{eff}}^2} \frac{1}{2\omega_0^3} \int_{-\infty}^\infty dy \frac{1}{(y^2 - 1)^2 + y^2 / Q^2}, \end{aligned}$$

where we have taken $y = \omega/\omega_0$. Using the quadratic formula, the denominator of the integrand can be rewritten as $(y^2 - r_+^2)(y^2 - r_-^2)$ with the roots $r_\pm^2 = 1 - 1/2Q^2 \pm i\sqrt{(1 - 1/4Q^2)/Q^2}$. In the limit $Q \gg 1$, these roots become $r_\pm^2 \approx 1 \pm i/Q$, and $r_\pm \approx 1 \pm i/2Q$. We can rewrite the integral as

$$\langle x^2 \rangle = \frac{S_{F,\text{th}}}{2\pi m_{\text{eff}}^2} \frac{1}{2\omega_0^3} \int_{-\infty}^\infty dy \frac{1}{(y - r_+)(y + r_+)(y - r_-)(y + r_-)} \quad (6.2)$$

which can be evaluated by contour integration. The integral in Eq. 6.2 is equal to the integral for standard semi-circular contour enclosing the upper half of the complex plane that contains poles at $+r_+$ and $-r_-$. Calculating the residues at these poles, we find

$$\begin{aligned} \langle x^2 \rangle &= \frac{S_{F,\text{th}}}{2\pi m_{\text{eff}}^2} \frac{2\pi i}{2\omega_0^4} \left(\frac{1}{2r_+ (r_+^2 - r_-^2)} + \frac{1}{2r_- (r_+^2 - r_-^2)} \right) \\ &\approx \frac{S_{F,\text{th}}}{2\pi m_{\text{eff}}^2} \frac{2\pi i}{2\omega_0^4} \left(\frac{Q}{2i} \right) \\ &\approx \frac{S_{F,\text{th}}}{4m_{\text{eff}}^2} \frac{Q}{\omega_0^3}. \end{aligned}$$

¹Unless otherwise specified, all power spectral densities discussed in this text will be single-sided.

This result combined with the Equipartition Theorem allows us to write the thermal force spectral density as

$$S_{F,\text{th}} = \frac{4kk_B T}{Q\omega_0} \quad (6.3)$$

where we have used $k = m_{\text{eff}}\omega_0^2$. We can also rewrite the relation $S_{x,\text{th}}(\omega) = |G(\omega)|^2 S_{F,\text{th}}$ in the form

$$S_{x,\text{th}}(\omega) = \frac{4\langle x^2 \rangle}{\omega_0 Q} \frac{1}{\left((\omega/\omega_0)^2 - 1\right)^2 + (\omega/\omega_0 Q)^2}. \quad (6.4)$$

The radiation pressure backaction force arises from the corpuscularity of the readout laser beam which is composed many photons each carrying a momentum $p = h/\lambda$. When a photon hits the cantilever and is reflected, it imparts a net impulse of $2h/\lambda$ onto the cantilever. A typical laser beam can be modeled as a series of propagating photons. The distance between adjacent photons is random and follows a Poisson distribution. Because the spacing between adjacent photons is random and uncorrelated, the intensity of the laser beam (the number of photons passing through a plane in space per unit time) possesses a fluctuating component. These “shot noise” fluctuations are also present in the number of impulses imparted on the cantilever per unit time and lead to a fluctuating component in the radiation pressure force [283].

Consider a Poissonian stream of particles each having a value q for some quantity (e.g. energy, electric charge, or momentum). If we denote by R the mean rate at which this quantity passes a particular point in space per unit time (e.g. power, electric current, or force, to match the previous examples for q), then the shot noise of the stream can be expressed as the power spectral density S_R of the fluctuations in this rate. This power spectral density is white and obeys [284]

$$S_R = 2qR. \quad (6.5)$$

For radiation pressure, we can take q to be the impulse kick per photon $2h/\lambda$ and R to be the rate of impulses on the cantilever, in other words the force F_{RP} , given by the impulse kick per photon $2h/\lambda$ times the rate of photons \dot{N} . We write the rate of photons in terms of the incident laser power P by dividing by the energy per photon hc/λ : $\dot{N} = \lambda P/hc$. We have

$$\begin{aligned} S_{F,\text{RP}} &= 2 \left(\frac{2h}{\lambda} \right) \left(\frac{2h}{\lambda} \frac{\lambda P}{hc} \right) \\ &= \frac{8hP}{\lambda c}. \end{aligned} \quad (6.6)$$

The highest power laser powers discussed in this text are $5 \mu\text{W}$. If we assume that the cantilever is perfectly reflective, Eq. 6.6 gives a radiation pressure force noise of $\sqrt{S_{F,\text{RP}}} = 8 \times 10^{-21} \text{ N}/\sqrt{\text{Hz}}$. This figure provides an upper bound on the radiation pressure force noise experienced by a partially reflective cantilever. On the other hand, using our refrigerator's base temperature of $T = 300 \text{ mK}$ and the smallest value of $k/Q\omega_0$ of all the cantilevers discussed in this text, Eq. 6.3 gives a minimum thermal force noise of $\sqrt{S_{F,\text{th}}} = 2 \times 10^{-18} \text{ N}/\sqrt{\text{Hz}}$, over two orders of magnitude larger than $\sqrt{S_{F,\text{RP}}}$. We will drop $S_{F,\text{RP}}$ from further analysis of the uncertainty in the cantilever frequency measurement.

6.1.2 Interferometer readout noise

Error in the interferometric detection of the cantilever's position arises from fluctuations both in the laser used to monitor the cantilever and in the detector used measure the laser signal. An ideal laser source contains fluctuations due to the shot noise effect discussed in the previous section. A real laser also possesses technical noise in both its intensity and wavelength. Any optical detection circuit based upon a photodiode contains several resistors and transistors which possess some voltage and current noise. In this section, we will compare these sources of uncertainty in units of optical intensity. As we are considering small fluctuations, the optical lever effect (see 5.3.1.1) will be ignored in each derivation.

We use Eq. 6.5 again to calculate the power fluctuations due to shot noise. Power P is the rate of passage of energy and so plays the role of R in Eq. 6.5. The energy associated with a single photon of wavelength λ can be written as hc/λ [281]. Thus the power fluctuations due to shot noise are $S_{P,\text{SN}} = 2hcP/\lambda$. The average power on the photodiode during the persistent current measurement is $P = (R_f + T_f^2 R_c)P_{\text{inc}}$ (see Eq. 5.2). Thus the laser power fluctuations due to shot noise are

$$S_{P,\text{SN}} = \frac{2hc \left(R_f + T_f^2 R_c \right) P_{\text{inc}}}{\lambda}. \quad (6.7)$$

In addition to the shot noise contribution, the intensity noise of a laser can also have a component which is technical in nature. Laser intensity fluctuations due to technical noise are often referred to as "relative intensity noise" and are proportional to the mean laser power. Relative intensity noise arises from noise in the laser's components such as fluctuations in the laser's driving current. Writing the sum of the mean laser power and its fluctuations due to relative intensity noise as $P + \delta P_{\text{RIN}}(t) = P(1 + \gamma(t))$, the power spectral density of the power fluctuations due to relative

intensity noise is $S_{P,\text{RIN}} = P^2 S_\gamma$. Again using $P = (R_f + T_f^2 R_c) P_{\text{inc}}$, we have

$$S_{P,\text{RIN}} = (R_f + T_f^2 R_c)^2 P_{\text{inc}}^2 S_\gamma. \quad (6.8)$$

The change in the interferometer power δP_λ due to a fluctuation $\delta\lambda$ in the wavelength can be written as $\delta P_\lambda = P_{\text{cant}}(\lambda + \delta\lambda) - P_{\text{cant}}(\lambda)$. With the use of Eq. 5.2, we have

$$\begin{aligned} \delta P_\lambda &= -2T_f \sqrt{R_c R_f} P_{\text{inc}} \left(\cos \left(\frac{4\pi}{\lambda + \delta\lambda} (x_0 + x_1) \right) - \cos \left(\frac{4\pi}{\lambda} (x_0 + x_1) \right) \right) \\ &\approx -2T_f \sqrt{R_c R_f} P_{\text{inc}} \left[\left(\cos \left(\frac{4\pi\delta\lambda}{\lambda^2} (x_0 + x_1) \right) - 1 \right) \cos \left(\frac{4\pi}{\lambda} (x_0 + x_1) \right) \right. \\ &\quad \left. + \sin \left(\frac{4\pi\delta\lambda}{\lambda^2} (x_0 + x_1) \right) \sin \left(\frac{4\pi}{\lambda} (x_0 + x_1) \right) \right] \\ &\approx -2T_f \sqrt{R_c R_f} P_{\text{inc}} \frac{4\pi\delta\lambda}{\lambda^2} x_0 \cos \left(\frac{4\pi}{\lambda} x_1 \right) \end{aligned} \quad (6.9)$$

where we have kept terms to first order in $\delta\lambda$. We have also assumed that the interferometer is operated such that $4\pi x_0/\lambda = 2\pi N + \pi/2$ and $x_0 \gg x_1$. When the cantilever is driven, the factor involving x_1 can have a time dependence. We find the upper bound of δP_λ by setting the $\cos(4\pi x_1/\lambda)$ factor to unity. With the relationship between δP_λ and $\delta\lambda$ given by Eq. 6.9, the upper bound for the power spectral density of laser intensity fluctuations can be written as

$$S_{P,\delta\lambda} = 4T_f^2 R_c R_f P_{\text{inc}}^2 \left(\frac{4\pi x_0}{\lambda^2} \right)^2 S_\lambda \quad (6.10)$$

where S_λ is the power spectral density of the laser's wavelength fluctuations.

Wavelength fluctuations are often specified by the full width at half maximum $\Delta\nu$ of the laser frequency lineshape. The power spectral density S_ν of laser frequency is given by $S_\nu = \Delta\nu/\pi$ [285]. We can re-express S_ν in terms of λ by using $\Delta\nu = c\Delta\lambda/\lambda^2$ to write

$$S_\lambda = \frac{\lambda^4}{\pi^2 c L_c}, \quad (6.11)$$

where $L_c = \lambda^2/\pi \Delta\lambda$ is the coherence length. When the wavelength of the light wave follows a lorentzian distribution with a full width at half maximum $\Delta\lambda$, the coherence length L_c corresponds to the characteristic length scale over which the autocorrelation of the laser's electric field amplitude decays.

The total power spectral density $S_{P,\text{int}}$ of the interferometer signal out of the photodetector is

$$S_{P,\text{int}} = S_{P,\text{SN}} + S_{P,\text{RIN}} + S_{P,\delta\lambda} + S_{P,pd}$$

where $S_{P,pd}$ is the voltage noise of the photodetector converted into units of optical power. On the highest gain setting (which was used for all measurements), the 2011 photoreceiver has a noise equivalent power specification of $\sqrt{S_{P,pd}} = 200 \text{ fW}/\sqrt{\text{Hz}}$. We compare this noise to the other noise figures discussed above by using typical values for the operating input power $P_{\text{inc}} = 20 \text{ nW}$, the reflectivities $R_f = .2$ and $R_c = .03$, the cavity length $x_0 = 8 \text{ mm}$, and the laser coherence length $L_c = 10 \text{ cm}$.² Eq. 6.7 gives a noise power due to shot noise of $\sqrt{S_{P,\text{SN}}} = 34 \text{ fW}/\sqrt{\text{Hz}}$, a factor of 6 below the detector's noise level. The relative intensity noise specification for the JDS Uniphase laser is $\sqrt{S_\gamma} = 10^{-8}/\sqrt{\text{Hz}}$ which corresponds to $\sqrt{S_{P,\text{RIN}}} = 44 \text{ aW}/\sqrt{\text{Hz}}$, negligible on the scale of the detector's noise.³ Eqs. 6.10 and 6.11 yield a noise of $46 \text{ fW}/\sqrt{\text{Hz}}$ for wavelength fluctuations, a factor of four below the detector's noise. So for the measurements discussed in this text, the photodetector's noise was the dominant noise source of the interferometer readout but was comparable in magnitude to the noise due to the laser.

For comparison with the force noise discussed in the previous section, it is most convenient to express both the force noise and interferometer noise in units of cantilever displacement. For the force noise, we calculate the uncertainty in cantilever position at the cantilever's resonance frequency $\omega = \omega_0$. Eqs. 6.1 and 6.43 give $S_{x,\text{th}}(\omega_0) = 4Qk_B T/\omega_0 k$. For $T = 300 \text{ mK}$ and typical cantilever parameters $Q = 10^5$, $\omega_0 = 2\pi \times 2 \text{ kHz}$, and $k = 10^{-3} \text{ N/m}$, the cantilever displacement uncertainty is $\sqrt{S_{x,\text{th}}} = 360 \text{ pm}/\sqrt{\text{Hz}}$. To convert interferometer power into cantilever displacement, we use $\delta P_{\text{cant}} \approx \delta x_1 (dP_{\text{cant}}/dx_1)$. Assuming the interferometer fringe position is optimized with $4\pi x_0/\lambda = 2\pi N + \pi/2$, differentiating Eq. 5.2 yields

$$\frac{dP_{\text{cant}}}{dx_1} = \frac{8\pi}{\lambda} T_f \sqrt{R_c R_f} P_{\text{inc}}$$

²The cavity length can be estimated from the period of oscillation of the interferometer signal with laser wavelength. The coherence length can be determined by comparing the depth of modulation of the interferometer signal with the rf modulation on (A) and with the rf modulation off (B). By assuming that, in the absence of rf modulation, the coherence length is much longer than the cavity length x_0 , the coherence length with the rf modulation can be found from the relation $A/B = \exp(-2x_0/L_c)$. The rf modulation was on for all persistent current measurements.

³This specification is valid between 20 MHz and 1 GHz. The frequencies of interest in the measurements discussed in this text were well below 20 MHz for which no relative intensity noise specification is given. No change in the noise out of the photodetector was observed when the laser turned on and off, so it is difficult to assign a magnitude to low frequency laser intensity noise other than to say that it is much less than $5 \times 10^{-4}/\sqrt{\text{Hz}}$, which would result in a noise level equal to the photodetector's on the photodetector output.

and thus

$$\begin{aligned}\sqrt{S_{x,\text{int}}} &= \frac{\lambda}{8\pi P_{\text{inc}} T_f \sqrt{R_c R_f}} \sqrt{S_{P,\text{int}}} \\ &= 10 \text{ pm}/\sqrt{\text{Hz}}.\end{aligned}$$

Within $\sim \omega_0/2\pi Q$ of the cantilever resonance frequency ω_0 , the uncertainty in the cantilever position is dominated by the noise $\sqrt{S_{x,\text{th}}}$ due to the thermal force. Away from ω_0 , this contribution is suppressed and the interferometer noise $\sqrt{S_{x,\text{int}}}$ dominates.

6.1.3 Measurement electronics noise

The highest gain setting of the 2011 photoreceiver was $1.65 \times 10^7 \text{ V/W}$. The photoreceiver's $200 \text{ fW}/\sqrt{\text{Hz}}$ noise level thus corresponds to a voltage noise of $3.3 \mu\text{V}/\sqrt{\text{Hz}}$. This value is well above the $40 \text{ nV}/\sqrt{\text{Hz}}$ input voltage noise of the lock-in amplifier (for 10 dB gain setting). Following the chain of electronics laid out in Fig. 5.6, the photoreceiver signal was passed into lock-in 1 and then into a set of filters. Lock-in 1 was typically operated at a gain of at least 12 (the gain factor for the 10 dB setting), meaning that photoreceiver's noise level into the filters was $40 \mu\text{V}/\sqrt{\text{Hz}}$ or higher, safely above the SRS filter's $300 \text{ nV}/\sqrt{\text{Hz}}$ input voltage noise. After the filters, the signal was passed through lock-in 2, which usually had a gain of 5 (for which the input noise was $100 \text{ nV}/\sqrt{\text{Hz}}$). The amplified photoreceiver noise was thus $200 \mu\text{V}/\sqrt{\text{Hz}}$ out of this lock-in. Finally, the signal was passed into the DAQ or the frequency counter in order to perform the frequency measurement. The DAQ input noise was $20 \text{ nV}/\sqrt{\text{Hz}}$ while that of the frequency counter was $66 \text{ nV}/\sqrt{\text{Hz}}$, both well below the amplified photoreceiver noise. Thus, the noise on the photoreceiver output (including both the photoreceiver's noise and that due to the cantilever's thermally driven motion) dominated the noise of all subsequent electronic components in the circuit.

The voltage output of the lock-in amplifier used to drive the piezoelectric actuator had an output voltage noise of $1 \mu\text{V}/\sqrt{\text{Hz}}$. Typically, the RMS amplitude of the voltage drive out of the lock-in amplifier was kept fixed at close to 1 V. When a smaller voltage drive was required, a voltage divider (composed of resistors whose Johnson noise was of order $40 \text{ nV}/\sqrt{\text{Hz}}$) was put between the lock-in output and the leads to the piezo.

6.2 Derivation of the error in the frequency measurement of a cantilever driven in a phase-locked loop

Several different authors have calculated the uncertainty in the frequency measurement of a resonator in a phase-locked loop [270, 286, 287]. Here we adopt the treatment of Yurke *et al.* [286] to the detection set-up used in the persistent current measurements (see Fig. 5.6). The total uncertainty $\sigma_{f,\text{tot}}$ in the measured cantilever frequency has two major contributions: the fluctuations $\sigma_{f,\text{cant}}$ present in the driven cantilever motion itself and the fluctuations $\sigma_{f,pd}$ due to noise added to the detection signal by the photodetector.

6.2.1 Fluctuations $\sigma_{f,\text{cant}}$ in the frequency of motion of the driven cantilever

We begin by rewriting Eq. 4.4 in the form

$$\ddot{X} + \frac{\omega_0}{Q}\dot{X} + \omega_0^2 X = \frac{F_d(t) + F_{\text{th}}(t)}{m_{\text{eff}}} \quad (6.12)$$

where X is the displacement of the cantilever tip, F_d is force drive applied to the piezoelectric actuator by the feedback circuit, and F_{th} is the thermal force discussed in 6.1.1. We write $X(t)$ in terms of its quadratures $X_1(t)$ and $X_2(t)$ as

$$X(t) = X_1(t) \cos \omega t + X_2(t) \sin \omega t. \quad (6.13)$$

The main frequency component of the driving force F_d and the cantilever's motion X will be taken to be ω . When ω is close to the resonant frequency ω_0 and the quality factor Q is large, the quadratures $X_1(t)$ and $X_2(t)$ vary on the time scale set by the ringdown time $\tau = 2Q/\omega_0$, which is much longer than the cantilever period $2\pi/\omega_0$.

We combine the two quadratures into a single quantity by introducing the complex amplitude

$$x(t) = X_1(t) - iX_2(t).$$

The cantilever displacement can be written in terms of $x(t)$ as

$$\begin{aligned}
X(t) &= |x(t)| \cos(\omega t + \arg x_0(t)) \\
&= \frac{1}{2} (x(t) e^{i\omega t} + x^*(t) e^{-i\omega t}).
\end{aligned} \tag{6.14}$$

Since the amplitude $x(t)$ varies slowly on the scale of the cantilever period, it can be thought of as the ω Fourier component of $X(t)$ evaluated over a time window that is centered at time t and that is much smaller than the cantilever's ringdown time τ . Throughout this section, we use an upper-cased symbol to denote a real-valued time dependent quantity (e.g. $X(t)$), the same upper-case symbol with a 1 or 2 subscript to denote that quantity's two quadratures (e.g. $X_1(t)$ and $X_2(t)$), and lower-case symbols for the quantity's complex amplitude (e.g. $x(t)$). For instance, we can write the driving force F_d and the thermal force noise F_{th} as

$$F_d(t) = F_{d,1} \cos \omega t + F_{d,2} \sin \omega t = \frac{1}{2} (f_d(t) e^{i\omega t} + f_d^* e^{-i\omega t})$$

and

$$F_{\text{th}}(t) = F_{\text{th},1} \cos \omega t + F_{\text{th},2} \sin \omega t = \frac{1}{2} (f_{\text{th}}(t) e^{i\omega t} + f_{\text{th}}^* e^{-i\omega t}).$$

We do not write out these definitions explicitly for every quantity. We will set $\omega = \omega_0$ below.

The driving force F_d is produced by a series of operations acting on X . First, the cantilever position X , monitored interferometrically, produces a voltage signal on the photodetector $V_{pd}(t) = G_{pd}(P_{\text{cant}}(t) + P_{N,\text{int}}(t))$, where G_{pd} is the gain of the photodetector in volts per watts, $P_{\text{cant}}(t)$ is the signal from the photodetector and $P_{N,\text{int}}(t)$ is the noise in units of optical power out of the photodetector (see 6.1.2). As discussed in 5.3.1.1, the interferometer signal $P_{\text{cant}}(t)$ has frequency components at the frequency ω of cantilever motion and each of its harmonics. Because of the bandpass filter in the feedback circuit, we keep only the fundamental component. Because the first harmonic of P_{cant} (see Eq. 5.6) is in phase with the cantilever position $X(t)$, the complex amplitude $p_{\text{cant}}(t)$ can be written as

$$\begin{aligned}
p_{\text{cant}}(t) &= P_{\text{inc}} \left(4T_f \sqrt{R_f R_c} J_1 \left(\frac{4\pi}{\lambda} U |x| \right) + 2T_f^2 R_c \epsilon U |x| \right) \frac{x}{|x|} \\
&\equiv R(|x|) x.
\end{aligned}$$

Here we have assumed that the cantilever is operated at the optimal fringe position (see 5.3.1.1). For a cantilever of length l excited in its m^{th} flexural mode, the factor $U = U_m(z_f/l)$ converts the displacement x of the tip to that at the position z_f monitored by the interferometer (see Eq. 4.1).

Continuing along the phase-locked loop diagram in Fig. 5.6, we pass from the photodetector to the lock-in amplifier. We combine the lock-in amplification factors together with the photodetector's gain in the quantity G_{pd} . As discussed in 6.1.3, we can ignore the input noise of all electronic components following the photodetector. The lock-in produces an output signal $V_{\text{piezo}}(t)$ whose frequency ω is set by the lock-in's internal feedback circuit in order to main a fixed phase ϕ_c , set externally by the user, relative to the lock-in's input $V_{pd}(t)$.⁴ The lock-in output's amplitude V_0 is also set by the user. We model this behavior of the lock-in as that of an ideal phase shifter and limiter plus a noise term $V_{N,d}(t)$, writing the complex amplitude v_{piezo} of the lock-in output as

$$v_{\text{piezo}} = V_0 e^{i\phi_c} \frac{G_{pd} (R(|x|)x + p_{N,pd})}{|G_{pd} (R(|x|)x + p_{N,pd})|} + v_{N,d}. \quad (6.15)$$

Denoting by β_{piezo} the amount of force exerted on the cantilever per applied voltage to the piezoelectric actuator, the complex amplitude f_d of the driving force is

$$f_d = \beta_{\text{piezo}} V_0 e^{i\phi_c} \frac{R(|x|)x + p_{N,\text{int}}}{|R(|x|)x + p_{N,\text{int}}|} + \beta_{\text{piezo}} v_{N,d} \quad (6.16)$$

In terms of the complex amplitudes, the equation of motion (Eq. 6.12) for the cantilever driven in a phase-locked loop becomes

$$2i\omega_0 \frac{dx}{dt} - (\omega_0^2 + 2\omega_0 \delta\omega) x + i \frac{\omega_0^2}{Q} x + \omega_0^2 x = \frac{f_d + f_{\text{th}}}{m_{\text{eff}}} \quad (6.17)$$

where $\delta\omega = \omega - \omega_0 \ll \omega_0$. We have dropped terms containing the factors $\delta\omega/Q$, $\delta\omega dx/dt$, $Q^{-1} dx/dt$ and d^2x/dt^2 , each of which we assume to be negligible due to the resonator's high Q and thus long ringdown time. We write

$$x = (X_0 + \delta X_0(t)) e^{i\phi_0 + i\phi(t)}. \quad (6.18)$$

Here, X_0 and ϕ_0 the real valued steady-state (independent of time) amplitude and phase of the complex amplitude x , and $\delta X_0(t)$ and $\phi(t)$ are the real valued fluctuations about these steady-

⁴In principle there could be additional phase shifts in the detection circuit which we do not discuss (e.g. the phase shift due to the band-pass filter). However, these shifts just result in an overall shift to ϕ_c which can be negated by our freedom to set the value of ϕ_c .

state values. We choose to shift the zero of t so that $\phi_0 = 0$. To leading order, we can write $x(t) \approx X_0 + \delta X_0(t) + iX_0\phi(t)$. The steady-state solution is given by setting $\delta X_0(t)$, $\phi(t)$ and all noise terms to zero. The steady-state solution can be written as

$$X_0 = e^{i\phi_c} \frac{\beta_{\text{piezo}} V_0}{m_{\text{eff}} \left(\frac{i\omega_0^2}{Q} - 2\omega_0 \delta\omega \right)}. \quad (6.19)$$

The steady-state amplitude X_0 and frequency offset $\delta\omega$ are determined by specifying V_0 and ϕ_c .

Ultimately, we are seeking an expression for the fluctuations of the phase-locked loop frequency when the loop is operated to drive the cantilever on resonance. These fluctuations of the loop's frequency are directly related to the fluctuations $\phi(t)$ in the loop's phase. We obtain an expression for $\phi(t)$ when the cantilever is driven resonantly by solving the equation of motion, Eq. 6.17, with the resonance condition $\delta\omega = 0$ and the expansion $x(t) \approx X_0 + \delta X_0(t) + iX_0\phi(t)$.

We now solve for $\phi(t)$. For $\delta\omega = 0$, the steady-state solution, Eq. 6.19, requires that $\phi_c = \pi/2$ and $X_0 = V_0 Q \beta_{\text{piezo}} / m_{\text{eff}} \omega_0^2$. With these relations, we can rewrite f_d (Eq. 6.16) as

$$\begin{aligned} f_d &= i \frac{m_{\text{eff}} \omega_0^2}{Q} X_0 \frac{R(|x|)x + p_{N,\text{int}}}{|R(|x|)x + p_{N,\text{int}}|} + \beta_{\text{piezo}} v_{N,d} \\ &\approx i \frac{m_{\text{eff}} \omega_0^2}{Q} X_0 \left(1 + i\phi + \frac{p_{N,\text{int}} - p_{N,\text{int}}^*}{2R(X_0)X_0} \right) + \beta_{\text{piezo}} v_{N,d} \\ &\approx i \frac{m_{\text{eff}} \omega_0^2}{Q} X_0 \left(1 + i\phi - i \frac{P_{N,\text{int},2}}{R(X_0)X_0} \right) + \beta_{\text{piezo}} v_{N,d}. \end{aligned} \quad (6.20)$$

where we have used the fact that for any real Γ and complex δ such that $|\delta| \ll \Gamma$,

$$\frac{\Gamma + \delta}{|\Gamma + \delta|} \approx 1 + \frac{\delta - \delta^*}{2\Gamma}.$$

Plugging this result for f_d as well as $\delta\omega = 0$ and $x(t) \approx X_0 + \delta X_0(t) + iX_0\phi(t)$ into the equation of motion (Eq. 6.17), we have

$$2 \left(\frac{d(\delta X_0)}{dt} + iX_0 \frac{d\phi}{dt} \right) + \frac{\omega_0}{Q} (X_0 + \delta X_0 + iX_0\phi) = \frac{\omega_0 X_0}{Q} \left(1 + i\phi - i \frac{P_{N,\text{int},2}}{R(X_0)X_0} \right) - \frac{i}{m_{\text{eff}} \omega_0} (\beta_{\text{piezo}} v_{N,d} + f_{\text{th}}). \quad (6.21)$$

Taking the imaginary part of Eq. 6.21 yields the following equation describing time evolution of

the phase fluctuations $\phi(t)$:

$$2\frac{d\phi}{dt} = -\frac{\omega_0}{Q} \left(\frac{P_{N,\text{int},2}}{R(X_0)X_0} \right) - \frac{1}{m_{\text{eff}}\omega_0 X_0} (\beta_{\text{piezo}}V_{N,d,1} + F_{\text{th},1}). \quad (6.22)$$

To find the time dependence of $\phi(t)$ we employ the Fourier transform

$$\phi(\xi) = \int_{-\infty}^{\infty} dt \phi(t) e^{-2\pi i \xi t}$$

and its inverse

$$\phi(t) = \int_{-\infty}^{\infty} d\xi \phi(\xi) e^{2\pi i \xi t}.$$

Each of $P_{N,\text{int},2}$, $V_{N,d,1}$, and $F_{\text{th},1}$ are quadrature amplitudes of uncorrelated fluctuating quantities which we assume have the properties of white noise. In particular, for quadrature amplitudes A_i and B_j of $A(t)$ and $B(t)$, we assume

$$\langle A_i(\xi) \rangle = 0 \quad (6.23)$$

$$\langle A_i(\xi) A_i(\xi') \rangle = S_A \delta(\xi + \xi') \quad (6.24)$$

$$\langle A_i(\xi) B_j(\xi') \rangle = 0. \quad (6.25)$$

where S_A is the power spectral density of A and $\langle \dots \rangle$ denotes averaging over the ensemble of possible $A(t)$ and $B(t)$. Taking the Fourier transform of Eq. 6.22, we find

$$\phi(\xi) = -\frac{1}{4\pi i \xi} \left(\frac{\omega_0}{Q} \left(\frac{P_{N,\text{int},2}(\xi)}{R(X_0)X_0} \right) + \frac{1}{m_{\text{eff}}\omega_0 X_0} (\beta_{\text{piezo}}V_{N,d,1}(\xi) + F_{\text{th},1}(\xi)) \right) \quad (6.26)$$

from which it follows that $\langle \phi(\xi) \rangle = 0$. Using Eqs. 6.25 and 6.26, we have

$$\langle \phi(\xi) \phi(\xi') \rangle = \frac{1}{16\pi^2 \xi^2} \delta(\xi + \xi') \left(\left(\frac{\omega_0}{QR(X_0)X_0} \right)^2 S_{P,\text{int}} + \left(\frac{1}{m_{\text{eff}}\omega_0 X_0} \right)^2 (\beta_{\text{piezo}}^2 S_{N,V,d} + S_{F,\text{th}}) \right) \quad (6.27)$$

where $S_{P,\text{int}}$ is the power spectral densities of the photodiode signal in units of optical power, $S_{N,V,d}$ is the voltage power spectral density of the lock-in output, and $S_{F,\text{th}}$ is the power spectral density of the thermal force acting on the cantilever (see 6.1.1). We will use this expression for $\langle \phi(\xi)\phi(\xi') \rangle$ to find the fluctuations in the phase-locked loop frequency momentarily.

We now consider the significance of the voltage noise $S_{N,V,d}$ of the lock-in output. As discussed

in 6.1.3, the feedback loop is typically operated with the voltage output of the lock-in at 1 V. In most cases, the cantilever tip is driven on resonance to an RMS amplitude of approximately

$$X_0 = \frac{1}{\sqrt{2}} \frac{1}{0.7} \frac{1.84\lambda}{4\pi} \approx 230 \text{ nm}$$

by this 1 V drive. This drive corresponds to the peak of J_1 in the first harmonic response of the interferometer given in Eq. 5.4. The factor of 0.7 in the expression above represents the scaling factor $U_m(z_f/l)$ for a typical detection position z_f . . On resonance, Eq. 4.9 gives the conversion between force F and displacement X_0 as $F = kX_0/Q$. For the typical values of $k = 10^{-3} \text{ N/m}$ and $Q = 10^5$, the force per voltage is

$$\begin{aligned} \beta_{\text{piezo}} &= \frac{F}{(1 \text{ V})} \\ &= \frac{kX_0}{Q(1 \text{ V})} \\ &= 2.3 \text{ fN/V}. \end{aligned}$$

Thus, the $1 \mu\text{V}/\sqrt{\text{Hz}}$ magnitude of $\sqrt{S_{N,V,d}}$ (see 6.1.3) corresponds to a force noise of $2.3 \text{ zN}/\sqrt{\text{Hz}}$, much less than the typical magnitude for the thermal force noise of 1 aN (see 6.1.1). Therefore, we now drop the $S_{N,V,d}$ term.

We now calculate the diffusion of the phase. Since $\langle \phi(\xi) \rangle = 0$, it follows that $\langle \phi(t) \rangle = 0$. The typical fluctuation $\delta\phi(\tau_M)$ in phase accumulated over time τ_M is given by

$$\begin{aligned} \delta\phi^2(\tau_M) &= \left\langle (\phi(t + \tau_M) - \phi(t))^2 \right\rangle \\ &= \left\langle \left(\int_{-\infty}^{\infty} d\xi \phi(\xi) e^{2\pi i \xi t} (e^{2\pi i \xi \tau_M} - 1) \right) \left(\int_{-\infty}^{\infty} d\xi' \phi(\xi') e^{2\pi i \xi' t} (e^{2\pi i \xi' \tau_M} - 1) \right) \right\rangle \\ &= \frac{S_\phi}{16\pi^2} \int_{-\infty}^{\infty} d\xi \frac{2 - e^{2\pi i \xi \tau_M} - e^{-2\pi i \xi \tau_M}}{\xi^2} \end{aligned} \quad (6.28)$$

where we have used

$$S_\phi = \omega_0^2 \left(\frac{S_{P,\text{int}}}{(QR(X_0)X_0)^2} + \frac{S_{F,\text{th}}}{(kX_0)^2} \right). \quad (6.29)$$

The integral in Eq. 6.28 can be evaluated with contour integration. We use the standard semi-circular contours with their flat sides along the real axis. The first two terms in the numerator of the integrand of Eq. 6.28 will have a negligible contribution along the semicircular arc enclosing the

upper half plane as its radius is taken to infinity, while the third term is negligible for such an arc enclosing the lower half plane (which introduces an extra minus sign in the first line of the equation below). To evaluate the integral, we replace the denominator of the integrand ξ^2 by $\xi^2 + \delta^2$ so that there are poles at $\xi = \pm i\delta$. We can then perform the integral using the calculus of residues to obtain

$$\begin{aligned}
\delta\phi^2(\tau_M) &= \frac{S_\phi}{16\pi^2} 2\pi i \left(\text{Res} \left[\frac{2 - e^{2\pi i \xi \tau_M}}{(\xi - i\delta)(\xi + i\delta)}, i\delta \right] - \text{Res} \left[\frac{-e^{-2\pi i \xi \tau_M}}{(\xi - i\delta)(\xi + i\delta)}, -i\delta \right] \right) \\
&= \frac{S_\phi}{16\pi^2} 2\pi i \left(\frac{2 - e^{-2\pi\delta\tau_M}}{2i\delta} - \frac{-e^{-2\pi\delta\tau_M}}{-2i\delta} \right) \\
&= \frac{S_\phi}{8\pi} \left(\frac{1 - e^{-2\pi\delta\tau_M}}{\delta} \right) \\
&\approx \frac{S_\phi}{4} \tau_M \\
&= \frac{\tau_M}{4} \omega_0^2 \left(\frac{S_{P,\text{int}}}{(QR(X_0)X_0)^2} + \frac{S_{F,\text{th}}}{(kX_0)^2} \right)
\end{aligned}$$

where in the next to last step we have taken $\delta \rightarrow 0$.

We now find the relation between a fluctuation $\delta\phi(\tau_M)$ of the resonator's phase over time τ_M and the corresponding fluctuation δf of the resonator's frequency. Over time τ_M , a resonator with period T undergoes $N = \tau_M/T$ oscillations. If the total fluctuation of the phase over τ_M is $\delta\phi$, then the fluctuation of the phase per oscillation is $\delta\phi/N$. Typically a resonator oscillates at a constant frequency and the phase

$$\phi = \frac{2\pi}{T} t$$

evolves linearly in time t . A fluctuation $\delta\phi/N$ in the phase over one period can be thought of as a fluctuation

$$\delta T = \frac{T}{2\pi} \left(\frac{\delta\phi}{N} \right) = \frac{T^2}{2\pi\tau_M} \delta\phi$$

in the period T . The corresponding fluctuation δf in frequency is given by

$$\begin{aligned}
\delta f &= \frac{1}{T} - \frac{1}{T + \delta T} \\
&\approx \frac{\delta T}{T^2} \\
&= \frac{\delta\phi}{2\pi\tau_M}.
\end{aligned} \tag{6.30}$$

Using Eq. 6.30 to convert the phase fluctuation $\delta\phi(\tau_M)$ into the fluctuation $\sigma_{f,\text{cant}}$ of the phase-

locked loop frequency over τ_M , we find

$$\begin{aligned}
\sigma_{f,\text{cant}}^2(\tau_M) &= \frac{\delta\phi^2(\tau_M)}{(2\pi\tau_M)^2} \\
&= \frac{f_0^2}{4\tau_M} \left(\frac{S_{P,\text{int}}}{(QR(X_0)X_0)^2} + \frac{S_{F,\text{th}}}{(kX_0)^2} \right) \\
&= \frac{1}{4\tau_M} \left(\frac{f_0^2 S_{P,\text{int}}}{Q^2 P_{\text{inc}}^2 \left(4T_f \sqrt{R_f R_c} J_1 \left(\frac{4\pi}{\lambda} U X_0 \right) + 2T_f^2 R_c \epsilon U X_0 \right)^2} + \frac{2f_0 k_B T}{\pi Q k X_0^2} \right) \quad (6.31)
\end{aligned}$$

where we have used the abbreviation $U = U_m(z_f/l)$. We reiterate now that $\sigma_{f,\text{cant}}$ is the typical fluctuation of the actual frequency at which the cantilever oscillates. Throughout the derivation, the cantilever's resonant frequency f_0 was assumed to be constant. The actual frequency of motion of the cantilever shows slight deviations from f_0 because the cantilever is driven by fluctuating forces (both the thermal noise force and the force created by noise in the phase-locked loop circuit being fed back to the piezoelectric actuator).

6.2.2 Frequency fluctuations $\sigma_{f,\text{int}}$ added to the cantilever signal by detector noise

So far, we have considered only the actual fluctuations of the phase of the cantilever's motion, either caused by noise forces intrinsic to the cantilever or transduced by the phase-locked loop circuit from noise in the cantilever position detection. Noise in the detection of the cantilever position can also lead to error in the inferred value of the frequency.

Typically, the cantilever frequency is measured by feeding the lock-in output signal $V_{\text{piezo}}(t)$ into a frequency counter. Following similar steps to those used deriving Eq. 6.20, the complex amplitude v_{piezo} (see Eq. 6.15) may be written as

$$\begin{aligned}
v_{\text{piezo}} &= iV_0 \frac{G_{pd}(R(|x|)x + p_{N,\text{int}})}{|G_{pd}(R(|x|)x + p_{N,\text{int}})|} \\
&\approx iV_0 \left(1 + i\phi - i \frac{P_{N,\text{int},2}}{R(X_0)X_0} \right)
\end{aligned}$$

From this expression, it can be seen that the fluctuating component of the lock-in output's phase is the sum of the fluctuating phase ϕ of the cantilever motion and another term, $-P_{N,\text{int},2}/R(X_0)X_0$, caused by the noise of the photodetector.⁵

⁵Following the observations of 6.1.1, we treat the noise of other electronic components, including the output

Using the approach of Ref. 286, we take the total measured fluctuating phase ϕ_{tot} to be a filtered form of the lock-in output's fluctuating phase $\phi - P_{N,\text{int},2}/R(X_0)X_0$:

$$\begin{aligned}\phi_{\text{tot}}(t) &= \frac{e^{-t/\tau_F}}{\tau_F} \int_{-\infty}^t dt' e^{t'/\tau_F} \left(\phi(t') - \frac{P_{N,\text{int},2}(t')}{R(X_0)X_0} \right) \\ &= \frac{e^{-t/\tau_F}}{\tau_F} \int_{-\infty}^{\infty} d\xi \int_{-\infty}^t dt' e^{t'/\tau_F} e^{2\pi i \xi t'} \left(\phi(\xi) - \frac{P_{N,\text{int},2}(\xi)}{R(X_0)X_0} \right) \\ &= \frac{e^{-t/\tau_F}}{\tau_F} \int_{-\infty}^{\infty} d\xi \frac{e^{t/\tau_F} e^{2\pi i \xi t}}{2\pi i \xi + 1/\tau_F} \left(\phi(\xi) - \frac{P_{N,\text{int},2}(\xi)}{R(X_0)X_0} \right) \\ &= \int_{-\infty}^{\infty} d\xi \frac{e^{2\pi i \xi t}}{1 + 2\pi i \xi \tau_F} \left(\phi(\xi) - \frac{P_{N,\text{int},2}(\xi)}{R(X_0)X_0} \right)\end{aligned}$$

where τ_F is the time constant of the filter. The average measured phase fluctuation $\langle \phi_{\text{tot}}(t) \rangle = \langle \phi_{\text{tot}}(\xi) \rangle = 0$ is zero because $\langle \phi(t) \rangle = \langle P_{N,\text{int},2}(\xi) \rangle = 0$. The total diffusion of the measured phase is

$$\begin{aligned}\delta\phi_{\text{tot}}^2(\tau_M) &= \left\langle (\phi_{\text{tot}}(t + \tau_M) - \phi_{\text{tot}}(t))^2 \right\rangle \\ &= \int_{-\infty}^{\infty} d\xi \int_{-\infty}^{\infty} d\xi' \left(\frac{e^{2\pi i \xi t} (e^{2\pi i \xi \tau_M} - 1)}{1 + 2\pi i \xi \tau_F} \right) \left(\frac{e^{2\pi i \xi' t} (e^{2\pi i \xi' \tau_M} - 1)}{1 + 2\pi i \xi' \tau_F} \right) \\ &\quad \times \left\langle \left(\phi(\xi) - \frac{P_{N,\text{int},2}(\xi)}{R(X_0)X_0} \right) \left(\phi(\xi') - \frac{P_{N,\text{int},2}(\xi')}{R(X_0)X_0} \right) \right\rangle.\end{aligned}$$

The phase correlation $\langle \phi(\xi)\phi(\xi') \rangle$ was given in Eq. 6.27 and can be abbreviated as

$$\langle \phi(\xi)\phi(\xi') \rangle = \frac{1}{16\pi^2} S_\phi(\xi) \delta(\xi + \xi').$$

Following our assumption, Eq. 6.24, that each noise source is white, we can write

$$\langle P_{N,\text{int},2}(\xi)P_{N,\text{int},2}(\xi') \rangle = S_{P,\text{int}}(\xi)\delta(\xi + \xi').$$

Using the expression for $\phi(\xi)$ given in Eq. 6.26, the cross-correlation term can be evaluated as

$$\begin{aligned}\left\langle \phi(\xi) \frac{P_{N,\text{int},2}(\xi')}{R(X_0)X_0} \right\rangle &= \left\langle -\frac{1}{4\pi i \xi} \left(\frac{\omega_0}{Q} \left(\frac{P_{N,\text{int},2}(\xi)}{R(X_0)X_0} \right) + \frac{\beta_{\text{piezo}} V_{N,d,1}(\xi) + F_{\text{th},1}(\xi)}{m_{\text{eff}} \omega_0 X_0} \right) \frac{P_{N,\text{int},2}(\xi')}{R(X_0)X_0} \right\rangle \\ &= -\frac{1}{4\pi i \xi} \frac{\omega_0}{Q} \frac{S_{P,\text{int}}(\xi) \delta(\xi + \xi')}{(R(X_0)X_0)^2}\end{aligned}$$

noise of the lock-in and the input noise of the frequency counter, to be negligible compared to the noise of the photodetector.

With these results, the measured phase diffusion is

$$\begin{aligned}
\delta\phi_{\text{tot}}^2(\tau_M) &= \int_{-\infty}^{\infty} d\xi \int_{-\infty}^{\infty} d\xi' \frac{-4e^{2\pi i(\xi+\xi')(t+\tau_M/2)} \sin(\pi\xi\tau_M) \sin(\pi\xi'\tau_M)}{(1+2\pi i\xi\tau_F)(1+2\pi i\xi'\tau_F)} \times \dots \\
&\quad \times \left(\frac{1}{16\pi^2} \frac{\delta(\xi+\xi')}{\xi^2} S_\phi + \frac{S_{P,\text{int}}}{(R(X_0)X_0)^2} \delta(\xi+\xi') + \dots \right. \\
&\quad \left. - \frac{1}{2} \frac{1}{2\pi i\xi} \frac{\omega_0}{Q} \frac{S_{P,\text{int}}}{R^2(X_0)} \delta(\xi+\xi') \right) \\
&= \int_{-\infty}^{\infty} d\xi \frac{4\sin^2(\pi\xi\tau_M)}{1+4\pi^2\xi^2\tau_F^2} \left(\frac{S_\phi}{16\pi^2\xi^2} + \frac{S_{P,\text{int}}}{(R(X_0)X_0)^2} - \frac{1}{4\pi i\xi} \frac{\omega_0}{Q} \frac{S_{P,\text{int}}}{(R(X_0)X_0)^2} \right) \\
&= \frac{S_\phi}{4} \int_{-\infty}^{\infty} d\xi \frac{1}{4\pi^2\xi^2} \frac{4\sin^2(\pi\xi\tau_M)}{1+4\pi^2\xi^2\tau_F^2} + \frac{S_{P,\text{int}}}{(R(X_0)X_0)^2} \int_{-\infty}^{\infty} d\xi \frac{4\sin^2(\pi\xi\tau_M)}{1+4\pi^2\xi^2\tau_F^2} \\
&= \frac{\tau_M S_\phi}{2\pi} \int_{-\infty}^{\infty} dx \frac{1}{x^2} \frac{\sin^2(x/2)}{1+(x/\alpha)^2} + \frac{2S_{P,\text{int}}}{\pi\tau_M (R(X_0)X_0)^2} \int_{-\infty}^{\infty} dx \frac{\sin^2(x/2)}{1+(x/\alpha)^2}
\end{aligned}$$

where we have used

$$\alpha = \tau_M/\tau_F.$$

We dropped the integral of the cross-term (the $1/\xi$ term) because it is anti-symmetric in ξ .

Evaluating the integrals in the expression for $\delta\phi_{\text{tot}}^2(\tau_M)$ with the help of Eqs. A.21 and A.22, we find

$$\delta\phi_{\text{tot}}^2(\tau_M) = \frac{S_\phi}{4} \left(\tau_M - \tau_F \left(1 - \exp\left(-\frac{\tau_M}{\tau_F}\right) \right) \right) + \frac{S_{P,\text{int}}}{(R(X_0)X_0)^2} \frac{1}{\tau_F} \left(1 - \exp\left(-\frac{\tau_M}{\tau_F}\right) \right).$$

Using Eq. 6.30 to convert phase to frequency, we find

$$\begin{aligned}
\sigma_{f,\text{tot}}^2(\tau_M) &= \frac{\delta_{\text{tot}}^2(\tau_M)}{(2\pi\tau_M)^2} \\
&= \frac{S_\phi}{16\pi^2\tau_M} \left(1 - \frac{\tau_F}{\tau_M} \left(1 - e^{-\frac{\tau_M}{\tau_F}} \right) \right) + \frac{S_{P,\text{int}}}{4\pi^2 (R(X_0)X_0)^2} \frac{1}{\tau_M^2\tau_F} \left(1 - e^{-\frac{\tau_M}{\tau_F}} \right). \quad (6.32)
\end{aligned}$$

This expression may also be written explicitly in terms of the different noise spectral densities as

$$\begin{aligned}
\sigma_{f,\text{tot}}^2(\tau_M) &= \frac{f_0^2}{4\tau_M} \frac{S_{P,\text{int}}}{Q^2 (R(X_0)X_0)^2} \left(1 - \frac{\tau_F}{\tau_M} \left(1 - \exp\left(-\frac{\tau_M}{\tau_F}\right) \right) \right) \\
&\quad + \frac{f_0^2}{4\tau_M} \frac{S_{F,\text{th}}}{(kX_0)^2} \left(1 - \frac{\tau_F}{\tau_M} \left(1 - \exp\left(-\frac{\tau_M}{\tau_F}\right) \right) \right) \\
&\quad + \frac{1}{4\pi^2} \frac{1}{\tau_M^2\tau_F} \frac{S_{P,\text{int}}}{(R(X_0)X_0)^2} \left(1 - \exp\left(-\frac{\tau_M}{\tau_F}\right) \right). \quad (6.33)
\end{aligned}$$

In the limit of long measurement times $\tau_M \gg \tau_F$, the fluctuations $\sigma_{f,\text{tot}}$ in the observed frequency may be written as

$$\sigma_{f,\text{tot}}^2 = \sigma_{f,\text{cant}}^2 + \sigma_{f,\text{int}}^2$$

with $\sigma_{f,\text{cant}}^2$ the actual fluctuations of the resonator given in Eq. 6.31 and

$$\sigma_{f,\text{int}}^2 = \frac{S_{P,\text{int}}}{4\pi^2 (R(X_0) X_0)^2} \frac{1}{\tau_M^2 \tau_F}$$

the additional fluctuations in the detected frequency due to the noise in the interferometer signal. Since $\sigma_{f,\text{cant}}^2 \propto \tau_M^{-1}$ and $\sigma_{f,\text{int}}^2 \propto \tau_M^{-2}$, there is a transitional value τ_M^* beyond which $\sigma_{f,\text{tot}}^2$ is dominated by the frequency fluctuations $\sigma_{f,\text{cant}}$ of the cantilever. For shorter times $\tau_M < \tau_M^*$, the fluctuations $\sigma_{f,\text{int}}$ added by the detector dominate.

Optimal filtering involves fixing $\alpha_F = \tau_M/\tau_F$ with $\alpha_F \gtrsim 1$. Using this condition to eliminate τ_F , we obtain

$$\begin{aligned} \sigma_{f,\text{tot}}^2(\tau_M) &= \frac{f_0^2}{4\tau_M} \frac{S_{P,\text{int}}}{Q^2 (R(X_0) X_0)^2} \left(1 - \frac{1}{\alpha_F} (1 - \exp(-\alpha_F))\right) \\ &+ \frac{f_0^2}{4\tau_M} \frac{S_{F,\text{th}}}{(kX_0)^2} \left(1 - \frac{1}{\alpha_F} (1 - \exp(-\alpha_F))\right) \\ &+ \frac{1}{4\pi^2} \frac{\alpha_F}{\tau_M^3} \frac{S_{P,\text{int}}}{(R(X_0) X_0)^2} (1 - \exp(-\alpha_F)). \end{aligned} \quad (6.34)$$

For optimal filtering, it remains the case that $\sigma_{f,\text{cant}}^2 \propto \tau_M^{-1}$, but now $\sigma_{f,\text{int}}^2 \propto \tau_M^{-3}$. In either case, we see that, by measuring for sufficiently long times τ_M , the fluctuations of the cantilever's phase can be made the dominant source of fluctuations in the detected frequency.

6.3 Optimal cantilever dimensions for measuring persistent currents

We now comment briefly on the choice of adjustable parameters for the persistent current measurements. When designing samples, we choose parameters that maximize the sensitivity defined as

$$\mathcal{S}_{pc} = \frac{\Delta f_{pc}}{\sqrt{(\sigma_{f,\text{tot}}(\tau_M))^2 \tau_M}} \quad (6.35)$$

where Δf_{pc} is the cantilever frequency shift due to the persistent current given in Eq. 4.26 and $\sigma_{f,\text{tot}}(\tau_M)$ is the uncertainty in a frequency measurement over time τ_M given in Eq. 6.33. Because Δf_{pc} depends non-linearly on several sample parameters and $\sigma_{f,\text{tot}}(\tau_M)$ trades off between two different sources of uncertainty, determining the optimal sample parameters is a complicated task. We do not have the space here to give this topic full justice but will outline some of its most important facets.

We begin by rewriting results from previous chapters in forms convenient for the present analysis. Eq. 4.26 gave the frequency shift Δf_{pc} due to the persistent current in a ring mounted at the cantilever tip as

$$\Delta f_{pc} = N^\sigma \frac{f_0}{2k} \frac{2\pi I_1}{\phi_0} \left(\pi r^2 B \cos \theta_0 \frac{\alpha}{l} \right)^2 \text{jinc} \left(2\pi \frac{\pi r^2 B}{\phi_0} \cos \theta_0 \frac{\alpha}{l} x_{\text{max}} \right). \quad (6.36)$$

Here we assume that the first harmonic $p = 1$ of the current is measured. Using Eq. 2.85 and assuming strong spin-orbit scattering, we can write the magnitude I_1 of the first harmonic of the typical persistent current⁶ as

$$I_1 \approx 0.028 \frac{eD}{r^2} \exp \left(-\frac{4k_B T r^2}{\hbar D} \right) \quad (6.37)$$

where $r = L/2\pi$ is the radius of the ring. The number of rings on the cantilever is given by N . The exponent σ determines how the total persistent current scales with N . When the sign of the persistent current varies randomly from ring to ring, $\sigma = 1/2$, and, when all the rings have a persistent current of the same sign, $\sigma = 1$. The maximum value of N for a given cantilever scales⁷ with the cantilever width w and length l and ring radius r as $N \propto wl/r^2$. The other parameters included in Eqs. 6.36 and 6.37 represent the same quantities as they did in Eqs. 2.85 and 4.26.

In the previous section, it was found that the fluctuations $\sigma_{f,\text{tot}}$ in the measured frequency were made up of two contributions, the fluctuations $\sigma_{f,\text{cant}}$ of the cantilever frequency and additional fluctuations $\sigma_{f,\text{int}}$ added to the measurement by the detector. In the limit that the thermal noise

⁶As discussed in 2.3.3, other persistent current mechanisms, such the average current due to either interacting or non-interacting electrons, have a similar exponential dependence on r , D , and T , with the interacting electron case also having the same D/r^2 prefactor.

⁷If a sufficiently large section of the cantilever is covered with rings, the cantilever mode shape factor α defined in Eq. 4.12 may no longer be constant. It is then necessary to integrate over the portion C of the cantilever covered with rings as $(\Delta f_{pc})_C = \int_C dz \Delta f_{pc}(\alpha(z))/l_C$ where z is the distance from the cantilever base and l_C is the length of the cantilever covered with rings. We ignore this mode shape dependence in our analysis. For the fundamental flexural mode, the factor α changes by only $\sim 10\%$ over the $\sim 40\%$ of the cantilever length closest to the tip.

contribution to $\sigma_{f,\text{tot}}$ is negligible ($S_{F,\text{th}} \approx 0$), the ratio between these two contributions is

$$\frac{\sigma_{f,\text{cant}}}{\sigma_{f,\text{pd}}} = \pi^2 \tau_M \tau_F \frac{f_0^2}{Q^2} \left(\frac{1}{1 - \exp\left(-\frac{\tau_M}{\tau_F}\right)} - \frac{\tau_F}{\tau_M} \right).$$

In the limit of $\tau_M/\tau_F \gg 1$, this ratio can be written as

$$\frac{\sigma_{f,\text{cant}}}{\sigma_{f,\text{int}}} = \frac{\tau_M \tau_F}{\tau^2}$$

where $\tau = Q/\pi f_0$ is the cantilever ringdown time. When $\tau_M, \tau_F \gg \tau$, the uncertainty $\sigma_{f,\text{int}}$ added to the measurement by the detector is negligible in comparison to $\sigma_{f,\text{cant}}$.

In principle, the contribution $\sigma_{f,\text{int}}$ can be made a negligible contribution $\sigma_{f,\text{tot}}$ for any set of sample parameters simply by measuring for a sufficiently long time τ_M . However, in the derivation of $\sigma_{f,\text{tot}}$ in the previous section, it was assumed that the cantilever resonant frequency f_0 was constant in time. In practice, the resonant frequency f_0 drifts slowly over time. When the measurement time τ_M is sufficiently long, this random drift leads to an increase in the total measured frequency uncertainty $\sigma_{f,\text{tot}}$. We found that this frequency drift led to an optimal measurement time of $\tau_M \approx 5$ s. For the samples listed in Table 7.1, the ringdown times $\tau \sim 20$ s were greater than this optimal value of τ_M , so $\sigma_{f,\text{int}}$ could not be neglected.

We now use the expressions reviewed so far in this section to write the sensitivity \mathcal{S}_{pc} in terms of parameters which can be controlled during sample fabrication and during measurement. In order to discuss the optimal choice of cantilever dimensions, we use the relations given in Section 4.2 to write the cantilever frequency and spring constant in terms of the cantilever dimensions as

$$f_0 = \beta_m \sqrt{\frac{E_Y}{12\rho}} \frac{t}{l^2} \quad (6.38)$$

$$k = \frac{\beta_m^2}{48} E_Y \frac{wt^3}{l^3} \quad (6.39)$$

where E_Y and ρ are the cantilever material's Young's modulus and density and β_m was defined implicitly by Eq. 4.2 for cantilever mode m . With these relations, we find

$$\mathcal{S}_{pc} = A_S \frac{\exp(-B_S r^2 T/D) r^{2-2\sigma} (\alpha B \cos \theta_0)^2 \text{jinc}(2\pi r^2 \alpha B \cos \theta_0 x_{\text{max}}/l)}{\sqrt{\frac{w^{2-2\sigma} S_{P,\text{int}}}{R^2 (x_{\text{max}})^2 x_{\text{max}}^2} \left(C_S \frac{t^6}{Q^2 l^{2+2\sigma}} + D_S \frac{t^4 l^{2-2\sigma}}{\tau_M \tau_F} \right) + E_S w^{1-2\sigma} t^2 l^{3-2\sigma} \frac{T}{Q x_{\text{max}}^2}}} \quad (6.40)$$

where we have grouped constants into the terms $A_S = 0.020 e$, $B_S = 4k_B/\hbar$, $C_S = (\beta_m^2 E_Y/48)^2$, $D_S = (\beta_m^2 E_Y \rho)/(192\pi^2)$ and $E_S = (k_B \beta_m \sqrt{E_Y \rho})/(4\pi\sqrt{3})$. Recall that $R(x)$ was defined above by

$$R(x_{\max}) x_{\max} = P_{\text{inc}} \left(4T_f \sqrt{R_f R_c} J_1 \left(\frac{4\pi}{\lambda} U x_{\max} \right) + 2T_f^2 R_c \epsilon U x_{\max} \right).$$

For simplicity, we have assumed that $\tau_F/\tau_M \gg 1$. The symbol x_{\max} has been used to denote amplitude of the cantilever tip.⁸

We now consider the choice of the parameters listed in Eq. 6.40 that maximizes the sensitivity \mathcal{S}_{pc} . The dependence of \mathcal{S}_{pc} on a few parameters is quite straightforward. Under all conditions, the sensitivity is improved by increasing the diffusion constant D and the mechanical quality factor Q and decreasing the temperature T and the cantilever thickness t . However, when the frequency uncertainty is dominated by the detector noise $\sigma_{f,\text{int}}$, \mathcal{S}_{pc} is not affected by Q . In this case, the sensitivity is improved by increasing the measurement time τ_M until another noise source becomes dominant (see the discussion above about the effect of resonant frequency drift on the frequency uncertainty).

While in the previous paragraph we discussed Q and t as independent variables, it is important to note that Q is not necessarily an independent parameter. Over the course of the persistent current experiment, samples have been fabricated two times each with $t \sim 110$ nm and $t \sim 340$ nm. For this limited number of fabrication runs, it has been observed that $Q_{340}/Q_{110} \sim 4 - 7$. Thus it appears that $Q \propto t^\delta$ for $\delta > 1$. It has previously been reported that $\delta \approx 1$ in silicon-nitride cantilevers [264]. In the same study, Q was found to depend only weakly on cantilever length in single crystal silicon cantilevers similar to the ones discussed in this text. As long as $\delta \leq 2$, the sensitivity is always improved by making t as small as possible, especially when the uncertainty $\sigma_{f,\text{tot}}$ is limited by the interferometer noise $S_{P,\text{int}}$. We also note that Q typically decreases with T . This dependence reinforces the trend noted above of increasing \mathcal{S}_{pc} with decreasing T .

The importance of the interferometer parameters P_{inc} , R_f , and R_c to \mathcal{S}_{pc} depends on the nature of the leading contribution to $S_{P,\text{int}}$. When the interferometer noise $S_{P,\text{int}}$ is dominated by shot noise or the detector's internal noise, the sensitivity increases with incident laser power P_{inc} until another noise contribution becomes dominant or the laser begins to heat the cantilever. If $S_{P,\text{int}}$ is dominated by the laser's technical noise, either intensity or wavelength fluctuations, the sensitivity

⁸The parameter x_{\max} is equivalent to X_0 from the previous section. We changed notation in the previous section in order to follow the convention of lower-case symbols for complex quantities and upper-case symbols for the real-valued equivalents.

is independent of P_{inc} . Also when $S_{P,\text{int}}$ is dominant, the sensitivity depends weakly on R_c and R_f , generally increasing with R_c and peaking for $R_f \approx .4$. The exact dependence of \mathcal{S}_{pc} on R_c and R_f is contingent upon the dominant contribution to $S_{P,\text{int}}$. Reflectivities of $R_c = .3$ and $R_f = .4$ achieve a factor of ~ 21 improvement over $R_c = .01$ and $R_f = .01$ when the photodetector noise dominates, and a factor of ~ 4 improvement when relative intensity noise or shot noise dominates. No improvement is seen when $S_{P,\text{int}}$ is dominated by wavelength fluctuations. These factors of improvement assume that the same source of noise remains dominant. Once one contribution to the noise is reduced to the same level as another source, further improvements will result in diminishing returns for \mathcal{S}_{pc} .

The choice of optimal cantilever width w depends upon the nature of the persistent current sample through the exponent σ . For a single ring sample, we can set $\sigma = 0$. Then the sensitivity increases as the width decreased for all noise sources. For a current of random sign, we have $\sigma = 1/2$. For this value of σ , \mathcal{S}_{pc} increases with decreasing w while the interferometer noise dominates and then is independent of w once the thermal force noise dominates. For a current with a well defined sign, $\sigma = 1$. In this case \mathcal{S}_{pc} increases with increasing w until the uncertainty due the interferometer noise dominates. Once it does, \mathcal{S}_{pc} becomes independent of w .

The dependence of \mathcal{S}_{pc} on the remaining experimental parameters is complicated by their appearance in the argument, $2\pi r^2 \alpha B \cos \theta_0 x_{\text{max}}/l$, of the jinc function in Eq. 6.40. The function $\text{jinc}(x)$ is peaked at $x = 0$ and drops to and remains below $\sim 10\%$ of its peak value once $x \gtrsim 1/2$ (see Fig. 4.5). Thus, r , $\alpha B \cos \theta_0$, x_{max} , and l must be chosen so that the combination $2\pi r^2 \alpha B \cos \theta_0 x_{\text{max}}/l$ remains less than $1/2$.

Disregarding the jinc factor, \mathcal{S}_{pc} scales as $(\alpha B \cos \theta_0)^2$. This quadratic dependence of \mathcal{S}_{pc} on $\alpha B \cos \theta_0$ is stronger than its dependence on r^2 , x_{max} , or l for all values of σ and all noise limits. Thus \mathcal{S}_{pc} is always increased by scaling down r^2 , x_{max} , or l so that $\alpha B \cos \theta_0$ may be increased. The maximum magnetic field B is generally set by the specifications of the equipment.⁹

The cantilever mode factor α is maximal at the cantilever tip and increases with the order of the flexural mode m . Thus optimal sensitivity is achieved when persistent current rings are placed near the cantilever tip and the highest possible order of flexural mode is used. For arrays of rings, the fraction of the cantilever length covered with rings must be decreased with increasing order of

⁹Our magnet was rated to produce fields up to 9 T. The maximum value of B used in the experiments discussed here was 8.4 T. The magnet quenched multiple times above 8.4 T during early cooldowns. It was decided that it was not worth risking further quenching to measure the persistent current between 8.4 T and 9 T. In principle, we could have continued measuring persistent currents at larger magnetic field strengths.

flexural mode. Otherwise, the variation of α across the cantilever length complicates the analysis of the frequency shift signal. The portion of the cantilever over which α is constant scales as $\alpha \propto \sim 2^m$ while α at the cantilever tip scales roughly as $\alpha \propto \sim 2.8m$. This dependence leads to the third order mode being optimal for $\sigma = 1$ and the sixth order mode being optimal for $\sigma = 1/2$.

In addition to its appearance in the expression for \mathcal{S}_{pc} , the angle θ_0 determines the degree of correlation of the persistent current oscillations in applied magnetic field. The magnetic field frequency $\beta_1 = \pi r^2 \sin \theta_0 / \phi_0$ of the first harmonic of the persistent current signal scales as $\sin \theta_0$. As discussed in 2.3.2.1, the typical persistent current oscillation is correlated on the magnetic field scale $\gamma B_{c,1}$, where $B_{c,1}$ was given by Eq. 2.79 and is independent of θ_0 . Assuming the geometrical factor γ depends only weakly on θ_0 , it is desirable to make $\gamma B_{c,1} \beta_1$ as large as possible. For the typical current, $\gamma B_{c,1} \beta_1$ is the number of oscillations of the persistent current that are correlated with each other in field. When this number becomes too small ($\lesssim 1$), the persistent current signal no longer follows a sinusoidal form and becomes difficult to distinguish from the frequency shift background. Additionally, for the case of the average persistent current, $\gamma B_{c,1} \beta_1$ sets the number of oscillations observable before the current is suppressed. A reasonable choice for the angle is $\theta_0 \approx 45^\circ$ because the $\cos^2 \theta_0$ prefactor of \mathcal{S}_{pc} decreases only by 1/2 as θ_0 is increased from 0° to 45° , while $\gamma B_{c,1} \beta_1$ increases strongly. Beyond $\theta_0 = 45^\circ$, the factor $\cos^2 \theta_0$ drops towards zero as θ_0 approaches 90° , while $\gamma B_{c,1} \beta_1$ varies only weakly. In the experiment, we initially used $\theta_0 = 6^\circ$ in order to maximize \mathcal{S}_{pc} and measure our first persistent current signal. We then adjusted θ_0 to 45° to obtain data with more oscillations per correlation field $B_{c,1}$.

Although the ring thickness t_r and linewidth w_r do not appear in the expression for \mathcal{S}_{pc} , they do affect the measurement through appearance in $B_{c,1} \propto (w_r t_r)^{-1/2}$. In order to maximize $\gamma B_{c,1} \beta_1$, the ring's cross-sectional dimensions should be made as small as possible. However, once the cross-sectional dimensions are reduced to roughly the same magnitude as the bulk elastic mean free path l_e , surface scattering becomes an important factor in the electron diffusion and the diffusion constant D is reduced. Since the current magnitude is suppressed exponentially in D , the cross-sectional dimensions of the rings should not be reduced to lengths much smaller than the value of the elastic mean free path in the absence of surface scattering.

Outside of the jinc factor, \mathcal{S}_{pc} scales with r as $\exp(-B_S r^2 T / D) r^{2-2\sigma}$. When $\sigma \neq 1$, this factor is optimized for $r_{\text{opt}} = \sqrt{(1-\sigma)\hbar D / 4k_B T}$. Using typical values of $D = 0.02 \text{ m}^2/\text{s}$ and $T = 0.3 \text{ K}$, the optimal radius is 252 nm for an array of rings with current of random sign ($\sigma = 1/2$) and 357 nm for

a single ring ($\sigma = 0$). These dimensions are similar to the ones used in the experiment. For an array of rings with well-defined sign ($\sigma = 1$), the factor $\exp(-B_S r^2 T/D) r^{2-2\sigma}$ decreases monotonically with r so that it is best to make the rings as small as possible lithographically. Because the average current is suppressed as magnetic flux penetrates the metal of the ring on the field scale $\gamma B_{c,1}$, the minimum r is set by the value that gives the minimum acceptable number of observable oscillations. As mentioned above this number is set by the factor $\gamma B_{c,1} \beta_1 \propto r$.

The final two parameters x_{\max} and l have the most complicated relationships to the sensitivity \mathcal{S}_{pc} . When the uncertainty is thermally limited, the sensitivity increases with decreasing l for all values of σ (i.e. for single rings and arrays of rings with persistent current of either random or well-defined sign). The dependence on l differs between the two contributions to the uncertainty due to noise $S_{P,\text{int}}$ in the interferometer. When uncertainty in the cantilever's frequency of motion caused by interferometer noise (the C_S term of Eq. 6.40) dominates, the sensitivity is improved with increasing l for all values of σ . This dependence on l follows the opposite trend as that followed when thermal noise dominates. When the uncertainty added to the measurement by noise in the interferometer (the D_S term of Eq. 6.40) dominates, the sensitivity is independent of l for an array of rings with well defined sign ($\sigma = 1$) and otherwise ($\sigma = 0$ or $1/2$) increases with decreasing l . This trend (except for the $\sigma = 1$ case) is the same as that followed when the sensitivity is limited by thermal noise. Adjusting l tunes the system from being thermally limited and being limited by one of the two contributions related to interferometer noise. Thus the optimal value of l depends on all of the other system parameters required to calculate the three contributions to the frequency uncertainty. These parameters include P_{inc} , R_c , R_f , Q , σ , among others.

Generally, there is an optimal value of x_{\max} for a given set of values of the other parameters in the experiment. When the frequency uncertainty $\sigma_{f,\text{tot}}$ is dominated by terms derived from the noise $S_{P,\text{int}}$ in the interferometric detection, the sensitivity scales as

$$\mathcal{S}_{pc} \propto R(x_{\max}) x_{\max} \text{jinc}(2\pi r^2 \alpha B \cos \theta_0 x_{\max}/l)$$

When the optical lever effect is small, $R(x_{\max}) x_{\max}$ typically has a maximum value for realistic values of x_{\max} . The value of x_{\max} producing this peak increases as the laser spot is moved toward the base of the cantilever where the cantilever motion (i.e. the parameter U) is smaller. When the frequency uncertainty is limited by $S_{P,\text{int}}$, it is preferable to position the laser spot as close to the cantilever tip as possible so that the argument of the jinc factor can be minimized (i.e. by

maximizing $R(x_{\max})x_{\max}$ with the smallest possible value of x_{\max}). When the frequency uncertainty is thermally limited, the sensitivity is proportional to

$$\mathcal{S}_{pc} \propto x_{\max} \text{jinc}(2\pi r^2 \alpha B \cos \theta_0 x_{\max} / l)$$

Because $x_{\max} \text{jinc}(Ax_{\max}) \propto J_1(Ax_{\max})$, the optimal value of x_{\max} in this case corresponds to the first peak of $J_1(2\pi r^2 \alpha B \cos \theta_0 x_{\max} / l)$ at $x_{\max} = 1.84l / 2\pi r^2 \alpha B \cos \theta_0$. If this value of x_{\max} occurs at a value above that optimizing $R(x_{\max})x_{\max}$ when the laser spot is at the cantilever tip and thus causes the interferometer noise to dominate (i.e. because $R(x_{\max})x_{\max}$ is small), the factor $R(x_{\max})x_{\max}$ can be optimized by moving the laser spot closer to the cantilever base as mentioned above. As was the case for l , the optimal choice of x_{\max} depends on several other parameters of the system.

There are a couple of caveats to our discussion of l and x_{\max} . In 4.2, we introduced the cantilever as a simple harmonic oscillator with restoring force $F_{\text{restoring}} = -kx$. For sufficiently large values of x/l , higher order corrections $F_{\text{restoring}}$ become non-negligible. These non-linearities must be included in the derivation of the uncertainty in the frequency measurement given in 6.2. In general, they lead to an increase in the uncertainty $\sigma_{f,\text{tot}}$. Additionally, the laser spot takes up a finite amount of space on the cantilever and must be kept a certain distance away from the rings in order to avoid heating them. Thus, when the sensitivity increases with decreasing l , there is a lower bound on l of $\sim 100 \mu\text{m}$.¹⁰

To summarize, we have seen that it is generally desirable to produce ring-cantilever samples with high diffusion constant D , cantilever reflectivity R_c , and quality factor Q and small thickness t . The ring samples should be located near the tip of the cantilever. The highest sensitivity in measuring these samples is achieved when the magnetic field B and incident laser power P_{inc} are maximized and the temperature T is minimized. The relationship between the sensitivity to the cantilever width w , cantilever thickness l , the sample orientation angle θ_0 , the cantilever mode m , the fiber reflectivity R_f , and the cantilever tip amplitude of motion x_{\max} depends on the details of the measurement. The sensitivity \mathcal{S}_{pc} peaks for fixed values of these parameters rather than scaling monotonically with them. The choice of the value for other parameters such the orientation angle θ_0 is less straightforward.

¹⁰This figure is obtained by assuming that the laser spot is $10 \mu\text{m}$ wide, that 40% of the cantilever is covered with rings, and that a $\sim 50 \mu\text{m}$ distance is kept between the rings and the laser spot (with the edge of the laser spot touching the edge of the cantilever base).

Finally, we note that the persistent current measurement in a uniform magnetic field is fundamentally a torque measurement. A torque τ experienced by a cantilever of length l is equivalent to a force of magnitude $F = \tau/l$ applied at the cantilever tip. This fact explains why the sensitivity to persistent currents scales inversely to cantilever length l whereas in force detection the sensitivity scales with l [266]. It is possible that a transducer designed more specifically for a torque rather than a force such as the ones described in Refs. 288–290 could achieve greater sensitivity than a cantilever.

6.4 Experimental characterization of the sensitivity of the cantilever detection apparatus

6.4.1 Cantilever and sample thermometry measurements

In 6.3, we saw that the sensitivity \mathcal{S}_{pc} of the persistent current measurement depends strongly on the temperature of the electrons in the ring and the temperature of the cantilever with the signal decreasing with temperature while the noise increases. One might think that mounting the cantilever chip on a sample stage in good thermal contact with a good cryostat cooled to a low bath temperature T_b would be sufficient to ensure that T_n and T_e are also cooled down. However, the requirements for fabricating a high sensitivity cantilever is at odds with those of achieving good thermal contact with the cantilever’s base. In particular, a high cantilever mechanical quality factor Q corresponds to a weak coupling of the cantilever to its external environment. Moreover, the extreme cantilever aspect ratio and the insulating properties of cantilever materials (such as silicon) contribute to the expectation of poor thermal conductivity for a high sensitivity cantilever. Additionally, the common detection mechanism of cantilever motion using a laser introduces a potentially strong source of heating into the system.

When we began planning the persistent current experiment, we were not aware any experimental investigation of both the temperature of a cantilever’s macroscopic degree of freedom T_n and that of its microscopic degrees of freedom (which should be equal to the temperature of the electrons T_e in a sample mounted on the end of the cantilever) below 1 K. Thurber *et al.* had previously performed careful measurements of the temperature of the microscopic degrees of freedom of a cantilever and their tracking of the bath temperature T_b from 4 K to 16 K by measuring the paramagnetism of solid air contamination on the cantilever [291]. Other experiments had been performed to study various

samples on the ends of cantilevers at temperatures as low as 250 mK, though concerns about possible discrepancies between the sample temperature and the bath temperature were not addressed directly [262, 292–294]. Measurements of the temperature of a resonator’s macroscopic degree of freedom by observing its Brownian motion had been performed at temperatures as low as 56 mK in nano-electromechanical systems [295] and as low as 220 mK in single crystal silicon cantilevers similar to those discussed in this text [296]. It is worth noting that in the latter measurement the bath temperature was 110 mK, so that decoupling of the cantilever noise temperature T_n from the bath temperature T_b was in fact observed. We decided to perform a preliminary thermometry experiment of both T_e and T_n on the same sample chip in order to assess the feasibility of the persistent current measurement and to provide an early milestone along the daunting ascent towards persistent current measurements [297].

Our cantilever thermometry measurements were performed on the commercial atomic force microscope cantilevers discussed in 5.1.1. The macroscopic temperature T_n was measured via the cantilever’s Brownian motion, while the microscopic temperature T_e was measured via observation of the superconducting transition of a macroscopic aluminum grain attached to the end of the cantilever. The measurements were not performed on the same cantilever but were performed on two cantilevers on the same sample chip during the same cool down. Cantilever detection was performed with a set-up similar to that described in 5.2.2 using a bare cleaved optical fiber kept at a distance of $\sim 100 \mu\text{m}$ from the cantilever.

6.4.1.1 Measurements of the cantilever’s noise temperature

The cantilever’s noise temperature T_n was extracted from measurements of the cantilever’s undriven motion at a series of bath temperatures T_b and incident laser powers P_{inc} . The amplified voltage signal from the photodiode (the lead connected to the “Frequency counter” in Fig. 5.6) was fed into the DAQ where it was digitized into an array of N voltage readings v_m spaced equally in time by Δt . Many such time series of the voltage were recorded, and for each one the single-sided power spectral density

$$S_V(f) = 2 \frac{\left| \sum_{m=0}^N v_m e^{-2\pi i f \Delta t m/N} \right|^2}{N \Delta t} \quad (6.41)$$

was computed. These power spectral densities were then averaged together. The resulting trace $S_V(f)$ was then converted into a cantilever amplitude of motion power spectral density S_x using

the conversion factor $\Gamma_{V \text{ to } x}$ discussed in Section 5.3.1.4 and defined in Eq. 5.8 to find

$$S_x(f) = \frac{\Gamma_{V \text{ to } x}^2}{2g_{\text{lock-in}}^2} S_V(f) \quad (6.42)$$

where $g_{\text{lock-in}}$ is the voltage gain between the lock-in's input (which was used to define $\Gamma_{V \text{ to } x}$) and its output ("signal monitor" on the 7265). Note that Eq. 6.41 gives the root-mean-square (RMS) voltage power spectral density and that the lock-in reading used to calculate $\Gamma_{V \text{ to } x}$ is also the RMS voltage. The conversion factor $\Gamma_{V \text{ to } x}$ has been defined so that it converts from RMS voltage to peak (not RMS) amplitude of motion at the cantilever tip. This choice of conversion factor explains the extra factor of 2 in Eq. 6.42.

The power spectral density was calculated using these short time trace sections because the cantilever is quite susceptible to external vibrations. Obvious outlier traces where the cantilever amplitude was several times as large as that observed in the majority of the traces could easily be identified and discarded. Additionally, because the undriven cantilever motion is a random quantity, the fluctuations of $S_x(f)$ for any one value of f in a single trace are as large as $S_x(f)$. It is only by averaging many traces that the measured $S_x(f)$ resembles the theoretically expected form. The effect of averaging many traces could also be accomplished by binning the frequency components of $S_x(f)$ from a single large time trace, but this method is susceptible to the effects of external vibrations described above.

The measured power spectral density curves were fit using Eq. 6.43 in the form

$$S_x(f) = \frac{2\langle x^2 \rangle}{\pi f_0 Q} \frac{1}{\left((f/f_0)^2 - 1 \right)^2 + (f/f_0 Q)^2} + S_{x,\text{int}} \quad (6.43)$$

where $S_{x,\text{int}}$ represents the constant offset in the power spectral density due to the noise of the interferometric measurement which was described in 6.1.2. The free parameters in the fit were $\langle x^2 \rangle$, f_0 , Q , and $S_{x,\text{int}}$. Fig. 6.1 shows the power spectral density of cantilever displacement taken at 4.2 K along with a fit to Eq. 6.43.¹¹ Fits were also performed with Q fixed to a value determined by ringdown measurements as described in 5.3.1.5. These fits produced less consistent results than the ones for which Q was allowed to vary. The fit gives $\langle x^2 \rangle$ directly. Alternatively, after subtracting the baseline noise $S_{x,\text{int}}$, the area under the data points of the $S_x(f)$ curve could be integrated near

¹¹The data in this figure were originally published in [297]. The scale of the vertical axis was incorrect in the original paper and has been corrected here.

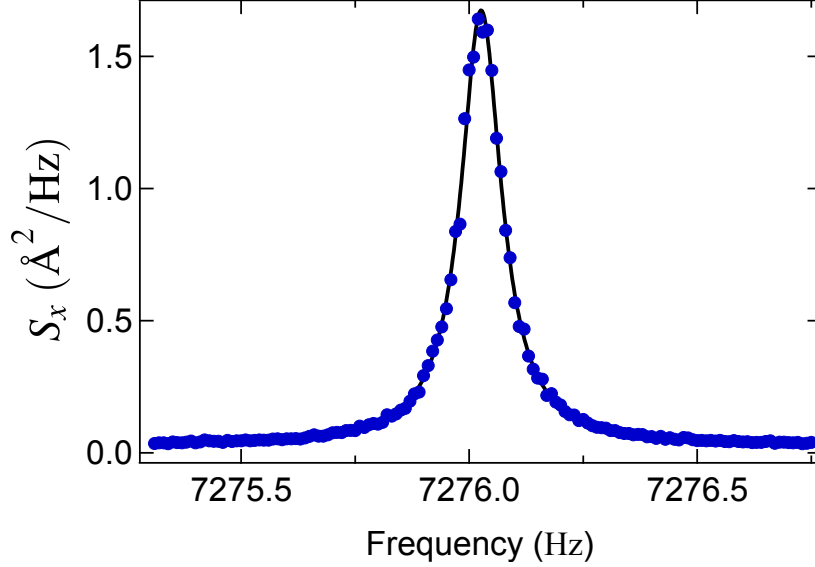


Figure 6.1: Power spectral density of cantilever motion. The data points shown were calculated from measurements of the cantilever’s undriven motion taken at 4.2 K using the procedure described in the text. The figure also shows a fit to Eq. 6.43. The extracted fitting parameters were $\langle x^2 \rangle = 0.28 \text{ \AA}^2$, $f_0 = 7276 \text{ Hz}$, $Q = 6.8 \times 10^4$, and $S_{x,\text{int}} = 0.029 \text{ \AA}^2/\text{Hz}$. The magnitude of the background $S_{x,\text{int}}$ is a factor of four greater than that expected for shot noise for the incident laser power of 150 nW.

the peak at f_0 to give $\langle x^2 \rangle$. This procedure gave similar results to the fits for $\langle x^2 \rangle$.

Measurements of $S_x(f)$ such as the one shown in Fig. 6.1 were repeated at a series of refrigerator temperatures using $P_{\text{inc}} = 150 \text{ nW}$ of power incident on the cantilever. The resulting trace of mean square cantilever displacement $\langle x^2 \rangle$ versus refrigerator temperature T_b is shown in Fig. 6.2, as is a linear fit. According to the equipartition theorem given in Eq. 6.1, the mean square displacement $\langle x^2 \rangle$ should be proportional to the cantilever temperature with constant of proportionality k_B/k . From Fig. 6.2, we can conclude that the cantilever temperature T_n tracks the refrigerator temperature down to its base temperature because the data matches the linear fit down to the lowest temperature and because the $\langle x^2 \rangle$ -intercept of the fit is consistent with zero within the uncertainty of the fit due to the scatter in the data. The presence of an external heat source preventing the cantilever from equilibrating with the refrigerator would lead to a saturation of $\langle x^2 \rangle$ at low temperature, while a non-zero $\langle x^2 \rangle$ -intercept would indicate an additional source vibrations to the thermal force noise. The ArrowTM TL8 cantilevers described in 5.1.1 had a specified spring constant of 0.03 N/m with values between 0.004 and 0.54 N/m typical. The slope of the fit in Fig. 6.2 corresponds to a spring constant of 0.02 N/m, consistent with these specifications. The spring constant can be calculated directly from the dimensions using Eq. 4.7. The uncertainty in cantilever thick-

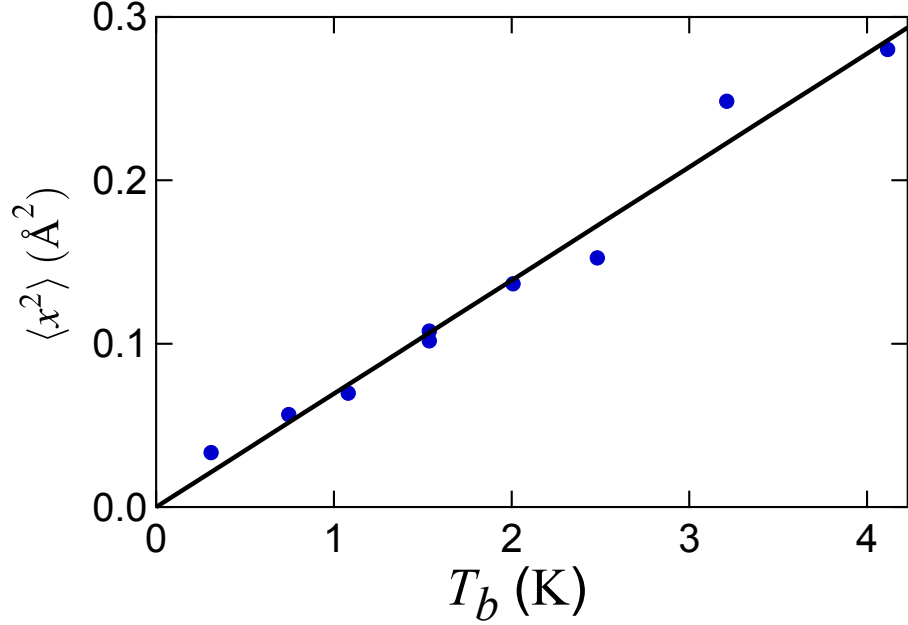


Figure 6.2: Mean square cantilever displacement versus refrigerator temperature. The data points represent the values of $\langle x^2 \rangle$ extracted from measurements such as the one shown in Fig. 6.1 at a series of refrigerator temperatures T_b . For each measurement, the incident laser power was 150 nW. The line represents a fit of the form $\langle x^2 \rangle = k_B T/k + x_{\text{off}}^2$ for k and x_{off}^2 . The best fit parameters were $k = 0.020$ N/m and $x_{\text{off}}^2 = 2.0 \times 10^{-3}$ \AA^2 .

ness (specified to be between 0.5 and 2.5 μm) results in the large uncertainty in the specification for the cantilever spring constant, which scales as the cube of the thickness. From the width and length measured in Fig. 5.1 and the measured frequency of 7276 Hz (Fig. 6.1), we estimate the cantilever thickness to be between 0.89 and 1.29 μm using Eqs. 4.5, 4.7, and 4.8. These two values were obtained defining the cantilever length to exclude and include the triangular tip, respectively. The spring constants corresponding to these dimensions are 0.036 and 0.11 N/m. We are not sure of the origin of the discrepancy between these values and our extracted value of 0.02 N/m for k .

In Ref. 296, a deviation of T_n from T_b was observed below 300 mK. The fact that this deviation of T_n from T_b was observed in Ref. 296 and not by us can be explained by the fact that the cantilever used in Ref. 296 had a smaller cross-section leading to increased phonon-boundary scattering [298]. Additionally, this deviation was observed only for $T_b \sim 100$ mK, below the range of temperatures measured by us. Presumably, these factors outweighed the fact that the cantilevers of Ref. 296 were fabricated from undoped silicon which should possess a larger thermal conductivity and a lower optical absorption coefficient than our doped silicon [298, 299]. We discuss the transport of heat through the cantilever further in 6.4.1.3.

6.4.1.2 Measurements of the electron temperature of a metallic sample at the end of a cantilever

We use the superconducting transition of an aluminum grain mounted on the end of the cantilever (Fig. 5.2) to determine the temperature T_e of the cantilever's microscopic degrees of freedom near its tip. In the presence of a static magnetic field, a bulk superconductor develops surface currents which screen the magnetic field from the superconductor's interior, a phenomenon known as the Meissner effect [300]. These screening currents and the superconductor's corresponding magnetic moment $\boldsymbol{\mu}$ are proportional to the applied magnetic field \mathbf{B} . From Eq. 4.15, the energy E of the superconductor in the magnetic field is proportional to B^2 . For an aspherical superconducting grain, we can write

$$E = m_0 B^2 N(\theta)$$

where m_0 is a constant of proportionality with units of A m^2 , θ is the angle between $\boldsymbol{\mu}$ and \mathbf{B} , and $N(\theta)$ is a shape anisotropy factor [301].

By Eq. 4.13, it follows that a cantilever mounted with a superconducting grain will exhibit a frequency shift proportional to B^2 . In the normal state, the grain should produce a negligible frequency shift. According to the BCS model, the critical field B_c at which a superconductor transitions to the normal state can be approximated within four percent by

$$B_c(T_e) = B_c(0) \sqrt{1 - \left(\frac{T_e}{T_c}\right)^2} \quad (6.44)$$

where T_e is the temperature of the superconductor and T_c is the superconducting transition temperature in the absence of an applied magnetic field [300, 302]. Thus, if T_c is known, Eq. 6.44 can be used to determine T_e of a superconducting sample on the end of a cantilever by measuring the cantilever frequency while sweeping the magnetic field and noting the magnitude of field at which the cantilever frequency stops changing quadratically with B and becomes independent of it.¹²

At a series of refrigerator temperatures T_b , we made such measurements of frequency as a function field for our aluminum grain-mounted cantilever. We began driving the cantilever in a phase-locked loop as described in 5.2.2. For each measurement, the incident laser power was

¹²We note here that Eq. 6.44 applies exactly only for a long, skinny superconductor oriented with its long axis parallel to the direction of the applied magnetic field. For a superconductor with a realistic shape, demagnetization effects will lead to magnetic flux penetration at a lower applied magnetic field than that given in Eq. 6.44. We do not attempt model these intermediate states in our analysis here.

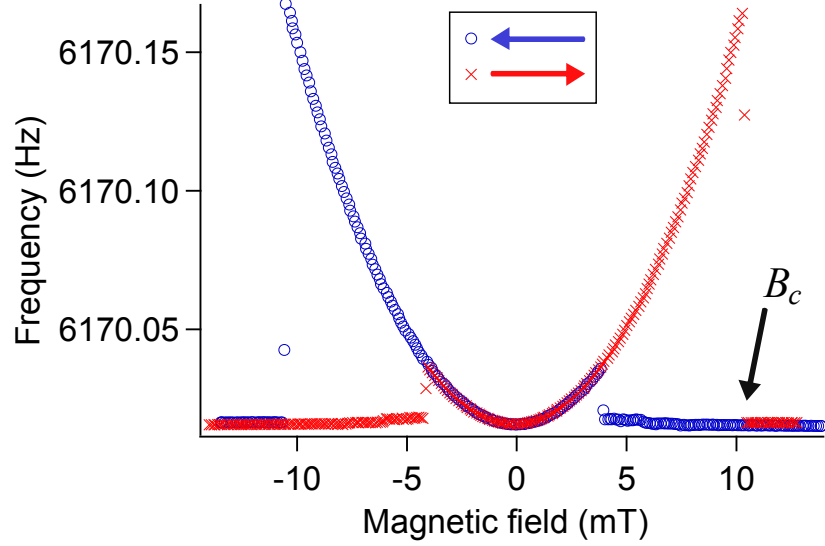


Figure 6.3: Resonant frequency versus magnetic field for the aluminum grain-mounted cantilever. As indicated in the inset, the red X's represent data taken as the magnetic field was swept from negative to positive values (upward), while the blue O's correspond to a sweep in the opposite direction (downward). The transition from the superconducting to the normal state at $B = 11.6$ mT is indicated as B_c in the figure for the upward sweep. The data shown were taken at a refrigerator temperature $T_b = 313$ mK and with an incident laser power of $P_{\text{inc}} = 25$ nW. For both sweeps, the initial magnetic field magnitude was larger than the largest magnetic field values shown in the figure.

$P_{\text{inc}} = 25$ nW. We initialized the system by sweeping the magnetic field well above the critical field B_c . We then swept the magnetic field continuously back through zero and through the critical field with the opposite sign of the initial field. Fig. 6.3 shows two such measurements, one for each direction of magnetic field sweep. As expected, the cantilever frequency exhibits a quadratic dependence on magnetic field near zero field and a sharp transition to independence from B at higher fields. We interpret the region of quadratic magnetic field dependence as the superconducting state and the flat regions as the normal state. In both sweeps, the aluminum grain transitions to the superconducting state well below B_c , exhibiting supercooling [303]. The transition back to the normal state where the frequency drops abruptly is assumed to occur at the critical field B_c .

The magnetic field produced by the solenoid displayed a small amount of hysteresis from sweep to sweep, which offset the frequency curves in B . The hysteresis was corrected for by fitting plots of frequency versus magnetic field with opposite sweep direction to second order polynomials. The data were then shifted so that their minima both located at zero magnetic field (see Fig. 6.3). The critical field B_c was taken to be the average of the observed B_c for the upward and downward sweeps.

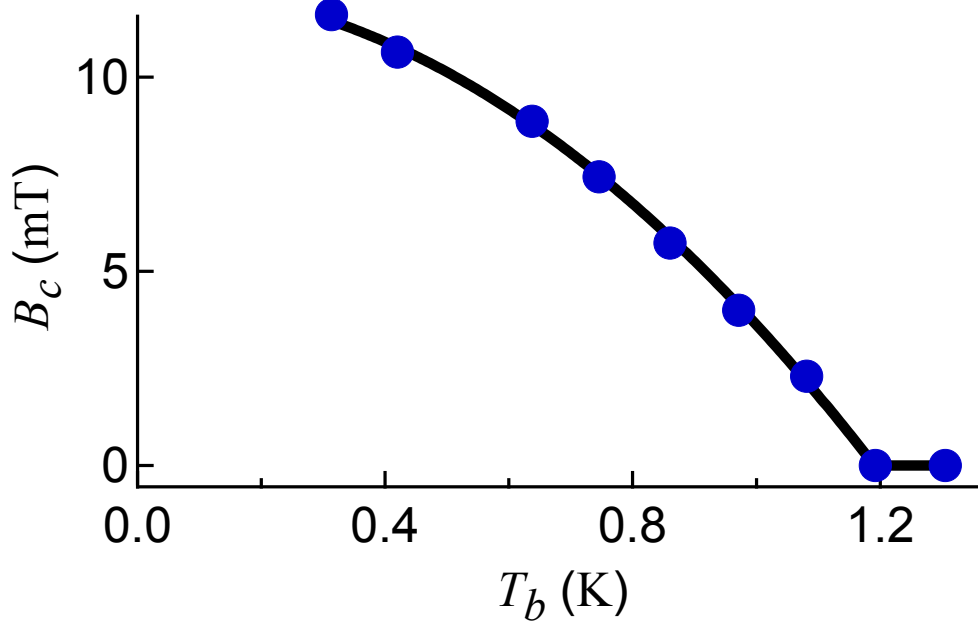


Figure 6.4: Superconducting critical field versus refrigerator temperature. The data points represent critical fields extracted from measurements of the cantilever frequency like the one shown in Fig. 6.3. The curve is a fit to the prediction of the BCS model for the critical field of a superconductor. A discussion of the fit is given in the text.

The measured critical field B_c as a function of refrigerator temperature T_b is shown in Fig. 6.4. These data were then fit to Eq. 6.44 for T_c and $B_c(0)$ using $T_e = T_b$. The fit, shown in Fig. 6.4, produced the values $T_c = 1.19$ K and $B_c(0) = 12.3$ mT. This value of T_c agrees within one percent of the bulk value of 1.18 K, while the critical field is larger than the bulk value of 10.5 mT. The discrepancy from the bulk value for $B_c(0)$ may be due to finite size effects, the grain’s aspherical shape, or trace impurities, each of which can increase $B_c(0)$ without changing the dependence of B_c on temperature [304]. We interpret the excellent match of the functional form of Eq. 6.44 with the data as evidence that the temperature T_e of the aluminum grain at the cantilever tip follows the temperature T_b of the refrigerator down to 313 mK for $P_{\text{inc}} = 25$ nW.

6.4.1.3 Effect of a localized heat source on the cantilever temperature

In order to test our conclusions from the previous sections that the cantilever’s noise temperature T_n and the cantilever’s microscopic temperature T_e could be deduced from measurements of the cantilever Brownian motion $\langle x^2 \rangle$ and the superconducting critical field B_c of the aluminum grain, we tested the effects of a local heat source on the measurements of T_n and T_e . In our case, the detection laser, operated at higher intensity than in the measurements discussed in the previous

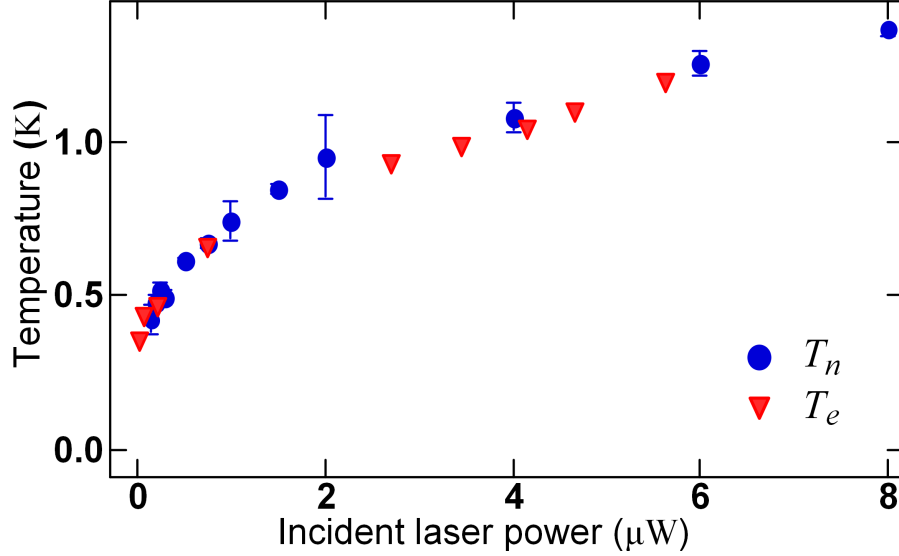


Figure 6.5: Measured cantilever temperature versus incident laser power. Both T_n (blue dots) and T_e (red triangles), found by the method in the text, are plotted against the incident laser power. As was the case for the measurements in the previous sections, the measurements of $\langle x^2 \rangle$ and B_c were performed on different cantilevers on the same chip. Further analysis of this data is given in the text and in Fig. 6.6.

sections, acted as the local heat source through the cantilever’s small but finite absorption of the incident optical power. The detection laser was directed at a point near the cantilever tip so that for appreciable absorbed power the cantilever no longer remains in equilibrium with the temperature T_b of the refrigerator at its base.

For our measurements of both $\langle x^2 \rangle$ and B_c , the laser spot was directed at a point $z_f = 400 \mu\text{m}$ from the cantilever base on the $\sim 500 \mu\text{m}$ long cantilever. The refrigerator was kept at its base temperature of $T_b = 310 \text{ mK}$. At each incident power P_{inc} , the cantilever motion $\langle x^2 \rangle$ was measured and used to infer T_n by inverting the fit from Fig. 6.2. Similarly, the fit in Fig. 6.4 was used to convert the measured values of B_c into T_e . Fig. 6.5 shows the extracted values of T_n and T_e versus the incident laser power.

Given that the silicon of the cantilever is an insulator, we assume that, in the steady state, any heat Q_H introduced to the cantilever at the position of the laser spot must be conducted to the base by phonons. According to Fourier’s law [56], the flow \mathbf{J}_Q of heat per unit time through a cross-section of unit area satisfies

$$\mathbf{J}_Q = -\kappa \nabla T \quad (6.45)$$

where κ is the thermal conductivity. At low temperatures, the phonon thermal conductivity of an

insulator is proportional to the specific heat at constant volume c_v , which itself is proportional to T^3 in the low temperature limit [56]. We write $\kappa = bT^3$. By integrating \mathbf{J}_Q over the cross-section $w \times t$ of the cantilever, we obtain the rate \dot{Q} of total heat transfer through the cantilever. Using z to denote the distance from the cantilever base, the rate of heat transfer out of the cantilever ($-z$ direction) is $\dot{Q}_{\text{out}} = wtbT^3 dT/dz$.

In a material for which the fraction of optical power lost per unit of distance is a constant, we can write the magnitude of optical power as a function of distance z traveled through the material as $P(z) = P(0)e^{-az}$, where a is the coefficient of absorption. For $az \ll 1$, we have $P(z) \approx P(0) - azP(0)$. Therefore, assuming all absorbed optical power is converted into heat, we can write the rate of heat transfer into the thin cantilever as $\dot{Q}_{\text{in}} = atP_{\text{inc}}$.

In the steady state, there is no build up of heat and $\dot{Q}_{\text{in}} = \dot{Q}_{\text{out}}$. For the cantilever, we have $P_{\text{inc}} = (wb/a)T^3 dT/dz$. Integrating this expression from the cantilever base at $z = 0$ to the laser spot at $z = z_f$, we find

$$\begin{aligned} z_f P_{\text{inc}} &= \int_0^{z_f} dz T^3 \frac{dT}{dz} \\ &= \frac{wb}{a} \int_{T_b}^{T_f} dT T^3 \\ &= \frac{wb}{4a} (T_f^4 - T_b^4) \end{aligned}$$

or

$$T_f^4 - T_b^4 = \frac{4az_f}{wb} P_{\text{inc}} \quad (6.46)$$

where T_f is the temperature of the cantilever at the spot of the laser. Since there is no heat sink at the tip of the cantilever, there is no heat flow from the laser spot towards the tip. Eq. 6.45 then requires that the temperature from the laser spot to the tip of the cantilever is constant and equal to T_f .

In Fig. 6.6, we plot $T_e^4 - T_b^4$ against P_{inc} using the data shown in Fig. 6.5. The Arrow cantilevers are doped such that their resistivity is specified to be on the order of $0.025 \Omega \text{ cm}$. This resistivity corresponds to a doping concentration of $\sim 1 - 2 \times 10^{18} \text{ cm}^{-3}$ [305]. For a similar doping concentration, the absorption coefficient of silicon has been measured to be $\sim 20 \text{ cm}^{-1}$ at 4 K [299]. Using this value along with $z_f = 400 \mu\text{m}$ and $w = 100 \mu\text{m}$, we fit the data to Eq. 6.46 and extract $b = 0.13 \text{ W K}^{-4} \text{ m}^{-1}$. This value is a factor of four smaller than that found previously in similarly

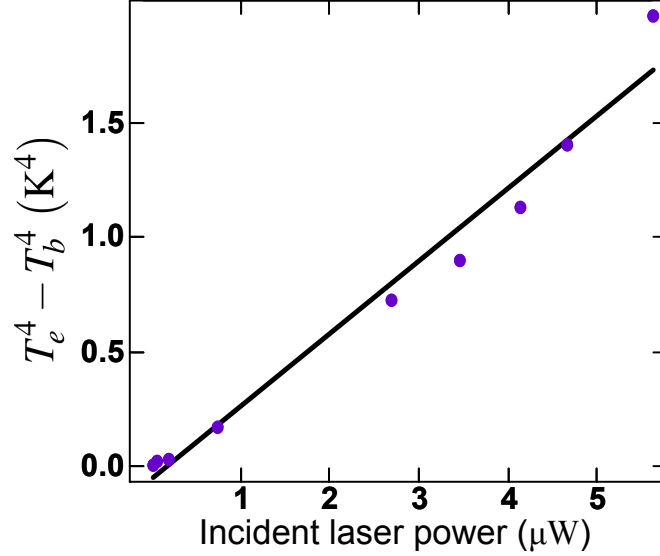


Figure 6.6: Comparison of observed cantilever heating to a phonon thermal conductivity model. We plot $T_e^4 - T_b^4$ against P_{inc} , in order to compare our data with Eq. 6.46 which predicts the two quantities to be proportional to each other. We fit the data to Eq. 6.46 with b as the only free parameter, obtaining $b = 0.13 \text{ W K}^{-4}\text{m}^{-1}$ as described in the text.

doped silicon [298, 306]. This discrepancy could be due to uncertainty in the exact doping level of the cantilever and also to finite size effects. We note that if the thermal conductivity coefficient b can be measured independently that the analysis performed here gives a direct measure of the absorption coefficient a . Usually a is deduced from measurements of optical transmission and reflection which do not distinguish between loss due to absorption and loss due to diffusive scattering.

We do not analyze the data for T_n because unlike T_e this quantity depends on the temperature of the entire cantilever, which is no longer a constant. We note, however, that in Fig. 6.5 T_e and T_n display a similar dependence on P_{inc} . This agreement between T_e and T_n can be explained by the fact that when $T_f \gtrsim 2T_b$ most of the drop temperature in temperature along the cantilever is located near to the cantilever base.¹³ Additionally, as noted above, the portion of the cantilever from the laser spot to the cantilever tip is at a constant temperature. Thus, the portion of the cantilever from its midpoint to its tip, the section responsible for most of the cantilever displacement, is at a fairly constant temperature. Since the laser spot was located at the same distance z_f for both the measurements of T_n and T_e , the temperature T_f at z_f should be the same for a given P_{inc} in both measurements. Thus, it is reasonable that these inferred temperatures are in agreement.

¹³This can be seen by replacing T_f and z_f by $T(z)$ and z in Eq. 6.46 and plotting $T(z)$.

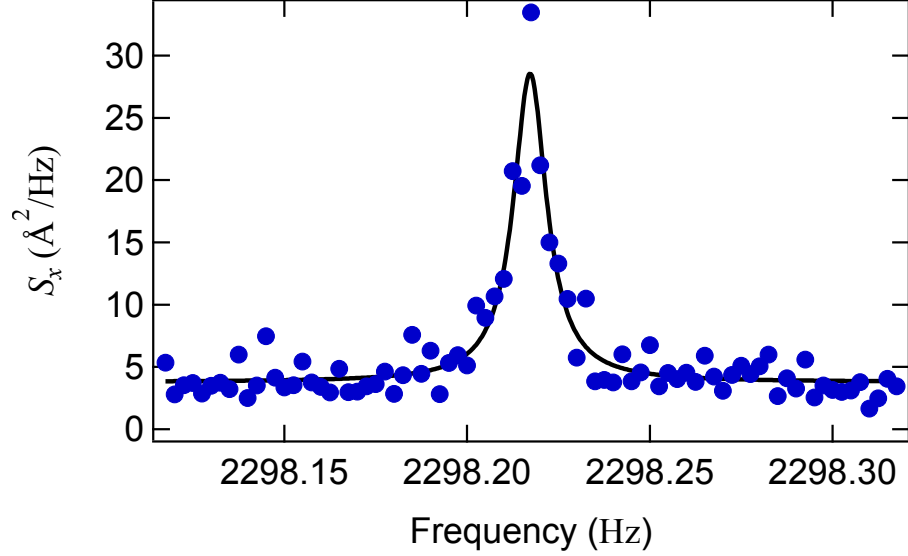


Figure 6.7: Power spectral density of cantilever displacement for sample CL14. The figure shows the power spectral density S_x obtained by the method described in 6.4.1.1 as well as a fit to Eq. 6.43. The results of the fit are discussed in the text. This data was taken with the Bragg reflector set-up with an incident laser power of $P_{\text{inc}} = 1.9 \text{ nW}$. The background noise level corresponds to a noise equivalent power of $0.29 \text{ pW}/\sqrt{\text{Hz}}$ for the photoreceiver-amplifier package.

6.5 Characterization of uncertainty in measurement of persistent current samples

We conclude this chapter by presenting data from a few different measurements characterizing the persistent current sensitivity \mathcal{S}_{pc} of the cantilevers used for the measurements discussed in this text. The parameters of these samples are collected in Tables 7.1 and 7.2.

In Fig. 6.7, the power spectral density S_x of cantilever displacement, obtained by the method outlined in 6.4.1.1, is shown for sample CL14. Also shown is a fit to the form of S_x given above in Eq. 6.43 for a white thermal noise force. The extracted best fit coefficients are $\langle x^2 \rangle = 2.5 \times 10^{-19} \text{ m}^2/\text{Hz}$, $f_0 = 2298.217 \text{ Hz}$, $Q = 2.1 \times 10^5$, and $S_{x,\text{int}} = 3.8 \times 10^{-20} \text{ m}^2/\text{Hz}$. Using the spring constant $k = 1.08 \times 10^{-3} \text{ N/m}$ deduced from the cantilever's dimensions, the equipartition theorem (Eq. 6.1) gives a cantilever noise temperature of $T_n = k\langle x^2 \rangle/k_B = 334 \text{ mK}$, in close agreement with the refrigerator temperature of $T_b = 323 \text{ mK}$, which was the base temperature for this set of persistent current measurements. Thus we see that T_n tracks T_b down to the base temperature of the refrigerator and that the thermal contribution dominates the force noise acting on the cantilevers used in the persistent current measurements.

In the next two figures, we display another characterization of the cantilever's thermal motion, this time measured while the cantilever was subjected to an external driving force. In the measurement discussed above, the cantilever was not subjected to an external driving force. In order to describe this measurement, we use the quadrature notation introduced in Eqs. 6.13 and 6.14. We alter the notation slightly to write the cantilever tip displacement $x(t)$ as

$$\begin{aligned} x(t) &= x_{\max}(t) \cos(\omega t + \phi(t)) \\ &= x_1(t) \cos \omega t + x_2(t) \sin \omega t. \end{aligned} \tag{6.47}$$

For $x \ll \lambda/2\pi$, the photodetector voltage is proportional to x , as explained in 5.3.1.4. In this case, the quadratures measured by lock-in 2 in Fig. 5.6 are proportional to x_1 and x_2 . The conversion from lock-in voltage to cantilever tip displacement was given in section 5.3.1.4.

We measured the quadratures x_1 and x_2 while driving the cantilever to a series small amplitudes $x_{\max} \ll \lambda/2\pi$. For these measurements, lock-in 2 was not operated in a phase-locked loop and instead took its reference from a stabilized clock signal at the frequency measured to be the cantilever's resonant frequency just before the measurement began.¹⁴ The measured quadratures for drives between 0 and 3 nm are shown for sample CL14 in Fig. 6.8.

When the lock-in's time constant is much less than the ringdown time τ of the cantilever, the timescale over which the cantilever amplitude can change appreciably, the lock-in voltage provides a real-time estimate of $x_1(t)$ and $x_2(t)$. By measuring x_1 and x_2 many times over a time span $t_M \gg \tau$, a statistically significant sample size of the random component of the cantilever's motion can be gathered. For CL14, the ringdown time τ was approximately 30 s. The data in Fig. 6.8 was taken with a lock-in time constant of 100 ms. At each value of the piezo driving voltage, the quadratures x_1 and x_2 were recorded approximately every 5 s over a 2000 s measurement time.

Because the cantilever equation of motion, Eq. 4.4, is linear, we can write $x_i(t) = x_{i,D} + x_{i,N}(t)$ for $i = 1, 2$ where $x_{i,D}$ is the quadrature amplitude due to the external resonant driving force which is constant in time and $x_{i,N}(t)$ is the quadrature amplitude due to the white fluctuating noise force. The time average of the quadrature amplitudes is $\langle x_i \rangle = x_{i,D}$. The standard deviation $\sigma(x_i)$ of the

¹⁴The clock signal is provided by an arbitrary waveform generator (33220A 20 MHz Function / Arbitrary Waveform Generator, Agilent, Santa Clara, CA) which is stabilized by the 10 MHz clock output of the frequency counter described in 5.2.2.5.

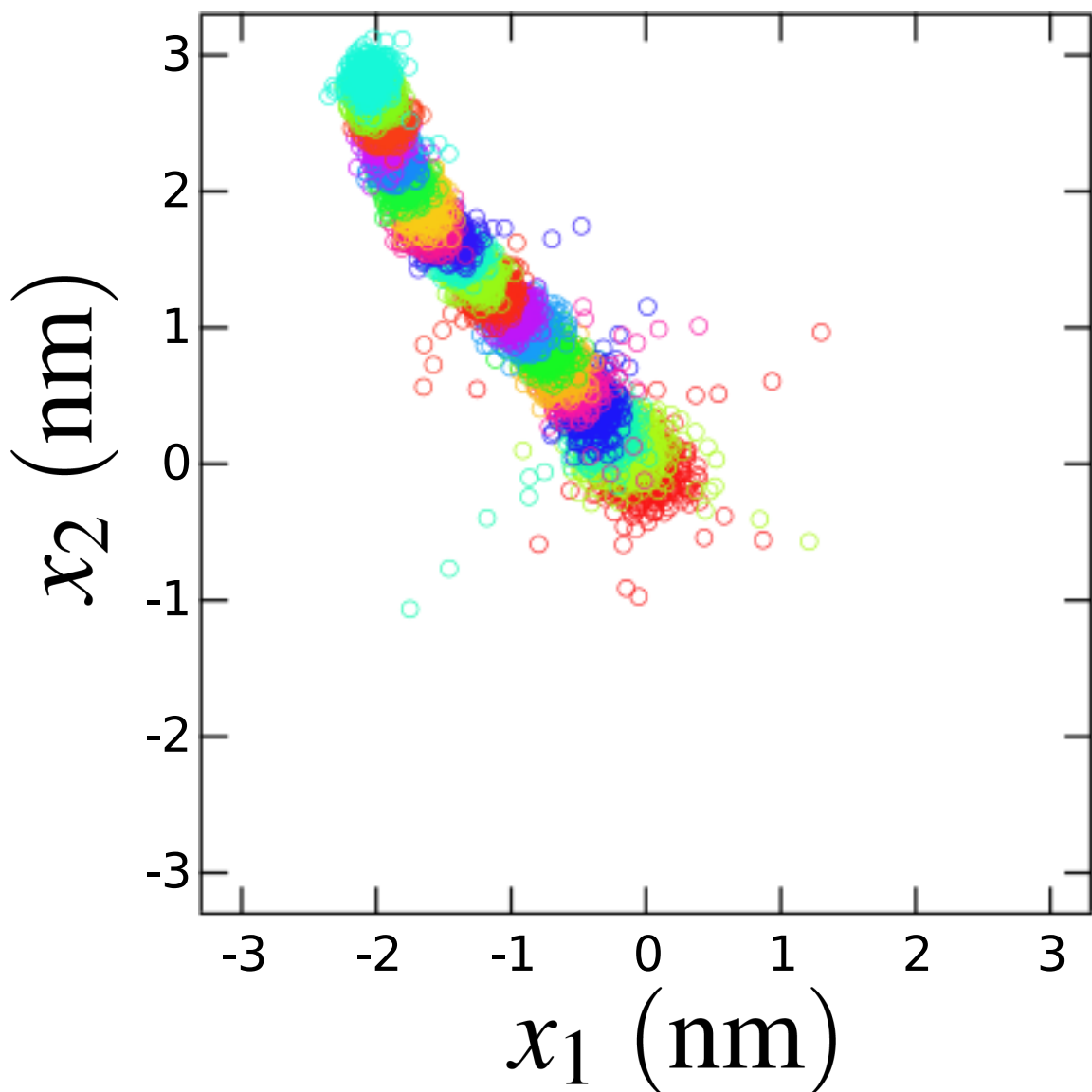


Figure 6.8: Quadratures of cantilever motion at a series of amplitudes of motion. Data points represent values of x_1 and x_2 measured by the method described in the text for sample CL14 at $T = 323$ mK. The quadratures were measured at a series of piezo drive voltages. Different values of the driving voltage are indicated by differently colored data points in the figure. The driving voltage was stepped to produce roughly 0.18 nm increments in the mean amplitude $\langle x_{\max} \rangle$. At each drive setting, 400 data points were taken at approximately 5 s intervals. A linear relationship between x_1 and x_2 is expected for a constant drive frequency. The slope of this line is related to the phase between the piezo drive voltage and the cantilever motion, but extra phase shifts in the measurement chain make the exact value of this phase uninteresting. Deviations from the linear relationship indicate a change in this phase and are likely due to the temporal drift of the cantilever's resonant frequency (see Fig. 5.14) which is not monitored during the measurement. As expected, the scatter about $(\langle x_1 \rangle, \langle x_2 \rangle)$ is uniform and independent of $\langle x_{\max} \rangle$.

quadrature amplitudes over time is given by

$$\begin{aligned}\sigma^2(x_i) &= \langle (x_i - \langle x_i \rangle)^2 \rangle \\ &= \langle x_{i,N}^2 \rangle.\end{aligned}$$

Since the $x_{i,N}$ are random and result from a white noise force with no special phase reference, we can take $\langle x_{i,N}^2 \rangle = \langle x_{1,N}^2 \rangle = \langle x_{2,N}^2 \rangle$. It appears that the noise source producing the scatter in Fig. 6.8 has no phase reference since the data set associated with each cantilever amplitude appears to have the same width in x_1 as in x_2 .

To discuss the total scatter of the cantilever amplitude, it is convenient to model the cantilever amplitude as a two component vector $\vec{x}_{\max} = x_1 \hat{i} + x_2 \hat{j}$. We have already done this to some extent by plotting the quadrature amplitudes together in the $x_1 x_2$ -plane in Fig. 6.8. From the two lines in Eq. 6.47, we can write

$$\begin{aligned}x_1 &= x_{\max} \cos \phi \\ x_2 &= -x_{\max} \sin \phi\end{aligned}$$

from which it follows that

$$x_{\max}^2 = x_1^2 + x_2^2.$$

Thus, the vectorial notation is justified as $|\vec{x}_{\max}| = x_{\max}$. With this \vec{x}_{\max} , we can define the time averages

$$\begin{aligned}\langle \vec{x}_{\max} \rangle &= \langle x_1 \rangle \hat{i} + \langle x_2 \rangle \hat{j} \\ &= x_{1,D} \hat{i} + x_{2,D} \hat{j}\end{aligned}$$

and

$$\begin{aligned}\langle x_{\max} \rangle &= |\langle \vec{x}_{\max} \rangle| \\ &= \sqrt{\langle x_1 \rangle^2 + \langle x_2 \rangle^2} \\ &= \sqrt{x_{1,D}^2 + x_{2,D}^2}.\end{aligned}$$

We can also define the typical size $\sigma(x_{\max})$ of the fluctuations of \vec{x}_{\max} by

$$\begin{aligned}\sigma^2(x_{\max}) &= \left\langle |\vec{x}_{\max} - \langle \vec{x}_{\max} \rangle|^2 \right\rangle \\ &= \left\langle |x_{1,N}\hat{i} + x_{2,N}\hat{j}|^2 \right\rangle \\ &= \sigma^2(x_1) + \sigma^2(x_2).\end{aligned}\tag{6.48}$$

In the absence of external drive, we have

$$\begin{aligned}\langle x^2 \rangle &= \langle x_{\max}^2 \rangle / 2 \\ &= \sigma^2(x_{\max}) / 2.\end{aligned}$$

Thus, by the Equipartition theorem, we have $\sigma(x_{\max}) = \sqrt{2\langle x^2 \rangle} = \sqrt{2k_B T/k}$. Since the driving voltage introduces a negligible force noise compared to the thermal force noise (see 6.2), the typical deviation $\sigma(x_{\max})$ from the mean amplitude vector $\langle \vec{x}_{\max} \rangle$ should be independent of amplitude $\langle x_{\max} \rangle$.

In Fig. 6.9, we plot $\sigma(x_{\max})$ for each set of quadrature data shown in Fig. 6.8 as a function of the mean amplitude $\langle x_{\max} \rangle$ associated with that set. We also mark $\sigma(x_{\max}) = 3.5 \times 10^{-9}$ nm, the value of the thermal limit expected for $T = 323$ mK and $k = 1.08 \times 10^{-3}$ N/m. Over most of the range of amplitudes, $\sigma(x_{\max})$ is close to the thermal limit, indicating that the piezo drive of the cantilever does not introduce any additional force noise. The larger magnitude of $\sigma(x_{\max})$ at low drive is not understood.

Finally, in Fig. 6.10, we present a measurement of the noise σ_f in the frequency measurement as a function of cantilever amplitude x_{\max} . The data shown in the figure were taken from measurements on sample CL17 of Table 7.1. For this measurement, the cantilever was driven in a phase-locked loop, and the driving voltage to the piezo was stepped in small increments so that the amplitude of motion observed by the fiber $x_{f,\max}$ spanned the full range of the first peak of $J_1(4\pi x_{f,\max}/\lambda)$ (see Eq. 5.4 describing the interferometer response). At each drive amplitude, the cantilever frequency was measured twenty times using the frequency counter with a gate time of $\tau_M = 5$ s.¹⁵ The data

¹⁵The data shown in Fig. 6.10 were taken during a measurement like the one shown in Fig. 7.11, which plots the frequency shift versus cantilever amplitude. At each cantilever amplitude, the frequency was measured twenty times and averaged for Fig. 7.11. The standard deviation of those frequency measurements was calculated for Fig. 6.10. I note this fact to point out that the data shown in Fig. 6.10 was taken from a measurement primarily intended to measure the persistent current, not to characterize the measurement uncertainty. Some parameters in the analysis below, namely $S_{P,\text{int}}$, R_c , and Q , were inferred by me from other measurements taken at about the same time as the

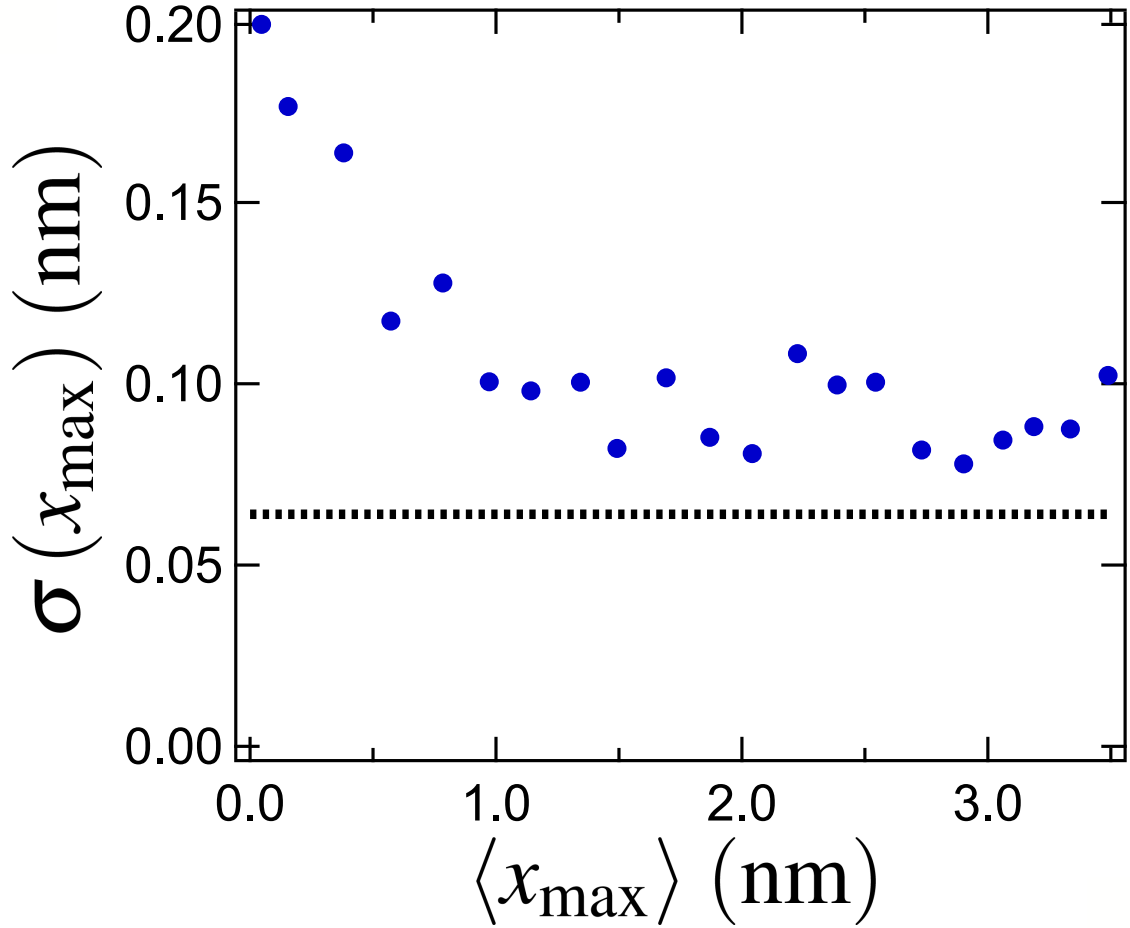


Figure 6.9: Standard deviation $\sigma(x_{\max})$ of cantilever amplitude versus mean cantilever amplitude $\langle x_{\max} \rangle$. The data points represent the values of $\sigma(x_{\max})$ calculated from the data in Fig. 6.8 with Eq. 6.48 plotted against the corresponding values of $\langle x_{\max} \rangle = \sqrt{\langle x_1 \rangle^2 + \langle x_2 \rangle^2}$ for each piezo drive setting. The dashed line indicates $\sigma(x_{\max}) = \sqrt{2k_B T/k}$ for measured temperature $T = 323$ mK and estimated spring constant $k = 1.08 \times 10^{-3}$ N/m of sample CL14.

shown (circles) in Fig. 6.10 represents the standard deviation of each of these twenty frequency measurements.

Fig. 6.10 also displays curves representing the frequency scatter expected from noise in the interferometric measurement and from thermal force noise. Using Eq. 6.31, we write the standard deviation of the frequency measurement due to the noise of the interferometric measurement as

The curves distinguish three contributions to the total frequency uncertainty $\sigma_{f,\text{tot}}$ given in Eq. 6.34: the typical fluctuation $\sigma_{f,\text{cant}}(S_{P,\text{int}} = 0)$ of the cantilever's frequency of motion in the absence of detector noise given by

$$\begin{aligned}\sigma_{f,\text{cant}}^2(S_{P,\text{int}} = 0) &= \frac{f_0^2}{4\tau_M} \frac{S_{F,\text{th}}}{(kx_{\text{max}})^2} \left(1 - \frac{1}{\alpha_F} (1 - \exp(-\alpha_F))\right) \\ &= \frac{1}{2\pi\tau_M} \frac{k_B T f_0}{Q k x_{\text{max}}^2} \left(1 - \frac{1}{\alpha_F} (1 - \exp(-\alpha_F))\right),\end{aligned}\quad (6.49)$$

the typical fluctuation $\sigma_{f,\text{cant}}(T = 0)$ of the cantilever's frequency of motion in the absence of the thermal noise force given by

$$\sigma_{f,\text{cant}}^2(T = 0) = \frac{f_0^2}{4\tau_M} \frac{S_{P,\text{int}}}{Q^2 (R(x_{\text{max}}) x_{\text{max}})^2} \left(1 - \frac{1}{\alpha_F} (1 - \exp(-\alpha_F))\right),\quad (6.50)$$

and the typical fluctuation $\sigma_{f,\text{int}}$ in the measured frequency due to noise in the interferometer signal given by

$$\sigma_{f,\text{int}}^2 = \frac{1}{4\pi^2} \frac{\alpha_F}{\tau_M^3} \frac{S_{P,\text{int}}}{(R(x_{\text{max}}) x_{\text{max}})^2} (1 - \exp(-\alpha_F)).\quad (6.51)$$

The total frequency uncertainty can be written as

$$\sigma_{f,\text{tot}} = \sqrt{\sigma_{f,\text{cant}}^2(S_{P,\text{int}} = 0) + \sigma_{f,\text{cant}}^2(T = 0) + \sigma_{f,\text{int}}^2}.\quad (6.52)$$

In these definitions, we have used $\alpha_F = \tau_F/\tau_M$ as was done in Section 6.2. In addition to the dimensions, spring constant and resonant frequency given for sample CL17 in Table 7.1, we use the observed parameters of $Q = 1.1 \times 10^5$, $P_{\text{inc}} = 24 \text{ nW}$, $R_f = .23$, $R_c = 0.009$, $\epsilon \approx 6.7 \times 10^{-3} \text{ nm}^{-1}$, $S_{P,\text{int}} = 0.29 \text{ pW}/\sqrt{\text{Hz}}$ and $U = U_1(249/449) = 0.40$ and $T = 323 \text{ mK}$ to plot the various contributions to the frequency uncertainty. Curves representing $\sigma_{f,\text{cant}}(S_{P,\text{int}} = 0)$, $\sigma_{f,\text{cant}}(T = 0)$, and $\sigma_{f,\text{int}}$ are each plotted assuming ideal filtering for which $\alpha_F = 1$. The measured frequency scatter measurement shown in Fig. 6.10. If these parameters had changed over time from the values I used, some systematic uncertainty would be introduced to the analysis. It is unlikely that any of these parameters would change by much more than a factor of 4.

σ_f is much larger than any of these curves and seems to agree with the total frequency uncertainty $\sigma_{f,\text{tot}}$ calculated using the above parameters and $\alpha_F = 150$. The total frequency uncertainty $\sigma_{f,\text{tot}}$ calculated for $\alpha_F = 150$ is ~ 10 times larger than the curve of $\sigma_{f,\text{tot}}$ found by assuming $\alpha_F = 1$.

The observed $35 \mu\text{Hz}$ minimum for σ_f was typical of all samples in Table 7.1. The measurement shown in Fig. 6.10 was performed with the fiber $z_f = 249 \mu\text{m}$ from the base of the $449 \mu\text{m}$ long cantilever. For most persistent current measurements discussed in this text, the fiber was positioned closer to the cantilever tip. This positioning results in a larger value for U and thus rescales the dependence of $\sigma_{f,\text{int}}$ and $\sigma_{f,\text{cant}}(T = 0)$ on x_{max} . The net effect of this rescaling is that the values of x_{max} indicated in Fig.6.10 are divided by ~ 2 for $\sigma_{f,\text{int}}$ and $\sigma_{f,\text{cant}}(T = 0)$. The dependence of the measured σ_f on x_{max} obeyed a similar rescaling with fiber position, with the relatively flat region of σ_f occurring between $x_{\text{max}} \approx 100 \text{ nm}$ and $x_{\text{max}} \approx 500 \text{ nm}$ (rather than between 200 nm and $1 \mu\text{m}$ as in Fig. 6.10). During the persistent current measurements, the cantilever amplitude x_{max} was on the order of $0.1 \mu\text{m}$, where the observed $\sigma_f \approx 35 \mu\text{Hz}$ was only a factor of ~ 3 larger than the expected magnitude of $\sigma_{f,\text{cant}}(S_{P,\text{int}} = 0)$, the contribution due to thermal force noise. Further study is necessary to understand the deviation of σ_f from the expected value in Fig. 6.10.¹⁶ However, the observed σ_f was sufficiently low to measure persistent currents with a signal to noise ratio over 30. These measurements will be discussed in the next chapter.

¹⁶Such study has been undertaken by my successors in the Harris Lab. In preliminary analysis, the transition of $\sigma_{f,\text{tot}}$ from the regime dominated by $\sigma_{f,\text{int}}$ to that dominated by $\sigma_{f,\text{cant}}(S_{P,\text{int}} = 0)$ (the thermally limited frequency uncertainty) has been observed by changing the measurement time τ_M . These measurements were performed on thinner, shorter cantilevers than those listed in Table 7.1. Decreasing the cantilever thickness increases $\sigma_{f,\text{cant}}(S_{P,\text{int}} = 0)$ while decreasing $\sigma_{f,\text{cant}}(T = 0)$ and leaving $\sigma_{f,\text{int}}$ unchanged and thus overall increases the relative importance of the $\sigma_{f,\text{cant}}(S_{P,\text{int}} = 0)$ contribution. Additionally, the shorter cantilevers had higher frequencies and lower quality factors and ringdown times. Consequently shorter measurement times, necessary to observe the cross-over from $\sigma_{f,\text{int}}$ to $\sigma_{f,\text{cant}}(S_{P,\text{int}} = 0)$, were possible. For these measurements, α_F was found to be ~ 1 . Thermally limited frequency uncertainty was also observed for cantilevers with lengths similar to those in Table 7.1 (but with $t = 110 \text{ nm}$).

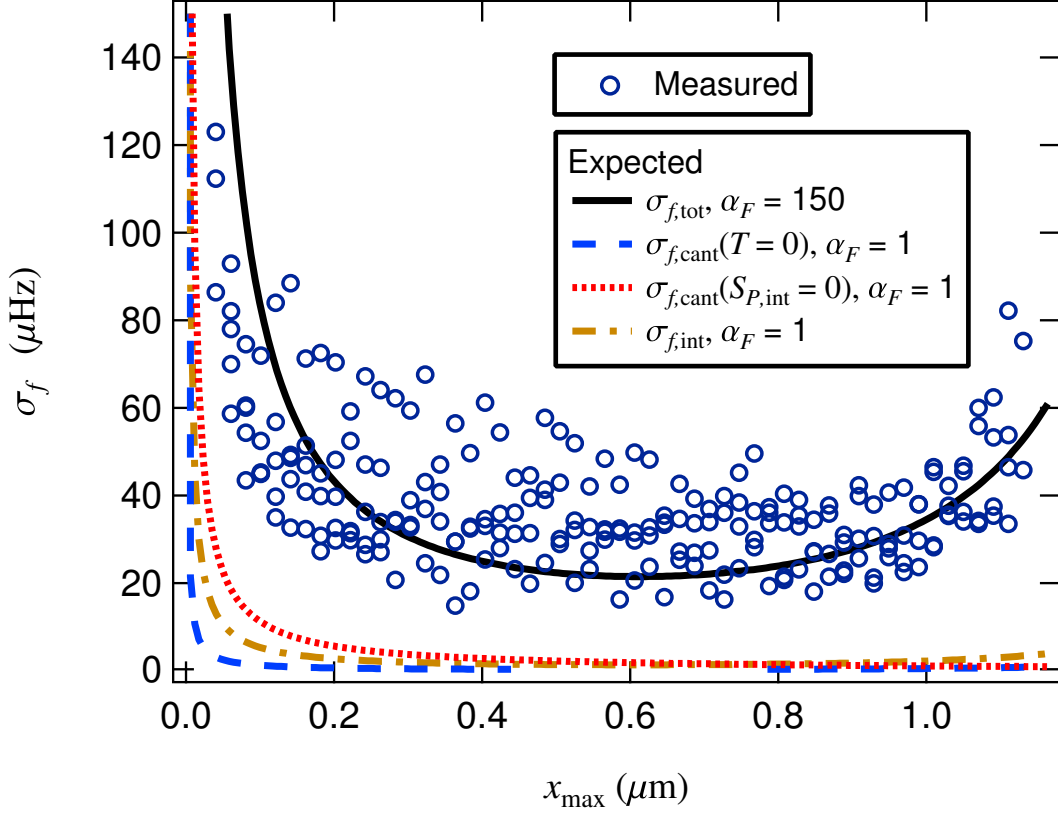


Figure 6.10: Measured frequency scatter as a function of cantilever amplitude. The measured σ_f data points (circles) represent the standard deviations of the cantilever frequency calculated from sets of twenty measurements taken at each value of the cantilever amplitude x_{\max} . The curves represent the expected frequency uncertainty calculated from Eqs. 6.49 through 6.52. For the parameters given in the text and $\alpha_F = 1$, it is expected that $\sigma_{f,\text{tot}}$ will be dominated by the thermal contribution $\sigma_{f,\text{cant}}(S_{P,\text{int}} = 0)$ except at the highest drives where the response of the interferometer drops to zero and the frequency uncertainty $\sigma_{f,\text{int}}$ added during the measurement by noise in the interferometer dominates. The contribution $\sigma_{f,\text{cant}}(T = 0)$ scales with x_{\max} in the same way as $\sigma_{f,\text{int}}$ and is smaller than $\sigma_{f,\text{int}}$ by a factor of ~ 4 for set of parameters given in the text and $\alpha_F = 1$. Also shown for reference is a curve of the expected $\sigma_{f,\text{tot}}$ for $\alpha_F = 150$. This curve, which is dominated by the $\sigma_{f,\text{int}}$ contribution, matches the data better the curves for $\alpha_F = 1$ and is ~ 10 times larger than $\sigma_{f,\text{tot}}(\alpha_F = 1)$.

Chapter 7

Data from and analysis of persistent current measurements

In this chapter, we first outline the procedure used to convert the measured trace of cantilever frequency versus magnetic field into persistent current versus magnetic field and then present the results of measurements of persistent currents in four different samples.

7.1 Signal processing of the measured cantilever frequency shift

7.1.1 Description of signal processing

In 4.4, we found that a persistent current signal of the form

$$I(B) = \text{Im} \left[\sum_p I_p e^{2\pi i p \beta_1 B} e^{i\psi_p} \right] \quad (7.1)$$

led to a cantilever frequency shift

$$\Delta f(B) = \text{Im} \left[FB^2 \sum_p 2\pi i p \beta_1 I_p e^{2\pi i p \beta_1 B} e^{i\psi_p} \text{jinc}(2\pi p \beta_1 GB) \right]. \quad (7.2)$$

In the preceding lines we have rewritten Eqs. 4.14 and 4.26 with $\beta_1 = A \sin \theta_0 / \phi_0$,

$$F = -\sqrt{N} \frac{f_0}{2k} \left(\frac{\alpha}{l} \right)^2 \frac{A \cos^2 \theta_0}{\sin \theta_0},$$

and $G = \alpha x_{\max} / l \tan \theta_0$. The quantity β_1 is the magnetic field frequency whose period corresponds to a magnetic flux of ϕ_0 threading a ring of area A lying on a plane at an angle θ_0 relative to the applied magnetic field B (see Figs. 4.2 and 4.3 for more clarification). If the applied magnetic field were threaded entirely through the ring's hole, the persistent current oscillation would possess non-zero coefficients I_p only for magnetic field frequencies $p\beta_1$ with p an integer. As described in 2.3.2.1, the magnetic field penetrating the metal of the ring introduces a finite range of correlation to the persistent current oscillation. This finite correlation broadens the peaks in the magnetic field frequency spectrum around each $p\beta_1$, allowing the coefficients I_p to be non-zero even for non-integer p . In the definition of F , we have included a factor of \sqrt{N} , where N is the number of rings on the cantilever. Following the discussion of 2.3, we expect that the amplitude I_p should vary randomly from ring to ring. Due to the finite magnetic field correlation, the phase ψ_p should also grow stochastically with applied field and be random for the values of magnetic applied in the measurements discussed below. Thus the amplitude of the total current in the array should be random with a typical magnitude \sqrt{N} larger than that of a single ring. Because of the inclusion of the \sqrt{N} factor in F , all quantities derived below representing current are scaled to correspond to the typical single ring current.

In the limit of small cantilever amplitude ($\beta_1 GB \ll 1$ for the range of B of interest), the jinc term is approximately unity, and the p^{th} complex Fourier coefficient $I_p e^{i\psi_p}$ of the persistent current is proportional to the p^{th} complex Fourier coefficient of $\Delta f(B) / B^2$. At finite cantilever amplitude, inference of the persistent current $I(B)$ from the cantilever frequency shift $\Delta f(B)$ is complicated by the $\text{jinc}(2\pi p \beta_1 GB)$ term, which depends on both the Fourier transform index p and the magnetic field B . We will now discuss two methods, which we will refer to as method A and method B, for estimating the persistent current $I(B)$ from the frequency shift $\Delta f(B)$ measured at finite cantilever amplitude.

For method A, we scale the entire trace $\Delta f(B)$ by a different function of B and p for each value of the index p and then infer the p^{th} component I_p from the Fourier transform of this scaled trace. Specifically, for a set of $M + 1$ measurements of $\Delta f(B)$ taken at regular intervals $\Delta B =$

$(B_{\max} - B_{\min})/M$ between B_{\min} and B_{\max} (with $B_{\max} > B_{\min} > 0$), we calculate

$$dI_p^A = \frac{1}{B_{\max} - B_{\min}} \sum_{n=0}^M \Delta B \frac{\Delta f(B_{\min} + n\Delta B)}{F(B_{\min} + n\Delta B)^2 \text{jinc}(2\pi p\beta_1 G(B_{\min} + n\Delta B))} e^{-2\pi i p\beta_1 (B_{\min} + n\Delta B)}, \quad (7.3)$$

which is the discrete form of the Fourier transform

$$\frac{1}{B_{\max} - B_{\min}} \int_{B_{\min}}^{B_{\max}} dB \frac{\Delta f(B)}{FB^2 \text{jinc}(2\pi p\beta_1 GB)} e^{-2\pi i p\beta_1 B}.$$

For $p\beta_1 GB_{\max} \lesssim 0.4$ for which the jinc function in the denominator does not pass through zero (see Fig. 4.5) and for $B_{\max} - B_{\min} \gg 1/p\beta_1$ (with all the usual caveats related to Fourier transform windowing and the Nyquist-Shannon sampling theorem), the coefficient dI_p^A satisfies

$$dI_p^A \approx 2\pi i p\beta_1 I_p e^{i\psi_p},$$

and thus we can define the approximate derivative of the current obtained by method A:

$$\begin{aligned} \frac{\partial I^A}{\partial B} &= \text{Im} \left[\sum_p dI_p^A e^{2\pi i p\beta_1 B} \right] \\ &\approx \text{Im} \left[\sum_p 2\pi i p\beta_1 I_p e^{2\pi i p\beta_1 B} e^{i\psi_p} \right] \\ &\approx \frac{\partial I}{\partial B}. \end{aligned}$$

Finally, we can numerically integrate $\partial I^A/\partial B$ with respect to B to obtain $I^A(B)$, the trace of persistent current versus magnetic field as estimated from $\Delta f(B)$ by method A.

Now we describe method B. The major difference between method A and method B is that in method B the trace $\Delta f(B)$ is scaled by a single function when performing Fourier analysis (rather than scaling $\Delta f(B)$ by a different function for each Fourier index p as was in done in method A). For method B, the trace $\Delta f(B)$ is divided by $FB^2 \text{jinc}(2\pi\beta_1 GB)$. In method A, this factor is used to convert from $\Delta f(B)$ to $\partial I/\partial B$ for $p = 1$ (i.e. for magnetic field frequency $\beta = \beta_1$). As with the definition of dI_p^A in method A, we define the coefficient

$$dI_p^B = \frac{1}{B_{\max} - B_{\min}} \sum_{n=0}^M \Delta B \frac{\Delta f(B_{\min} + n\Delta B)}{F(B_{\min} + n\Delta B)^2 \text{jinc}(2\pi\beta_1 G(B_{\min} + n\Delta B))} e^{-2\pi i p\beta_1 (B_{\min} + n\Delta B)}$$

and then the inverse Fourier transform integral

$$\frac{\partial I^B}{\partial B} = \text{Im} \left[\sum_p dI_p^B e^{2\pi i p \beta_1 B} \right].$$

We write these expressions simply to mirror the presentation of method A given above. Because $\Delta f(B)$ is scaled by the same function for all p when calculating dI_p^B , we can also write

$$\frac{\partial I^B}{\partial B} = \frac{\Delta f(B)}{FB^2 \text{jinc}(2\pi\beta_1 GB)}.$$

When the only contribution to $\Delta f(B)$ is from a persistent current oscillation $I(B)$ with frequency components close to β_1 , we have

$$\frac{\partial I^B}{\partial B} \approx \frac{\partial I}{\partial B}.$$

As with method A, we can numerically integrate $\partial_B I^B$ to obtain I^B .

The preceding steps are adequate for a measurement free from noise and systematic error. In practice, it is necessary to remove a smooth background from the $\Delta f(B)$ trace found by using either a polynomial fit or a smoothing function prior to finding I^A or I^B . A second background subtraction is often desirable as a final step to remove low frequency drift caused by the interaction of the integration of $\partial_B I$ with the noise in the $\Delta f(B)$ trace (i.e. the remaining low frequency noise that was not removed by the first background subtraction step).

Typically, method A gives a more accurate estimation of the persistent current than method B. However, the argument of the jinc function in the denominator of the expression (Eq. 7.3) defining dI_p^A will go to zero for some values of the Fourier index p which we call p_{zero} . Since the first zero of the $\text{jinc}(x)$ is at $x \approx 2\pi \times 0.61$,

$$p_{\text{zero}} \approx \frac{0.61}{\beta_1 GB_{\text{min}}} \quad (7.4)$$

where B_{min} is the minimum magnitude of the magnetic field in the trace being analyzed. For p near these p_{zero} , the coefficients dI_p^A become unrealistically large. The reason for this behavior is that for the chosen cantilever amplitude x_{max} (contained in the factor G) the cantilever frequency shift Δf is simply not sensitive to the components p of the persistent current near these p_{zero} (as can be seen from Eq. 7.2 or Fig. 4.5).

In order to avoid introducing a large component to the persistent current with magnetic field

frequency

$$\begin{aligned}\beta_{\text{zero}} &= p_{\text{zero}}\beta_1 \\ &= \frac{0.61}{GB_{\text{min}}},\end{aligned}\tag{7.5}$$

we set all of the dI_p^A coefficients with $p \geq p_{\text{zero}}$ to zero before finding $\partial_B I^A$. This procedure is essentially a strong low-pass filtering of the data. All of the data discussed below was analyzed in this way. However, we also analyzed the data using method B which, though slightly less accurate, requires less processing of the data. In this way, we verified that the persistent current inferred by method A did not introduce or remove any significant features to the persistent current trace $I^A(B)$ which were not present in the frequency shift trace $\Delta f(B)$.

For most of the measurements of samples CL11 and CL15 at $\theta_0 = 6^\circ$ and sample CL14 at 45° , the lowest p_{zero} was close to $p = 2$. Thus these measurements were not sensitive to the $h/2e$ component of the persistent current oscillation. For these combinations of sample and angle, we also performed measurements at reduced cantilever amplitudes and found no evidence of the second harmonic of the persistent current signal within the uncertainty of our measurement. This result was not surprising as the expected magnitude of the higher harmonics of the current based on Eq. 2.85 was below our sensitivity for these samples.

In some instances, we plot the data in the form

$$I'_{A,B}(B) \equiv \frac{1}{2\pi\beta_1} \frac{\partial I^{A,B}}{\partial B}$$

and

$$I_p^{A,B} \equiv \frac{1}{2\pi\beta_1} dI_p^{A,B}\tag{7.6}$$

in order to minimize the number of processing steps applied to the raw data. The quantity $I'_{A,B}(B)$ has units of current and should have the same amplitude as $I(B)$ for features with magnetic field frequencies close to β_1 . The quantity $I_p^{A,B}$ also has units of current.

7.1.2 Step-by-step walk-through of signal processing

We now walk through the conversion of measured cantilever frequency to persistent current using method A on a typical data set. For this data set, sample CL15 (see Tables 7.1 and 7.2) was driven

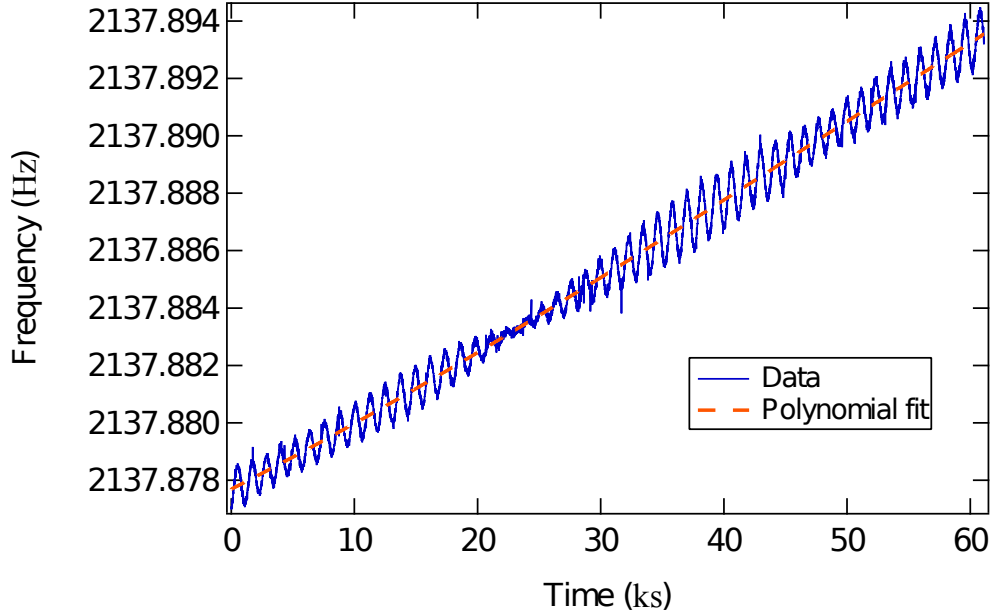


Figure 7.1: Frequency versus time for a typical data set. The frequency of cantilever CL15 was measured seven times at a fixed value of magnetic field with each measurement lasting approximately five seconds. The magnetic field was then increased by 0.5 mT over a time scale of 20 seconds. Oscillations of the persistent current can clearly be seen on top of a time-dependent drift of the cantilever frequency. Also shown is a third order polynomial fit to the frequency, which is then subtracted from the frequency data to produce the curve in Fig. 7.2.

in a phase-locked loop as described in 5.2.2 and 5.3.1. The resonant frequency of the cantilever was measured seven times by the frequency counter with a gate time of 5 seconds while the magnetic field was held constant. The magnetic field was then increased by 0.5 mT. This measure and step process was repeated from 7.3 T to 7.9 T.

Prior to beginning the sweep of the magnetic field, the excitation of the cantilever was calibrated following the procedure described in 5.3.1.4. During the scan, the cantilever was driven with a tip amplitude $x_{\max} = 31$ nm. The cantilever was mounted at an angle $\theta_0 = 45^\circ$ relative to the magnetic field, which for CL15 corresponded to a magnetic field frequency $\beta_1 = 94 \text{ T}^{-1}$ and a magnetic field period $B_1 = \beta_1^{-1} = 10.7$ mT. The temperature of the refrigerator was 360 mK.

Figure 7.1 shows the raw frequency data versus measurement time as well as a third order polynomial fit. Oscillations due to the persistent current are clearly present in the raw data on top of a smooth frequency drift. Immediately after the data shown in Fig. 7.1 was taken, the direction of the magnetic field step was reversed. While the oscillations were also reversed, the nearly linear drift was unaffected. This observation indicates that the drift of the cantilever's resonant frequency

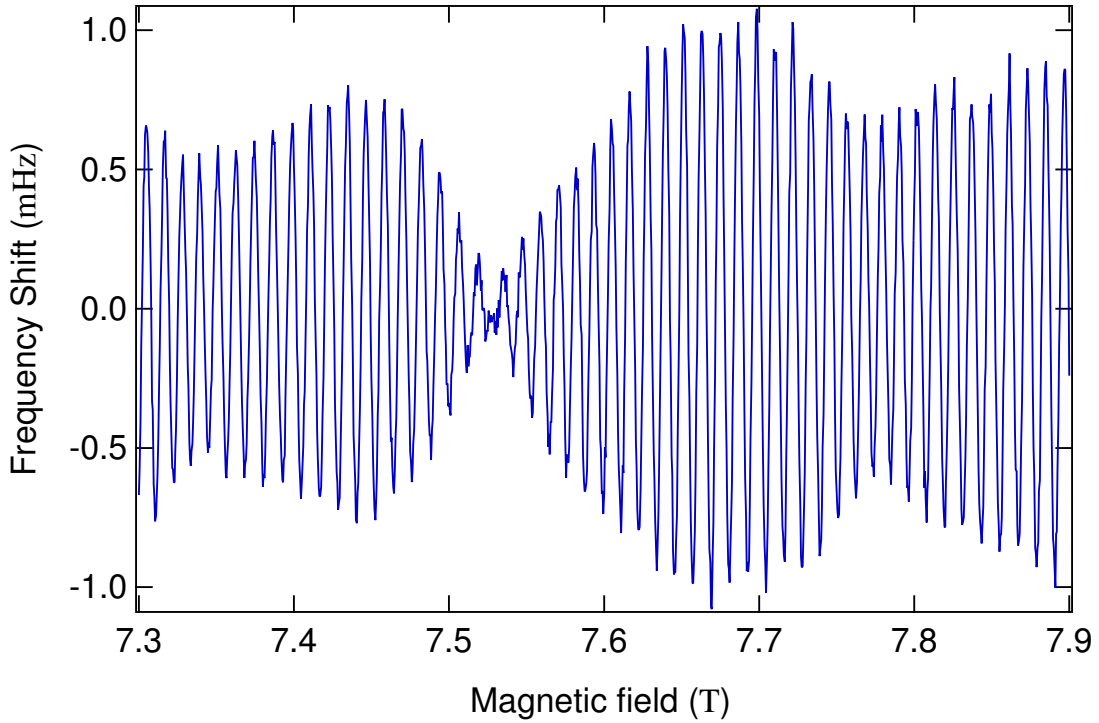


Figure 7.2: Frequency shift versus magnetic field for a typical data set. The figure shows the frequency shift $\Delta f(B)$ obtained by removing the smooth background from the data shown in Fig. 7.1 and averaging together the data points taken at the same value of magnetic field B . Oscillations with a period close to the expected ϕ_0 periodicity $B_1 = 10.7$ mT can be seen.

was purely time-dependent and independent of magnetic field.¹

Fig. 7.2 shows the frequency shift $\Delta f(B)$, the result of subtracting the polynomial fit from the data in Fig. 7.1 and then averaging together all of the measurements recorded at the same value of the magnetic field. A few errant data points from Fig. 7.1, selected for being several times the typical frequency scatter away from the other frequency recordings at the same magnetic field, were discarded before performing this averaging. Fig. 7.3 displays the discrete Fourier transform of the frequency shift trace defined as

$$\Delta f(\beta = \beta_1 p) = \frac{1}{B_{\max} - B_{\min}} \int_{B_{\min}}^{B_{\max}} dB \Delta f(B) e^{-2\pi i p \beta_1 B}. \quad (7.7)$$

A strong peak located close to the expected value of β_1 is visible in the spectrum.

¹It was not always the case that the frequency drift was independent of magnetic field. This field dependence could possibly be due to a magnetic field dependence of the cantilever quality factor. Alternatively, an electrostatic interaction between the cantilever and detection fiber could lead to a magnetic field dependence of the cantilever frequency if the magnetic field caused the sample stage to tilt and thus the distance between the cantilever and fiber to change.

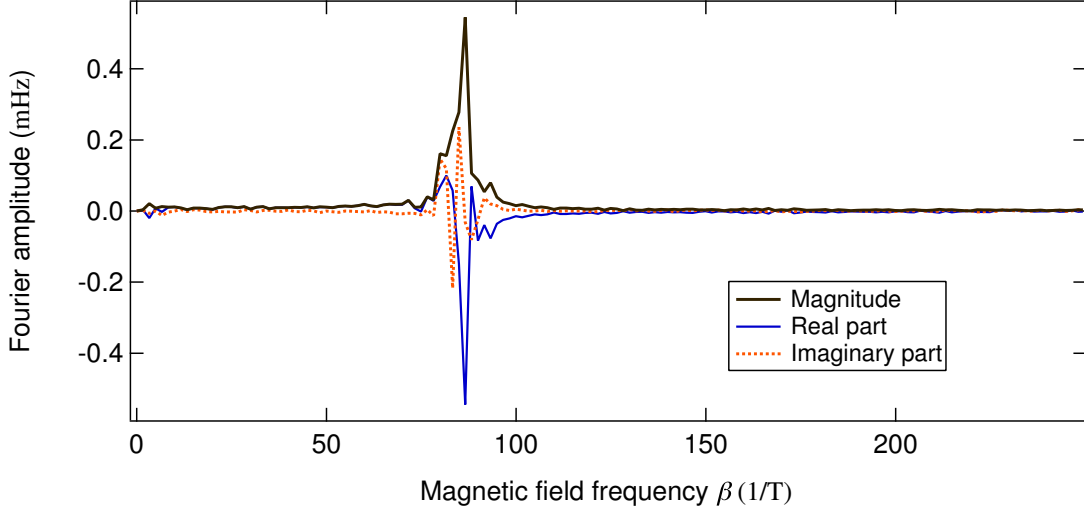


Figure 7.3: Frequency shift versus magnetic field frequency β for a typical data set. The Fourier spectrum of the $\Delta f(B)$ trace shown in Fig. 7.2 is plotted for low values of the magnetic field frequency β . A peak is located close to the expected magnetic field periodicity of $\beta = 94 \text{ T}^{-1}$. The peak has an irregular shape due to the small number of correlation fields $B_{c,p=1}$ spanned by the data in Fig. 7.2. The white fluctuating background seen above $\beta = 150 \text{ T}^{-1}$ maintains a roughly constant level of fluctuations out to $\beta = 10^3 \text{ T}^{-1}$.

Fig. 7.4 shows the coefficients I_p^A calculated from Eqs. 7.3 and 7.6. The I_p^A are the Fourier coefficients of the magnetic field derivative $\partial_B I$ of the persistent current inferred by method A. The coefficients I_p^A are plotted versus magnetic field frequency $\beta = \beta_1 p$. Because of the scaling introduced in Eq. 7.6, the I_p^A have units of current with the coefficients near $\beta = \beta_1$ possessing similar amplitudes to those of the corresponding Fourier coefficients I_p^A of the persistent current trace $I(B)$.

In the inset of Fig. 7.4, the coefficients I_p^A are shown over a wider range of magnetic field frequency β . A large peak can be seen between $\beta \approx 829 \text{ T}^{-1}$ and $\beta \approx 904 \text{ T}^{-1}$. For these values of β , the expression $\text{jinc}(2\pi p \beta_1 G B)$ passes through zero for $B = B_{\text{max}} = 7.9 \text{ T}$ and $B = B_{\text{min}} = 7.3 \text{ T}$ respectively. Within this peak, the denominator of Eq. 7.3 becomes very small for some value of B and thus causes the coefficients I_p^A to be large. Because no such feature was present in the Fourier transform of the frequency shift and no lower harmonics of the persistent current other than the fundamental can be seen in the spectrum, we can take this peak to be purely an artifact of the signal processing procedure.

Fig. 7.5 shows the scaled magnetic field derivative $I^A = \partial_B I^A / (2\pi\beta_1)$ of the persistent current found by taking the inverse Fourier transform of the spectrum shown in Fig. 7.4. Like Fig. 7.4,

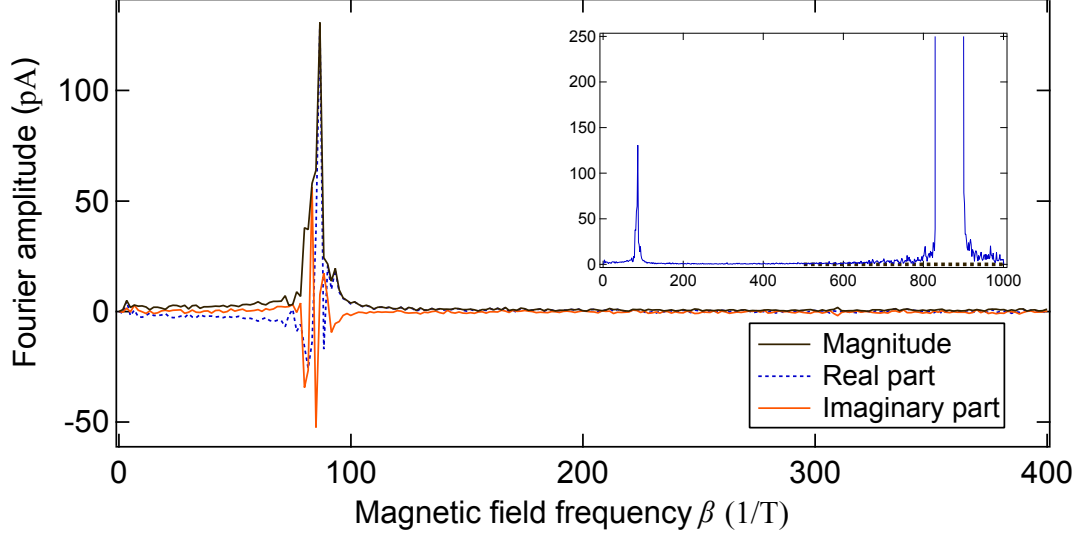


Figure 7.4: Fourier coefficients I_p^A for a typical data set. The Fourier coefficients dI_p^A were calculated from the frequency shift $\Delta f(B)$ shown in Fig. 7.2 using Eq. 7.3 and the values specified in the text and in Tables 7.1 and 7.2 for CL15. The traces shown in the figure represent the scaled form of the coefficients $I_p^A = dI_p^A / (2\pi\beta_1)$ introduced in Eq. 7.6. This scaling converts the current derivative coefficient dI_p^A into a quantity I_p^A with units of current and similar magnitude to the current for $\beta \sim \beta_1$. The coefficients dI_p^A are plotted versus $\beta = \beta_1 p$. The inset shows I_p^A over the full range of β calculable from the data. Above $\beta = 500 \text{ T}^{-1}$, and especially between 829 and 904 mT^{-1} , the values of the coefficients I_p^A are enhanced due to an effect described in the text.

the data in Fig. 7.5 represents the derivative of the current but is scaled to have units of current as described in 7.1.1. For the calculation of I^A , all of the values of dI_p^A corresponding to $\beta > 500 \text{ T}^{-1}$ (the region marked by the black dashed line in the inset of Fig. 7.4) were set to zero. This operation amounts to performing a low-pass filter of the data. This region of high β was removed because it was quite clear that no observable persistent current signal was present within it and because the white noise in the spectrum of Δf (Fig. 7.3) was being significantly amplified in this range (see discussion above) leading to the large peak in the inset of Fig. 7.4. Because the fractional change in magnetic field is fairly small over the range shown, $I^A(B)$ in Fig. 7.5 looks qualitatively similar to $\Delta f(B)$ in Fig. 7.2. The frequency shift $\Delta f(B)$ and inferred I^A from measurements of sample CL15 over a wider range of magnetic field are shown in Fig. 7.6.

Fig. 7.7 displays the integral with respect to magnetic field of the data representing $I^A = \partial_B I^A / (2\pi\beta_1)$ in Fig. 7.5. The scale factor $(2\pi\beta_1)^{-1}$ used for I^A has been removed so that curve in Fig. 7.7 depicts the persistent current $I^A(B)$ as a function of magnetic field. Numerical integration of the data has the undesirable side effect of magnifying low frequency noise. This magnification can be seen in Fig. 7.8 which shows the Fourier transform coefficients $I_p^A(\beta)$ of the current trace

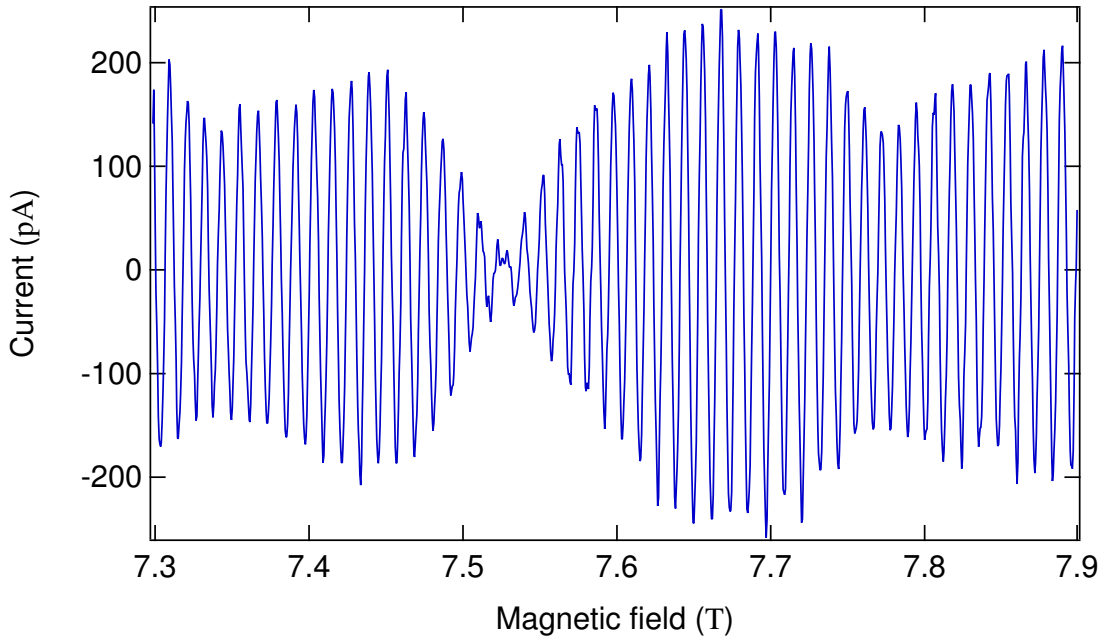


Figure 7.5: Derivative of persistent current I'^A versus magnetic field for a typical data set. The curve shown is the inverse transform of the coefficients $I_p'^A$ shown in Fig. 7.4 with the coefficients corresponding to $\beta > 500 \text{ T}^{-1}$ (black dashed line in the inset of Fig. 7.4) set to zero. This curve is the field derivative $\partial_B I^A$ scaled by $(2\pi\beta_1)^{-1}$ so that it has units of current.

$I^A(B)$ shown in Fig. 7.7. The spectrum $I_p^A(\beta)$ in Fig. 7.8 looks quite similar to the spectrum $I_p'^A(\beta)$ shown 7.4 other than an added spike at low frequency (indicated by a black bar in Fig. 7.8).

The added low frequency noise can be removed in several ways. In Fig. 7.7, we show both a ninth order polynomial fit to $I^A(B)$ and the result of a lowest-order regression smoothing (LOESS) routine with a window of 60 mT on $I^A(B)$. Subtracting either of these curves from $I^A(B)$ removes most of the low frequency fluctuations. A similar result is obtained by performing a high-pass filter on $I^A(B)$. This filter can be realized by setting to zero all of the low frequency components spanned by the black bar in Fig. 7.8 and then taking the inverse transform. The difference between the current trace and the LOESS smoothed trace is plotted in Fig. 7.9 and represents the final form of the inferred current $I^A(B)$ from the measured cantilever frequency $f(B)$.

In calculating the current trace $I^A(B)$, we twice removed smooth backgrounds and also integrated the data once. These operations correspond to high and low pass filters respectively. We also low-pass filtered the dI_p^A to remove high frequency components of the noise which were strongly magnified by the conversion of frequency shift to current derivative. All of these filters were applied to ranges of the magnetic field frequency β spectrum well separated from the persistent current

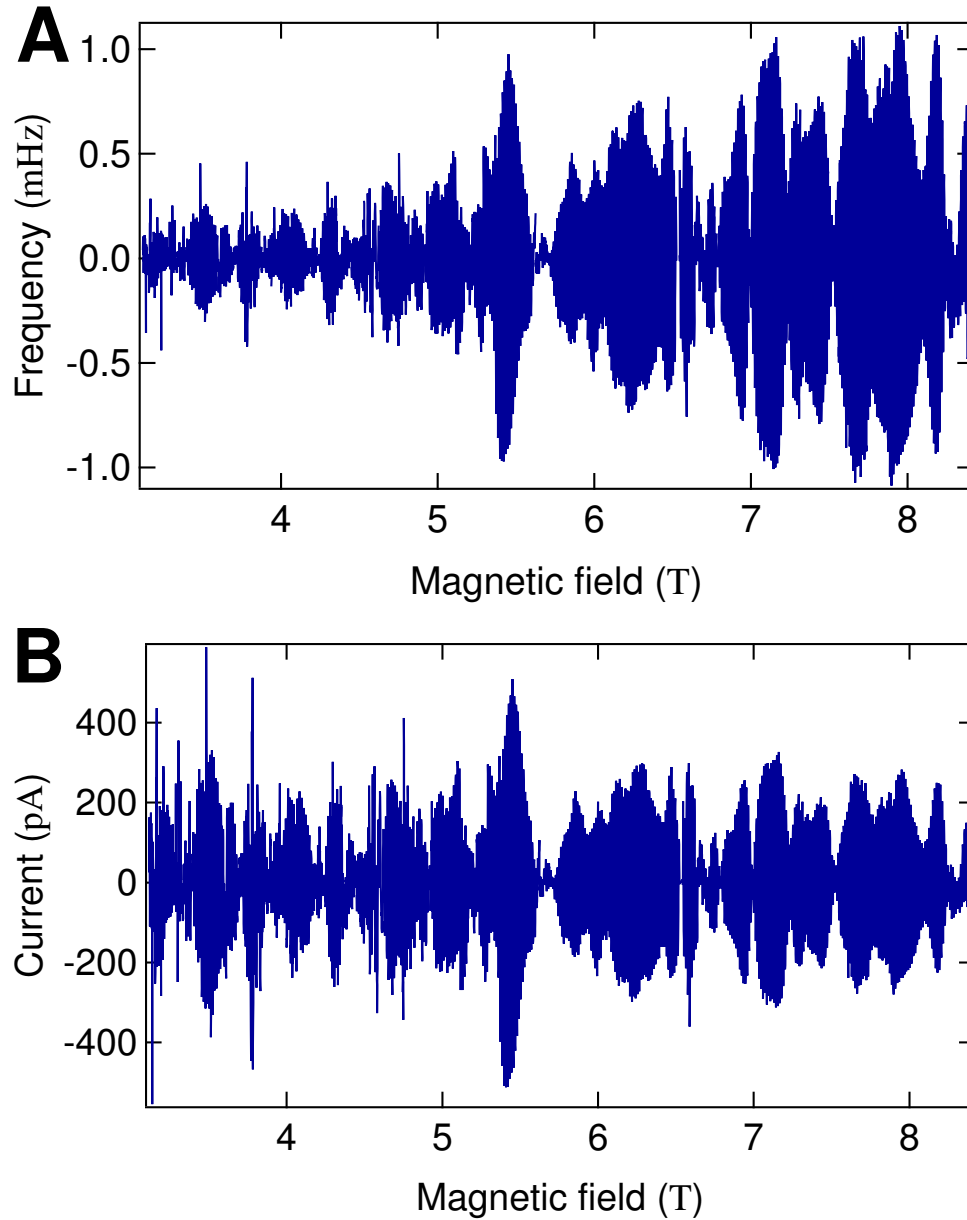


Figure 7.6: Frequency shift and inferred persistent current derivative I'^A over a large range of magnetic field. Panel A shows all of the frequency shift Δf data taken on sample CL15 at $\theta_0 = 45^\circ$ and $T = 360$ mK. The data shown was taken in a series of different magnetic field scans at different points in time. A smooth background has been removed from each $\Delta f(B)$ trace. The cantilever amplitude was held constant during a single scan but varied in between scans so that the argument of the jinc factor in Eq. 7.2 was relatively constant across the entire field range. Panel B shows the inferred scaled current derivative $I'^A(B)$ calculated by the method described in the text. The data between 7.3 T and 7.9 T match that shown in Fig. 7.5 (on the scale of Fig. 7.6, the individual oscillations of the persistent current can not be made out). Despite the wide variation of the typical amplitude of the oscillations in $\Delta f(B)$, the amplitude of the oscillations in I'^A remain roughly constant over the entire range of magnetic field.

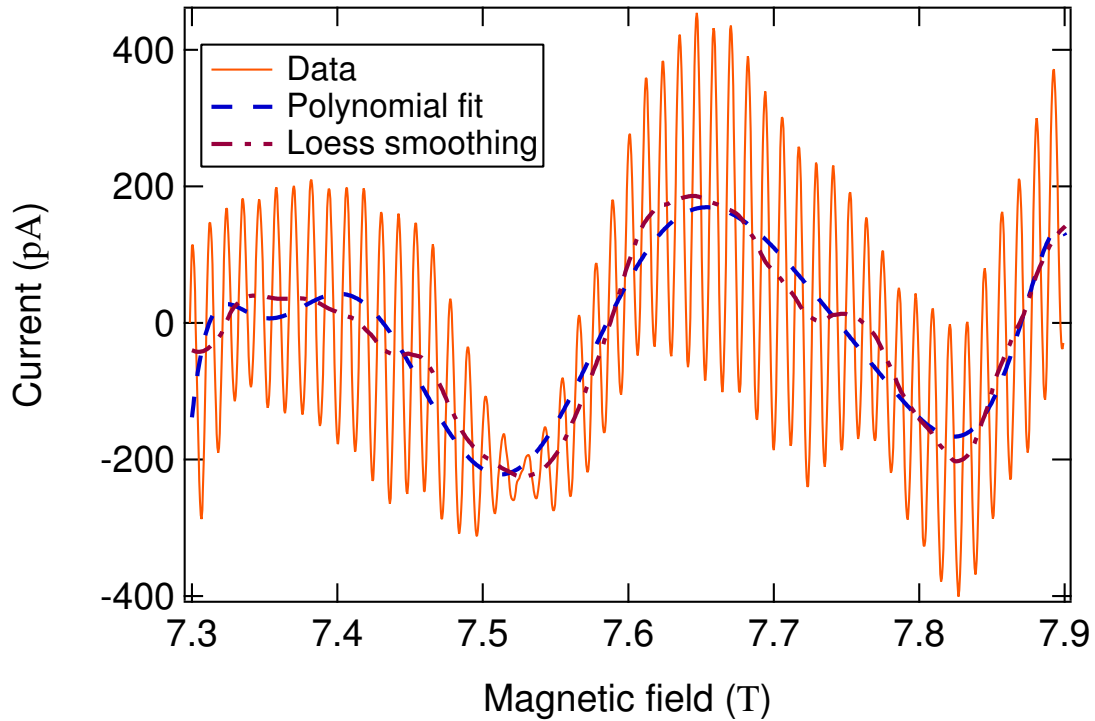


Figure 7.7: Persistent current I^A versus magnetic field without background subtraction for a typical data set. The curve shown represents the persistent current $I^A(B)$ and is found by numerically integrating the curve $I^A(B)$ shown in Fig. 7.5 (and multiplying by $2\pi\beta_1$ to remove the extra scale factor used in that figure). The process of integration introduces large low frequency fluctuations to $I^A(B)$. These fluctuations can also be seen in the Fourier spectrum of $I^A(B)$ shown in Fig. 7.8. Two approximations of the low frequency fluctuations are also shown in the figure: a ninth order polynomial fit (dashed line) and a lowest-order regression smoothing with a window of 60 mT (dot-dashed line).

features and should not affect the analysis of the persistent current data. This conclusion can be seen by noting that the main feature in the Fourier spectra of Figs. 7.3, 7.4, and 7.8 is largely unchanged throughout the signal processing routine. However, these filtering steps are the reason that the trace of $I^A(B)$ in Fig. 7.9 appears slightly smoother than the $\Delta f(B)$ trace in Fig. 7.2.

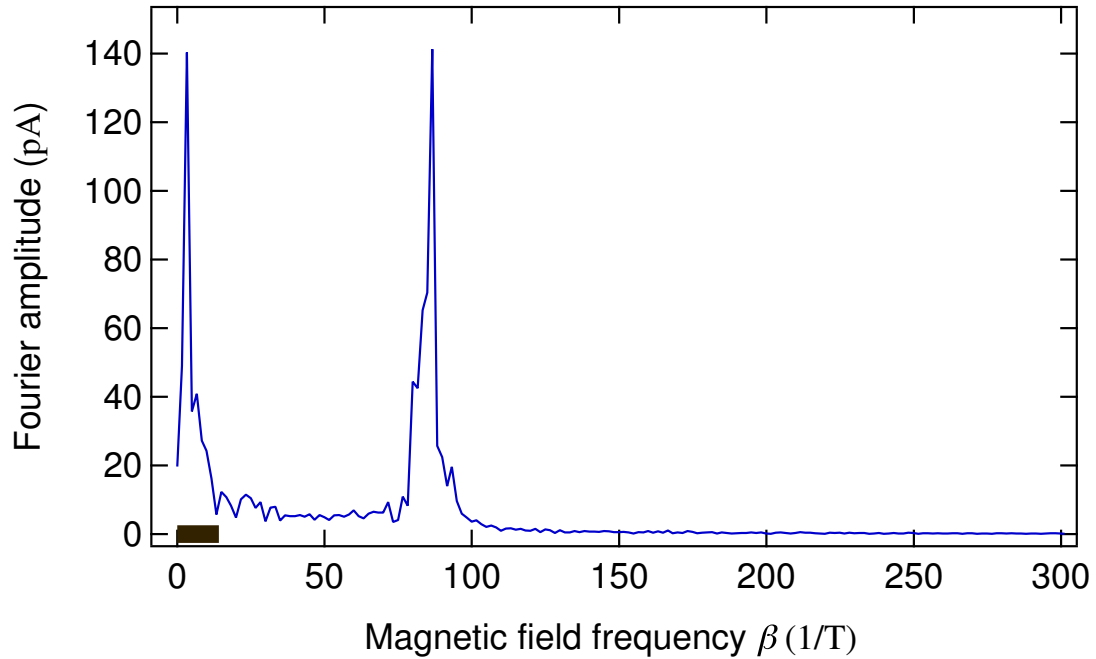


Figure 7.8: Fourier transform of the persistent current for a typical data set. The Fourier coefficients $I_p^A(\beta)$ of the current $I^A(B)$ plotted in Fig. 7.7 are shown versus magnetic field frequency $\beta = \beta_{1p}$. Low frequency fluctuations enhanced by the integration process are indicated by a black bar.

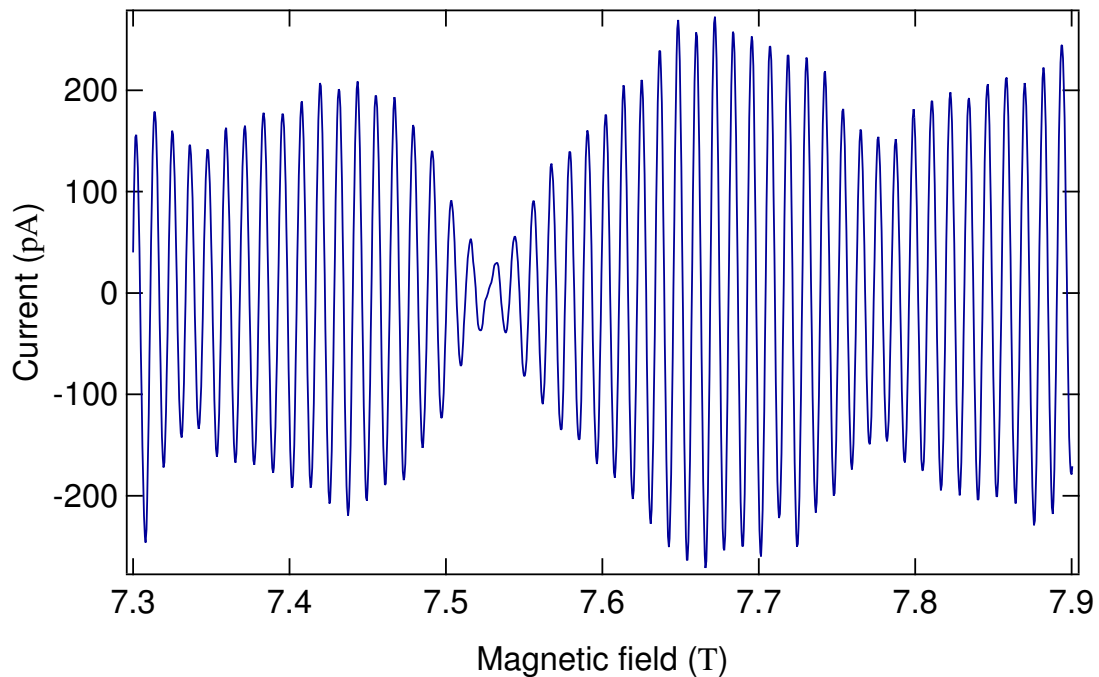


Figure 7.9: Persistent current versus magnetic field with smooth background removed for a typical data set. The persistent current $I^A(B)$ inferred from the data in Fig. 7.1 is plotted versus magnetic field B . This curve was obtained by taking the difference of the persistent current trace and the lowest-order regression smoothing trace both shown in Fig. 7.7.

7.2 Persistent current measurement diagnostics

Before discussing our main experimental results regarding persistent currents, we review several diagnostic measurements which were made in order to check the validity of the persistent current signal processing procedure outlined in 7.1 and the validity of the torsional magnetometry technique more generally.

Figs. 7.10, 7.11, and 7.12 each display a different test of Eq. 4.26 and Section 7.1. Each of the figures displays data taken on sample CL17 of Tables 7.1 and 7.2 at an angle of $\theta_0 = 6^\circ$. In Fig. 7.10, panel A shows the frequency shift $\Delta f(B)$ measured over a region of magnetic field B for a series of different values of the cantilever amplitude x_{\max} , while panel B displays the current $I^A(B)$ inferred by method A of 7.1 for value of x_{\max} . While the features in the frequency shift data vary by over a factor of 2, the traces representing the inferred value of the current show good agreement.

Fig. 7.11 provides a more direct check of Eq. 4.26 for the cantilever frequency shift due to the persistent current by showing measurements of the cantilever frequency as a function of cantilever amplitude at fixed values of the magnetic field. For simplicity, we assume that the Fourier series expansion of the persistent current given in Eq. 7.1 contains only one non-zero term so that the current can be written in the form

$$I(B) = I_p \sin(2\pi p \beta_1 B + \psi_p).$$

Eq. 7.2 for the change in resonant frequency of the cantilever due to the persistent current can then be written as

$$\Delta f_{pc}(x_{\max}, B) = FB^2 2\pi p \beta_1 I_p \cos(2\pi p \beta_1 B + \psi_p) \text{jinc} \left(2\pi p \beta_1 \frac{\alpha}{l \tan \theta_0} x_{\max} B \right).$$

The expected frequency shift should reach its maximum magnitude when the current $I(B)$ crosses through zero and $\cos(2\pi p \beta_1 B + \psi_p) = \pm 1$.

For Fig. 7.11, the frequency shift Δf was measured as a function of the cantilever amplitude x_{\max} at two fixed values of the magnetic field B . These measurements were made on sample CL17 with an angle θ_0 of 6° between the cantilever beam and the applied magnetic field. The cantilever was excited in its second flexural mode in order to increase the argument of the jinc function in the expression for Δf_{pc} without requiring larger values of x_{\max} . A comparison of measurements

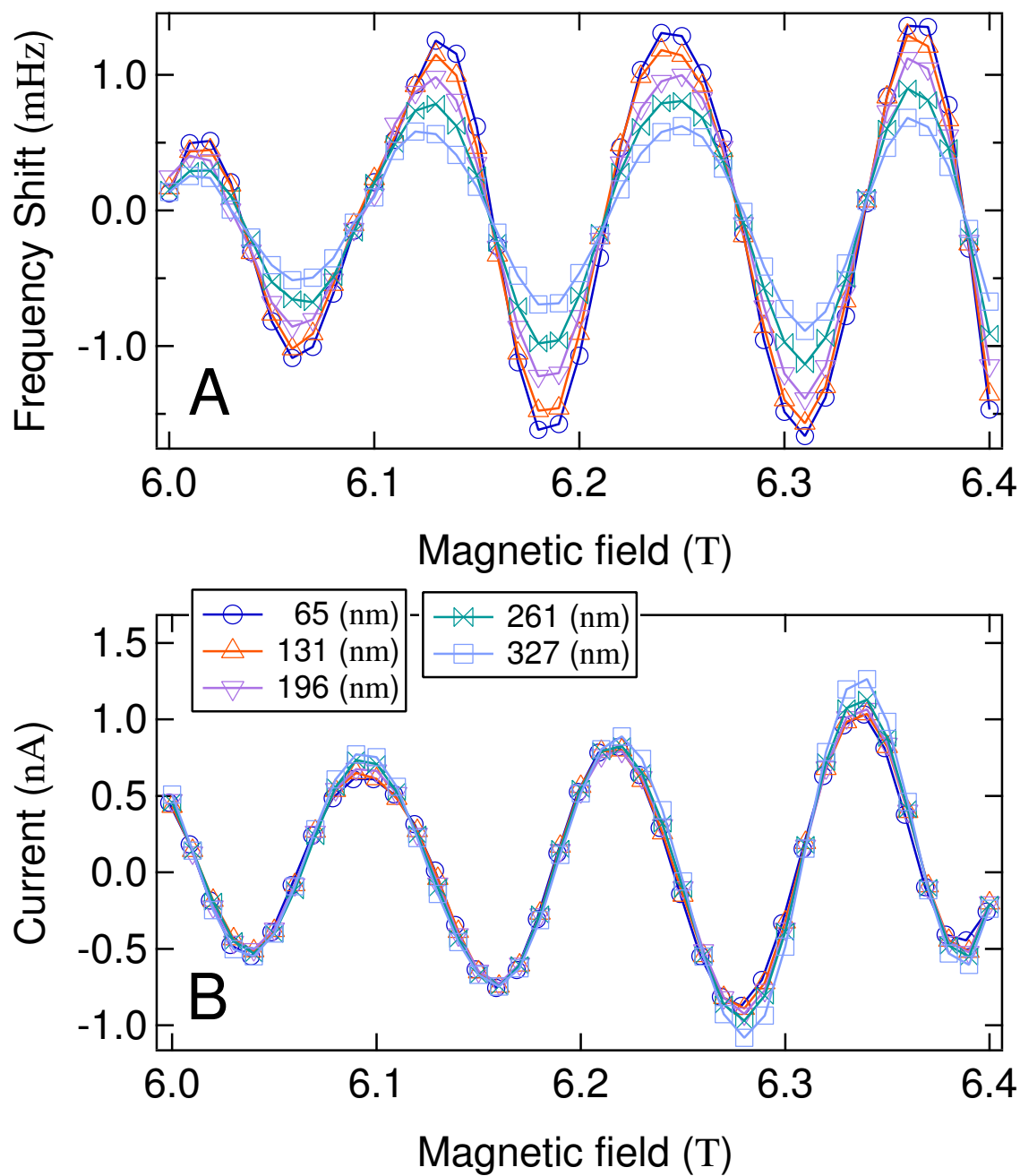


Figure 7.10: Frequency shift and inferred persistent current versus magnetic field for a series of cantilever amplitudes. The data shown were taken on sample CL17 at $T = 323$ mK. The angle θ_0 between the cantilever beam and the magnetic field was 6° . The persistent current traces were calculated using method A of 7.1.1.

performed using the cantilever's first and second flexural modes are discussed below and shown in Fig. 7.12. A list of the cantilever parameters relevant to the calculation of Δf_{pc} that depend on mode index is given in the discussion concerning Fig. 7.12.

The two values of the magnetic field used in this measurement (indicated by the arrows in the upper trace in Fig. 7.11) were chosen to correspond to adjacent magnetic field positions B_u and B_d where the current trace $I(B)$ passed through zero with an upward and downward slope respectively. The measured frequency shifts $\Delta f(x_{\max}, B_u)$ and $\Delta f(x_{\max}, B_d)$ are shown in the inset of the lower plot of Fig. 7.11. Both traces show a similar trend of increasing frequency with cantilever amplitude, possibly the result of an electrostatic interaction between the cantilever and the nearby optical fiber tip or of a small mechanical non-linearity of the cantilever.

In order to eliminate this background trend of the frequency shift present at both B_u and B_d , the net frequency shift $\Delta f_{pc}(x_{\max})$ was found by subtracting the frequency shift measured at the two magnetic field values:

$$\Delta f_{pc}(x_{\max}) = \Delta f(x_{\max}, B_d) - \Delta f(x_{\max}, B_u).$$

The measured frequency shift difference Δf_{pc} is represented by the dots in the lower plot of Fig. 7.11. Taking $B \equiv (B_u + B_d)/2$, $I_p \equiv I_p(B_u) \approx I_p(B_d)$, $\cos(2\pi p \beta_1 B_u + \psi_p) = +1$, and $\cos(2\pi p \beta_1 B_d + \psi_p) = -1$, the expected frequency shift difference $\Delta f_{pc}(x_{\max})$ is

$$\Delta f_{pc}(x_{\max}) = \frac{f_0}{k} \frac{2\pi p}{\phi_0} I_{pS} \left(AB \cos \theta_0 \frac{\alpha}{l} \right)^2 \text{jinc} \left(2\pi p \frac{AB}{\phi_0} \cos \theta_0 \frac{\alpha}{l} x_{\max} \right). \quad (7.8)$$

A curve calculated using Eq. 7.8 with $I_p = 4 \text{ nA}$ and $p = 0.93$ is also shown in the lower plot of Fig. 7.11 and agrees well with the measured Δf_{pc} data. The 4 nA value for I_p is close to the 3.1 nA peak-to-peak amplitude observed in the trace $I(B)$ of current versus magnetic field (upper plot of figure). The seven percent deviation of p from unity is well within the range of expected fluctuations of the persistent current oscillation frequency due to magnetic field penetrating the ring's finite linewidth (see the discussion in 7.3.2 below). If p is fixed to unity inside the argument of the jinc function in Eq. 7.8, the same curve can be generated by changing the ring radius from 308 nm to 297 nm, well within the ring's 115 nm linewidth.

Fig. 7.12 shows two traces of the current $I(B)$ inferred from measurements of the frequency shift $\Delta f(B)$ taken while different flexural modes of the cantilever were excited. For these two mea-

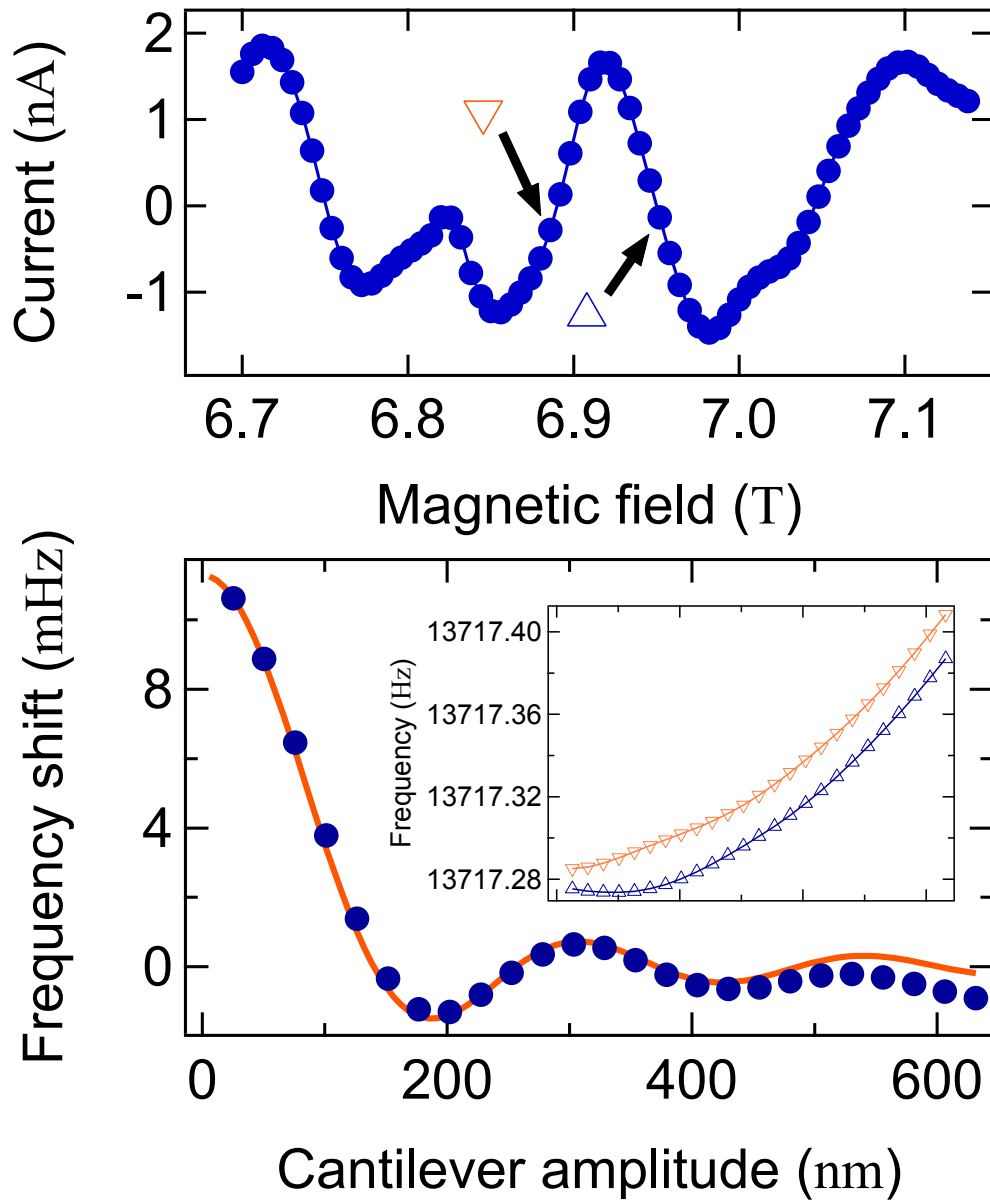


Figure 7.11: Frequency shift versus cantilever amplitude. In the upper plot the full $I(B)$ trace is shown over the magnetic field range of interest for the amplitude scan measurements of the lower plot. To generate the data shown in the lower plot, the resonant frequency of cantilever CL17 was measured at $B_u = 6.885$ T and $B_d = 6.95$ T (indicated by arrows in the upper plot) as a function of cantilever amplitude x_{\max} . For these measurements, the angle θ_0 between the cantilever beam and the magnetic field was 6° , the temperature T was 323 mK, and the cantilever was excited in its second flexural mode. The measured frequency as a function cantilever amplitude at both field values is shown in the inset of the lower plot with the frequency measured at B_u represented by downward pointing triangles and that measured at B_d by upward pointing triangles. The large lower plot shows the difference $\Delta f_{pc}(x_{\max}) = \Delta f(x_{\max}, B_d) - \Delta f(x_{\max}, B_u)$ (dots) between the measured frequency shifts at the two magnetic field values. Also shown is a curve calculated using Eq. 7.8. The accuracy of the match between the curve and the data is discussed in the text.

measurements, the fundamental flexural mode of the cantilever with resonant frequency $f_0 = 2186$ Hz and the second order flexural mode with resonant frequency $f_0 = 13,718$ Hz were excited. Beyond the resonant frequency, the parameters in Eq. 4.26 that varied with flexural mode were the spring constant k (1.34×10^{-3} N/m for the fundamental mode, 5.27×10^{-2} N/m for the second order mode) and the mode shape derivative α (1.38 for the fundamental mode, 4.78 for the second order mode). The two traces shown in Fig. 7.12 exhibit good agreement in terms of current magnitude and magnetic field features. The discrepancy in the two traces near 7.2 T could possibly be due to different resonances in the sample holder in this region of magnetic field. Similar variation between traces can be observed in Fig. 7.15 for which both measurements were performed while exciting the cantilever's fundamental mode.

In addition to providing another confirmation of the accuracy of Eq. 4.26, the independence of the inferred current from the cantilever flexural mode can also be viewed as independence of the current from cantilever excitation frequency in the low kilohertz regime relevant to the cantilever torsional magnetometry technique discussed here. Thus the inferred persistent current magnitude can be taken to be the equilibrium value. This result is not surprising as almost all of the timescales related to the ring sample (the correlation energy E_c , the electron phase coherence time τ_ϕ , the electron elastic scattering time τ_e , the decay time associated with the ring inductance (L/R where L is the ring inductance and R the ring resistance), the temperature T , and the Zeeman splitting E_Z of the electron) are on order of one gigahertz or higher. One notable exception, the single level spacing at the Fermi energy, is still greater than 200 kHz for each sample.

Figs. 7.13, 7.14, and 7.15 show the results of measurements performed to verify the independence of the inferred persistent current trace $I(B)$ from various configurations of the experimental apparatus. In Fig. 7.13, the current traces $I(B)$ detected for a series of values of the optical power of the cantilever detection laser are shown over a small range of magnetic field. These measurements were performed at the refrigerator's base temperature of 323 mK. For 80 nW or less incident on the cantilever, little variation in the current traces is observed, and even for the trace taken with 800 nW only a moderate deviation is evident. Outside of Fig. 7.13, the incident laser power on the cantilever was kept to 5 nW or less, a range for which the ring sample could be assumed to be in thermal equilibrium with the refrigerator. Although we did not thoroughly characterize the optical absorption of the samples listed in Table 7.1, we note that Fig. 7.13 indicates less sensitivity to laser power than was observed in Fig. 6.6. As the cantilevers from these two sets of measurements

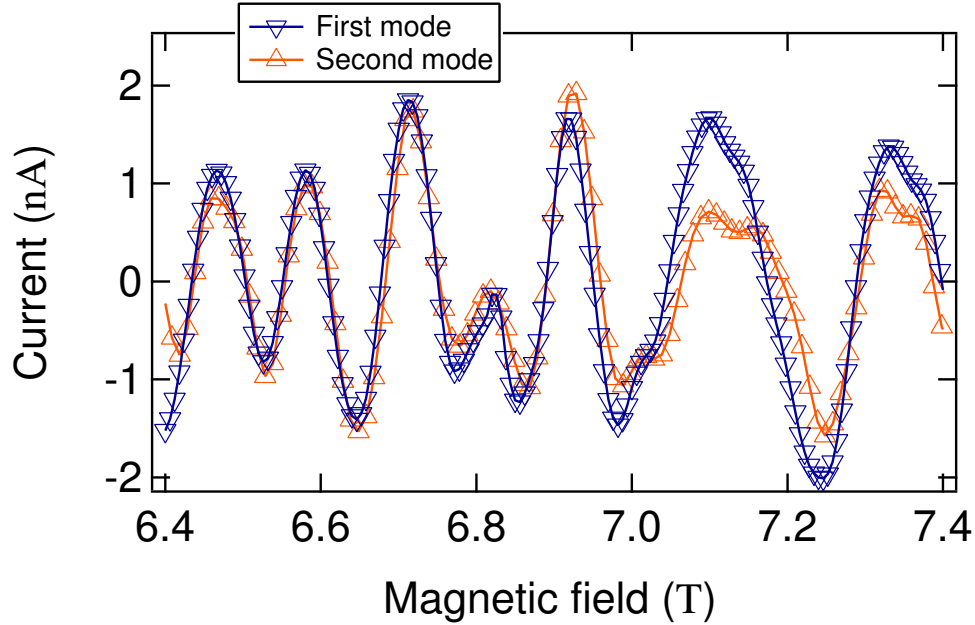


Figure 7.12: Persistent current measurements taken while exciting the first and second flexural modes of the cantilever. The two traces were calculated from measurements of the cantilever frequency shift of sample CL17 using method A of 7.1.1. The measurements were taken with a temperature T of 323 mK and an angle θ_0 of 6° between the cantilever beam and magnetic field.

had similar dimensions (see 5.1.1 and Table 7.1), we surmise that lower level of doping (resistivities of $\sim 0.025 \Omega \text{ cm}$ for the Arrow cantilevers and $\sim 20 \Omega \text{ cm}$ for the persistent current samples) accounted for the decreased sensitivity to incident laser power.

Fig. 7.14 presents measurements of the persistent current for three different modes of operation of the solenoid (see 5.2.1 for a description of the experimental apparatus). The solenoid consisted of a large coil of superconducting material closed electrically by a small section of superconducting wire referred to as the “persistent switch.” By operating a nearby heater, the persistent switch could be driven normal, creating a resistive “break” of the closed superconducting loop.

Most measurements of the persistent current were performed with the persistent switch heater turned on and with the electrical current in the solenoid sourced by a room temperature power supply. For Fig. 7.14, measurements of the cantilever frequency were performed with the persistent switch heater turned off but current from the external supply still flowing through the leads down to the magnet. In order to change the magnetic field in between measurements of the cantilever frequency, the persistent switch heater was turned on and the current supplied by the external supply ramped up or down. Additionally, measurements were performed with the persistent switch heater turned off and the current in the magnet leads ramped down to zero. For these measurements,

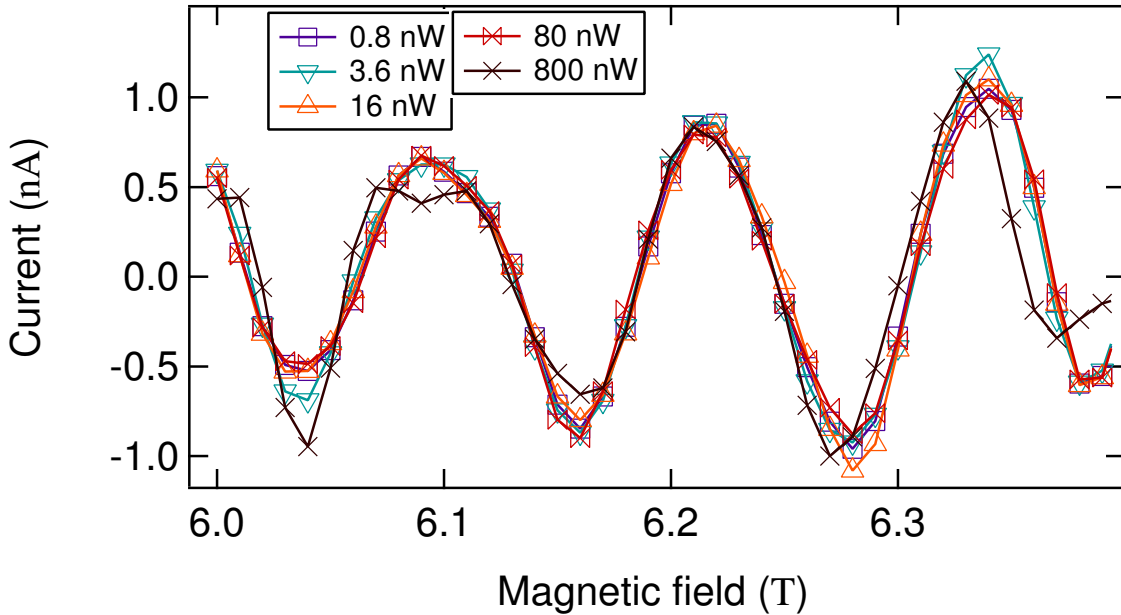


Figure 7.13: Persistent current versus magnetic field for a series of readout laser powers. The persistent current is clearly unaffected by the incident power of the detection laser for powers up to 80 nW. Only slight variations in the current trace are visible for 800 nW. The measurements shown were taken with a temperature T of 323 mK and an angle θ_0 of 6° between the cantilever beam and magnetic field.

all electrical connections to the cryostat other than the leads to the piezoelectric actuator and the leads to the magnet were disconnected. Little variation in the current was observed for these three different modes of solenoid operation. We did not attempt measurements in which the magnet leads were physically disconnected from room temperature electronics. However, we note that magnetic field fluctuations in the solenoid due to voltage noise coupled to the magnet leads from the room temperature electronics should be strongly suppressed due to the solenoid's large (19 H) inductance.

In Fig. 7.15, the persistent current traces measured with the magnet operated in both polarities are compared. For the trace representing the negative magnetic polarity, the sign of both the current I and the magnetic field B are inverted. The two traces show good agreement with each other. This result is as expected since time reversal invariance requires that $I(-B) = -I(B)$.

We also measured the frequency shift signal due to the supercurrent in the rings near $B \approx 0$ T. While the frequency shift signal is roughly proportional to B^2 and thus small at low field, the current in the superconducting state was over a thousand times larger in magnitude than that in the normal state and was observable at fields as low as ~ 15 mT. A rough analysis of the measurements of the rings in the superconducting state is given in Appendix F. The transition temperature of the

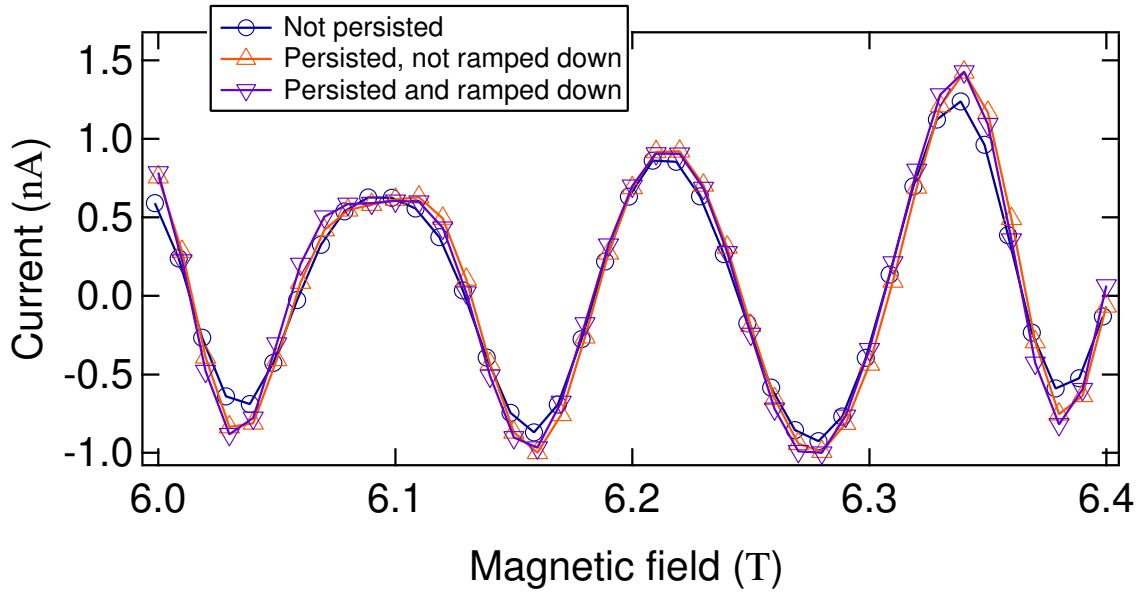


Figure 7.14: Persistent current versus magnetic field observed with the magnet in different modes of operation. Measurements were performed on sample CL17 with the solenoid not persisted (persistent switch heater on), the solenoid persisted but the leads not ramped down (persistent switch heater off), and the solenoid persisted and the leads ramped down (persistent switch heater off, no external current sourced to magnet) as described in the text. The measurements shown were taken with a temperature T of 323 mK and an angle θ_0 of 6° between the cantilever beam and magnetic field.

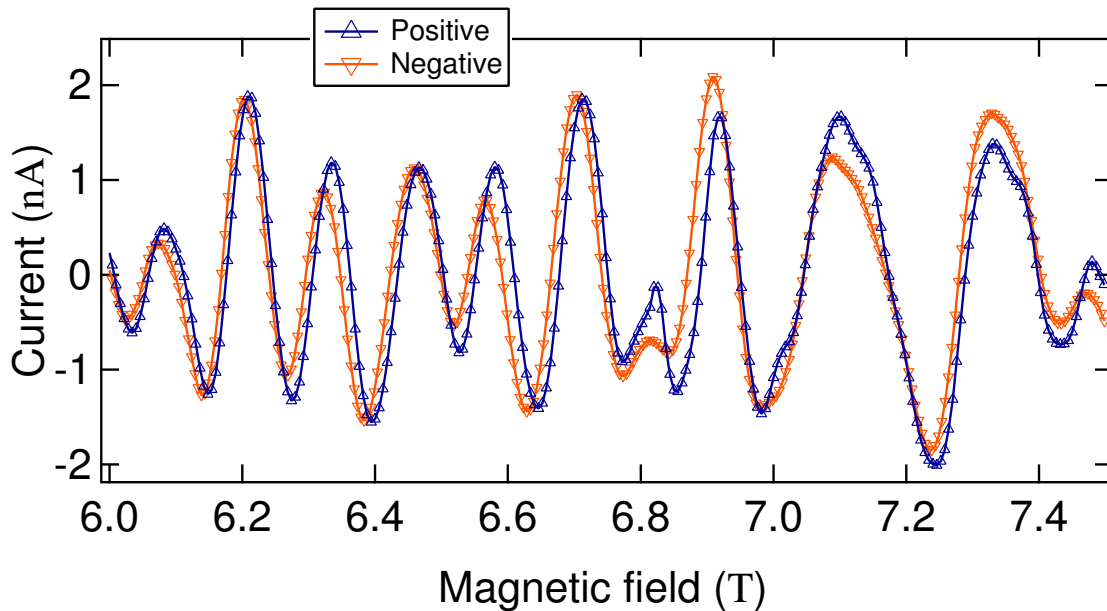


Figure 7.15: Persistent current versus magnetic field measured for both magnet polarities. For the measurements with negative magnet polarity, both the current and the magnetic field axis have been reversed. The measurements shown were taken on sample CL17 with a temperature T of 323 mK and an angle θ_0 of 6° between the cantilever beam and magnetic field.

rings was found to be consistent with transport measurements of a co-deposited wire (see Appendix E) and close to the bulk value for aluminum (see Fig. 6.4 and accompanying discussion). The magnetic field dependence and inferred magnitude of the current in the superconducting state were similar to those observed in previous measurements, indicating that the rings were of good quality and that our modeling of the cantilever was accurate.

7.3 Persistent current measurements

We now present our main experimental results and interpret them using the theoretical picture developed in Chapter 2. The measured samples are described in Tables 7.1 and 7.2. These samples were all contained on one sample chip and thus could all be measured in the same cooldown. The measurements described in this section were taken in two cooldowns, one with the sample oriented with the angle θ_0 between the cantilever beam and the magnetic field at 6° and one with $\theta_0 = 45^\circ$. Persistent currents have also been observed in other cooldowns and with other samples created in a different fabrication run.

7.3.1 Qualitative discussion

In Fig. 7.16, measurements of rings with three different circumferences L are shown between $B = 6.7$ T and 7.2 T for $\theta_0 = 6^\circ$ and $T = 323$ mK. The magnetic field period of the persistent current oscillation (the magnetic field necessary to thread h/e through the ring) is inversely proportional to the ring's area and thus to L^2 . Qualitatively, this trend is borne out in Fig. 7.16 where the magnetic field scale of the typical feature is seen to increase with decreasing L . Additionally, in Eq. 2.85 it was predicted that the typical magnitude $I^{\text{typ}}(T) = \langle I^2(T) \rangle^{1/2}$ scales roughly as

$$I^{\text{typ}} \propto \frac{1}{R^2} \exp(-aL^2T/D)$$

with a a constant and D the diffusion constant of the metal. The data in Fig. 7.16 is qualitatively consistent with this relationship as the size scale of the persistent current increases with decreasing L .

In Figs. 7.17 and 7.18, the current observed in samples CL15 and CL17 is shown for both $\theta_0 = 6^\circ$ and $\theta_0 = 45^\circ$ over the same 0.5 T field region as shown in Fig. 7.16. The magnetic field scale $B_{h/e}$

Sample	l (μm)	w (μm)	f_0 (Hz)	k (mN/m)	Q ($\times 10^5$)
CL11	459	40	2091	0.63	1.2
CL14	438	60	2298	1.08	1.6
CL15	454	60	2138	0.97	1.3
CL17	449	80	2186	1.34	1.2

Table 7.1: Cantilever parameters of persistent current samples. The cantilever widths w were measured optically, and the cantilever resonant frequencies f_0 were measured using the detection arrangement described in Chapter 5. The cantilever thickness t was measured to be 340 nm using the instrument mentioned in D.1. The cantilever length l and spring constant k were calculated using the values from the other measurements and Eqs. 4.5 and 4.7. The cantilever length measured optically was not used due to uncertainty caused by over-etching of the silicon handle layer on which the cantilever was mounted. The length values given above are consistent with the values observed optically. The listed cantilever quality factors Q represent typical measured values. The quality factor varied with temperature and over time. More details about the cantilevers are given in 5.1.2 and D.1.

Sample	L (μm)	w_r (nm)	t_r (nm)	N	h_A (μm)
CL11	5.0	85	90	242	30
CL14	2.6	85	90	1	n/a
CL15	2.6	85	90	990	18
CL17	1.9	115	90	1680	20

Table 7.2: Ring specifications of persistent current samples. The mean circumference L and linewidth w_r of the aluminum rings as measured by a scanning electron microscope are given for each sample. The thickness t_r of the deposited aluminum was measured by an atomic force microscope. For each array, the amount of distance h_A spanned by the array along the cantilever's long dimension is given, as is the number N of rings in the array. Each array was located at the tip of the cantilever with a $5 \mu\text{m}$ margin from the three edges of the cantilever. The single ring was also located $5 \mu\text{m}$ from the cantilever tip and was centered along the cantilever's width dimension.

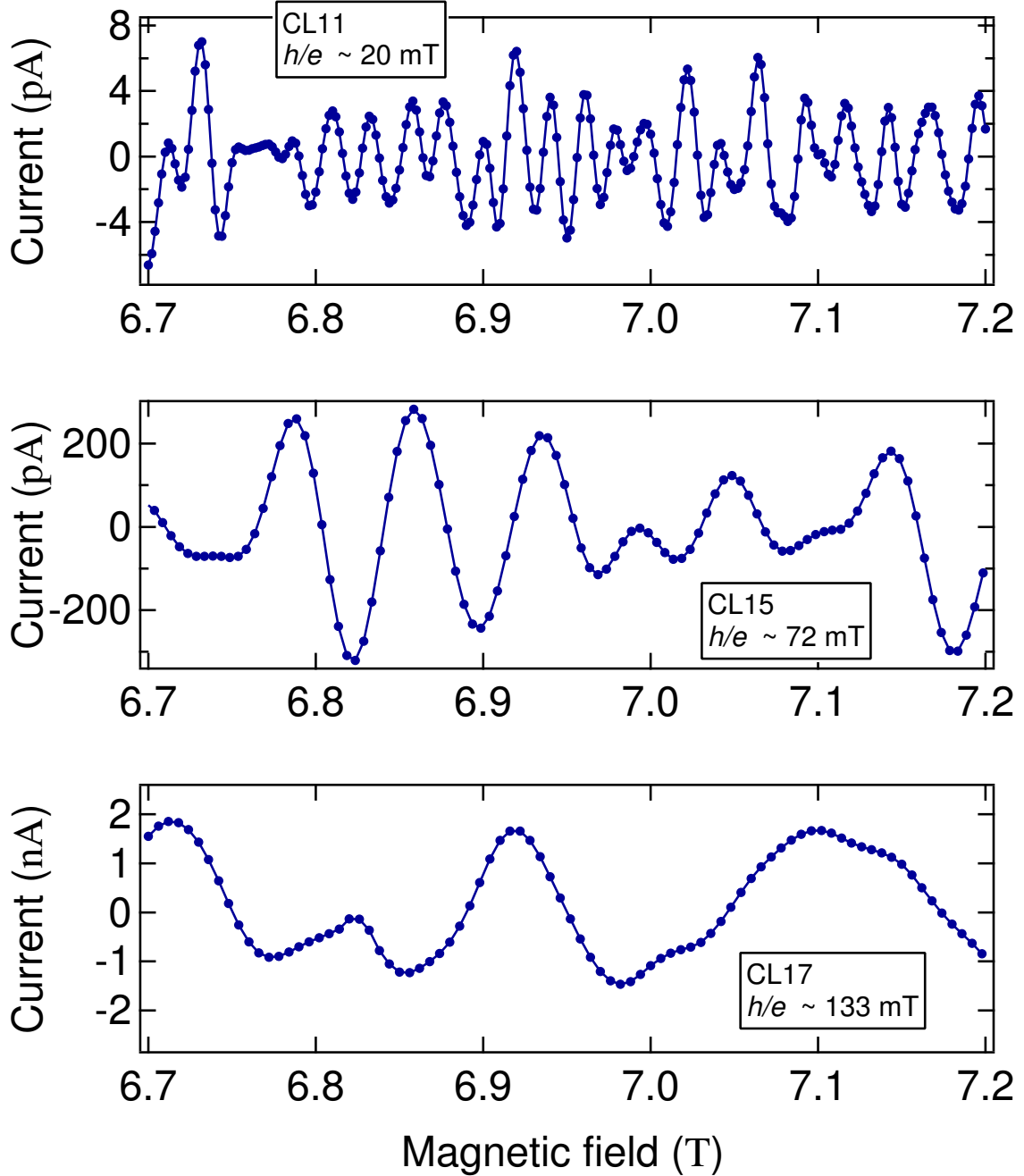


Figure 7.16: Comparison of persistent current measured for samples with three different ring sizes. From top to bottom, the observed current for samples CL11, CL15, and CL17 of Tables 7.1 and 7.2 are shown in order of decreasing ring size. Each trace is labeled with the expected magnetic field scale $1/\beta_1$ for threading h/e through the mean ring radius with an angle θ_0 of 6° between the magnetic field and the plane of the rings. As ring size decreases, both the magnetic field scale and the current magnitude of typical features increases. The measurements shown were taken at $T = 323 \text{ mK}$.

associated with threading a flux quantum h/e through the mean ring radius can be written as

$$B_{h/e} = \frac{1}{\beta_1} = \frac{4\pi\phi_0}{L^2 \sin \theta_0}.$$

Thus one expects the period of the oscillation to decrease as θ_0 increases from 0° to 90° . This trend is clearly followed by the data in both Figs. 7.17 and 7.18.

The effect of the angle θ_0 on the persistent current was addressed briefly in 2.3.2.1 in which the consequences of magnetic field penetrating the metal portions of the ring was discussed. For the most part, Section 2.3.2.1 discussed the magnetic field penetrating the metal in terms of the toroidal field model. It was found that the magnetic flux through the metal introduced a finite scale B_c of correlation to the persistent current oscillation. It was also argued that this field scale would need to be rescaled by a factor of order unity for a different geometrical arrangement between the ring and the applied magnetic field. That the observed persistent current oscillation has a finite range of correlation is evident in Figs. 7.17 and 7.18, especially in the data taken with $\theta_0 = 45^\circ$ for which more oscillations fit into the 0.5 T field range shown. The analysis of Section 2.3.2.1 predicted no change in the typical magnitude of the current, and indeed the current magnitudes in Figs. 7.17 and 7.18 are of the same order of magnitude for both orientations.

In Section 7.1.1, the frequency shift was scaled by a factor of \sqrt{N} to determine the current per ring where N is the number of rings on the cantilever. This choice of scaling was justified by citing the fact that the persistent current discussed in 2.3 is random in sign. Additionally, near the end of Section 2.3.3.2 it was argued that for moderate ring to ring variation the phase of oscillation in magnetic field should be random from ring to ring in the regime of magnetic field over which the measurements discussed in this section were performed.²

The \sqrt{N} scaling is justified as follows. The frequency of a cantilever containing an array of N rings is affected by the total current I_Σ of all of the rings in the array. The quantity I_Σ can be written as

$$I_\Sigma = \sum_{j=1}^N I_j$$

where I_j is the current in the j^{th} ring. Writing the Fourier series expansion with respect to magnetic

²The effect of magnetic flux through the metal discussed in Section 2.3.2.1 also leads to a random phase. We point out the other source of phase randomization because fewer assumptions about the nature of the persistent current were required to derive it.

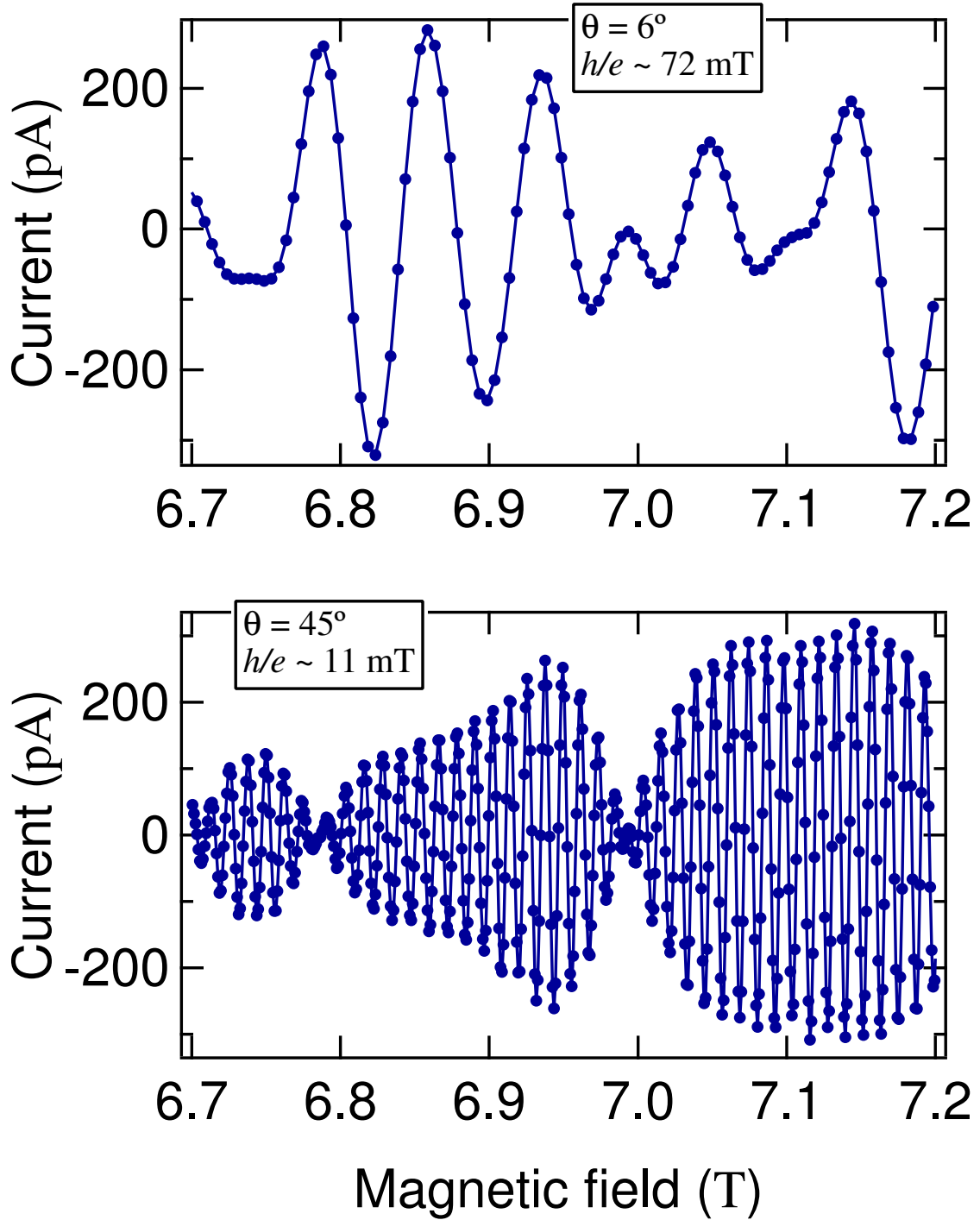


Figure 7.17: Comparison of persistent current observed in sample CL15 for two different angles θ_0 . The current inferred from measurements with $\theta_0 = 6^\circ$ and $T = 323 \text{ mK}$ (top graph) and $\theta_0 = 45^\circ$ and $T = 365 \text{ mK}$ (bottom graph) are shown. The expected h/e periodicity in terms of applied magnetic field is given with each plot for the mean ring radius and specified angle θ_0 .

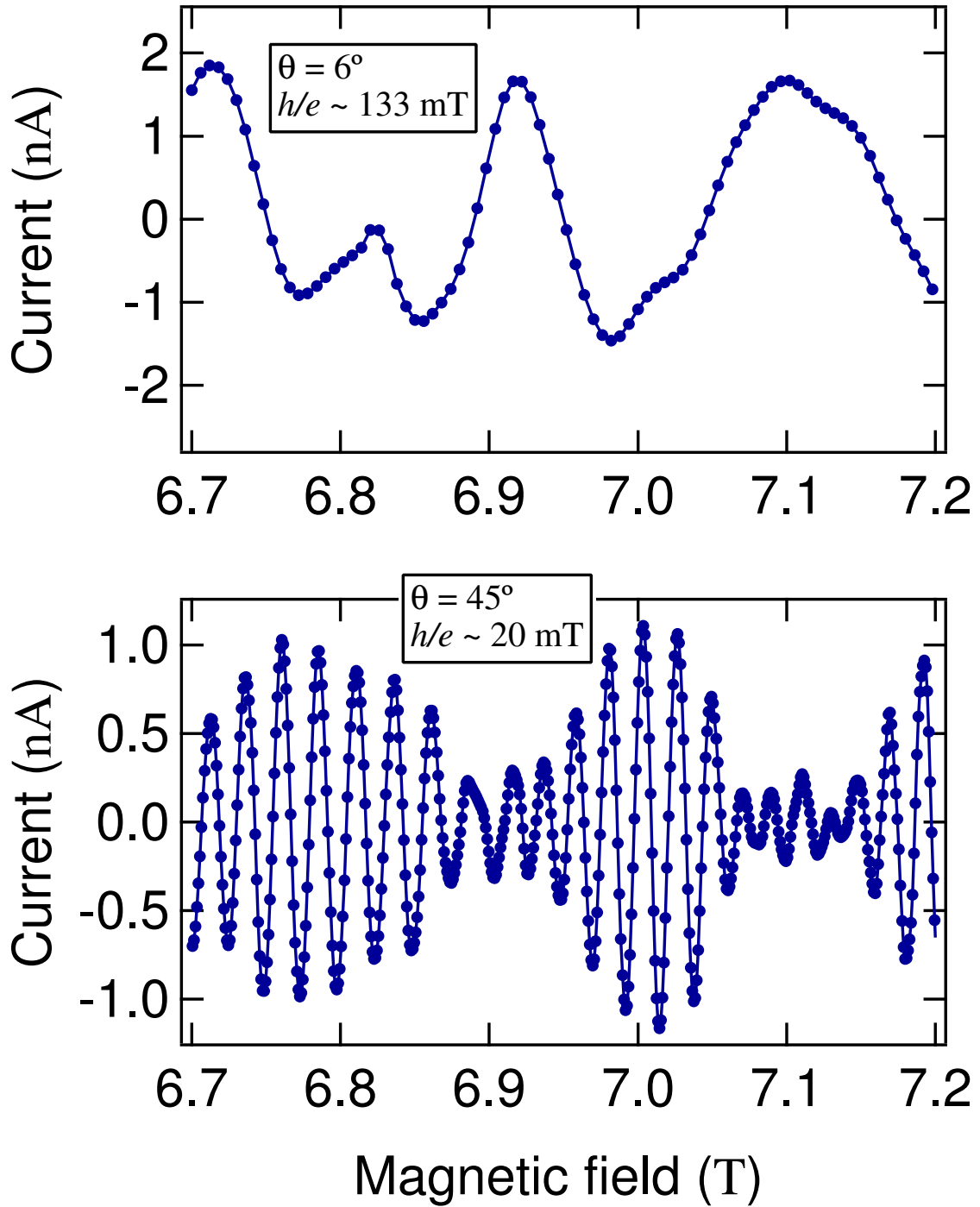


Figure 7.18: Comparison of persistent current observed in sample CL17 for two different angles θ_0 . The current inferred from measurements with $\theta_0 = 6^\circ$ and $T = 323 \text{ mK}$ (top graph) and $\theta_0 = 45^\circ$ and $T = 365 \text{ mK}$ (bottom graph) are shown. The expected h/e periodicity in terms of applied magnetic field is given with each plot for the mean ring radius and specified angle θ_0 .

field of the j^{th} ring as

$$I_j(B) = \text{Im} \left[\sum_p I_{j,p} e^{2\pi i p \beta_1 B} e^{i\psi_p} \right],$$

the p^{th} coefficient of the expansion

$$I_\Sigma(B) = \text{Im} \left[\sum_p I_{\Sigma,p} e^{2\pi i p \beta_1 B} e^{i\psi_p} \right]$$

of the total current can be written as

$$I_{\Sigma,p} = \sum_{j=1}^N I_{j,p}.$$

For a cantilever with an array of rings, the coefficient I_p in Eq. 4.26 relating the frequency shift and the persistent current becomes $I_{\Sigma,p}$. The central limit theorem of probability theory states that, when all of the $I_{j,p}$ satisfy $\langle I_{j,p} \rangle = 0$ and $\sqrt{\langle I_{j,p}^2 \rangle} = I_p^{\text{typ}}$, the sum $I_{\Sigma,p}$ satisfies $\langle I_{\Sigma,p} \rangle = 0$ and $\sqrt{\langle I_{\Sigma,p}^2 \rangle} = \sqrt{N} I_p^{\text{typ}}$ in the limit of large N . According to the central limit theorem, the typical magnitude of the current in the array is a factor of \sqrt{N} larger than the single ring current. Therefore, when the total current trace from an array of rings is rescaled by \sqrt{N} , the resulting trace has the same typical magnitude as the trace from a single ring. We note that more generally the central limit theorem requires that in the limit of large N the total current amplitude $I_{\Sigma,p}$ in an array should follow the normal distribution with zero mean and a standard deviation of $\sqrt{N} I_p^{\text{typ}}$.

Fig. 7.19 displays an experimental result in support of the \sqrt{N} scaling. In the figure, the current observed for samples CL14 and CL15 are plotted between 8.1 and 8.4 T for $\theta_0 = 45^\circ$ and $T = 365$ mK. The two samples both contain rings with the same circumference $L = 2.6 \mu\text{m}$, but CL15 had an array of 990 rings fabricated on its tip whereas sample CL14 had only a single ring.³ Nevertheless, with the frequency shift from CL15 converted into a current per ring using the \sqrt{N} scaling, the current was observed to be of the same order of magnitude, ~ 200 pA, for both rings. A more quantitative comparison of the current magnitude observed for each sample will be provided below.

³The chip also contained single ring samples with ring radii of 540 nm and 793 nm. No current was observed in these samples, but, given the diffusion constants (see below) and the scatter in the cantilever frequency, the signal to noise ratio for these samples was expected to be less than one.

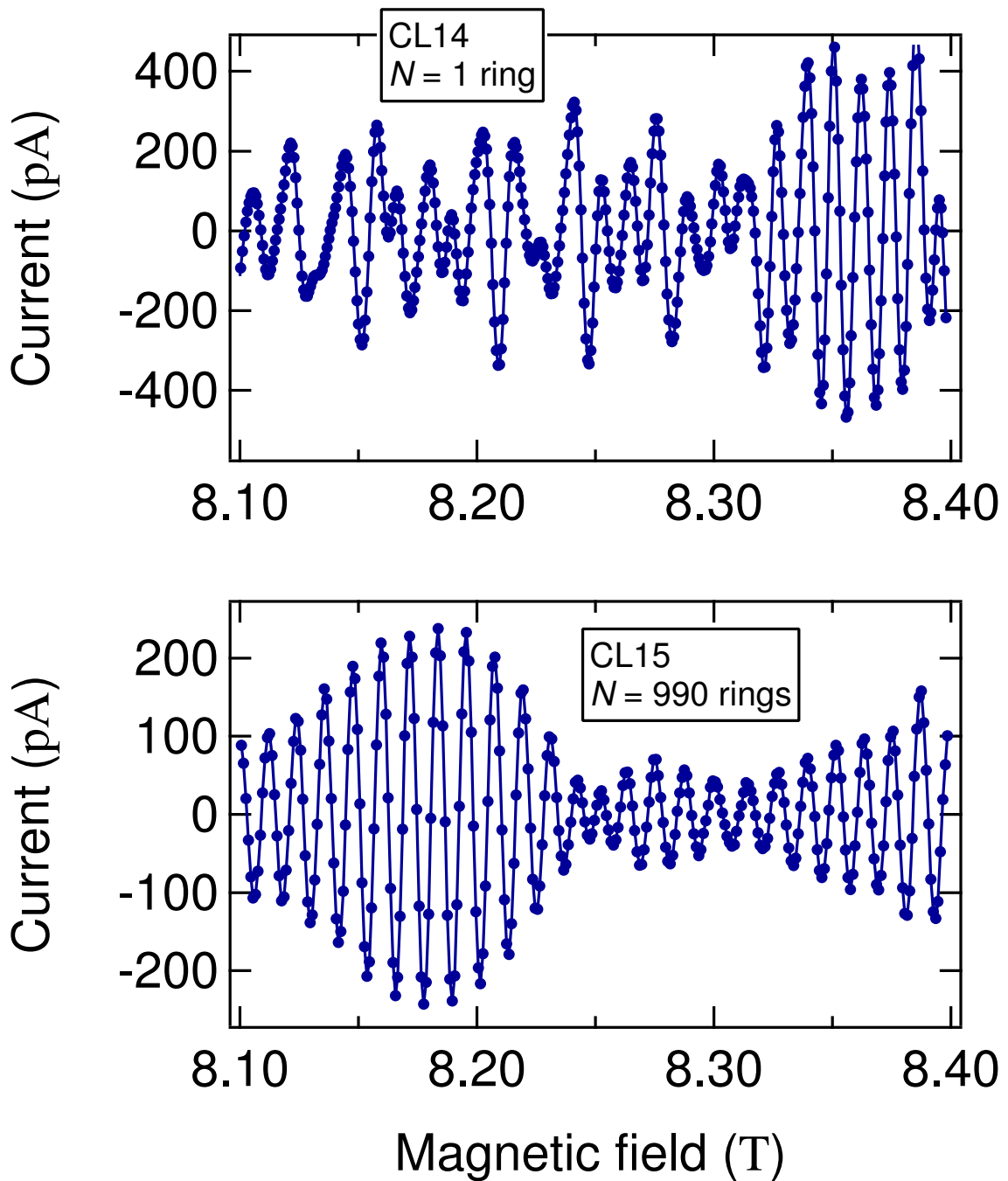


Figure 7.19: Comparison of the persistent current signal from a single ring with the signal from an array of rings. The inferred persistent current per ring for samples CL14 (upper plot) and CL15 (lower plot) are shown for $\theta_0 = 45^\circ$ and $T = 365$ mK between 8.1 and 8.4 T. The cantilevers and rings of both samples are nominally the same with the main difference that sample CL14 had only a single ring while sample CL15 had an array of 990 rings. With the signal scaled to represent the current per ring as described in the text, both samples show similar current magnitudes and magnetic field dependence.

7.3.2 Quantitative discussion

In order to test the theoretical picture of Chapter 2 more directly, we measured each sample listed in Tables 7.1 and 7.2 over as wide a range of magnetic field and temperature as possible. The large magnetic field scans were all performed at the refrigerator’s base temperature with the sample chip oriented at both $\theta_0 = 6^\circ$ and $\theta_0 = 45^\circ$ relative to the magnetic field. Plots of the inferred persistent current versus magnetic field from these measurements are presented in 7.3.3. Measurements at different temperatures were performed over small regions of magnetic field as described below.

The main result of Chapter 2 that can be tested by our measurements is Eq. 2.85 which specifies the persistent current correlation function $\langle I(\phi, B_M)I(\phi', B'_M) \rangle$ in the presence of finite temperature, spin-orbit scattering, and Zeeman splitting. We do this by determining the magnitude $I_{p,\text{meas}}^{\text{typ}}$ of the typical current at a series of temperatures for each sample and comparing this quantity to $I_p^{\text{typ}}(T, E_Z, E_{SO})$ given in Eq. 2.86.⁴ We now describe the procedure used to determine the measured typical current $I_{p,\text{meas}}^{\text{typ}}$. In discussing our experimental results, we treat ϕ as the magnetic flux threading the mean radius of the ring and write $\phi/\phi_0 = \beta_1 B$ as was done in Eq. 7.2.

7.3.2.1 Power spectral density of the persistent current

According to 2.3.2.1, the magnetic field B of the experimental arrangement differs from the toroidal magnetic field B_M considered in that section through a geometrical factor γ of order unity. We define this factor by the relation $B = \gamma B_M$. The finite range of correlation in applied magnetic field can then be written as $\gamma B_{c,p}$ where $B_{c,p}$ was introduced in 2.3.2.1 as the correlation range in terms of the toroidal field B_M for the p^{th} harmonic of the current.

The finite correlation in applied magnetic field of the persistent current oscillation implies that measurements of the persistent current made in one ring at values of B separated by $\Delta B \gg \gamma B_{c,p}$ are uncorrelated and thus effectively independent measurements of the persistent current for that ring. By measuring the current over a field range $B_0 \gg \gamma B_{c,p}$, we can build up a data set of many independent measurements of the current. The uncertainty in the calculated cumulants of such a finite, correlated data set has been derived previously [307] and will be used below to find the uncertainty in our measurements.

The finite correlation in applied magnetic field B of the persistent current oscillation also leads to a broadening of the peak located at $\beta = p\beta_1$ associated with the p^{th} harmonic of the current.

⁴For clarity, we add the subscript “meas” to the magnitude extracted from the data rather than that expected from theory.

We can rewrite the persistent current autocorrelation function of Eq. 2.85 in terms of the applied field B as

$$\langle I(B)I(B+B') \rangle = \sum_{p=1}^{\infty} (I_p^{\text{typ}}(T, E_Z, E_{SO}))^2 \cos(2\pi p\beta_1 B') K_p\left(\frac{B'}{\gamma B_{c,p}}\right)$$

where $I_p^{\text{typ}}(T, E_Z, E_{SO})$ was given in Eq. 2.86 and K_p is the autocorrelation function

$$K_p(x) = \frac{c_p^T(T, B_{c,p}x, E_Z, E_{SO})}{c_p^T(T, 0, E_Z, E_{SO})} \quad (7.9)$$

normalized so that $K_p(0) = 1$ and rescaled in B so that an argument of $x = 1$ corresponds to $B_M = B_{c,p}$. For $T = 0$ and $E_{SO} \gg E_c$, the Fourier transform of $K_p(x)$ is a peak centered at zero with a half-width at half-maximum of $\Delta \sim 1/6$. Consequently, the Fourier transform of $\langle I(B)I(B+B') \rangle$ with respect to B' consists of a series of peaks located at $\beta = p\beta_1$ and possessing half widths at half maximum of

$$\Delta\beta_p \approx \frac{1}{12\gamma B_{c,p}} \quad (7.10)$$

for each positive integer p . From Fig. 2.28, it can be seen that the correlation scale $B_{c,p}$ increases slightly with temperature and thus that $\Delta\beta_p$ decreases. We note that the Fourier transform of $\langle I(B)I(B+B') \rangle$ is equal to the power spectral density $S_I(\beta)$ of the persistent current.

In Figs. 7.20 through 7.25, we plot the power spectral densities $S_I(\beta)$ associated with each of the measured persistent current traces (see Section 7.3.3 for the complete traces). The power spectral densities are calculated from the data by

$$S_I(\beta) = \frac{2}{B_0} \left| \sum_{j=0}^{M-1} \Delta B I_j \exp(2\pi i j \beta \Delta B) \right|^2.$$

Here the $\{I_j\}$ are the M values of the current arranged in order of ascending magnetic field $B_j = B_i + j\Delta B$ with B_i the initial value of B and ΔB the magnetic field spacing. We use $B_0 = (M-1)\Delta B$ to indicate the range of magnetic field spanned by the measurement. Also shown in each plot are bars spanning the regions from $p\beta_1 - \Delta\beta_p$ to $p\beta_1 + \Delta\beta_p$ for $p = 1, 2$ in order to indicate the expected peak location and width of the first two harmonics of the persistent current. For these bars, we use the zero-temperature value for $\Delta\beta_p$ given in Eq. 7.10 with γ set to 1.

In all of the power spectral density plots shown, peaks are visible in the spectrum close to the

bars associated with the first harmonic of the persistent current oscillation. For the spectra with more well-defined peaks, the peaks appear to be centered at $\sim 90\%$ of the expected value for β_1 . This discrepancy in magnetic field frequency could be due to an offset error in the values of the orientation angle θ_0 of the cantilever chip relative to the applied magnetic field. An offset error of $\sim -6^\circ$ in θ_0 would be necessary to account for the observed discrepancy at a nominal angle of 45° . Such an offset in θ_0 would result in an underestimation of the current magnitude by $\sim 10\%$. However, we estimate that the offset angle should not be larger than 1° . We propose an alternative explanation of the discrepancy below. To account for the observed discrepancy at a nominal angle of 6° , an error of $\sim -0.5^\circ$ is required and results in a negligible error in the inferred persistent current magnitude.

Inaccuracy in defining the effective mean area A of the ring from its geometrical arrangement in the applied magnetic field could be responsible for the discrepancy in the observed magnetic field frequency. In 2.3, the finite linewidth of the ring is taken into account by modeling the applied magnetic field as an idealized Aharonov-Bohm flux plus a toroidal magnetic field. It is possible that an accurate model for the experimental geometry of a uniform magnetic field applied at angle to the plane of the ring would calculate the flux ϕ_{tot} threading the ring using a different area than the area corresponding to the mean radius of the ring⁵ and thus a different expression for the expected frequency β_1 . Using $\beta_1 = \pi R_{\text{eff}}^2 \sin \theta_0 / \phi_0$ with the nominal value for θ_0 , the observed values of β_1 correspond to values for the effective radius R_{eff} that are $\sim 5\%$ smaller than the nominal mean radii and thus still within the nominal linewidths of the rings. It is unlikely that there is a significant error in the dimensions of the rings as these dimensions were measured with a scanning electron microscope.

The clearest peaks were obtained for samples CL15 and CL17 at $\theta_0 = 45^\circ$. For these two measurements, the widest range ($B_0 > 5$ T) of magnetic field was studied and the greatest number M_{eff} of statistically independent measurements (see discussion below for a precise definition of M_{eff}) were obtained. The peaks in the spectra of the other measurements appear uneven due to the lower number of independent measurements. The spectra for samples CL15 and CL17 at $\theta_0 = 45^\circ$ are plotted on a log scale in Figs. 7.20 and 7.21. The suppression of the spectrum floor at low β is the result of the background subtraction steps (which act as high pass filters) performed during the frequency to current conversion (see Section 7.1). The downward sloping trend of $S_I(\beta)$ for higher

⁵By which we mean the area $\pi R^2 \sin \theta_0$ covered when a circle with a radius R equal to the mean radius of the ring is projected onto a plane perpendicular to the direction of the applied magnetic field.

values of β is produced by the intervening integration step that converts the current derivative $\partial_B I$ into the current I . The cantilever frequency spectrum $S_f(\beta)$ at high β is flat.

During the discussion of the conversion from frequency shift $\Delta f(B)$ to current $I(B)$, it was mentioned (see e.g. Fig. 7.4) that the coefficient dI_p^A , which is related to the value $S_I(\beta)$ of the power spectral density of the current at $\beta = p\beta_1$, was set to zero for $p \gtrsim p_{\text{zero}} = 0.6/\beta_1 GB_i$ (for which the argument of the jinc factor in Eq. 7.2 goes to zero) where B_i was the lowest value of B in the $\Delta f(B)$ trace. For Figs. 7.20 through 7.25, only frequencies β below this cut-off frequency $\beta_{\text{zero}} = p_{\text{zero}}\beta_1 = 0.6/GB_i$ are shown. In all cases, the feature in the spectrum located close to the expected value of β_1 ends distinctly below this cut-off frequency.

For the measurements performed at $\theta_0 = 6^\circ$ for which the magnetic field frequency is lower, one might worry that subtractions of a smooth background from the data (performed in going from Fig. 7.1 to Fig. 7.2 and from Fig. 7.7 to Fig. 7.8 in the walk-through of method A given in 7.1.2) remove part of the persistent current signal. We do not believe this to be the case. For samples CL15 and CL17, the signal to noise ratio is quite large, comparable to that observed at $\theta_0 = 45^\circ$. An indication of the repeatability of the signal for sample CL17 is given by the figures of 7.1.2 which show comparisons of the current inferred from measurements made under several different experimental arrangements. No feature appeared consistently in the spectrum of the cantilever frequency f at the low values of β removed by the background subtraction.

Sample CL11 had a lower signal to noise ratio due to its weaker persistent current. We believe the lowest peak in the spectrum $S_I(\beta)$ Fig. 7.25 is actually not due to the persistent current. The drift of the cantilever frequency f over time results in an enhanced amount of noise in the low β region of the spectrum that falls off as β^{-x} for $x > 0$. Removal of the smooth background reduces the magnitude of the spectral components at the lowest β , resulting in a peak-like shoulder that, for sample CL11, is of comparable size to the persistent current signal. Separation of the persistent current signal from the background is aided by measuring the current at different temperatures. At higher temperature, the features at higher values of β decay while the low β shoulder does not. We discuss the signal from sample CL11 further in Section 7.3.3.

In the measurement of sample CL17 at $\theta_0 = 45^\circ$, we were able to observe the second harmonic ($p = 2$) of the current. In Fig. 7.20, the second harmonic peak is difficult to discern as it is only slightly larger than the background. From Eqs. 2.85 and 4.26, it can be seen that the frequency shift Δf due to the p^{th} harmonic of the persistent current is proportional to $p^{-0.5} \exp(-p^2 k_B T / E_c)$.

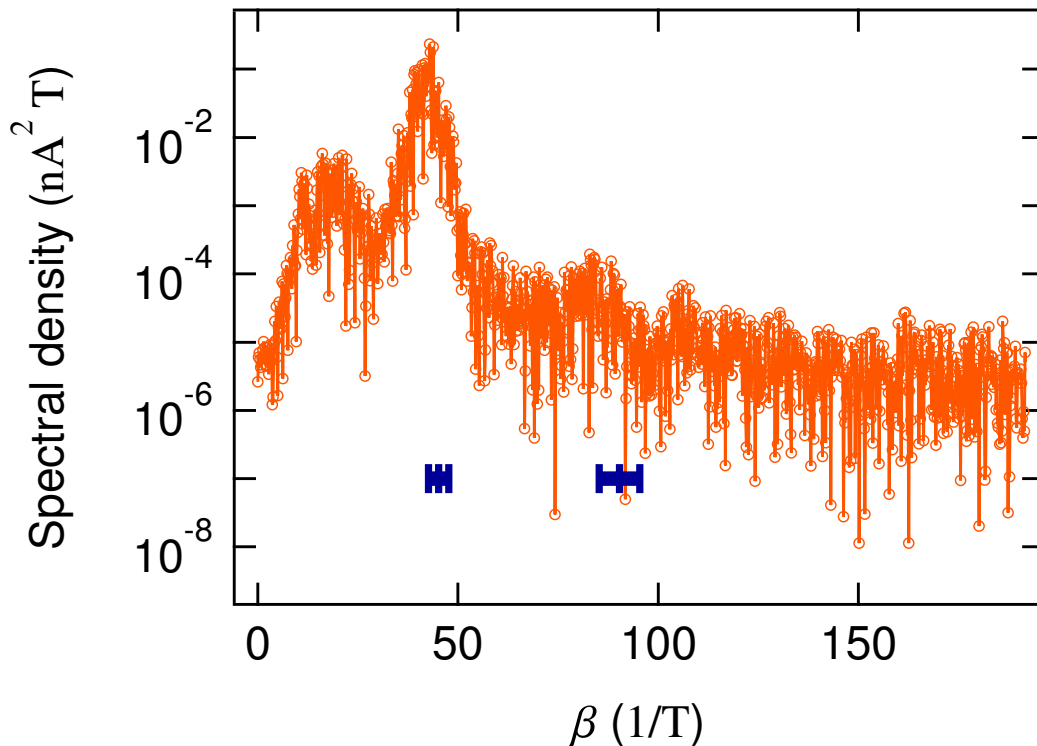


Figure 7.20: Persistent current power spectral density for sample CL17 at 45° . Horizontal bars indicate the expected location β_p and width $\Delta\beta_p$ of the peaks associated with the persistent current. The first harmonic peak is clearly visible. As discussed in the text, a small second harmonic peak is also present. The total current under the first harmonic peak is 653 pA while that under the second is 27 ± 9 pA. The data shown was taken at $T = 365$ mK.

Thus the signal from higher harmonics is reduced compared to the fundamental and more strongly suppressed by the effect of finite temperature. Additionally, the correlation field $B_{c,p}$ associated with the p^{th} harmonic scales as p^{-1} . Thus the width $\Delta\beta_p$ of the p^{th} peak in $S_I(\beta)$ grows linearly with p . This effect contributes to the difficulty in observing the second harmonic peak as the smaller persistent current power is spread out over a wider range of β . When we measure the current over a small range of magnetic field closer to the correlation field $B_{c,p=2}$, we observe a stronger peak for the second harmonic of the current. Such a measurement is shown below in Figs. 7.27 and 7.28. That this feature decays much more strongly with temperature than the peak associated with the first harmonic is a strong confirmation that it is indeed the second harmonic of the persistent current oscillation.

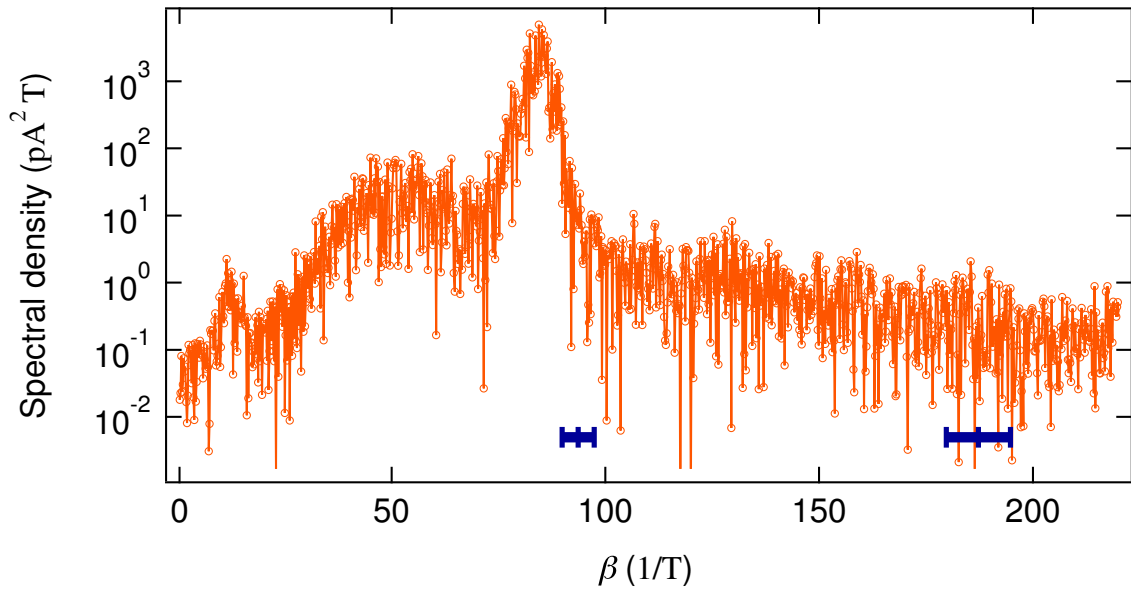


Figure 7.21: Persistent current power spectral density for sample CL15 at 45° . Horizontal bars indicate the expected location β_p and width $\Delta\beta_p$ of the peaks associated with the persistent current. The first harmonic peak is clearly visible. No second harmonic peak is detected above the level of the noise background. The total current under the first harmonic peak is 131 pA. The data shown was taken at $T = 365$ mK.

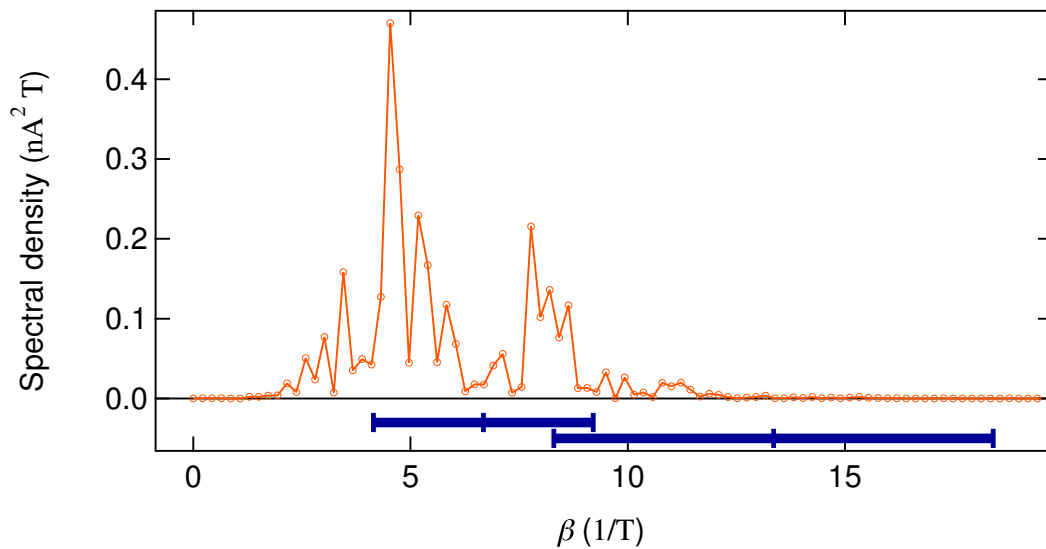


Figure 7.22: Persistent current power spectral density for sample CL17 at 6° . All of the features present in the spectrum are associated with the first harmonic of the persistent current signal. Horizontal bars indicate the expected location β_p and width $\Delta\beta_p$ of the peaks associated with the persistent current. At this small angle θ_0 , the magnetic field frequencies β_p of the persistent current harmonics are not much larger than the widths $\Delta\beta_p$ of the associated peaks. The second harmonic, which was barely detectable at $\theta_0 = 45^\circ$, is indistinguishable from the slightly larger background observed for $\theta_0 = 6^\circ$. The total current associated with all features is 693 pA. The data shown was taken at $T = 323$ mK.

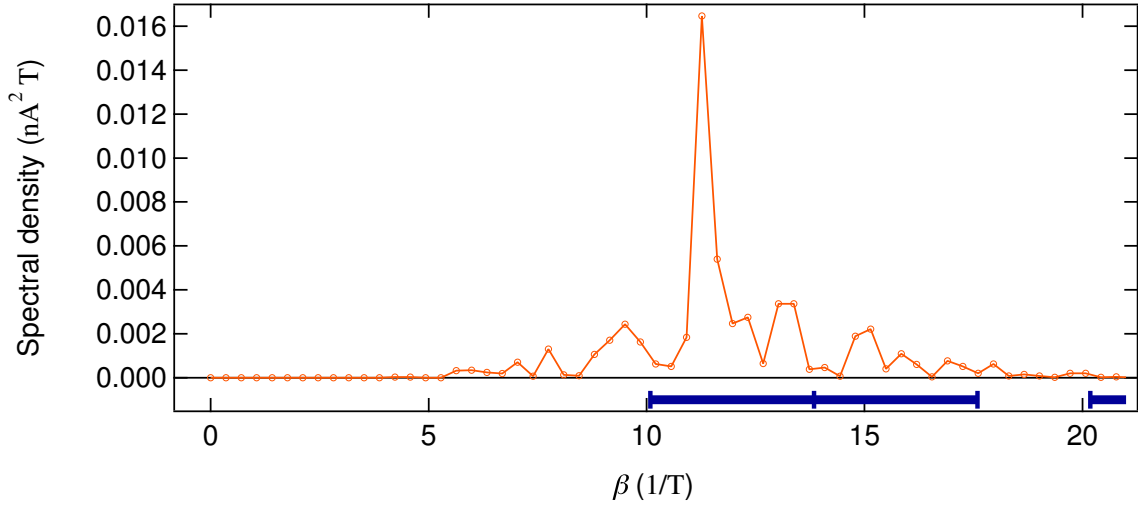


Figure 7.23: Persistent current power spectral density for sample CL15 at 6° . A broad peak associated with the persistent current is visible. Horizontal bars indicate the expected location β_p and width $\Delta\beta_p$ of the peaks associated with the persistent current. Most of the region of the spectrum associated with the second harmonic is above the cut-off frequency $\beta_{\text{zero}} = 21 \text{ T}^{-1}$ beyond which the measurement was insensitive to the persistent current. The large spike in the middle of the peak is presumably due to insufficient averaging associated with the small number of measured statistically independent sections of the persistent current signal. The total current under the peak is 133 pA. The data shown was taken at $T = 323 \text{ mK}$.

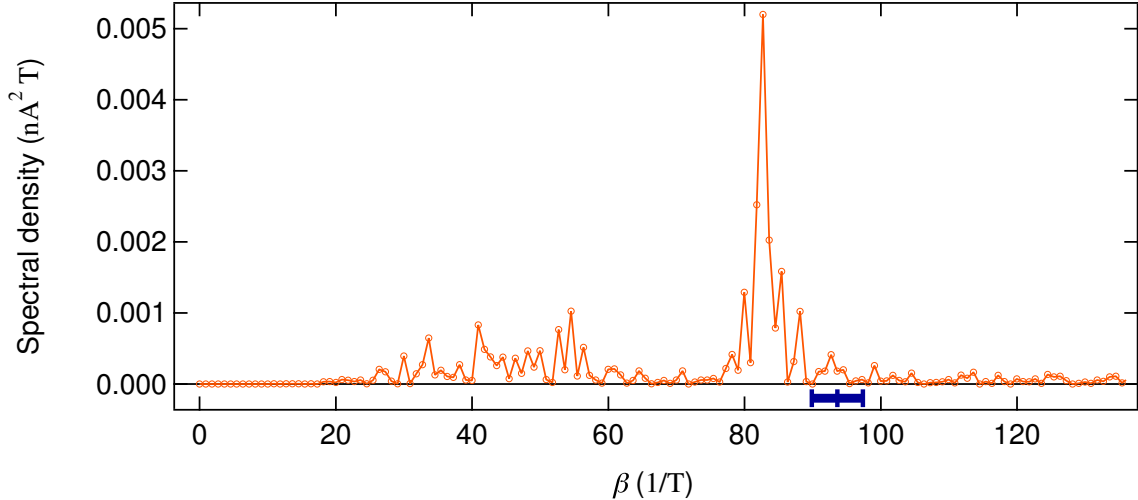


Figure 7.24: Persistent current power spectral density for sample CL14 at 45° . The horizontal bar indicates the expected location β_p and width $\Delta\beta_p$ of the peak associated with the first harmonic of the persistent current signal. A strong peak due to the persistent current is present at values of β just below the region covered by this bar. The cut-off frequency β_{zero} discussed in the text occurs at $\beta = 136 \text{ T}^{-1}$, below the region of the spectrum associated with the second harmonic. A low, broad peak is located at lower values of β than the large peak near the expected location of the first harmonic of the persistent current signal. This smaller peak is the remnant of the low β noise removed during the subtraction of the smooth background. The total current under the peak is 116 pA. The data shown was taken at $T = 365 \text{ mK}$.

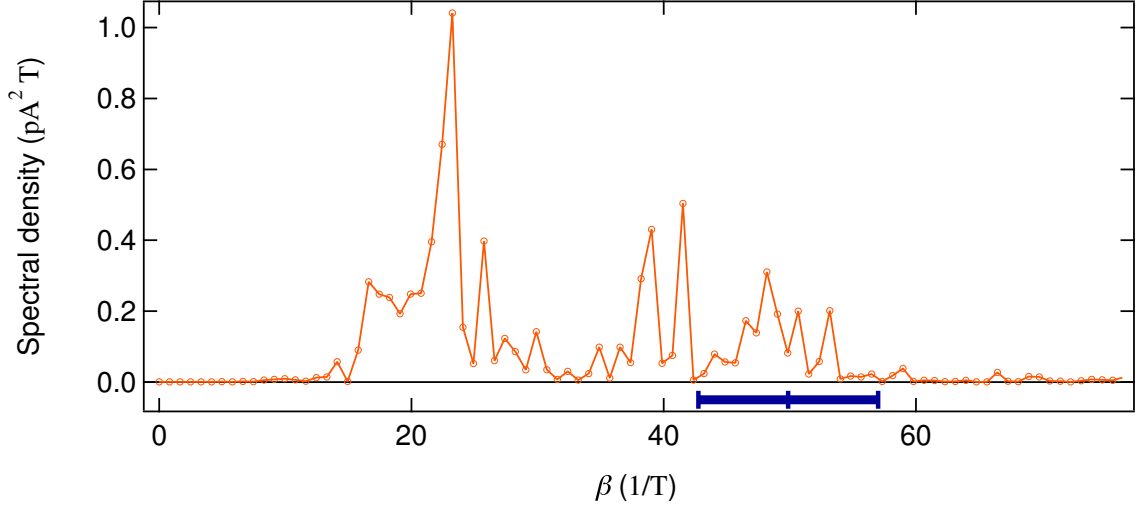


Figure 7.25: Persistent current power spectral density for sample CL11 at 6° . The horizontal bar indicates the expected location β_p and width $\Delta\beta_p$ of the peak associated with the first harmonic of the persistent current signal. The wide peak above the bar and the two slightly taller peaks located just below it in β are due to the persistent current. The larger peak closer to $\beta = 20 \text{ T}^{-1}$ is the shoulder left by the removal of the smooth background from the low β noise in the $\Delta f(B)$ and $I(B)$ traces (see discussion in text and Fig. 7.50). The cut-off frequency β_{zero} at which the measurement was insensitive to the persistent current occurs at $\beta = 82 \text{ T}^{-1}$, below the region of the spectrum associated with the second harmonic. Total current associated with the features which we attribute to the persistent current is 1.7 pA . The data shown was taken at $T = 323 \text{ mK}$.

7.3.2.2 Determination of the temperature dependence from the measured persistent current

We determined the measured typical current $I_{p,\text{meas}}^{\text{typ}}(T_b)$ at the refrigerator's base temperature T_b by finding the area under the peak of the power spectral densities $S_I(\beta)$ shown in Figs. 7.20 through 7.25. To do this, we first fit a curve $b(\beta)$ to each spectral density $S_I(\beta)$ excluding the region dominated by the peak. The fitted background curve $b(\beta)$ for $S_I(\beta)$ of sample CL17 at $\theta_0 = 45^\circ$ is shown in Fig. 7.26. The measured typical current $I_{p,\text{meas}}^{\text{typ}}(T_b)$ is taken to be the square root of the area under $S_I(\beta)$ minus the area under $b(\beta)$ in the vicinity of the peak:

$$\begin{aligned} (I_{p,\text{meas}}^{\text{typ}}(T_b))^2 &= \int_{\beta_p^-}^{\beta_p^+} d\beta (S_I(\beta) - b(\beta)) \\ &= \sum_{\beta_j = \beta_p^-}^{\beta_p^+} \Delta\beta (S_I(\beta_j) - b(\beta_j)) \end{aligned}$$

where $\Delta\beta = 1/B_0$ is the point spacing in β of the power spectral density $S_I(\beta)$ calculated from the measured current data. The bounds of the integration, β_p^- and β_p^+ , are chosen to be outside

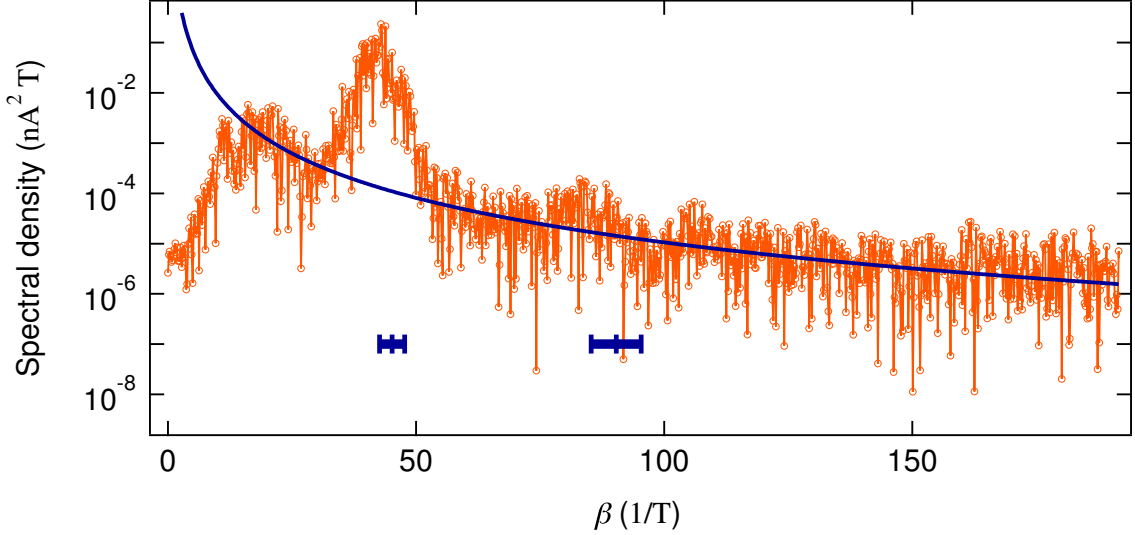


Figure 7.26: Fit to the background of the persistent current power spectral density for sample CL17 at 45° . The data (circles) and horizontal bars are the same as those shown in Fig. 7.20. The solid line added in this plot represents a fit $b(\beta)$ to the spectrum $S_I(\beta)$ close to, but outside of, the peak associated with the first harmonic of the persistent current signal. The curve shown represents $b(\beta) = (8.1 \times 10^{-23} \text{ A}^2 \text{ T})(\beta \times 1 \text{ T})^{-2.9}$. For each persistent current sample and orientation θ_0 , the square of the typical current was determined by finding the area under the peak in $S_I(\beta)$ minus the area under the background $b(\beta)$ over the same region of β .

of, but close to, the edges of the peak. Their precise locations are not critical since the quantity $S_I(\beta) - b(\beta)$ is zero on average outside of the peak.

For each measurement, the background fit was of the form

$$b(\beta) = X\beta^{-Y}$$

with X and Y fitting parameters. The value $I_{p,\text{meas}}^{\text{typ}}(T_b)$ of the typical current inferred from each large magnetic field scan is given in the caption of the corresponding power spectral density plot (Figs. 7.20 through 7.25). For each first harmonic, the error in the calculated typical current $I_{p,\text{meas}}^{\text{typ}}(T_b)$ due to fluctuations in the background were a few percent or less and thus negligible compared to the systematic uncertainty both due to error in the angle θ_0 discussed above and due to the finite number M_{eff} of statistically independent measurements of the current discussed below. The uncertainty in the second harmonic of the signal from sample CL17 due to the background measurement noise was about 33%.

In order to characterize the temperature dependence of the typical current, we measured the persistent current of each sample over a small region of magnetic field at a series of temperatures.

Some of the persistent current traces $I(B)$ measured for sample CL17 at $\theta_0 = 45^\circ$ are shown in Fig. 7.27. The magnitude of the Fourier transform of all persistent current traces measured for this sample are shown in Fig. 7.28. In both figures, the features of the persistent current show little change with temperature other than an overall scaling of the current amplitude. In the Fourier transform, a second peak associated with the second harmonic of the persistent current signal is visible. As expected from Eq. 2.85, this peak decays much more quickly than the first harmonic peak. The second harmonic signal was only observable for sample CL17 and only at $\theta_0 = 45^\circ$.

For each measurement temperature T in the temperature series, we infer a current magnitude $I_{p,M}^{TS}(T)$ for the p^{th} harmonic of the persistent current signal from the size of the corresponding peak in the Fourier spectrum.⁶ The typical current magnitude $I_{p,M}^{\text{typ}}(T)$ at temperature T is then found by scaling the temperature series magnitude by $I_{p,M}^{\text{typ}}(T_b)/I_{p,M}^{TS}(T_b)$, a factor which relates the magnitude $I_{p,M}^{TS}$ of the current measured over the small region used for the temperature series to the typical magnitude $I_{p,M}^{\text{typ}}$ of the current inferred from measurements over a large range of magnetic field at the base temperature T_b . That is,

$$I_{p,M}^{\text{typ}}(T) = I_{p,M}^{TS}(T) \left(\frac{I_{p,M}^{\text{typ}}(T_b)}{I_{p,M}^{TS}(T_b)} \right).$$

The inferred typical current magnitudes $I_{p,M}^{\text{typ}}(T)$ for each sample, each angle θ_0 , each harmonic p , and all temperatures are shown in Fig. 7.29 along with fits described below.

This scaling procedure assumes that, as the temperature is varied, the magnitude of the current measured in the small region of field chosen for the temperature series maintains the same proportionality to the typical current determined from a measurement over a large region of magnetic field. From Eq. 2.85 and Fig. 2.28, it can be seen that the magnetic field scale of the correlation of the persistent current signal is expected to increase with temperature. This increasing correlation of the persistent current signal with temperature should lead to a change in its shape and thus to a change in the proportionality between the current magnitude within a particular small region of magnetic field and its value averaged over a large region of magnetic field. This effect produces a systematic error in our inferred magnitude of the typical current.

For the range of temperatures covered by our measurements (see Fig. 7.29), the magnetic field scale $B_{1/2}(T)$ of the persistent current autocorrelation function, which we define as the magnetic

⁶We characterized the size of the peak by averaging the two or three highest points defining the peak. An alternative method would be to integrate the peak in the power spectral density. As the shape of the peak was largely unchanged with temperature, the exact method chosen should not be critical.

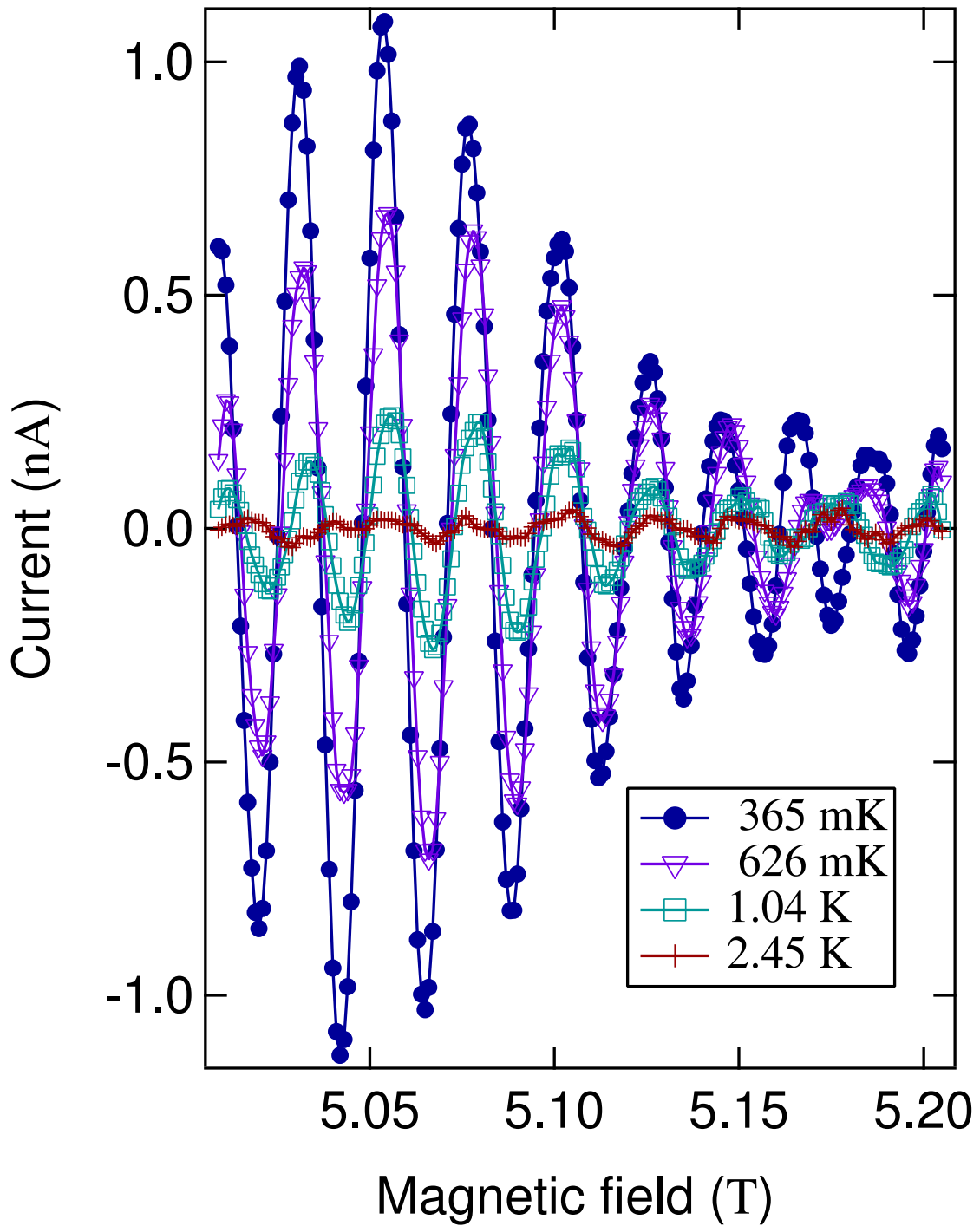


Figure 7.27: Persistent current versus magnetic field for a series of temperatures. The traces shown were taken on sample CL17 with $\theta_0 = 45^\circ$ and $T = 0.365, 0.420, 0.626, 0.831, 1.04,$ and 2.45 K. Varying the temperature produces an overall scaling of the data while largely leaving the shape of the trace unchanged. Fourier transforms of the traces shown are plotted in Fig. 7.28.

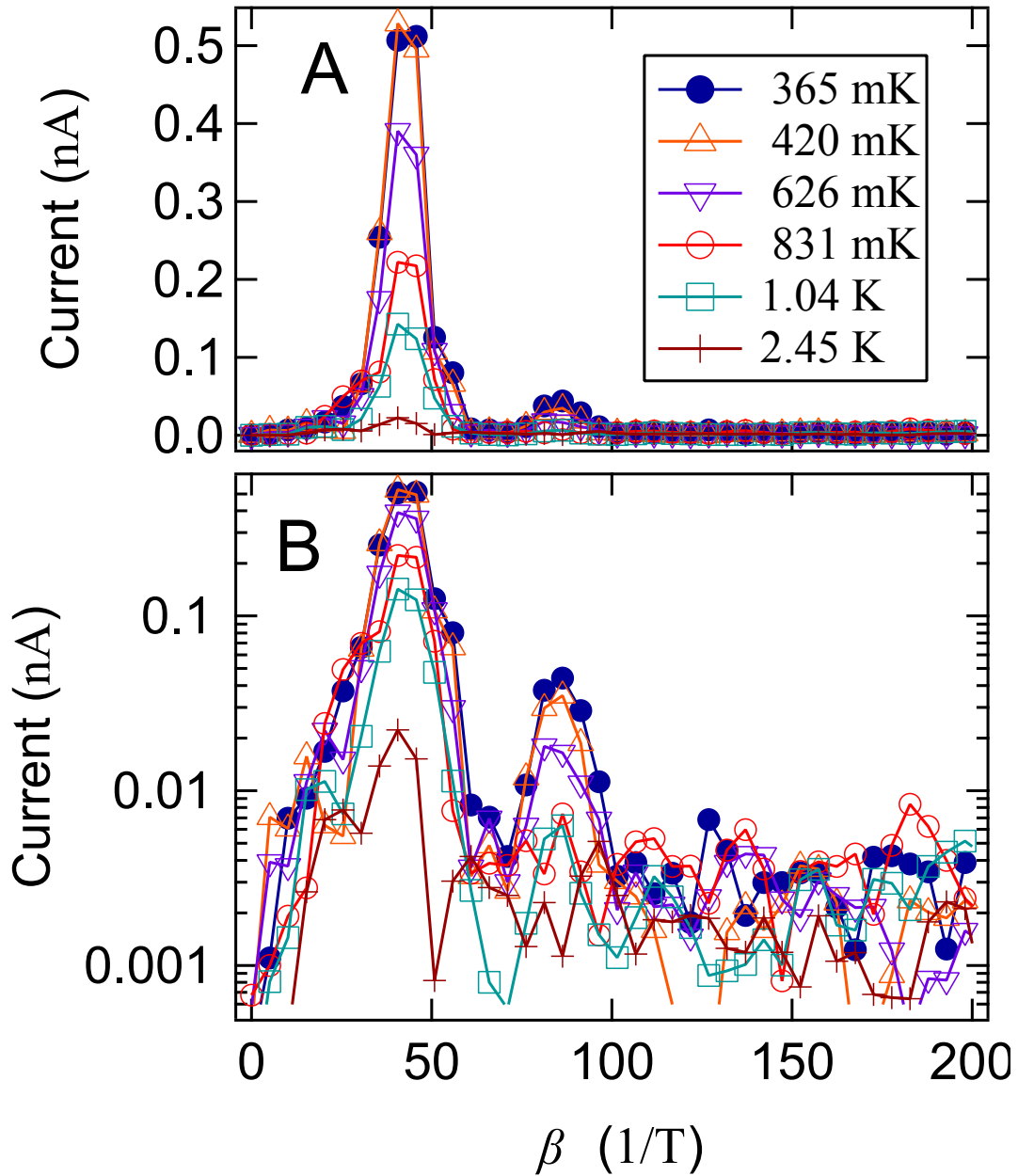


Figure 7.28: Fourier transform of the persistent current signal for a series of temperatures. The magnitude $|I(\beta)|$ of the Fourier transform of the persistent current traces measured for sample CL17 at θ_0 is shown for $T = 0.365, 0.420, 0.626, 0.831, 1.04,$ and 2.45 K. Panels A and B show the same data on linear and log scales respectively. Peaks in the spectrum at $\beta \approx 42 \text{ T}^{-1}$ and $\beta \approx 84 \text{ T}^{-1}$ represent the first and second harmonics of the persistent current signal respectively. The size of these peaks is used to calculate the data shown in Fig. 7.29 for the temperature dependence of the typical current. Several of the persistent current traces $I(B)$ corresponding to the Fourier transforms above are shown in Fig. 7.27. The Fourier transform $I(\beta)$ was calculated using the form given in Eq. 7.7 for the Fourier transform of $\Delta f(B)$.

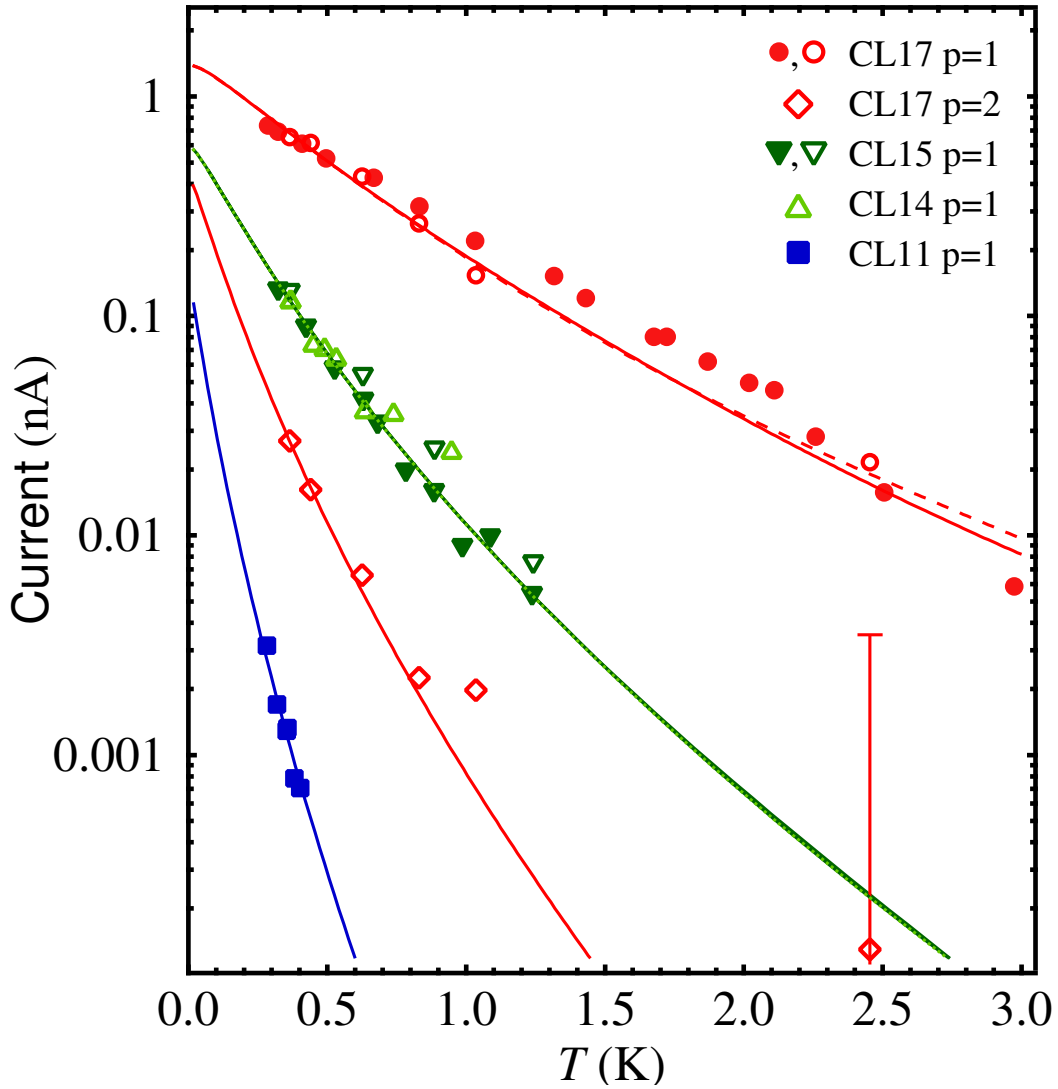


Figure 7.29: Typical magnitude of the persistent current versus temperature. The data points show the inferred magnitude $I_{p,M}^{\text{typ}}(T)$ of the current for each sample. Fits to Eq. 7.11 are also shown and are described in Section 7.3.2.3. Solid markers represent measurements taken with an angle $\theta_0 = 6^\circ$ between the plane of the rings and the applied magnetic field, while for hollow markers $\theta_0 = 45^\circ$. For sample CL17, the magnitude of the second harmonic of the current is represented by diamonds. For each other sample, only the first harmonic was observable. The error bars associated with noise in the cantilever frequency measurement were roughly the size of the markers or smaller except where indicated explicitly. The value for the diffusion constant D extracted from the fits are given in Table 7.3.

field scale $B_{1/2}$ satisfying $\langle I(\phi, B)I(\phi, B + B_{1/2}) \rangle = (1/2)\langle I(\phi, B)I(\phi, B) \rangle$ (see Fig. 2.28), roughly doubles. The size ΔB_{TS} of the magnetic field region studied for each temperature series was $\Delta B_{TS} \sim 1.5B_{1/2}(T_b)$, where T_b was the base temperature of the refrigerator. Thus at the highest temperature T_{\max} , $\Delta B_{TS} \sim 0.75B_{1/2}(T_{\max})$. In principle, one could expect a systematic error of $\lesssim 33\%$ in the inferred $I_{p,M}^{\text{typ}}(T_{\max})$ due the change in $B_{1/2}(T)$ as T increases from T_b to T_{\max} . In practice, we expect this error to be less for our measurements as we did not observe significant changes in the shape of the persistent current signal in our temperature series measurements.⁷ It would be interesting, but time consuming, to measure the persistent current over a large range $B_0 \gg B_{1/2}$ of magnetic field at a series of temperatures to investigate changes in the correlation scale of the persistent current signal with temperature.

For samples CL11 and CL17 at $\theta_0 = 6^\circ$, measurements were taken at $T \approx 285$ mK, below the nominal base temperature $T_b = 323$ mK. This lower temperature was achieved by filling the 1K pot with helium, closing the needle valve connecting it to the helium bath, and then pumping it down to the lowest possible temperature (~ 1.8 K). We used this procedure sparingly because it provided a low temperature only for a short duration (until the 1K pot was empty) and introduced additional measurement noise due to the vibrations of the pump. In the case of CL11 (largest rings and thus smallest characteristic temperature), the increase in current magnitude was large enough to offset the increase in noise, while for CL17 the signal was large enough that the signal to noise ratio was still large even with the added noise.

The inferred typical current magnitudes $I_{p,M}^{\text{typ}}(T)$ plotted in Fig. 7.29 represent measurements for which several parameters were varied. The ring circumference was varied by over a factor of two, going from $L = 1.9 \mu\text{m}$ (CL17) to $5.0 \mu\text{m}$ (CL11). Measurements were taken on two separate cooldowns each corresponding to a different angle θ_0 between the magnetic field and the plane of the rings, with $\theta_0 = 6^\circ$ represented by solid markers and $\theta_0 = 45^\circ$ by hollow markers. As expected, no dependence on the angle θ_0 is observed for the two samples, CL15 and CL17, measured in both orientations. For $L = 2.6 \mu\text{m}$, the inferred typical current per ring for a single ring (CL14) and an array of 990 rings (CL15) are both plotted and show good agreement, justifying the \sqrt{N} scaling of the arrays discussed above. Finally, for sample CL17, the magnitudes of both the first and second harmonics of the persistent current are shown.

⁷This result could be related to the fact that, rather than a typical region, we specifically chose regions where the current magnitude was largest for the temperature series.

7.3.2.3 Analysis of the temperature dependence of the persistent current

In order to compare the data shown in Fig. 7.29 to the theoretical picture discussed in 2.3, we fit the data for each sample using Eq. 2.86 for $I_p^{\text{typ}}(T, E_Z, E_{SO})$. The quantity $I_p^{\text{typ}}(T, E_Z, E_{SO})$ depends on D and L through the correlation energy E_c . Each sample was fit individually, but for each sample the data from both angles θ_0 and harmonics p were all used in a single fit. The only parameter varied during the fitting routine was the diffusion constant D . The sample circumference L was fixed to the value corresponding to the mean radius measured with a scanning electron microscope and listed in Table 7.2. The spin-orbit scattering length L_{SO} was held fixed to $1.1 \mu\text{m}$, the value obtained from transport measurements of a co-deposited wire (see Appendix E). To account for Zeeman splitting, the actual fitting function took the form

$$I_{p,\text{fit}}^{\text{typ}}(T, D) = \sqrt{\frac{\int_{B_{M,\text{min}}}^{B_{M,\text{max}}} dB (I_p^{\text{typ}}(T, E_Z(B), E_{SO}))^2}{B_{M,\text{max}} - B_{M,\text{min}}}} \quad (7.11)$$

where $B_{M,\text{min}}$ and $B_{M,\text{max}}$ were the minimum and maximum magnetic field values of the big magnetic field sweep (see 7.3.3) used to determine $I_{p,M}^{\text{typ}}(T_b)$. The quantity $I_{p,\text{fit}}^{\text{typ}}(T, D)$ given in Eq. 7.11 represents the average of the typical square magnitude of the current for the region of magnetic field over which the persistent current was measured.⁸

The curves resulting from fits of the typical persistent current data to Eq. 7.11 are shown in Fig. 7.29. For sample CL17, two curves are shown with the dashed curve corresponding to $\theta_0 = 45^\circ$ and the solid curve to $\theta_0 = 6^\circ$. The measurements for the two angles were made over regions of magnetic field (and corresponding ranges of E_Z) different enough to produce the slight separation between the curves at high temperature. Both curves are part of one single fit to the data from sample CL17 using Eq. 7.11. Only one curve is shown for samples CL14 and CL15. The same curve fit the data from both samples independently.

The fits shown in Fig. 7.29 agree well with the measured temperature dependence of the persistent current. The fitting function has roughly an exponential form $I_p^D \exp(-T/T_p)$ where both the amplitude $I_p^D = I_p^{\text{typ}}(T = 0, E_Z, E_{SO})$ and characteristic temperature T_p are proportional

⁸It is not clear that this is the best way to account for the effect of the Zeeman splitting. An alternative approach would be to use one value for $E_Z(B)$ with B chosen to be a value from within the measurement range, such as the midpoint. In any case, different methods for accounting for the Zeeman splitting produce only small changes in the form of $I_{p,\text{fit}}^{\text{typ}}(T, D)$ for the range of Zeeman splitting E_Z and temperature spanned by the measurements shown in Fig. 7.29. In fact, different methods of accounting for the finite Zeeman splitting in the form of $I_{p,\text{fit}}^{\text{typ}}(T, D)$ produce fits to the data with the same fitted diffusion constants D , although the fit curves look slightly different (with differences similar to the two curves in Fig. 7.29 fit to the first harmonic data from sample CL17).

Sample	D (m ² /s)	I_1^D (nA)	T_1 (mK)	γ	M_{eff}	$\eta(M_{\text{eff}})$ (%)
CL11	0.0196	0.15	62	(2.5)	(29)	(13)
CL14	0.0195	0.61	228	1.1	12	21
CL15	0.0195	0.61	228	1.1, (2.5)	57, (14)	9.4, (19)
CL17	0.0234	1.43	513	0.83, (2.8)	78, (20)	8.0, (16)

Table 7.3: Extracted parameters for persistent current samples. The diffusion constants D are the values inferred from the fits to $I_{p,\text{fit}}^{\text{typ}}(T, D)$ (Eq. 7.11) shown in Fig. 7.29. The magnitude $I_1^D = I_{p=1}^{\text{typ}}(T = 0, E_Z = \infty, E_{SO})$ of the persistent current in the zero-temperature, large Zeeman splitting limit (see Eq. 2.86) and the characteristic temperature T_1 (see Eq. 2.73) are calculated for the first harmonic from the fitted value for D and the value of L given in Table 7.2. The spin-orbit scattering length is fixed to $L_{SO} = 1.1 \mu\text{m}$, the value found in transport measurements (see Table E.1). The geometrical factors γ were found from fits to the autocorrelation of the persistent current shown in Figs. 7.30 through 7.35. The effective number M_{eff} of independent realizations and the fractional standard error $\eta(M_{\text{eff}})$ in the typical current are calculated from γ using Eqs. 7.12 and 7.15. For these last three quantities (see discussion in Section 7.3.2.4), values in parentheses correspond to measurements at $\theta_0 = 6^\circ$ and those without parentheses to measurements at $\theta_0 = 45^\circ$.

to the only fitting parameter, the diffusion constant D .⁹ Table 7.3 lists the values of the fitted diffusion constant D and of $I_p^{\text{typ}}(T = 0, E_Z, E_{SO})$ and T_p calculated for the first harmonic of each sample using fitted D .

A further confirmation of the accuracy of the theoretical picture of Section 2.3.1 (and Eq. 2.85 in particular) is provided by a comparison of the fitted diffusion constants D from the different samples. The values of D found for samples CL11, CL14, and CL15 all agree within the 6% error margin which we discuss below. The value of D obtained for sample CL17 was $\sim 20\%$ larger than the values obtained for the other samples. While a 20% discrepancy is reasonable for different measurements of the diffusion constant, we note that the ring linewidth $w_r = 115 \text{ nm}$ of sample CL17 was somewhat larger than the linewidth $w_r = 85 \text{ nm}$ of the other samples. Additionally, scanning electron microscopy of other samples on the same chip (see Fig. D.7) revealed that features with the wider linewidth of sample CL17 had much more uniform sidewalls than features with the thinner linewidth of the other samples. If boundary scattering contributed significantly to electron diffusion in our samples, one would expect that the wider sample with smoother sidewalls would possess a larger value of D .

Comparison with the diffusion constant D_p found from transport measurements of a co-deposited

⁹For the sake of clarity, we reiterate that for sample CL17 both harmonics of the persistent current are fit simultaneously for one value of the diffusion constant D . In this case, there are essentially two characteristic temperatures, $T_{p=1}$ and $T_{p=2}$.

wire provides another check of the accuracy of our analysis. In Appendix E the diffusion constant of transport sample WL115 is reported as $D_\rho = 0.0259 \pm 0.0014 \text{ m}^2/\text{s}$. Sample WL115 was co-deposited with the persistent current samples and had nominally the same linewidth $w_w = 115 \text{ nm}$ as sample CL17. That the diffusion constants obtained from transport and persistent current measurements agree to within $\sim 10\%$, roughly the combined experimental uncertainty for the two measurements, is a strong endorsement for the theoretical picture reviewed in Section 2.3.1.

7.3.2.4 Analysis of persistent current autocorrelation and estimation of statistical uncertainty of persistent current magnitude

We now discuss the sources of uncertainty in our measurements of the persistent current and in the extraction of the diffusion constant D . As discussed in chapters 2 and 3, the amplitude of the persistent current is expected to be a random quantity and to follow the normal distribution with a mean of zero and a standard deviation given by $I_p^{\text{typ}}(T, E_Z, E_{SO})$ (see Eq. 2.86). For the arrays, we expect that the current per ring (using \sqrt{N} scaling) will follow this distribution regardless of the distribution for the single ring current because of the central limit theorem. With the inference of any value found by averaging over measurements of a probabilistic quantity, there is an accompanying uncertainty due to the finite number of measurements entering into the statistical average. For M measurements of a quantity x following the normal distribution with mean $\langle x \rangle = 0$, it can be shown that the fractional standard error $\eta(M)$ due to finite sampling in the typical value $x^{\text{typ}} = \sqrt{\langle x^2 \rangle}$ of x is [308, 309]

$$\eta(M) \equiv \frac{\delta x^{\text{typ}}}{x^{\text{typ}}} = \sqrt{\frac{1}{2M}}. \quad (7.12)$$

For the persistent current measurements, the form of the standard error in the estimation of the typical current $I_{p,M}^{\text{typ}}$ is not as simple as Eq. 7.12. The finite correlation of the persistent current amplitude makes unclear what number should be used for the number of measurements M . In Ref. 307, Tsypliyatyev *et al.* derive expressions for the standard error of the cumulants calculated from a data set with a finite range of correlation. From their results one finds that the fractional error in the typical magnitude (which is related to the second cumulant when the mean is zero) satisfies

$$\frac{\delta I_p^{\text{typ}}}{I_p^{\text{typ}}} = \sqrt{\frac{\gamma B_{c,p}}{B_0}} \sqrt{\int_0^\infty dx (K_p(x))^2} \quad (7.13)$$

where $K_p(x)$ is the normalized and scaled correlation function¹⁰

$$K_p(x) = \frac{\langle I_p(B_M) I_p(B_M + B_{c,p}x) \rangle}{\langle I_p^2(B_M) \rangle}, \quad (7.14)$$

B_0 is the magnetic field range of the persistent current measurement and $B_{c,p}$ is the toroidal magnetic field correlation scale given in Eq. 2.79. γ is the geometrical factor that, for a given geometrical arrangement of the ring in the applied magnetic field, relates the toroidal field $B_{c,p}$ to a quantity $\gamma B_{c,p}$ which is expressed in units of the applied field. This expression is valid for a large measurement field range $B_0 \gg B_{c,p}$. At $T = 0$, $\int_0^\infty dx (K_p(x))^2 \approx 1.8$, so that

$$\frac{\delta I_p^{\text{typ}}}{I_p^{\text{typ}}} \approx \sqrt{1.8 \frac{\gamma B_{c,p}}{B_0}}.$$

We define an effective number of independent realizations M_{eff} of the persistent current as

$$M_{\text{eff}} = \frac{1}{2 \int_0^\infty dx (K_p(x))^2} \frac{B_0}{\gamma B_{c,p}} \quad (7.15)$$

by equating Eq. 7.13 for the statistical uncertainty in the typical persistent current magnitude with Eq. 7.12 for the uncertainty in a finite number of measurements of a normally distributed quantity.¹¹ At $T = 0$, $M_{\text{eff}} = B_0/3.6\gamma B_{c,p}$. From Fig. 2.28, it can be seen that the correlation of the persistent current is slightly enhanced at finite temperature and spin-orbit scattering and thus that M_{eff} is reduced from its value at $T = 0$.

In order to estimate M_{eff} for each measurement of $I_{p,M}^{\text{typ}}$, we analyze the autocorrelation of the large persistent current traces shown in 7.3.3. We calculate the autocorrelation $\langle I(B)I(B+B') \rangle_M$ of the persistent current data using

$$\begin{aligned} \langle I(B) I(B + j\Delta B) \rangle_M &= \frac{1}{P - j - 1} \sum_{k=0}^{P-j-1} I(B_{\min} + k\Delta B) I(B_{\min} + (j+k)\Delta B) \\ &\approx \frac{1}{B_0} \int_{B_{\min}}^{B_{\min}+B_0} dB' I(B') I(B' + j\Delta B) \end{aligned} \quad (7.16)$$

where B_{\min} is the minimum magnetic field measured, P is the total number of magnetic field values measured, and ΔB is the magnetic field spacing between measurements of the persistent current.

¹⁰We can also write $K_p(x)$ in terms of the notation of 2.3 (see e.g. Eq. 2.85 and subsequent formulae) as $K_p(x) = c_p^T(T, B_{c,p}x, E_Z, E_{SO})$.

¹¹Because the signal to noise ratio for the second harmonic signal observed for sample CL17 was so low, we do not analyze its autocorrelation function. Since we only consider the first harmonic, we do not index M_{eff} by p .

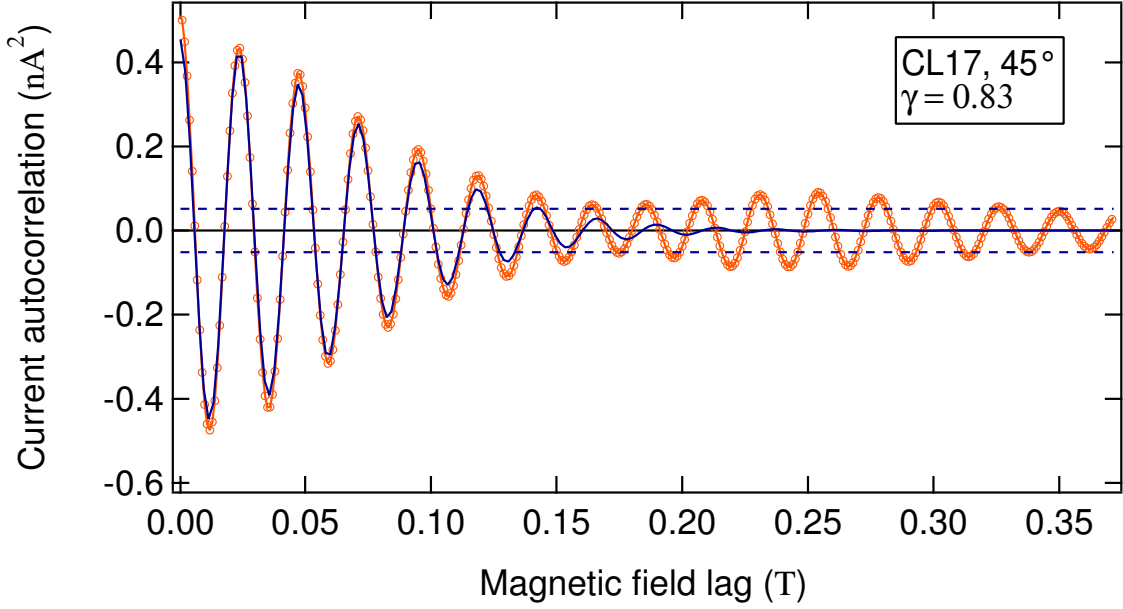


Figure 7.30: Persistent current autocorrelation for sample CL17 at $\theta_0 = 45^\circ$. Circles represent the autocorrelation of the data shown in Figs. 7.36 through 7.38. The curve is a fit to Eq. 7.17 as described in the text with $\gamma = 0.83$ and $p = 0.83$. The estimated standard error in the autocorrelation (dashed horizontal lines) is $\sqrt{2}\eta(M_{\text{eff}}) = 11\%$ of its value at zero magnetic field lag B' . Fluctuations of this magnitude are present at large B' where the autocorrelation is expected to be small.

The resulting traces of the autocorrelation $\langle I(B)I(B+B') \rangle_M$ versus the magnetic field lag B' are shown in Figs. 7.30 through 7.35. The measurements of samples CL17 (Fig. 7.30) and CL15 (7.31) at $\theta_0 = 45^\circ$ resulted in the nicest looking autocorrelation traces. As we shall see shortly, these two measurements achieved the highest values of M_{eff} and represent the best averaging over the statistical distribution of the persistent current for our measurements.

We analyze the autocorrelation data by fitting each trace to the first harmonic component of Eq. 2.85 which we rewrite in the form

$$\langle I(B)I(B+B') \rangle = (I_{p=1}^{\text{typ}})^2 \cos(2\pi p\beta_1 B') c_{p=1}^T \left(T, \frac{B'}{\gamma}, E_Z = \infty, E_{SO} \right). \quad (7.17)$$

In Eq. 7.17, we take the limit of large Zeeman splitting, $E_Z \rightarrow \infty$, because finite Zeeman splitting results in only small corrections to the autocorrelation function for the temperatures at which the large magnetic field traces were measured. For fitting the correlation function of the first harmonic, the coefficient p is fixed to 1 for both the persistent current typical magnitude $I_{p=1}^{\text{typ}}$ and the normalized correlation function $c_{p=1}^T$. However, in the argument of $\cos(2\pi p\beta_1 B')$, the coefficient

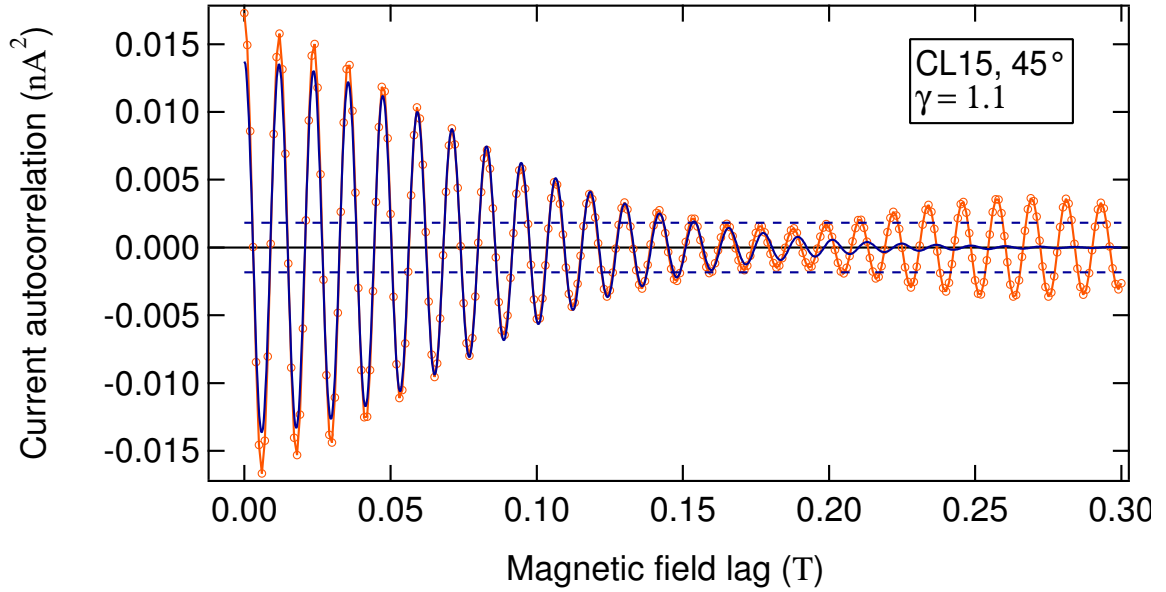


Figure 7.31: Persistent current autocorrelation for sample CL15 at $\theta_0 = 45^\circ$. Circles represent the autocorrelation of the data shown in Figs. 7.39 through 7.42. The curve is a fit to Eq. 7.17 as described in the text with $\gamma = 1.1$ and $p = 0.90$. The estimated standard error in the autocorrelation (dashed horizontal lines) is $\sqrt{2}\eta(M_{\text{eff}}) = 13\%$ of its value at zero magnetic field lag B' . Fluctuations of this magnitude are present at large B' where the autocorrelation is expected to be small.

p is allowed to vary as it is critical for the accuracy of the fit that the oscillating term have the correct period. The other free parameter varied during the fitting routine is the geometrical factor γ . The diffusion constant D is held fixed to its fitted value listed in Table 7.3. The parameters L and θ_0 are fixed to their nominal values, and L_{SO} is fixed to the value found in transport measurements (see Appendix E).

The curves associated with the best fits of Eq. 7.17 to the autocorrelation data are plotted in Figs. 7.30 through 7.35. The fitted values of the geometrical factor γ are shown in each figure and are collected in Table 7.3. The fitted values of the coefficient p are listed in each figure caption. As expected, all of the fitted values for γ are of order unity. With one exception (sample CL17 at $\theta_0 = 6^\circ$), the fitted values of p were all between 0.8 and 0.9, slightly below the expected value $p = 1$ but consistent with the location of the peaks in the power spectral densities (Figs. 7.20 through 7.25) discussed earlier. Also shown in Table 7.3 are the values of M_{eff} and $\eta(M_{\text{eff}})$ found using Eqs. 7.12 and 7.15 and the values of γ found from the fits to the persistent current autocorrelation data.

At large magnetic field lag (B' in Eq. 7.17), the autocorrelation function $\langle I(B)I(B+B') \rangle$ decays to zero. The autocorrelation calculated from each measured persistent current trace (see Figs. 7.30

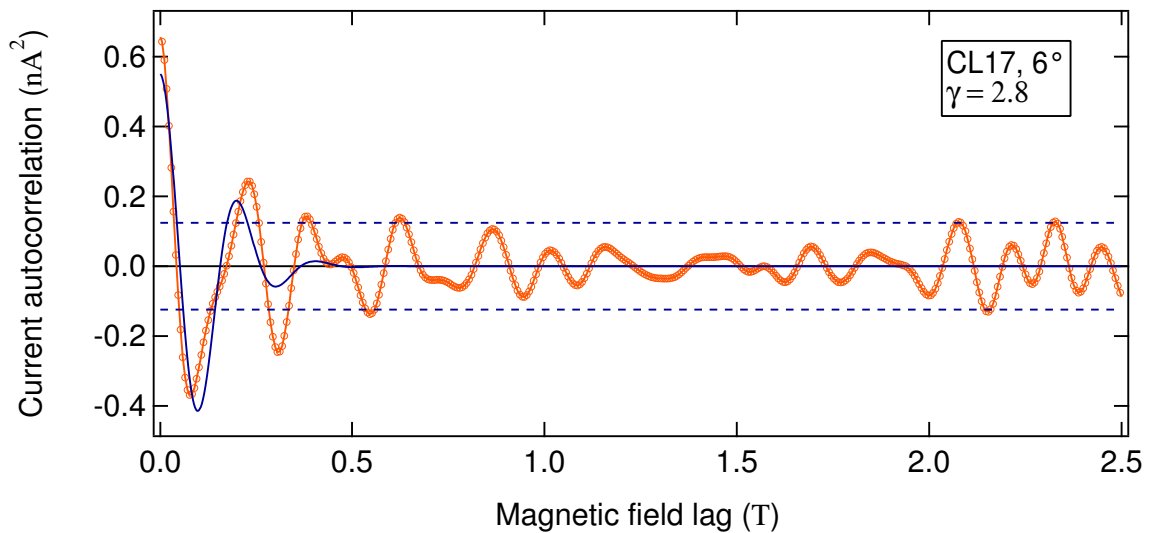


Figure 7.32: Persistent current autocorrelation for sample CL17 at $\theta_0 = 6^\circ$. Circles represent the autocorrelation of the data shown in Fig. 7.43. The curve is a fit to Eq. 7.17 as described in the text with $\gamma = 2.8$ and $p = 0.63$. Forcing $p = 1$ in the expression for the magnetic field frequency $\beta = \pi R^2 \sin \theta_0 / \phi_0$ would require a radius R of 244 nm to match the frequency β for $p = 0.63$ and R the mean radius. This value is close to the inner radius of 250 nm for sample CL17. The estimated standard error in the autocorrelation (dashed horizontal lines) is $\sqrt{2}\eta(M_{\text{eff}}) = 23\%$ of its value at zero magnetic field lag B' . Fluctuations of this magnitude are present at large B' where the autocorrelation is expected to be small. These fluctuations show a wide range of frequencies, consistent with the large peak width $\Delta\beta_1$ relative to the peak location β_1 in the power spectral density (Fig. 7.22).

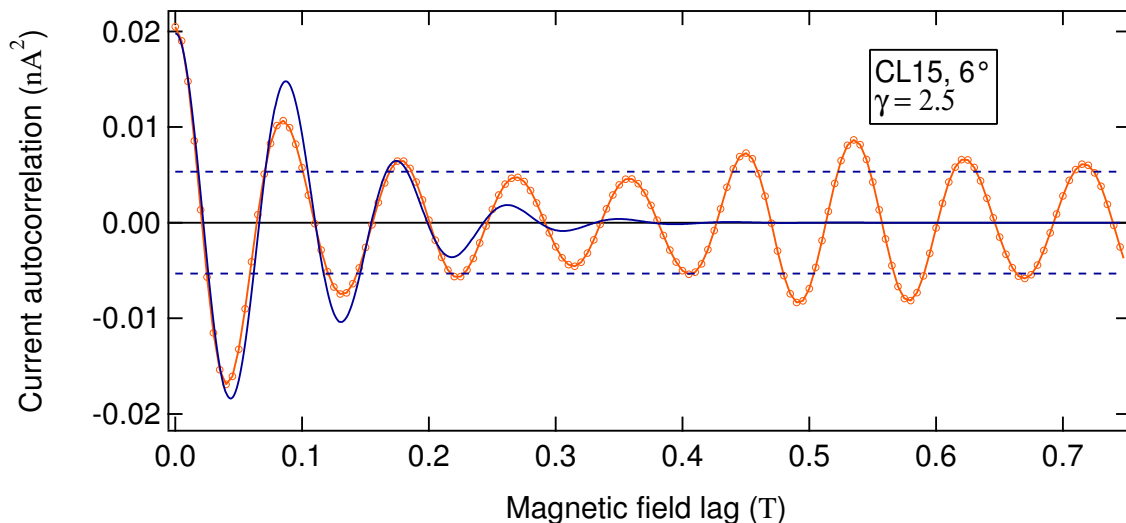


Figure 7.33: Persistent current autocorrelation for sample CL15 at $\theta_0 = 6^\circ$. Circles represent the autocorrelation of the data shown in Fig. 7.44. The curve is a fit to Eq. 7.17 as described in the text with $\gamma = 2.5$ and $p = 0.82$. The estimated standard error in the autocorrelation (dashed horizontal lines) is $\sqrt{2}\eta(M_{\text{eff}}) = 27\%$ of its value at zero magnetic field lag B' . Fluctuations of this magnitude are present at large B' where the autocorrelation is expected to be small.

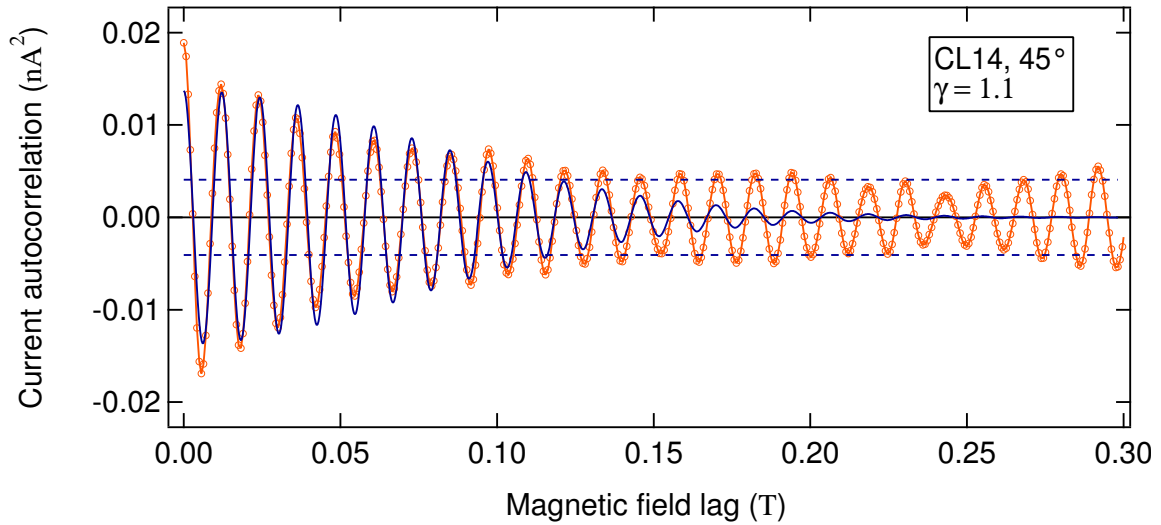


Figure 7.34: Persistent current autocorrelation for sample CL14. Circles represent the autocorrelation of the data shown in Fig. 7.45. In calculating the autocorrelation, the features with magnetic field frequency β less than 60 T^{-1} (see Fig. 7.24) were removed. As discussed in the text, we attribute these features to the slowly varying background and not to the persistent current. The curve is a fit to Eq. 7.17 as described in the text with $\gamma = 1.1$ and $p = 0.88$. The estimated standard error in the autocorrelation (dashed horizontal lines) is $\sqrt{2}\eta(M_{\text{eff}}) = 30\%$ of its value at zero magnetic field lag B' . Fluctuations of this magnitude are present at large B' where the autocorrelation is expected to be small.

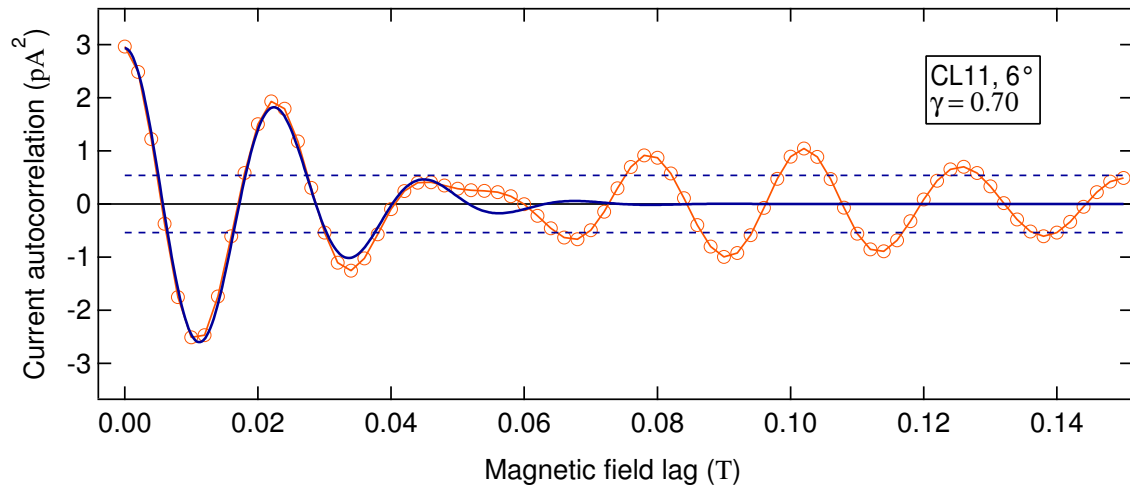


Figure 7.35: Persistent current autocorrelation for sample CL11. Circles represent the autocorrelation of the data shown in Fig. 7.46. In calculating the autocorrelation, the features with magnetic field frequency β less than 30 T^{-1} (see Fig. 7.25) were removed. As discussed in the text, we attribute these features to the slowly varying background and not to the persistent current. The curve is a fit to Eq. 7.17 as described in the text with $\gamma = 0.70$ and $p = 0.90$. The estimated standard error in the autocorrelation (dashed horizontal lines) is $\sqrt{2}\eta(M_{\text{eff}}) = 18\%$ of its value at zero magnetic field lag B' . Fluctuations of this magnitude are present at large B' where the autocorrelation is expected to be small.

through 7.35), however, continues to oscillate at a finite, varying amplitude. Once the field lag B' is large enough that $\langle I(B)I(B+B') \rangle \ll \langle I^2(B) \rangle$, the autocorrelation calculation essentially involves averaging the product of M_{eff} uncorrelated values of the persistent current. Thus, the standard error $\sigma(\langle I(B)I(B+B') \rangle)$ in the autocorrelation due to the finite measurement size is

$$\begin{aligned} \sigma(\langle I(B)I(B+B') \rangle) &= \frac{\langle I^2(B) \rangle}{\sqrt{M_{\text{eff}}}} \\ &= \sqrt{2}\eta(M_{\text{eff}})\langle I^2(B) \rangle \end{aligned}$$

where we have assumed that the measurement has M_{eff} independent realizations as calculated with Eq. 7.15.¹² The magnitude of the autocorrelation at large magnetic field lag in Figs. 7.30 through 7.35 is consistent with $\sqrt{2}\eta(M_{\text{eff}})\langle I^2(B) \rangle$ for the values of $\eta(M_{\text{eff}})$ listed in Table 7.3. The region of magnetic field lag B' covered by each fit extended from $B' = 0$ to the value of B' at which $\langle I(B)I(B+B') \rangle \approx \sqrt{2}\eta(M_{\text{eff}})\langle I^2(B) \rangle$. That the phase of the autocorrelation begins to drift at large B' (e.g. in Fig. 7.30) is further indication that the large magnitude of the autocorrelation at large B' is due to random fluctuations in the persistent current trace.

The relatively large magnitude of the fluctuations in the autocorrelation make an accurate analysis difficult. Other than the autocorrelation of samples CL15 and CL17 at $\theta_0 = 45^\circ$, each measured autocorrelation has an estimated error of over 25% of its value $\langle I^2(B) \rangle$ at zero magnetic field lag B' , and thus the values for the geometrical factor γ extracted from fits to these autocorrelations must be taken only as rough estimates. For samples CL15 and CL17 at $\theta_0 = 45^\circ$, we estimate an uncertainty of $\sim 25\%$ in the best fit values for γ .¹³

With this analysis of the persistent current autocorrelation, we have estimated fractional uncertainties $\eta(M_{\text{eff}})$ ranging from 8 to 19% for the magnitude of the typical persistent current inferred from the large field traces. As these magnitudes were used to scale all of the current versus temperature data shown in Fig. 7.29, the same fractional error is present in each of these traces. This uncertainty leads to an over- or under-scaling of the entire current versus temperature trace and does not introduce any scatter to the data points.

¹²This expression for the error in the autocorrelation is only valid provided that $B' \ll B_0$. Otherwise, M_{eff} must be recalculated with B_0 replaced with $B_0 - B'$ in Eq. 7.15 because only the overlapping magnetic field region of length $B_0 - B'$ contributes to the persistent current autocorrelation calculated using Eq. 7.16. Also, it is possible that my expression is a factor of $\sqrt{2}$ too small. This factor does not change the qualitative conclusions drawn here.

¹³Unlike measurement noise which is uncorrelated from point to point, the fluctuations in the autocorrelation due to finite sample size are correlated in magnetic field lag B' . This correlation complicates the estimation of the uncertainty in the fitted values for γ . We took sections of the autocorrelation at large B' , shifted them down to $B' = 0$, and then added or subtracted them from the autocorrelation data. By fitting these new forms of the autocorrelation, we got an idea of the sensitivity of γ to the typical fluctuations in the autocorrelation.

The scatter present in the current versus temperature plot is due to the fluctuations of the cantilever frequency discussed in Chapter 6. Considering the persistent current data in the magnetic field frequency β domain, drift of the cantilever frequency over a long time scale leads to increased noise at low β (see e.g. Figs. 7.25 and 7.50), but otherwise the noise in the persistent current spectrum is fairly flat and independent of temperature. This flat persistent current background can be seen in Fig. 7.28 which plots the Fourier transform of the persistent current for sample CL17 at several different temperatures. For sample CL17, the background noise was on the order of 30 pA. The background noise levels were roughly 0.5, 10, and 3 pA for samples CL11, CL14, and CL15 respectively. Statistical error in the fitting routine for D due to this background scatter was about 2%.

The final possible error to consider in the analysis of the current versus temperature data is the error in the nominal temperature of the refrigerator. Based on the manufacturer's specifications for the thermometer and comparison of its reading to fixed temperature points, we estimate an error of about 7% in the thermometer reading. As the current's temperature dependence is roughly exponential, the error in the temperature is much more significant in fitting the data than the error in the current magnitude.

Taking all of these sources of error into account (statistical uncertainty in the current magnitude, scatter in the cantilever frequency, and error in the thermometer calibration), we estimate an uncertainty in the fitted values for the diffusion constant of 7%. The uncertainty in the analysis of the autocorrelation data and the extracted values of γ was discussed above. In that case, the uncertainty was dominated by the standard error due to the finite sample size and varied between measurements (see discussion above).

7.3.3 Complete persistent current traces

In this section, we present, in Figs. 7.36 through 7.46, the complete current versus magnetic field traces which were analyzed in Sections 7.3.1 and 7.3.2. These traces were calculated, using method A, from measurements of the cantilever frequency performed at the refrigerator's base temperature T_b , which was 323 mK for $\theta_0 = 6^\circ$ and 365 mK for $\theta_0 = 45^\circ$.¹⁴

¹⁴We define the base temperature as the temperature of the refrigerator when the helium-3 was condensed and all heat sources turned off. It was possible to reach slightly lower temperatures by also pumping on the 1K pot, but these temperatures could only be sustained for short periods of time. The base temperature was different for the two angles θ_0 because different wiring arrangements led to different heat loads on the refrigerator during the two cooldowns.

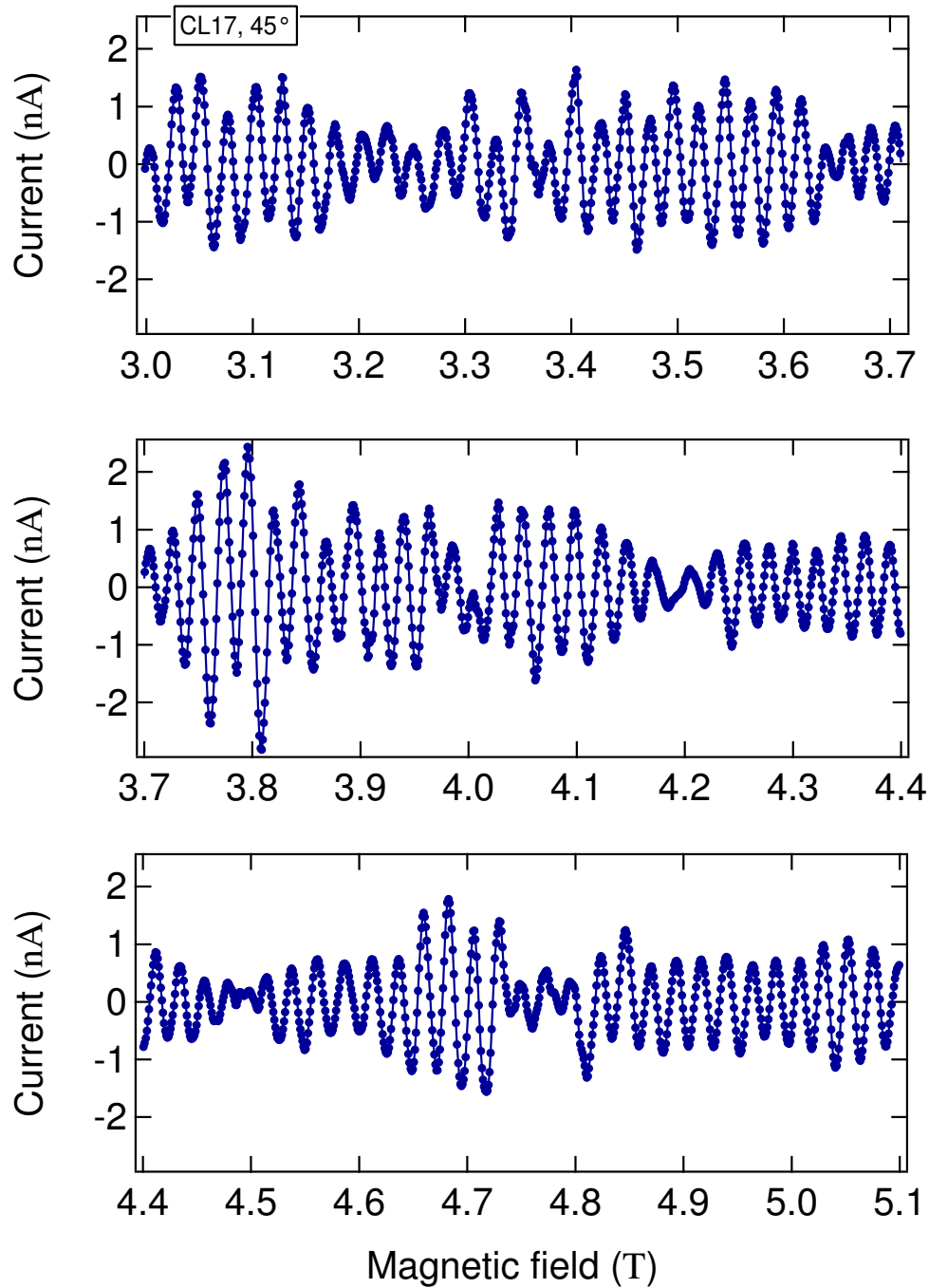


Figure 7.36: Full current versus magnetic field trace for CL17 at 45°, part 1. The data shown were recorded at 365 mK and converted from frequency shift to current using method A described in 7.1.

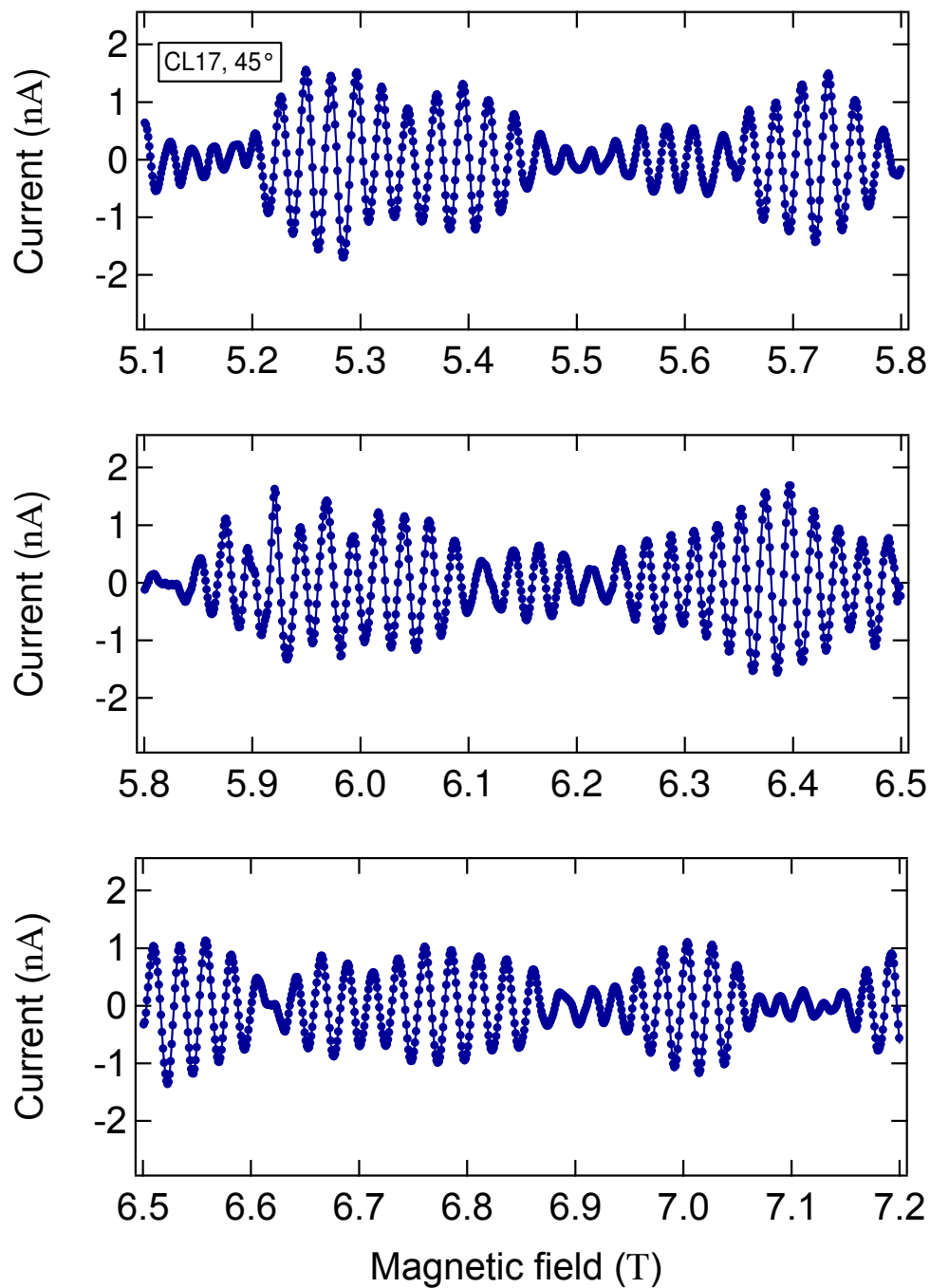


Figure 7.37: Full current versus magnetic field trace for CL17 at 45° , part 2. The data shown were recorded at 365 mK and were converted from frequency shift to current using method A described in 7.1.

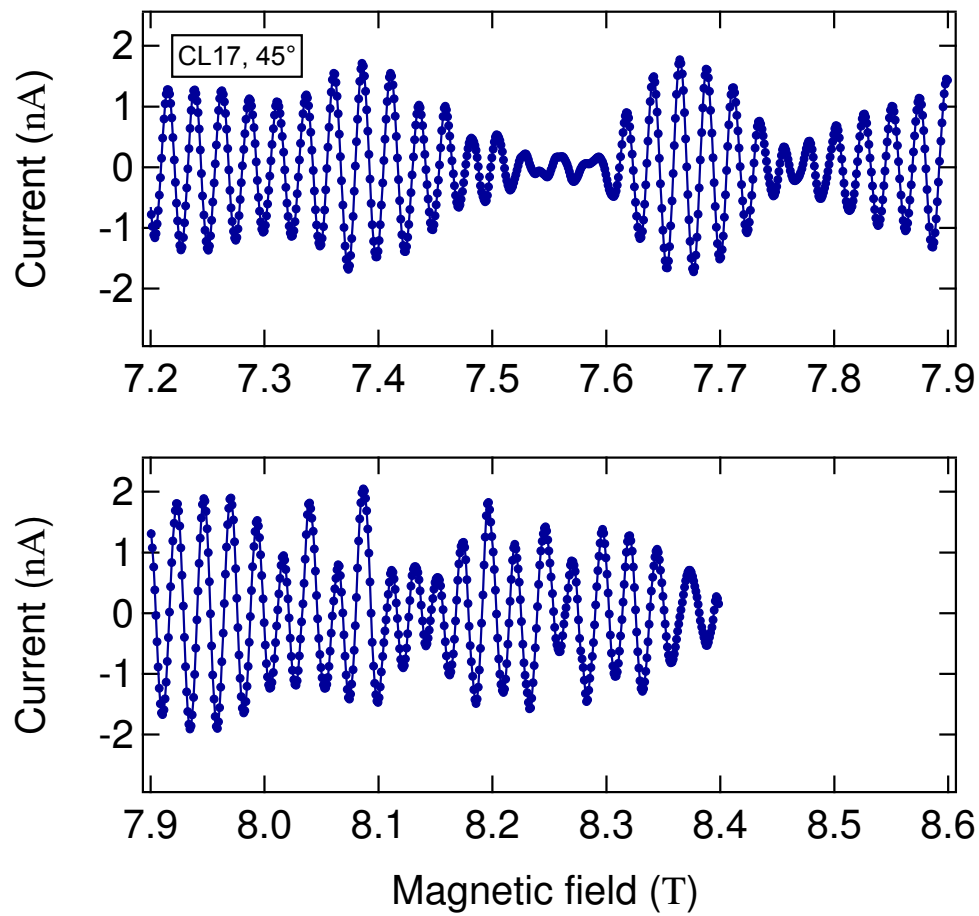


Figure 7.38: Full current versus magnetic field trace for CL17 at 45° , part 3. The data shown were recorded at 365 mK and converted from frequency shift to current using method A described in 7.1.

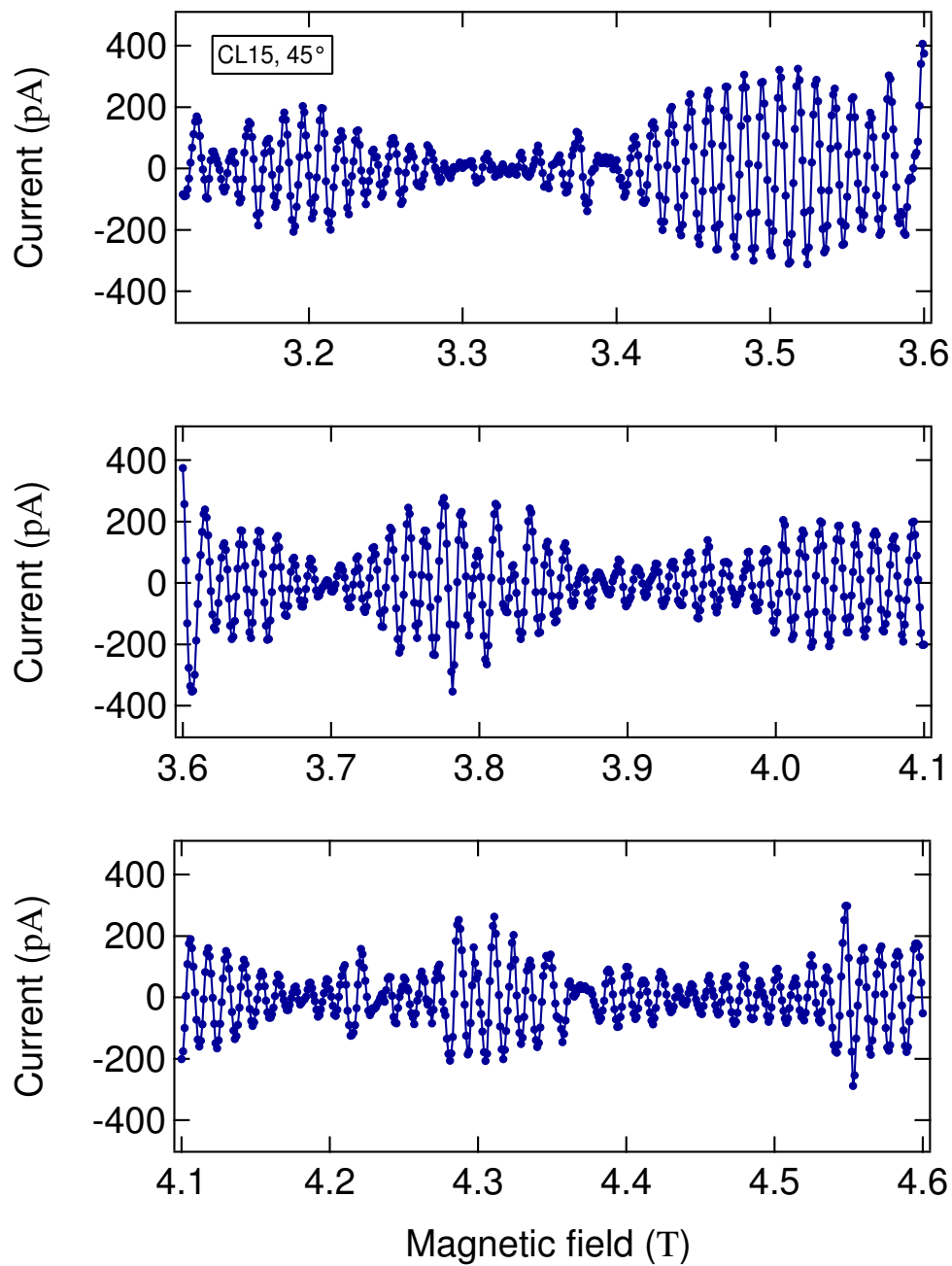


Figure 7.39: Full current versus magnetic field trace for CL15 at 45° , part 1. The data shown were recorded at 365 mK and converted from frequency shift to current using method A described in 7.1.

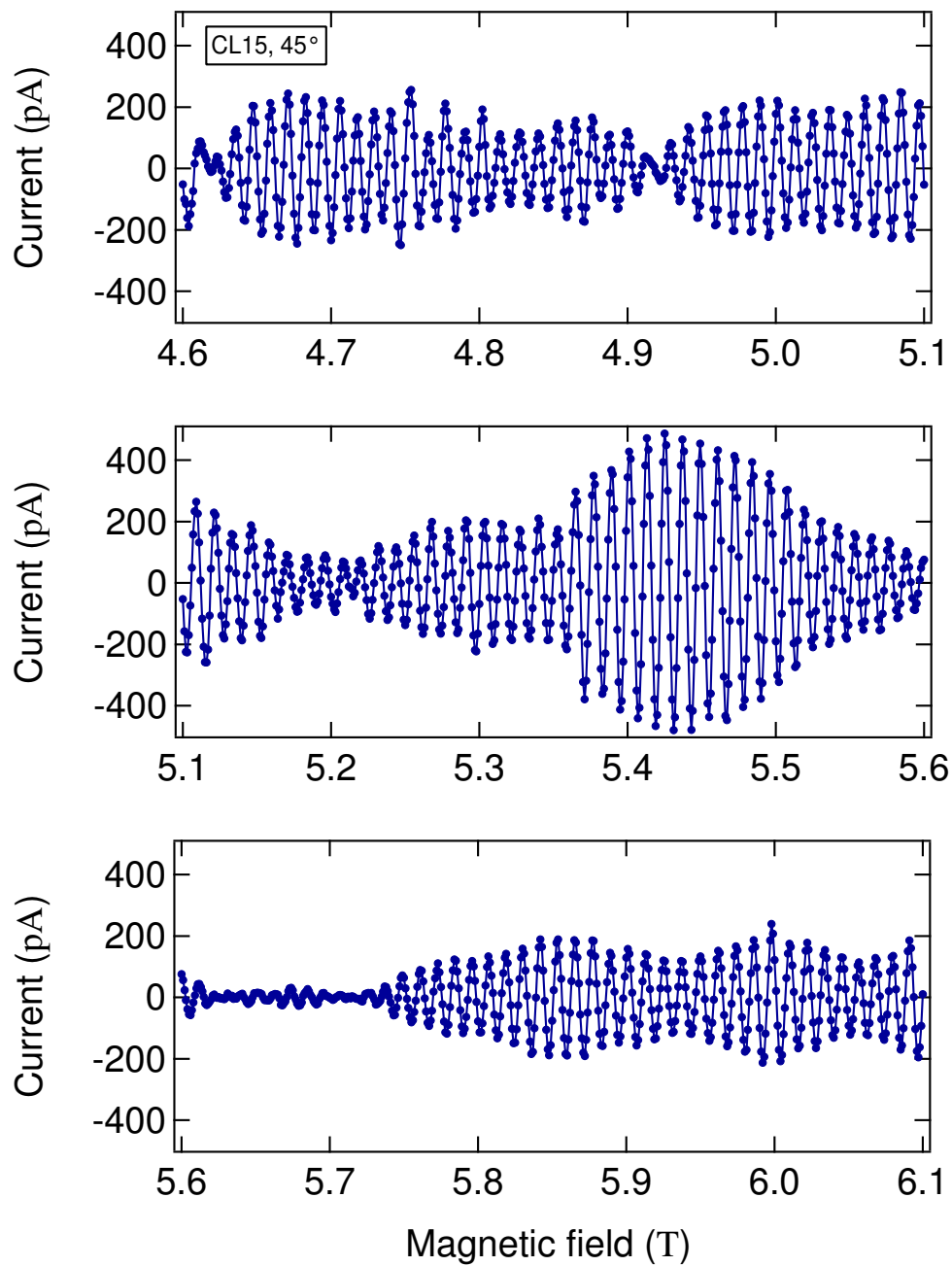


Figure 7.40: Full current versus magnetic field trace for CL15 at 45° , part 2. The data shown were recorded at 365 mK and converted from frequency shift to current using method A described in 7.1.

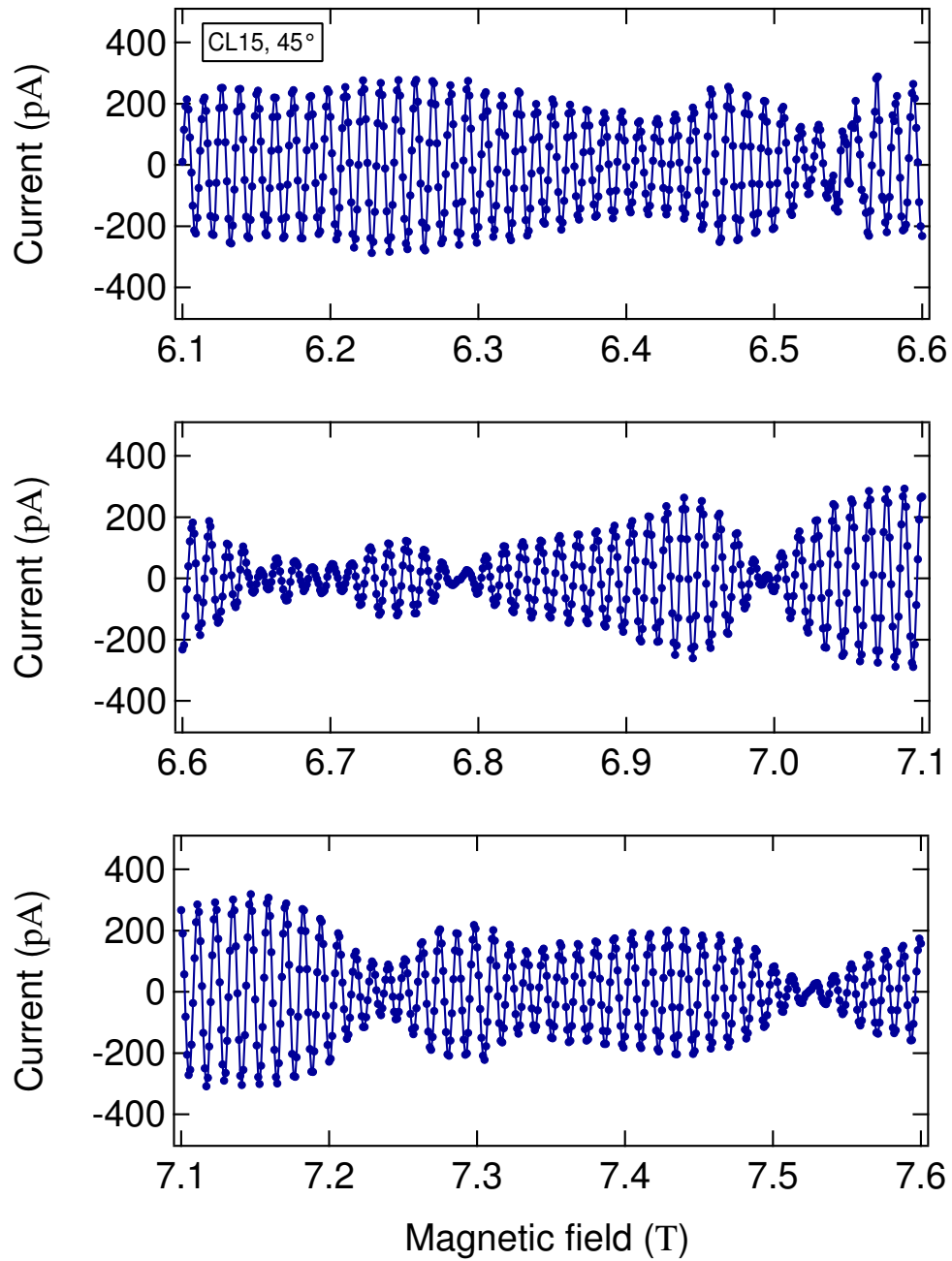


Figure 7.41: Full current versus magnetic field trace for CL15 at 45° , part 3. The data shown were recorded at 365 mK and converted from frequency shift to current using method A described in 7.1. Due to intermittent noise in the measurement, the data between 6.528 T and 6.537 T was not usable. We approximated this section by replicating the data from the oscillation just below 6.528 T.

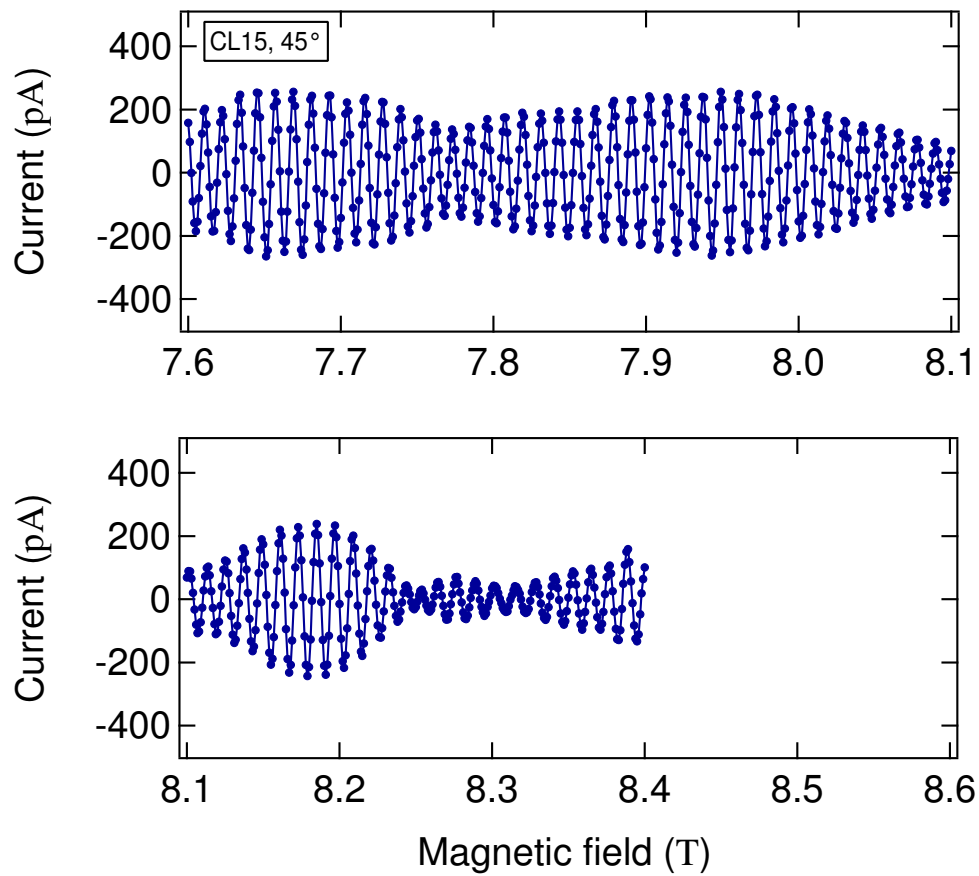


Figure 7.42: Full current versus magnetic field trace for CL15 at 45°, part 4. The data shown were recorded at 365 mK and converted from frequency shift to current using method A described in 7.1.

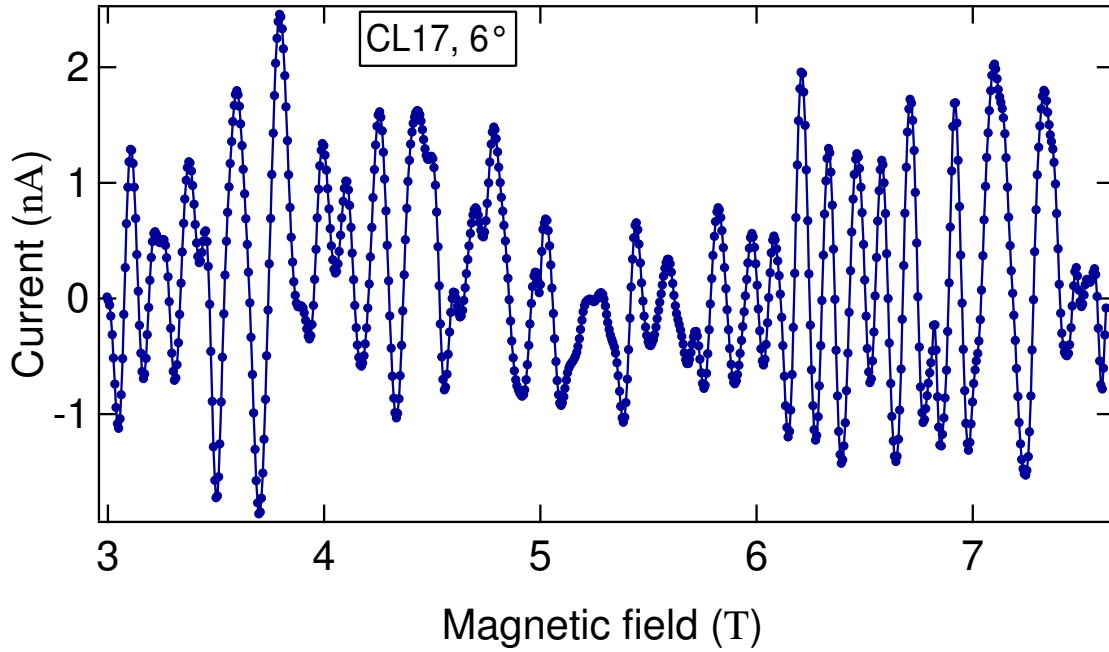


Figure 7.43: Full current versus magnetic field trace for CL17 at 6°. The data shown were recorded at 323 mK and converted from frequency shift to current using method A described in 7.1.

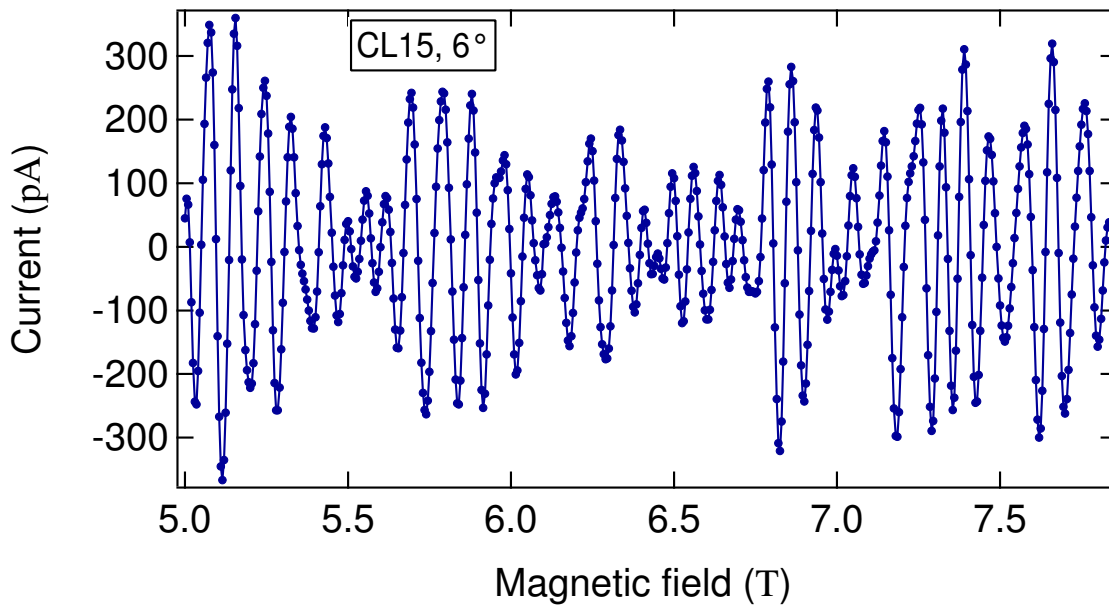


Figure 7.44: Full current versus magnetic field trace for CL15 at 6°. The data shown were recorded at 323 mK and converted from frequency shift to current using method A described in 7.1.

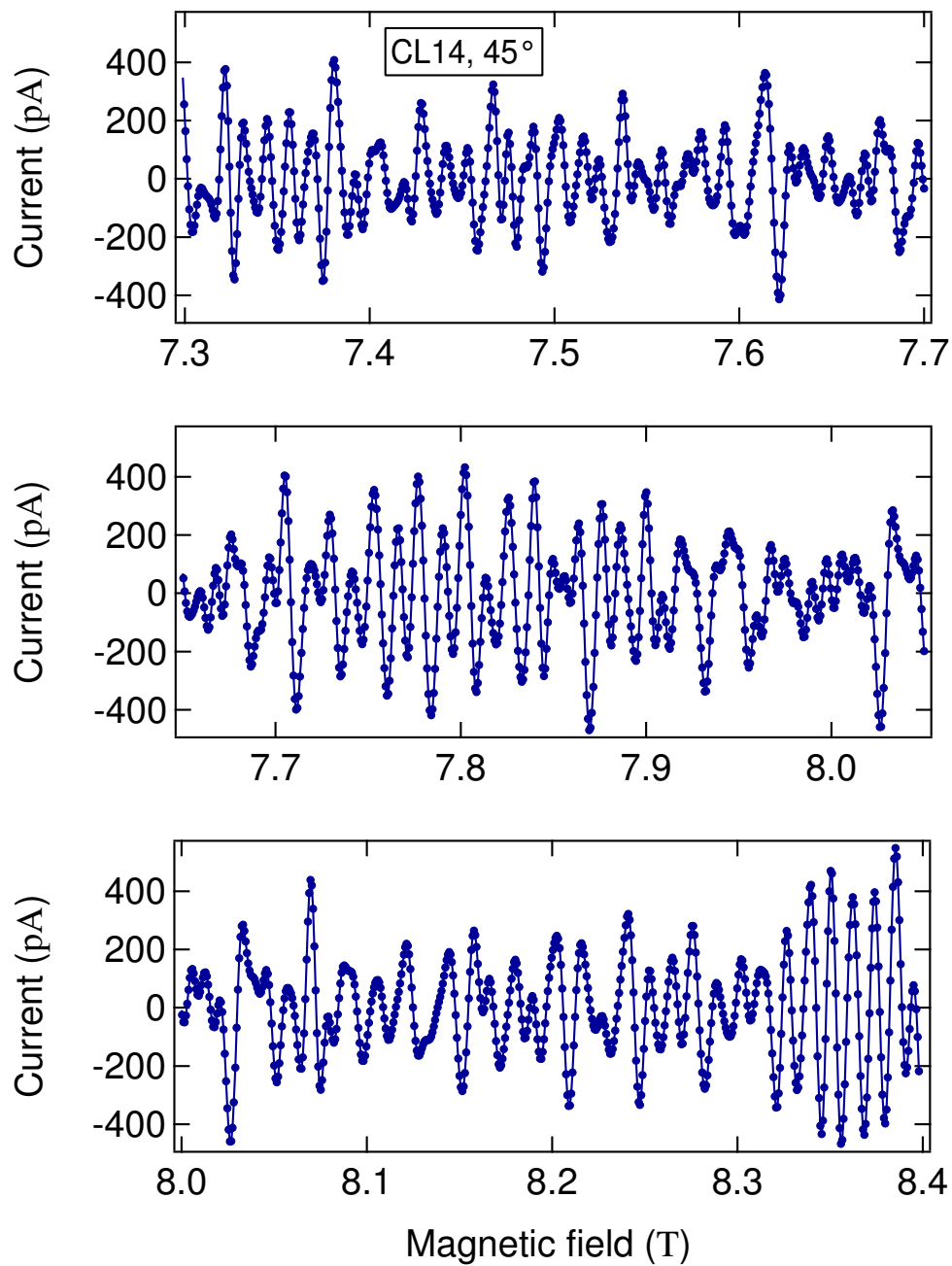


Figure 7.45: Full current versus magnetic field trace for CL14 at 45° . The data shown were recorded at 365 mK and converted from frequency shift to current using method A described in 7.1.

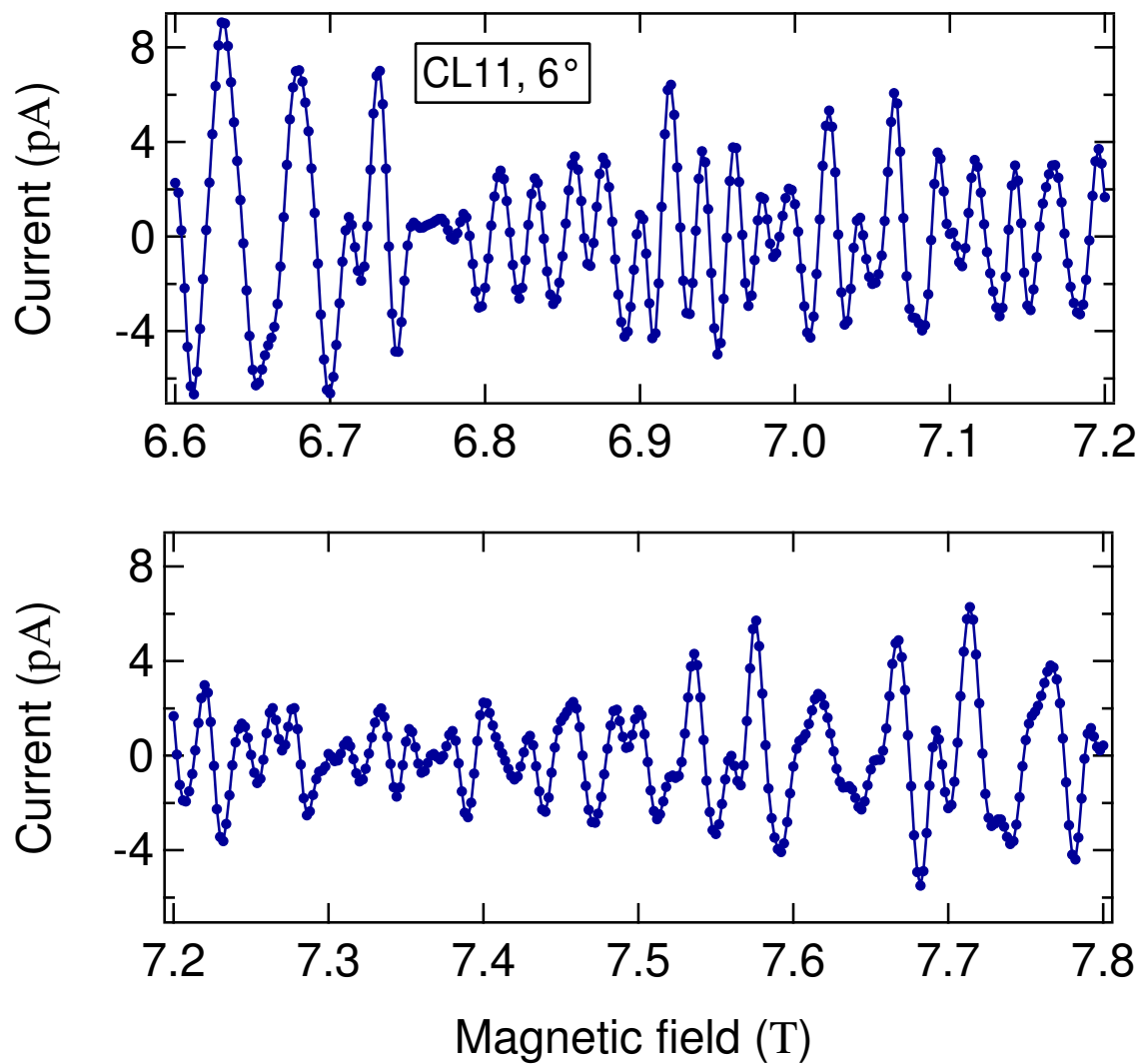


Figure 7.46: Full current versus magnetic field trace for CL11 at 6° . The data shown were recorded at 323 mK and converted from frequency shift to current using method A described in 7.1.

As discussed in Sections 7.3.1 and 7.3.2, the signal to noise ratios from samples CL11 (large rings) and CL14 (single ring) were smaller than those from samples CL15 and CL17, which had bigger arrays of smaller rings. At high field, the absolute signal to noise ratio for the latter two samples ranged from 30 to 40, making analysis quite straightforward. For samples CL11 and CL14, the total signal to noise ratio for the large magnetic field scans was between 5 and 10.

The weaker signal for samples CL11 and CL14 necessitated driving the cantilevers hard so that the cut-off frequency β_{zero} (see Eq. 7.5), above which the cantilever frequency shift is insensitive, was somewhat close to β_1 , the expected magnetic field frequency of the persistent current. In the data processing steps of method A, it is necessary to filter out the components β_{zero} to avoid introducing artifacts to the data. It was also necessary to remove the smooth background which was of comparable magnitude to the persistent current signal. Between these filtering steps and the other data processing performed in converting the cantilever frequency shift into a persistent current, one could be concerned that the persistent current signals for samples CL11 and CL14 were mere artifacts of the signal processing routine.

To dispel these concerns, we present in Figs. 7.47 and 7.49 the raw frequency shift versus magnetic field data for samples CL14 and CL11. The only processing that has been performed on the data is the removal of a smooth, slowly drifting background. In Figs. 7.48 and 7.50, we show the power spectral densities of the two traces of frequency shift versus magnetic field.

In the spectrum of Fig. 7.48, the peak due to the persistent current in the single ring of sample CL14 can clearly be seen. The peak is located at $\sim 80 \text{ T}^{-1}$. Measurements taken at the same angle $\theta_0 = 45^\circ$ on another sample (CL15) with rings of the same size found a peak at the same location (see Fig. 7.21). The roll-off at low β due to the subtraction of the smooth background can also be made out in Fig. 7.21 at around $\beta \approx 25 \text{ T}^{-1}$, well below the location of the persistent current peak.

The spectrum for sample CL11 (Fig. 7.50) is similar to that of CL14 (Fig. 7.48). As with the spectrum for CL14, the low β suppression due to the subtraction of the smooth background occurs at $\sim 25 \text{ T}^{-1}$. Above this point, the spectrum begins to descend, following the usual $S_f \propto \beta^{-1+\delta}$ behavior of low frequency noise. This trend is visible from 25 to 35 T^{-1} and above 60 T^{-1} . Between 35 and 60 T^{-1} , a broad peak is present on top of this low frequency background in the spectrum. We attribute this peak to the persistent current. As indicated by the horizontal bar this peak is roughly in the expected location for $\theta_0 = 6^\circ$ and the dimensions of sample CL11.

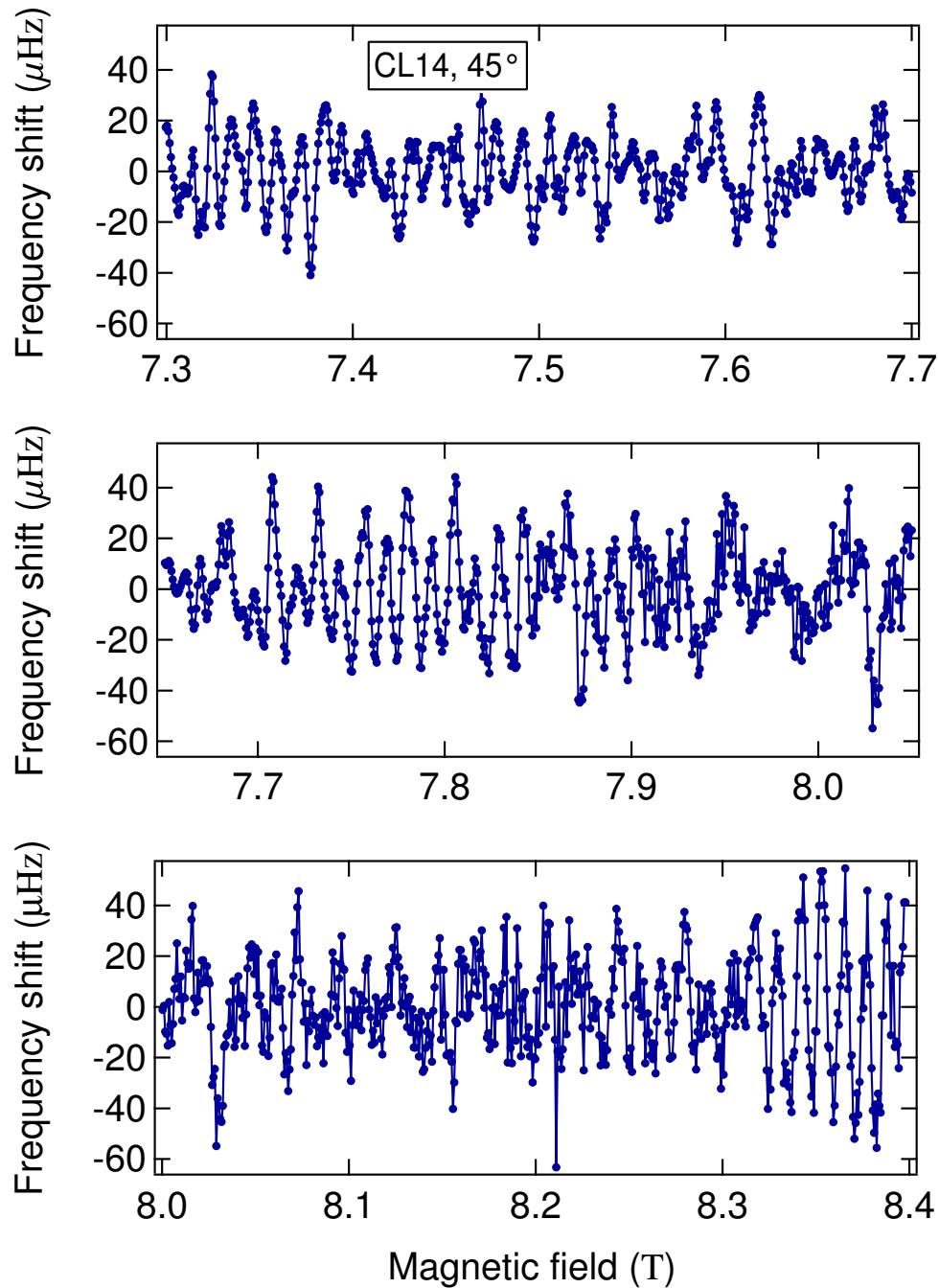


Figure 7.47: Full frequency shift versus magnetic field trace for CL14 at 45° . The data shown plot the full data set of cantilever frequency shift versus magnetic field for sample CL14 at $T_b = 365 \text{ mK}$. A smooth background has been subtracted from the cantilever frequency to remove its slow drift in time. Otherwise, no manipulation of the data has been performed. The size of the persistent current signal varies with magnetic field with large amplitude oscillations visible near 7.35, 7.75, and 8.35 T. The power spectral density of the trace is shown in Fig. 7.48.

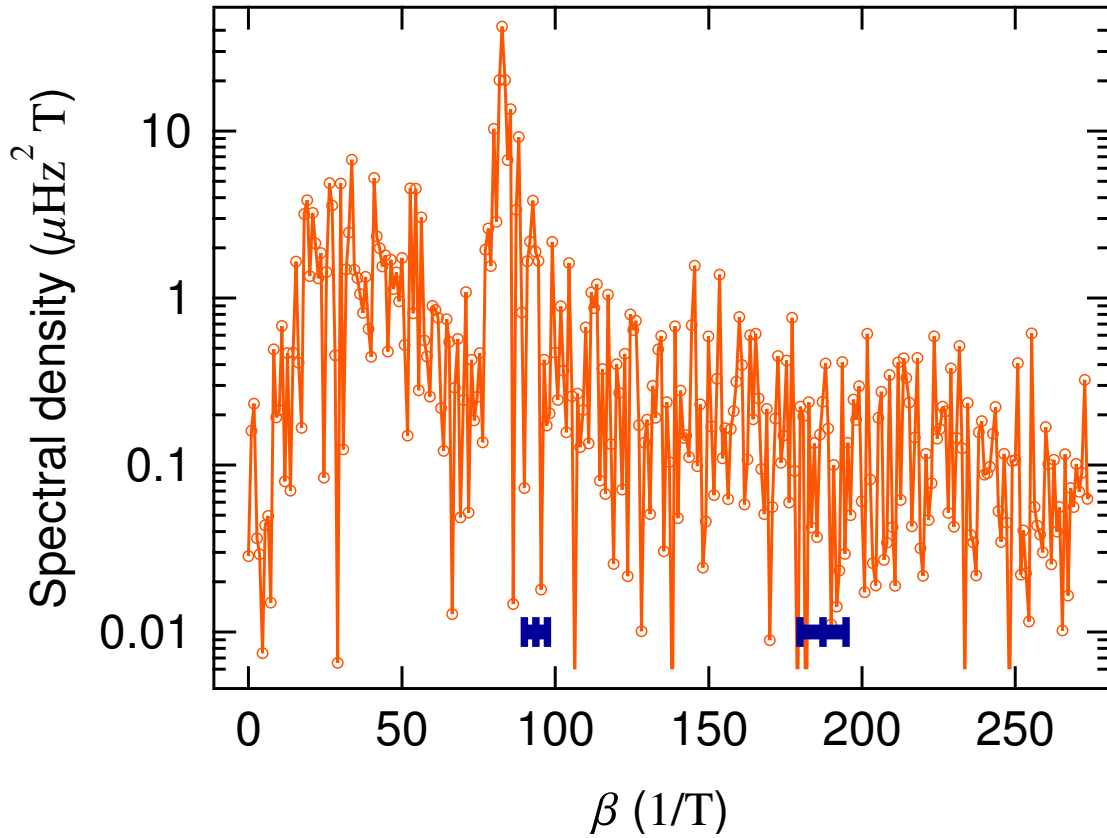


Figure 7.48: Spectral density of the measured frequency shift for CL14 at 45° . The data shown represent the power spectral density of the frequency shift versus magnetic field trace (Fig. 7.47) for sample CL14 taken with $\theta_0 = 45^\circ$ and $T = 365$ mK. The horizontal bars represent the expected locations and widths of the peaks in the spectrum expected for the first two harmonics of the persistent current signal using the nominal experimental parameters. A clear peak is visible just below the expected location of the first harmonic.

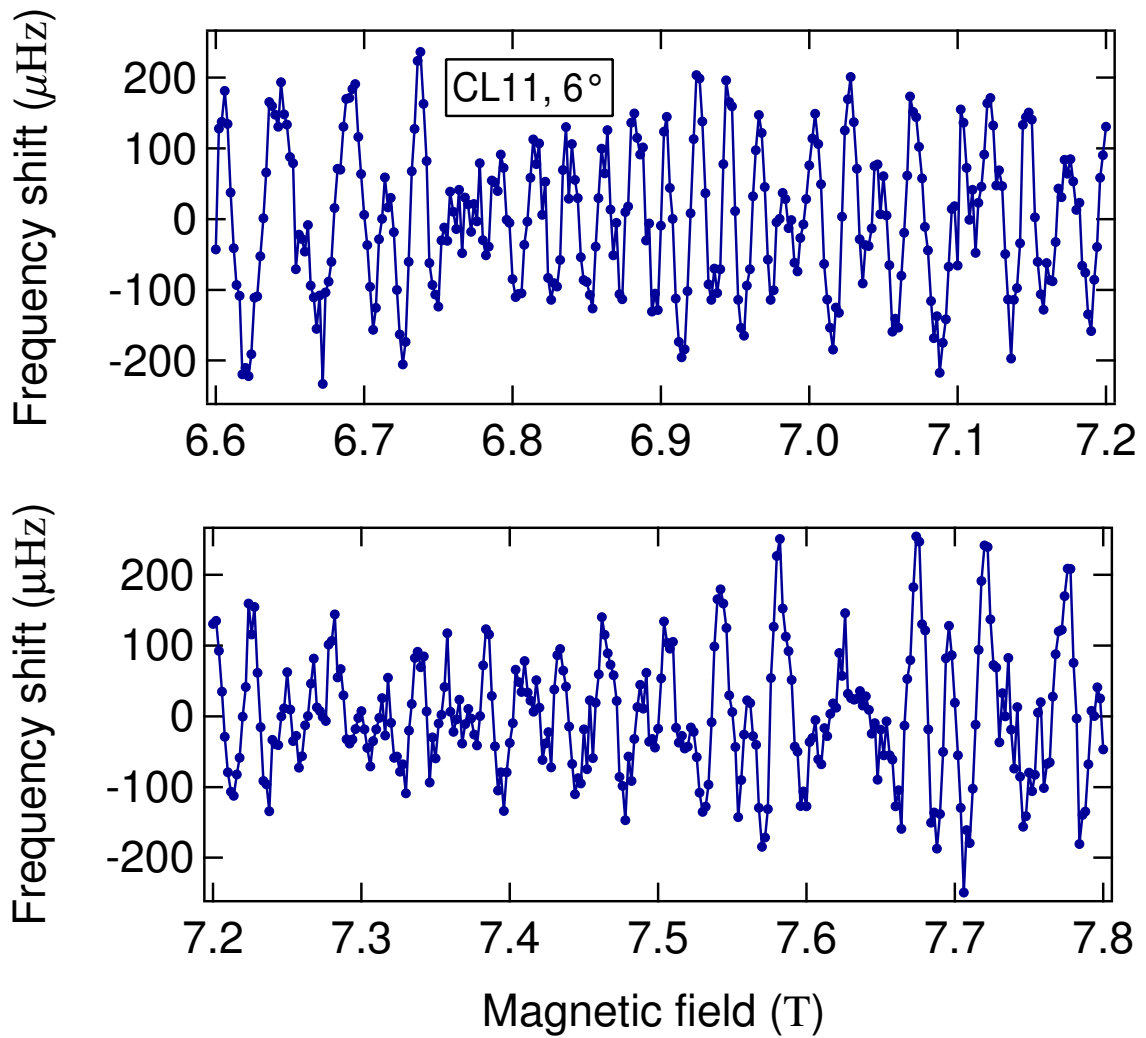


Figure 7.49: Full frequency shift versus magnetic field trace for CL11 at 6° . The data shown plot the full data set of cantilever frequency shift versus magnetic field for sample CL11 at $T_b = 323$ mK. A smooth background has been subtracted from the cantilever frequency to remove its slow drift in time. Otherwise, no manipulation of the data has been performed. The size of the persistent current signal varies with magnetic field with large amplitude oscillations visible near 6.9 T. The power spectral density of the trace is shown in Fig. 7.50.

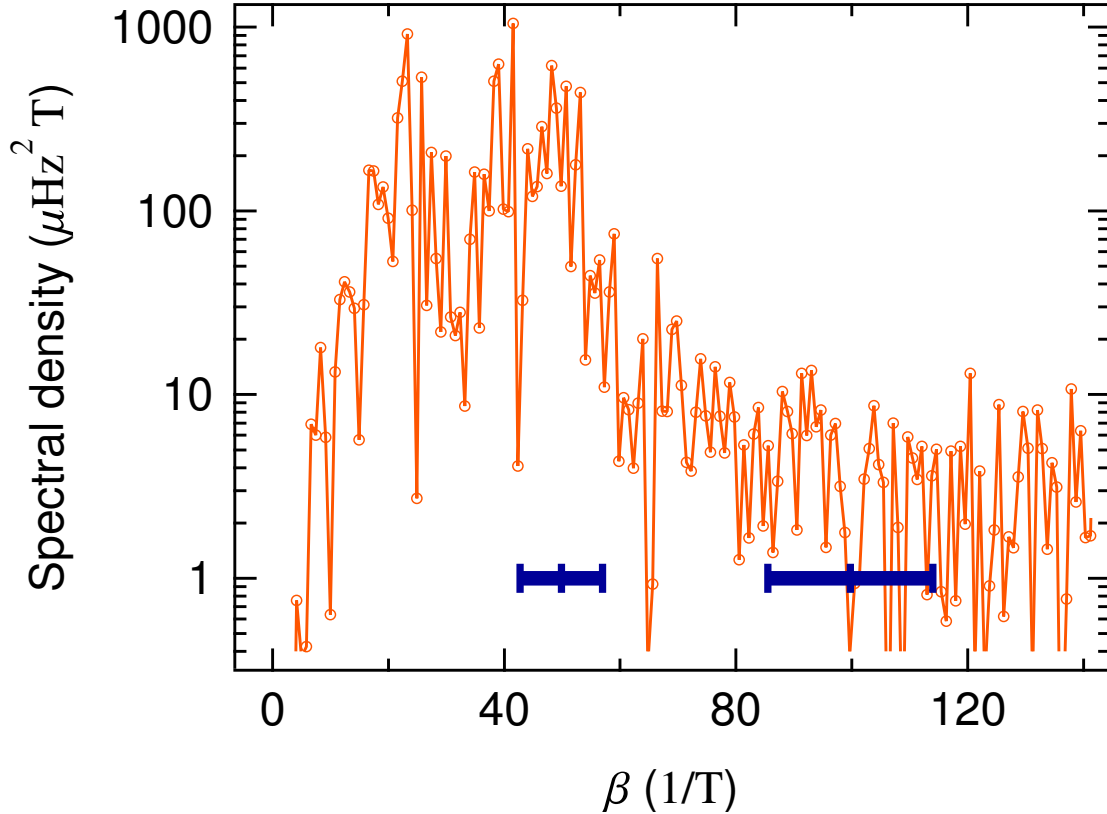


Figure 7.50: Spectral density of the measured frequency shift for CL11 at 6° . The data shown represent the power spectral density of the frequency shift versus magnetic field trace (Fig. 7.49) for sample CL11 taken with $\theta_0 = 6^\circ$ and $T = 323$ mK. The horizontal bars represent the expected locations and widths of the peaks in the spectrum expected for the first two harmonics of the persistent current signal using the nominal experimental parameters. The peak at 25 T^{-1} was created by the subtraction of the smooth background which suppresses the low β components of the spectrum. Above 25 T^{-1} , the remaining low β noise results in a downward sloping trend in the spectrum. On top of this trend, a peak is present between 35 and 60 T^{-1} , roughly the expected location of the first harmonic of the persistent current signal. We attribute this peak to the persistent current.

Chapter 8

Outlook

In the preceding chapters, I have described the magnetometer developed in the Harris lab for the study of persistent currents in normal metal rings and reported measurements of persistent currents in arrays of aluminum rings. I would like to conclude by highlighting some simple experiments that build upon the results reported here. Before doing so, I will describe the place of those results within the context of previous persistent current measurements.

We studied the dependence of the typical current¹ on several parameters that had not previously been varied and extended the range of variation of several other parameters. We reported the largest signal to noise ratio of all measurements of the typical current and observed many more independent realizations M_{eff} of the persistent current than all previous measurements combined. We observed the typical current in an environment free from high frequency electromagnetic radiation, avoiding a source of potential systematic error present in previous measurements.²

We performed the first measurements of the typical current in strong magnetic fields. Previous measurements,³ all of which used SQUIDs, had been restricted to fields $\lesssim 10$ mT, whereas our measurements spanned a magnetic field range 270 times larger, achieving a maximum field of 8.4 T. We increased the highest temperature at which the persistent current had been observed by a factor of five to 2.5 K. We performed the first direct study of the effect of ring size on the current's

¹The typical current was defined in Chapter 1 as the contribution to the persistent current which varies randomly from ring to ring.

²There is no published prediction for the effects of high frequency radiation on the typical current. See Chapter 3 for a discussion of related effects. In previous measurements, the sample was exposed to high frequency radiation due to the Josephson oscillations in the measurement SQUID.

³These experiments, Refs. 2, 3, 10, are reviewed in Chapter 3. In this chapter, we compare directly to the other measurements of the typical current. Many of our statements about previous work apply equally well to measurements of the average persistent current as well.

magnitude and temperature dependence. We did this by measuring co-deposited rings of three significantly different sizes. For each previous experiment, only one characteristic temperature was observed. We reported the first definitive observation of the second harmonic of the typical persistent current. Ref. 3 also reported a signal with $h/2e$ flux periodicity but could not differentiate the contributions from the typical current and the average current. We studied for the first time the dependence of the persistent current on its orientation in the applied magnetic field by measuring the same samples at two different angles with respect to magnetic field. We measured aluminum rings (all previous measurements of the typical persistent current studied gold rings).

We reported a greater absolute signal to noise ratio and a greater sensitivity to persistent currents than previous measurements of the typical current. Our largest signal to noise ratio was ~ 40 , achieved with sample CL17 of Table 7.2, while the signal to noise ratio of previous measurements was typically $\lesssim 7$. Because the persistent current signal scales differently with ring size for the torsional magnetometry and SQUID measurements, it is difficult to compare the persistent current sensitivity of measurements made on rings of different sizes. Still, our measured current magnitude of ~ 0.7 pA for sample CL11 ($L = 5 \mu\text{m}$) is much lower than the ~ 200 pA minimum current magnitude reported in other experiments on similar rings ($L = 3.6 \mu\text{m}$ for Ref. 234; $L = 8 \mu\text{m}$ for Ref. 3). Our signal to noise ratio does not display as large of an improvement over previous measurements as our persistent current sensitivity because we measured at higher temperatures where the persistent current was suppressed. Operating at lower temperatures would increase our signal to noise ratio, especially for larger rings which have smaller characteristic temperatures. The signal to noise ratio and persistent current sensitivity could also be increased by covering a larger fraction of the cantilever with rings and by making thermally limited measurements of the cantilever frequency.⁴

The improvement in sensitivity was due in part to the significantly larger magnetic field range accessible with torsional magnetometry. The large number of observed persistent current oscillations aided the task of distinguishing the persistent current signal from the measurement's smooth background. Previous experiments were much more sensitive to the measurement background. These measurements were performed over a small range near zero magnetic field for which only a small number of oscillations were observed and over which paramagnetic effects led to a large

⁴As discussed in 6.5, the measurements reported in Chapter 7 did not reach the thermal limit. Recently, thermally limited measurements have been performed in the Harris lab with thinner (110 nm) cantilevers. For these measurements, the cantilever frequency was obtained using the Hilbert transform technique mentioned in 5.2.2.5.

background magnetization signal.

Beyond aiding in the analysis of the measurement, the large magnetic field range enabled the study of new physics. We measured the persistent current signal over many correlation fields $B_{c,p}$ and so were able to confirm the predictions of 2.3.2.1 and Ref. 42 for the effect of magnetic flux piercing the metal on the autocorrelation of the persistent current oscillation. In previous measurements, it was not possible to apply a magnetic field much greater than the correlation field $B_{c,p}$. With our measurement range $B_0 \gg B_{c,p}$, we were able to acquire $M_{\text{eff}} \approx 210$ independent measurements of the persistent current magnitude,⁵ a figure approximately seven times the total number of samples studied previously. The large values of M_{eff} for each sample allowed for accurate estimates of the typical current magnitude.

There are several ways of making further use of cantilever torsional magnetometry to study persistent currents. The simplest extension of the work performed so far is to make additional measurements of individual rings over a wide magnetic field range. Such measurements would enable the study of the statistics of the persistent current beyond its typical magnitude and test the prediction cited in Chapter 3 that the persistent current magnitude is normally distributed. Single ring measurements are required because, as discussed in 7.3, the central limit theorem requires that the distribution of the total current in an array of rings tends toward the normal distribution regardless of the underlying single ring distribution. An example of the analysis that would be performed on such single ring measurements is given in Appendix G for the measurements on the arrays of rings reported in Chapter 7. The analysis in Appendix G shows that the measured set of values of the persistent current in the arrays is consistent with a normal distribution. This result confirms the applicability of the central limit theorem but does not provide much information about the underlying single ring distribution.

The one single ring measurement discussed in Chapter 7 contained $M_{\text{eff}} \approx 12$ independent samples of the persistent current (see Table 7.3 and accompanying discussion). While the size of this data set was sufficient to infer the magnitude of the typical current with reasonable statistical uncertainty, a larger data set is necessary to study the properties of the current's statistical distribution beyond its variance. By redesigning the sample chip to contain many cantilevers with single rings, a much larger number M_{eff} of independent realizations of the persistent current could be observed. The signal to noise ratio could also potentially be improved by using cantilevers with dimensions

⁵This number is the sum of all of the M_{eff} listed in Table 7.3.

chosen by following the considerations reviewed in 6.3. Together with Manuel Castellanos Beltran, I have fabricated such samples. At the time of writing, measurements of these samples are underway in the Harris lab.⁶

The effects of high frequency electromagnetic radiation on the persistent current could be studied by cantilever torsional magnetometry. To study these effects on the typical current in a strong magnetic field, the only necessary modification to the current experimental apparatus is the addition of a radiation source coupled to the persistent current sample. Many works investigating the non-equilibrium currents induced by external radiation were mentioned in Chapter 3. However, none of these works discusses the typical current in a metal ring. I am not aware of any published work studying the effect of electromagnetic radiation on the typical persistent current in a normal metal ring.

Cantilever torsional magnetometry could also be applied to the study of the average persistent current at low magnetic field. The fact that the frequency shift signal scales quadratically with magnetic field was a great advantage in the study of the typical persistent current because it meant that the persistent current was observable over a large magnetic field range. However, one of the most intriguing puzzles in the persistent current literature is the unexpected magnitude and sign of the average current. This contribution to the persistent current is only present at low magnetic field.

With a modified cantilever design, it is possible to study this average contribution to the persistent current as well. Because the total current in the array scales as the ring number N , the signal to noise ratio increases with cantilever size.⁷ Using Eq. 2.94 for the average current I^{ee} due to electron-electron interactions and assuming that the thermal motion of the cantilever produces the leading contribution to the noise in the frequency measurement (see Eq. 6.31), one finds a sensitivity \mathcal{S}_{pc} (defined in Eq. 6.35) of $\sim 8.2 (1/\sqrt{\text{Hz}})$ for a cantilever $400 \mu\text{m}$ long, 2 mm wide, and 110 nm thick covered with an array of 1.3×10^6 rings with radii of 250 nm and cross-sections of 30 nm by 30 nm . This figure for the sensitivity was calculated for a temperature of 323 mK and for gold rings each with a diffusion constant $D = 0.014 \text{ m}^2/\text{s}$ (corresponding to an elastic mean free path of $l_e = 30 \text{ nm}$) and an effective electron-electron interaction coefficient $\lambda_{\text{eff}} = 0.333$. For

⁶To add to the credibility of the measurements discussed in Chapter 7, I note that a persistent current signal has already been measured in many additional single ring samples. These new samples were part of a round of fabrication distinct from the one in which the samples discussed in Chapter 7 were created, indicating good repeatability for the entire process of measuring persistent currents with cantilever torsional magnetometry.

⁷For the typical current, the signal to noise ratio decreases with cantilever length and is independent of cantilever width when the measurement is limited by the thermal motion of the cantilever. See 6.3.

these figures, the persistent current should be observable at least between ~ 50 mT and ~ 250 mT, a span covering ~ 15 oscillations.

Other modifications to the cantilever design and experimental apparatus could potentially improve sensitivity to persistent currents. In 4.3, it was noted that a measurement using a strong magnetic field gradient could achieve a sensitivity comparable to that of the uniform field measurements discussed in most of this text. Such a magnetic field gradient measurement could be performed at low magnetic field and, unlike the low magnetic field measurement described above, would require a small array of rings so that each ring would experience a similar magnetic field gradient strength. Also, as mentioned in 6.3, geometries other than the cantilevered beam could be more sensitive to persistent currents [288–290].

Finally, cantilever torsional magnetometry could be used to study persistent currents in other materials. Semiconductor rings in the ballistic regime are of particular interest. Many predictions regarding the persistent current in the ballistic regime have been made and remain untested (see Chapter 3). Another potential system is a superconductor such as niobium with a large critical magnetic field. If the critical field is large enough (~ 1 T), the sensitivity would be sufficient to observe persistent current in the normal state across the transition into the superconducting state.

Appendix A

Mathematical relations

A.1 Poisson summation formula

A.1.1 General formula

The Poisson summation formula relates the infinite sum of a function with evenly spaced arguments

$$\sum_n f(\phi + n\phi_0) = F(\phi) \quad (\text{A.1})$$

to its Fourier transform

$$\tilde{f}(p/\phi_0) = \int_{-\infty}^{\infty} d\phi f(\phi) e^{-2\pi i p \phi / \phi_0}.$$

The formula is useful in the calculation of persistent currents where sums over all the states in the ring often take the form of Eq. A.1. The identity is shown by noting that $F(\phi)$ is periodic in ϕ with period ϕ_0 and can be expanded in a Fourier series:

$$\begin{aligned} F(\phi) &= \sum_p \left(\frac{1}{\phi_0} \int_0^{\phi_0} d\phi' F(\phi') e^{-2\pi i p \phi' / \phi_0} \right) e^{2\pi i p \phi / \phi_0} \\ &= \sum_n \sum_p \left(\frac{1}{\phi_0} \int_0^{\phi_0} d\phi' f(\phi' + n\phi_0) e^{-2\pi i p \phi' / \phi_0} \right) e^{2\pi i p \phi / \phi_0} \\ &= \sum_n \sum_p \left(\frac{1}{\phi_0} \int_{-n\phi_0}^{-(n-1)\phi_0} d\phi' f(\phi') e^{2\pi i p n} e^{-2\pi i p \phi' / \phi_0} \right) e^{2\pi i p \phi / \phi_0} \\ &= \sum_p \sum_n \left(\frac{1}{\phi_0} \int_{-n\phi_0}^{-(n-1)\phi_0} d\phi' f(\phi') e^{-2\pi i p \phi' / \phi_0} \right) e^{2\pi i p \phi / \phi_0} \end{aligned}$$

$$\begin{aligned}
F(\phi) &= \sum_p \left(\frac{1}{\phi_0} \int_{-\infty}^{\infty} d\phi' f(\phi') e^{-2\pi i p \phi' / \phi_0} \right) e^{2\pi i p \phi / \phi_0} \\
\sum_n f(\phi + n\phi_0) &= \frac{1}{\phi_0} \sum_p \tilde{f}\left(\frac{p}{\phi_0}\right) e^{2\pi i p \phi / \phi_0}.
\end{aligned} \tag{A.2}$$

The last line is the Poisson summation formula.

A.1.2 Application to $\nu(\varepsilon, \phi)$ for the one-dimensional ring

The density of states for a system with discrete energy levels such as the one-dimensional ring considered in 2.1 can be written in the form

$$\nu(\varepsilon) = \sum_n \delta(\varepsilon - \varepsilon_n)$$

where the sum is over the discrete energy levels ε_n .

For the one-dimensional ring, the energy levels, given in Eq. 2.4, take the form

$$\varepsilon_n(\phi) = \varepsilon_0(\phi + n\phi_0)$$

with

$$\varepsilon_0(\phi) = \frac{\hbar^2}{2mL^2} \left(\frac{\phi}{\phi_0} \right)^2.$$

Thus, the density of states for the one-dimensional ring matches the form of the Poisson summation formula in Eq. A.2 with $f(\phi) = \delta(\varepsilon - \varepsilon_0(\phi))$. We can evaluate the Fourier transform as

$$\begin{aligned}
\tilde{f}\left(\frac{p}{\phi_0}\right) &= \int_{-\infty}^{\infty} d\phi \delta(\varepsilon - \varepsilon_0(\phi)) e^{-2\pi i p \phi / \phi_0} \\
&= \int_{-\infty}^{\infty} d\phi \frac{mL^2 \phi_0^2}{\hbar^2 |\phi|} \left(\delta\left(\phi - \sqrt{\frac{2mL^2 \phi_0^2 \varepsilon}{\hbar^2}}\right) + \delta\left(\phi + \sqrt{\frac{2mL^2 \phi_0^2 \varepsilon}{\hbar^2}}\right) \right) e^{-2\pi i p \phi / \phi_0} \\
&= \frac{2mL^2 \phi_0^2}{\hbar^2} \sqrt{\frac{\hbar^2}{2mL^2 \phi_0^2 \varepsilon}} \cos\left(\frac{2\pi p}{\phi_0} \sqrt{\frac{2mL^2 \phi_0^2 \varepsilon}{\hbar^2}}\right) \\
&= \sqrt{\frac{2mL^2 \phi_0^2}{\hbar^2 \varepsilon}} \cos\left(2\pi p \sqrt{\frac{2mL^2 \varepsilon}{\hbar^2}}\right).
\end{aligned}$$

In the second line we use the identity $\delta(g(x)) = \sum_i \delta(x - x_i) / |g'(x_i)|$ where the x_i are the values

of x for which $g(x) = 0$. The density of states is then

$$\begin{aligned}
\nu(\varepsilon, \phi) &= \frac{1}{\phi_0} \sum_p \sqrt{\frac{2mL^2\phi_0^2}{h^2\varepsilon}} \cos\left(2\pi p \sqrt{\frac{2mL^2\varepsilon}{h^2}}\right) e^{2\pi i p \phi / \phi_0} \\
&= \sum_{p>0} \sqrt{\frac{2mL^2}{h^2\varepsilon}} \cos\left(2\pi p \sqrt{\frac{2mL^2\varepsilon}{h^2}}\right) \cos\left(2\pi p \frac{\phi}{\phi_0}\right) \\
&\quad + \sqrt{\frac{2mL^2}{h^2\varepsilon}}.
\end{aligned} \tag{A.3}$$

A.2 Fourier transform of $\operatorname{sech}^2(t)$

Here we derive the Fourier transform of $\operatorname{sech}^2(t)$

$$\mathcal{F}[\operatorname{sech}^2(t), \omega] = \int_{-\infty}^{\infty} dt \operatorname{sech}^2(t) e^{-i\omega t}$$

by contour integration. We begin by noting

$$\begin{aligned}
\operatorname{sech}^2(t + i\pi) &= \frac{4}{(e^t e^{i\pi} + e^{-t} e^{-i\pi})^2} \\
&= \frac{4}{(e^t + e^{-t})^2} \\
&= \operatorname{sech}^2(t).
\end{aligned}$$

We thus choose the contour C bounded by $(-\infty, \infty)$, $(\infty, \infty + i\pi)$, $(\infty + i\pi, -\infty + i\pi)$, and $(-\infty + i\pi, -\infty)$. The two segments at ∞ give negligible contributions to the total integral. Thus

$$\begin{aligned}
\oint_C dz \operatorname{sech}^2(z) e^{-i\omega z} &= \int_{-\infty}^{\infty} dt \operatorname{sech}^2(t) e^{-i\omega t} + \int_{\infty}^{-\infty} dt \operatorname{sech}^2(t + i\pi) e^{-i\omega t} e^{\pi\omega} \\
&= (1 - e^{\pi\omega}) \int_{-\infty}^{\infty} dt \operatorname{sech}^2(t) e^{-i\omega t}.
\end{aligned}$$

The function $\operatorname{sech}^2(z)$ has poles at $z = i\pi/2 + i\pi n$ for integer n . The only pole enclosed by C is $z = i\pi/2$. To find the residue, we find the Taylor expansion of the numerator $e^{-i\omega z}$ and the denominator $\cosh^2(z)$ about $z = i\pi/2$:

$$e^{-i\omega z} \approx e^{\pi\omega/2} - i\omega e^{\pi\omega/2} \left(z - i\frac{\pi}{2}\right) + \mathcal{O}\left(\left(z - i\frac{\pi}{2}\right)^2\right)$$

and

$$\begin{aligned}
\cosh^2(z) &\approx \cosh^2\left(i\frac{\pi}{2}\right) + 2\sinh\left(i\frac{\pi}{2}\right)\cosh\left(i\frac{\pi}{2}\right)\left(z - i\frac{\pi}{2}\right) \\
&\quad + 2\left(\sinh^2\left(i\frac{\pi}{2}\right) + \cosh^2\left(i\frac{\pi}{2}\right)\right)\frac{\left(z - i\frac{\pi}{2}\right)^2}{2} \\
&\quad + 8\sinh\left(i\frac{\pi}{2}\right)\cosh\left(i\frac{\pi}{2}\right)\frac{\left(z - i\frac{\pi}{2}\right)^3}{3!} + \mathcal{O}\left(\left(z - i\frac{\pi}{2}\right)^4\right) \\
&\approx 0 + 0 - \left(z - i\frac{\pi}{2}\right)^2 + 0 + \mathcal{O}\left(\left(z - i\frac{\pi}{2}\right)^4\right).
\end{aligned}$$

These expansions allow us to find the Laurent series

$$\begin{aligned}
\operatorname{sech}^2(z)e^{-i\omega z} &= \frac{e^{\pi\omega/2} - i\omega e^{\pi\omega/2}\left(z - i\frac{\pi}{2}\right) + \mathcal{O}\left(\left(z - i\frac{\pi}{2}\right)^2\right)}{-\left(z - i\frac{\pi}{2}\right)^2 + \mathcal{O}\left(\left(z - i\frac{\pi}{2}\right)^4\right)} \\
&= -\frac{e^{\pi\omega/2} - i\omega e^{\pi\omega/2}\left(z - i\frac{\pi}{2}\right) + \mathcal{O}\left(\left(z - i\frac{\pi}{2}\right)^2\right)}{\left(z - i\frac{\pi}{2}\right)^2}\left(1 + \mathcal{O}\left(\left(z - i\frac{\pi}{2}\right)^2\right)\right) \\
&= -\frac{e^{\pi\omega/2}}{\left(z - i\frac{\pi}{2}\right)^2} + \frac{i\omega e^{\pi\omega/2}}{\left(z - i\frac{\pi}{2}\right)} + \mathcal{O}\left(\left(z - i\frac{\pi}{2}\right)^0\right).
\end{aligned}$$

Thus we find

$$\begin{aligned}
\int_{-\infty}^{\infty} dt \operatorname{sech}^2(t) e^{-i\omega t} &= \frac{1}{1 - e^{\pi\omega}} \oint_C dz \operatorname{sech}^2(z) e^{-i\omega z} \\
&= \frac{2\pi i}{1 - e^{\pi\omega}} \operatorname{Res}\left[\operatorname{sech}^2(z) e^{-i\omega z}, i\frac{\pi}{2}\right] \\
&= -\frac{2\pi\omega e^{\pi\omega/2}}{1 - e^{\pi\omega}} \\
&= \frac{\pi\omega}{\sinh\left(\frac{\pi\omega}{2}\right)}. \tag{A.4}
\end{aligned}$$

We note in particular that

$$\begin{aligned}
\lim_{\omega \rightarrow 0} \int_{-\infty}^{\infty} dt \operatorname{sech}^2(t) e^{-i\omega t} &= \lim_{\omega \rightarrow 0} \frac{\pi\omega}{\sinh\left(\frac{\pi\omega}{2}\right)} \\
&= 2,
\end{aligned}$$

so that, as noted in Section 2.2,

$$\int_{-\infty}^{\infty} d\varepsilon \frac{\operatorname{sech}^2\left((\varepsilon - \varepsilon_F)/2k_B T\right)}{4k_B T} = 1$$

while the integrand itself peaks at a value of $1/4k_B T$ at $\varepsilon = \varepsilon_F$ and thus becomes more and more sharply peaked as $T \rightarrow 0$.

A.3 Integral of $\text{sech}^2(\sigma + \frac{\varepsilon}{2})\text{sech}^2(\sigma - \frac{\varepsilon}{2})$ in current-current correlation function calculation

In the calculation of the current-current function at finite temperature in Section 2.3.1.2, the following integral is encountered:

$$\int_{-\infty}^{\infty} d\sigma \text{sech}^2\left(\sigma + \frac{\varepsilon}{2}\right) \text{sech}^2\left(\sigma - \frac{\varepsilon}{2}\right).$$

Using

$$\begin{aligned} \cosh\left(\sigma + \frac{\varepsilon}{2}\right) \cosh\left(\sigma - \frac{\varepsilon}{2}\right) &= \frac{1}{4} \left(e^{\sigma+\varepsilon/2} + e^{-\sigma-\varepsilon/2} \right) \left(e^{\sigma-\varepsilon/2} + e^{-\sigma+\varepsilon/2} \right) \\ &= \frac{1}{4} \left(e^{2\sigma} + e^{\varepsilon} + e^{-\varepsilon} + e^{-2\sigma} \right) \end{aligned}$$

and defining $x = e^{2\sigma}$ and $x_0 = e^{\varepsilon}$, we can rewrite the σ integration as

$$\begin{aligned} \int_{-\infty}^{\infty} d\sigma \text{sech}^2\left(\sigma + \frac{\varepsilon}{2}\right) \text{sech}^2\left(\sigma - \frac{\varepsilon}{2}\right) &= \int_{-\infty}^{\infty} d\sigma \left(\frac{4}{e^{2\sigma} + e^{\varepsilon} + e^{-\varepsilon} + e^{-2\sigma}} \right)^2 \\ &= \int_0^{\infty} dx \frac{1}{2x} \left(\frac{4}{x + x_0 + x_0^{-1} + x^{-1}} \right)^2 \\ &= 8 \int_0^{\infty} dx \frac{x}{(x^2 + (x_0 + x_0^{-1})x + 1)^2}. \end{aligned}$$

The quadratic formula gives the roots of the denominator as

$$\begin{aligned} x_{\pm} &= \frac{-(x_0 + x_0^{-1}) \pm \sqrt{(x_0 + x_0^{-1})^2 - 4}}{2} \\ &= \frac{-(x_0 + x_0^{-1}) \pm \sqrt{(x_0^{-1} - x_0)^2}}{2} \\ &= -x_0^{\pm 1}. \end{aligned}$$

The integrand can then be rewritten as

$$\begin{aligned}
\int_{-\infty}^{\infty} d\sigma \operatorname{sech}^2\left(\sigma + \frac{\varepsilon}{2}\right) \operatorname{sech}^2\left(\sigma - \frac{\varepsilon}{2}\right) &= 8 \int_0^{\infty} dx \frac{x}{(x^2 + (x_0 + x_0^{-1})x + 1)^2} \\
&= 8 \int_0^{\infty} dx \frac{x}{(x - x_+)^2 (x - x_-)^2} \\
&= 8 \frac{\partial^2}{\partial x_+ \partial x_-} \int_0^{\infty} dx \frac{x}{(x - x_+)(x - x_-)}.
\end{aligned}$$

We can factor the denominator by solving for A and B in

$$\begin{aligned}
\frac{x}{(x - x_+)(x - x_-)} &= \frac{A}{x - x_+} + \frac{B}{x - x_-} \\
&= \frac{A(x - x_-) + B(x - x_+)}{(x - x_+)(x - x_-)}
\end{aligned}$$

which requires

$$\begin{aligned}
A + B &= 1 \\
Ax_- + Bx_+ &= 0
\end{aligned}$$

and gives

$$\begin{aligned}
A &= \frac{x_+}{x_+ - x_-} \\
B &= \frac{-x_-}{x_+ - x_-}.
\end{aligned}$$

With this factorization, the integral can now be evaluated explicitly to find

$$\begin{aligned}
\int_{-\infty}^{\infty} d\sigma \operatorname{sech}^2\left(\sigma + \frac{\varepsilon}{2}\right) \operatorname{sech}^2\left(\sigma - \frac{\varepsilon}{2}\right) &= \\
&= 8 \frac{\partial^2}{\partial x_+ \partial x_-} \int_0^{\infty} dx \left(\frac{A}{x - x_+} + \frac{B}{x - x_-} \right) \\
&= 8 \frac{\partial^2}{\partial x_+ \partial x_-} \left(\frac{x_+}{x_+ - x_-} \ln(x - x_+) - \frac{x_-}{x_+ - x_-} \ln(x - x_-) \right) \Bigg|_0^{\infty} \\
&= 8 \frac{\partial}{\partial x_-} \left(\frac{\ln(x - x_+)}{x_+ - x_-} - \frac{x_+}{(x_+ - x_-)^2} \ln(x - x_+) + \dots \right. \\
&\quad \left. - \frac{x_+}{x_+ - x_-} \frac{1}{x - x_+} + \frac{x_-}{(x_+ - x_-)^2} \ln(x - x_-) \right) \Bigg|_0^{\infty}
\end{aligned}$$

$$\begin{aligned}
\int_{-\infty}^{\infty} d\sigma \operatorname{sech}^2\left(\sigma + \frac{\varepsilon}{2}\right) \operatorname{sech}^2\left(\sigma - \frac{\varepsilon}{2}\right) &= \\
&= 8 \left(\frac{\ln(x-x_+)}{(x_+ - x_-)^2} - \frac{2x_+}{(x_+ - x_-)^3} \ln(x-x_+) + \dots \right. \\
&\quad - \frac{x_+}{(x_+ - x_-)^2} \frac{1}{x-x_+} + \frac{1}{(x_+ - x_-)^2} \ln(x-x_-) + \dots \\
&\quad \left. - + \frac{2x_-}{(x_+ - x_-)^3} \ln(x-x_-) - \frac{x_-}{(x_+ - x_-)^2} \frac{1}{(x-x_-)} \right) \Big|_0^{\infty} \\
&= 8 \left(- \frac{x_+ + x_-}{(x_+ - x_-)^3} \ln(x-x_+) + \frac{x_+ + x_-}{(x_+ - x_-)^3} \ln(x-x_-) + \dots \right. \\
&\quad \left. - \frac{1}{(x_+ - x_-)^2} \left(\frac{x_+}{x-x_+} + \frac{x_-}{x-x_-} \right) \right) \Big|_0^{\infty} \\
&= \frac{-8}{(x_+ - x_-)^2} \left(\frac{x_+ + x_-}{x_+ - x_-} \ln\left(\frac{x-x_+}{x-x_-}\right) + \frac{x_+}{x-x_+} + \frac{x_-}{x-x_-} \right) \Big|_0^{\infty} \\
&= \frac{8}{(x_+ - x_-)^2} \left(\frac{x_+ + x_-}{x_+ - x_-} \ln\left(\frac{x_+}{x_-}\right) - 2 \right).
\end{aligned}$$

Restoring $x_{\pm} = -e^{\pm\varepsilon}$, we have

$$\begin{aligned}
\int_{-\infty}^{\infty} d\sigma \operatorname{sech}^2\left(\sigma + \frac{\varepsilon}{2}\right) \operatorname{sech}^2\left(\sigma - \frac{\varepsilon}{2}\right) &= \frac{8}{(e^{\varepsilon} - e^{-\varepsilon})^2} \left(\frac{e^{\varepsilon} + e^{-\varepsilon}}{e^{\varepsilon} - e^{-\varepsilon}} (2\varepsilon) - 2 \right) \\
&= 4 \frac{\varepsilon \cosh \varepsilon - \sinh \varepsilon}{\sinh^3 \varepsilon}.
\end{aligned} \tag{A.5}$$

We note that the expression

$$f_2(\varepsilon) = \frac{\varepsilon \cosh \varepsilon - \sinh \varepsilon}{\sinh^3 \varepsilon}$$

can be written in the more compact form

$$f_2(\varepsilon) = 4 \frac{\partial^2}{\partial \varepsilon^2} \left(\frac{\varepsilon}{1 + e^{-2\varepsilon}} \right).$$

A.4 Summation form of the normalized temperature dependence of the current-current correlation function

In Eq. 2.71 we introduce the function

$$g_D(x, y) = \text{Re} \left(\int_{-\infty}^{\infty} d\varepsilon \left(\frac{\varepsilon \cosh \varepsilon - \sinh \varepsilon}{\sinh^3 \varepsilon} \right) \left(1 + \sqrt{x + iy\varepsilon} + \frac{(x + iy\varepsilon)}{3} \right) \exp \left(-\sqrt{x + iy\varepsilon} \right) \right) \quad (\text{A.6})$$

where x and y are real, positive numbers set by parameters of the persistent current ring system. Note that despite the complex components of the integrand the function $g_D(x, y) = g_D^*(x, y)$ is always real. The first factor of the integral

$$\lim_{\varepsilon \rightarrow 0} \left(\frac{\varepsilon \cosh \varepsilon - \sinh \varepsilon}{\sinh^3 \varepsilon} \right) = \frac{1}{3}$$

is finite as $\varepsilon \rightarrow 0$. However, for $\varepsilon \rightarrow 2\pi iN$ with N a non-zero integer, this factor has a third order pole. Away from these poles, the entire integrand decays to zero as $|\varepsilon| \rightarrow \infty$ in the lower half plane due to the $\sinh^3 \varepsilon$ term in the denominator and the $\exp(-\sqrt{x + iy\varepsilon})$ in the numerator because $\text{Re}(-\sqrt{x + iy\varepsilon}) < 0$. The function $g_D(x, y)$ can thus be evaluated by contour integration with the contour following the real axis and enclosing the lower half of the complex plane. Because the integrand is a complicated function with third order poles, calculating the residues by hand is quite tedious. Using the Series command of Mathematica to evaluate the Laurent series at $i\pi N$, we find

$$\begin{aligned} g_D(x, y) &= \\ &= -2\pi i \sum_{N=-1}^{-\infty} \text{Res} \left[\left(\frac{\varepsilon \cosh \varepsilon - \sinh \varepsilon}{\sinh^3 \varepsilon} \right) \left(1 + \sqrt{x + iy\varepsilon} + \frac{(x + iy\varepsilon)}{3} \right) \exp \left(-\sqrt{x + iy\varepsilon} \right), 2\pi iN \right] \end{aligned} \quad (\text{A.7})$$

$$\begin{aligned} &= -2\pi i \sum_{N=-1}^{-\infty} \left(-i \frac{N\pi y^2}{24} \exp \left(-\sqrt{x - \pi N y} \right) \right) \\ &= \frac{\pi^2 y^2}{12} \sum_{N=1}^{\infty} N \exp \left(-\sqrt{x + \pi N y} \right). \end{aligned} \quad (\text{A.8})$$

Typically, the summation in Eq. A.8 agrees with numerical evaluation of the integral over the experimentally relevant range $y > 2.5$ when the first twenty terms are kept.

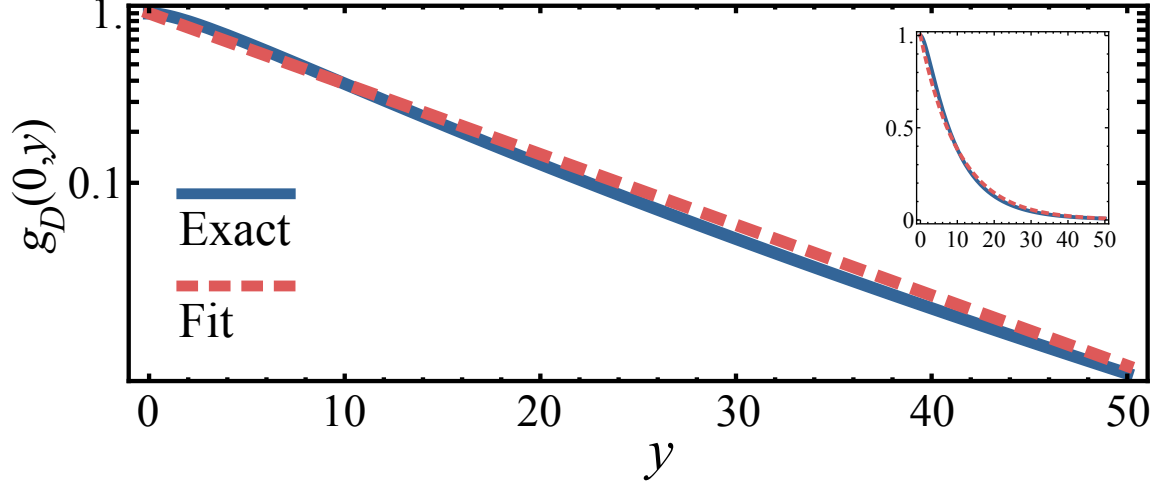


Figure A.1: Exponential fit to $g_D(0, y)$. The solid curve shows a numerical evaluation of the integral given in Eq. A.6 for $g_D(0, y)$. The dashed curve shows the exponential $\exp(-0.095y)$ obtained from a best fit for a in $\exp(-ay)$ to the solid curve over the range $y < 50$.

When Zeeman splitting is considered, the quantity ε is shifted to $\varepsilon + w$ where w is a real number. Effectively, this replaces x in the expression for $g_D(x, y)$ by $x + iw y$. This change does not affect the location or evaluation of the poles of $g_D(x, y)$. However, it does make the integral in Eq. A.6 complex. We then can not drop the operation of taking the real part of the integral. The more general result for complex x is then

$$g_D(x, y) = \frac{\pi^2 y^2}{12} \sum_{N=1}^{\infty} N \operatorname{Re} \left(\exp \left(-\sqrt{x + \pi N y} \right) \right).$$

Finally, we note that for $x = 0$, the function $g_D(x, y)$ is approximately exponential in y over the experimentally relevant parameter range $y < 50$, following the form

$$g_D(0, y) \approx \exp(-0.096y)$$

obtained by a numerical fit to $g_D(0, y)$ over this range. The accuracy of this exponential approximation is demonstrated in Fig. A.1. A slightly better fit can be achieved by allowing the prefactor of the exponential to deviate from 1. In all analysis of data in this text, the exact form for $g_D(x, y)$ is used. The exponential approximation is only used when modeling the dependence of the signal to noise ratio on the various properties of the ring and cantilever system.

A.5 Trigonometric identities

Many useful relations can be derived from algebraic manipulations of Euler's formula,

$$e^{i\theta} = \cos \theta + i \sin \theta.$$

The main ones used in this text are

$$\cos(A + B) = \cos A \cos B - \sin A \sin B, \quad (\text{A.9})$$

$$\sin(A + B) = \sin A \cos B + \cos A \sin B, \quad (\text{A.10})$$

$$\cos^2 \theta = \frac{1 + \cos(2\theta)}{2}, \quad (\text{A.11})$$

$$\sin^2 \theta = \frac{1 - \cos(2\theta)}{2}. \quad (\text{A.12})$$

From these relations it is easily seen that

$$\int_0^1 d\theta \sin(2\pi m\theta) \sin(2\pi n\theta) = \frac{\delta_{mn}}{2}, \quad (\text{A.13})$$

$$\int_0^1 d\theta \cos(2\pi m\theta) \cos(2\pi n\theta) = \frac{\delta_{mn}}{2}, \quad (\text{A.14})$$

$$\int_0^1 d\theta \sin(2\pi m\theta) \cos(2\pi n\theta) = 0. \quad (\text{A.15})$$

A.6 Jacobi-Anger expansion

The Jacobi-Anger expansion provides a convenient way of expressing nested sinusoidal functions in terms of a sum over sinusoidal functions that are no longer nested. In Ref. [51], the Bessel functions J_n are defined in terms of the generating function $g(x, t)$ as

$$\begin{aligned} g(x, t) &= e^{(x/2)(t-1/t)} \\ &= \sum_{n=-\infty}^{\infty} J_n(x) t^n. \end{aligned} \quad (\text{A.16})$$

Then, for $t = e^{i\theta}$,

$$g(x, e^{i\theta}) = e^{ix \sin \theta} = \sum_{n=-\infty}^{\infty} J_n(x) e^{in\theta}.$$

By expanding the right-hand side of Eq. A.16 one can show that $J_{-n}(x) = (-1)^n J_n(x)$. The real and imaginary parts of Eq. ?? simplify to

$$\begin{aligned}\cos(x \sin \theta) &= \sum_{n=-\infty}^{\infty} J_n(x) \cos(n\theta) \\ &= \sum_{n=-\infty}^{\infty} J_{2n}(x) \cos(2n\theta) \\ &= J_0(x) + 2 \sum_{n=1}^{\infty} J_{2n}(x) \cos(2n\theta)\end{aligned}\tag{A.17}$$

$$\begin{aligned}\sin(x \sin \theta) &= \sum_{n=-\infty}^{\infty} J_n(x) \sin(n\theta) \\ &= 2 \sum_{n=1}^{\infty} J_{2n-1}(x) \sin((2n-1)\theta).\end{aligned}\tag{A.18}$$

We obtain the comparable expressions for $\cos \theta$ by taking $\theta \rightarrow \theta + \pi/2$ which gives

$$\begin{aligned}\cos(x \cos \theta) &= \sum_{n=-\infty}^{\infty} (-1)^n J_{2n}(x) \cos(2n\theta) + \sum_{n=-\infty}^{\infty} (-1)^n J_{2n-1}(x) \sin((2n-1)\theta) \\ &= \sum_{n=-\infty}^{\infty} (-1)^n J_{2n}(x) \cos(2n\theta) \\ &= J_0(x) + 2 \sum_{n=1}^{\infty} (-1)^n J_{2n}(x) \cos(2n\theta)\end{aligned}\tag{A.19}$$

$$\begin{aligned}\sin(x \cos \theta) &= \sum_{n=-\infty}^{\infty} (-1)^n J_{2n}(x) \sin(2n\theta) - \sum_{n=-\infty}^{\infty} (-1)^n J_{2n-1}(x) \cos((2n-1)\theta) \\ &= \sum_{n=-\infty}^{\infty} (-1)^{n+1} J_{2n-1}(x) \cos((2n-1)\theta) \\ &= 2 \sum_{n=1}^{\infty} (-1)^{n+1} J_{2n-1}(x) \cos((2n-1)\theta).\end{aligned}\tag{A.20}$$

Eqs. A.17, A.18, A.19, and A.20 are collectively referred to as the Jacobi-Anger expansion.

A.7 Select integral identities

A.7.1 $\frac{\sin^2(x/2)}{1+(x/\alpha)^2}$

By taking $x \rightarrow -x$ and reversing the direction of integration for part of the integrand, we can write

$$\begin{aligned} \int_{-\infty}^{\infty} dx \frac{\sin^2(x/2)}{1+(x/\alpha)^2} &= \frac{1}{4} \int_{-\infty}^{\infty} dx \frac{2 - e^{ix} - e^{-ix}}{1+(x/\alpha)^2} \\ &= \frac{1}{4} \int_{-\infty}^{\infty} dx \frac{2 - e^{ix}}{1+(x/\alpha)^2} - \frac{1}{4} \int_{\infty}^{-\infty} (-dx) \frac{e^{ix}}{1+(x/\alpha)^2} \\ &= \frac{1}{4} \int_{-\infty}^{\infty} dx \frac{2 - e^{ix}}{1+(x/\alpha)^2} - \frac{1}{4} \int_{-\infty}^{\infty} dx \frac{e^{ix}}{1+(x/\alpha)^2} \\ &= \frac{1}{2} \int_{-\infty}^{\infty} dx \frac{1 - e^{ix}}{1+(x/\alpha)^2}. \end{aligned}$$

The latter integral has poles at $\pm i\alpha$ and is easily evaluated using the standard infinite semi-circular contour in the upper half plane bordering the real axis:

$$\begin{aligned} \int_{-\infty}^{\infty} dx \frac{\sin^2(x/2)}{1+(x/\alpha)^2} &= 2\pi i \operatorname{Res} \left[\frac{1}{2} \frac{\alpha^2 (1 - e^{ix})}{(x + i\alpha)(x - i\alpha)}, i\alpha \right] \\ &= \frac{\pi}{2} \alpha (1 - e^{-\alpha}). \end{aligned} \tag{A.21}$$

A.7.2 $\frac{1}{x^2} \frac{\sin^2(x/2)}{1+(x/\alpha)^2}$

Using the same manipulations as in the previous section, we can rewrite the integrand as

$$\int_{-\infty}^{\infty} dx \frac{1}{x^2} \frac{\sin^2(x/2)}{1+(x/\alpha)^2} = \frac{1}{2} \int_{-\infty}^{\infty} dx \frac{1}{x^2} \frac{1 - e^{ix}}{1+(x/\alpha)^2}.$$

This integrand has second order pole on the real axis. We use the standard trick of shifting this second order pole to $\pm\delta$ by changing x^{-2} to $(x^2 + \delta^2)^{-1}$. The integral can then be evaluated using the standard infinite semi-circular contour in the upper half plane bordering the real axis

$$\begin{aligned} \int_{-\infty}^{\infty} dx \frac{1}{x^2 + \delta^2} \frac{\sin^2(x/2)}{1+(x/\alpha)^2} &= \\ &= 2\pi i \left(\operatorname{Res} \left[\frac{1}{2} \frac{1}{x^2 + \delta^2} \frac{\alpha^2 (1 - e^{ix})}{\alpha^2 + x^2}, i\alpha \right] + \operatorname{Res} \left[\frac{1}{2} \frac{1}{x^2 + \delta^2} \frac{\alpha^2 (1 - e^{ix})}{\alpha^2 + x^2}, i\delta \right] \right) \\ &= \frac{\pi}{2} \left(\frac{1}{-\alpha^2 + \delta^2} \right) \alpha (1 - e^{-\alpha}) + \frac{\pi}{2} \frac{1}{\delta} \frac{\alpha^2 (1 - e^{-\delta})}{\alpha^2 + \delta^2} \end{aligned}$$

$$\int_{-\infty}^{\infty} dx \frac{1}{x^2 + \delta^2} \frac{\sin^2(x/2)}{1 + (x/\alpha)^2} =$$

$$\approx -\frac{\pi}{2} \frac{1}{\alpha} (1 - e^{-\alpha}) + \frac{\pi}{2}$$

where in the last line we have taken the limit $\delta \rightarrow 0$. Thus we have

$$\int_{-\infty}^{\infty} dx \frac{1}{x^2} \frac{\sin^2(x/2)}{1 + (x/\alpha)^2} = \frac{\pi}{2} \left(1 - \frac{1}{\alpha} (1 - e^{-\alpha}) \right). \quad (\text{A.22})$$

Appendix B

Green functions in mesoscopics

The best introduction to the Green function techniques used in mesoscopic physics that I have found is the text of Akkermans and Montambaux [36]. In this appendix, I will review a few properties of Green functions relevant to the calculation of persistent currents. Many of these results come from chapter three of Akkermans and Montambaux. The main purpose of this appendix is to introduce enough of the Green function formalism to describe what the diffuson and cooperon are. The diffuson and cooperon are central to the calculation of the persistent current measurements discussed in this text.

B.1 General properties

For a system governed by the Hamiltonian $\hat{H} = \hat{H}_0 + \hat{V}$ with \hat{H}_0 the Hamiltonian of a free particle, a complete characterization amounts to solving the Schrödinger equation

$$i\hbar \frac{\partial \psi}{\partial t} = \hat{H} \psi$$

for $\psi(t)$. Formally, this equation can be solved¹ by the time evolution Green function $\hat{G}(t) = \exp(-i\hat{H}t/\hbar)$ for which $\psi(t) = \hat{G}(t)\psi(0)$. It is often more convenient in computations to make use

¹Here we are assuming that \hat{V} is time independent.

of the retarded \hat{G}^R and advanced \hat{G}^A Green functions

$$\begin{aligned}\hat{G}^R(t) &= -i\theta(t) \exp(-i\hat{H}t/\hbar) \\ \hat{G}^A(t) &= i\theta(-t) \exp(-i\hat{H}t/\hbar)\end{aligned}$$

where $\theta(t)$ is the Heaviside function ($\theta(t) = 1$ for $t > 0$ and 0 otherwise). Because of the Heaviside functions, these Green functions are related to propagation forward and backward in time respectively.

Consider the expectation value² of $\hat{G}^{R,A}(t)$ for the n^{th} eigenstate of the Hamiltonian with eigenenergy ε_n ,

$$\begin{aligned}\langle n | \hat{G}^{R,A}(t) | n \rangle &= \mp i\theta(\pm t) \langle n | \exp(-i\hat{H}t/\hbar) | n \rangle \\ &= \mp i\theta(\pm t) \exp(-i\varepsilon_n t/\hbar).\end{aligned}$$

Taking the Fourier transform with respect to t , we find

$$\begin{aligned}\langle n | \hat{G}^{R,A}(\varepsilon) | n \rangle &= \int_{-\infty}^{\infty} dt \langle n | \hat{G}^{R,A}(t) | n \rangle e^{i\varepsilon t/\hbar} \\ &= -i \int_0^{\pm\infty} dt \exp(i(\varepsilon - \varepsilon_n)t/\hbar) \\ &= -\hbar \frac{\exp(i(\varepsilon - \varepsilon_n)t/\hbar)}{\varepsilon - \varepsilon_n} \Big|_0^{\pm\infty}.\end{aligned}$$

This last expression contains an oscillating term that is not well-defined at $\pm\infty$. This oscillating term can be eliminated if we give each eigenenergy a small imaginary component $\varepsilon_n \rightarrow \varepsilon_n \mp i\gamma$. In this case,

$$\begin{aligned}\langle n | \hat{G}^{R,A}(\varepsilon) | n \rangle &= \lim_{t \rightarrow \infty} \hbar \frac{1 - e^{-\gamma|t|/\hbar} \exp(i(\varepsilon - \varepsilon_n)t/\hbar)}{\varepsilon - \varepsilon_n \pm i\gamma} \\ &= \hbar \frac{1}{\varepsilon - \varepsilon_n \pm i\gamma}.\end{aligned}\tag{B.1}$$

²This term is just used formally for the mathematical quantity under consideration. The Green function does not represent a physical observable.

One result of complex analysis is that

$$\lim_{\gamma \rightarrow 0} \frac{1}{\varepsilon - \varepsilon_n \pm i\gamma} = \text{p.p.} \left(\frac{1}{\varepsilon - \varepsilon_n} \right) - i\pi\delta(\varepsilon - \varepsilon_n)$$

where p.p. represents the principal part. With this expression, the density of states

$$\nu(\varepsilon) = \sum_n \delta(\varepsilon - \varepsilon_n) \quad (\text{B.2})$$

can be written using Green functions as

$$\begin{aligned} \nu(\varepsilon) &= \mp \frac{1}{\pi\hbar} \sum_n \text{Im} \left(\langle n | \hat{G}^{R,A}(\varepsilon) | n \rangle \right) \\ &= \mp \frac{1}{\pi\hbar} \text{Im} \left(\text{Tr} \left(\hat{G}^{R,A}(\varepsilon) \right) \right). \end{aligned} \quad (\text{B.3})$$

In particular, we can take the trace over the position states to write

$$\nu(\varepsilon) = \mp \frac{1}{\pi\hbar} \text{Im} \left(\int d\mathbf{r} G^{R,A}(\mathbf{r}, \mathbf{r}, \varepsilon) \right). \quad (\text{B.4})$$

The integral in this expression can be thought of as the spatial average of the probability amplitude associated with all closed paths followed by a particle with energy ε .

Returning to Eq. B.1, we note that the operator $\hat{G}^{R,A}(\varepsilon)$ can be formally extended beyond the energy eigenstate basis as

$$\hat{G}^{R,A}(\varepsilon) = \frac{\hbar}{\varepsilon - \hat{H} \pm i\gamma}, \quad (\text{B.5})$$

where the matrix element between any two states can be calculated as

$$\langle k | \hat{G}^{R,A}(\varepsilon) | k' \rangle = \sum_n \langle k | n \rangle \langle n | \hat{G}^{R,A}(\varepsilon) | n \rangle \langle n | k' \rangle.$$

In particular we can write the real space representation in the form

$$\begin{aligned} G^{R,A}(\mathbf{r}, \mathbf{r}', \varepsilon) &= \langle \mathbf{r} | \hat{G}^{R,A}(\varepsilon) | \mathbf{r}' \rangle \\ &= \sum_n \langle \mathbf{r} | n \rangle \langle n | \hat{G}^{R,A}(\varepsilon) | n \rangle \langle n | \mathbf{r}' \rangle \\ &= \sum_n \frac{\phi_n^*(\mathbf{r}') \phi_n(\mathbf{r})}{\varepsilon - \varepsilon_n \pm i\gamma} \end{aligned} \quad (\text{B.6})$$

where the $\phi_n(\mathbf{r}) = \langle \mathbf{r} | n \rangle$ are the energy eigenfunctions. We note in passing that, if we define the non-local density of states as

$$\nu(\mathbf{r}, \mathbf{r}', \varepsilon) = \sum_n \phi_n^*(\mathbf{r}') \phi_n(\mathbf{r}) \delta(\varepsilon - \varepsilon_n), \quad (\text{B.7})$$

we can write

$$\nu(\mathbf{r}, \mathbf{r}', \varepsilon) = \mp \frac{1}{\pi \hbar} \text{Im} G^{R,A}(\mathbf{r}, \mathbf{r}', \varepsilon)$$

in analogy with the previous expression for $\nu(\varepsilon)$. From Eqs. B.1 and B.5, it follows that the imaginary part of the operators $\hat{G}^{R,A}(\varepsilon)$ can be formally defined as

$$\text{Im} \hat{G}^R(\varepsilon) = \frac{\hat{G}^R(\varepsilon) - \hat{G}^A(\varepsilon)}{2i} \quad (\text{B.8})$$

and

$$\text{Im} \hat{G}^A(\varepsilon) = \frac{\hat{G}^A(\varepsilon) - \hat{G}^R(\varepsilon)}{2i}. \quad (\text{B.9})$$

Denoting by G_0 the Green functions associated with $\hat{H} = \hat{H}_0$ and taking $\gamma \rightarrow 0$, we can write

$$\begin{aligned} (\varepsilon - \hat{H}) \hat{G}^{R,A}(\varepsilon) &= \hbar \\ \hat{G}_0^{R,A}(\varepsilon) (\varepsilon - \hat{H}_0) &= \hbar. \end{aligned}$$

From these relations it follows that

$$\begin{aligned} \hat{G}_0^{R,A}(\varepsilon) &= \hat{G}_0^{R,A}(\varepsilon) \frac{(\varepsilon - \hat{H})}{\hbar} \hat{G}^{R,A}(\varepsilon) \\ &= \hat{G}_0^{R,A}(\varepsilon) \frac{(\varepsilon - \hat{H}_0)}{\hbar} \hat{G}^{R,A}(\varepsilon) - \hat{G}_0^{R,A}(\varepsilon) \frac{\hat{V}}{\hbar} \hat{G}^{R,A}(\varepsilon) \\ &= \hat{G}^{R,A}(\varepsilon) - \hat{G}_0^{R,A}(\varepsilon) \frac{\hat{V}}{\hbar} \hat{G}^{R,A}(\varepsilon), \end{aligned}$$

from which we obtain the recursive expression for $\hat{G}^{R,A}(\varepsilon)$

$$\hat{G}^{R,A}(\varepsilon) = \hat{G}_0^{R,A}(\varepsilon) + \hat{G}_0^{R,A}(\varepsilon) \frac{\hat{V}}{\hbar} \hat{G}^{R,A}(\varepsilon). \quad (\text{B.10})$$

Generally, the potential \hat{V} is taken to be a small perturbation so that $\hat{G}^{R,A}$ and $\hat{G}_0^{R,A}$ are similar. In that case, corrections of successively higher orders in \hat{V} can be found for $\hat{G}^{R,A}$ by substituting

the right-hand side of Eq. B.10 for the factor of $\hat{G}^{R,A}$ in that same right-hand side. That is,

$$\hat{G}^{R,A} \approx \hat{G}_0^{R,A} + \hat{G}_0^{R,A} \frac{\hat{V}}{\hbar} \hat{G}_0^{R,A} + \hat{G}_0^{R,A} \frac{\hat{V}}{\hbar} \hat{G}_0^{R,A} \frac{\hat{V}}{\hbar} \hat{G}_0^{R,A} + \dots$$

This equation is known as the Dyson equation.

We assume that the perturbing potential is a function of position and can be written as $\langle \mathbf{r} | \hat{V} | \mathbf{r}' \rangle = V(\mathbf{r}) \delta(\mathbf{r} - \mathbf{r}')$ and that the function $V(\mathbf{r})$ varies randomly with each individual realization of a conducting material due to microscopic defects. The Dyson equation then has the following spatial representation

$$G^{R,A}(\mathbf{r}) \approx G_0^{R,A}(\mathbf{r}) + \frac{1}{\hbar} \int d\mathbf{r}_1 G_0^{R,A}(\mathbf{r}_1) V(\mathbf{r}_1) G_0^{R,A}(\mathbf{r} - \mathbf{r}_1) + \frac{1}{\hbar^2} \int d\mathbf{r}_1 \int d\mathbf{r}_2 G_0^{R,A}(\mathbf{r}_1) V(\mathbf{r}_1) G_0^{R,A}(\mathbf{r}_2 - \mathbf{r}_1) V(\mathbf{r}_2) G_0^{R,A}(\mathbf{r} - \mathbf{r}_2) + \dots \quad (\text{B.11})$$

A simple but accurate model for the disorder in a metal is Gaussian white noise.³ For Gaussian noise, all cumulants are zero except for the second. We will not write down the general formula for the cumulants but will only note that the result of all cumulants other than the second being zero is that all of the odd moments of disorder (e.g. $\langle V(\mathbf{r}_1) \rangle$, $\langle V(\mathbf{r}_1)V(\mathbf{r}_2)V(\mathbf{r}_3) \rangle$, $\langle \prod_{p=1}^{2n+1} V(\mathbf{r}_p) \rangle$, etc. where $\langle \dots \rangle$ denotes an average over disorder realization⁴) are zero and all of the even moments can be written as a polynomial consisting only of second moments $\langle V(\mathbf{r}_1)V(\mathbf{r}_2) \rangle$ (i.e. $\langle V(\mathbf{r}_1)V(\mathbf{r}_2)V(\mathbf{r}_3)V(\mathbf{r}_4) \rangle$ can be written as the sum of the products $\langle V(\mathbf{r}_1)V(\mathbf{r}_2) \rangle \langle V(\mathbf{r}_3)V(\mathbf{r}_4) \rangle$, $\langle V(\mathbf{r}_1)V(\mathbf{r}_3) \rangle \langle V(\mathbf{r}_2)V(\mathbf{r}_4) \rangle$, and $\langle V(\mathbf{r}_1)V(\mathbf{r}_4) \rangle \langle V(\mathbf{r}_2)V(\mathbf{r}_3) \rangle$). For white noise, the disorder potential has no spatial correlation so $\langle V(\mathbf{r}_1)V(\mathbf{r}_2) \rangle = \hbar^2 B \delta(\mathbf{r}_1 - \mathbf{r}_2)$. Thus the disorder averaged Green function (with dependence

³Gaussian noise is actually a sufficient assumption for the results we discuss, but white noise is a reasonable assumption as well.

⁴Hopefully, the difference between quantum expectation value and disorder average is clear from context. The other standard notation for averaging, $\overline{\dots}$, is already made use of in Chapter 2. All expectation values below use unabbreviated “bra” and “ket” notation.

on ε suppressed) is

$$\begin{aligned}
\langle G^{R,A}(\mathbf{r}) \rangle &= G_0^{R,A}(\mathbf{r}) + B \int d\mathbf{r}_1 d\mathbf{r}_2 \delta(\mathbf{r}_1 - \mathbf{r}_2) G_0^{R,A}(\mathbf{r}_1) G_0^{R,A}(\mathbf{r}_2 - \mathbf{r}_1) G_0^{R,A}(\mathbf{r} - \mathbf{r}_2) \\
&\quad + B^2 \int d\mathbf{r}_1 d\mathbf{r}_2 d\mathbf{r}_3 d\mathbf{r}_4 \delta(\mathbf{r}_1 - \mathbf{r}_2) \delta(\mathbf{r}_3 - \mathbf{r}_4) G_0^{R,A}(\mathbf{r}_1) G_0^{R,A}(\mathbf{r}_2 - \mathbf{r}_1) G_0^{R,A}(\mathbf{r}_3 - \mathbf{r}_2) \\
&\quad \quad \quad \times G_0^{R,A}(\mathbf{r}_4 - \mathbf{r}_3) G_0^{R,A}(\mathbf{r} - \mathbf{r}_4) \\
&\quad + B^2 \int d\mathbf{r}_1 d\mathbf{r}_2 d\mathbf{r}_3 d\mathbf{r}_4 \delta(\mathbf{r}_1 - \mathbf{r}_3) \delta(\mathbf{r}_2 - \mathbf{r}_4) G_0^{R,A}(\mathbf{r}_1) G_0^{R,A}(\mathbf{r}_2 - \mathbf{r}_1) G_0^{R,A}(\mathbf{r}_3 - \mathbf{r}_2) \\
&\quad \quad \quad \times G_0^{R,A}(\mathbf{r}_4 - \mathbf{r}_3) G_0^{R,A}(\mathbf{r} - \mathbf{r}_4) \\
&\quad + B^2 \int d\mathbf{r}_1 d\mathbf{r}_2 d\mathbf{r}_3 d\mathbf{r}_4 \delta(\mathbf{r}_1 - \mathbf{r}_4) \delta(\mathbf{r}_2 - \mathbf{r}_3) G_0^{R,A}(\mathbf{r}_1) G_0^{R,A}(\mathbf{r}_2 - \mathbf{r}_1) G_0^{R,A}(\mathbf{r}_3 - \mathbf{r}_2) \\
&\quad \quad \quad \times G_0^{R,A}(\mathbf{r}_4 - \mathbf{r}_3) G_0^{R,A}(\mathbf{r} - \mathbf{r}_4) \\
&\quad + \mathcal{O}(B^4)
\end{aligned}$$

which simplifies to

$$\begin{aligned}
\langle G^{R,A}(\mathbf{r}) \rangle &= G_0^{R,A}(\mathbf{r}) + B \int d\mathbf{r}_1 G_0^{R,A}(\mathbf{r}_1) G_0^{R,A}(0) G_0^{R,A}(\mathbf{r} - \mathbf{r}_1) \\
&\quad + B^2 \int d\mathbf{r}_1 d\mathbf{r}_3 G_0^{R,A}(\mathbf{r}_1) G_0^{R,A}(0) G_0^{R,A}(\mathbf{r}_3 - \mathbf{r}_1) G_0^{R,A}(0) G_0^{R,A}(\mathbf{r} - \mathbf{r}_3) \\
&\quad + B^2 \int d\mathbf{r}_1 d\mathbf{r}_2 G_0^{R,A}(\mathbf{r}_1) G_0^{R,A}(\mathbf{r}_2 - \mathbf{r}_1) G_0^{R,A}(\mathbf{r}_1 - \mathbf{r}_2) G_0^{R,A}(\mathbf{r}_2 - \mathbf{r}_1) G_0^{R,A}(\mathbf{r} - \mathbf{r}_2) \\
&\quad + B^2 \int d\mathbf{r}_1 d\mathbf{r}_2 G_0^{R,A}(\mathbf{r}_1) G_0^{R,A}(\mathbf{r}_2 - \mathbf{r}_1) G_0^{R,A}(0) G_0^{R,A}(\mathbf{r}_1 - \mathbf{r}_2) G_0^{R,A}(\mathbf{r} - \mathbf{r}_1) \\
&\quad + \mathcal{O}(B^4).
\end{aligned}$$

This expression is simpler in momentum space as the correlation integrals become simple products:

$$\begin{aligned}
\langle G^{R,A}(\mathbf{k}) \rangle &= \int d\mathbf{r} \langle G^{R,A}(\mathbf{r}) \rangle e^{-i\mathbf{k}\cdot\mathbf{r}} \\
&= G_0^{R,A}(\mathbf{k}) + G_0^{R,A}(\mathbf{k}) \left(B G_0^{R,A}(\mathbf{r} = 0) G_0^{R,A}(\mathbf{k}) \right) \\
&\quad + G_0^{R,A}(\mathbf{k}) \left(B G_0^{R,A}(\mathbf{r} = 0) G_0^{R,A}(\mathbf{k}) \right)^2 \\
&\quad + G_0^{R,A}(\mathbf{k}) \left(B^2 \int d\mathbf{r}_2 e^{-i\mathbf{k}\cdot\mathbf{r}_2} \left(G_0^{R,A}(\mathbf{r}_2) \right)^2 G_0^{R,A}(-\mathbf{r}_2) G_0^{R,A}(\mathbf{k}) \right) \\
&\quad + G_0^{R,A}(\mathbf{k}) \left(B^2 G_0^{R,A}(\mathbf{r} = 0) \int d\mathbf{r}_2 G_0^{R,A}(\mathbf{r}_2) G_0^{R,A}(-\mathbf{r}_2) G_0^{R,A}(\mathbf{k}) \right) \\
&\quad + \mathcal{O}(B^4).
\end{aligned}$$

From this expression, it can (perhaps) be seen that $\langle G^{R,A}(\mathbf{k}) \rangle$ is a geometric series of geometric series of terms involving successively higher orders of B .⁵ That is, we can write

$$\langle G^{R,A}(\mathbf{k}) \rangle = G_0^{R,A}(\mathbf{k}) + G_0^{R,A}(\mathbf{k}) \sum_{n=1}^{\infty} \left(\Sigma^{R,A}(\mathbf{k}, \varepsilon) G_0^{R,A}(\mathbf{k}) \right)^n$$

with $\Sigma^{R,A}(\mathbf{k}, \varepsilon) = \sum_{n=1}^{\infty} \Sigma_n^{R,A}$ and

$$\begin{aligned} \Sigma_1^{R,A}(\mathbf{k}, \varepsilon) &= \sum_{n=1}^{\infty} \left(B G_0^{R,A}(\mathbf{r}=0) \right)^n \\ \Sigma_2^{R,A}(\mathbf{k}, \varepsilon) &= \sum_{n=1}^{\infty} \left(B^2 \int d\mathbf{r}_2 e^{-i\mathbf{k}\cdot\mathbf{r}_2} \left(G_0^{R,A}(\mathbf{r}_2) \right)^2 G_0^{R,A}(-\mathbf{r}_2) \right)^n \\ \Sigma_3^{R,A}(\mathbf{k}, \varepsilon) &= \sum_{n=1}^{\infty} \left(B^2 G_0^{R,A}(\mathbf{r}=0) \int d\mathbf{r}_2 G_0^{R,A}(\mathbf{r}_2) G_0^{R,A}(-\mathbf{r}_2) \right)^n \end{aligned} \quad (\text{B.12})$$

with the series for $\Sigma_n^{R,A}$ with $n > 3$ being series involving B^m for $m > 2$. With this expansion for $\langle G^{R,A}(\mathbf{k}) \rangle$, we can write

$$\begin{aligned} \langle G^{R,A}(\mathbf{k}) \rangle &= G_0^{R,A}(\mathbf{k}) + G_0^{R,A}(\mathbf{k}) \sum_{n=1}^{\infty} \left(\Sigma^{R,A}(\mathbf{k}, \varepsilon) G_0^{R,A}(\mathbf{k}) \right)^n \\ &= G_0^{R,A}(\mathbf{k}) \left(\sum_{n=0}^{\infty} \left(\Sigma^{R,A}(\mathbf{k}, \varepsilon) G_0^{R,A}(\mathbf{k}) \right)^n \right) \\ &= \frac{G_0^{R,A}(\mathbf{k})}{1 - \Sigma^{R,A}(\mathbf{k}, \varepsilon) G_0^{R,A}(\mathbf{k})}. \end{aligned}$$

Using the form of Eq. B.1 for $G_0^{R,A}(\mathbf{k})$ (since the free Hamiltonian \hat{H}_0 is diagonal in \mathbf{k}), we have

$$\langle G^{R,A}(\mathbf{k}, \varepsilon) \rangle = \frac{\hbar}{\varepsilon - \varepsilon(\mathbf{k}) - \hbar \Sigma^{R,A}(\mathbf{k}, \varepsilon)}.$$

From this expression, we can see that the real part of $\Sigma^{R,A}(\mathbf{k}, \varepsilon)$ gives a shift to the energy of state \mathbf{k} due to the disorder average while the imaginary part of $\Sigma^{R,A}(\mathbf{k}, \varepsilon)$ plays the role of γ .

The condition of weak disorder can be formulated as $k_F l_e \gg 1$ where k_F is the wave vector of electrons at the Fermi level and l_e is the elastic mean free path which can be conceptualized as the average distance between collisions with the disorder potential for a freely propagating electron. It is defined by the relation $l_e = v_F \tau_e$ where v_F is the velocity of electrons at the Fermi level and τ_e

⁵This conclusion might be best drawn from a diagrammatic framework which we will not introduce here.

is the elastic scattering time (the average time between collisions). It can be shown that for $n > 1$

$$\frac{\Sigma_n^{R,A}(\mathbf{k}, \varepsilon)}{\Sigma_1^{R,A}(\mathbf{k}, \varepsilon)} \propto \left(\frac{1}{k(\varepsilon) l_e} \right)^m$$

with $m \geq 1$. Since we are usually concerned with $\varepsilon \sim \varepsilon_F$, these terms may be neglected in the limit of weak disorder. From Eq. B.12, we see that $\Sigma_1(\mathbf{k}, \varepsilon)$, usually referred to as the self-energy, does not depend on \mathbf{k} . Since the real part of Σ_1 just gives a constant shift to energy levels $\varepsilon(\mathbf{k})$, we will neglect it.

To find the imaginary part of the self energy, we make the further approximation of dropping the higher order terms in B , leaving

$$\begin{aligned} \Sigma_1^{R,A} &\approx B G_0^{R,A}(\mathbf{r} = 0) \\ &= B \langle \mathbf{r} = 0 | G_0^{R,A} | \mathbf{r} = 0 \rangle \\ &= B \sum_{\mathbf{k}, \mathbf{k}'} \langle \mathbf{r} = 0 | \mathbf{k} \rangle \langle \mathbf{k} | G_0^{R,A} | \mathbf{k}' \rangle \langle \mathbf{k}' | \mathbf{r} = 0 \rangle \\ &= B \frac{1}{V_d} \sum_{\mathbf{k}} \langle \mathbf{k} | G_0^{R,A} | \mathbf{k} \rangle \\ &= \frac{B}{V_d} \text{Tr} G_0^{R,A} \end{aligned}$$

where we have used the fact that $G_0^{R,A}$ is diagonal in \mathbf{k} and $\langle \mathbf{r} = 0 | \mathbf{k} \rangle = V_d^{-1/2}$ where V_d is the volume of the system. Using Eq. B.3, we have

$$\text{Im} \Sigma_1^{R,A}(\varepsilon) = \pm \pi \hbar \frac{B}{V_d} \nu_0(\varepsilon) \quad (\text{B.13})$$

where $\nu_0(\varepsilon)$ is the density of states in the absence of disorder. As a comparison, Fermi's golden rule (see e.g. Ref. [310]) states that the rate of transition $R_{\mathbf{k} \rightarrow \mathbf{k}'}$ from state \mathbf{k} to \mathbf{k}' to leading order in the perturbation V is

$$R_{\mathbf{k} \rightarrow \mathbf{k}'} = \frac{2\pi}{\hbar} \left| \langle \mathbf{k} | \hat{V} | \mathbf{k}' \rangle \right|^2 \delta(\varepsilon(\mathbf{k}) - \varepsilon(\mathbf{k}')).$$

By summing up the transition rates to all possible states, we get the total rate of decay which we

refer to as the inverse lifetime

$$\begin{aligned}\tau^{-1}(\mathbf{k}) &= \int d\mathbf{k}' \left(\frac{V_d}{(2\pi)^d} \right) R_{\mathbf{k} \rightarrow \mathbf{k}'} \\ &= \frac{2\pi}{\hbar} \int d\mathbf{k}' \left(\frac{V_d}{(2\pi)^d} \right) |\langle \mathbf{k} | \hat{V} | \mathbf{k}' \rangle|^2 \delta(\varepsilon(\mathbf{k}) - \varepsilon(\mathbf{k}')).\end{aligned}$$

Since

$$\begin{aligned}\langle \mathbf{k} | \hat{V} | \mathbf{k}' \rangle &= \int d\mathbf{r} \langle \mathbf{k} | \mathbf{r} \rangle \langle \mathbf{r} | \mathbf{k}' \rangle V(\mathbf{r}) \\ &= \frac{1}{V_d} \int d\mathbf{r} e^{i(\mathbf{k}' - \mathbf{k}) \cdot \mathbf{r}} V(\mathbf{r}),\end{aligned}$$

the disorder average is

$$\begin{aligned}\left\langle |\langle \mathbf{k} | \hat{V} | \mathbf{k}' \rangle|^2 \right\rangle &= \left(\frac{1}{V_d} \right)^2 \int d\mathbf{r} d\mathbf{r}' e^{i(\mathbf{k}' - \mathbf{k}) \cdot (\mathbf{r} - \mathbf{r}')} \langle V(\mathbf{r}) V(\mathbf{r}') \rangle \\ &= \left(\frac{\hbar}{V_d} \right)^2 B \int d\mathbf{r} d\mathbf{r}' e^{i(\mathbf{k}' - \mathbf{k}) \cdot (\mathbf{r} - \mathbf{r}')} \delta(\mathbf{r} - \mathbf{r}') \\ &= \frac{\hbar^2 B}{V_d}\end{aligned}$$

and thus the disorder average of the inverse lifetime is

$$\begin{aligned}\langle \tau^{-1}(\mathbf{k}) \rangle &= \frac{2\pi\hbar B}{V_d} \int d\mathbf{k}' \left(\frac{V_d}{(2\pi)^d} \right) \delta(\varepsilon(\mathbf{k}) - \varepsilon(\mathbf{k}')) \\ &= \frac{2\pi\hbar B}{V_d} \int_0^\infty dk' \left(\frac{V_d}{(2\pi)^d} \right) \frac{\delta(k - k')}{d\varepsilon/dk} k'^{d-1} \int d\Omega_{d-1} \\ &= \frac{2\pi\hbar B}{V_d} \frac{dk}{d\varepsilon} \frac{d}{dk} \left(\frac{V_d}{(2\pi)^d} \frac{k^d}{d} \int d\Omega_{d-1} \right) \\ &= \frac{2\pi\hbar B}{V_d} \frac{dk}{d\varepsilon} \frac{dN}{dk} \\ &= \frac{2\pi\hbar B}{V_d} \nu_0(\varepsilon)\end{aligned}\tag{B.14}$$

where $\int d\Omega_{d-1}$ represents integration of the $d-1$ angular degrees of freedom in d -dimensional space and N is the number of energy levels. We are usually interested in \mathbf{k} near the Fermi energy in which case $\langle \tau^{-1}(\mathbf{k}) \rangle$ is the elastic scattering time τ_e mentioned above. For ε near ε_F , Eqs. B.13 and B.14

give

$$\text{Im}\Sigma_1^{R,A}(\varepsilon) = \pm \frac{1}{2\tau_e}.$$

We now consider some different forms of the Green functions. Since momentum $\hat{P} = \hbar\hat{k}$ commutes with \hat{H}_0 , the Green function can be written as

$$\begin{aligned} \langle G^{R,A}(\mathbf{k}, \varepsilon) \rangle &= \langle \mathbf{k} | \hat{G}^{R,A}(\varepsilon) | \mathbf{k} \rangle \\ &= \frac{\hbar}{\varepsilon - \frac{\hbar^2 k^2}{2m} \pm \frac{i\hbar}{2\tau_e}}, \end{aligned} \quad (\text{B.15})$$

where in the first line on the right hand both the expectation value and disorder average are taken.

In real space, the Green function becomes

$$\begin{aligned} G^{R,A}(\mathbf{r}, \varepsilon) &= \langle \mathbf{r} = 0 | \hat{G}^{R,A}(\varepsilon) | \mathbf{r} \rangle \\ &= \sum_{\mathbf{k}'} \langle \mathbf{r} = 0 | \mathbf{k}' \rangle \langle \mathbf{k}' | \hat{G}^{R,A}(\varepsilon) | \mathbf{k}' \rangle \langle \mathbf{k}' | \mathbf{r} \rangle \\ &= \int d\mathbf{k}' \left(\frac{V_d}{(2\pi)^d} \right) \left(\frac{1}{\sqrt{V_d}} \right) G^{R,A}(\mathbf{k}', \varepsilon) \left(\frac{e^{-i\mathbf{k}' \cdot \mathbf{r}}}{\sqrt{V_d}} \right) \\ &= \frac{1}{(2\pi)^d} \int d\mathbf{k}' G^{R,A}(\mathbf{k}', \varepsilon) e^{-i\mathbf{k}' \cdot \mathbf{r}} \end{aligned}$$

which is just the Fourier transform of $G^{R,A}(\mathbf{k}, \varepsilon)$ (V_d is the system volume). Taking the disorder average of both sides, this integral can be easily evaluated in one dimension by using the calculus of residues with the standard contour following the real axis and then enclosing the upper half plane.

The result is

$$\begin{aligned} \int dk' \langle G^{R,A}(k', \varepsilon) \rangle e^{-ik'r} &= \int dk' \frac{2m}{\hbar^2} \frac{e^{-ik'r}}{k^2 - k'^2 \pm im/\hbar\tau_e} \\ &\approx \frac{2m}{\hbar^2} 2\pi i \text{Res} \left[\frac{e^{-ik'r}}{\left(k \pm i\frac{m}{2\hbar\tau_e k} - k' \right) \left(k \pm i\frac{m}{2\hbar\tau_e k} + k' \right)}, \pm k + i\frac{m}{2\hbar\tau_e k} \right] \\ &= \frac{2m}{\hbar^2} 2\pi i \frac{1}{2} \frac{e^{\mp ikr} \exp\left(-\frac{m}{2\hbar\tau_e k}\right)}{\pm k + i\frac{m}{2\hbar\tau_e k}}, \end{aligned}$$

which gives

$$\langle G_0^{R,A}(r, \varepsilon) \rangle = \pm \frac{m}{\hbar^2 k} e^{\mp ikr} \left(\frac{\exp\left(-\frac{m}{2\hbar\tau_e k} r\right)}{1 \mp i \frac{m}{2\hbar\tau_e k^2}} \right)$$

where we have used $\varepsilon = \hbar^2 k^2 / 2m$. A similar but more lengthy calculation in three dimensions gives

$$\langle G_0^{R,A}(\mathbf{r}, \varepsilon) \rangle = -\frac{m}{2\pi} \frac{e^{\mp ikr}}{r} \exp\left(-\frac{m}{2\hbar\tau_e k} r\right).$$

At the Fermi level, k becomes k_F and $\hbar k_F / m$ is the Fermi velocity v_F . Using the relation $l_e = v_F \tau_e$, we can write the disorder averaged Green function as

$$\langle G_0^{R,A}(\mathbf{r}, \varepsilon) \rangle = -\frac{m}{2\pi} \frac{e^{\mp ikr}}{r} \exp\left(-\frac{r}{2l_e}\right). \quad (\text{B.16})$$

The one-dimensional function $\langle G_0^{R,A}(r, \varepsilon) \rangle$ similarly has the factor of $\exp(-r/2l_e)$.

We can use the form of $\langle G^{R,A}(\mathbf{k}, \varepsilon) \rangle$ given in Eq. B.3 to find the disorder average of the density of states as

$$\begin{aligned} \langle \nu(\varepsilon) \rangle &= \mp \frac{1}{\pi \hbar} \langle \text{Im} \left(\text{Tr} \left(\hat{G}^{R,A}(\varepsilon) \right) \right) \rangle \\ &= \mp \frac{1}{\pi \hbar} \sum_{\mathbf{k}'} \text{Im} \left(\frac{\hbar}{\varepsilon - \varepsilon(\mathbf{k}') \pm i\hbar/2\tau_e} \right) \\ &= \frac{1}{\pi \hbar} \sum_{\mathbf{k}'} \left(\frac{\hbar(\hbar/2\tau_e)}{(\varepsilon - \varepsilon(\mathbf{k}'))^2 + (\hbar/2\tau_e)^2} \right) \\ &= \frac{1}{\pi \hbar} \sum_{\mathbf{k}'} \int d\eta \delta(\eta - \varepsilon(\mathbf{k}')) \left(\frac{\hbar(\hbar/2\tau_e)}{(\varepsilon - \eta)^2 + (\hbar/2\tau_e)^2} \right) \\ &= \frac{1}{\pi} \int d\eta \left(\frac{\hbar(\hbar/2\tau_e)}{(\varepsilon - \eta)^2 + (\hbar/2\tau_e)^2} \right) \nu_0(\eta) \end{aligned} \quad (\text{B.17})$$

where we have used the expressions for ν given in Eqs. B.2 and B.3.

B.2 The diffuson and cooperon

Having introduced the Green function and derived its form after averaging over disorder, we now shift focus to the diffuson and cooperon. The Green function allows the calculation of the wave function amplitude for any set of parameters (position, momentum, time, energy, etc.) given the

wave function amplitude for some initial set of parameters. The diffusion and cooperon represent contributions to the *probability* of measuring a particle with a given set of parameters given some initial set of values for those parameters. Space does not allow for a full derivation of these quantities (see Chapters 4 and 5 of Ref. 36 for an introduction; this section is based on that text), but we will try to give enough description of these quantities to give some physical intuition for the calculation of the persistent current in the diffusive regime given in Section 2.3.

For a Gaussian wavepacket $\psi(\mathbf{r}, \varepsilon)$ of energy ε with energy width σ_ε centered at position \mathbf{r} at time $t = 0$, which can be specified by

$$\psi(\mathbf{r}', t; \mathbf{r}, \varepsilon) = \sum_n \chi_n^*(\mathbf{r}) \chi_n(\mathbf{r}) \exp\left(-i\frac{\varepsilon_n t}{\hbar}\right) \exp\left(-\frac{(\varepsilon_n - \varepsilon)^2}{4\sigma_\varepsilon^2}\right)$$

where the χ_n and ε_n are eigenstates and eigenenergies of the exact Hamiltonian \hat{H} , it can be shown that

$$P(\mathbf{r}, \mathbf{r}', \omega) = \frac{V_d}{2\pi\nu_0(\varepsilon)} \langle G^R(\mathbf{r}, \mathbf{r}', \varepsilon) G^A(\mathbf{r}', \mathbf{r}, \varepsilon - \hbar\omega) \rangle \quad (\text{B.18})$$

where

$$P(\mathbf{r}, \mathbf{r}', \omega) = \int dt P(\mathbf{r}, \mathbf{r}', t) e^{-i\omega t}$$

is the Fourier transform of

$$P(\mathbf{r}, \mathbf{r}', t) = \langle |\psi(\mathbf{r}', t; \mathbf{r}, \varepsilon)|^2 \rangle,$$

the disorder-averaged probability of measuring the particle at position \mathbf{r}' at time $t > 0$ [36].

The disorder average of the product $G^R G^A$ in Eq. B.18 is in principle a difficult quantity to calculate. It can be shown that for three dimensions, when the product $\langle G^R G^A \rangle$ in Eq. B.18 is replaced by $\langle G^R \rangle \langle G^A \rangle$, that the Fourier transform of the resulting quantity $P_0(\mathbf{r}, \mathbf{r}', \omega)$ is

$$\begin{aligned} P_0(\mathbf{r}, \mathbf{r}', t) &= \frac{V_d}{2\pi\nu_0(\varepsilon)} \langle G^R(\mathbf{r}, \mathbf{r}', \varepsilon) \rangle \langle G^A(\mathbf{r}', \mathbf{r}, \varepsilon - \hbar\omega) \rangle \\ &= \frac{\delta(|\mathbf{r}' - \mathbf{r}| - v(\varepsilon)t)}{4\pi|\mathbf{r} - \mathbf{r}'|^2} \exp\left(-\frac{t}{\tau_e}\right) \end{aligned} \quad (\text{B.19})$$

which describes a spherical plane wave originating at point \mathbf{r} and traveling at speed $v(\varepsilon)$ while decaying on the timescale τ_e . From this result it is seen that replacing $\langle G^R G^A \rangle$ by $\langle G^R \rangle \langle G^A \rangle$ amounts to discarding all contributions to $P(\mathbf{r}, \mathbf{r}', t)$ in which the particle scatters off the disorder potential. The timescale τ_e was introduced in the previous section as the typical timescale on

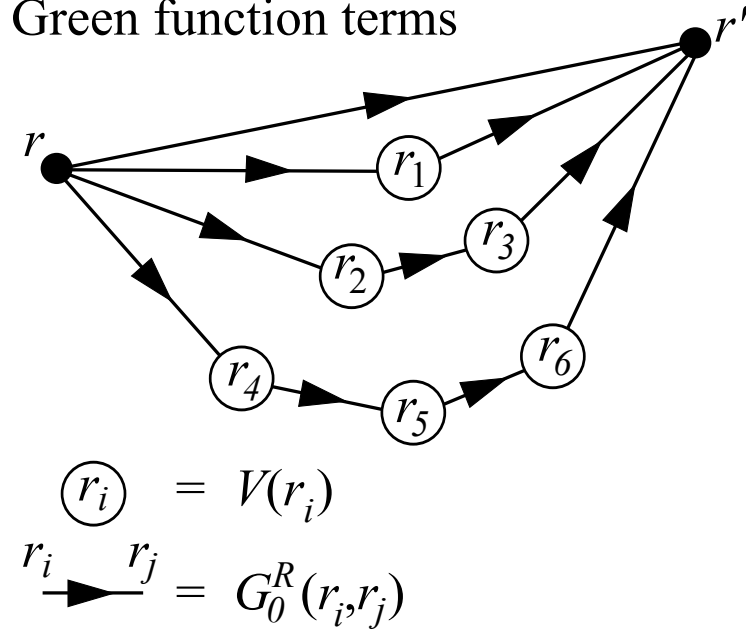


Figure B.1: Contributions to the Green function in the presence of disorder. The different paths represent integrands of first four terms of Eq. B.11. The total Green function $G^R(\mathbf{r}, \mathbf{r}')$ is found by summing the integral of each path over each r_i .

which a state \mathbf{k} scatters off the disorder potential into a state \mathbf{k}' with $|\mathbf{k}'| = |\mathbf{k}|$. The diffuson and cooperon represent the contributions to $P(\mathbf{r}, \mathbf{r}', t)$ which involve scattering off the disorder potential and survive the disorder averaging.

To see what other terms still contribute after disorder averaging, we consider the form of $G^{R,A}$ in the presence of a disorder potential V as given by the Dyson equation (Eq. B.11). Each term in the Dyson equation represents a series of free propagations broken up by scatterings off of the potential $V(\mathbf{r})$, as illustrated in Fig. B.1 for $G^R(\mathbf{r}, \mathbf{r}')$. The product $G^R G^A$ is the sum of terms composed of one set of scatterings for G^R (i.e. one path between \mathbf{r} and \mathbf{r}' in Fig. B.1) and one set of scatterings for G^A . For the white noise potential which we have been considering, the potential V has no spatial correlation ($\langle V(\mathbf{r}_i)V(\mathbf{r}_j) \rangle = \delta(\mathbf{r}_i - \mathbf{r}_j)$). Thus, for $\langle G^R G^A \rangle$ only the cross terms of $G^R G^A$ which contain the same set of $V(\mathbf{r}_i)$ will survive the average over disorder.

Next we consider the complex phases of the different terms contributing to $G^{R,A}$. From Eq. B.16, we see that the phase associated with $G_0^{R,A}(\mathbf{r}_i, \mathbf{r}_j, \varepsilon)$ is $\mp k(\varepsilon)|\mathbf{r}_j - \mathbf{r}_i|$. Since $V(r)$ is taken to be real, the phases of the $G_0^{R,A}(\mathbf{r}_i, \mathbf{r}_j, \varepsilon)$ add up to give the total phase $\mp k(\varepsilon)L_m$ where L_m is the length of the m th path between r and r' . For paths m and m' meeting the constraint stipulated above of scattering off the potential V at the same set of points $\{\mathbf{r}_i\}$, with path m corresponding

Diffuson terms

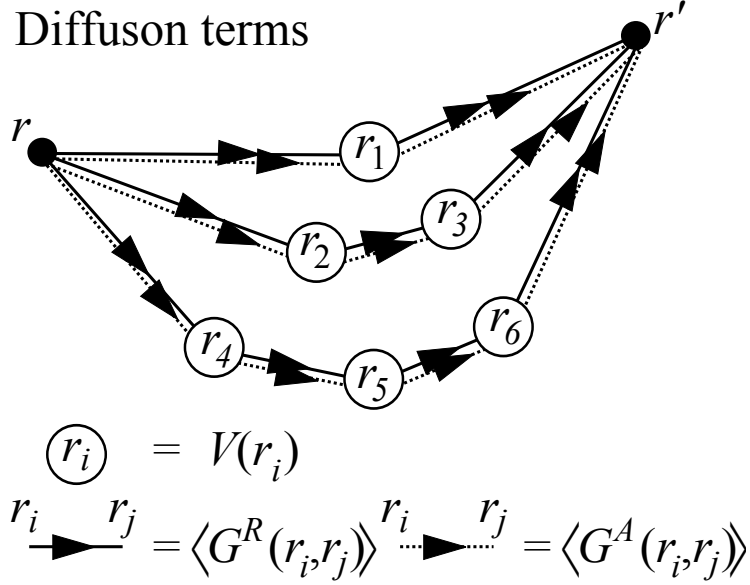


Figure B.2: Contributions to the diffuson. One term of the contributions to the diffuson of each order in V up to the third is shown in the figure. The diffuson represents all terms in $\langle G^R G^A \rangle$ for which both the term from G^R and the term from G^A follow the exact same path. The accumulated phases are thus equal in magnitude and opposite in sign, giving no net phase. In the actual calculation, the $G_0^{R,A}$'s of Fig. B.1 are replaced by $\langle G^{R,A} \rangle$. To find the diffuson, each of these terms must be integrated over all of the r_i .

to one term in G^R and path m' to one in G^A , the corresponding contribution to the phase of $G^R G^A$ will generally be $\gg 1$ unless the paths m and m' follow the $\{r_i\}$ in the exact same sequence because the average distance between scatterers is l_e and $k_F l_e \gg 1$ in the weak disorder limit. The terms where m and m' are identical do survive the disorder average. The sum of all such terms is collectively known as the diffuson contribution to $\langle G^R G^A \rangle$. Some of the terms contributing to the diffuson are shown in Fig. B.2.

The phase associated with $G^{R,A}$ does not depend on the direction of propagation. Thus, the phase $k(L_m - L_{m'})$ will also be zero when m' represents the path through the same set of scattering sites $\{r_i\}$ but in reverse order. As long as r is close to r' , the terms corresponding to pairs of reversed scattering paths will also survive averaging over disorder. The sum of all such terms is known as the cooperon contribution to $\langle G^R G^A \rangle$. One term contributing to the cooperon is shown in Fig. B.2.

The diffuson contribution to $\langle G^R G^A \rangle$ when multiplied by $V_d/2\pi\nu_0(\varepsilon)$ leads to a contribution $P_d(\mathbf{r}, \mathbf{r}', \omega)$ to $P(\mathbf{r}, \mathbf{r}', \omega)$. By summing the terms shown in Fig. B.2 and taking the disorder average,

Cooperon term

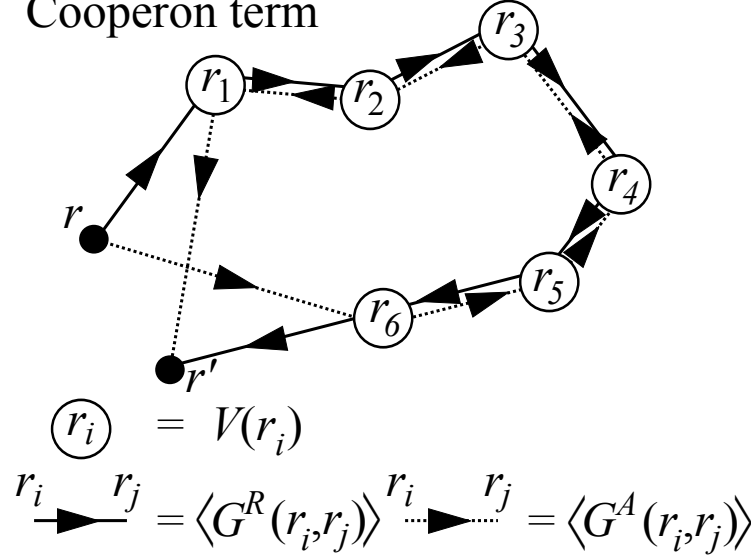


Figure B.3: Contribution to the cooperon. One sixth order contribution to the cooperon is shown. The path associated with the $\langle G^R \rangle$'s through the scattering sites is reversed from the path followed by the $\langle G^A \rangle$'s. Just as with the diffuson terms in Fig. B.2, the net phase of each term due to traveling through the sequence $\{r_i\}$ is zero. However, here the connections to \mathbf{r} and \mathbf{r}' are not identical. The cooperon contributes significantly only when \mathbf{r} and \mathbf{r}' are close. In the calculation of the persistent current, only closed paths around the ring for which $\mathbf{r}' = \mathbf{r}$ are important so the cooperon is on equal footing with the diffuson.

this contribution can be written in the form

$$\begin{aligned}
 P_d(\mathbf{r}, \mathbf{r}', \omega) = & \frac{V_d}{2\pi\nu_0(\varepsilon)} \left(B \int d\mathbf{r}_1 \langle G^R(\mathbf{r}, \mathbf{r}_1) \rangle \langle G^A(\mathbf{r}_1, \mathbf{r}) \rangle \langle G^R(\mathbf{r}_1, \mathbf{r}') \rangle \langle G^A(\mathbf{r}', \mathbf{r}_1) \rangle \right. \\
 & + B^2 \int d\mathbf{r}_1 d\mathbf{r}_2 \langle G^R(\mathbf{r}, \mathbf{r}_1) \rangle \langle G^A(\mathbf{r}_1, \mathbf{r}) \rangle \langle G^R(\mathbf{r}_1, \mathbf{r}_2) \rangle \langle G^A(\mathbf{r}_2, \mathbf{r}_1) \rangle \times \dots \\
 & \dots \times \langle G^R(\mathbf{r}_2, \mathbf{r}') \rangle \langle G^A(\mathbf{r}', \mathbf{r}_2) \rangle + \dots \\
 & \left. + \dots \right), \tag{B.20}
 \end{aligned}$$

where all of the $\langle G^R \rangle$'s are at energy ε and the $\langle G^A \rangle$'s are at energy $\varepsilon + \hbar\omega$. The diffuson contribution P_d also admits the simpler iterative expression

$$P_d(\mathbf{r}, \mathbf{r}', \omega) = \frac{2\pi\nu(\varepsilon)}{V_d} \int d\mathbf{r}_1 d\mathbf{r}_2 P_0(\mathbf{r}, \mathbf{r}_1, \omega) \Gamma_d(\mathbf{r}_1, \mathbf{r}_2) P_0(\mathbf{r}_2, \mathbf{r}', \omega) \tag{B.21}$$

with

$$\Gamma_d(\mathbf{r}_1, \mathbf{r}_2) = B\delta(\mathbf{r}_1 - \mathbf{r}_2) + B \int d\mathbf{r}_3 \Gamma_d(\mathbf{r}_1, \mathbf{r}_3) \left(\frac{2\pi\nu_0(\varepsilon)}{V_d} P_0(\mathbf{r}_3, \mathbf{r}_2) \right) \tag{B.22}$$

where each term is also a function of ω . In the diffusive regime $\Gamma(\mathbf{r}_1, \mathbf{r}_3)$ changes slowly on the scale of l_e and that by Eq. B.19 P_0 decays exponentially on this scale, $\Gamma_d(\mathbf{r}_1, \mathbf{r}_3)$ can be expanded about \mathbf{r}_2 in a Taylor series, changing Eq. B.22 to a differential form. Using the same assumptions, $\Gamma_d(\mathbf{r}, \mathbf{r}')$ can be taken outside of the integral in Eq. B.21 and can be seen to be proportional to $P_d(\mathbf{r}, \mathbf{r}', \omega)$, which thus also admits this differential form (see Ref. [36] for the details of this calculation). The resulting differential *diffusion* equation for P_d is

$$(-i\omega - D\nabla'^2) P_d(\mathbf{r}, \mathbf{r}', \omega) = \delta(\mathbf{r} - \mathbf{r}') \quad (\text{B.23})$$

where $D = v_F l_e / d$ is the diffusion constant and ∇'^2 operates on \mathbf{r}' . In the limit of $\mathbf{r}' \rightarrow \mathbf{r}$ relevant to the calculation of persistent currents, the analogous cooperon contribution $P_c(\mathbf{r}, \mathbf{r}', \omega)$ is identical to $P_d(\mathbf{r}, \mathbf{r}', \omega)$.

B.2.1 Density of states correlation function

In the calculation of the typical magnitude of the fluctuations of the persistent current over different disorder configurations, the quantity of interest is $\langle \nu(\varepsilon) \nu(\varepsilon - \hbar\omega) \rangle$. By Eqs. B.4, B.8, and B.9, this quantity can be written as

$$\begin{aligned} \langle \nu(\varepsilon) \nu(\varepsilon - \hbar\omega) \rangle &= \\ &= \left(\frac{1}{2\pi\hbar} \right)^2 \int d\mathbf{r} d\mathbf{r}' \langle (G^R(\mathbf{r}, \mathbf{r}, \varepsilon) - G^A(\mathbf{r}, \mathbf{r}, \varepsilon)) (G^R(\mathbf{r}', \mathbf{r}', \varepsilon - \hbar\omega) - G^A(\mathbf{r}', \mathbf{r}', \varepsilon - \hbar\omega)) \rangle. \end{aligned} \quad (\text{B.24})$$

The procedure of identifying terms which survive averaging over disorder follows the same principles as given above for $P_d(\mathbf{r}, \mathbf{r}', \omega)$. Restricting our focus to paths following the same (or reversed) sequence of scatterers, the terms $G^R G^R$ and $G^A G^A$ become negligible since each factor picks up a phase kL_m giving a total phase of $2kL_m \gg 1$ which is essentially random. The other terms $G^R G^A$ contain contributions such as those shown in Fig. B.4 which survive disorder averaging. Summing up all such terms results in

$$\begin{aligned} \langle \nu(\varepsilon) \nu(\varepsilon - \hbar\omega) \rangle_{d,c} &= \\ &= \left(\frac{1}{2\pi\hbar} \right)^2 \sum_{\pm} \int d\mathbf{r} d\mathbf{r}' (P_d(\mathbf{r}, \mathbf{r}', \pm\omega) P_d(\mathbf{r}', \mathbf{r}, \pm\omega) + P_c(\mathbf{r}, \mathbf{r}', \pm\omega) P_c(\mathbf{r}', \mathbf{r}, \pm\omega)). \end{aligned} \quad (\text{B.25})$$

The correlation in energy of the density of states contains contributions from all possible closed paths traversed by both diffusons and cooperons. Although it is not especially illuminating, the diffuson/cooperon contribution $\langle \nu(\varepsilon)\nu(\varepsilon - \hbar\omega) \rangle_{d,c}$ to the energy correlation function of the density of states can also be viewed as the Fourier transform of the convolution $\int dt P_{d,c}(\mathbf{r}, \mathbf{r}', t) P_{d,c}(\mathbf{r}', \mathbf{r}, \tau - t)$ in time of the two halves of a closed path traversed by a diffuson or cooperon. The connection of this component of the density of states correlation function to the probability of completing a closed path hints at its connection to the persistent current calculation as it is closed paths around the ring which result in a current.

Denoting by $\phi_n(\mathbf{r})$ the eigenfunctions of $-D\nabla^2$ for the system under consideration with eigenvalues $E_n^{d,c}$,⁶ we can write down the eigenfunction expansion,

$$P_{d,c}(\mathbf{r}, \mathbf{r}', \omega) = \sum_n a_n(\mathbf{r}) \phi_n(\mathbf{r}').$$

Substituting this form into Eq. B.23 along with the representation $\delta(\mathbf{r} - \mathbf{r}') = \sum_n \phi_n^*(\mathbf{r}) \phi_n(\mathbf{r}')$, we have

$$\sum_n (-i\omega - DE_n^{d,c}) a_n(\mathbf{r}) \phi_n(\mathbf{r}') = \sum_n \phi_n^*(\mathbf{r}) \phi_n(\mathbf{r}')$$

from which we conclude

$$P_{d,c}(\mathbf{r}, \mathbf{r}', \omega) = \sum_n \frac{\phi_n^*(\mathbf{r}) \phi_n(\mathbf{r}')}{i\omega + DE_n^{d,c}}. \quad (\text{B.26})$$

This result allows us to write

$$\begin{aligned} \int d\mathbf{r} d\mathbf{r}' P_d(\mathbf{r}, \mathbf{r}', \omega) P_d(\mathbf{r}', \mathbf{r}, \omega) &= \sum_{n,n'} \int d\mathbf{r} d\mathbf{r}' \left(\frac{\phi_n^*(\mathbf{r}) \phi_n(\mathbf{r}')}{i\omega + DE_n^{d,c}} \right) \left(\frac{\phi_{n'}^*(\mathbf{r}') \phi_{n'}(\mathbf{r})}{i\omega + DE_{n'}^{d,c}} \right) \\ &= \sum_{n,n'} \int d\mathbf{r} \delta_{nn'} \left(\frac{\phi_n^*(\mathbf{r})}{i\omega + DE_n^{d,c}} \right) \left(\frac{\phi_{n'}(\mathbf{r})}{i\omega + DE_{n'}^{d,c}} \right) \\ &= \sum_n \left(\frac{1}{i\omega + DE_n^{d,c}} \right)^2 \end{aligned}$$

where we have used the orthonormality condition $\int d\mathbf{r}' \phi_n^*(\mathbf{r}') \phi_{n'}(\mathbf{r}') = \delta_{nn'}$. With this result, we

⁶Currently $E_n^{d,c}$ is the same for both the diffuson and cooperon. They are different in the presence of a magnetic field as discussed below.

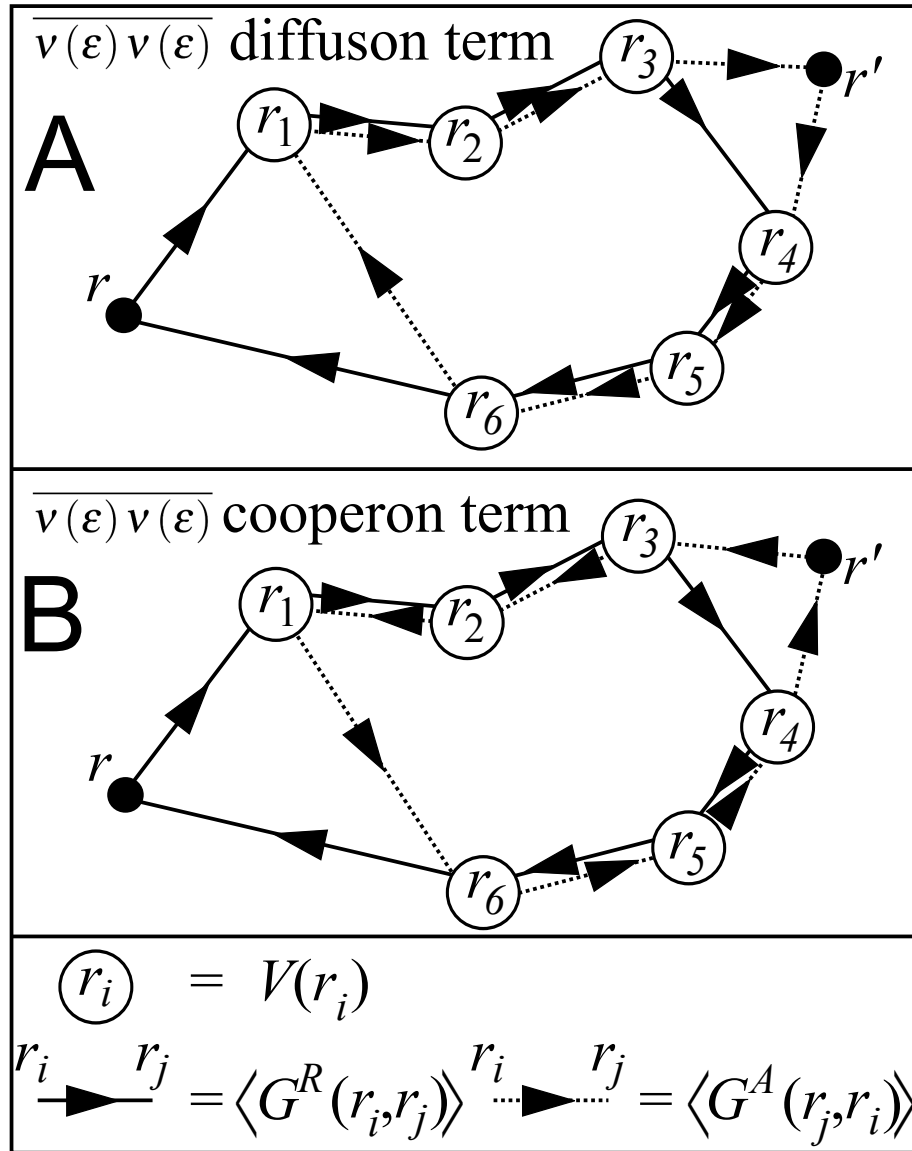


Figure B.4: Long-range contributions of the diffuson and cooperon to the density of states correlation function. In panel A, the paths from r_1 to r_3 and from r_4 to r_6 involve diffuson-like propagation, while in panel B these paths involve cooperon-like propagation. Because of the short range nature of $\langle G^R(\mathbf{r}, \mathbf{r}_i) \rangle$, there must be scatterers close to points \mathbf{r} and \mathbf{r}' (e.g. in the drawings \mathbf{r} must be close to \mathbf{r}_1 and \mathbf{r}_6 while \mathbf{r}' must be close to \mathbf{r}_3 and \mathbf{r}_4). In this case, summing all the terms like those shown panels A and B results in contributions $P_d(\mathbf{r}, \mathbf{r}', \omega)P_d(\mathbf{r}', \mathbf{r}, \omega)$ and $P_c(\mathbf{r}, \mathbf{r}', \omega)P_c(\mathbf{r}', \mathbf{r}, \omega)$ respectively.

can rewrite the diffuson and cooperon contributions to the density of states correlation function as

$$\begin{aligned}\langle \nu(\varepsilon) \nu(\varepsilon - \hbar\omega) \rangle_{d,c} &= \left(\frac{1}{2\pi\hbar} \right)^2 \sum_{\pm} \sum_n \left(\left(\frac{1}{\pm i\omega + DE_n^d} \right)^2 + \left(\frac{1}{\pm i\omega + DE_n^c} \right)^2 \right) \\ &= 2 \left(\frac{1}{2\pi\hbar} \right)^2 \sum_n \operatorname{Re} \left(\left(\frac{1}{i\omega + DE_n^d} \right)^2 + \left(\frac{1}{i\omega + DE_n^c} \right)^2 \right).\end{aligned}\quad (\text{B.27})$$

It is also possible to create terms from the $G^R G^A$ product that survive averaging over disorder for which \mathbf{r} and \mathbf{r}' are on the same side of the path through the scatterers such as those shown in Fig. B.4. These terms consist of a single diffuson or a single cooperon. They follow the form (see Ref. 36)

$$\langle \nu(\varepsilon) \nu(\varepsilon - \hbar\omega) \rangle_{d,c} = \frac{\nu_0 L^d}{\pi} \operatorname{Re} \int d\mathbf{r} d\mathbf{r}' (g(\mathbf{r} - \mathbf{r}', \varepsilon) P_d(\mathbf{r}', \mathbf{r}, \omega) + g(\mathbf{r} - \mathbf{r}', \varepsilon) P_c(\mathbf{r}, \mathbf{r}', \omega))$$

where L^d is the system volume and

$$g(\mathbf{r}) = \frac{\sin(k(\varepsilon)r)}{k(\varepsilon)r} \exp\left(-\frac{r}{2l_e}\right).$$

Upon averaging over disorder, the free propagation between \mathbf{r} and \mathbf{r}' and the scattering sites decays exponentially on the length scale l_e resulting in the $g(\mathbf{r})$ factors in the expression. Due to the short range nature of $g(\mathbf{r})$, these terms are not significant upon spatial integration and we neglect them in the discussion below. They can be significant though when calculating the local density of states correlation function, giving a contribution

$$\begin{aligned}\langle \nu(\mathbf{r}, \mathbf{r}, \varepsilon) \nu(\mathbf{r}', \mathbf{r}', \varepsilon - \hbar\omega) \rangle_{\text{SR}} \\ = \frac{\nu_0 L^d}{\pi} \operatorname{Re} (g(\mathbf{r} - \mathbf{r}', \varepsilon) P_d(\mathbf{r}', \mathbf{r}, \omega) + g(\mathbf{r} - \mathbf{r}', \varepsilon) P_c(\mathbf{r}, \mathbf{r}', \omega)).\end{aligned}\quad (\text{B.28})$$

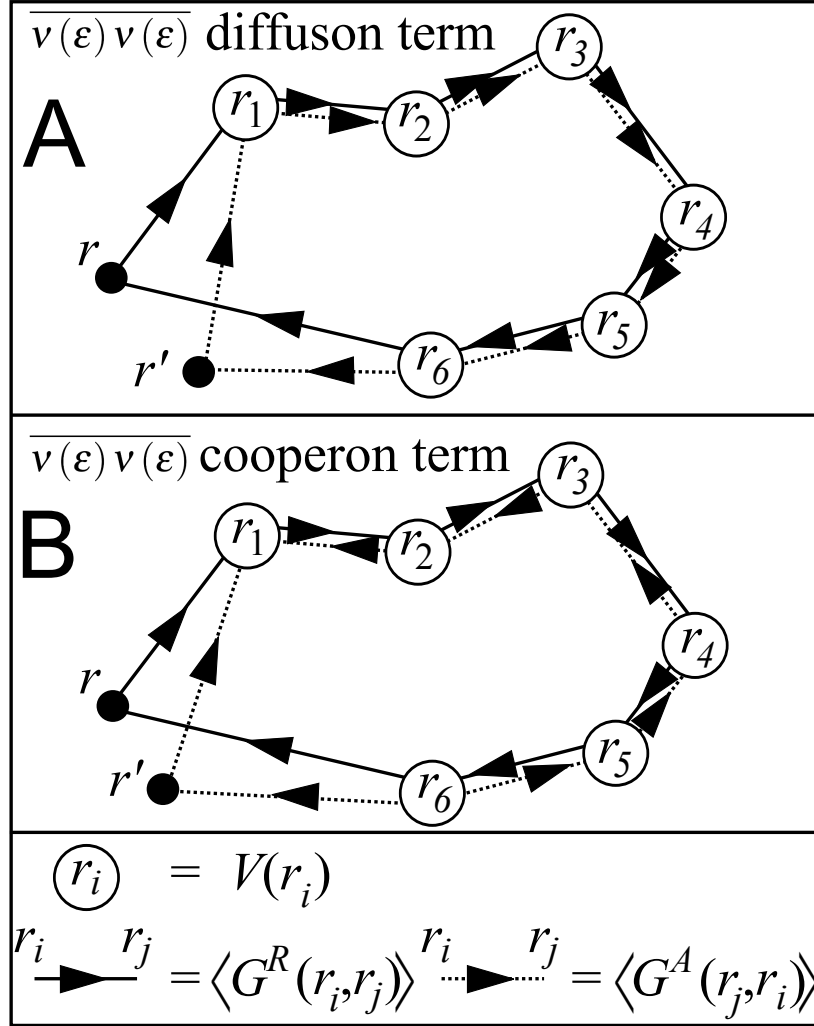


Figure B.5: Short-range contributions of the diffuson and cooperon to the density of states correlation function. In panel A, r_1 and r_6 are connected by diffuson-like propagation, while in panel B the connection is cooperon-like. In contrast to Fig. B.4, \mathbf{r} and \mathbf{r}' must be close to each other due to the short range nature of $\langle G^R(\mathbf{r}, \mathbf{r}_i) \rangle$. Summing all of the terms like those shown in the figure leads to contributions of the form $g(\mathbf{r} - \mathbf{r}')P_d(\mathbf{r}, \mathbf{r}', \omega)$ and $g(\mathbf{r} - \mathbf{r}')P_c(\mathbf{r}, \mathbf{r}', \omega)$ where $g(\mathbf{r} - \mathbf{r}')$ decays exponentially with $|\mathbf{r} - \mathbf{r}'|/l_e$.

B.2.2 Magnetic field effects

Now we address the question of how a finite magnetic field affects the results of this appendix, in particular Eq. B.27. In Section 2.1.1, we discuss the gauge transformation for a vector potential \mathbf{A} that takes

$$\psi(\mathbf{r}) \rightarrow \psi'(\mathbf{r}) = \psi(\mathbf{r}) \exp\left(i\frac{e}{\hbar} \int_{\mathbf{r}_0}^{\mathbf{r}} d\mathbf{r}_1 \cdot \mathbf{A}(\mathbf{r}_1)\right).$$

With this transformation, $\psi'(\mathbf{r})$ represents the same state as $\psi(\mathbf{r})$ but with $\mathbf{A} = 0$ in the Hamiltonian. In that section, we argued that this result held for regions where $\mathbf{B} = \nabla \times \mathbf{A} = 0$. However, the result can be extended to regimes where \mathbf{A} varies slowly in space [36, 44]. Using Eq. B.6 and indicating gauge transformed Green functions and eigenfunctions by G' and ϕ' , we can relate the transformed Green function to the untransformed one as

$$\begin{aligned} G'^{R,A}(\mathbf{r}, \mathbf{r}', \varepsilon) &= \sum_n \frac{\phi_n'^*(\mathbf{r}') \phi_n'(\mathbf{r})}{\varepsilon - \varepsilon_n \pm i\gamma} \\ &= \sum_n \frac{\left(\exp\left(-i\frac{e}{\hbar} \int_{\mathbf{r}_0}^{\mathbf{r}'} d\mathbf{r}_1 \cdot \mathbf{A}(\mathbf{r}_1)\right) \phi_n^*(\mathbf{r}')\right) \left(\exp\left(i\frac{e}{\hbar} \int_{\mathbf{r}_0}^{\mathbf{r}} d\mathbf{r}_1 \cdot \mathbf{A}(\mathbf{r}_1)\right) \phi_n(\mathbf{r})\right)}{\varepsilon - \varepsilon_n \pm i\gamma} \\ &= \exp\left(i\frac{e}{\hbar} \int_{\mathbf{r}'}^{\mathbf{r}} d\mathbf{r}_1 \cdot \mathbf{A}(\mathbf{r}_1)\right) \sum_n \frac{\phi_n^*(\mathbf{r}') \phi_n(\mathbf{r})}{\varepsilon - \varepsilon_n \pm i\gamma} \\ &= \exp\left(i\frac{e}{\hbar} \int_{\mathbf{r}'}^{\mathbf{r}} d\mathbf{r}_1 \cdot \mathbf{A}(\mathbf{r}_1)\right) G^{R,A}(\mathbf{r}, \mathbf{r}', \varepsilon). \end{aligned}$$

Thus, the magnetic field can be incorporated by giving the Green function $G^{R,A}(\mathbf{r}, \mathbf{r}', \varepsilon)$ a phase shift of $i\frac{e}{\hbar} \int_{\mathbf{r}'}^{\mathbf{r}} d\mathbf{r}_1 \cdot \mathbf{A}(\mathbf{r}_1)$. The diffuson $P_d(\mathbf{r}, \mathbf{r}', \varepsilon)$ involves products $\langle G^R(\mathbf{r}_i, \mathbf{r}_j) \rangle \langle G^A(\mathbf{r}_j, \mathbf{r}_i) \rangle$ of Green functions with the $\{\mathbf{r}_i\}$ following a path from \mathbf{r} to \mathbf{r}' . In the persistent current calculation, we are concerned with the quantity $\langle \nu(\varepsilon, B) \nu(\varepsilon - \hbar\omega, B') \rangle$, which by Eq. B.24 can be seen to involve $\langle G^R \rangle$ terms corresponding to B and $\langle G^A \rangle$ terms corresponding to B' . Using \mathbf{A} and \mathbf{A}' as the corresponding vector potentials for B and B' , we see that

$$\begin{aligned} &\langle G'^{R,A}(\mathbf{r}, \mathbf{r}', B) \rangle \langle G'^{R,A}(\mathbf{r}', \mathbf{r}, B') \rangle \\ &= \exp\left(i\frac{e}{\hbar} \int_{\mathbf{r}'}^{\mathbf{r}} d\mathbf{r}_1 \cdot \mathbf{A}(\mathbf{r}_1)\right) \exp\left(i\frac{e}{\hbar} \int_{\mathbf{r}}^{\mathbf{r}'} d\mathbf{r}_1 \cdot \mathbf{A}'(\mathbf{r}_1)\right) \langle G^{R,A}(\mathbf{r}, \mathbf{r}', 0) \rangle \langle G^{R,A}(\mathbf{r}', \mathbf{r}, 0) \rangle \\ &= \exp\left(i\frac{e}{\hbar} \int_{\mathbf{r}'}^{\mathbf{r}} d\mathbf{r}_1 \cdot (\mathbf{A}(\mathbf{r}_1) - \mathbf{A}'(\mathbf{r}_1))\right) \langle G^{R,A}(\mathbf{r}, \mathbf{r}', 0) \rangle \langle G^{R,A}(\mathbf{r}', \mathbf{r}, 0) \rangle \end{aligned}$$

Thus, for vector potentials \mathbf{A} and \mathbf{A}' , the diffuson $P_d(\mathbf{r}, \mathbf{r}', \varepsilon)$ picks up the extra phase $i\frac{e}{\hbar} \int_{\mathbf{r}'}^{\mathbf{r}} d\mathbf{r}_1 \cdot (\mathbf{A}(\mathbf{r}_1) - \mathbf{A}'(\mathbf{r}_1))$. Similarly the cooperon involves terms of the form $\langle G^R(\mathbf{r}_i, \mathbf{r}_j) \rangle \langle G^A(\mathbf{r}_i, \mathbf{r}_j) \rangle$ and picks up a phase $i\frac{e}{\hbar} \int_{\mathbf{r}'}^{\mathbf{r}} d\mathbf{r}_1 \cdot (\mathbf{A}(\mathbf{r}_1) + \mathbf{A}'(\mathbf{r}_1))$. We use the notation

$$\mathbf{A}_{\pm} = \mathbf{A} \pm \mathbf{A}'.$$

When the Taylor expansion derivation leading to Eq. B.23 is performed in the presence of a magnetic field, the relation

$$\nabla P_{d,c}(\mathbf{r}, \mathbf{r}', \varepsilon, \mathbf{A}_{\mp}) = \exp\left(i\frac{e}{\hbar} \int_{\mathbf{r}'}^{\mathbf{r}} d\mathbf{r}_1 \cdot \mathbf{A}_{\mp}\right) \left(\nabla + i\frac{e}{\hbar} \mathbf{A}_{\mp}\right) P_{d,c}(\mathbf{r}, \mathbf{r}', \varepsilon, 0)$$

results in the new diffusion equation

$$\left(-i\omega - D \left(\nabla' + i\frac{e}{\hbar} \mathbf{A}_{\mp}\right)^2\right) P_{d,c}(\mathbf{r}, \mathbf{r}', \omega) = \delta(\mathbf{r} - \mathbf{r}'). \quad (\text{B.29})$$

With this result, we can write the field dependent form of the density of states correlation function as

$$\langle \nu(\varepsilon, B) \nu(\varepsilon - \hbar\omega, B') \rangle_{d,c} = 2 \left(\frac{1}{2\pi\hbar}\right)^2 \sum_{\mp} \sum_n \text{Re} \left(\left(\frac{1}{i\omega + DE_n(B_{\mp})} \right)^2 \right) \quad (\text{B.30})$$

where the $E_n^{d,c}(B_{\mp})$ are the eigenvalues in the expression

$$\left(\nabla' + i\frac{e}{\hbar} \mathbf{A}_{\mp}\right)^2 P_{d,c}(\mathbf{r}, \mathbf{r}', \omega) = E_n^{d,c}(B_{\mp}) P_{d,c}(\mathbf{r}, \mathbf{r}', \omega). \quad (\text{B.31})$$

The boundary conditions for $P_{d,c}$ are that

$$\tilde{\mathbf{n}} \cdot \left(\nabla' + i\frac{e}{\hbar} \mathbf{A}_{\mp}\right) P_{d,c}(\mathbf{r}, \mathbf{r}', \omega) = 0 \quad (\text{B.32})$$

for reflecting boundaries with $\tilde{\mathbf{n}}$ the vector normal to the surface of the boundary [36, 42].

B.2.3 Spin effects

We now address effects related to the electron spin. In the absence of any effect to break the degeneracy of the two spin states \uparrow and \downarrow , the spatial characterization of the two spin states is

identical and we can write

$$\nu(\varepsilon) = \nu(\varepsilon, \uparrow) + \nu(\varepsilon, \downarrow)$$

where both $\nu(\varepsilon, \uparrow)$ and $\nu(\varepsilon, \downarrow)$ are just the density of states $\nu(\varepsilon)$ considered in the preceding portion of this appendix. Now we consider applying a magnetic field \mathbf{B} . In a magnetic field, the electron Hamiltonian picks up a term

$$\hat{H}_Z = \frac{g\mu_B}{2} \boldsymbol{\sigma} \cdot \mathbf{B}, \quad (\text{B.33})$$

and with its spin aligned (anti-aligned) with the field the electron has a Zeeman energy

$$E_Z = (-) \frac{g\mu_B}{2} B \quad (\text{B.34})$$

where $\boldsymbol{\sigma}$ is the vector of Pauli matrices, $g \approx 2$ is the gyromagnetic ratio of the electron in the medium under consideration and μ_B is the Bohr magneton.

We now consider the correlation function of the density of states. Reserving the ε argument of $\nu(\varepsilon)$ for the energy ε_s associated with the electron's spatial degrees of freedom but allowing $\varepsilon = \varepsilon_s + E_Z$ to denote the total energy and taking \uparrow to be the spin direction aligned with the magnetic field, we can write

$$\nu(\varepsilon_s, B, \uparrow) = \nu(\varepsilon - E_Z, B, \uparrow)$$

and

$$\nu(\varepsilon_s, B, \downarrow) = \nu(\varepsilon + E_Z, B, \downarrow)$$

where the expressions on the right-hand side correspond to the same density of states expression discussed in previous sections where spin degeneracy was assumed (the $\uparrow\downarrow$ label has only been added for clarity). Using the fact that under the limits considered the density of states correlation function $\langle \nu(\varepsilon)\nu(\varepsilon - \hbar\omega) \rangle$ depends only on the energy difference $\hbar\omega$, we can write

$$\begin{aligned} \langle \nu(\varepsilon, B) \nu(\varepsilon - \hbar\omega, B') \rangle &= \left\langle (\nu(\varepsilon - E_Z, B, \uparrow) + \nu(\varepsilon + E_Z, B, \downarrow)) \times \dots \right. \\ &\quad \left. \dots (\nu(\varepsilon - \hbar\omega - E_Z, B', \uparrow) + \nu(\varepsilon - \hbar\omega + E_Z, B', \downarrow)) \right\rangle \\ &= \langle \nu(\varepsilon, B, \uparrow) \nu(\varepsilon - \hbar\omega, B', \uparrow) \rangle + \langle \nu(\varepsilon, B, \uparrow) \nu(\varepsilon - \hbar\omega + 2E_Z, B', \downarrow) \rangle + \dots \\ &\quad + \langle \nu(\varepsilon, B, \downarrow) \nu(\varepsilon - \hbar\omega - 2E_Z, B', \uparrow) \rangle + \langle \nu(\varepsilon, B, \downarrow) \nu(\varepsilon - \hbar\omega, B', \downarrow) \rangle \end{aligned}$$

where we assumed that $E'_Z \approx E_Z$ since we are usually interested in magnetic field differences small on the scale of the total field. From this result, we see that two terms, the $\uparrow\uparrow$ and $\downarrow\downarrow$ ones, match the expression found for the spin degenerate case while the other two terms, $\uparrow\downarrow$ and $\downarrow\uparrow$, are shifted in energy by $\pm 2E_Z$. The effect of the Zeeman splitting is to separate in energy the orbital energy levels for two spin orientations. When considering the correlation of the density of states, the spin up levels maintain the same level of correlation with themselves because they are all shifted by the same energy and the disorder averaged correlation function is independent of the absolute energy ε . The case is the same for the spin down levels. The correlation between the two spin states, however, changes as the correlated orbitals become shifted in energy relative each by a total amount $2E_z$. In the presence of Zeeman splitting, we can rewrite Eq. B.30 as

$$\begin{aligned} \langle \nu(\varepsilon, B) \nu(\varepsilon - \hbar\omega, B') \rangle_{d,c} = & \\ = 2 \left(\frac{1}{2\pi\hbar} \right)^2 \sum_{\mp} \sum_n \operatorname{Re} \left(2 \left(\frac{1}{i\omega + DE_n(B_{\mp})} \right)^2 + \left(\frac{1}{i\omega + 2i\frac{E_Z}{\hbar} + DE_n(B_{\mp})} \right)^2 + \right. & \\ \left. \dots + \left(\frac{1}{i\omega - 2i\frac{E_Z}{\hbar} + DE_n(B_{\mp})} \right)^2 \right) & \end{aligned} \quad (\text{B.35})$$

with the eigenvalues $E_n(B_{\mp})$ unaffected by the Zeeman splitting.

Another important spin effect⁷ is that of spin-orbit scattering.⁸ Gauge invariance of the electromagnetic field requires that a pure electric field \mathbf{E} in one inertial reference frame becomes a superposition of electric and magnetic fields in another reference frame moving at velocity \mathbf{v} relative to the first, with the magnetic field given by $\mathbf{B} = -\mathbf{v} \times \mathbf{E}/c^2$. An electron moving at velocity $\dot{\mathbf{r}}$ through a disorder potential V experiences an electric field given by $-\nabla V/e$ and thus a magnetic field $\dot{\mathbf{r}} \times \nabla V/ec^2$ in its rest frame. The spin of the electron couples to this magnetic field and thus to the disorder potential. The Zeeman energy contribution to the Hamiltonian (Eq. B.33) for this effective magnetic field takes the form

$$\hat{H}_{SO} = \frac{g\mu_B}{2ec^2} \boldsymbol{\sigma} \cdot (\dot{\mathbf{r}} \times \nabla V),$$

⁷We neglect a third important spin effect, the interaction of the electron spin with magnetic impurities, because for the conditions relevant to the measurements discussed in this text the magnetic field is strong enough to polarize the magnetic impurities and weaken their ability to interact with the electron spins.

⁸As is the case with much of this appendix, this section is adapted from Ref. 36.

which for spin states α and β has matrix elements of the form

$$\begin{aligned}\langle \mathbf{k}'\beta | \hat{H}_{SO} | \mathbf{k}\alpha \rangle &= \frac{g\mu_B}{2ec^2} \langle \beta | \boldsymbol{\sigma} | \alpha \rangle \cdot \langle \mathbf{k}' | (\hat{\mathbf{r}} \times \nabla V) | \mathbf{k} \rangle \\ &= \frac{g\mu_B}{2ec^2} \langle \beta | \boldsymbol{\sigma} | \alpha \rangle \cdot \left(\frac{\hbar \mathbf{k}'}{m} \times i\mathbf{k}V(\mathbf{k} - \mathbf{k}') \right) \\ &= \left(i \frac{g\mu_B \hbar}{2emc^2} k'kV(\mathbf{k} - \mathbf{k}') \right) \boldsymbol{\sigma}_{\beta\alpha} \cdot (\tilde{\mathbf{k}}' \times \tilde{\mathbf{k}}).\end{aligned}$$

The prefactor of this last term can be treated as new disorder potential V_{SO} which depends on the spin of the electrons in addition to the wavevectors.

The derivations of the diffuson, cooperon and density of states correlation function of the preceding sections can be repeated adding this new disorder potential to the original one which was independent of spin. The major difference in the derivation is that now components of the electron spins must be tracked. This means that, for example, in Fig. B.3 the solid and dashed lines entering the r_i must be assigned spin components α and β , and the lines exiting must be assigned spin components γ and δ , since the potential V_{SO} can mix spin components. The derivation including spin-orbit scattering is best performed in reciprocal space, rather than real space which was used in the derivation above. Rather than develop this framework to present the full derivation (see e.g. Ref. 36), we simply state the results. Eq. B.31 for the eigenvalues of the diffuson⁹ is modified to include spin, taking the form

$$\left(\left(\nabla' + i \frac{e}{\hbar} \mathbf{A}_{\mp} \right)^2 + H_{D,SO} \right) \mathbf{P}_d(\mathbf{r}, \mathbf{r}', \omega) = E_n^d(B_{\mp}) \mathbf{P}_d(\mathbf{r}, \mathbf{r}', \omega)$$

where the diffuson $\mathbf{P}_d(\mathbf{r}, \mathbf{r}', \omega)$ is now a spinor and in the $\{ | \uparrow\uparrow \rangle, | \uparrow\downarrow \rangle, | \downarrow\uparrow \rangle, | \downarrow\downarrow \rangle \}$ basis $H_{D,SO}$

⁹The cooperon term is slightly different because the reversed paths have opposite wavevectors and thus experience the opposite effective magnetic field form of the spin-orbit interaction. The operator analogous to $H_{D,SO}$ is

$$H_{C,SO} = \frac{2}{3D\tau_{SO}} \begin{bmatrix} 2 & 0 & 0 & 0 \\ 0 & 1 & -1 & 0 \\ 0 & -1 & 1 & 0 \\ 0 & 0 & 0 & 2 \end{bmatrix}.$$

This term leads to the mixing of the $| \uparrow\downarrow \rangle$ and $| \downarrow\uparrow \rangle$ spin pairs and so to an interplay with the Zeeman shifts experienced by these pairs. Incorporating the Zeeman terms by changing the 1's on the diagonal to $1 + (3D\tau_{SO}/2)2iE_Z$ and $1 - (3D\tau_{SO}/2)2iE_Z$, the eigenvalues are found to be $4/3D\tau_{SO}$, $4/3D\tau_{SO}$, and

$$\frac{2}{3D\tau_{SO}} \pm \sqrt{\left(\frac{2}{3D\tau_{SO}} \right)^2 - 4 \left(\frac{E_Z}{\hbar D} \right)^2}.$$

takes the form

$$H_{D,SO} = \frac{2}{3D\tau_{SO}} \begin{bmatrix} 1 & 0 & 0 & -1 \\ 0 & 2 & 0 & 0 \\ 0 & 0 & 2 & 0 \\ -1 & 0 & 0 & 1 \end{bmatrix}$$

where τ_{SO} can be defined from the disorder average of V_{SO} in a similar manner to τ_e being defined for V in Eq. B.14. The unnormalized eigenvectors are $|\uparrow\uparrow\rangle + |\downarrow\downarrow\rangle$, $|\uparrow\uparrow\rangle - |\downarrow\downarrow\rangle$, $|\uparrow\downarrow\rangle$, and $|\downarrow\uparrow\rangle$, and the corresponding eigenvalues are 0, $4/3D\tau_{SO}$, $4/3D\tau_{SO}$, and $4/3D\tau_{SO}$. Comparing with the spin pairings for the Zeeman splitting, we see that the two terms shifted by $\pm E_Z$ are eigenvectors of $H_{D,SO}$ both with eigenvalue $4/3D\tau_{SO}$, while the two terms unaffected by the Zeeman splitting are now split by the spin-orbit scattering. Incorporating these eigenvalues, the full form for the diffuson contribution to the density of states correlation function becomes

$$\begin{aligned} \langle \nu(\varepsilon, B) \nu(\varepsilon - \hbar\omega, B') \rangle_d = & \\ = 2 \left(\frac{1}{2\pi\hbar} \right)^2 \sum_{\mp} \sum_n \text{Re} & \left(\left(\frac{1}{i\omega + DE_n(B_-)} \right)^2 + \left(\frac{1}{i\omega + \frac{4}{3\tau_{SO}} + DE_n(B_-)} \right)^2 + \right. \\ & \dots + \left(\frac{1}{i\omega + 2i\frac{E_Z}{\hbar} + \frac{4}{3\tau_{SO}} + DE_n(B_-)} \right)^2 \\ & \left. \dots + \left(\frac{1}{i\omega - 2i\frac{E_Z}{\hbar} + \frac{4}{3\tau_{SO}} + DE_n(B_-)} \right)^2 \right). \end{aligned} \quad (\text{B.36})$$

Appendix C

Classical perturbation theory using action-angle variables

C.1 Classical mechanics formalism

In this appendix, we will outline the steps involved in calculating the change in frequency of a periodic system due to a perturbation using the action-angle variables in the Hamilton-Jacobi formalism. To that end, we begin in this section by briefly reviewing the basic concepts of the Hamilton-Jacobi formalism and action-angle variables. For more detail, see [268].¹

C.1.1 Hamiltonian mechanics

In one dimension, the classical Hamiltonian $H = H(q, p)$ can be obtained from the Lagrangian $L = T - V$ by the Legendre transformation $H = p\dot{q} - L$. Here q is a generalized coordinate with canonically conjugate momentum $p = \partial_{\dot{q}}L$, and T and V are the kinetic and potential energies of

¹I recommend looking at the second edition as well as the third. The second edition covers classical perturbation theory in one dimension which is all that is needed for deriving the finite amplitude correction to the persistent current signal and is much simpler notationally than the higher dimensional case.

the system under consideration.² The modified Hamilton's variational principle,

$$\delta \int_{t_1}^{t_2} dt \left(pq - \dot{H}(q, p) \right) = 0,$$

leads to Hamilton's equations of motion,

$$\begin{aligned} \dot{q} &= \frac{\partial H}{\partial p} \\ \dot{p} &= -\frac{\partial H}{\partial q}. \end{aligned}$$

C.1.2 Canonical transformations

The key concept behind the Hamilton-Jacobi formalism and action-angle variables is the canonical transformation. A canonical transformation is a transformation from coordinates (q, p) to coordinates (η, J) such that the new coordinates satisfy Hamilton's equations of motion

$$\begin{aligned} \dot{\eta} &= \frac{\partial K}{\partial J} \\ \dot{J} &= -\frac{\partial K}{\partial \eta} \end{aligned}$$

for some function $K(\eta, J)$. Generally, this kind of coordinate transformation requires

$$p\dot{q} - H = J\dot{\eta} - K + \frac{dF}{dt} \tag{C.1}$$

so that the modified Hamilton's principle holds in both coordinates systems.³ Typically, F is written as a function of one of the old coordinates and one of the new coordinates so that it connects the two coordinate systems. We will restrict ourselves to the case where F has no explicit time dependence ($\partial_t F = 0$).

The simplest form of F is $F = F(q, \eta)$. In this case, Eq. (C.1) becomes

$$p\dot{q} - H = J\dot{\eta} - K + \frac{\partial F}{\partial q}\dot{q} + \frac{\partial F}{\partial \eta}\dot{\eta}.$$

²Although our actual perturbation ultimately arises from electrons moving in a magnetic field, we will treat the perturbation solely as a modification to the analytic function defining the cantilever's potential energy landscape and so ignore modifications to the Lagrangian and Hamiltonian relevant for the case of a charged particle in an applied magnetic field. For simplicity, we also ignore the case of H depending explicitly on time.

³Because the end points in time t_1 and t_2 are fixed, dF/dt does not change the variation.

This relation only holds provided that

$$\begin{aligned} p &= \frac{\partial F}{\partial q} \\ J &= -\frac{\partial F}{\partial \eta} \\ K &= H. \end{aligned}$$

Other pairs of coordinates can be used but require Legendre transformations in order to follow the same form as $F(q, \eta)$. For the action-angle variable analysis to follow, we will use the transformation function $W(q, J)$, known as Hamilton's characteristic function in the literature, for which $F = W(q, J) - J\eta$. With this transformation function, Eq. (C.1) takes the form

$$p\dot{q} - H = J\dot{\eta} - K + \frac{\partial W}{\partial q}\dot{q} + \frac{\partial W}{\partial J}\dot{J} - J\dot{\eta} - \eta\dot{J}$$

which is satisfied when

$$p = \frac{\partial W}{\partial q} \tag{C.2}$$

$$\eta = \frac{\partial W}{\partial J} \tag{C.3}$$

$$K = H. \tag{C.4}$$

C.1.3 Hamilton-Jacobi formalism

In the Hamilton-Jacobi formalism, a transformation is chosen to make the new Hamiltonian K take a simple form. With our restricted assumptions of one degree of freedom and no explicit time dependence in H , the transformation we seek is one where $K = E(J)$ for some function E (with $E(J)$ constant because J is). In this case where the generalized coordinate η does not appear in the Hamiltonian, it is called *cyclic*.

Hamilton's equations of motion are easily solved in the case of cyclic coordinates. The generalized momentum obeys

$$\dot{J} = -\frac{\partial K}{\partial \eta} = 0,$$

which requires J to be a constant. The equation of motion for the generalized position,

$$\dot{\eta} = \frac{\partial E}{\partial J} \equiv f_0,$$

has the solution

$$\eta = f_0 t + \eta_0. \quad (\text{C.5})$$

Given the initial conditions (q_0, p_0) at $t = t_0$, the relation $p = \partial_q W(q, J)$ can be inverted to give $J = J(q_0, p_0)$, which can then be combined with the relation $\eta = \partial_P W(q, J)$ to give $\eta_0 = \eta_0(q_0, p_0)$. In essence, this procedure shifts the problem from solving the original equations of motion to solving the Hamilton-Jacobi equation

$$H\left(q, \frac{\partial W}{\partial q}\right) = E(J)$$

for $W(q, J)$ (the constant of integration involved in going from $\partial_q W$ to W is trivial since only derivatives of W are needed to obtain the equations of motion). The solutions of the equations of motion for (η, J) were derived above. The relations $\eta = \partial_J W(q, J)$ and $p = \partial_q W(q, J)$ can be inverted to give $q(\eta, J)$ and $p(\eta, J)$.

C.1.4 Action-angle variables

Action-angle variables are a particular choice of coordinates obtained using the Hamilton-Jacobi procedure for the case of a periodic system. By a “periodic system,” we mean one where the solutions of the equations of motion trace out closed curves in (q, p) phase space. The angle variable is the transformed position, while the action variable is its canonically conjugate momentum. We define the action variable⁴ by

$$J = \oint dq p(q, E) + A_0 \quad (\text{C.6})$$

where $p(q, E)$ comes from inverting $H(q, p) = E$, and A_0 can be any constant independent of q and p . As usual, Hamilton’s characteristic function $W(q, J)$ connects the original coordinates to the action-angle variables.

The usefulness of the action-angle variables is revealed by considering the change in the angle

⁴This name comes from the usage of this integral in the form $\int dt \dot{q} p$ in the formulation of the principle of least action. It has the units of angular momentum. The angle coordinate is so named because the canonical conjugate of angular momentum is an angle.

variable over one period,

$$\begin{aligned}
\Delta\eta &= \oint dq \frac{\partial\eta}{\partial q} \\
&= \oint dq \frac{\partial^2 W}{\partial q \partial J} \\
&= \frac{d}{dJ} \oint dq \frac{\partial W}{\partial q} \\
&= \frac{d}{dJ} \oint dq p \\
&= \frac{d}{dJ} (J - A_0) \\
&= 1
\end{aligned}$$

where we have used Eqs. (C.2), (C.3), and (C.6) and the fact that J is independent of q . From the equation of motion for η , Eq. (C.6), we have $1 = f_0\tau$ where τ is the period of the system in units of time. Thus we see that $f_0 = \partial_J E$ is the frequency of the system. In principle, this procedure allows one to determine the frequency of the system without solving the equations of motion.

C.1.5 Action-angle variables of the simple harmonic oscillator

Now we will briefly set up the action-angle formalism for the case of a simple harmonic oscillator for application to the study of the cantilever's motion discussed in Chapter (4). The Hamiltonian

$$H_0(q, p) = \frac{p^2}{2m} + \frac{1}{2}m\omega_0^2 q^2 = E$$

can be rearranged as

$$p = \sqrt{2mE - m^2\omega_0^2 q^2}$$

with m the mass of the oscillator. The action variable can then be written as

$$\begin{aligned}
J &= \oint dq p \\
&= 4 \int_0^{\sqrt{\frac{2E}{m\omega_0^2}}} dq \sqrt{2mE - m^2\omega_0^2 q^2} \\
&= \frac{2\pi E}{\omega_0}.
\end{aligned}$$

where we have used the fact that $dqp > 0$ to rewrite the integral over a quarter of a period. We see immediately that the frequency is $f_0 = \partial_J E = \omega_0/2\pi$ as expected. We note that J can also be written in terms of the maximum displacement from equilibrium q_{\max} as

$$J = \pi m \omega_0 q_{\max}^2.$$

Using the relation for the angle variable $\eta = f_0 t + \eta_0$ found above in Eq. C.5, the well known solutions

$$\begin{aligned} q(t) &= \sqrt{\frac{2E}{m\omega_0^2}} \sin(2\pi f_0 t + \phi_0) \\ p(t) &= \sqrt{2mE} \cos(2\pi f_0 t + \phi_0) \end{aligned}$$

can be rewritten in terms of the action-angle variables as

$$\begin{aligned} q &= \sqrt{\frac{J}{2\pi^2 m f_0}} \sin 2\pi\eta \\ p &= \sqrt{2m f_0 J} \cos 2\pi\eta \end{aligned} \tag{C.7}$$

where we have set $\phi_0 = 2\pi\eta_0$.

C.2 Perturbation theory with action-angle variables

We will now review the calculation of the frequency of a periodic system subject to a small perturbation. An analysis using action-angle variables is particularly well suited to this task since the frequency of the system has a particularly simple form. We write the Hamiltonian in the original coordinate system as

$$H(q, p, \varepsilon) = H_0(q, p) + \varepsilon H_1(q, p)$$

where $H_0(q, p)$ is the Hamiltonian describing the unperturbed periodic system and ε is a dimensionless variable parametrizing the strength of the perturbation. The unperturbed Hamiltonian H_0 can be transformed into $K(\eta, J)$ where η and J are the angle and action variables described in the preceding section. For small perturbations the system remains periodic and the perturbed Hamiltonian H can be transformed to $\mathcal{K}(\zeta, j)$ where ζ and j are now the angle and action variables

for the system described by H . The transformation $(q, p) \rightarrow (\eta, J)$ is just a set of analytic relations between variables independent of the form of the Hamiltonian and so remains canonical when the perturbation is added. By the construction of (η, J) , $q(\eta, J)$ and $p(\eta, J)$ are periodic in η with period 1. However, when $\varepsilon \neq 0$, (η, J) are no longer action-angle variables. It is thus no longer guaranteed that J is a constant nor that η is linear in time.

In the presence of the perturbation, the Hamiltonians of both the old and new action-angle variables are functions of ε and can be expanded as

$$K(\eta, J, \varepsilon) = K_0(J) + \varepsilon K_1(\eta, J) + \varepsilon^2 K_2(\eta, J) + \dots$$

and

$$\mathcal{K}(j, \varepsilon) = \mathcal{K}_0(j) + \varepsilon \mathcal{K}_1(j) + \varepsilon^2 \mathcal{K}_2(j) + \dots$$

where \mathcal{K} is independent of ζ because it was constructed to be the Hamiltonian for the action-angle variables of the perturbed system. The two sets of coordinates are related by a canonical transformation which we can write as $W(\eta, j)$ in keeping with the notation developed in the previous section. This function also admits an expansion in ε :

$$W(\eta, j, \varepsilon) = \eta j + \varepsilon W_1(\eta, j) + \varepsilon^2 W_2(\eta, j) + \dots$$

where the form of the first term has been constructed so that W gives the trivial transformation $J \rightarrow j$, $\eta \rightarrow \zeta$ when $\varepsilon = 0$.

Now we will solve for the first correction to the frequency $\partial_j \mathcal{K}_1$. We make use of the fact that K and \mathcal{K} must be equal for each order of ε . Using $J \approx j + \varepsilon \partial_\eta W_1(\eta, j)$, we can rewrite K to first order in ε as

$$\begin{aligned} K(\eta, j, \varepsilon) &\approx K_0(j + \varepsilon \partial_\eta W_1(\eta, j)) + \varepsilon K_1(\eta, j + \varepsilon \partial_\eta W_1(\eta, j)) \\ &\approx K_0(j) + \varepsilon [\partial_j K_0(j) \partial_\eta W_1(\eta, j) + K_1(\eta, j)]. \end{aligned}$$

Equating powers of ε , we have

$$\begin{aligned} \mathcal{K}_0(j) &= K_0(j) \\ \mathcal{K}_1(j) &= \partial_j K_0(j) \partial_\eta W_1(\eta, j) + K_1(\eta, j). \end{aligned} \tag{C.8}$$

To carry the analysis further, we need to consider closely the properties of $W_1(\eta, j)$. When the system moves through one period, the angle variables must satisfy $\zeta \rightarrow \zeta + 1$ and $\eta \rightarrow \eta + 1$ for all values of ε . Since

$$\zeta = \eta + \varepsilon \partial_j W_1(\eta, j) + \dots,$$

it must hold that $\partial_j W_m$ is periodic in η with period 1 for each m . Similarly, although J is no longer constant in the presence of the perturbation, it can still be written in terms of q and p . The relation

$$J = j + \varepsilon \partial_\eta W_1 + \dots \quad (\text{C.9})$$

thus implies that $\partial_\eta W_m$ is also periodic in η with period 1 for each m . The Fourier expansion

$$\partial_\eta W_m = \sum_n C_n^m(j) e^{2\pi i n \eta} \quad (\text{C.10})$$

can be integrated to give

$$W_m = \sum_{n \neq 0} \frac{C_n^m(j)}{2\pi i n} e^{2\pi i n \eta} + D^m(j) + C_0^m(j) \eta.$$

Taking the derivative with respect to j , we find

$$\partial_j W_m = \sum_{n \neq 0} \frac{\partial_j C_n^m(j)}{2\pi i n} e^{2\pi i n \eta} + \partial_j D^m(j) + \partial_j C_0^m(j) \eta.$$

For $\partial_j W_m$ to be periodic in η , the quantity $\partial_j C_0^m$ must be zero, and thus C_0^m must be independent of η and j . From Eqs. C.9 and C.10, we see that all of the C_0^m effectively shift J by a constant that depends only on ε . The action variable J as defined in Eq. C.6 includes an arbitrary offset A .

We are thus free to shift J appropriately to set all $C_0^m = 0$.

With all $C_0^m = 0$, we can now evaluate Eq. C.8 by average both sides over a period. This averaging gives

$$\begin{aligned} \mathcal{K}_1(j) &= \int_0^1 d\eta (\partial_j K_0(j) \partial_\eta W_1(\eta, j) + K_1(\eta, j)) \\ &= \int_0^1 d\eta K_1(\eta, j). \end{aligned} \quad (\text{C.11})$$

To first order, the correction to the frequency of the system is thus

$$\delta f_0 \approx \varepsilon \frac{\partial}{\partial j} \int_0^1 d\eta K_1(\eta, j). \quad (\text{C.12})$$

From Eqs. C.8 and C.11, it is possible to solve for $\partial_\eta W_1$. To find the second order correction \mathcal{K}_2 , all that is needed is to carry out the Taylor expansions to second order and use the values of $\mathcal{K}_1(j)$ and $\partial_\eta W_1(\eta, j)$ from the first order calculation. Successively higher order terms can be found by iterating this procedure.

Appendix D

Persistent current cantilever-with-ring sample fabrication

The actual samples discussed in this text were fabricated at the Cornell NanoScale Facility (CNF) at Cornell University, Ithaca, NY, USA except for the aluminum deposition which took place in the Devoret/Schoelkopf thermal evaporator in Becton Engineering and Applied Science Center, Yale University, New Haven, CT, USA. The details of the recipe were developed largely by Ania Jayich and Rob Ilic with guidance from Jack Harris and some input from myself. Some preliminary work was performed at Yale with the assistance of Luigi Frunzio and use of the Devoret lab's FEI scanning electron microscope (SEM) (FEI Company, Hillsboro, OR, USA).

Below is a detailed recipe for the single crystal silicon cantilevers with integrated rings reported on in this text.¹ Samples were made over several iterations with slight tweaks to the recipe each time. The recipe as presented represents a recommended fabrication procedure for the production of

¹Ring/wire feature sizes obtained by this recipe were 80-130 nm. In order to achieve smaller feature sizes, a thinner e-beam resist is likely needed. To obtain a smooth coat of a thinner resist it would be preferable to perform the e-beam lithography before the frontside photolithography for the cantilevers. We attempted one run of this alternate recipe. Because we did not achieve the desired feature sizes (we got ~ 100 nm rather than the target 30 nm, possibly due to overexposure with the e-beam), I will not include the alternate recipe in this thesis. Further refinements to our recipe are necessary to achieve these smaller features. When aiming for the smallest possible feature sizes with e-beam lithography, it is common practice to write on suspended membranes to minimize electron backscattering off the substrate. It is worth considering reversing the major steps in the recipe below, performing the backside etch first, then writing the frontside e-beam pattern and depositing the metal, and defining the cantilevers with frontside photolithography last.

future samples rather than a step-by-step record of any one previous fabrication run. All numbers in the recipe below should be treated as starting points in future fabrication processes. When using a new tool for the first time or an old tool after a long lapse, it is highly recommended to consult with the tool manager about recent tool performance and calibrations and to adjust the recipe accordingly. Also, when using a chemical unfamiliar to you, always check for its container compatibility before pouring it!

D.1 Cantilever-with-ring fabrication recipe

1. Photolithography mask creation

- (a) Create mask designs for all three stages of lithography (frontside photolithography, backside photolithography, electron beam (e-beam) lithography) by computer.
 - i. Lay out mask designs with a computer aided design (CAD) program (See Fig. D.2). We used the L-Edit Pro software (Tanner EDA, www.tannereda.com, Monrovia, CA, USA).
 - ii. Put global alignment marks on the mask of each stage of lithography. These marks should line up on each mask so that the sequential lithography steps can be aligned to each other. We used two crosses, located on opposite sides of the wafer.²
 - iii. Export masks to appropriate format for mask writing tools. In our case, this format was the semiconductor standard GDSII.
- (b) Write photolithography masks with mask writer.
 - i. We used five inch chrome photomasks provided by the CNF. These masks are five inch squares of glass about an eighth of an inch thick with a thin film of chrome evaporated on one side and a layer of photoresist on top of the chrome.
 - ii. We used two mask writing tools at the CNF, the DWL 66 laser lithography system (Heidelberg Instruments Mikrotechnik GmbH, Heidelberg, Germany) and the GCA Mann 3600F pattern generator (this is an old machine. GCA / D. W. Mann is

²A convenient choice for alignment marks on the photolithography masks is a large window to be etched from the mask with a large unetched cross centered inside of it. This configuration provides a large transparent viewing area for hunting for marks on different layers when performing alignment. We never did this during any of my fabrication runs. Instead we had large transparent crosses for alignment marks. Such marks provide only a narrow viewing window for searching for marks through the mask. It is advisable to consult with the managers of the lithography tools requiring alignment when choosing the dimensions and geometry of alignment marks.

no longer in business. Its intellectual properties have been sold several times and are currently controlled by Ultratech, San Jose, CA, USA). The tools have slightly different capabilities, but our mask features were realizable in both. The deciding factor in which mask writer was used was tool availability.

iii. Many companies offer mask writing services. This step could be outsourced if no mask writer is available.

(c) Develop mask photoresist and etch chrome.

i. At the CNF, these two steps can be done using the Steag-Hamatech HMP 900 mask processing system (HamaTech APE GmbH & Co. KG, Sternenfels, Germany). The Hamatech system contains a spinner and a chemical sprayer and is preprogrammed with recipes for chrome photomask development and etching.

ii. For photoresist, AZ 300 MIF (AZ Electronic Materials USA Corp., Somerville, NJ, USA) developer is used. The main working component of the developer is tetramethylammonium hydroxide (TMAH).

iii. For chrome etching, CR-14 Chromium Etchant (Cyantek Corporation, Fremont, CA, USA) is used. The main active ingredients of the etchant are ceric ammonium nitrate and acetic acid.

2. Preliminary preparation of silicon wafers

(a) Obtain four inch diameter silicon-on-insulator wafers to fabricate the persistent current samples.

i. Some wafers used in early stages of the experiment were obtained from Shin-Etsu (SEH America, Inc., Vancouver, WA, USA), but all of the samples in which normal state persistent currents were actually observed were obtained from Soitec (Soitec USA, Inc., Peabody, MA, USA).

ii. Specifically, we used Soitec's Unibond wafer, part number G4P-022-01. These wafers are manufactured with a 340 nm top silicon layer, a 1 μm thick buried silicon dioxide layer, and 450 μm silicon handle layer. Soitec's Unibond wafer production process, which involves bonding a silicon wafer weakened at well-defined depth by hydrogen implantation to a handle wafer, produces thin but highly uniform top silicon layers, well suited to wafer-scale parallel production of cantilevers of ~ 100 nm thickness.

- iii. Soitec's Unibond wafers are not mass produced. As a small-volume customer, we were restricted in our purchases of SOI wafers to whatever was leftover in Soitec's inventory. In one instance, we could only obtain six inch diameter wafers. We had those wafers resized to four inch diameter by MPE (Micro Precision Engineering, Greenville, TX, USA).
- (b) Clean wafer. We used a standard MOS clean recipe required at the CNF before using any MOS compatible tool in the facility (such as the furnace described in the oxidation step). The MOS clean recipe consisted of the following steps.
 - i. Submerge wafer in 6:1:1 DI water:H₂O₂:NH₄OH bath for 10 minutes.
 - ii. Submerge wafer in 6:1:1 DI water:H₂O₂:HCl bath for 10 minutes.
- (c) Thin down frontside silicon layer to desired cantilever thickness. This step is not necessary if the wafers begin with an acceptable thickness (the main experimental results reported in this text used 340 nm thick cantilevers which were not thinned down). A wafer map of the final device layer silicon thickness (see Fig. D.1) should be recorded regardless of whether the wafer needs etching.
 - i. Oxidize wafer in thermal oxidation furnace.
 - A. ~44% of thermally grown oxide grows down into the existing silicon. So to remove 44 nm of Si, 100 nm of SiO₂ must be grown and etched.
 - B. Put wafers into furnace facing frontside-to-frontside and backside-to-backside when processing multiple wafers. This arrangement helps to maintain frontside polish through the oxidation process.
 - C. For removal of large amounts of silicon, we used the CNF's CMOS Wet Oxidation Furnace to perform a wet oxide etch with HCl at 1000°C. These parameters grow SiO₂ at an approximate rate of 5 to 9 nm/min. Note that this rate is tool specific and nonlinear in time.
 - D. For removal of fine amounts of silicon, we used the CNF's CMOS Dry Oxide Furnace to perform a dry oxide etch with HCl at 1000°C. These parameters grow SiO₂ at an approximate rate of 1 nm/min. Note that this rate is tool specific and nonlinear in time.
 - ii. Etch oxide in HF for about three minutes (100 nm/min etch rate).

- iii. Check remaining silicon thickness. We used a microscope equipped with the F40 optical film thickness measurement instrument (Filmetrics, San Diego, CA, USA).
 - iv. Iterate steps i-iii until desired frontside silicon thickness is achieved.
- (d) Deposit 1.2 μm of oxide on backside of wafer.
- i. We used the CNF's GSI PECVD (plasma-enhanced chemical vapor deposition) tool (Ultradep, Group Sciences, Inc., San Jose, CA; this company went out of business several years ago). The tool's standard oxide recipe uses a temperature of 400°C and a gas mix of SiH_4 , N_2O , and N_2 and produces oxide with 290 MPa compressive stress. This recipe's nominal deposition rate is 260 nm/min.
 - ii. The purpose of this step is to produce an extra mask layer for the backside etch step. It is not strictly necessary if the backside photoresist is baked sufficiently.
 - iii. Measure the deposited oxide thickness if possible and note it for when the oxide will be etched during the backside wafer processing.
3. Frontside cantilever definition (all steps performed to frontside of wafer)
- (a) Spin ~ 7 mL MicroPrime MP-P20 photoresist primer (Shin-Etsu MicroSi, Phoenix, AR, USA) at 4000 rpm for 30 seconds on frontside of wafer.
 - (b) Spin ~ 14 mL Megaposit SPR220-3.0 photo resist (Rohm and Haas Electronic Materials LLC, Marlboro, MA, USA) at 4000 rpm for 60 seconds on frontside of wafer.³
 - (c) Bake for 90 seconds at 115°C on hotplate. (At the CNF, we used the BLE-150 hotplate which has a lid and the ability to lift the wafer off the plate when the timer is up).
 - (d) Expose the photoresist using the frontside mask (if this is the first mask used on the wafer, alignment is not critical) with 12 mW/cm² for 5 seconds. At the CNF, we used the EV620 mask aligner (EV Group GmbH, St. Florian am Inn, Austria) in soft contact mode.
 - (e) Bake for 90 seconds at 115°C on hotplate.

3

i. Make sure the lid is closed for all spinning steps as the composition of the photoresist can be different when spun with the lid open, leading to inconsistent photolithography results.

- (f) Develop photoresist with AZ 300 MIF for 60 seconds. At the CNF, we used the STEAG-Hamatech HMP 900 system with a double puddle process (recipe 6). If developing by hand, spray clean with de-ionized (DI) water and blow dry with clean N₂ gas.
- (g) Examine developed photoresist in an optical microscope. If the resist does not match the expected pattern of the mask, remove it by spinning the wafer with acetone and try repeating steps (a) through (g).
- (h) Etch frontside silicon using a CF₄ reactive ion etch (RIE).
 - i. We used the Oxford PlasmaLab 80+ RIE System (Oxford Instruments, Tubney Woods, Abingdon, Oxfordshire, UK).
 - ii. For all RIE work, a 10 minute oxygen clean is recommended prior to putting samples in the tool and after every ~30 minutes of tool use. The standard oxygen clean recipe for the Oxford 80 used 30 sccm of O₂ at 60 mtorr and 150 W of RF power.
 - iii. The standard CF₄ etch recipe for the Oxford 80 used 30 sccm of CF₄ at 40 mtorr and 150 W of RF power. Other tool parameters were an 80 V DC bias and -10° for the chilled house water. The nominal tool etch rate was ~40 nm/min. We etched for 20 minutes to be sure the silicon was totally gone. It is advisable to check with the tool manager about the standard etch recipe and etch rate when using a new tool. Be careful about overetching because the CF₄ etch can etch both Si and SiO₂.
 - iv. We used pieces of quartz to pin the wafer in place and keep it from sliding around on the etcher's electrode.
- (i) Examine etch in optical microscope. A thin film (such as one composed of residual silicon) should have strong color, usually a bright purple, blue, or red. If possible, check film thicknesses with a film measurement tool. If it appears that the silicon is not totally etched, submit the wafer to further reactive ion etching.
- (j) Remove the remaining photoresist and clean the wafer.
 - i. Spin off photoresist with acetone.
 - ii. Consider cleaning the wafer with a stronger cleaning agent. At the CNF, we would either use the STEAG-Hamatech HMP 900 to run a wafer cleaning recipe which spun hot Pirhana Nano-strip solution (Cyantek Corporation, Fremont, CA, USA) on the wafer. This solution is primarily sulfuric acid with small amounts of peroxymonosul-

furic acid and hydrogen peroxide. Alternatively, we used the two stage hot photoresist bath which had tanks of AZ 300T photoresist stripper (AZ Electronic Materials USA Corp., Somerville, NJ, USA), which is composed of 1-Methyl-2-pyrrolidone (NMP), 1,2-Propanediol, and TMAH.

4. Electron beam lithography (all steps performed to frontside of wafer)⁴

- (a) Spin 5.5% poly(methylmethacrylate) (PMMA) in Anisole (NANOTM 495K A5.5% PMMA Positive Radiation Sensitive Resist, Microchem, Newton, MA, USA) at 2000 rpm for 60 seconds.
- (b) Bake wafer on hotplate at 170°C for 10 minutes.
- (c) Spin 2% PMMA in methyl isobutyl ketone (MIBK) (NANOTM 950K M2% PMMA Positive Radiation Sensitive Resist, Microchem, Newton, MA, USA) at 4000 rpm for 60 seconds.
- (d) Bake wafer at 170°C for 10 minutes
- (e) Write e-beam pattern with electron beam writing tool.
 - i. At the CNF, we used the JEOL JBX-9300FS Electron Beam Lithography System (JEOL Ltd., Tokyo, Japan).
 - ii. For fine features (namely the rings and transport measurement wires), we used a 1.6 nA beam current and a dosage of 1200 $\mu\text{C}/\text{cm}^2$ (aperture 3 on the JEOL e-beam tool). However, our features always ended up overexposed with fabricated linewidths about 40% greater than expected.
 - iii. For big features (bond pads and leads to transport samples), we used a 140 nA beam current and 2000 $\mu\text{C}/\text{cm}^2$ (aperture 8 on the JEOL e-beam tool).
 - iv. More detail might be desired regarding the e-beam writing procedure. However, the e-beam tool is sophisticated and expensive, requiring extensive training to be operated autonomously. During my time working on the persistent current experiment, none of the members of the Harris Lab achieved full independence with the tool. Some of the finer points of the e-beam writer operation were handled by Rob Ilic and Daron Westly of the CNF.

⁴We use a bilayer e-beam resist for improved lift-off. The lower resist layer is removed more easily by the e-beam so that an undercut is formed below the top resist layer. The top resist layer defines the feature size during evaporation. During lift-off, solvent is able to enter the space between the lower resist layer and the evaporated metal and so remove the remaining resist more easily than if the resist were flush with the metal.

- (f) Develop e-beam resist by dipping wafer in 1:3 MIBK:IPA (a mixture of solvents) for 2 minutes. Use very slight agitation for ~ 20 seconds. (Precise solvent specifications: MIBK (4-methyl-2-pentanone, Sigma-Aldrich, Saint Louis, MO, USA) and IPA (2-propanol, Mallinckrodt Baker, Phillipsburg, NJ, USA).
- (g) Descum wafer in barrel etcher (P2000 Branson International Plasma Corp. (long out of business), Hayward, CA, USA) for 2 minutes at 150 W.

5. Metal deposition and lift-off

- (a) Deposit metal.⁵ For the experiments discussed in the text 99.999% pure aluminum (Alfa Aesar, Ward Hill, MA, USA) was used.⁶ Here is a detailed procedure for our aluminum deposition with the PLASSYS electron beam evaporator (PLASSYS-BESTEK, Marolles-en Hurepoix, France):
 - i. Mount wafer. The PLASSYS we used was design for three inch wafers. We used double sided 1 mil Kapton[®] tape (KaptonTape.com, Torrance, CA, USA) to secure our four inch wafers to the sample mount. There was just barely enough clearance for the four inch wafer in the evaporator.
 - ii. Pump down sample load-lock and then open valve to evaporation chamber. We usually pumped on the load-lock for at least four hours before opening the valve to the electron beam evaporation chamber. A typical chamber pressure was 3×10^{-8} torr after opening the valve.
 - iii. Run titanium sweep of chamber. A typical chamber pressure after running a Ti sweep was 1×10^{-8} torr.
 - iv. Evaporate aluminum at ~ 1 nm/s.

⁵We deposited aluminum at Yale using the Devoret/Schoelkopf PLASSYS electron beam evaporator. This evaporator was chosen because its application was the creation of Josephson tunnel junctions for qubits with long coherence times. Long coherence times are linked to cleanliness of the aluminum, which we also wanted for our persistent current samples. The variety of materials allowed in the evaporator was highly limited (mainly just aluminum and titanium though copper, gold, and possibly a couple others had been used in the past), and none of them were magnetic. Previous work has shown a link between electron phase coherence and magnetic impurities at low magnetic field [55, 311], and it has been predicted that magnetic impurities could have an effect on persistent currents (see e.g. [128, 131, 312] or Chapter 3 for more detail). We also tested the fabrication of gold rings though we never measured them. The gold evaporation was outsourced to Jose Aumentado, NIST, Boulder, CO, USA. We made some preliminary lift-off tests and had mild success with the same lift-off procedure described here for aluminum. Typically 99% of the ring centers lifted off but that might not be good enough when creating arrays of hundreds of thousands of rings. Also, we observed that some of the gold rings lifted off of the silicon entirely. At least one more wafer should be tested for lift-off using the procedure given here as the starting point for finding one that works with gold rings.

⁶Concentrations of some impurities as provided by Alfa Aesar: 0.5 ppm Fe, 0.07 ppm Mn, 0.017 ppm Cr, <0.002 ppm Ni. The overall impurity concentration was specified as 10 ± 5 ppm.

- v. Wait 5 minutes for aluminum to cool.
 - vi. Treat aluminum with static oxidation using 3 torr of O₂ for 10 minutes. The purpose of this step is to oxidize the aluminum with a clean, controlled source of oxygen. If this step is skipped, the aluminum will still oxidize ~3-5 nm in from the surface, but the oxidation will be uncontrolled and other impurities could enter the aluminum as well.
- (b) Lift off e-beam resist.
- i. Put wafer in a solution of ~90% methylene chloride (MeCl)⁷ (Dichloromethane, Sigma-Aldrich, Saint Louis, MO, USA) and ~10% acetone (Mallinckrodt Baker, Inc., Phillipsburg, NJ, USA).
 - A. Holding the wafer upside down allows gravity to aid in the lift-off process.
 - B. We machined a Teflon ring with lip to hold the wafer in place upside down without touching the frontside of the wafer.
 - C. Use a screw-top lid for the MeCl container because it evaporates quickly. Do not tighten the lid all the way because the evaporating MeCl can make the lid very difficult to loosen.
 - ii. Let sample sit for 5 minutes. Then ultrasound container for 20 seconds.
 - iii. Let sample sit for 1 hour. Then ultrasound container for 20 seconds. This step can be repeated several times.
 - iv. Let sample sit for ~8 hours (typically overnight).
 - v. Ultrasound container for 3 minutes just before removing wafer.
 - vi. Spray wafer with IPA while removing it from MeCl. MeCl evaporates quickly and leaves an unwanted residue.
 - vii. Rinse wafer in a fresh container of IPA. Ultrasound this container for 20 seconds.
 - viii. Blow wafer dry with clean N₂ gas.
 - ix. Examine wafer in optical microscope.⁸ It is possible to image metal features at this point with an SEM (see Fig. D.7) and an atomic force microscope (AFM) (see Fig.

⁷Some people feel very strongly about not using MeCl, and it is banned in some facilities. We had much greater success with MeCl than we did with pure acetone for the aluminum lift-off.

⁸A. Even with feature sizes smaller than the diffraction limit, it is possible to distinguish rings for which the center has lifted off from rings for which it has not (if you see two sorts of rings, then one of those sorts is probably rings that have not lifted off properly). If it appears that not all rings have lifted off, the wafer can be returned to MeCl and further ultrasounding can be attempted. If the wafer can be imaged before being dried off, that

D.8) to determine their linewidths and thickness. These measurements can also be delayed until step 9.

6. Backside wafer photolithography

- (a) Spin ~ 7 mL MicroPrime MP-P20 photoresist primer at 4000 rpm for 30 seconds on frontside of wafer.⁹
 - i. Spin Megaposit SPR220-7.0 photo resist (Rohm and Haas Electronic Materials LLC, Marlboro, MA, USA) at 3000 rpm for 60 seconds on frontside of wafer.¹⁰ The purpose of this resist is to protect the deposited metal during subsequent processing steps.
 - ii. Bake for 3 minutes at 115°C using hotplate (again, at the CNF, we used the BLE-150 hotplate).
 - iii. Spin ~ 7 mL MicroPrime MP-P20 photoresist primer at 4000 rpm for 30 seconds on backside of wafer.
 - iv. Spin Megaposit SPR220-7.0 photo resist at 3000 rpm for 60 seconds on backside of wafer. (See note on previous use of SPR220-7.0 above).
 - v. Bake wafer for 2 minutes at 115°C. Do not put the wafer directly onto the hotplate with photoresist on both sides! Put the wafer facedown onto the polished face of a spare silicon wafer and then bake with the clean side of this wafer in contact with the hotplate. After baking, the wafers will need to be pried apart. Intentionally misaligning the wafer flats when putting them together can help with prying the wafers apart.
 - vi. Expose backside of wafer with 12 mW/cm² for 14 seconds using backside alignment to line up the backside mask to the features on the front of the wafer. At the CNF, we used the EV620 mask aligner.

would be worth considering. We had inconsistent results when trying to re-lift off the rings after drying them off.

⁹Good advice: always test the spinner at low speed before spinning and always be aware of the location of the stop button when starting a high speed spin. At this point in the fabrication procedure, a lot of time has been invested into the wafer and the frontside metal is currently exposed. Extra care is called for here.

¹⁰This resist is really thick. The easiest way to spin it on the wafer is to pour the resist onto the wafer directly from the bottle. Pour enough to create a circle of about 2 inch diameter in the center of the wafer. When using this technique, always clean the edge of the bottle top before and after pouring the resist out to prevent contamination of the resist with dried resist residue.

- vii. Allow the photoresist to rehydrate for at least 2 hours.¹¹
- viii. Bake for 2 minutes at 115°C. Use a same procedure as previous bake step.
- ix. Develop photoresist in dish of AZ 300 MIF for 2 minutes. Agitate the wafer gently by hand over this time.
- x. Spray wafer with DI water and blow dry with clean N₂ gas.
- xi. Bake wafer in oven for 8 hours at 90°C. At the CNF, we put the wafer in a standard quartz wafer cassette to hold it in the oven.

7. Backside wafer etching

- (a) If PECVD oxide was deposited on the backside of the wafer:
 - i. Reactive ion etch the backside of the wafer with CF₄ in 20 minute intervals to remove oxide (see CF₄ recipe in step 3(h)iii).
 - A. Run 5-10 minute O₂ cleans in between etches (plus one before beginning etching of course) with the wafer removed from the etcher.
 - B. Any color on the etched areas means that the oxide has not been fully etched. Repeat previous steps until all oxide is removed.
 - ii. Check depth of windows with profilometer if desired. At the CNF, we used a P-10 surface profiler (KLA-Tencor, Milpitas, CA, USA).
- (b) Deep reactive ion etch (DRIE) the backside features (windows underneath the cantilevers) through the handle down to the oxide.
 - i. NOTE: at the CNF, we used the Unaxis ICP 770 deep silicon etcher (OC Oerlikon (formerly Unaxis), Pfäffikon, Schwyz, Switzerland) and the following detailed steps were developed based on that tool's performance.
 - ii. NOTE: DRIE typically employs a Bosch process which consists of a loop of deposition of a passivation layer and a standard reactive ion etch. The etch step is somewhat directional so that during each loop the passivation layer is etched away from the bottom of the trench before it is etched away from the sides. Silicon is then etched away from the bottom. Then the passivation layer is deposited again before being completely removed from the sides. In this way, a highly directional etch is

¹¹The wafer must be kept out of UV light at this time. If storing in a wafer box with screw-top lid, keep the lid a little bit loose.

achieved. Ideally, the etch is highly selective to silicon over silicon dioxide so that the oxide can serve as an etch stop and make up for non-uniformity in etch rate across the wafer. At the CNF, we used the standard etch recipe saved as 0trench in the Unaxis software. Typical recipe performance was $0.7 \mu\text{m}$ per loop and 4 loops/min. This recipe loop had three steps with the following parameters:

- A. Deposition: 5 seconds of 70 sccm C_4F_8 , 2 sccm SF_6 , 100 sccm Ar at 24 mtorr with $\text{RF1} = 0.1 \text{ W}$ and $\text{RF2} = 850 \text{ W}$ (RF powers).
 - B. Etch 1: 2 seconds of 2 sccm C_4F_8 , 70 sccm SF_6 , 40 sccm Ar at 23 mtorr with $\text{RF1} = 8 \text{ W}$ and $\text{RF2} = 850 \text{ W}$.
 - C. Etch 2: 5 seconds of 2 sccm C_4F_8 , 100 sccm SF_6 , 40 sccm Ar at 23 mtorr with $\text{RF1} = 8 \text{ W}$ and $\text{RF2} = 850 \text{ W}$ (RF powers).
- iii. Run 20-50 loops of DRIE recipe on a junk silicon wafer. If the wafer looks black, there is a problem with the tool that should be addressed. Otherwise, proceed.
 - iv. Etch $\sim 100 \mu\text{m}$ into the wafer (~ 150 loops of 0trench).
 - v. Check etch depth with profilometer. Check several regions of the wafer. The etch rates of the center of the wafer and the perimeter might be fairly different.
 - vi. Etch the rest of silicon handle layer. This process may be broken up into steps to allow for further checks of the etch rate or to work around tool availability.
 - vii. Inspect wafer in an optical microscope. A thin remaining layer of silicon can appear light colored but opaque (see Fig. D.5). The photoresist can appear to have features but is more cloudy and transparent than the silicon.

8. Cantilever release

- (a) Break off some chips with tweezers. I prefer carbon coated tweezers (758TW0000, Techni-Tool, Worcester, PA, USA) to minimize damage to the sample chips.
- (b) Etch Bosch polymer residue on sample chips.
 - i. Lay down a strip of double-sided Kapton tape on the edge of a cleaved piece of a silicon wafer.
 - ii. Rough up the exposed side of the tape with tweezers so it is not excessively sticky. It can be difficult to remove the silicon chips from fresh Kapton tape without damaging them.

- iii. Stick some sample chips¹² cantilever-side up onto the tape with the cantilever window portion of the chips hanging off the edge of the silicon piece (this arrangement makes it easy to pull the samples off the tape afterwards).
 - iv. Weakly tape the silicon pieces to a silicon wafer which you can pin down in the RIE chamber with quartz pieces. Do not tape the pieces directly to the RIE chamber electrode.
 - v. RIE the samples (after the standard O₂ clean of the chamber) with 5 sccm CF₄, 30 sccm O₂ at 60 mtorr and 150 W of RF power for 3-4 minutes.
 - vi. Remove the samples from the silicon pieces and then retape them to the silicon pieces upside down, again with the cantilever windows hanging off of the sides (this time this arrangement is important since the you do not want the fragile topside membrane of the cantilever windows to touch anything).¹³
 - vii. Again tape the silicon pieces to a wafer and secure it in the RIE chamber.
 - viii. RIE the samples (after the standard O₂ clean of the chamber) with 5 sccm CF₄, 30 sccm O₂ at 60 mtorr and 150 W of RF power for 5-6 minutes.
 - ix. The preceding etches can be varied from batch to batch of sample chips. During early fabrication runs, it was discovered that the Bosch process of the DRIE left a bit of residue which made it difficult for the buffered oxide etchant (BOE) to etch the oxide and this RIE step solved this problem. If performance of the DRIE tool changes, this step might need to be adjusted.
- (c) Etch silicon dioxide membrane with 6:1 BOE with surfactant.
- i. Prepare the BOE with surfactant (Buffered etch 6:1 w/OHS; semi grade, Fujifilm Electronic Materials U.S.A., Inc., North Kingstown, RI, USA).
 - A. Pour ~0.5 L into a plastic container (NOT GLASS!).
 - B. Add a few drops of Triton X surfactant (Triton X-100, Sciencelab.com, Inc., Houston, TX, USA).

¹²The exact number depends on the level of confidence in the subsequent steps. As a first pass, I would recommend about 1/6 of the chips be used in the first batch. This batch should favor the least desirable chips (e.g. those suspected of damage or possibly on the edge of area of metal deposition) but should also sample different areas of the wafer. Breaking things up prevents one disaster from ruining all of the work done up to this point.

¹³A convenient way I devised for flipping the sample chips was to set them right side up in a row on a flat surface and then to press the silicon piece tape first down onto the sample chips so that they would all stick to the silicon piece with the windows off the edge. I always ended up damaging some chips when I tried the alternative of flipping the chips one by one and sticking them to the tape upside down.

- C. Add magnetic stirrer and put container on magnetic stirrer base stand. Agitate the liquid steadily but weakly enough not to cause bubbles/turbulence.
- D. Put stand capable of holding up the silicon pieces with the taped sample chips over the magnetic stirrer.
- E. Make sure Triton X has been dissolved into BOE. The Triton X requires some agitation to dissolve.
 - ii. Put one silicon piece with sample chips taped to it onto stand in the BOE with the backside of the sample chips facing up.¹⁴
 - iii. Blow out air bubble from sample chip windows with pipette. Air bubbles will prevent BOE from etching the oxide membrane.
 - iv. For 1 μm oxide layer, keep chips in BOE for 20 minutes.¹⁵
 - v. Rinse chips in three to four stages of ~ 0.5 L DI water.
 - vi. Turn chips right side up in the last stage of water (or an earlier stage of water).
 - vii. Remove chips from silicon piece in the last stage of water.¹⁶
- (d) Put chips face up in warm (at least 80°C¹⁷) 1165 (Microposit™ Remover 1165, Rohm and Haas Electronics Materials LLC, Marlborough, MA, USA) to remove protective frontside photoresist until resist stops visibly dissolving.
- (e) Transfer some chips to a dish of IPA (to rinse) and then to a dish of DI water. Examine the chips.¹⁸ If chips look okay, proceed. If the cantilevers appear compromised in some way (e.g. there is residual oxide or the cantilevers are warped), make note of the

¹⁴It is recommended to do one silicon piece at a time in the BOE as the situation can become hectic when multiple pieces are involved. Handling the silicon pieces with the weakly attached sample chips in the BOE using tweezers, gloves, mask and apron can be tricky. Try practicing with an empty silicon piece first to get a feel for how the silicon piece will slide around on the stand in the BOE. Also, practice taking the silicon piece out of the BOE quickly. Etch times can get stretched out due to difficulty in grabbing the silicon pieces quickly. Finally, be gentle with the silicon pieces in the BOE. The tape should be only weakly holding the sample chips. It is possible for them to fall off of the silicon pieces and get sucked into the magnetic stirrer if handled too roughly. If this happens frequently, do not rough up the Kapton tape so much with the tweezers (also, consider fresh tape between Bosch etches).

¹⁵

A. The nominal etch rate for BOE is 100 nm/min. However, poor circulation in windows necessitates a longer etch time. Also, by the time unetched oxide (see Fig. D.6) can be identified, it is too late to perform further etching so it is advisable to overetch a little bit. On the other hand, it is possible for the BOE to get under the photoresist and keep etching sideways under the cantilever, possibly to ill effect. If there is evidence of strong undercutting in an early batch, the BOE time can be reduced in subsequent batches.

¹⁶I like to do this after flipping the whole silicon piece over to avoid mishandling of individual sample chips. It is pretty easy to pull the sample chips off the silicon piece after it has been flipped over. It is recommended to remove the chips now because they will fall off on their own in the next step.

¹⁷This temperature was the highest allowed at the CNF for 1165.

¹⁸Looking at a dish of water under the optical microscope might be against the cleanroom rules. If it is, do not blame me if you get in trouble for it.

deficiencies and adjust the release procedure in future batches to try to correct them.

- (f) Return sample chips to warm 1165 and leave them there for ~ 1 hour.
 - (g) Rinse the chips in 2-3 stages of IPA.
 - (h) Use a critical point dryer (CPD) to dry off the cantilevers.
 - i. Without critical point drying, the cantilevers will be deformed by surface tension when allowed to dry in ambient conditions (typically, the cantilevers are pulled down and become stuck to the chip).
 - ii. At the CNF, we used the tousimis[®] Automegasamdri[®]-915B, series B supercritical point dryer (Tousimis, Rockville, MD, USA).
 - iii. We used custom Teflon pieces to hold the sample chips in the CPD. These pieces were Teflon rectangles a few millimeters thick with one through-hole drilled into each. A square groove forming a shallow step (less than the thickness of the silicon wafer) was milled off the edge of each Teflon piece. A Teflon piece could then be screwed down onto a sample chip with the sample chip under the stepped groove.
 - iv. Thinner cantilevers suffered some attrition in the critical point dryer. We tried to position the cantilevers away from holes in the sample holder boat and away from entry and exit holes in the critical point dryer in order to shield the cantilevers from turbulence.
9. Examine chips in optical microscope (see Fig. D.9), scanning electron microscope (see Figs. D.7, D.10, D.11 and D.12), and atomic force microscope (see Fig. D.8). We avoided imaging samples with the SEM that we wanted to use to study persistent currents, but we do not think the SEM would have any serious negative effects on the persistent current samples.

D.2 Supplementary figures related to sample fabrication

In this section, we present some drawings and images related to fabrication of the cantilever-with-ring samples relevant to the discussions in Chapter 5 and the preceding section of this appendix.

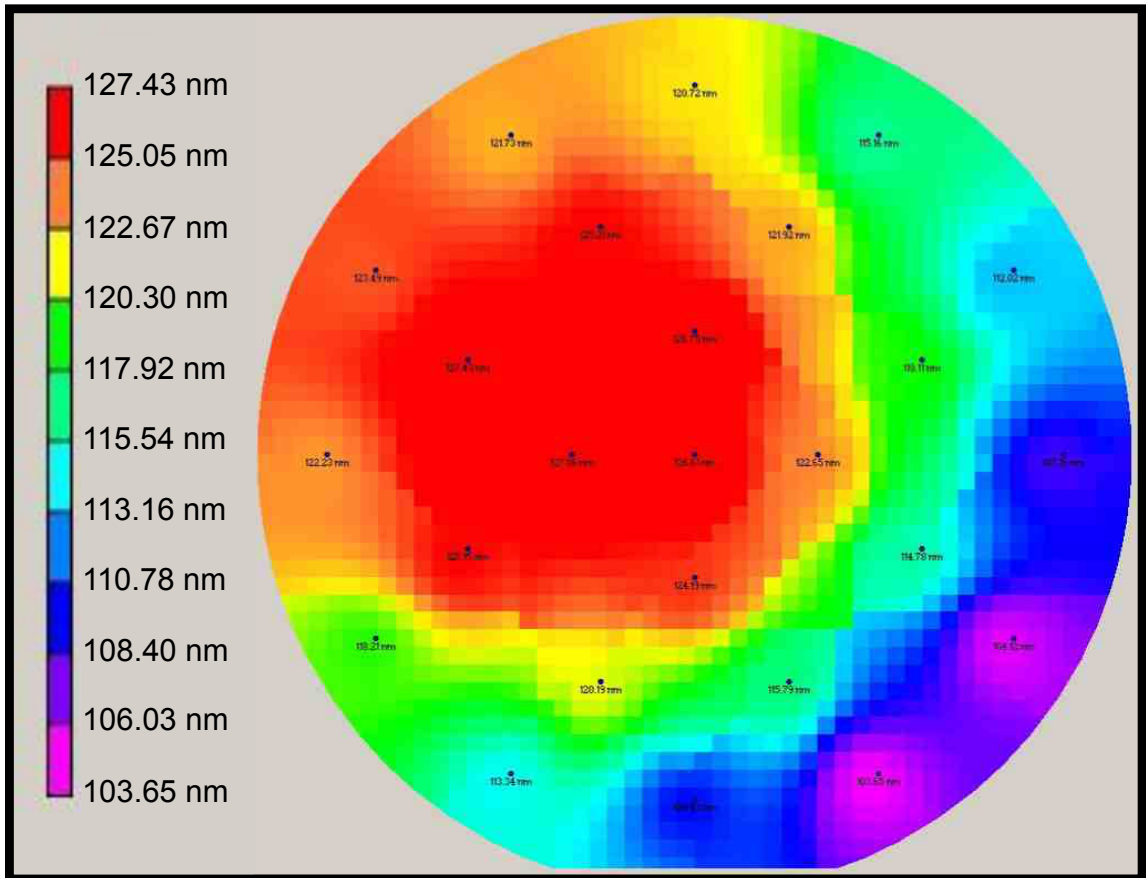


Figure D.1: Wafer map displaying typical Soitec SOI wafer uniformity. The wafer shown began with a 340 nm device layer and was thinned down to ~ 114 nm. The 25 nm spread in thickness is typical for these wafers and can actually be a bit smaller in the wafers prior to thinning. Wafers obtained from other suppliers that were thinned down from an initial thickness of $1 \mu\text{m}$ had much greater variations in their final thicknesses.

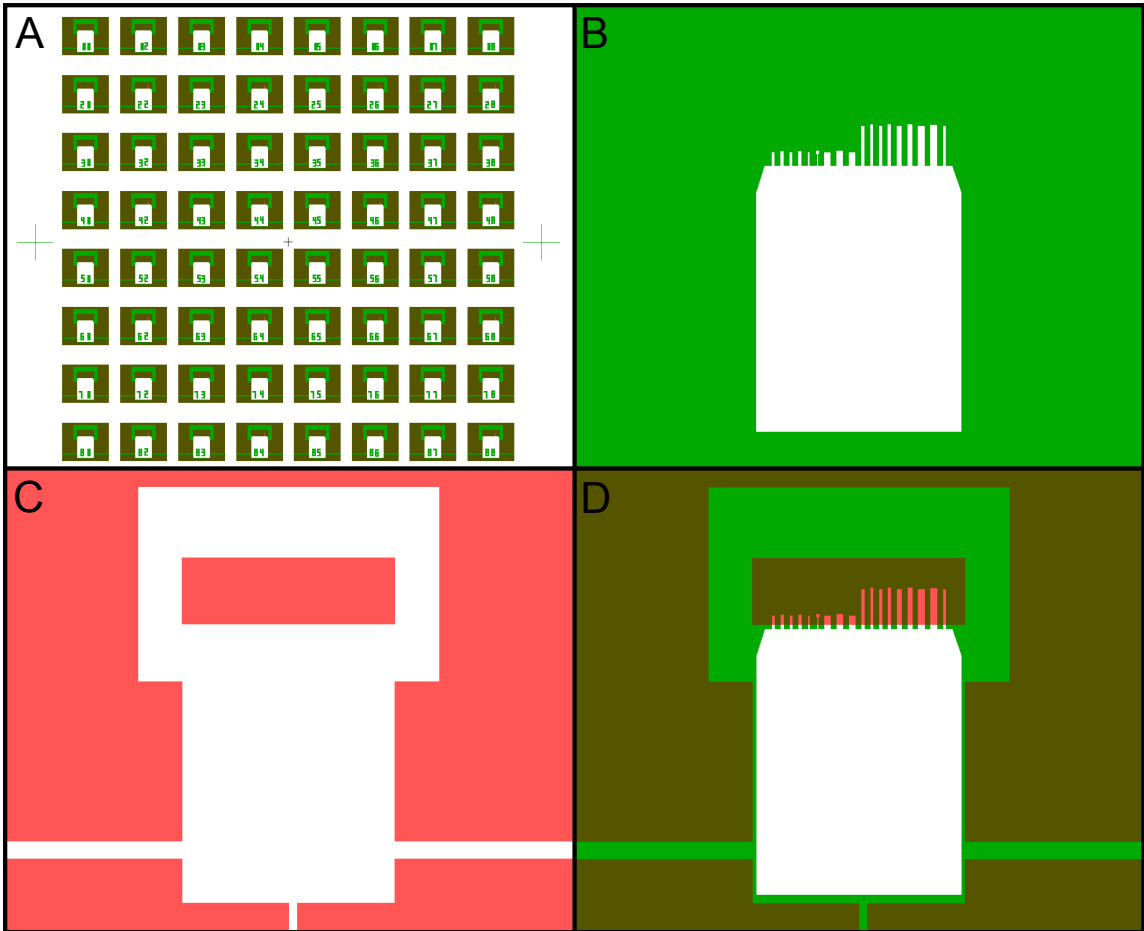


Figure D.2: Images of cantilever sample mask designs. Panel A shows the wafer die with both frontside and backside patterns overlaid in a manner similar to panel D. Global alignment marks are visible on the two sides of the pattern (see the note accompanying step 1(a)ii of Section D.1 for a suggestion for better alignment mark design). Panel B shows the frontside pattern of one sample chip. The colored area is etched away during frontside fabrication. The samples discussed in Chapter 7 were part of a chip made with this pattern. Panel C shows the backside pattern of each sample chip. Again, the colored area is etched away (during the deep reactive ion etch step). The beams near the bottom of the chip hold the chip to the wafer after this etch step. Panel D shows the frontside and backside etch masks overlaid. In later iterations of the sample mask, cantilevers were added to the top of the chip window to make more efficient use of space and increase the number of samples available in one cooldown. The cantilever bases on the frontside mask were also pulled further down the chip to make the design less susceptible to overetching of the window during the deep reactive ion etch.

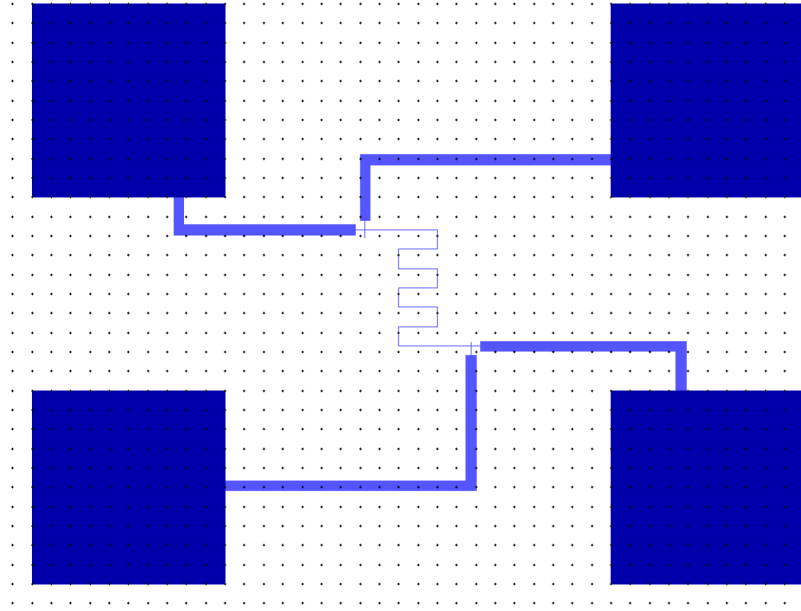


Figure D.3: Image of transport sample mask design. The large squares are $100\ \mu\text{m}$ on each side and were used for wire bonding to the transport sample (the thin wire in the center of the image). The large leads were $5\ \mu\text{m}$ wide. The sample wire shown has a linewidth of $80\ \text{nm}$ and a length of $\sim 280\ \mu\text{m}$. This mask design was used for the measurements discussed in E.

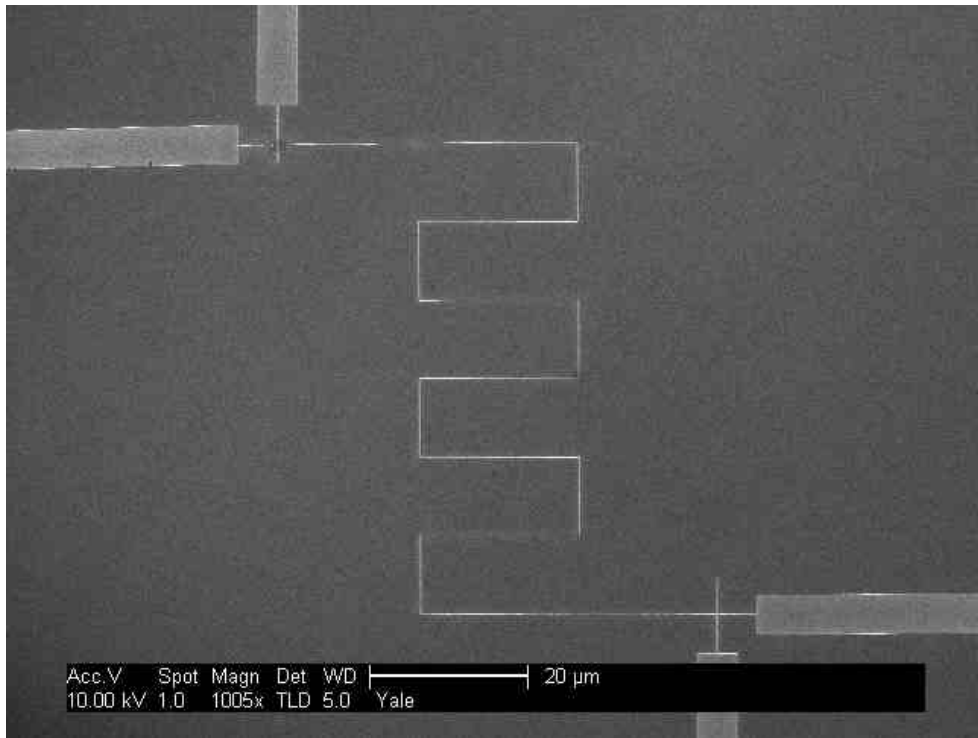


Figure D.4: Scanning electron micrograph of transport sample WL115. The figure shows the sample discussed in E with dimensions given in Table E.1. The sample mask design is shown in Fig. D.3. Magnified images of the wire are shown in Fig. D.7.

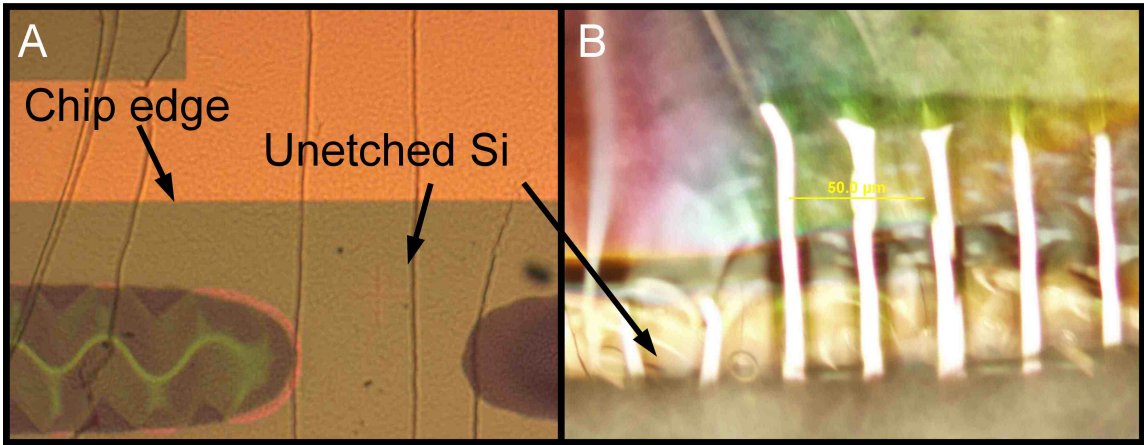


Figure D.5: Optical microscope images of underetched silicon surrounding two sample chips. The figure shows images taken during the deep reactive ion etch step of sample fabrication. Panel A shows an image taken from the frontside of the wafer while panel B displays the view from the backside. The frontside photoresist can distort the shape of the sample chip, but from both sides of the chip evidence of underetched silicon (opaque areas indicated in figure) can be made out.

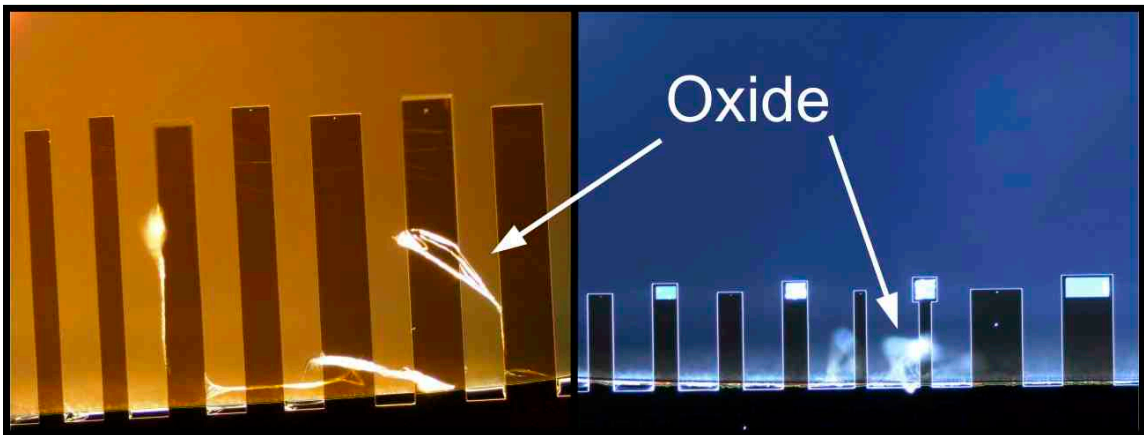


Figure D.6: Optical microscope images of residual oxide film on two cantilever sample chips. The oxide renders the affected cantilevers unusable. The residual oxide film can be minimized by blowing out any air bubbles in the sample chip windows during the BOE etch step and etching for a sufficient amount of time.

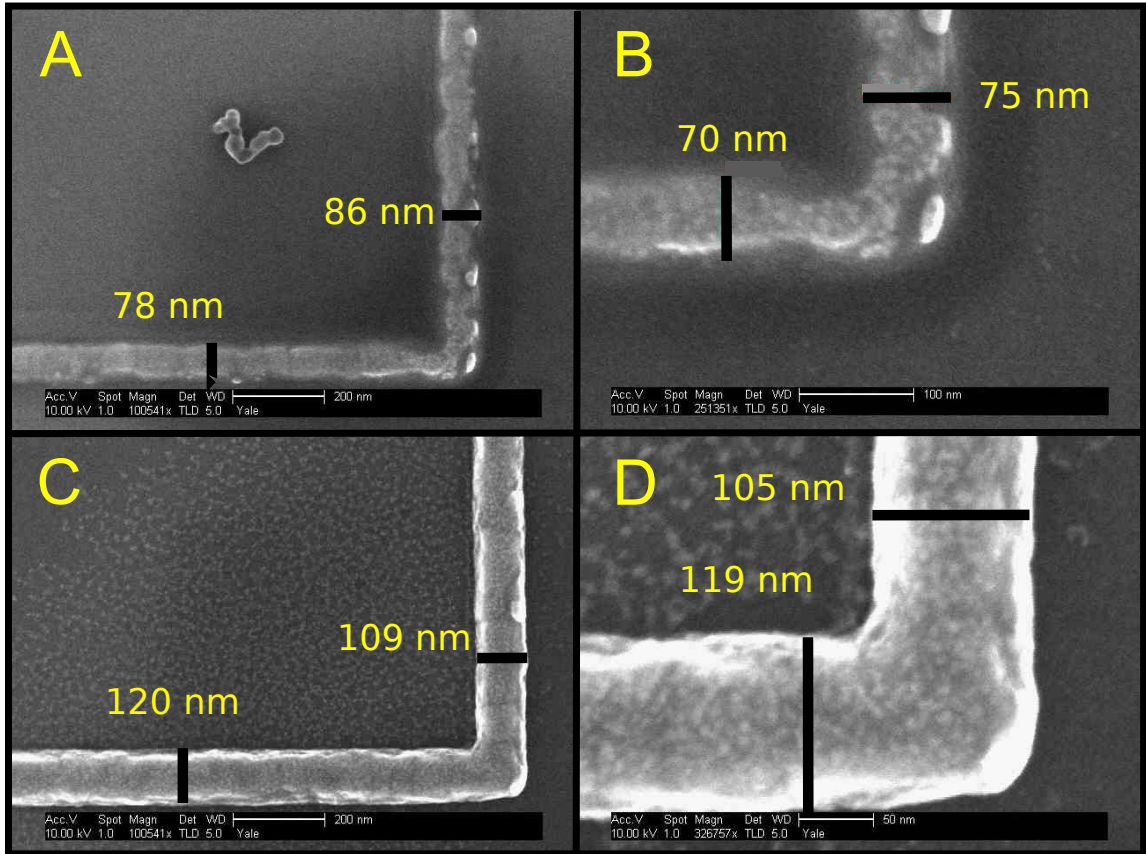


Figure D.7: Images of aluminum wires displaying characteristic linewidths of measured samples. Panels A and B show SEM images at two different magnifications of a corner of an aluminum meander with linewidth 85 ± 15 nm (see scale bars in figure). The target linewidth programmed into the e-beam tool for this sample was 65 nm, the same as samples CL11, CL14, and CL15 in Table 7.2. Panels C and D show SEM images at two different magnifications of a corner of an aluminum meander (sample WL115 in Table E.1) with linewidth 116 ± 6 nm (see scale bars in figure). The target linewidth programmed into the e-beam tool for this sample was 80 nm, the same as sample CL17 in Table 7.2. We note also that the wider linewidth sample appears to have a more uniform surface. This surface uniformity might be related to the observed overexposure in both samples.

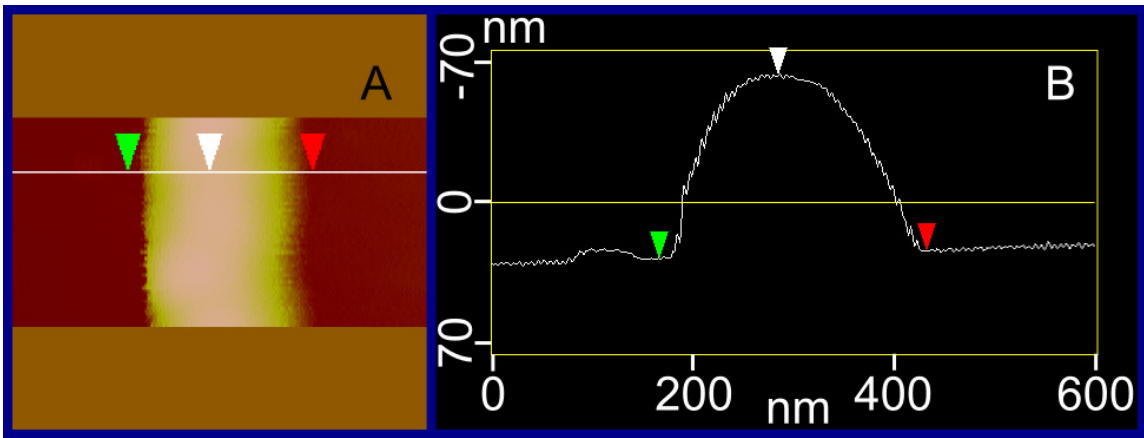


Figure D.8: Atomic force microscope analysis of persistent current sample thickness. Panel A shows a surface map of a section of the wire (sample WL115 in Table E.1) displayed in panels C and D of Fig. D.7. Panel B plots the line drawn through the sample in panel A. The height difference between the left and middle markers is 91.6 nm, and the difference between the right and middle markers is 87.6 nm. Overall, the sample height is estimated to be 90 ± 2 nm.

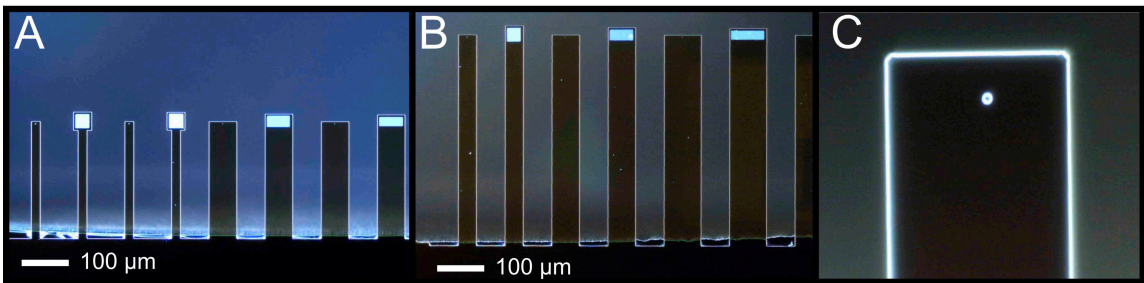


Figure D.9: Dark field optical microscope images of cantilevers. In dark-field, the arrays and single rings (panel C) are clearly visible. The cantilever in panel C has a width of $40 \mu\text{m}$ and supports a ring of diameter $1.5 \mu\text{m}$ and 115 nm linewidth.

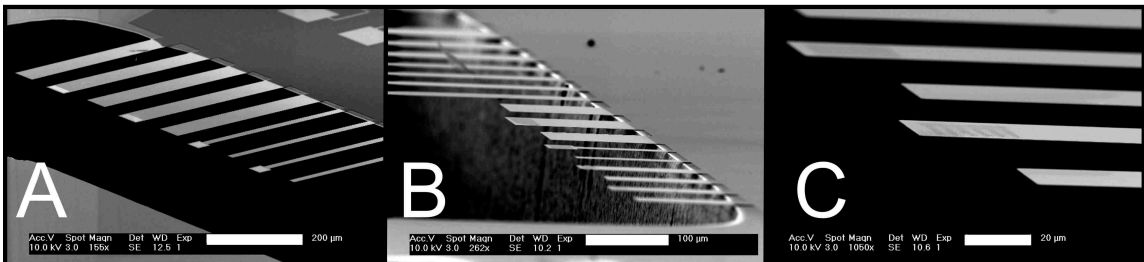


Figure D.10: Scanning electron micrographs of sample chip: side views. The three panels display successive magnifications of a sample chip viewed from the side at different angles. These images allow the extreme aspect ratio of the cantilevers to be appreciated. The scale bars for panels A, B, and C are $200 \mu\text{m}$, $100 \mu\text{m}$, and $20 \mu\text{m}$ respectively.

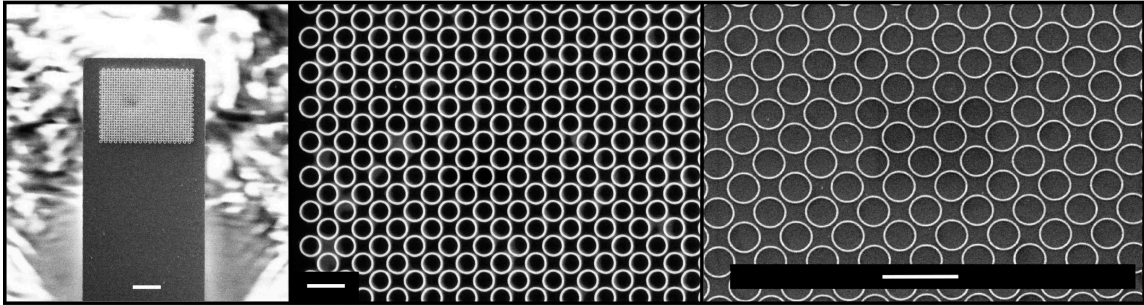


Figure D.11: Overhead scanning electron micrographs of cantilever with array of rings. Each panel was taken from a different sample. From left to right, the scale bars are $10\ \mu\text{m}$, $2\ \mu\text{m}$, and $5\ \mu\text{m}$.

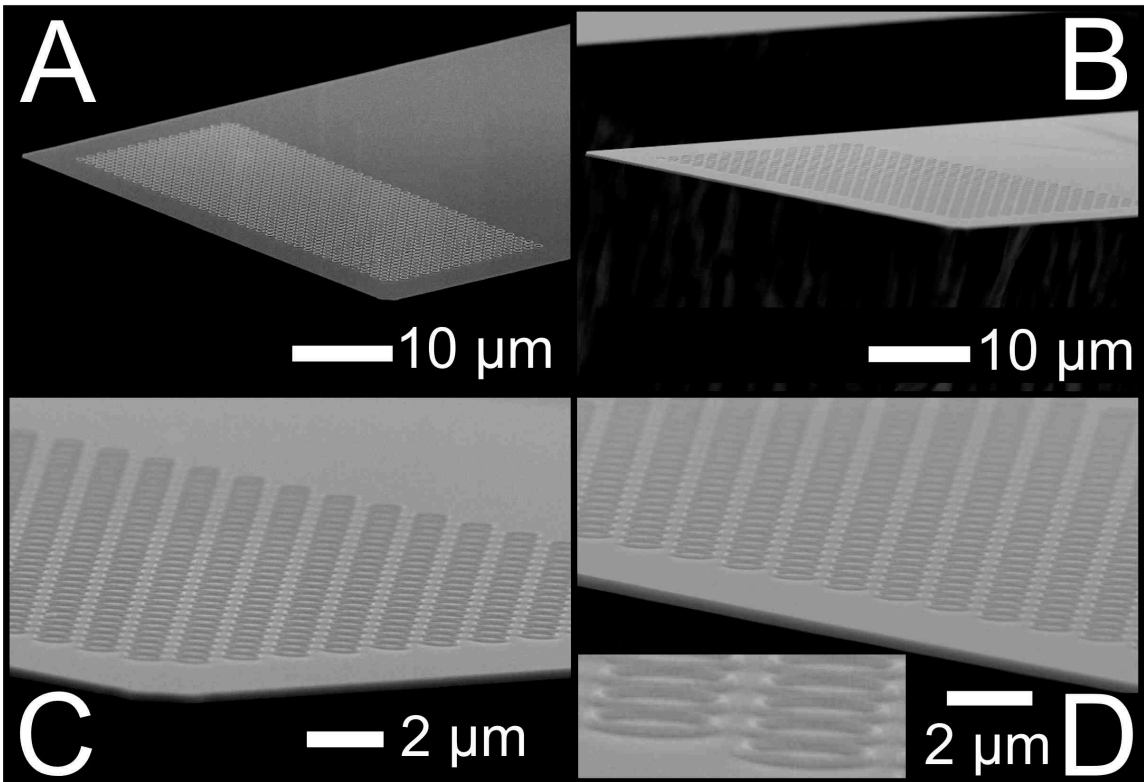


Figure D.12: Angled scanning electron micrographs of array of rings on end of cantilever. In the lower panels, the thickness of the cantilever can be discerned. The inset in panel D shows a region of the main image in panel D at three times stronger magnification.

Appendix E

Transport characterization of persistent current samples

The persistent current samples consisted of small isolated aluminum rings fabricated on the ends of pliable cantilevers less than $1\ \mu\text{m}$ thick. Because it would be nearly impossible to perform transport measurements on these rings directly, we also included wires in the same e-beam mask defining the rings and so deposited these wires onto the chip simultaneously with the rings as described in 5.1.2 and D. These wires allowed us to obtain values of the diffusion constant D , the electron phase coherence length L_ϕ and spin-orbit scattering length L_{SO} for comparison with the results from the persistent current measurements.

All measurements were performed using the bridge circuit and following the procedure detailed in Sections 5.2.3 and 5.3.2. The same sample which we refer to as WL115 (see Table E.1 and Fig. D.4), was used for all measurements.

Name	L (μm)	w (nm)	t (nm)	D_ρ (cm^2/s)	D_{B_c} (cm^2/s)	L_{SO} (μm)
WL115	289	115 ± 5	90 ± 2	259 ± 14	122 ± 5	1.10 ± 0.25

Table E.1: Dimensions and properties of sample WL115. The table gives the wire's length L , linewidth w , and thickness t . Also listed are the diffusion constant calculated from the wire's resistance D_ρ and from its superconducting critical field D_{B_c} . The measured wire resistance was $R = 285 \pm 7\ \Omega$, which corresponds to a resistivity of $\rho = 1.02 \pm 0.06 \times 10^{-8}\ \Omega\ \text{cm}$. The final entry gives the wire's spin-orbit scattering length L_{SO} , found from low field magnetoresistance measurements in the normal state. The wire's electron phase coherence length L_ϕ is not shown because it varies with temperature. At $T = 2\ \text{K}$, L_ϕ was observed to be about $5\ \mu\text{m}$. The measurements of D_ρ , D_{B_c} , L_{SO} , and L_ϕ are described in the subsequent sections.

E.1 Transport measurements of the diffusion constant

E.1.1 Resistance measurement

Sample WL115's resistivity ρ was obtained by measuring the total change in resistance R of the sample at 360 mK as the magnetic field was swept through the wire's superconducting critical field. From Fig. E.1 we take $R = 286 \pm 7 \Omega$ with the relatively large uncertainty for a resistance measurement due to the broadening of the superconducting transition. Using the dimensions of Table E.1 the corresponding resistivity $\rho = \frac{wt}{L}R$ is $(1.02 \pm 0.06) \times 10^{-8} \Omega \text{ m}$.

The diffusion constant D can be calculated using the Einstein relation

$$\rho^{-1} = e^2 \eta D \quad (\text{E.1})$$

with e the electron charge and η the electron density of states per unit volume at the Fermi level. The density of states can be written in terms of the free electron density n and the Fermi energy ε_F as $\eta = 3n/2\varepsilon_F$. With $n = 1.81 \times 10^{29} \text{ m}^{-3}$ and $\varepsilon_F = 11.5 \text{ eV}$ for aluminum [56], the wire's measured resistivity corresponds to a diffusion constant of $D_\rho = 0.0259 \pm 0.014 \text{ m}^2/\text{s}$. To avoid confusion in the following sections, we denote this value of D as D_ρ .

E.1.2 Superconducting critical field measurement

The wire's superconducting critical field B_c was measured as a function of temperature T near the wire's superconducting transition temperature T_c . In the Ginzburg Landau framework valid for a dirty superconductor near T_c , the superconducting critical field for a thin wire lying on a plane normal to the applied magnetic field can be written as

$$B_c(T) = \frac{\sqrt{12h}}{\pi e w \sqrt{D}} \sqrt{k_B(T_c - T)} \quad (\text{E.2})$$

where h is Planck's constant and k_B is the Boltzmann constant [300]. For a superconductor with known linewidth w , a measurement of B_c as a function of T allows one to determine both D and T_c .

The superconducting critical field was measured by sweeping the magnetic field at different

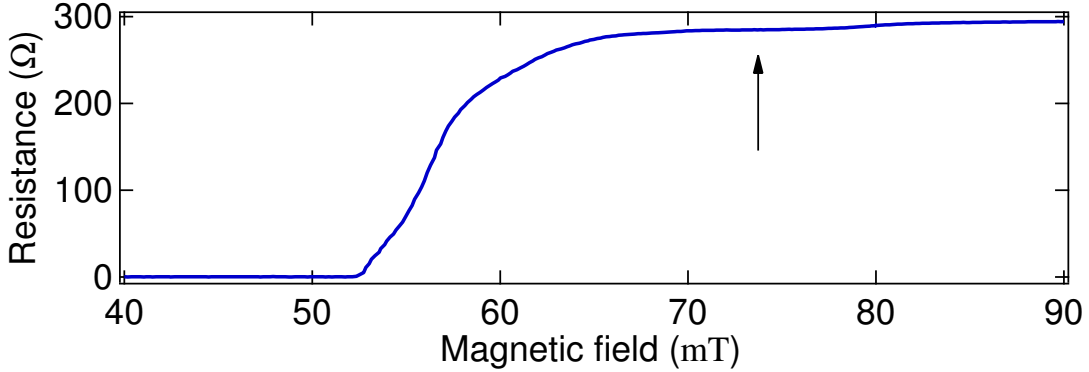


Figure E.1: Magnetic field sweep through the superconducting transition of sample WL115. Due to finite size effects, the wire’s superconducting critical field is enhanced and the superconducting to normal transition is broadened as a function of magnetic field. We take the normal state resistance R to be the value of the resistance at ~ 74 mT where resistance as a function of magnetic field is relatively flat. We assign a 7Ω uncertainty to this value of resistance to account for the ambiguity in choosing the value of the magnetic field for which the sample is fully in the normal state. The sample resistance continues to vary with magnetic field in the normal state presumably due to classical magnetoresistance. The temperature during this measurement was 365 mK, well below the superconducting transition temperature $T_c \approx 1.2$ K. The magnetic field was swept up from zero field through the superconducting transition. Due to the loss of a sample lead as described in 5.2.3, the sample resistance had to be inferred from the change in resistance across the superconducting transition rather than from a direct four point measurement.

sample temperatures and observing the change in resistance from the normal to the superconducting state. The superconducting critical field was taken to be the field at which the wire resistance reached a fixed fraction γ_R of the normal state resistance. Fig. E.2 shows the extracted values of B_c when $\gamma_R = 0.1$. A different choice for γ_R simply offsets all of the data points in Fig. E.2 by a constant amount. From Eq. E.2, it can be seen that such a shift in T will result in an equal shift in the inferred value of T_c but will not affect the determination of D . Choosing $\gamma_R = 0.5$ produces a shift of +20 mK in T_c relative to the value found for $\gamma_R = 0.1$. In addition to the measured $B_c(T)$, Fig. E.2 shows a fit to Eq. E.2. The extracted fit parameters are $T_c = 1.19$ K and $D_{B_c} = 0.0122 \pm 0.0005 \text{ m}^2/\text{s}$. We denote this value of D as D_{B_c} .

The fitted value of D_{B_c} is a factor of two smaller than that which was found for D_ρ . We note that Eq. E.2 is applicable only when the electrons’ elastic scattering length l_e is much smaller than the wire’s transverse dimensions w and t . If we use the value of D_ρ determined above for the diffusion constant D and $v_F = 2.0 \times 10^6$ m/s as the Fermi velocity of aluminum, we find a value of $l_e = 3D/v_F = 40$ nm. This indicates that $l_e \sim w, d$, and hence that Eq. E.2 is not valid. As a result we do not consider D_{B_c} to have a physical meaning and include it here only for completeness.

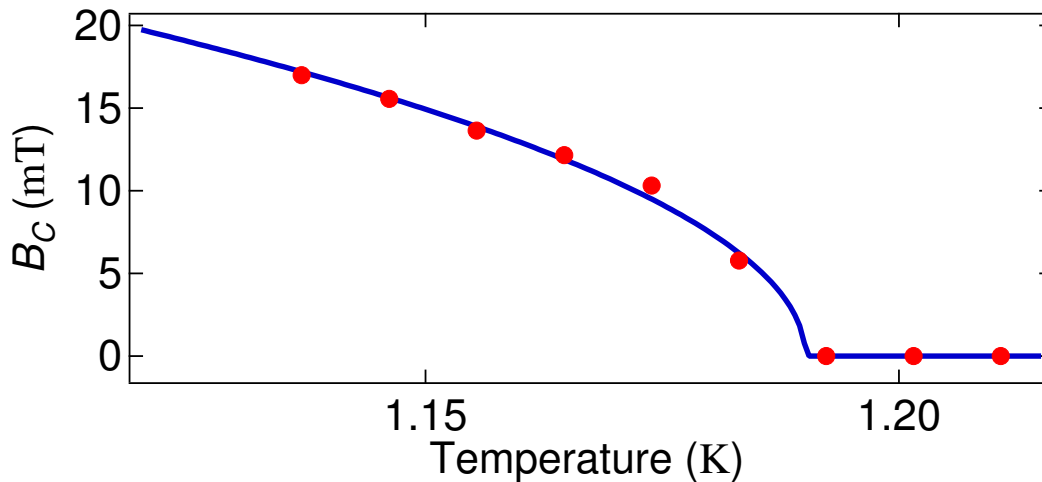


Figure E.2: Superconducting critical field of transport sample versus temperature. The superconducting critical field was extracted from measurements of resistance as a function of magnetic field (similar to the one shown in Fig. E.1) as described in the text. A fit to Eq. E.2 is also shown. Analysis of the results of the fit is provided in the text.

Discrepancies between D_{B_c} and D_ρ due to the breakdown of Eq. E.2 have been noted previously [313].

E.2 Determination of electron phase coherence length and spin-orbit scattering length from low field magnetoresistance measurements

The electron phase coherence and spin orbit scattering lengths were extracted from measurements of the magnetoresistance of sample WL115 at temperatures above T_c . As mentioned in 5.2.3, these measurements were first performed in aluminum wires two decades ago at Yale and have been reviewed previously [314].¹

E.2.1 Theoretical predictions for the magnetoresistance of thin wires

The coherent interference of time reversed trajectories leads to an increase in the probability for a quasiparticle to return to its original position and thus to an increase in electrical resistance R , a phenomenon known as weak localization. The presence of a magnetic field B suppresses weak

¹All of the equations in the next section are derived from relations given in this paper.

localization by breaking time reversal symmetry and allows a direct measure of electron phase coherence through the resulting magnetoresistance. Spin orbit scattering can also modify the spin components of time reversed paths and thus the weak localization contribution to conductivity.

The analytic form for the weak localization correction to the resistance R in a magnetic field B is given by

$$\begin{aligned} \frac{\delta R^{WL}}{R} &\equiv \frac{R(B) - R(B=0)}{R(B=0)} \\ &= \frac{3}{2} f_1\left(B, b(L_2)\right) - \frac{1}{2} f_1\left(B, b(L_\phi)\right) \end{aligned} \quad (\text{E.3})$$

where L_ϕ is electron phase coherence length and

$$L_2 = \frac{1}{\sqrt{L_\phi^{-2} + \frac{4}{3} L_{SO}^{-2}}}$$

with L_{SO} is the spin orbit scattering length. The function f_1 is given by²

$$f_1\left(B, B_1\right) = R_\square \frac{e^2}{\pi \hbar} \left(\frac{b(w)}{B_1}\right)^{1/2} \left(\left(1 + \frac{B^2}{48b(w)B_1}\right)^{-1/2} - 1 \right)$$

with $R_\square = \rho/t$ the sheet resistance per square unit of the wire. The field scale $b(w)$ is given by

$$b(l) = \frac{\hbar}{4el^2}$$

where l is in units of length. This form for the weak localization correction to the magnetoresistance is derived from a perturbative calculation and is valid for $B < 12b(w)$ (approximately 300 mT for sample WL115) [314].

Just above T_c , superconducting fluctuations result in a small, temperature dependent population of Cooper pairs, which reduce the resistance of the metal. Further above T_c , in the temperature range relevant to our magnetoresistance measurements, Cooper pairs from superconducting fluctuations are too short-lived to contribute directly to the conductivity. However, after a Cooper pair decays, the two electron quasiparticle wave functions are still correlated and provide a contribution to the conductivity, known as the Maki-Thompson contribution, which behaves similarly to the direct contribution of a Cooper pair as long as the electrons maintain phase coherence. Because all

²This definition of f_1 differs by a constant offset from the definition given in Ref. 314. This offset makes $f_1(0, B_1) = 0$.

Cooper pairs are composed of electrons in the singlet state, spin orbit scattering does not affect the Maki-Thompson contribution to the conductivity.

The correlation between quasiparticles formed by the decay of a Cooper pair has a theoretically similar description to the cooperon which describes weak localization and thus both effects have similar analytic forms for their contributions to the magnetoresistance. Specifically, the Maki-Thompson correction to the resistance obeys

$$\begin{aligned}\frac{\delta R^{MT}}{R} &\equiv \frac{R(B) - R(B=0)}{R(B=0)} \\ &= -\beta \left(\frac{T}{T_c} \right) f_1 \left(B, b(L_\phi) \right)\end{aligned}\quad (\text{E.4})$$

where $\beta(t)$ is a function introduced by Larkin which diverges logarithmically as $t \rightarrow 1$. Eq. E.4 is valid provided that $\hbar D/L_\phi^2 \ll k_B T \ln(T/T_c)$ and $B \ll (k_B T/4De) \ln(T/T_c)$.

E.2.2 Measurement and analysis of low field magnetoresistance measurements

Magnetoresistance measurements were made at a series of wire temperatures above T_c between 1.6 and 12.6 K. Because of the limitations on the validity of Eq. E.4, measurements could only be made at relatively high temperatures compared to those for which we measured persistent currents. Fig. E.3 shows magnetoresistance measurements with fits to the sum of Eqs. E.3 and E.4 for three different temperatures. The exact form of the fitting function used was

$$\frac{\delta R}{R} = \frac{\delta R^{WL}(B - B_o)}{R} + \frac{\delta R^{MT}(B - B_o)}{R} - \frac{\delta R_o}{R}$$

where B_o and δR_o correct for possible trapped flux in the solenoid applying the magnetic field and for the imbalance between the two sides of the resistance bridge at $B = 0$. Besides B_o and δR_o , the only free parameter was L_ϕ . Some preliminary analysis also varied L_{SO} as described below. In Fig. E.3, each data set and fit curve are shifted by B_o in B and $\delta R_o/R$ in $\delta R/R$ so that the extreme point of each fit curve is located at the origin.

Note the first condition, $\hbar D/L_\phi^2 \ll k_B T \ln(T/T_c)$, for the validity of Eq. E.4 is satisfied for T as low as ~ 1.35 K where $\hbar D/L_\phi^2 \approx 100 k_B T \ln(T/T_c)$. However, the second condition, $B \ll (k_B T/4De) \ln(T/T_c)$, restricts the valid range of magnetic fields to relatively small values over the

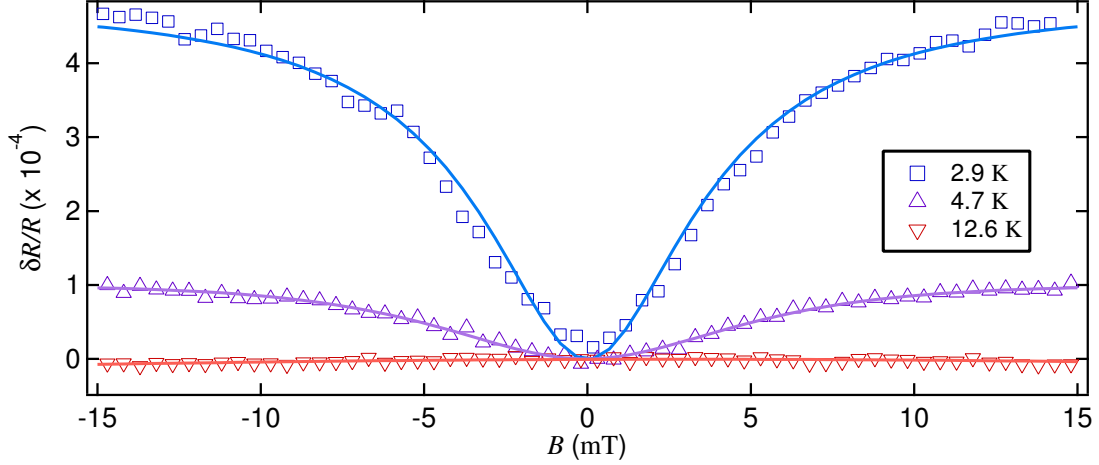


Figure E.3: Magnetoresistance of sample WL115 at several temperatures. Superconducting fluctuations (as well as spin-orbit scattering) result in a reduction in the sample resistance at zero magnetic field which is evident in the data from 2.9 K and 4.7 K. Weak localization causes an increase in resistance at zero magnetic field. The weak localization correction to the resistance dominates once the temperature is far enough from T_c for superconducting fluctuations to be sufficiently suppressed (12.6 K data). The curves in the figure shows fits to the sum of Eqs. E.3 and E.4 for L_ϕ with L_{SO} fixed to $1.1 \mu\text{m}$. Analysis of the fits is provided in the text. Each fit curve and data set has been shifted as described in the text.

range of temperatures relevant to our measurements. For 1.6 K, the second condition should be valid for fields much less than 0.43 mT. By 4 K, the field range is restricted to $\ll 6$ mT and by 10 K, $\ll 25$ mT. Due to the small size of the magnetoresistance signal for field ranges of less than ~ 3 mT, all magnetoresistance data were fit to Eq. E.4 over a field range of 15 mT, as indicated in Fig. E.3. The extracted L_ϕ does depend weakly on the size of the fit range. For example, at 2.4 K where the expression is valid for $B \ll 2$ mT, the fitted L_ϕ increases by 20% as the fit range is increased from 3 mT to 30 mT. Previous efforts have produced modifications to Eq. E.4 which allow it to be applied to wider ranges of magnetic field and temperature, but no modifications have addressed the range of temperatures and magnetic fields relevant to our magnetoresistance measurements [315, 316].

From fits to the magnetoresistance data in which both L_ϕ and L_{SO} are varied, we verified that spin-orbit scattering contributes significantly to the magnetoresistance only at higher temperatures where the Maki-Thompson contribution is small. For temperatures above 4 K, the magnetoresistance data were fit with both L_ϕ and L_{SO} as fitting parameters. In this range, L_{SO} was measured to be $1.10 \pm 0.25 \mu\text{m}$ and observed to be independent of temperature. Following this analysis, the data for the whole temperature range was fit with L_{SO} fixed to $1.1 \mu\text{m}$ and L_ϕ as the only free

parameter. In Fig. E.4, the values of L_ϕ found in this way are plotted versus temperature.

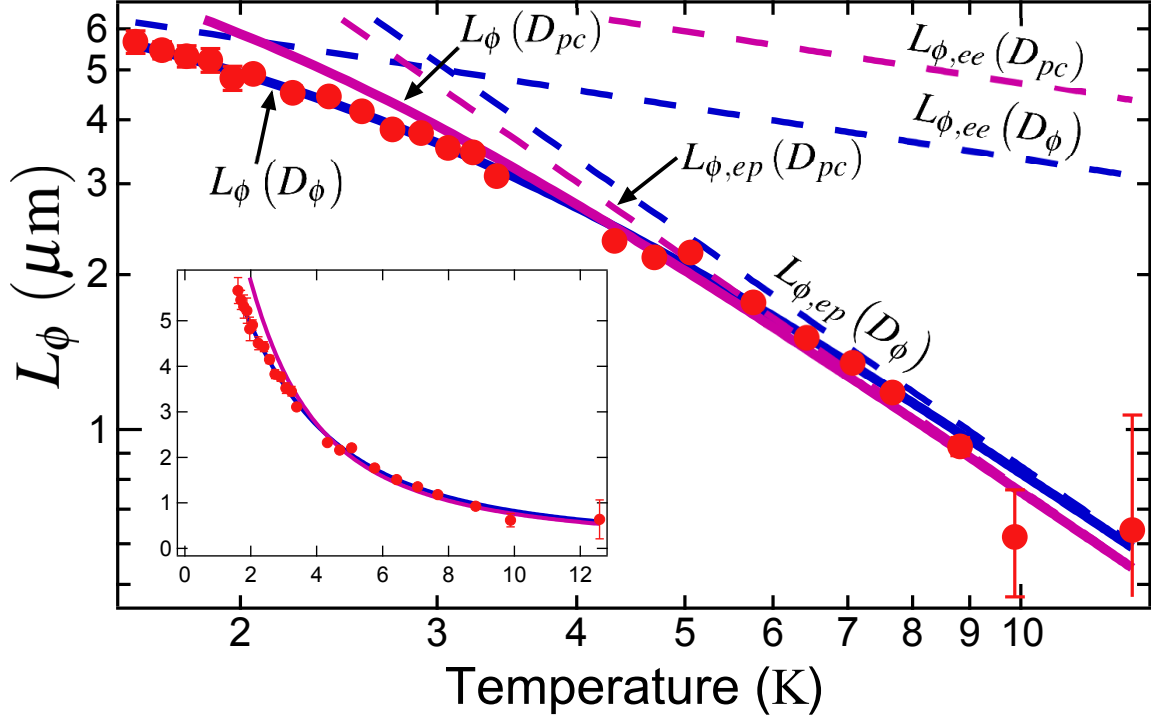


Figure E.4: Fitted electron phase coherence length for sample WL115 versus temperature. The data points were extracted from fits to the magnetoresistance as described in the text. There are also several curves shown. The curves labeled as functions of D_ϕ were obtained from fits in which the diffusion constant D was a fitting parameter (as was A_{ep}), while those labeled as functions of D_{pc} were calculated from fits in which D was fixed to the value $D_{pc} = 0.024 \text{ m}^2/\text{s}$. The dashed curves labeled $L_{\phi,ep}$ and $L_{\phi,ee}$ represent the values of L_ϕ calculated from the extracted parameters of these fits assuming $L_{\phi,ep} = \sqrt{D\tau_{ep}}$ and $L_{\phi,ee} = \sqrt{D\tau_{ee}}$, respectively. We note that the non-linearity of the data points as a function of T on the log-log scale indicates that we observe the cross-over from the regime where L_ϕ is dominated by the electron-electron interaction to that dominated by the electron-phonon interaction. A more detailed description and analysis of the fitting procedure is provided in the text. The inset shows the data on a linear scale, as well as the fitted curves $L_\phi(D_\phi)$ and $L_\phi(D_{pc})$.

The electron phase coherence length is limited to a finite value due to scattering processes in which electrons change energy. For the temperature regime of our measurements, the processes expected to be dominant are electron-phonon and electron-electron scattering. Scattering from magnetic impurities should be negligible for our high purity aluminum film (see Appendix D for a description of the aluminum source). The electron-phonon phase scattering rate τ_{ep}^{-1} follows the form

$$\tau_{ep}^{-1} = A_{ep}T^3 \quad (\text{E.5})$$

The electron phonon coefficient has previously been reported as $A_{ep} = 9.1 \times 10^6 \text{ s}^{-1}\text{K}^{-3}$ for bulk

aluminum [314, 317]. For the conditions of our measurement, the electron-electron phase scattering rate τ_{ee}^{-1} was observed in Ref. [311, 318] to be dominated by the process of multiple collisions with small energy transfers and to follow the form³

$$\begin{aligned}\tau_{ee}^{-1} &= A_{ee}T^{2/3} \\ &= \left(\frac{R_{\square} e^2 k_B \sqrt{D}}{2\sqrt{2}\hbar^2 w} \right)^{2/3} T^{2/3}.\end{aligned}\tag{E.6}$$

The total electron phase breaking rate τ_{ϕ}^{-1} is the sum of these two rates, $\tau_{\phi}^{-1} = \tau_{ep}^{-1} + \tau_{ee}^{-1}$. The blue lines in Fig. E.4 show a fit to the measured $L_{\phi}(T)$ using Eqs. E.5 and E.6 and the relation $L_{\phi} = \sqrt{D\tau_{\phi}}$ with A_{ep} and D as the free parameters. We denote this fitted value of D as D_{ϕ} . The fitted values are $A_{ep} = (1.21 \pm 0.07) \times 10^7 \text{ s}^{-1}\text{K}^{-3}$ and $D_{\phi} = 0.0044 \pm 0.0002 \text{ m}^2/\text{s}$.

While D_{ϕ} differs from D_{ρ} and D_{pc} , the value of D extracted from the persistent current measurements, we note that L_{ϕ} is roughly proportional to $D^{1/2}$ and so provides a relatively weak constraint on D . To illustrate this point, Fig. E.4 also show fits (purple lines) with D_{ϕ} fixed to $0.024 \text{ m}^2/\text{s}$ (the value of D_{pc} for the persistent current sample with comparable linewidth to WL115) and A_{ep} as the only fitting parameter. The best fit value of A_{ep} was $(4.09 \pm 0.04) \times 10^7 \text{ s}^{-1}\text{K}^{-3}$ in this case. As can be seen from Fig. E.4, $D_{\phi} = D_{pc}$ provides reasonable agreement with the data, producing slightly higher values of L_{ϕ} at the lowest temperatures. We note that using the bulk value for A_{ep} rather than our fitted values would also result in larger values for L_{ϕ} . These two predictions of larger magnitudes of L_{ϕ} are consistent with the findings of Refs. [315, 316] that fitting the magnetoresistance data over a larger magnetic field range than that specified for Eq. E.4 results in lower magnitudes for the extracted L_{ϕ} . Thus, the values in Fig. E.4 can be taken as rough lower bounds on $L_{\phi}(T)$. As our primary intent in measuring $L_{\phi}(T)$ is to demonstrate that $L_{\phi}(T)$ is greater than the circumference of the persistent current rings $L = 1.9$ to $5.0 \mu\text{m}$, such an interpretation is sufficient for our needs.

³There appears to be some disagreement in the literature over the numerical prefactor multiplying D in this expression. Compare Refs. 311, 318–320. The expression used here produces the largest value of D .

Appendix F

Measurements of persistent currents in the superconducting state

We measured persistent currents with the rings in the superconducting state as well as the normal state. Measurements of the superconducting rings provided a method of checking the quality of the deposited aluminum and the angle between the cantilever.

We analyze the measurements of the superconducting state using the Ginzburg-Landau theory for superconductivity [300]. As the analysis serves mainly a diagnostic role, we make use of some approximations that simplify the results notationally. A more accurate numerical analysis is possible. The cases of a one dimensional ring [300] and a ring with finite linewidth [200] in a magnetic field perpendicular to the ring plane have been considered previously. Here we modify these results to account for the angle between the applied magnetic field and the plane of the ring.

In the Ginzburg-Landau theory, the free energy density of the superconductor is written as

$$f = f_{n0} + \alpha |\psi|^2 + \frac{\beta}{2} |\psi|^4 + \frac{1}{4m} \left| \left(\frac{\hbar}{i} \nabla + 2e\mathbf{A} \right) \psi \right|^2$$

with

$$\alpha = -\frac{\hbar^2}{4m\xi^2}$$

and

$$\beta = \frac{\mu_0 e^2 \hbar^2}{2} \frac{\lambda_{\text{eff}}^2}{\xi^2}.$$

Here f_{n0} is the free energy density of the normal state, ψ is the complex order parameter, m and e are the mass and charge of the electron, ϕ_0 is the normal state flux quantum h/e , μ_0 is the magnetic permeability of the superconductor, λ_{eff} is the effective penetration depth (see Eq. 3.119 of Ref. 300), and ξ is the Ginzburg-Landau coherence length. If the value of ψ would lead to $f > f_{n0}$, then ψ is replaced with 0 and the superconductor is taken to be in the normal state. The total free energy $F = \int d^3\mathbf{r} f$ of the superconductor is found by integrating f over the volume of the superconductor.

The current density \mathbf{J} of the superconductor is given by

$$\mathbf{J} = -\frac{e}{m} |\psi|^2 (\hbar \nabla (\arg \psi) + 2e\mathbf{A}). \quad (\text{F.1})$$

For a superconductor surrounded by an insulator, the boundary condition ensuring that no current leaves the superconductor is

$$\tilde{\mathbf{n}} \cdot \left(\frac{\hbar}{i} \nabla - 2e\mathbf{A} \right) \psi = 0 \quad (\text{F.2})$$

where $\tilde{\mathbf{n}}$ is a unit vector normal to the surface of the superconductor. To determine the current in a superconductor, one finds the order parameter ψ which satisfies the boundary conditions and minimizes the free energy F . Then this ψ is plugged into Eq. F.1 above.

We now consider a superconducting ring with radius R , thickness t , and linewidth w centered at the origin so that its axis of rotational symmetry is the z -axis. A magnetic field \mathbf{B} is applied at an angle θ relative to the z -axis in the xz -plane. We decompose the magnetic field into perpendicular $\mathbf{B}_\perp = B \sin \theta \tilde{\mathbf{z}}$ and in-plane $\mathbf{B}_M = B \cos \theta \tilde{\mathbf{x}}$ components.

The boundary conditions (Eq. F.2) complicate the form of ψ . To simplify the derivation, we will treat \mathbf{B}_\perp exactly but will use the toroidal field model introduced in Section 2.3.2.1 to account for \mathbf{B}_M . Following Eq. 2.6, we write the vector potential \mathbf{A}_\perp associated with \mathbf{B}_\perp in cylindrical coordinates (r, a, z) (with a the azimuthal coordinate) as

$$\mathbf{A}_\perp = \frac{B_\perp r}{2} \tilde{\mathbf{a}}.$$

For the toroidal field, we imagine breaking the ring and unbending it to form a rectangular bar of length $2\pi R$. Then we replace the rectangular cross-section with a circular one of radius $\sqrt{wt/\pi}$. The volume $2\pi wtR$ of this cylinder is then the same as that of the ring. The vector potential \mathbf{A}_M

associated with \mathbf{B}_M can be written as

$$\mathbf{A}_M = \frac{B_M r_M}{2} \tilde{\mathbf{a}}_M$$

where (r_M, a_M, z_M) are the cylindrical coordinates corresponding to the cylinder created by transforming the ring in the manner just described with the z_M -axis running down the center of the cylinder.

With these conventions, both \mathbf{A}_\perp and \mathbf{A}_M are everywhere parallel to the surface of the ring. We can then use the form of the order parameter found previously in Refs. 300 and 200, namely

$$\psi = |\psi| e^{ina}$$

where n is an integer so that ψ is single valued in a . Because $\tilde{\mathbf{n}} \cdot \nabla \psi = 0$ over the surface of the ring, the boundary conditions (Eq. F.2) are satisfied. Integrating the free energy density over the ring with this form for ψ , one finds

$$F \approx F_{n0} + V \left(\alpha |\psi|^2 + \frac{\beta}{2} |\psi|^4 \right) + \frac{|\psi|^2}{4m} \left(2\pi t \left(\hbar^2 n^2 \left(\frac{w}{R} + \frac{w^3}{12R^3} \right) + \hbar n e B_\perp R w + e^2 B_\perp^2 \left(R^3 w + \frac{1}{4} R w^3 \right) \right) + e^2 \gamma^2 B_M^2 w^2 t^2 R \right)$$

where F_{n0} is the integral of f_{n0} over the ring and, as in Section 7.3.2.4, we multiply B_M by a geometrical factor γ to account for the difference between the toroidal field model and the field configuration of the experiment. In performing the integration, it was assumed that $w \ll R$. In order to drop higher order terms

To find the value of $|\psi|$ that minimizes F , we solve $\partial_{|\psi|} F = 0$. Using the abbreviated form

$$F = C + D |\psi|^2 + E |\psi|^4,$$

the free energy is minimized for

$$|\psi|^2 = -\frac{D}{2E}.$$

With this form of $|\psi|^2$, the free energy can be written as

$$F = C - \frac{D^2}{4E}.$$

Explicitly, the coefficients C , D and E are

$$C = F_{n0} + V \frac{B^2}{2\mu_0}$$

$$D = V \left(\alpha + \frac{\hbar^2}{4mR^2} \left(\left(n + \frac{\phi_\perp}{\phi_0/2} \right)^2 + \frac{w^2}{4R^2} \left(\frac{n^2}{3} + \frac{\phi_\perp^2}{(\phi_0/2)^2} \right) + \frac{\pi \gamma^2 B_M^2 R^2 w t}{2 (\phi_0/2)^2} \right) \right)$$

$$E = V \frac{\beta}{2}$$

where $\phi_\perp = \pi R^2 B_\perp$ is the flux threading the mean radius of the ring. One may then evaluate F for each value of n to determine the value that minimizes F . Integrating $\tilde{\mathbf{a}} \cdot \mathbf{J}$ (see Eq. F.1) over the ring cross-section gives the current in the ring as

$$I = \frac{e\hbar}{m\beta} \frac{1}{R} \frac{wt}{R} \left(n \left(1 + \frac{w^2}{12R^2} \right) + \frac{\phi_\perp}{\phi_0/2} \right) \times \left(\alpha + \frac{\hbar^2}{4mR^2} \left(\left(n + \frac{\phi_\perp}{\phi_0/2} \right)^2 + \frac{w^2}{4R^2} \left(\frac{n^2}{3} + \frac{\phi_\perp^2}{(\phi_0/2)^2} \right) + \frac{\pi \gamma^2 B_T^2 R^2 w t}{2 (\phi_0/2)^2} \right) \right).$$

In the limit of $w \ll R$ and $B_T \rightarrow 0$, the free energy and thus current become periodic in ϕ_\perp with period $\phi_0/2$. Additionally, for $\xi \ll R$ so that α dominates the second line in the expression for I , the current takes on a sawtooth shape similar to I_{N+0} of Fig. 2.4.

In Section 4.3, the frequency shift of the cantilever was found to be proportional to the second derivative of the energy with respect to angle θ . For the superconducting ring the frequency shift is then

$$\begin{aligned} \Delta f_{sc} &= N \frac{f_0}{2k} \left(\frac{\alpha_m(z_r)}{l} \right)^2 \frac{\partial^2 F}{\partial \theta^2} \\ &= -N \frac{(\phi_0/2)^2 V}{16\pi^2 \mu_0 \lambda_{\text{eff}}^2} \frac{f_0}{2k} \left(\frac{\alpha_m(z_r)}{l} \right)^2 \\ &\quad \times \frac{\partial^2}{\partial \theta^2} \left(-\frac{1}{\xi} + \frac{\xi}{R^2} \left(\left(n + \frac{\phi_\perp}{\phi_0/2} \right)^2 + \frac{w^2}{4R^2} \left(\frac{n^2}{3} + \frac{\phi_\perp^2}{(\phi_0/2)^2} \right) + \frac{\pi \gamma^2 B_M^2 R^2 w t}{2 (\phi_0/2)^2} \right) \right)^2 \quad (\text{F.3}) \end{aligned}$$

where N is the number of rings in the array and f_0 , k , $\alpha_m(z_r)$, and l are properties of the cantilever defined in Section 4.3. To evaluate this expression, one must restore the dependence on θ for $\phi_\perp = \pi R^2 B \sin \theta$ and $B_M = B \cos \theta$. We do not write the full form for the frequency shift Δf_{sc} because it is very long. When measuring a superconducting sample, the unknown parameters in the expression for Δf_{sc} are γ , n , λ_{eff} , and ξ . The geometrical factor γ adjusts the overall shape

Sample	l (μm)	w (μm)	f_0 (Hz)	k (mN/m)	Q ($\times 10^5$)
CL10	439	40	2287	1.1	1.2

Table F.1: Cantilever parameters of superconducting ring sample. The cantilever width w was measured optically, and the cantilever resonant frequency f_0 was measured using the detection arrangement described in Chapter 5. The cantilever thickness t was measured to be 340 nm using the instrument mentioned in Section D.1. The cantilever length l and spring constant k were calculated using the values from these measurements and Eqs. 4.5 and 4.7. The cantilever length measured optically was not used due to uncertainty caused by over-etching of the silicon handle layer on which the cantilever was mounted. The listed cantilever quality factor Q is a typical value. The quality factor varied with temperature and over time. More details about the cantilevers are given in Sections 5.1.2 and D.1.

Sample	L (μm)	w_r (nm)	t_r (nm)	N
CL10	5.0	85	90	1

Table F.2: Superconducting ring specifications. The mean circumference L and linewidth w_r of the aluminum ring were measured by a scanning electron microscope. The thickness t_r of the deposited aluminum was measured by an atomic force microscope. The ring was located $5 \mu\text{m}$ from the cantilever tip and was centered along the cantilever’s width dimension.

of the curve $\Delta f_{sc}(B)$ and affects the location of the transition to the normal state. The winding number n must always be an integer and jumps discontinuously as a function of magnetic field B , roughly at half integral values of $\phi_{\perp}/(\phi_0/2)$ where the value of n minimizing F changes. The penetration depth λ_{eff} scales the entire Δf_{sc} curve. The coherence length ξ sets the critical field at which superconductivity is quenched.

A frequency shift due to the rings’ superconductivity was observed at low magnetic field for each sample listed in Tables 7.1 and 7.2. For measurements of superconducting rings, the frequency shift signal Δf_{sc} increases with ring radius R . For this reason, we present representative measurements of the superconducting state from a sample with the largest ring size. For simplicity, we consider sample CL10 which contained a single ring with the same dimensions as the rings of sample CL11. The dimensions of sample CL10 are given in Tables F.1 and F.2.

The frequency shift observed for sample CL10 at $\theta_0 = 6^\circ$ and $T = 1.05 \text{ mK}$ is shown in Fig. F.1. This measurement was taken as the magnetic field was stepped up from below -60 mT to above 60 mT . The frequency shift exhibits regular jumps at values of the magnetic field at which the winding number n increases by 1 as the state of the ring jumps to a state with a lower free energy $F(B, n)$. In Fig. F.1, a triangle is located along the $\Delta f_{sc} = 0$ line at the magnetic field

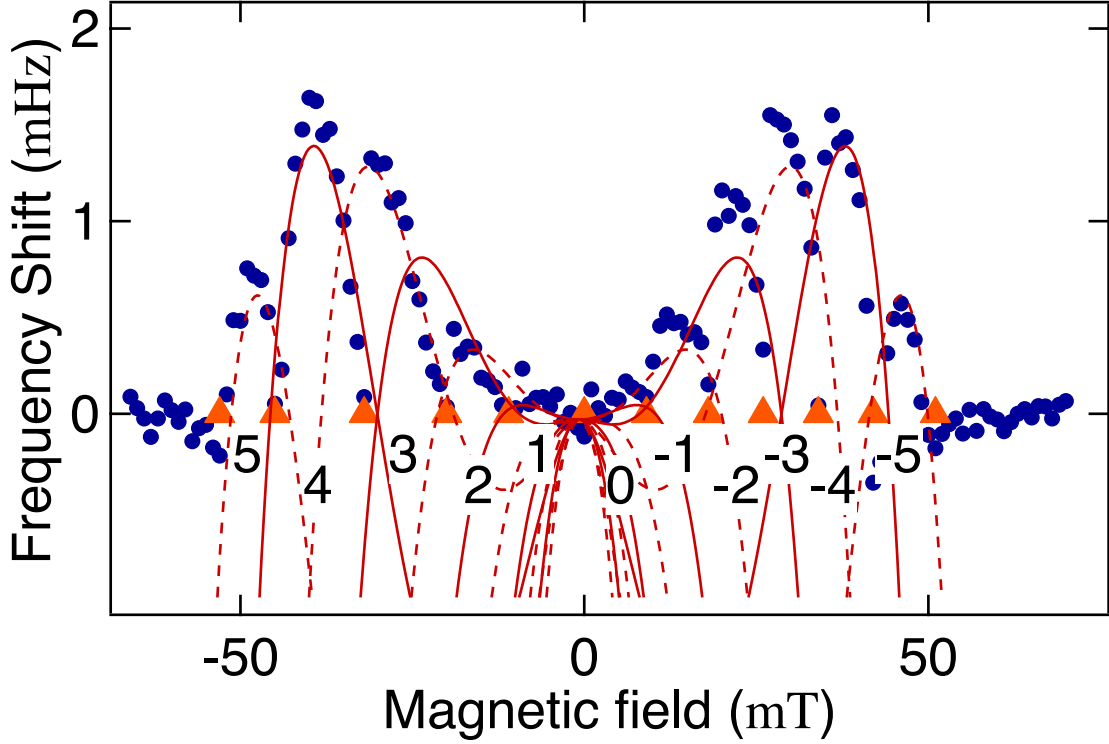


Figure F.1: Frequency shift due to superconductivity in sample CL10. The cantilever frequency was measured at $\theta_0 = 6^\circ$ and $T = 1.05$ K while sweeping the magnetic field from $B < -60$ mT to $B > 60$ mT. The frequency shift (dots) was found by subtracting a fourth order polynomial to the trace of frequency versus magnetic field. The polynomial coefficients were determined by fitting the cantilever frequency in the magnetic field regions where the frequency shift was expected to be negligible ($|B| \lesssim 5$ mT and $|B| \gtrsim 55$ mT). A series of jumps is visible in the measured frequency shift. These jumps occur at points in B (triangles) where the winding number n changes by 1. The magnetic field regions between jumps are labeled by the value of n that best matches the observed frequency shift. The curves representing $\Delta f_{sc}(B, n)$ are plotted for each of these values of n and for the values of λ_{eff} , ξ , and γ found with the fit shown in Fig. F.2. For even n , Δf_{sc} is drawn with a solid curve, while for odd n the curve is dashed.

value of each jump. The frequency shift is clearly asymmetric about $B = 0$ T, indicating that the ring experiences some metastability and that the winding number n does not change at exactly the value of B at which $F(B, n) = F(B, n - 1)$.¹

We use Eq. F.3 to analyze the frequency shift Δf_{sc} . In order to account for the observed metastability of the superconducting state, the value of n was held fixed over each region of the magnetic field between the observed jumps in Δf_{sc} . At each jump in Δf_{sc} , n was incremented by 1. The particular values of n used were chosen to provide the best match to the data. In practice,

¹We focus on a single ring sample in part because it is possible that the locations of the jumps in n could vary from ring to ring in the array samples.

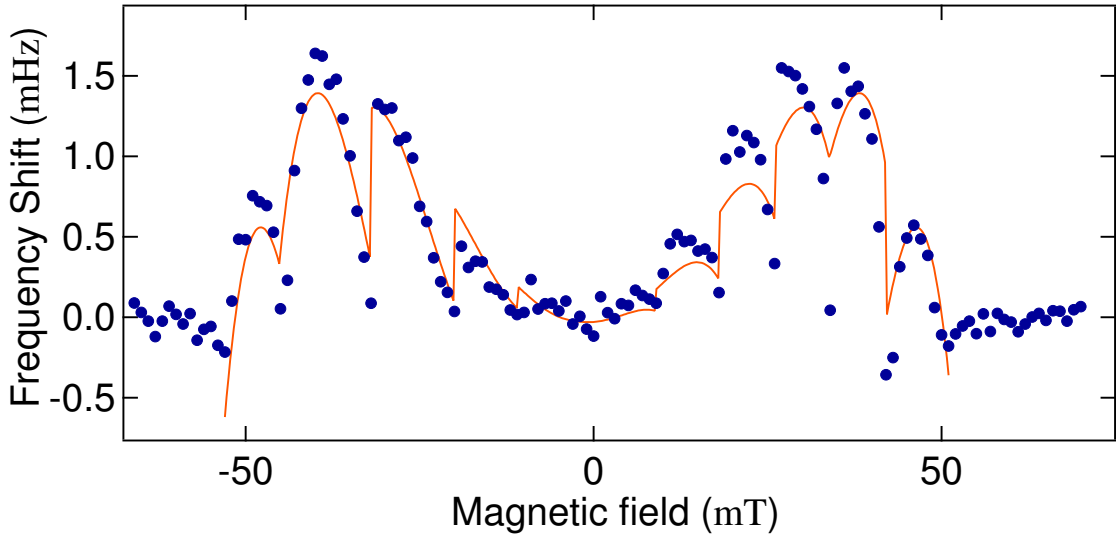


Figure F.2: Fit to frequency shift of sample CL10 at low magnetic field. The same measured frequency shift (dots) as shown in Fig. F.1 is reproduced here. A fit (solid curve) to Eq. F.3 is also shown. During the fitting routine, the value of n was held to integer values that varied with magnetic field region as indicated in Fig. F.1. The geometric factor γ was held to 1 while λ_{eff} and ξ were varied. The fitting routine also allowed for overall offsets in the frequency shift ($-30 \mu\text{Hz}$) and the magnetic field (-0.7 mT). The best fit coefficients, $\lambda_{\text{eff}} = 145 \text{ nm}$ and $\xi = 366 \text{ nm}$, are in reasonable agreement with previous measurements of aluminum rings. The deviations of the observed frequency shift from the fitted curve could be due to corrections to the Ginzburg-Landau model away from T_c .

the set of values of n was always symmetric about $n = 0$ (i.e. if $+n$ were present, so was $-n$). The region of field between each jump in Δf_{sc} is labeled by the appropriate value for n in Fig. F.1. The frequency shift curves $\Delta f_{sc}(B, n)$ associated with each n are also shown in Fig. F.1 for a particular set of λ_{eff} , ξ , and γ .

In Fig. F.2, the measured frequency shift for sample CL10 at $\theta_0 = 6^\circ$ and $T = 1.05 \text{ mK}$ is shown again along with a fit to Eq. F.3. During the fitting routine, the value of n was fixed to the values shown in Fig. F.1 as discussed above. At $\theta_0 = 6^\circ$, the frequency shift Δf_{sc} has a similar dependence on the coherence length ξ and the geometrical factor γ . To achieve a reliable fit, the geometrical factor was fixed to $\gamma = 1$ because it is expected to be of order unity. The fitted superconductor parameters were $\lambda_{\text{eff}} = 145 \text{ nm}$ and $\xi = 366 \text{ nm}$. These values are in reasonable agreement with those found in previous measurements of superconducting aluminum rings [200].

In Fig. F.3, the frequency shift observed for sample CL10 at $\theta_0 = 6^\circ$ is shown at a series of temperatures between 300 mK and 1.2 K. The strength of the signal decreases with temperature and appears to vanish near $T \approx 1.18 \text{ K}$ as expected for aluminum (see Fig. 6.4). Similar curves

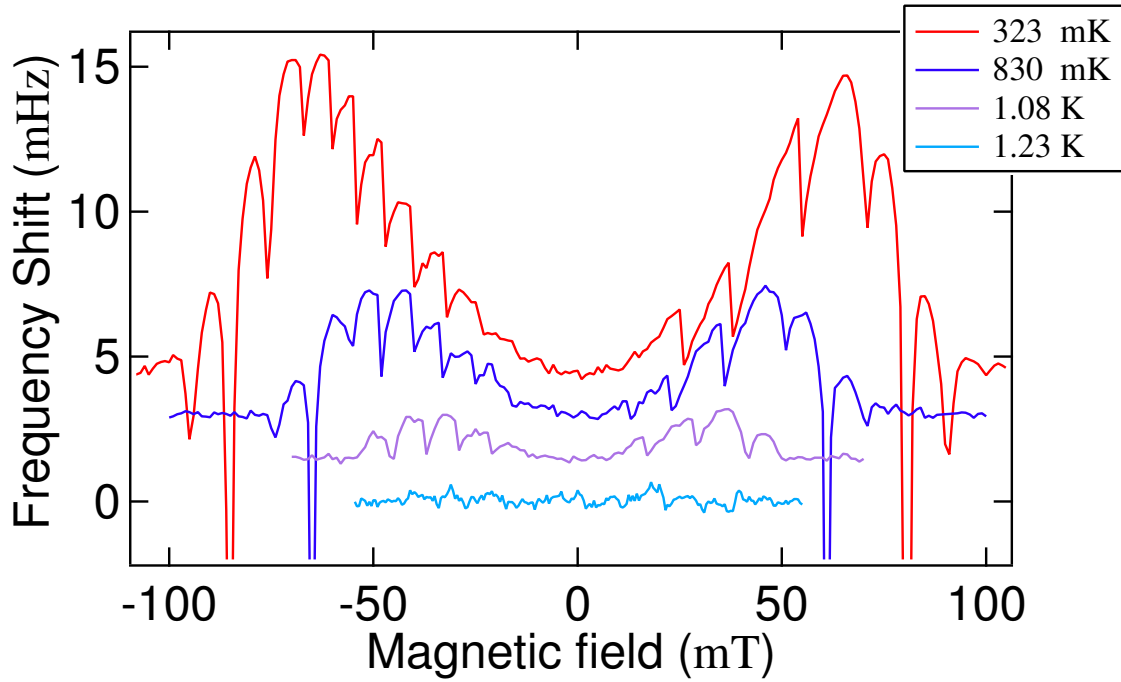


Figure F.3: Frequency shift observed for sample CL10 in the superconducting state at several temperatures. All curves were recorded at $\theta_0 = 6^\circ$ by first sweeping the magnetic field above 100 mT and then stepping it down while recording the cantilever frequency. Smooth backgrounds were removed by the method described for the measurement shown in Fig. F.1. The curves are each offset from each other by 1.5 mT. In descending order the curves represent measurements taken at $T = 0.32, 0.83, 1.08,$ and 1.23 K. As expected, the strength of the superconducting signal and the magnitude of the critical magnetic field decrease with temperature and vanish near $T \approx 1.2$ K.

were observed for each sample listed in Tables 7.1 and 7.2. The magnetic field scale of the jumps in the frequency shift was observed to change with ring size, with the smallest rings exhibiting only one or two jumps before going normal.

Appendix G

Cumulants of the persistent current in arrays of rings

We present a brief analysis of the statistical distribution of the persistent current based on the measurements of samples CL15 and CL17 at $\theta_0 = 45^\circ$. The sample parameters are given in Tables 7.1 and 7.2. The full data sets for these measurements are shown in Section 7.3.3. As discussed in Section 7.3.1, we measure the total current summed over the many rings making up the array on each of these samples. By the central limit theorem, we expect the total current in each sample to follow the normal distribution regardless of the underlying distribution of the persistent current for a single ring. Thus, the analysis presented here is mostly a check of the accuracy of our measurement. To test the predictions regarding the single ring distribution discussed in Section 3.1, more measurements of samples with single rings must be performed.

We analyze the two quadratures of the persistent current signal. The quadratures are found by making use of the Hilbert transform. To calculate the Hilbert transform $I_H(B)$ of a signal $I(B)$, one finds the Fourier transform

$$I(\beta) = \int_{-\infty}^{\infty} dB I(B) e^{-2\pi i \beta B},$$

defines

$$I_H(\beta) = \begin{cases} I(\beta) & \beta > 0 \\ 0 & \beta = 0 \\ -I(\beta) & \beta < 0 \end{cases},$$

and then finds the inverse Fourier transform

$$I_H(B) = \int_{-\infty}^{\infty} d\beta I_H(\beta) e^{2\pi i\beta B}.$$

When a signal $I(B) = I_0 \sin(2\pi\beta_0 B)$ is a monotone oscillation, the Hilbert transform $I_H(B) = I_0 \cos(2\pi\beta_0 B)$ is also a monotone oscillation with the same frequency but shifted in phase. In this case, the amplitude of the oscillation can be found by taking $\sqrt{I^2(B) + I_H^2(B)} = I_0$. Similarly, a signal possessing a slowly varying amplitude $I_0(B)$ and containing a finite range of frequencies (such as the range of frequencies exhibited by the peaks in the spectra shown in Figs. 7.20 and 7.21 for samples CL17 and CL15) can be written as $I(B) = I_0(B) \sin(2\pi\beta_0 B + \phi(B))$. As long as $I_0(B)$ and $\phi(B)$ vary slowly enough, the Hilbert transform satisfies $I_H(B) \approx I_0(B) \cos(2\pi\beta_0 B + \phi(B))$, so that the instantaneous amplitude still satisfies

$$I_0(B) = \sqrt{I^2(B) + I_H^2(B)}. \quad (\text{G.1})$$

The instantaneous phase $\phi(B)$ can also be found by

$$\phi(B) = \arg(I(B) + iI_H(B)) - 2\pi\beta_0 B. \quad (\text{G.2})$$

For a more thorough review of the properties of the Hilbert transform, see Ref. 321.

To analyze the persistent current signals of samples CL15 and CL17, we found the Hilbert transform of the current versus magnetic field trace and then calculated the instantaneous current magnitude $I_0(B)$ and phase $\phi(B)$ using Eqs. G.1 and G.2. The magnitude and phase found for sample CL17 are plotted versus magnetic field in Fig. G.1. In calculating the phase, the function $\arg(I(B) + iI_H(B))$ was first unwrapped by adding 2π whenever the phase jumped discontinuously from $+\pi$ to $-\pi$. A line was fit and subtracted from this unwrapped trace to determine $\phi(B)$. For both samples, the slope of the fitted line was approximately $2\pi\beta_0$ where β_0 is the location of the center of the peak in the Fourier spectrum (see Figs. 7.20 and 7.21).

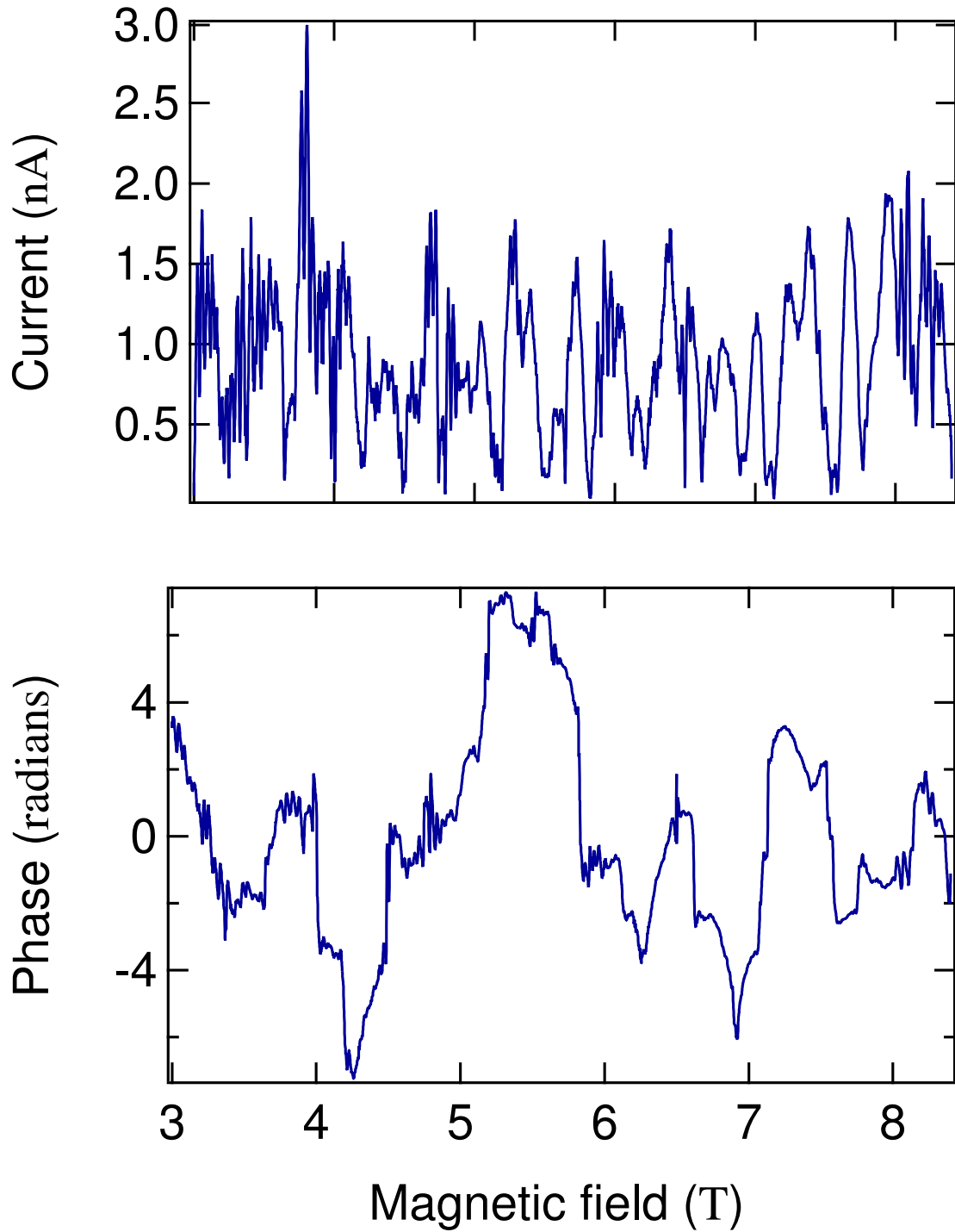


Figure G.1: Magnitude and phase of the persistent current signal. The current magnitude $I_0(B)$ (top graph) and phase $\phi(B)$ (bottom graph) were calculated as described in the text from the current versus magnetic field trace shown in Figs. 7.36 through 7.38. This trace was measured with sample CL17 at $\theta_0 = 45^\circ$ and $T = 365$ mK.

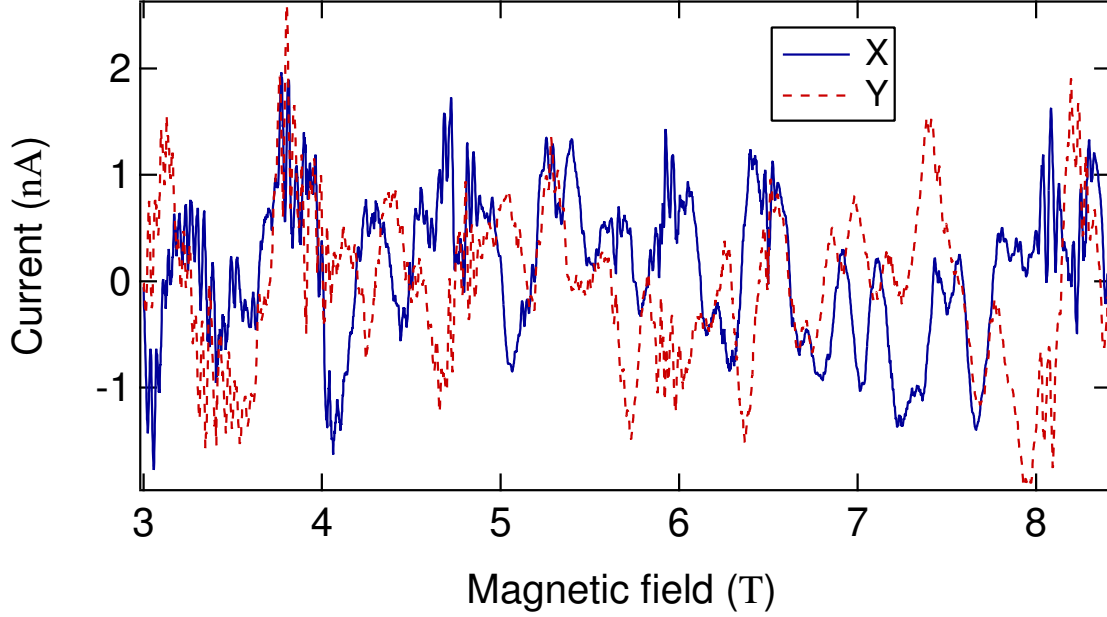


Figure G.2: Quadratures of the persistent current signal. The quadratures X_I (solid line) and Y_I (dashed line) were calculated from the magnitude and phase shown in Fig. G.1 using the definitions given in Eqs. G.3 and G.4.

From the current magnitude $I_0(B)$ and phase $\phi(B)$, the quadratures of the persistent current calculation can be defined as

$$X_I(B) = I_0(B) \cos(\phi(B)) \quad (\text{G.3})$$

$$Y_I(B) = I_0(B) \sin(\phi(B)). \quad (\text{G.4})$$

Fig. G.2 plots the quadratures associated with the magnitude and phase shown in Fig. G.1 for sample CL17. In Fig. G.3, the autocorrelation, calculated using Eq. 7.16, is shown for both quadratures of the signal from sample CL17. As expected, the magnitude and magnetic field range of this correlation agrees with those observed in Fig. 7.30 for the current versus magnetic field trace $I(B)$. Additionally, the cross-correlation of the two quadratures, defined by

$$\langle X_I(B) Y_I(B + j\Delta B) \rangle_M = \frac{1}{P - |j| - 1} \sum_{k=0}^{P - |j| - 1} X_I(B_{\min} + k\Delta B) Y_I(B_{\min} + (j + k)\Delta B), \quad (\text{G.5})$$

shows no significant correlation. In the definition, for both traces X_I and Y_I , B_{\min} is the minimum value of B , ΔB is the spacing in B between successive points, and P is the total number of points.

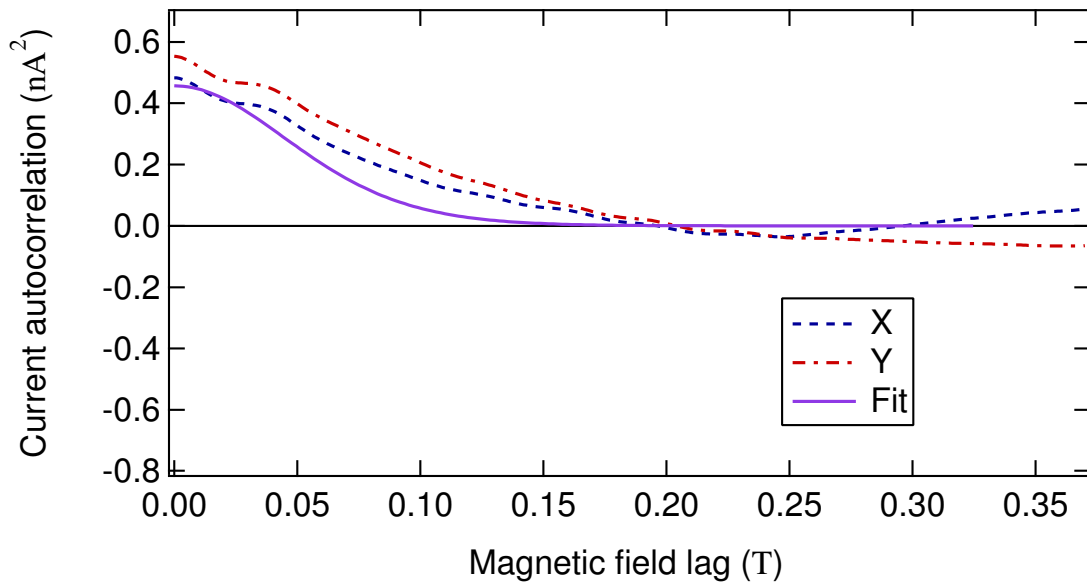


Figure G.3: Autocorrelation of the persistent current quadratures. The autocorrelation of the X_I (dashed line) and Y_I (dot-dashed line) quadratures from Fig. G.2 were calculated using Eq. 7.16. Also shown is the solid line representing the envelope of the fit to the oscillating autocorrelation of the persistent current signal given in Fig. 7.30. Each quadrature is correlated on roughly the same scale within the level of uncertainty associated with the finite magnetic field range of the measurement. For the autocorrelation, one expects an error of $2\eta(M_{\text{eff}})$, which for this sample is 16% (see Table 7.3).

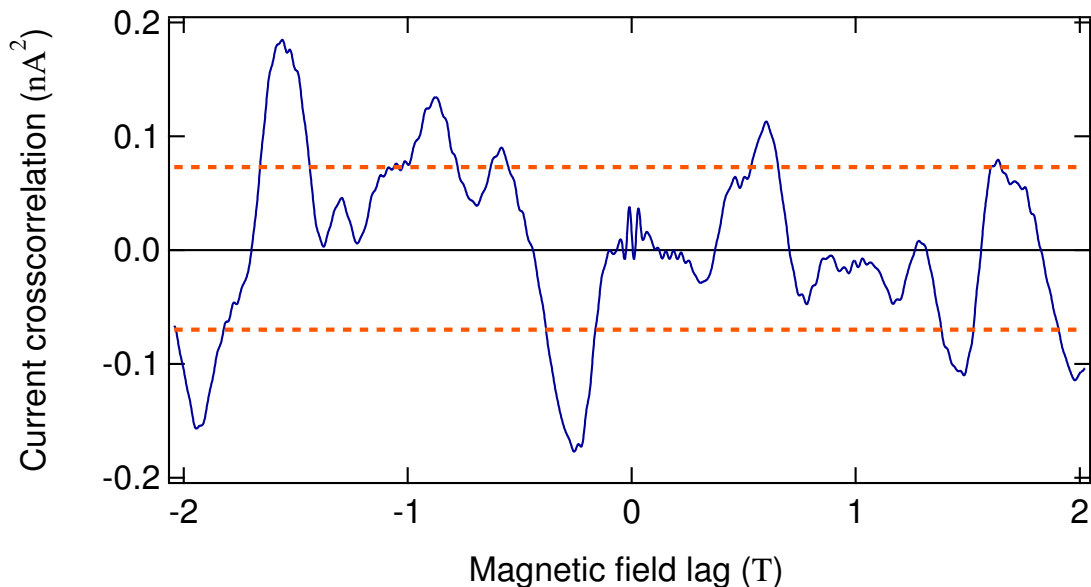


Figure G.4: Cross-correlation of the persistent current quadratures. The cross correlation (solid line) of the two quadratures shown in Fig. G.3 was calculated using Eq. G.5. The horizontal dashed lines represent the uncertainty $2\eta(M_{\text{eff}})(I^{\text{typ}})^2$ expected for the finite range of magnetic field measured and the observed correlation of the persistent current signal. The lack of a significant deviation from the horizontal lines indicates that the two quadratures are uncorrelated.

To assess the distribution of the quadrature amplitudes we calculate the cumulants of the quadratures. The j^{th} moment μ_j of a set of numbers $\{r_k\}$ is defined as the average of the j^{th} power of those numbers

$$\mu_j = \frac{1}{N} \sum_{k=1}^N r_k^j.$$

The cumulants κ_j are another set of numbers related to the moments. The cumulants can be easier to work with analytically in some instances but are not as easy to write down as the moments. When the mean $\mu_1 = 0$, the cumulants κ_j can be defined in terms of the moments μ_j by the relation

$$\exp\left(\sum_{j=1}^{\infty} \frac{t^j \kappa_j}{j!}\right) = 1 + \sum_{j=1}^{\infty} \frac{\mu_j t^j}{j!}. \quad (\text{G.6})$$

For a normal distribution with $\mu_1 = 0$ and $\mu_2 = (I^{\text{typ}})^2$, the probability $P(I)$ of measuring an amplitude I is

$$P(I) = \frac{1}{\sqrt{2\pi} I^{\text{typ}}} \exp\left(-\frac{I^2}{2(I^{\text{typ}})^2}\right).$$

For such a distribution, $\kappa_2 = (I^{\text{typ}})^2$ and $\kappa_j = 0$ for $j \neq 2$. More information about moments and cumulants is given in Ref. 308.

As discussed in Section 7.3.2, the inference of any quantity from a set of measurements with a random contribution has some error related to the finite number of measurements averaged together to calculate that quantity. When the quantity being measured is correlated from measurement to measurement, as is the case for the persistent current measured as a function of magnetic field, the determination of this error is not straightforward. In Ref. 307, Tsyplatyev *et al.* give the error $\delta\kappa_j$ in the j^{th} cumulant κ_j for such a set of correlated data as

$$\delta\kappa_j = \sqrt{\kappa_2^j j! \frac{B_c}{B_0} \int_{-\infty}^{\infty} dx (K_p(x))^j}$$

where B_0 is the range of the measurement field B , B_c is a characteristic field scale of the correlation and $K_p(x)$ is the normalized and scaled correlation function for the measured quantity. The correlation function $K_p(x)$ was discussed further in Section 7.3.2 and given explicitly for the persistent current in Eq. 7.9.

The measured cumulants for samples CL15 and CL17 are shown in Fig. G.5. The plotted

cumulants have been normalized as

$$\kappa_j^N = \frac{\kappa_j}{(I^{\text{typ}})^j}$$

where κ_j is the unnormalized cumulant and I^{typ} is the typical current given by Eq. 2.86 for the measurement temperature $T = 365$ mK and the value of the diffusion constant found from a fit to the temperature dependence of the persistent current (see Table 7.3). Also shown are bars representing the normalized error

$$\begin{aligned} \delta\kappa_j^N &= \frac{\delta\kappa_j}{(I^{\text{typ}})^j} \\ &= \sqrt{j! \frac{B_c}{B_0} \int_{-\infty}^{\infty} dx (K_p(x))^j} \end{aligned} \quad (\text{G.7})$$

appropriate for a normal distribution with zero mean and $\kappa_2 = (I^{\text{typ}})^2$. These bars are centered at $\kappa_j^N = 1$ for $j = 2$ and $\kappa_j^N = 0$ for $j \neq 2$, the positions expected for a normal distribution. The cumulants are plotted up to fifth order where $\delta\kappa_j^N \approx 1$. The measured cumulants agree well the values expected for the normal distribution given the uncertainty specified by Eq. G.7. We reiterate that this agreement only confirms the applicability of the central limit theorem to our arrays of rings and consequently the accuracy of our data analysis procedure. To test the claim that the persistent current in an individual ring follows the normal distribution, larger data sets of individual rings must be measured.

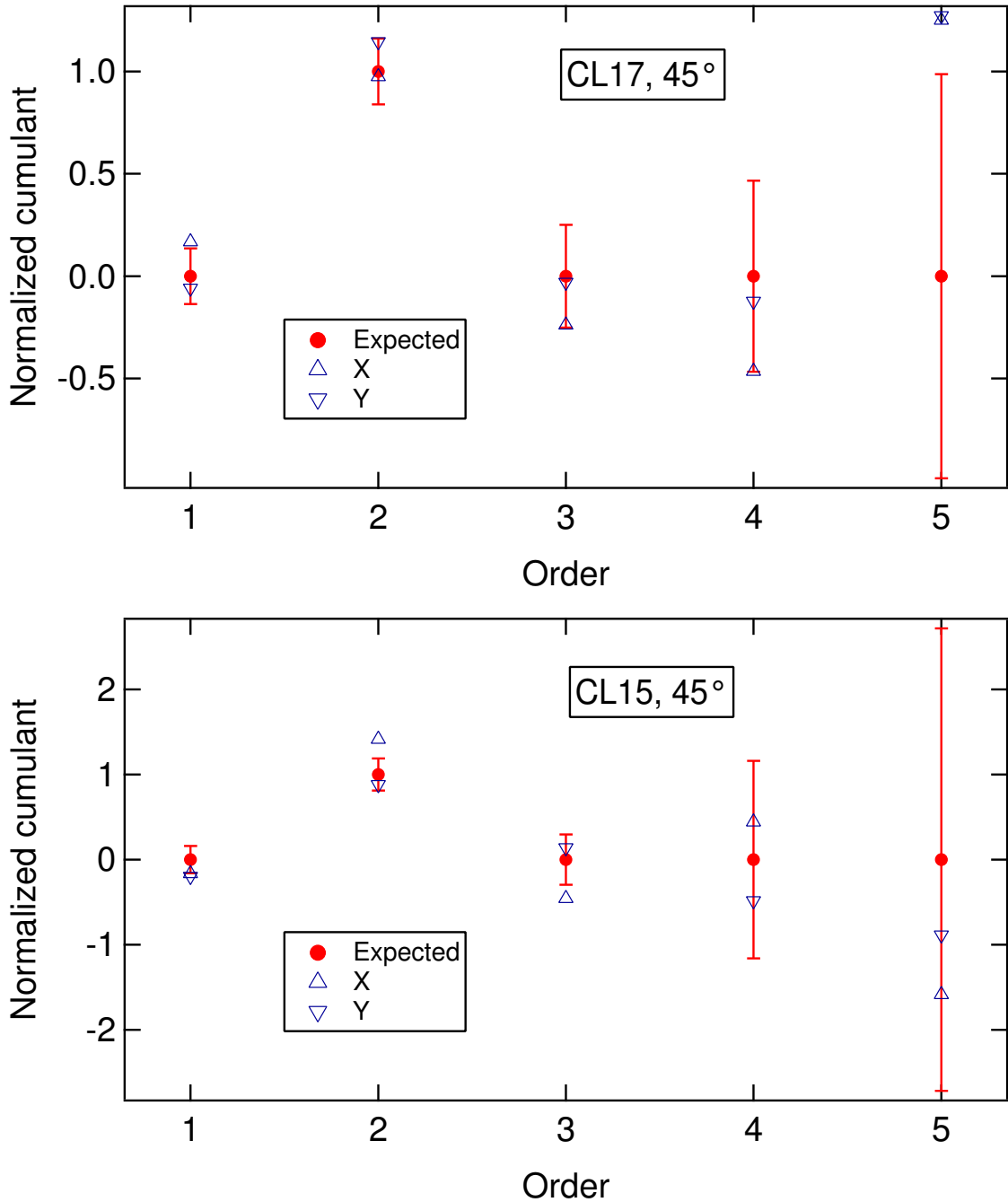


Figure G.5: Cumulants of the persistent current for samples CL15 and CL17. The normalized cumulants κ_j^N are shown for the measurements of both sample CL17 (top graph) and CL15 (bottom graph) at $\theta_0 = 45^\circ$ and $T = 365$ mK. The cumulants were calculated for both the X_I (upward pointing triangles) and Y_I (downward pointing triangles) quadratures and then divided by $(I^{\text{typ}})^j$, the j th power of the typical current expected from analysis of the temperature dependence of the current (see the discussion in the text). The quadratures of sample CL17 are shown in Fig. G.2. The normalized cumulants κ_j^N (dots) expected for the normal distribution with zero mean are also shown above, as are the corresponding normalized uncertainties $\delta\kappa_j^N$ (vertical bars) given by Eq. G.7. Most of the measured cumulants fall within the expected uncertainties, indicating that the measured values of the persistent current are consistent with the normal distribution.

Bibliography

- [1] M. Büttiker, Y. Imry, and R. Landauer, “Josephson behavior in small normal one-dimensional rings,” *Physics Letters A*, vol. 96, no. 7, pp. 365–367, Jul. 1983.
- [2] V. Chandrasekhar, R. A. Webb, M. J. Brady, M. B. Ketchen, W. J. Gallagher, and A. Kleinsasser, “Magnetic response of a single, isolated gold loop,” *Physical Review Letters*, vol. 67, no. 25, pp. 3578–3581, Dec. 1991.
- [3] E. M. Q. Jariwala, P. Mohanty, M. B. Ketchen, and R. A. Webb, “Diamagnetic persistent current in diffusive normal-metal rings,” *Physical Review Letters*, vol. 86, no. 8, pp. 1594–1597, Feb. 2001.
- [4] L. P. Lévy, G. Dolan, J. Dunsmuir, and H. Bouchiat, “Magnetization of mesoscopic copper rings: Evidence for persistent currents,” *Physical Review Letters*, vol. 64, no. 17, pp. 2074–2077, Apr. 1990.
- [5] B. Reulet, M. Ramin, H. Bouchiat, and D. Mailly, “Dynamic response of isolated Aharonov-Bohm rings coupled to an electromagnetic resonator,” *Physical Review Letters*, vol. 75, no. 1, pp. 124–127, Jul. 1995.
- [6] R. Deblock, Y. Noat, B. Reulet, H. Bouchiat, and D. Mailly, “ac electric and magnetic responses of nonconnected Aharonov-Bohm rings,” *Physical Review B*, vol. 65, no. 7, p. 075301, Jan. 2002.
- [7] R. Deblock, R. Bel, B. Reulet, H. Bouchiat, and D. Mailly, “Diamagnetic orbital response of mesoscopic silver rings,” *Physical Review Letters*, vol. 89, no. 20, p. 206803, Oct. 2002.
- [8] D. Mailly, C. Chapelier, and A. Benoît, “Experimental observation of persistent currents in

- GaAs-AlGaAs single loop,” *Physical Review Letters*, vol. 70, no. 13, pp. 2020–2023, Mar. 1993.
- [9] W. Rabaud, L. Saminadayar, D. Mailly, K. Hasselbach, A. Benoît, and B. Etienne, “Persistent currents in mesoscopic connected rings,” *Physical Review Letters*, vol. 86, no. 14, pp. 3124–3127, Apr. 2001.
- [10] H. Bluhm, N. C. Koshnick, J. A. Bert, M. E. Huber, and K. A. Moler, “Persistent currents in normal metal rings,” *Physical Review Letters*, vol. 102, no. 13, p. 136802, Mar. 2009.
- [11] N. A. J. M. Kleemans, I. M. A. Bominaar-Silkens, V. M. Fomin, V. N. Gladilin, D. Granados, A. G. Taboada, J. M. García, P. Offermans, U. Zeitler, P. C. M. Christianen, J. C. Maan, J. T. Devreese, and P. M. Koenraad, “Oscillatory persistent currents in self-assembled quantum rings,” *Physical Review Letters*, vol. 99, no. 14, p. 146808, Oct. 2007.
- [12] D. Prober, (private communication).
- [13] N. Trivedi and D. A. Browne, “Mesoscopic ring in a magnetic field: Reactive and dissipative response,” *Physical Review B*, vol. 38, no. 14, pp. 9581–9593, Nov. 1988.
- [14] K. B. Efetov, “Dynamic persistent currents in mesoscopic rings,” *Physical Review Letters*, vol. 66, no. 21, pp. 2794–2797, May 1991.
- [15] M. Janßen, U. Gummich, J. Hajdu, and O. Viehweger, “Linear response, persistent currents and related problems,” *Annalen der Physik*, vol. 505, no. 4, pp. 361–380, 1993.
- [16] F. Marchesoni, “Persistent currents in mesoscopic rings: A stochastic model,” *Journal of Statistical Physics*, vol. 70, no. 1-2, pp. 247–256, 1993.
- [17] V. E. Kravtsov and V. I. Yudson, “Direct current in mesoscopic rings induced by high-frequency electromagnetic field,” *Physical Review Letters*, vol. 70, no. 2, pp. 210–213, Jan. 1993.
- [18] V. E. Kravtsov, “Disorder-induced resonance nonlinear response of metal rings with quasi-ballistic transport of electrons,” *Physics Letters A*, vol. 172, no. 6, pp. 452–456, Jan. 1993.
- [19] A. G. Aronov and V. E. Kravtsov, “Nonlinear properties of disordered normal-metal rings with magnetic flux,” *Physical Review B*, vol. 47, no. 20, pp. 13409–13419, May 1993.

- [20] B. Reulet and H. Bouchiat, “ac conductivity of mesoscopic rings: The discrete-spectrum limit,” *Physical Review B*, vol. 50, no. 4, pp. 2259–2272, Jul. 1994.
- [21] G. M. Genkin and G. A. Vugalter, “Resonance absorption of a high-frequency electromagnetic field in a mesoscopic ring,” *Physics Letters A*, vol. 189, no. 5, pp. 415–418, Jun. 1994.
- [22] Y. Galperin and O. Entin-Wohlman, “Nonequilibrium orbital magnetization of strongly localized electrons,” *Physical Review B*, vol. 54, no. 13, pp. 9346–9352, Oct. 1996.
- [23] G. P. Berman, E. N. Bulgakov, D. K. Campbell, and I. V. Krive, “Quantum nonlinear resonance and quantum chaos in Aharonov-Bohm oscillations in mesoscopic semiconductor rings,” *Physical Review B*, vol. 56, no. 16, pp. 10 338–10 354, Oct. 1997.
- [24] P. Kopietz and A. Völker, “Non-linear response and electron-electron interactions in mesoscopic metal rings,” *The European Physical Journal B - Condensed Matter and Complex Systems*, vol. 3, no. 3, pp. 397–405, Jul. 1998.
- [25] O. Keller and G. Wang, “Angular-momentum photon drag in a mesoscopic metallic ring in the presence of a persistent current,” *Optics Communications*, vol. 178, no. 4-6, pp. 411–430, May 2000.
- [26] V. I. Yudson, E. Kanziiper, and V. E. Kravtsov, “Limits of the dynamical approach to the nonlinear response of mesoscopic systems,” *Physical Review B*, vol. 64, no. 4, p. 045310, Jun. 2001.
- [27] O. L. Chalaev and V. E. Kravtsov, “Aharonov-Bohm magnetization of mesoscopic rings caused by inelastic relaxation,” *Physical Review Letters*, vol. 89, no. 17, p. 176601, Oct. 2002.
- [28] V. Yudson and V. Kravtsov, “Electron kinetics in isolated mesoscopic rings driven out of equilibrium,” *Physical Review B*, vol. 67, no. 15, p. 155310, 2003.
- [29] L. Arrachea, “dc response of a dissipative driven mesoscopic ring,” *Physical Review B*, vol. 70, no. 15, p. 155407, Oct. 2004.
- [30] A. Matos-Abiague and J. Berakdar, “Photoinduced charge currents in mesoscopic rings,” *Physical Review Letters*, vol. 94, no. 16, p. 166801, Apr. 2005.

- [31] J. Dajka, A. Vourdas, S. Zhang, and E. Zipper, “The influence of entangled photons on distant persistent currents,” *Journal of Physics: Condensed Matter*, vol. 18, no. 4, pp. 1367–1379, 2006.
- [32] D. Cohen, T. Kottos, and H. Schanz, “Rate of energy absorption by a closed ballistic ring,” *Journal of Physics A: Mathematical and General*, vol. 39, no. 38, pp. 11 755–11 771, 2006.
- [33] I. O. Kulik, “Mesoscopic Aharonov-Bohm loops in a time-dependent potential: Quasistationary electronic states and quantum transitions,” *Physical Review B*, vol. 76, no. 12, p. 125313, 2007.
- [34] A. S. Moskalenko, A. Matos-Abiague, and J. Berakdar, “Nonequilibrium charge dynamics of light-driven rings threaded by a magnetic flux,” *Europhysics Letters*, vol. 78, no. 5, p. 57001, 2007.
- [35] N. C. Koshnick, H. Bluhm, M. E. Huber, and K. A. Moler, “Fluctuation superconductivity in mesoscopic aluminum rings,” *Science*, vol. 318, no. 5855, pp. 1440–1443, Nov. 2007.
- [36] E. Akkermans and G. Montambaux, *Mesoscopic Physics of Electrons and Photons*. New York, NY: Cambridge University Press, 2007.
- [37] H. Cheung, Y. Gefen, and E. K. Riedel, “Isolated rings of mesoscopic dimensions. Quantum coherence and persistent currents,” *IBM Journal of Research and Development*, vol. 32, no. 3, pp. 359–371, 1988.
- [38] H. Cheung, Y. Gefen, E. K. Riedel, and W. Shih, “Persistent currents in small one-dimensional metal rings,” *Physical Review B*, vol. 37, no. 11, pp. 6050–6062, Apr. 1988.
- [39] V. Ambegaokar and U. Eckern, “Coherence and persistent currents in mesoscopic rings,” *Physical Review Letters*, vol. 65, no. 3, pp. 381–384, Jul. 1990.
- [40] B. L. Altshuler, Y. Gefen, and Y. Imry, “Persistent differences between canonical and grand canonical averages in mesoscopic ensembles: Large paramagnetic orbital susceptibilities,” *Physical Review Letters*, vol. 66, no. 1, pp. 88–91, Jan. 1991.
- [41] E. K. Riedel and F. von Oppen, “Mesoscopic persistent current in small rings,” *Physical Review B*, vol. 47, no. 23, pp. 15 449–15 459, Jun. 1993.

- [42] E. Ginossar, L. I. Glazman, T. Ojanen, F. von Oppen, W. E. Shanks, A. C. Bleszynski-Jayich, and J. G. E. Harris, “Mesoscopic persistent currents in a strong magnetic field,” *Physical Review B*, vol. 81, no. 15, p. 155448, Apr. 2010.
- [43] W. Ehrenberg and R. E. Siday, “The refractive index in electron optics and the principles of dynamics,” *Proceedings of the Physical Society. Section B*, vol. 62, no. 1, pp. 8–21, 1949.
- [44] Y. Aharonov and D. Bohm, “Significance of electromagnetic potentials in the quantum theory,” *Physical Review*, vol. 115, no. 3, pp. 485–491, 1959.
- [45] R. D. Mattuck, *A Guide to Feynman Diagrams in the Many-Body Problem*, 2nd ed. Mineola, NY: Dover Publications, Jun. 1992.
- [46] H. Cheung, E. K. Riedel, and Y. Gefen, “Persistent currents in mesoscopic rings and cylinders,” *Physical Review Letters*, vol. 62, no. 5, pp. 587–590, Jan. 1989.
- [47] E. K. Riedel, H. Cheung, and Y. Gefen, “Persistent currents in mesoscopic normal metal rings,” *Physica Scripta*, vol. T25, pp. 357–361, 1989.
- [48] M. Yip, J. Zheng, and H. Cheung, “Persistent current of one-dimensional perfect rings under the canonical ensemble,” *Physical Review B*, vol. 53, no. 3, pp. 1006–1009, Jan. 1996.
- [49] A. Schmid, “Persistent currents in mesoscopic rings by suppression of charge fluctuations,” *Physical Review Letters*, vol. 66, no. 1, pp. 80–83, Jan. 1991.
- [50] L. Saminadayar, C. Bäuerle, and D. Mailly, “Equilibrium properties of mesoscopic quantum conductors,” in *Encyclopedia of Nanoscience and Nanotechnology*, H. S. Nalwa, Ed. Valencia, CA: American Scientific, 2004, vol. 3, pp. 267–285.
- [51] G. B. Arfken and H. J. Weber, *Mathematical Methods for Physicists*, 5th ed. San Diego, CA: Academic Press, 2001.
- [52] I. O. Kulik, “Flux quantization in a normal metal,” *Soviet Journal of Experimental and Theoretical Physics Letters*, vol. 11, pp. 275–277, Apr. 1970.
- [53] P. A. Lee and A. D. Stone, “Universal conductance fluctuations in metals,” *Physical Review Letters*, vol. 55, no. 15, pp. 1622–1625, Oct. 1985.

- [54] P. A. Lee, A. D. Stone, and H. Fukuyama, “Universal conductance fluctuations in metals: Effects of finite temperature, interactions, and magnetic field,” *Physical Review B*, vol. 35, no. 3, pp. 1039–1070, Jan. 1987.
- [55] F. Pierre and N. O. Birge, “Dephasing by extremely dilute magnetic impurities revealed by Aharonov-Bohm oscillations,” *Physical Review Letters*, vol. 89, no. 20, p. 206804, Oct. 2002.
- [56] N. W. Ashcroft and N. D. Mermin, *Solid State Physics*, 1st ed. Fort Worth, TX: Harcourt, Inc., Jan. 1976.
- [57] F. von Oppen and E. K. Riedel, “Average persistent current in a mesoscopic ring,” *Physical Review Letters*, vol. 66, no. 1, pp. 84–87, Jan. 1991.
- [58] V. Ambegaokar and U. Eckern, “Comment on “Persistent currents in mesoscopic rings by suppression of charge fluctuations”,” *Physical Review Letters*, vol. 67, no. 22, p. 3192, Nov. 1991.
- [59] U. Eckern, “Coherence and destruction of coherence in mesoscopic rings,” *Zeitschrift für Physik B Condensed Matter*, vol. 82, no. 3, pp. 393–398, Oct. 1991.
- [60] H. Bouchiat, G. Montambaux, L. P. Levy, G. Dolan, and J. Dunsmuir, “Persistent currents in mesoscopic rings: Ensemble average and half-flux-quantum periodicity,” in *Quantum coherence in mesoscopic systems*, B. Kramer, Ed. New York, NY: Plenum Press, 1991, pp. 245–260.
- [61] L. P. Lévy, “Persistent currents in mesoscopic copper rings,” *Physica B: Condensed Matter*, vol. 169, no. 1-4, pp. 245–256, Feb. 1991.
- [62] U. Eckern and A. Schmid, “Persistent currents of single mesoscopic rings,” *Europhysics Letters*, vol. 18, no. 5, pp. 457–462, 1992.
- [63] —, “Stochastic fluctuations of persistent currents in mesoscopic rings,” *Annalen der Physik*, vol. 505, no. 2, pp. 180–200, 1993.
- [64] R. A. Smith and V. Ambegaokar, “Systematic calculation of moments of flux-dependent currents in single mesoscopic rings,” *Europhysics Letters*, vol. 20, no. 2, pp. 161–166, 1992.
- [65] U. Eckern and P. Schwab, “Normal persistent currents,” *Advances in Physics*, vol. 44, no. 5, pp. 387–404, 1995.

- [66] H. J. Bussemaker and T. R. Kirkpatrick, “Effective-field-theory approach to persistent currents,” *Physical Review B*, vol. 56, no. 8, pp. 4529–4540, 1997.
- [67] M. Houzet, “Distribution function of persistent current,” *Physical Review B*, vol. 82, no. 16, p. 161517, 2010.
- [68] A. C. Bleszynski-Jayich, W. E. Shanks, B. Peaudecerf, E. Ginossar, F. von Oppen, L. Glazman, and J. G. E. Harris, “Persistent currents in normal metal rings,” *Science*, vol. 326, no. 5950, pp. 272–275, Oct. 2009.
- [69] N. Bohr, “I. On the constitution of atoms and molecules,” *Philosophical Magazine Series 6*, vol. 26, no. 151, pp. 1–25, 1913.
- [70] R. B. Dingle, “Some magnetic properties of metals. IV. Properties of small systems of electrons,” *Proceedings of the Royal Society of London. Series A, Mathematical and Physical Sciences*, vol. 212, no. 1108, pp. 47–65, Apr. 1952.
- [71] P. Ehrenfest, “Opmerkingen over het diamagnetisme van vast bismuth,” *Physica*, vol. 5, pp. 388–391, 1925.
- [72] —, “Bemerkungen uber den diamagnetismus von festem wismut,” *Zeitschrift für Physik*, vol. 58, pp. 719–721, Nov. 1929.
- [73] L. Landau, “Diamagnetismus der metalle,” *Zeitschrift für Physik*, vol. 64, no. 9-10, pp. 629–637, 1930.
- [74] R. Peierls, “Zur theorie des diamagnetismus von leitungselektronen,” *Zeitschrift für Physik*, vol. 80, no. 11-12, pp. 763–791, 1933.
- [75] —, “Zur theorie des diamagnetismus von leitungselektronen. II. Starke magnetfelder,” *Zeitschrift für Physik*, vol. 81, no. 3-4, pp. 186–194, 1933.
- [76] M. Blackman, “On the diamagnetic susceptibility of bismuth,” *Proceedings of the Royal Society A: Mathematical, Physical and Engineering Sciences*, vol. 166, no. 924, pp. 1–15, 1938.
- [77] L. Pauling, “The diamagnetic anisotropy of aromatic molecules,” *The Journal of Chemical Physics*, vol. 4, no. 10, pp. 673–677, 1936.

- [78] F. London, “Théorie quantique des courants interatomiques dans les combinaisons aromatiques,” *Journal de Physique et le Radium*, vol. 8, no. 10, pp. 397–409, 1937.
- [79] F. Hund, “Rechnungen über das magnetische Verhalten von kleinen Metallstücken bei tiefen Temperaturen,” *Annalen der Physik*, vol. 424, no. 1-2, pp. 102–114, 1938.
- [80] N. Byers and C. N. Yang, “Theoretical considerations concerning quantized magnetic flux in superconducting cylinders,” *Physical Review Letters*, vol. 7, no. 2, pp. 46–49, Jul. 1961.
- [81] F. Bloch, “Off-diagonal long-range order and persistent currents in a hollow cylinder,” *Physical Review*, vol. 137, no. 3A, pp. A787–A795, Feb. 1965.
- [82] —, “Flux quantization and dimensionality,” *Physical Review*, vol. 166, no. 2, pp. 415–423, Feb. 1968.
- [83] M. Schick, “Flux quantization in a one-dimensional model,” *Physical Review*, vol. 166, no. 2, pp. 404–414, Feb. 1968.
- [84] L. Gunther and Y. Imry, “Flux quantization without off-diagonal long range order in a thin hollow cylinder,” *Solid State Communications*, vol. 7, no. 18, pp. 1391–1394, Sep. 1969.
- [85] M. Büttiker, Y. Imry, and M. Y. Azbel, “Quantum oscillations in one-dimensional normal-metal rings,” *Physical Review A*, vol. 30, no. 4, pp. 1982–1989, Oct. 1984.
- [86] “Flux-sensitive effects in normal metal loops,” vol. 480.
- [87] M. Büttiker, “Quantum oscillations in ultrasmall normal loops and tunnel junctions,” *Physica Scripta*, vol. T14, pp. 82–88, 1986.
- [88] A. A. Shablo, T. P. Narbut, S. A. Tyurin, and I. M. Dmitrenko, “Quantization of magnetic flux at temperatures above the superconducting transition temperature,” *JETP Letters*, vol. 19, no. 7, pp. 246–247, 1974.
- [89] D. Y. Sharvin and Y. V. Sharvin, “Magnetic-flux quantization in a cylindrical film of a normal metal,” *JETP Letters*, vol. 34, no. 5, pp. 272–275, 1981.
- [90] C. P. Umbach, S. Washburn, R. B. Laibowitz, and R. A. Webb, “Magnetoresistance of small, quasi-one-dimensional, normal-metal rings and lines,” *Physical Review B*, vol. 30, no. 7, pp. 4048–4051, Oct. 1984.

- [91] R. A. Webb, S. Washburn, C. P. Umbach, and R. B. Laibowitz, “Observation of h/e Aharonov-Bohm oscillations in normal-metal rings,” *Physical Review Letters*, vol. 54, no. 25, pp. 2696–2699, Jun. 1985.
- [92] S. Washburn and R. A. Webb, “Aharonov-Bohm effect in normal metal quantum coherence and transport,” *Advances in Physics*, vol. 35, no. 4, pp. 375–422, 1986.
- [93] H. Cheung and E. K. Riedel, “Energy spectrum and persistent current in one-dimensional rings,” *Physical Review B*, vol. 40, no. 14, pp. 9498–9501, Nov. 1989.
- [94] E. Riedel, “Persistent currents in mesoscopic rings,” in *Quantum Coherence in Mesoscopic Systems*, B. Kramer, Ed. New York, NY: Plenum Press, 1991, pp. 261–276.
- [95] G. Montambaux, H. Bouchiat, D. Sigeti, and R. Friesner, “Persistent currents in mesoscopic metallic rings: Ensemble average,” *Physical Review B*, vol. 42, no. 12, pp. 7647–7650, Oct. 1990.
- [96] Y. Imry, “Persistent currents in mesoscopic normal metal rings,” in *Quantum Coherence in Mesoscopic Systems*, B. Kramer, Ed. New York, NY: Plenum Press, 1991, pp. 221–236.
- [97] A. S. Cattaneo, A. Gamba, and I. V. Kolokolov, “Statistics of the one-electron current in a one-dimensional mesoscopic ring at arbitrary magnetic fields,” *Journal of Statistical Physics*, vol. 76, no. 3-4, pp. 1065–1074, 1994.
- [98] J. Danon and P. W. Brouwer, “Non-Gaussian fluctuations of mesoscopic persistent currents,” *Physical Review Letters*, vol. 105, no. 13, p. 136803, 2010.
- [99] E. Akkermans and G. Montambaux, “Conductance and statistical properties of metallic spectra,” *Physical Review Letters*, vol. 68, no. 5, pp. 642–645, Feb. 1992.
- [100] B. D. Simons and B. L. Altshuler, “Universalities in the spectra of disordered and chaotic systems,” *Physical Review B*, vol. 48, no. 8, pp. 5422–5438, 1993.
- [101] A. Szafer and B. L. Altshuler, “Universal correlation in the spectra of disordered systems with an Aharonov-Bohm flux,” *Physical Review Letters*, vol. 70, no. 5, pp. 587–590, Feb. 1993.
- [102] D. Braun and G. Montambaux, “Universal spectral correlations in diffusive quantum systems,” *Physical Review B*, vol. 50, no. 11, pp. 7776–7785, 1994.

- [103] G. Montambaux, “Spectral statistics of disordered metals in the presence of several Aharonov-Bohm fluxes,” *Physical Review B*, vol. 55, no. 19, pp. 12 833–12 835, May 1997.
- [104] H. Feldmann, E. P. Nakhmedov, and R. Oppermann, “Distribution function of the local density of states of a one-channel weakly disordered ring in an external magnetic field,” *Physical Review B*, vol. 62, no. 4, pp. 2401–2415, Jul. 2000.
- [105] A. Müller-Groeling, H. A. Weidenmüller, and C. H. Lewenkopf, “Interacting electrons in mesoscopic rings,” *Europhysics Letters*, vol. 22, no. 3, pp. 193–198, 1993.
- [106] P. Kopietz, “Universal persistent currents in mesoscopic metal rings due to long-range Coulomb interactions,” *Physical Review Letters*, vol. 70, no. 20, p. 3123, May 1993.
- [107] —, “Universal persistent currents in mesoscopic metal rings due to long-range Coulomb interactions,” *Physical Review Letters*, vol. 71, no. 2, p. 306, Jul. 1993.
- [108] G. Vignale, “Comment on “Universal persistent current in mesoscopic metal rings due to long-range Coulomb interactions”,” *Physical Review Letters*, vol. 72, no. 3, p. 433, Jan. 1994.
- [109] P. Kopietz, “Kopietz replies,” *Physical Review Letters*, vol. 72, no. 3, p. 434, Jan. 1994.
- [110] A. Altland and Y. Gefen, “Comment on “Universal persistent currents in mesoscopic metal rings due to long-range Coulomb interactions”,” *Physical Review Letters*, vol. 72, no. 18, p. 2973, May 1994.
- [111] P. Kopietz, “Kopietz replies,” *Physical Review Letters*, vol. 72, no. 18, p. 2974, May 1994.
- [112] H. Kato and D. Yoshioka, “Suppression of persistent currents in one-dimensional disordered rings by the Coulomb interaction,” *Physical Review B*, vol. 50, no. 7, pp. 4943–4946, 1994.
- [113] A. Müller-Groeling and H. A. Weidenmüller, “Persistent currents in one- and two-dimensional mesoscopic rings: Influence of the Coulomb interaction, impurity scattering, and periodic potential,” *Physical Review B*, vol. 49, no. 7, pp. 4752–4767, Feb. 1994.
- [114] L. Wendler and V. M. Fomin, “Persistent currents in finite-width mesoscopic rings. The role of the interchannel coupling and of the electron-electron interaction,” *physica status solidi (b)*, vol. 191, no. 2, pp. 409–447, 1995.

- [115] R. Berkovits and Y. Avishai, "Significant interaction-induced enhancement of persistent currents in 2D disordered cylinders," *Europhysics Letters*, vol. 29, no. 6, pp. 475–480, 1995.
- [116] G. S. Jeon and M. Y. Choi, "Persistent currents in annuli: Effects of disorder and Coulomb interaction," *Journal of Physics: Condensed Matter*, vol. 8, no. 24, pp. 4429–4440, 1996.
- [117] T. Giamarchi and B. S. Shastry, "Persistent currents in a one-dimensional ring for a disordered Hubbard model," *Physical Review B*, vol. 51, no. 16, pp. 10 915–10 922, Apr. 1995.
- [118] M. Ramin, B. Reulet, and H. Bouchiat, "Electron-electron interactions in one- and three-dimensional mesoscopic disordered rings: A perturbative approach," *Physical Review B*, vol. 51, no. 8, pp. 5582–5585, Feb. 1995.
- [119] Y. Li and Z. Ma, "Exactly solvable model for persistent currents in the presence of hard-core interaction in one-dimensional mesoscopic ring," *Journal of the Physical Society of Japan*, vol. 65, pp. 1519–1522, 1996.
- [120] P. Schmitteckert and U. Eckern, "Phase coherence in a random one-dimensional system of interacting Fermions: A density-matrix renormalization-group study," *Physical Review B*, vol. 53, no. 23, pp. 15 397–15 400, Jun. 1996.
- [121] C. A. Stafford and D. F. Wang, "Interaction-induced enhancement and oscillations of the persistent current," *Physical Review B*, vol. 56, no. 8, pp. R4383–R4386, 1997.
- [122] M. Schechter, Y. Oreg, Y. Imry, and Y. Levinson, "Magnetic response of disordered metallic rings: Large contribution of far levels," *Physical Review Letters*, vol. 90, no. 2, p. 026805, Jan. 2003.
- [123] U. Eckern, P. Schwab, and V. Ambegaokar, "Comment on "Magnetic response of disordered metallic rings: Large contributions of far levels"," *Physical Review Letters*, vol. 93, no. 20, p. 209701, Nov. 2004.
- [124] M. Schechter, Y. Oreg, Y. Imry, and Y. Levinson, "Schechter et al. reply:," *Physical Review Letters*, vol. 93, no. 20, p. 209702, Nov. 2004.
- [125] L. P. Chau and P. Kopietz, "Linear magnetic response of disordered metallic rings: Large contribution from forward-scattering interactions," *Physical Review B*, vol. 70, no. 15, p. 155317, Oct. 2004.

- [126] H. Yoshioka and H. Fukuyama, “Fluctuations of Josephson currents and persistent currents in mesoscopic spin glass systems,” *Journal of the Physical Society of Japan*, vol. 62, pp. 612–623, 1993.
- [127] U. Eckern, “Persistent current fluctuations in mesoscopic rings in the presence of spin effects,” *Physica Scripta*, vol. T49A, pp. 338–342, 1993.
- [128] P. Schwab, “Impurity spin dynamics and quantum coherence in mesoscopic rings,” Ph.D. dissertation, Universität Augsburg, 1996.
- [129] P. Schwab and U. Eckern, “Impurity spin dynamics and quantum coherence in mesoscopic rings,” *Annalen der Physik*, vol. 508, pp. 57–87, 1996.
- [130] W. Häusler, “Persistent current of correlated, spin carrying electrons,” *Czechoslovak Journal of Physics*, vol. 46, no. 0, pp. 2403–2404, Apr. 1996.
- [131] P. Schwab and U. Eckern, “Persistent current induced by magnetic impurities,” *Zeitschrift für Physik B Condensed Matter*, vol. 103, no. 1, pp. 97–103, Apr. 1997.
- [132] H. Bary-Soroker, O. Entin-Wohlman, and Y. Imry, “Effect of pair breaking on mesoscopic persistent currents well above the superconducting transition temperature,” *Physical Review Letters*, vol. 101, no. 5, p. 057001, 2008.
- [133] —, “Pair-breaking effect on mesoscopic persistent currents,” *Physical Review B*, vol. 80, no. 2, p. 024509, 2009.
- [134] J. D. Maynard, “A possible explanation for the discrepancy in electron persistent current amplitudes: A superfluid persistent current analog,” *Journal of Low Temperature Physics*, vol. 89, no. 1, pp. 155–158, Oct. 1992.
- [135] M. Büttiker, “Characteristic potentials for mesoscopic rings threaded by an Aharonov-Bohm flux,” *Physica Scripta*, vol. T54, pp. 104–110, 1994.
- [136] R. Kirczenow, “Why are large persistent currents observed in small gold rings?” *Journal of Physics: Condensed Matter*, vol. 7, no. 10, pp. 2021–2035, 1995.
- [137] C. S. Unnikrishnan, “Persistent currents and role of ‘whispering gallery modes’,” *Physica B: Condensed Matter*, vol. 223-224, pp. 634–636, Jun. 1996.

- [138] F. V. Kusmartsev, “N-electron train effect on the enhancement of persistent current,” *Physics Letters A*, vol. 232, no. 1-2, pp. 135–142, Jul. 1997.
- [139] C. Stelzer and W. Schweizer, “Mesoscopic normal-metal rings in a magnetic field,” *Physical Review B*, vol. 62, no. 11, pp. 7275–7282, 2000.
- [140] V. M. Apel, G. Chiappe, and M. J. Sánchez, “Enhancement of persistent currents due to confinement in metallic samples,” *Physical Review Letters*, vol. 85, no. 19, pp. 4152–4155, Nov. 2000.
- [141] I. Tomita, “Persistent current in a one-dimensional correlated disordered ring,” *Physica A: Statistical Mechanics and its Applications*, vol. 308, no. 1-4, pp. 1–14, May 2002.
- [142] S. S. Chowdhury, P. S. Deo, A. K. Roy, and M. Manninen, “Large diamagnetic persistent currents,” *New Journal of Physics*, vol. 10, no. 8, p. 083014, 2008.
- [143] H. Chen and J. Ding, “Persistent current in finite-width ring with surface disorder,” *Physica B: Condensed Matter*, vol. 403, no. 12, pp. 2015–2020, Jun. 2008.
- [144] J. Feilhauer and M. Moško, “Conductance and persistent current in quasi-one-dimensional systems with grain boundaries,” arXiv:1012.0702v1, Nov. 2010.
- [145] E. Akkermans, A. Auerbach, J. E. Avron, and B. Shapiro, “Relation between persistent currents and the scattering matrix,” *Physical Review Letters*, vol. 66, no. 1, pp. 76–79, Jan. 1991.
- [146] S. Bandopadhyay, P. S. Deo, and A. M. Jayannavar, “Quantum current magnification in a multichannel mesoscopic ring,” *Physical Review B*, vol. 70, no. 7, p. 075315, 2004.
- [147] M. Pascaud and G. Montambaux, “Magnetization of mesoscopic disordered networks,” *Europhysics Letters*, vol. 37, no. 5, pp. 347–352, 1997.
- [148] —, “Persistent currents on networks,” *Physical Review Letters*, vol. 82, no. 22, pp. 4512–4515, May 1999.
- [149] Y. Imry, “Mesoscopic physics and the fundamentals of quantum mechanics,” *Physica Scripta*, vol. T76, no. 1, pp. 171–178, 1998.

- [150] J. Cayssol, T. Kontos, and G. Montambaux, “Isolated hybrid normal/superconducting ring in a magnetic flux: From persistent current to Josephson current,” *Physical Review B*, vol. 67, no. 18, p. 184508, May 2003.
- [151] D. Loss and P. M. Goldbart, “Persistent currents from Berry’s phase in mesoscopic systems,” *Physical Review B*, vol. 45, no. 23, pp. 13 544–13 561, Jun. 1992.
- [152] X. Gao and T. Qian, “Aharonov-Anandan phase and persistent currents in a mesoscopic ring,” *Physical Review B*, vol. 47, no. 12, pp. 7128–7131, Mar. 1993.
- [153] S. Kawabata, “Berry phase and persistent current in disordered mesoscopic rings,” *Physical Review B*, vol. 60, no. 12, pp. R8457–R8460, 1999.
- [154] N. Yu and M. Fowler, “Persistent current of a Hubbard ring threaded with a magnetic flux,” *Physical Review B*, vol. 45, no. 20, pp. 11 795–11 804, May 1992.
- [155] S. Fujimoto and N. Kawakami, “Persistent currents in mesoscopic Hubbard rings with spin-orbit interaction,” *Physical Review B*, vol. 48, no. 23, pp. 17 406–17 412, Dec. 1993.
- [156] R. A. Römer and A. Punnoose, “Enhanced charge and spin currents in the one-dimensional disordered mesoscopic Hubbard ring,” *Physical Review B*, vol. 52, no. 20, pp. 14 809–14 816, Nov. 1995.
- [157] P. Schmitteckert, R. A. Jalabert, D. Weinmann, and J. Pichard, “From the Fermi glass towards the Mott insulator in one dimension: Delocalization and strongly enhanced persistent currents,” *Physical Review Letters*, vol. 81, no. 11, pp. 2308–2311, 1998.
- [158] E. Gambetti-Césare, D. Weinmann, R. A. Jalabert, and P. Brune, “Disorder-induced enhancement of the persistent current for strongly interacting electrons in one-dimensional rings,” *Europhysics Letters*, vol. 60, no. 1, pp. 120–126, 2002.
- [159] A. A. Zvyagin, T. V. Bandos, and P. Schlottmann, “Persistent current oscillations in a metallic ring embedding a quantum dot,” *Czechoslovak Journal of Physics*, vol. 46, no. S4, pp. 2409–2410, Aug. 1996.
- [160] A. A. Zvyagin and P. Schlottmann, “Finite-size effects in a metallic multichannel ring with Kondo impurity: Persistent currents and magnetoresistance,” *Physical Review B*, vol. 54, no. 21, pp. 15 191–15 199, Dec. 1996.

- [161] V. Ferrari, G. Chiappe, E. V. Anda, and M. A. Davidovich, "Kondo resonance effect on persistent currents through a quantum dot in a mesoscopic ring," *Physical Review Letters*, vol. 82, no. 25, pp. 5088–5091, Jun. 1999.
- [162] H. Eckle, H. Johannesson, and C. A. Stafford, "Kondo impurity in a mesoscopic ring: Charge persistent current," *Journal of Low Temperature Physics*, vol. 118, no. 5, pp. 475–483, Mar. 2000.
- [163] K. Kang and S. Shin, "Mesoscopic Kondo effect in an Aharonov-Bohm ring," *Physical Review Letters*, vol. 85, no. 26, pp. 5619–5622, Dec. 2000.
- [164] A. A. Zvyagin, "Comment on "Mesoscopic Kondo effect in an Aharonov-Bohm ring"," *Physical Review Letters*, vol. 87, no. 17, p. 179704, Oct. 2001.
- [165] K. Kang and S. Y. Cho, "Kang and Cho reply:," *Physical Review Letters*, vol. 87, no. 17, p. 179705, Oct. 2001.
- [166] I. Affleck and P. Simon, "Detecting the Kondo screening cloud around a quantum dot," *Physical Review Letters*, vol. 86, no. 13, pp. 2854–2857, Mar. 2001.
- [167] H. Hu, G. Zhang, and L. Yu, "Mesoscopic Kondo screening effect in a single-electron transistor embedded in a metallic ring," *Physical Review Letters*, vol. 86, no. 24, pp. 5558–5561, Jun. 2001.
- [168] H. Eckle, H. Johannesson, and C. A. Stafford, "Kondo resonance in a mesoscopic ring coupled to a quantum dot: Exact results for the Aharonov-Bohm-Casher effects," *Physical Review Letters*, vol. 87, no. 1, p. 016602, Jun. 2001.
- [169] I. Affleck and P. Simon, "Comment on "Kondo resonance in a mesoscopic ring coupled to a quantum dot: Exact results for the Aharonov-Bohm-Casher effects"," *Physical Review Letters*, vol. 88, no. 13, p. 139701, Mar. 2002.
- [170] H. Eckle, H. Johannesson, and C. A. Stafford, "Eckle et al. reply:," *Physical Review Letters*, vol. 88, no. 13, p. 139702, Mar. 2002.
- [171] S. Y. Cho, K. Kang, C. K. Kim, and C. Ryu, "Spin fluctuation and persistent current in a mesoscopic ring coupled to a quantum dot," *Physical Review B*, vol. 64, no. 3, p. 033314, Jun. 2001.

- [172] E. V. Anda, C. Busser, G. Chiappe, and M. A. Davidovich, “Kondo effect and persistent currents in a mesoscopic ring: Numerically exact results,” *Physical Review B*, vol. 66, no. 3, p. 035307, Jul. 2002.
- [173] H. Luo, S. Wang, and C. Jia, “Magnetic flux effects in an Aharonov-Bohm ring with an inserted quantum dot,” *Physical Review B*, vol. 66, no. 23, p. 235311, Dec. 2002.
- [174] E. S. Sørensen and I. Affleck, “Kondo screening cloud around a quantum dot: Large-scale numerical results,” *Physical Review Letters*, vol. 94, no. 8, p. 086601, Feb. 2005.
- [175] M. Moskalets and M. Büttiker, “Hidden quantum pump effects in quantum coherent rings,” *Physical Review B*, vol. 68, no. 7, p. 075303, 2003.
- [176] —, “Quantum pumping: Coherent rings versus open conductors,” *Physical Review B*, vol. 68, no. 16, p. 161311, Oct. 2003.
- [177] H. Zhou, U. Lundin, and S. Y. Cho, “Geometric phases of scattering states in a ring geometry: Adiabatic pumping in mesoscopic devices,” *Journal of Physics: Condensed Matter*, vol. 17, no. 7, pp. 1059–1066, 2005.
- [178] N. Tong and M. Vojta, “Signatures of a noise-induced quantum phase transition in a mesoscopic metal ring,” *Physical Review Letters*, vol. 97, no. 1, p. 016802, Jul. 2006.
- [179] P. Cedraschi, V. V. Ponomarenko, and M. Büttiker, “Zero-Point fluctuations and the quenching of the persistent current in normal metal rings,” *Physical Review Letters*, vol. 84, no. 2, pp. 346–349, Jan. 2000.
- [180] P. Cedraschi and M. Büttiker, “Zero-point fluctuations in the ground state of a mesoscopic normal ring,” *Physical Review B*, vol. 63, no. 16, p. 165312, Apr. 2001.
- [181] A. Semenov and A. D. Zaikin, “Persistent current noise,” *Journal of Physics: Conference Series*, vol. 248, p. 012034, 2010.
- [182] A. Barone, T. Hakioglu, and I. O. Kulik, “Quantum computation with Aharonov-Bohm qubits,” arXiv:cond-mat/0203038, Mar. 2002.
- [183] I. O. Kulik, “Persistent currents in mesoscopic loops and networks,” *Turkish Journal of Physics*, vol. 27, no. 5, pp. 395–417, 2003.

- [184] —, “Quantum computation with persistent-current Aharonov-Bohm qubits and qugates,” *Nanotech 2003*, vol. 2, pp. 153–156, 2003.
- [185] —, “Quantum computation with Aharonov-Bohm qubits,” in *Toward the Controllable Quantum States - Proceedings of the International Symposium on Mesoscopic Superconductivity and Spintronics (MS+S2002)*, Atsugi, Kanagawa, Japan, 2003, pp. 302–307.
- [186] —, “Spontaneous and persistent currents in superconductive and mesoscopic structures (Review),” *Low Temperature Physics*, vol. 30, no. 7, pp. 528–534, 2004.
- [187] E. Zipper, M. Kurpas, M. Szelać, J. Dajka, and M. Szopa, “Flux qubit on a mesoscopic nonsuperconducting ring,” *Physical Review B*, vol. 74, no. 12, p. 125426, 2006.
- [188] M. Szopa, E. Zipper, M. Szelać, and M. Kurpas, “Coherent quantum dynamics of mesoscopic metallic ring with a barrier,” *Journal of Physics: Conference Series*, vol. 30, pp. 224–229, 2006.
- [189] M. Kurpas, J. Dajka, and E. Zipper, “Decoherence in flux qubits on mesoscopic nonsuperconducting rings,” *physica status solidi (b)*, vol. 244, no. 7, pp. 2470–2475, 2007.
- [190] G. L. Giorgi and F. de Pasquale, “Quantum oscillations of the persistent current in a normal loop,” *Physical Review B*, vol. 75, no. 6, p. 064501, Feb. 2007.
- [191] M. Kurpas, J. Dajka, and E. Zipper, “Coherent coupling of two semiconducting flux qubits,” *Journal of Physics: Conference Series*, vol. 104, p. 012004, 2008.
- [192] M. Szelać and M. Szopa, “Persistent currents in distorted quantum ring,” *Journal of Physics: Conference Series*, vol. 104, p. 012006, 2008.
- [193] M. Szopa and E. Zipper, “Flux qubits on semiconducting quantum ring,” *Journal of Physics: Conference Series*, vol. 213, p. 012006, 2010.
- [194] J. Dajka, M. Szopa, A. Vourdas, and E. Zipper, “Persistent currents in the presence of nonclassical electromagnetic fields,” *Physical Review B*, vol. 69, no. 4, p. 045305, Jan. 2004.
- [195] —, “The influence of non-classical electromagnetic fields on persistent currents,” *physica status solidi (b)*, vol. 242, no. 2, pp. 296–302, 2005.

- [196] D. I. Tsomokos, C. C. Chong, and A. Vourdas, “Electron interference in mesoscopic devices in the presence of nonclassical electromagnetic fields,” *Journal of Optics B: Quantum and Semiclassical Optics*, vol. 7, no. 6, pp. R73–R87, 2005.
- [197] I. Pakuła, “Quantum gambling using mesoscopic ring qubits,” *physica status solidi (b)*, vol. 244, no. 7, pp. 2513–2515, 2007.
- [198] M. Kurpas and E. Zipper, “Entanglement of flux qubits through a joint detection of photons,” *physica status solidi (b)*, vol. 246, no. 5, pp. 961–964, 2009.
- [199] H. Bary-Soroker, O. Entin-Wohlman, and Y. Imry, “Persistent currents of noninteracting electrons,” *Physical Review B*, vol. 82, no. 14, p. 144202, Oct. 2010.
- [200] X. Zhang and J. C. Price, “Susceptibility of a mesoscopic superconducting ring,” *Physical Review B*, vol. 55, no. 5, pp. 3128–3140, Feb. 1997.
- [201] C. H. van der Wal, A. C. J. ter Haar, F. K. Wilhelm, R. N. Schouten, C. J. P. M. Harmans, T. P. Orlando, S. Lloyd, and J. E. Mooij, “Quantum superposition of macroscopic persistent-current states,” *Science*, vol. 290, no. 5492, pp. 773–777, Oct. 2000.
- [202] V. Ambegaokar and U. Eckern, “Nonlinear diamagnetic response in mesoscopic rings of superconductors above T_c ,” *Europhysics Letters*, vol. 13, no. 8, pp. 733–738, 1990.
- [203] F. von Oppen and E. K. Riedel, “Flux-periodic persistent current in mesoscopic superconducting rings close to T_c ,” *Physical Review B*, vol. 46, no. 5, pp. 3203–3206, 1992.
- [204] G. Schwiete and Y. Oreg, “Persistent current in small superconducting rings,” *Physical Review Letters*, vol. 103, no. 3, p. 037001, Jul. 2009.
- [205] C. W. J. Beenakker, H. van Houten, and A. A. M. Staring, “Influence of Coulomb repulsion on the Aharonov-Bohm effect in a quantum dot,” *Physical Review B*, vol. 44, no. 4, pp. 1657–1662, Jul. 1991.
- [206] P. Pietiläinen and T. Chakraborty, “Interacting-electron states and the persistent current in a quantum ring,” *Solid State Communications*, vol. 87, no. 9, pp. 809–812, Sep. 1993.
- [207] S. Viefers, P. Koskinen, P. S. Deo, and M. Manninen, “Quantum rings for beginners: Energy spectra and persistent currents,” *Physica E: Low-dimensional Systems and Nanostructures*, vol. 21, no. 1, pp. 1–35, Feb. 2004.

- [208] D. Loss, “Parity effects in a Luttinger liquid: Diamagnetic and paramagnetic ground states,” *Physical Review Letters*, vol. 69, no. 2, pp. 343–347, Jul. 1992.
- [209] D. Loss and T. Martin, “Absence of spontaneous persistent current for interacting Fermions in a one-dimensional mesoscopic ring,” *Physical Review B*, vol. 47, no. 8, pp. 4619–4630, Feb. 1993.
- [210] D. Schmeltzer, “Persistent current for a Luttinger liquid,” *Physical Review B*, vol. 47, no. 12, pp. 7591–7593, Mar. 1993.
- [211] Y. Avishai, Y. Hatsugai, and M. Kohmoto, “Persistent currents and edge states in a magnetic field,” *Physical Review B*, vol. 47, no. 15, pp. 9501–9512, Apr. 1993.
- [212] D. Eliyahu, R. Berkovits, M. Abraham, and Y. Avishai, “Mesoscopic persistent-current correlations in the presence of strong magnetic fields,” *Physical Review B*, vol. 49, no. 20, pp. 14 448–14 455, May 1994.
- [213] L. S. Georgiev and M. R. Geller, “Magnetic-moment oscillations in a quantum Hall ring,” *Physical Review B*, vol. 70, no. 15, p. 155304, Oct. 2004.
- [214] A. A. Odintsov, W. Smit, and H. Yoshioka, “Persistent current and correlation effects in carbon nanotubes,” *Europhysics Letters*, vol. 45, no. 5, pp. 598–604, 1999.
- [215] S. Latil, S. Roche, and A. Rubio, “Persistent currents in carbon nanotube based rings,” *Physical Review B*, vol. 67, no. 16, p. 165420, Apr. 2003.
- [216] M. Szopa, M. Margańska, E. Zipper, and M. Lisowski, “Coherence of persistent currents in multiwall carbon nanotubes,” *Physical Review B*, vol. 70, no. 7, p. 075406, 2004.
- [217] M. Margańska, M. Szopa, and E. Zipper, “Orbital magnetic moments in pure and doped carbon nanotubes,” *Physical Review B*, vol. 72, no. 11, p. 115406, 2005.
- [218] I. I. Cotaescu and E. Papp, “Signatures of the Dirac electron in the flux dependence of total persistent currents in isolated Aharonov–Bohm rings,” *Journal of Physics: Condensed Matter*, vol. 19, no. 24, p. 242206, 2007.
- [219] S. Bellucci, A. A. Saharian, and V. M. Bardeghyan, “Induced Fermionic current in toroidally compactified spacetimes with applications to cylindrical and toroidal nanotubes,” *Physical Review D*, vol. 82, no. 6, p. 065011, 2010.

- [220] P. Michetti and P. Recher, “Bound states and persistent currents in topological insulator rings,” arXiv:1011.5166, Nov. 2010.
- [221] B. G. Levi, “Experiments remove resistance to the notion of persistent currents,” *Physics Today*, vol. 45, no. 4, pp. 17–19, 1992.
- [222] U. Eckern, “Sind dauerströme noch normal?” *Physik in unserer Zeit*, vol. 25, no. 4, pp. 152–157, 1994.
- [223] Y. Imry and U. Sivan, “Recent developments in mesoscopic physics,” *Solid State Communications*, vol. 92, no. 1-2, pp. 83–87, Oct. 1994.
- [224] G. Montambaux, “Spectral fluctuations in disordered metals,” in *Quantum Fluctuations: Les Houches, LXIII*, S. Reynaud, E. Giacobino, and J. Zinn-Justin, Eds. Elsevier, 1997, p. 387, [Available at arXiv:cond-mat/9602071v2].
- [225] Y. Noat, B. Reulet, H. Bouchiat, and D. Mailly, “Signature of phase coherence in mesoscopic systems,” *Physica A: Statistical Mechanics and its Applications*, vol. 263, no. 1-4, pp. 187–196, Feb. 1999.
- [226] H. Bouchiat, “New clues in the mystery of persistent currents,” *Physics*, vol. 1, p. 7, Jul. 2008.
- [227] N. O. Birge, “Sensing a small but persistent current,” *Science*, vol. 326, no. 5950, pp. 244–245, Oct. 2009.
- [228] M. Wilson, “Sensitive cantilevers detect the persistent currents in normal-metal rings,” *Physics Today*, vol. 62, no. 12, p. 17, 2009.
- [229] M. Büttiker and M. Moskalets, “From Anderson localization to mesoscopic physics,” *International Journal of Modern Physics B*, vol. 24, no. 12-13, pp. 1555–1576, 2010.
- [230] D. Mailly, C. Chapelier, and A. Benoît, “Persistent currents in a GaAs-AlGaAs single loop,” *Physica Scripta*, vol. T55, pp. 72–76, 1994.
- [231] A. M. Jayannavar and P. S. Deo, “Persistent currents and conductance of a metal loop connected to electron reservoirs,” *Physical Review B*, vol. 49, no. 19, pp. 13 685–13 690, May 1994.

- [232] —, “Persistent currents in the presence of a transport current,” *Physical Review B*, vol. 51, no. 15, pp. 10 175–10 178, Apr. 1995.
- [233] T. P. Pareek, P. S. Deo, and A. M. Jayannavar, “Effect of impurities on the current magnification in mesoscopic open rings,” *Physical Review B*, vol. 52, no. 20, pp. 14 657–14 663, Nov. 1995.
- [234] H. Bluhm, “Magnetic response measurements of mesoscopic superconducting and normal metal rings,” Ph.D. dissertation, Stanford University, Palo Alto, CA, 2008.
- [235] P. Peregrinus, *The Letter of Petrus Peregrins on the Magnet, A. D. 1269*, 1st ed. New York, NY: McGraw-Hill Book Co., 1904.
- [236] D. Gubbins and E. Herrero-Bervera, *Encyclopedia of Geomagnetism and Paleomagnetism*. Springer, 2007.
- [237] P. Gauss, “Intensitas vis magneticae terrestris ad mensuram absolutam revocata. [Abstract],” *Abstracts of the Papers Printed in the Philosophical Transactions of the Royal Society of London*, vol. 3, pp. 166–174, 1830.
- [238] P. K. Hoch, “A key concept from the electron theory of metals: history of the Fermi surface 1933–60,” *Contemporary Physics*, vol. 24, no. 1, pp. 3–23, 1983.
- [239] W. J. de Haas and P. M. van Alphen, “Oscillations in the magnetization of bismuth,” *Leiden Commun.*, vol. 208d, p. 212a, 1930.
- [240] D. Shoenberg and M. Z. Uddin, “The magnetic properties of bismuth. I. Dependence of susceptibility on temperature and addition of other elements,” *Proceedings of the Royal Society of London. Series A, Mathematical and Physical Sciences (1934-1990)*, vol. 156, no. 889, pp. 687–701, 1936.
- [241] —, “The magnetic properties of bismuth. II. the de Haas-van Alphen effect,” *Proceedings of the Royal Society of London. Series A, Mathematical and Physical Sciences (1934-1990)*, vol. 156, no. 889, pp. 701–720, 1936.
- [242] D. Shoenberg, “The magnetic properties of bismuth. III. Further measurements on the de Haas-van Alphen effect,” *Proceedings of the Royal Society of London. Series A, Mathematical and Physical Sciences (1934-1990)*, vol. 170, no. 942, pp. 341–364, 1939.

- [243] —, “The Rutherford Memorial Lecture, 1980: Magnetic oscillations in metals,” *Proceedings of the Royal Society of London. A. Mathematical and Physical Sciences*, vol. 379, no. 1776, pp. 1–14, Jan. 1982.
- [244] R. G. Wheeler, “The early history of cryogenic research at Yale,” Dunham Lab, Yale University, New Haven, CT, Mar. 2006.
- [245] J. A. Marcus, “The de Haas-van Alphen effect in a single crystal of zinc,” *Physical Review*, vol. 71, no. 8, p. 559, Apr. 1947.
- [246] —, “Magnetic susceptibility of zinc at liquid hydrogen temperatures,” *Physical Review*, vol. 76, no. 3, pp. 413–416, 1949.
- [247] S. G. Sydoriak and J. E. Robinson, “Magnetic susceptibility of zinc at liquid helium temperatures,” *Physical Review*, vol. 75, no. 1, pp. 118–131, Jan. 1949.
- [248] T. G. Berlincourt, “The de Haas-van Alphen effect in enriched tin isotopes,” *Physical Review*, vol. 88, no. 2, pp. 242–248, Oct. 1952.
- [249] J. H. E. Griffiths and J. R. MacDonald, “An oscillation type magnetometer,” *Journal of Scientific Instruments*, vol. 28, no. 2, pp. 56–58, 1951.
- [250] U. Gradmann, W. Kummerle, and R. Tham, “High sensitivity torsion magnetometers for oligatomic films,” *Applied Physics A: Materials Science & Processing*, vol. 10, no. 3, pp. 219–225, Jul. 1976.
- [251] M. R. Schaapman, P. C. M. Christianen, J. C. Maan, D. Reuter, and A. D. Wieck, “A multipurpose torsional magnetometer with optical detection,” *Applied Physics Letters*, vol. 81, no. 6, pp. 1041–1043, 2002.
- [252] K. Petersen, “Silicon as a mechanical material,” *Proceedings of the IEEE*, vol. 70, no. 5, pp. 420–457, 1982.
- [253] R. N. Kleiman, G. K. Kaminsky, J. D. Reppy, R. Pindak, and D. J. Bishop, “Single-crystal silicon high-Q torsional oscillators,” *Review of Scientific Instruments*, vol. 56, no. 11, pp. 2088–2091, 1985.
- [254] G. Binnig, C. F. Quate, and C. Gerber, “Atomic force microscope,” *Physical Review Letters*, vol. 56, no. 9, pp. 930–933, Mar. 1986.

- [255] Y. Martin and H. K. Wickramasinghe, “Magnetic imaging by “force microscopy” with 1000 Å resolution,” *Applied Physics Letters*, vol. 50, no. 20, pp. 1455–1457, 1987.
- [256] J. J. Sáenz, N. García, P. Grütter, E. Meyer, H. Heinzelmann, R. Wiesendanger, L. Rosenthaler, H. R. Hidber, and H. Güntherodt, “Observation of magnetic forces by the atomic force microscope,” *Journal of Applied Physics*, vol. 62, no. 10, pp. 4293–4295, 1987.
- [257] P. L. Gammel, L. F. Schneemeyer, J. V. Wasczak, and D. J. Bishop, “Evidence from mechanical measurements for Flux-Lattice melting in single-crystal $\text{YBa}_2\text{Cu}_3\text{O}_7$ and $\text{Bi}_{2.2}\text{Sr}_2\text{Ca}_{0.8}\text{Cu}_2\text{O}_8$,” *Physical Review Letters*, vol. 61, no. 14, pp. 1666–1669, Oct. 1988.
- [258] D. Rugar, C. S. Yannoni, and J. A. Sidles, “Mechanical detection of magnetic resonance,” *Nature*, vol. 360, no. 6404, pp. 563–566, Dec. 1992.
- [259] D. Rugar, R. Budakian, H. J. Mamin, and B. W. Chui, “Single spin detection by magnetic resonance force microscopy,” *Nature*, vol. 430, no. 6997, pp. 329–332, Jul. 2004.
- [260] C. L. Degen, M. Poggio, H. J. Mamin, C. T. Rettner, and D. Rugar, “Nanoscale magnetic resonance imaging,” *Proceedings of the National Academy of Sciences*, vol. 106, no. 5, pp. 1313–1317, Feb. 2009.
- [261] J. G. E. Harris, D. D. Awschalom, F. Matsukura, H. Ohno, K. D. Maranowski, and A. C. Gossard, “Integrated micromechanical cantilever magnetometry of $\text{Ga}_{1-x}\text{Mn}_x\text{As}$,” *Applied Physics Letters*, vol. 75, no. 8, pp. 1140–1142, 1999.
- [262] J. G. E. Harris, R. Knobel, K. D. Maranowski, A. C. Gossard, N. Samarth, and D. D. Awschalom, “Magnetization measurements of magnetic two-dimensional electron gases,” *Physical Review Letters*, vol. 86, no. 20, pp. 4644–4647, May 2001.
- [263] A. N. Cleland, *Foundations of Nanomechanics: From Solid-State Theory to Device Applications*. Berlin: Springer-Verlag, 2003.
- [264] K. Yasumura, T. Stowe, E. Chow, T. Pfafman, T. Kenny, B. Stipe, and D. Rugar, “Quality factors in micron- and submicron-thick cantilevers,” *Microelectromechanical Systems, Journal of*, vol. 9, no. 1, pp. 117–125, 2000.
- [265] E. M. Purcell, *Electricity and Magnetism*, 2nd ed. Boston, MA: McGraw-Hill, 1985.

- [266] J. A. Sidles, J. L. Garbini, K. J. Bruland, D. Rugar, O. Züger, S. Hoen, and C. S. Yannoni, “Magnetic resonance force microscopy,” *Reviews of Modern Physics*, vol. 67, no. 1, pp. 249–265, Jan. 1995.
- [267] A. C. Bleszynski-Jayich, W. E. Shanks, B. R. Ilic, and J. G. E. Harris, “High sensitivity cantilevers for measuring persistent currents in normal metal rings,” *Journal of Vacuum Science & Technology B: Microelectronics and Nanometer Structures*, vol. 26, no. 4, pp. 1412–1416, Jul. 2008.
- [268] H. Goldstein, C. P. Poole, and J. L. Safko, *Classical Mechanics*, 3rd ed. Addison Wesley, Jun. 2001.
- [269] D. Rugar and P. Grütter, “Mechanical parametric amplification and thermomechanical noise squeezing,” *Physical Review Letters*, vol. 67, no. 6, pp. 699–702, 1991.
- [270] T. R. Albrecht, P. Grütter, D. Horne, and D. Rugar, “Frequency modulation detection using high-Q cantilevers for enhanced force microscope sensitivity,” *Journal of Applied Physics*, vol. 69, no. 2, pp. 668–673, 1991.
- [271] T. Albrecht, P. Grütter, D. Rugar, and D. Smith, “Low-temperature force microscope with all-fiber interferometer,” *Ultramicroscopy*, vol. 42-44, no. Part 2, pp. 1638–1646, Jul. 1992.
- [272] A. Arimoto, M. Ojima, N. Chinone, A. Oishi, T. Gotoh, and N. Ohnuki, “Optimum conditions for the high frequency noise reduction method in optical videodisc players,” *Applied Optics*, vol. 25, no. 9, pp. 1398–1403, May 1986.
- [273] M. Ojima, A. Arimoto, N. Chinone, T. Gotoh, and K. Aiki, “Diode laser noise at video frequencies in optical videodisc players,” *Applied Optics*, vol. 25, no. 9, pp. 1404–1410, May 1986.
- [274] T. Fukuma, M. Kimura, K. Kobayashi, K. Matsushige, and H. Yamada, “Development of low noise cantilever deflection sensor for multienvironment frequency-modulation atomic force microscopy,” *Review of Scientific Instruments*, vol. 76, no. 5, p. 053704, 2005.
- [275] P. Santhanam, “Localization and superconductivity in thin films and narrow wires of aluminum,” Dissertation, Yale University, New Haven, CT, 1985.

- [276] M. Rooks, “Electron beam lithography of quantum interference devices for electron transport studies,” Dissertation, Yale University, New Haven, CT, 1987.
- [277] S. Wind, “Electron quantum interference and transport in ultrasmall metal structures,” Dissertation, Yale University, New Haven, CT, 1987.
- [278] V. Chandrasekhar, “Electron interference in small metal wires and loops,” Dissertation, Yale University, New Haven, CT, 1989.
- [279] J. D. Jackson, *Classical Electrodynamics*, 3rd ed. New York, NY: Wiley, Aug. 1998.
- [280] H. R. Philipp and E. A. Taft, “Optical constants of silicon in the region 1 to 10 eV,” *Physical Review*, vol. 120, no. 1, pp. 37–38, Oct. 1960.
- [281] E. Hecht, *Optics*, 2nd ed. Reading, MA: Addison-Wesley, May 1987.
- [282] R. K. Pathria, *Statistical Mechanics*, 2nd ed. Boston, MA: Butterworth-Heinemann, Aug. 1996.
- [283] W. A. Edelstein, J. Hough, J. R. Pugh, and W. Martin, “Limits to the measurement of displacement in an interferometric gravitational radiation detector,” *Journal of Physics E: Scientific Instruments*, vol. 11, no. 7, pp. 710–712, 1978.
- [284] M. Devoret, “Noise, amplification, and dissipation: Shot noise,” Class lecture, Yale University, New Haven, CT, Dec. 2006.
- [285] “Relative intensity noise, phase noise, and linewidth,” Application Note, JDS Uniphase, Milpitas, CA, 2006.
- [286] B. Yurke, D. S. Greywall, A. N. Pargellis, and P. A. Busch, “Theory of amplifier-noise evasion in an oscillator employing a nonlinear resonator,” *Physical Review A*, vol. 51, no. 5, pp. 4211–4229, May 1995.
- [287] A. Hajimiri and T. Lee, “A general theory of phase noise in electrical oscillators,” *Solid-State Circuits, IEEE Journal of*, vol. 33, no. 2, pp. 179–194, Feb. 1998.
- [288] M. D. Chabot and J. T. Markert, “Microfabrication of single-crystal silicon multiple torsional oscillators,” in *Materials and Device Characterization in Micromachining II*, Y. Vladimirovsky and C. R. Friedrich, Eds., vol. 3875. Santa Clara, CA, USA: SPIE, 1999, pp. 104–112.

- [289] N. Lobontiu, B. Ilic, E. Garcia, T. Reissman, and H. G. Craighead, “Modeling of nanofabricated paddle bridges for resonant mass sensing,” *Review of Scientific Instruments*, vol. 77, no. 7, p. 073301, 2006.
- [290] L. Haiberger, M. Weingran, and S. Schiller, “Highly sensitive silicon crystal torque sensor operating at the thermal noise limit,” *Review of Scientific Instruments*, vol. 78, no. 2, p. 025101, 2007.
- [291] K. R. Thurber, L. E. Harrell, and D. D. Smith, “Temperature measurement at the end of a cantilever using oxygen paramagnetism in solid air,” *Journal of Applied Physics*, vol. 93, no. 7, pp. 4297–4299, 2003.
- [292] M. P. Schwarz, M. A. Wilde, S. Groth, D. Grundler, C. Heyn, and D. Heitmann, “Sawtoothlike de Haas-van Alphen oscillations of a two-dimensional electron system,” *Physical Review B*, vol. 65, no. 24, p. 245315, Jun. 2002.
- [293] J. G. E. Harris, R. Knobel, K. D. Maranowski, A. C. Gossard, N. Samarth, and D. D. Awschalom, “Damping of micromechanical structures by paramagnetic relaxation,” *Applied Physics Letters*, vol. 82, no. 20, pp. 3532–3534, 2003.
- [294] H. J. Mamin, M. Poggio, C. L. Degen, and D. Rugar, “Nuclear magnetic resonance imaging with 90-nm resolution,” *Nat Nano*, vol. 2, no. 5, pp. 301–306, May 2007.
- [295] M. D. LaHaye, O. Buu, B. Camarota, and K. C. Schwab, “Approaching the quantum limit of a nanomechanical resonator,” *Science*, vol. 304, no. 5667, pp. 74–77, Apr. 2004.
- [296] H. J. Mamin and D. Rugar, “Sub-atto-newton force detection at millikelvin temperatures,” *Applied Physics Letters*, vol. 79, no. 20, pp. 3358–3360, 2001.
- [297] A. C. Bleszynski-Jayich, W. E. Shanks, and J. G. E. Harris, “Noise thermometry and electron thermometry of a sample-on-cantilever system below 1 kelvin,” *Applied Physics Letters*, vol. 92, no. 1, p. 013123, 2008.
- [298] M. Asheghi, K. Kurabayashi, R. Kasnavi, and K. E. Goodson, “Thermal conduction in doped single-crystal silicon films,” *Journal of Applied Physics*, vol. 91, no. 8, pp. 5079–5088, Jan. 2002.

- [299] P. E. Schmid, “Optical absorption in heavily doped silicon,” *Physical Review B*, vol. 23, no. 10, pp. 5531–5536, May 1981.
- [300] M. Tinkham, *Introduction to Superconductivity*, 2nd ed. Mineola, NY: Dover Publications, Inc., Jun. 2004.
- [301] E. C. Stoner and E. P. Wohlfarth, “A mechanism of magnetic hysteresis in heterogeneous alloys,” *Philosophical Transactions of the Royal Society of London. Series A, Mathematical and Physical Sciences*, vol. 240, no. 826, pp. 599–642, May 1948.
- [302] J. Bardeen, L. N. Cooper, and J. R. Schrieffer, “Theory of superconductivity,” *Physical Review*, vol. 108, no. 5, pp. 1175–1204, Dec. 1957.
- [303] T. E. Faber, “The phase transition in superconductors. IV. Aluminium,” *Proceedings of the Royal Society of London. Series A. Mathematical and Physical Sciences*, vol. 231, no. 1186, pp. 353–367, 1955.
- [304] M. Devoret, (private communication).
- [305] “Resistivity & mobility calculator/graph for various doping concentrations in silicon,” Aug. 2010, <http://cleanroom.byu.edu/ResistivityCal.phtml>.
- [306] D. Fortier and K. Suzuki, “Effect of p donors on thermal phonon scattering in Si,” *Journal de Physique*, vol. 37, no. 2, pp. 143–147, 1976.
- [307] O. Tsypliyatyev, I. L. Aleiner, V. I. Fal’ko, and I. V. Lerner, “Applicability of the ergodicity hypothesis to mesoscopic fluctuations,” *Physical Review B*, vol. 68, no. 12, p. 121301, 2003.
- [308] M. Kendall, *Advanced Theory of Statistics*, 3rd ed. London, England, UK: Charles Griffin & Co. Ltd., 1947, vol. 1.
- [309] I. P. Castro, *An Introduction to the Digital Analysis of Stationary Signals*. Bristol, England, UK: CRC Press, 1989.
- [310] R. Shankar, *Principles of Quantum Mechanics*. New York, NY: Plenum Press, 1994.
- [311] F. Pierre, A. B. Gougam, A. Anthore, H. Pothier, D. Esteve, and N. O. Birge, “Dephasing of electrons in mesoscopic metal wires,” *Physical Review B*, vol. 68, no. 8, p. 085413, 2003.

- [312] U. Eckern and P. Schwab, “Persistent currents versus phase breaking in mesoscopic metallic samples,” *Journal of Low Temperature Physics*, vol. 126, no. 3, pp. 1291–1304, Feb. 2002.
- [313] P. Lafarge, P. Joyez, D. Esteve, C. Urbina, and M. H. Devoret, “Two-electron quantization of the charge on a superconductor,” *Nature*, vol. 365, no. 6445, pp. 422–424, 1993.
- [314] P. Santhanam, S. Wind, and D. E. Prober, “Localization, superconducting fluctuations, and superconductivity in thin films and narrow wires of aluminum,” *Physical Review B*, vol. 35, no. 7, pp. 3188–3206, Mar. 1987.
- [315] J. M. Gordon and J. B. Hansen, “Superconducting-fluctuation conductivity of one-dimensional wires in a magnetic field,” *Physical Review B*, vol. 32, no. 9, pp. 6039–6041, Nov. 1985.
- [316] J. M. Gordon and A. M. Goldman, “Electron inelastic scattering in aluminum films and wires at temperatures near the superconducting transition,” *Physical Review B*, vol. 34, no. 3, pp. 1500–1507, 1986.
- [317] W. E. Lawrence and A. B. Meador, “Calculation of the order-parameter relaxation times in superconducting aluminum,” *Physical Review B*, vol. 18, no. 3, pp. 1154–1161, 1978.
- [318] S. Wind, M. J. Rooks, V. Chandrasekhar, and D. E. Prober, “One-dimensional electron-electron scattering with small energy transfers,” *Physical Review Letters*, vol. 57, no. 5, pp. 633–636, 1986.
- [319] B. L. Altshuler and A. Aronov, “Electron-electron interactions in disordered conductors,” in *Electron-Electron Interactions in Disordered Systems*, A. L. Efros and M. Pollak, Eds. New York, NY: Elsevier, 1985, pp. 1–153.
- [320] I. L. Aleiner, B. L. Altshuler, and M. E. Gershenson, “Waves in random media,” *Waves in Random Complex Media*, vol. 9, no. 2, pp. 201–240, 1999.
- [321] N. E. Huang, Z. Shen, S. R. Long, M. C. Wu, H. H. Shih, Q. Zheng, N. Yen, C. C. Tung, and H. H. Liu, “The empirical mode decomposition and the Hilbert spectrum for nonlinear and non-stationary time series analysis,” *Proceedings of the Royal Society of London. Series A: Mathematical, Physical and Engineering Sciences*, vol. 454, no. 1971, pp. 903–995, Mar. 1998.